Power Plant Burners for Bio-Dust Combustion

Johansen, Joakim Myung

Publication date:
2015

Document Version
Publisher's PDF, also known as Version of record

Technical University of Denmark

Power Plant Burners for Bio-Dust Combustion

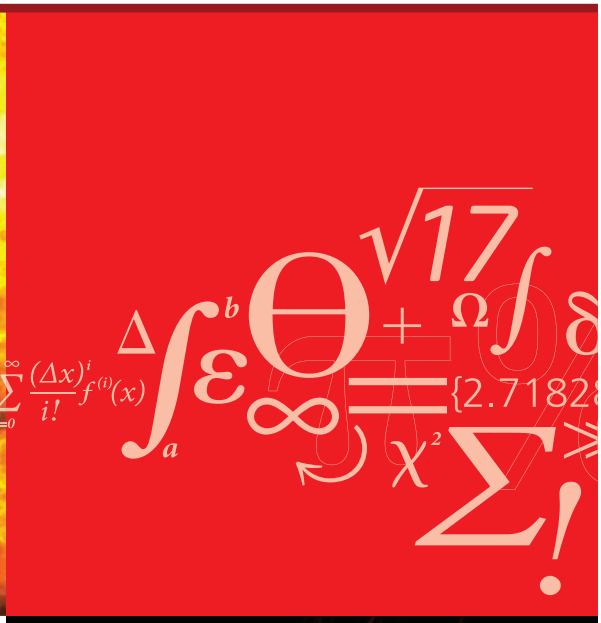

PhD Thesis
Doctor of Philosophy

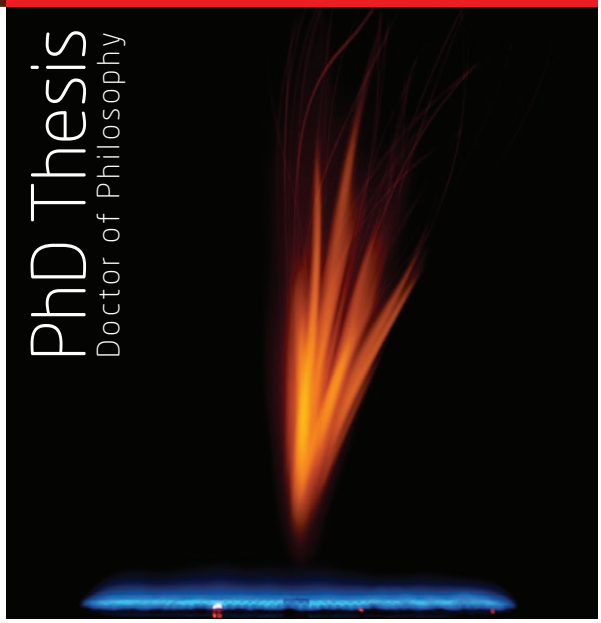

Joakim M. Johansen

2015

DTU Chemical Engineering
Department of Chemical and Biochemical Engineering

{2.7182818284}ϑφερτυθιοπσδφγηξκλ

PhD Thesis

Power Plant Burners for Bio-Dust Combustion

2015

Joakim M. Johansen

Technical University of Denmark
Department of Chemical and Biochemical Engineering

In cooperation with

Stanford University
Department of Mechanical Engineering

Clausthal University of Technology
Faculty of Energy and Management Science

Joakim@jmjohansen.com

DTU Chemical Engineering
Combustion and Harmful Emission Control Research Centre
Department of Chemical and Biochemical Engineering
Technical University of Denmark

Søltofts Plads
Building 229
2800 Kongens Lyngby, Denmark
Phone +45 4525 2800
kt@kt.dtu.dk
www.kt.dtu.dk

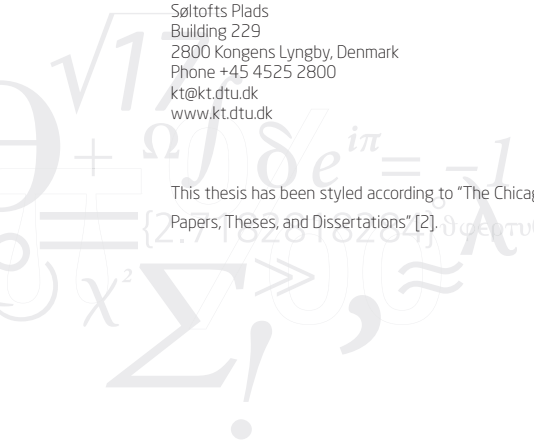

This thesis has been styled according to "The Chicago Manual of Style" [1] and "A Manual for Writers of Research Papers, Theses, and Dissertations" [2].

Abstract

The present study contributes to the establishment of a scientific basis for the development of the next generation of biomass burners. It combines experimental and modeling work in lab-, pilot-, and full-scale and seeks to both define and fulfil the current needs for developing better predictive tools that can be used to advance the burner technology.

The devolatilization kinetics of biomass particles were evaluated at operational conditions relevant to suspension fired pulverized fuel (PF) combustion: Particle heating rates on the order of 10^4–$10^5\,\mathrm{K \cdot s^{-1}}$ and gas phase peak temperatures of 1405–1667 K were obtained in a laminar entrained flow reactor (LFR) heated by an under-stoichiometric CH_4/H_2 pilot flame. Pine wood, miscanthus, KCl doped (1.5 wt. %) pine wood, and leached miscanthus were fed to the reactor in two particle size fractions (63–90 μm and 106–125 μm) and extracted during devolatilization at residence times between 4 and 200 ms. Particle temperature and residence time histories were derived from computational fluid dynamics (CFD) simulations coupled to the experimental results through an iterative update of the devolatilization kinetics. The results indicated that the devolatilization could be described by a single first order reaction (SFOR) mechanism and an Arrhenius type rate expression but with noticeably faster kinetics than previously reported in the literature. The faster kinetics were attributed to the improved characterization in the particle property history. The kinetic investigation was accompanied by a morphology study showing comprehensive transformation of the solid phase as heat-up and devolatilization progressed. The solid phase underwent a melting phase, changing the geometrical appearance from a needle shaped parent fuel to near spherical char particles. The transformation appeared to progress faster for high ash content fuels and did not occur to significant degree until after completion of the devolatilization for low ash wood pine.

A one dimensional heat transport model coupled with a simultaneous drying and devolatilization model was developed and validated against experimental data for particles between 63 μm and 10.9 mm. The model was based on the SFOR mechanism but required separate kinetics for high and low temperature devolatilization in order to cover the relevant intervals of heating rates and particle temperatures. The effective heating rate experienced by the particle is to extent defined by the initial heat capacity of the particle and thus the thermal histories for a typical biodust particle size distribution (PSD) entering a full-scale burner span wide in heating rates and temperatures. The model was used to evaluate the inherent error when using an isothermal assumption in biodust combustion. A preliminary Biot-number analysis showed how biodust particles are never to be assumed isothermal under conditions relevant to PF combustion. Comparison of the 1D model to a corresponding isothermal model established how the isothermal approach overestimated the required devolatilization time for small particles (89 μm) by 10–20 %, depending on the reaction conditions. Contrary, the isothermal model would significantly underestimate the required time for complete

devolatilization of particles larger than a few hundred microns. The predicted total devolatilization time for a 490 μm particle using the isothermal approach was found to be 20–30 % shorter than the corresponding 1D model predictions, depending on the reaction conditions. While the deviations exceeded 50 % for a 1.6 mm particle.

An engineering fix to the heat transport limited devolatilization process has been developed, allowing for direct implementation into the commercial CFD code ANSYS®FLUENT®(v.13.5–15.07). The method is based on discrete particle size intervals, each with their own specific set of apparent devolatilization kinetics based on the simulation results of the stand-alone single particle devolatilization model. The implementation into FLUENT®can be achieved by the inherent discrete phase functions and adds no additional strain to the computational requirements.

A model fuel was derived based on the devolatilization study, case study results from full-scale campaigns, and literature surveys. It includes recommended devolatilization kinetics, PSDs, physical and chemical properties, and characterization of the evolving gases. The formulation of the fuel properties makes it readily implementable to ANSYS® FLUENT®.

Full-scale measurements were carried out at Amager power station (AMV) and Herning power station (HEV). With focus on the near burner field, intrusive probe measurements of the gas phase temperature and species concentrations as well as optical observations in both the infrared (IR) and visible spectrum (VIS) were used to characterize flame responses to changes in the operating conditions. A method for fast flame mapping was developed and allowed for the characterization of multiple flames. The burners at AMV and HEV, although similar in thermal output and construction, produced fundamentally different flames. A high mass flow of the particle laden primary air (PA) penetrated the internal recirculation zone (IRZ) produced by the swirling combustion air at AMV. IR imaging of the flame showed cold particles penetrating more than a quarl diameter into the flame with only little radial dispersion. Flame instabilities were easily provoked by changes to the operational conditions, destabilizing the IRZ.

The HEV burner was operated at lower PA flows. The air was primarily introduced as pre-heated through the tertiary air (TA) register at high velocity. This created an IRZ strong enough to deflect the particle laden PA flow and divert the particles into the shear layer between the PA and the combustion air. Flame instabilities were much harder to provoke but could be induced by destabilizing the IRZ by decreasing the swirl number.

The full-scale campaigns provide fundamental understanding of flame response behavior to a range of changes to the operational conditions. They provide quantitative validation material for CFD simulations of the specific burners. The flames represent textbook flame types and thus the parametric study can be used on a qualitative basis to evaluate versatility of numerical studies on similar burners, providing much needed full-scale data to the literature.

Resumé (Danish)

Denne afhandling bidrager til opbygningen af et videnskabeligt grundlag for udviklingen af næste generation af biomassebrændere. Afhandlingen kombinerer eksperimential og modelleringsarbejde i laboratorie-, pilot- og fuldskala. Den har til formål at definere og opfylde de aktuelle behov, der eksisterer med henblik på at udvikle nye og forbedre eksisterende værktøjer til at sikre fremgang i brænderteknologi.

Frigivelsen af flygtige bestandele fra biomassepartikler blev evalueret under betingelser relevante for suspensionsfyret forbrænding af pulveriseret brændsel: Partikelopvarmningshastigheder i størrelsesordenen 10^4–$10^5\,\mathrm{K}\cdot\mathrm{s}^{-1}$ og gas temperaturer på 1405–1667 K blev opnået i en laminar entrained flow reaktor (LFR) opvarmet ved en understøkiometrisk CH_4/H_2 pilot flamme. Fire brændsler: Fyr, elefantgræs, KCl-dopet fyr og udvasket elefantgræs blev tilført reaktoren i to partikelstørrelsesfraktioner (63–90 μm og 106–125 μm). Prøveudtagning blev foretaget af de delvist afgassede brændsler ved opholdstider mellem 4 og 200 ms. Partikeltemperatur- og partikelopholdstidshistoriker blev beregnet ved hjælp af numerisk fluid mekaniksimuleringer (CFD) koblet til de eksperimentelle resultater ved iterativt at opdatere den anvendte afgasningskinetik. Resultaterne indikerede, at frigivelsen af flygtige bestandele kunne beskrives ved hjælp af en enkelt første ordens reaktion (SFOR) og et Arrhenius-type hastighedsudtryk. Den afledte kinetik blev fundet væsentligt hurtigere, end hvad der tidligere er blevet rapporteret i litteraturen, hvilket må tilskrives den forbedrede karakterisering af partikelhistorik. Udviklingen i partikelmorfologi blev undersøgt sideløbende med afgasningskinetikken. Analyserne viste, hvordan fastfasen undergik en smeltefase, der blandt andet ændrede partiklens geometriske udseende fra et nåleformet udgangspunkt til en nær sfærisk kokspartikel. Omdannelsen syntes at foregå tidligere for brændsler med højt askeindhold, dvs. allerede under delvis afgasning. Brændsler med lavt askeindhold undergik ikke nogen nævneværdig omdannelse, før afgasningen var tilendebragt.

En endimensionel varmetransportmodel kombineret med en tørring- og en afgasningsmodel blev udviklet og valideret mod eksperimentelle data for partikler mellem 63 μm and 10.9 mm. Modellen er basert på en SFOR-meknaisme, men et behov for særskilte kinetikudtryk for høj og lav temperatur blev fundet nødvendigt, med henblik på at kunne dække de relevante intervaller af opvarmningshastigheder og partikeltemperaturer. Den effektive opvarmningshastighed, den enkelte partikel oplever, er i vidt omfang defineret af den oprindelige varmekapacitet af partiklen. Dermed spænder de termiske historikker bredt i både opvarmningshastighed og endelig partikeltemperatur for en typisk partikelstørrelsesfordeling (PSD) af biostøv, der bruges i suspensionsfyrede kraftværker. Den endimensionelle afgasningsmodel blev anvendt til at vurdere den fejl, der indføres ved brug af en antagelse om isoterme partikler. En indledende Biot-tal analyse viste, at en antagelse om isoterme partikler aldrig vil kunne retfærdiggøres for biostøvpartikler under betingelser relevante for suspensionsfyring. Sammenligning af

den endimensionelle model med den tilsvarende isoterme model viste, hvordan de beregnede reaktionstider for fuld afgasning af små partikler, 89 μm, blev overestimeret med 10–20 % af den isoterme model. Omvendt underestimerede den isoterme model afgasningstiden væsenligt for partikler større end et par hundrede mikrometer. Reaktionstiden for fuldstændig omsætning af en 490 μm partikel blev beregnet til at være 20–30 % kortere ved at antage isoterme partikler. Afvigelser på over 50 % blev beregnet for en partikel på 1.6 mm i diameter.

En metode der kan kompensere for den varmetransportbegrænsede afgasning og som samtidig er direkte implementerbar i den kommercielle CFD-kode ANSYS®FLUENT®(v.13.5–15.07) er blevet udviklet. Metoden er baseret på diskrete partikelstørrelsesintervaller, der hver især tildeles en specifik afgasningskinetik, der korrigerer for den beregnede varmetransport for den enkelte partikelstørrelse. Den korrigerede kinetik er beregnet ud fra den endimensionelle afgasningsmodel. Metoden kan implementeres i FLUENT®ved brug af de indbyggede funktioner og medfører ingen yderligere beregningsmæssig belastning.

Et modelbrændsel er blevet konstrueret ud fra afgasningsstudiet, typiske eksempler fra fuldskalakampagnerne og litteratursøgninger. Modelbrændslet inkluderer information om afgasningskinetik, partikelstørrelsesdistributioner, fysiske og kemiske egenskaber samt karakterisering af de flygtige bestandele. Formuleringen af modelbrænselsegenskaberne gør dem direkte implementerbare i ANSYS®FLUENT®.

Der er blevet udført fuldskalamålinger på Amagerværket (AMV) og Herningværket (HEV) med fokus på nærbrænderområdet. Ved hjælp af probemålinger af gassammensætning og gasfasetemperatur samt optiske observationer i både infrarødt (IR) og visuelt spektrum (VIS) er flammerne og deres respons til ændringer i driftsbetingelserne blevet karakteriseret. En metode til hurtig kortlægning af flammeegenskaber blev udviklet og muliggjorde karakterisering af flere flammer og driftsindstillinger. Brænderne på AMV og HEV, der trods flere ligheder (termisk effekt og opbygning), producerede fundamentalt forskellige flammer. Et højt masseflow af den partikellastede primærluft (PA) medførte en fuldt penetreret indre recirculationszone (IRZ) stabiliseret af den tangentielt hvirvlende forbrændingsluft. IR billeder af flammen viser, hvordan kolde partikler penetrerer mere end en quarl diameter ind i flammen med kun lille radiel spredning. Flammeinstabilitet kunne let fremprovokeres ved destabilisering af IRZen via ændringer i driftsindstillingerne.

HEV brænderen blev opereret med et lavere PA-masseflow og luften blev primært tilført ved høj hastighed som tertiær luft (TA). Dette stabiliserede en IRZ kraftig nok til at afbøje den partikellastede PA-luft og ledte partiklerne ind i grænselaget mellem PA og forbrændingsluft. Flammen fremstod væsenligt mere stabil, men instabilitet kunne fremprovokeres ved at sænke swirl-tallet og dermed svække IRZen.

Fuldskalakampagnerne giver en grundlæggende forståelse af flammerepsons til en række ændringer i driftindstillingerne. De udgør et kvantitativt valideringsmateriale for CFD-simuleringer af de specifikke brændere. Flammerne repræsenterer typemodeller af flammer, og parameterstudiet udgør derfor et ideelt udgangspunkt for at evaluere alsidigheden af numeriske beregninger af lignende brændere.

Preface and Acknowledgements

This thesis is written in partial fulfilment of the doctors degree in philosophy (PhD) at the Technical University of Denmark. The study was carried out in the period of September 2011 to March 2015 at the Technical University of Denmark (DTU), Department of Chemical and Biochemical Engineering in the Combustion and Harmful Emission Control research centre as well as at Stanford University, Department of Mechanical Engineering in the High-Temperature Gasdynamics Laboratory, and Clausthal University of Technology (TUC), Faculty of Energy and Management Science at the Institute of Energy Processes Engineering and Fuel Technology. The work has been carried out as part of the power Generation from REnewable ENergy (GREEN) research centre funded by Innovation Fund Denmark (formerly the Danish Council for Strategic Research).

I would like to thank my academic advisers Professor Peter Glarborg, lic.techn. and Associate Professor Peter A. Jensen from DTU for their dedication to the field and to my project. With a unique combination of expertise and competences, qualified guidance was always at present.

A sincere thanks to Professor Reginald Mitchell, ScD for many inspiring discussions and for hosting me in his laboratories at Stanford University and to his students, especially Mr. Matthew Tilghmann and Mr. Eli Goldstein, PhD-candidates for helping me to settle down 5000 miles from home.

Many thanks for a fruitful collaboration to Professor Roman Weber, PhD. and Senior Scientist Marco Mancini, PhD from TUC. Your guidance and help in getting me up to speed in CFD simulations has been indispensable to me and to my project. Also Mr. An Marcell Beckmann, Stefan Brinker and Yunus Poyraz are gratefully acknowledged for their help in operating the pilot-scale facilities at Clausthal University of Technology.

A great deal of work and effort has gone into planning, executing and post processing the three full-scale campaigns at Amager and Herning power plants. A task that would not have been possible without the insight, dedication and willingness of the GREEN WP3 participants. Especially I would like to thank Senior Scientist Sønnik Clausen, PhD, Senior Scientist Alexander Fateev, PhD and Technician Karsten L. Nielsen from DTU for developing the tools and equipment and carrying out the experimental campaigns in a most professional order. Likewise, has the cooperation with our industrial partners been very fruitful and thus I would like to thank both DONG Energy Power, Vattenfall and HOFOR for letting us carry out an academic study

on their power plants. This appreciation goes both to the GREEN project members, Søren L. Hvid (now Rambøll), PhD, Jimmy Andersen, PhD, Ole M. Madsen, PhD from DONG, Maria Tonell, MSc (now HOFOR) and Mogens Berg, PhD (now COWI) from Vattenfall and Johan Wadenbäck, PhD (formerly Vattenfall) from HOFOR but also to the people at the power plants for excellent service and cooperation during the campaigns — I am sorry for the long working hours.

I am grateful to the industrial CFD brain trust: Lisbeth Myllerup, PhD from Burmeister and Wain Energy, Jan Eriksson, PhD from Vattenfall and Søren L. Hvid, PhD from Rambøll (formerly DONG) for their help, interest in my project and eagerness to share knowledge and ideas. Your help and experience in the power industry and in numerical modeling have been a great help in bridging academic research and industrial application — I am continuing my work with CFD and I have your numbers...

During my study I have been visiting many different locations across the world. A lot of people have contributed to an inspiring and pleasant work environment. But especially my colleagues at CHEC (Combustion and Harmful Emission Control) at DTU Chemical Engineering, faculty, PhD-candidates, technical and administrative staff should receive a great thanks for creating a friendly, yet professional environment with mutual respect and free flow of informations and knowledge.

Thank you to the students I have had the privilege to supervise during my study: Mr. Rasmus Ø. Gadsbøll, MSc Eng and Mr. Jesper Thomsen, MSc Eng from DTU Mechanical Engineering (now elsewhere) for excellent and enthusiastic work on chemical kinetics and particle behavior.

Finally, many thanks to family and friends for their support and complete lack of understanding of my project and choice of career... There is more to combustion than just lighting a match — not much, but some...

Joakim M. Johansen
Technical University of Denmark
Spring 2015

Contents

List of Figures

List of Tables

Abbreviations

ABCD	Advanced biomass and coal devolatilization
AMV	Amager power station
APH	Air pre-heater
AS	Air split
b-CPD	Biomass chemical percolation devolatilization
CA	Carrier air
CCD	Charge-coupled device
CFD	Computational fluid dynamics
CHP	Combined heat and power
CPD	Chemical percolation devolatilization
CW	Cooling water
DAEM	Distributed activation energy model
d.a.f.	Dry and ash free
DO	Discrete ordinates
DPM	Discrete phase model
DRW	Discrete random walk
DSC	Differential scanning calorimetry
DTA	Differential thermal analysis
DTG	Derivative thermogravemetry
DTGS	Deuterated triglycine sulfate
EDX	Energy-dispersive x-ray spectroscopy
EFR	Entrained flow reactor
ERZ	External recirculation zone
EWT	Enhanced wall treatment
FBR	Fixed bed reactor
FSP	Fiber saturation point
FTIR	fourier transform infrared spectroscopy
GREEN	Power Generation from REnewable ENergy
HEV	Herning power station
HHV	Higher heating value
HR	Heating rate
HTVY	High temperature volatile yield
IRZ	Internal recirculation zone
LDA	Laser doppler anemometry

LFR	Laminar entrained flow reactor
LHV	Lower heating value
NC	Number correlation
PA	Primary air
PF	Pulverized fuel
PSD	Particle size distribution
RANS	Reynold averaged Navier-Stokes
RNG	Renormalization Group
RSM	Reynold stress model
SATP	Standard ambient temperature and pressure
SCR	Selective catalytic reduction
SEM	Scanning electron microscopy
SF	Shape factor
SFOR	Single first order reaction
SNOR	Single n^{th} order reaction
STA	Simultaneous thermal analysis
std	Standard deviation
TA	Tertiary air
TGA	Thermogravimetric analysis
UBC	Unburned hydrocarbons
UV	Ultraviolet
VIS	Visible spectrum
WP	Work package

Notation

Greek letters

β	TGA heating rate	$\mathrm{K \cdot min^{-1}}$
χ	Conversion	—
ε	Emissivity	—
λ	Thermal conductivity	$\mathrm{J\,(m \cdot s \cdot K)^{-1}}$
Λ	Mean free pathway	m
μ	Viscosity	$\mathrm{Pa \cdot s}$
Ω	Angular velocity	$\mathrm{rad \cdot s^{-1}}$
ω	Tangential velocity	$\mathrm{m \cdot s^{-1}}$
φ	Porosity	—
ρ	Density	$\mathrm{kg \cdot m^{-3}}$
σ	Distribution spread	—
σ	Stefan-Boltzmann's constant	$\mathrm{J \cdot s^{-1} \cdot m^{-1} \cdot K^{-4}}$
τ_m	Macro-mixing time scale	s
ξ	Material property	—
y^+	Dimensionless wall distance	—

Subscripts

0	Initial
ad	Adiabatic
bound	Bound water
c	Char
c	Chord length
c	Critical limit
cond	Conduction
drag	Drag upon a particle
ds	Desorption
e	External (emissivity)
eff	Effective
eq	Equivalent
ext	External
Fe	Ferret diameter
f	Fuel
fiber	Solid structure fiber
free	Free water
fsp	Fiber saturation point
g	Gas

g	Gravity	
i	Index	
i	Present time step	
i	Internal (emissivity)	
k	Rate constant	s^{-1}
l	Liquid water	
Ma	Martin diameter	
min	minimum	
max	Maximum	
m	Mass weighted	
N	Elapsed time step	
por	Solid structure pore	
p	Particle	
R	Outer radius	m
r	Radius	m
r	Radiation	
T	Tar	
Y	Water	
vap	Evaporation	
vol	Volume	
V	Volatile	
w	Wall	

Roman letters

A	Area	m^2
A	Effective thermal conductivity model constant	—
A	Pre-exponential factor	s^{-1} or $s^{-1} \cdot K^{-1/2}$
a	Acceleration	$m \cdot s^{-2}$
Bi	Biot number	—
c_p	Specific heat capacity	$J\,(kg \cdot K)^{-1}$
d	Diameter	m
D	Characteristic burner diameter	m
D	Quarl diameter	m
ΔH	Enthalpy of reaction	$J \cdot kg^{-1}$
$\bar{d}$	Mean diameter	m
E_a	Activation energy	$J \cdot mol^{-1}$
$\bar{E}_a$	Mean activation energy	$J \cdot mol^{-1}$
$\vec{F}$	Force vector	$\left(kg \cdot m \cdot s^{-2}\right) \hat{\mathbf{u}}$
$g\,(z)$	Dummy function	
h	Heat transfer coefficient	$J\,(s \cdot K)^{-1}\,m^{-2}$
I	Temperature integral	
k	Rate constant	s^{-1}
m	Mass	kg
H	Enthalpy	$kJ \cdot mol^{-1}$
MW	Molecular weight	$g \cdot mol^{-1}$

n	Exponent	—
n	Reaction order	—
Nu	Nusselts number	—
Pr	Prandtl number	—
Q	Burner throughput	$\mathrm{kg \cdot s^{-1}}$
q	Heat flux	$\mathrm{J \cdot s^{-1} \cdot m^{-2}}$
r	Radius	m
R	Outer radius	m
R	Universal gas constant	$\mathrm{J\,(mol \cdot K)^{-1}}$
Re	Reynolds number	—
S	Swirl number	—
S	Entropy	$\mathrm{J \cdot mol^{-1}}$
T	Temperature	K
t	Time	s
U	Characteristic burner velocity	$\mathrm{m \cdot s^{-1}}$
u	Axial velocity	$\mathrm{m \cdot s^{-1}}$
$\vec{u}$	Velocity vector	$\left(\mathrm{m \cdot s^{-1}}\right) \hat{\mathbf{u}}$
V	Volatile fraction	—
V	Volume	$\mathrm{m^3}$
v	Velocity	$\mathrm{m \cdot s^{-1}}$
$\dot{w}$	Rate of water evaporation	$\mathrm{kg \cdot s^{-1} \cdot m^{-3}}$
x	Distance	m
Y	Water fraction	—
Y_d	Distribution function	—
z	Einstein temperature function	$\mathrm{K^{-1}}$

Superscripts

0	Reference value
$*$	Initial
$\prime$	Parameter variation value
s	Skeletal

Introduction

In recent decades, central power and heat production through thermal conversion of biomass has gained ground concurrently with the political agenda both on a national and an international level. Fossil fuel combustion constitutes the largest part of the anthropogenic emission of green house gases [3]. The development of high efficiency biomass plants is required in order to balance the fluctuating power production from wind mills and other alternative utility sources, while still striving towards a CO_2-neutral energy profile. Direct combustion or co-combustion of biomass provides an economic advantage over the indirect combustion through thermal conversion processes to e.g. the transportation sector [4]. In addition, thermal plants are a necessary need in the provision of district heating.

Development and implementation of high efficiency biomass combustion technology is arguably the best near-term solution to provide stable and CO_2-neutral centralized power and district heating to larger cities and industrial areas.

Biomass differs from conventional solid fossil fuels (traditionally coal) in a number of essential areas; including both chemical composition and physical structure and appearance. Thus, direct utilization of existing high efficiency pulverized heat and power facilities is not an optimal option when considering biodust as the fuel. The fibrous nature of the biomass complicates particle pretreatment implying larger and oddly shaped fuel particles; changing aerodynamics and particle size distributions. In addition, the larger fraction of volatile components changes the conditions at which stable flames are achieved. A fast development of the technology aiming to convert existing high efficiency burner installations has been conducted in Denmark throughout the past couple of decades. However, technical difficulties lower the efficiency and limit the operational flexibility both with regards to biomass type and quantity.

The transition to renewable energy is rapidly progressing in Denmark. Danish power plants have been obligated to implement biomass combustion technologies since 1993 [5] in the attempt to lower the overall CO_2-emissions. The continued interest in actively developing sustainable technologies has been the focus of several studies on the operational centralized power plants both in Denmark [6–10] and abroad [11]. The development of the future heat and power production in Denmark is to a large extend regulated by the 2030 framework of the European Commission [12] but also by national initiatives

[13]. The Danish 2050 plans aim towards a 100 % CO_2-neutral energy sector, including stationary (central, decentral, and household) production of heat and power and the transport sector. The use of coal as feed for the Danish heat and power production is terminated in 2030, while the use of oil is gradually phased out until 2035. Windmills play a significant role in the Danish energy infrastructure and will by 2020 cover 50 % of the power production. This motivates for the development of high efficiency and fuel flexible thermal power plants to cover the central heat production and supplement the still growing share of windmills.

Introduction to the GREEN Center

The power Generation from REnewable ENergy (GREEN) research center is based on seven work packages (WPs), cf. figure 1, covering the life cycle of biomass fuel from the growth of new and improved energy crops (WP1), characterizing the fuel for combustion purposes (WP2), establishing a scientific basis for the development of new burner designs (WP3), post flame activities in ash transformation, deposition, and additives (WP4), development of novel corrosion resistant super-heater materials (WP5), characterization of $DeNO_x$ catalyst deactivation (WP6), and finally the re-utilization of ash (WP7).

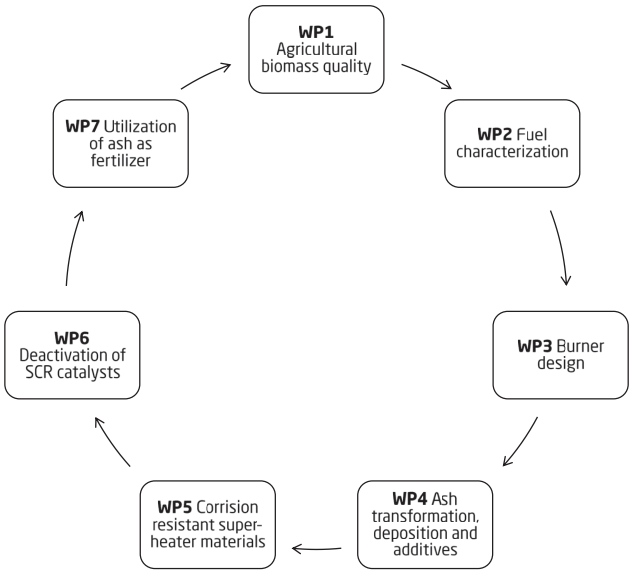

Figure 1 An overview of the WPs covered by GREEN.

WP3: Burner Design

This PhD project will primarily include work related to WP3 on burner development. WP3 is closely related to fuel characterization (WP2) and works to relate the laboratory characterizations to observations made through full-scale campaigns.

Objectives

This work aims to establish a scientific basis for the development of a new generation of biomass burners designed to facilitate high efficiency and fuel flexibility combined with good particle burn-out and stable flame capabilities of 100 % biodust fueled plants. The project will link fuel properties to flame properties, considering both fluid dynamic effects due to the differences in particle characters and chemical effects due to changes in chemical composition and chemical kinetics.

Structure of the Thesis

The thesis is written as a monograph and constructed from five parts:

I Introduction and Fundamentals
In this part biomass combustion fundamentals are presented. The basic literature on biomass characterization and thermochemical processes is briefly introduced.

II Devolatilization of Small Biomass Particles
This part describes the kinetically controlled devolatilization process. The near isothermal particles are studied at both low and high heating rates and a selection of phenomenological mechanisms are employed to model the processes. Part II form the basis for publication A, appendix A.

III Devolatilization of Larger Biomass Particles
For industrial purposes, the isothermal particle assumption only apply to a fraction of the particles introduced to a boiler. This part examines the influence of heat transport limitations and develops engineering fixes that can be implemented to commercial CFD codes. The combined chapters of part III form the basis for publication B, appendix B.

IV Full-Scale Measurements
Three full-scale campaigns have been carried out, two of which are reported in this part. This covers a comprehensive review of the experimental results and their comparisons.

V Recapitulations and Conclusions
Main summary, work in progress and suggestions to further work.

Part I

Introduction and Fundamentals

"If we knew what it was we were doing,

it would not be called research, would it?"

—Albert Einstein

CHAPTER 1

Thermochemical Conversion of Biomass

This thesis aims to provide scientific material for the development of swirl stabilized PF burners. Suspension firing of solid fuels is interesting for commercial use primarily due to its high combustion efficiency, wide utilization, and its large capacity [14, 15]. However, poor fuel versatility makes this combustion technology subject to ongoing research. This chapter will introduce the fundamentals of suspension fired biomass combustion.

1.1 Wall Mounted Burners

In general, two generic main categories of suspension fired technologies exist, defined by the type of employed burner installation [15, 16]: Swirl burners introduce combustion air to the furnace through an annular ring surrounding the primary air/fuel jet at a tangential angle, hence, creating the swirling motion. This rotating motion gives rise to a low pressure zone adjacent to the primary nozzle exit, causing hot combustion gases to reflux and thereby ignite newly introduced fuel. This self sustaining behavior implies an independence between each burner installation. The second category of suspension fired combustion technologies includes jet-nozzle array burners. These installations use no, or only little swirling motion in the combustion air. Flame ignition and stabilization relies primarily on a cooperative placement of the burners [17]. Batteries of burners are commonly installed at the corners of the furnace tower, introducing the jet of air and fuel tangentially to a vertical cylinder at the center of the furnace. Hence, multiple jets creates a single flame.

1.1.1 Flame Stabilization

Swirling jets are the main objective of this work. Multiple independent wall mounted burners introduces both fuel and combustion air to the furnace. Flame stability in relation to front wall mounted burners is usually described as a "'lit-back" flame, i.e. a flame that ignites within, or very near the burner quarl [18]. Lifted flames, i.e. flames that ignite in the far-field, or downstream of any internal recirculation zones can only be stabilized if the incoming radiation is strong and is generally not considered as favourable operation. Strong radiation is rarely the case in utility boilers where heat is extracted through the boiler walls leaving the boundary conditions well below the gas phase temperature.

Instead swirling flames are stabilized by two primary mechanisms:

- Swirl stabilization
- Bluff body attachment

The swirl stabilization (including quarl design) manipulates the flow pattern of the flame by introducing pressure differences in the flame induced by velocity gradients, defining the macromixing properties of the flow field. The primary job of the swirling flow stabilization mechanism is to control the convective heat transport to the near burner field and the mixing between fuel lean and fuel rich zones [19]. The fuel is transported from the mills to the nozzle suspended in the primary air. The fuel-air mixture is introduced to the furnace through a central tube, or inner annulus, at velocities adjusted to the desired mixing functionalities, as will be described later. The maximum velocity is usually limited to around $20\,\mathrm{m}\cdot\mathrm{s}^{-1}$ restricted by flame stability considerations; e.g. blow off, nozzle erosion, etc. [16]. Combustion air is introduced at high velocity (60–$80\,\mathrm{m}\cdot\mathrm{s}^{-1}$) through an outer annulus. However, the flow velocities may vary from burner to burner. The primary objective of the rotating secondary air flow is to induce a pressure defect at the nozzle exit due to the forward directed inertial forces. This creates a low pressure zone close to the nozzle outlet inducing a velocity gradient perpendicular to the primary flow [16, 20]. As the degree of swirl, or the angular-to-linear-momentum ratio, reaches a critical value, vortex breakdown will occur and a toroidal recirculation is established in the central region of the jet. Controlling this toroidal recirculation pattern is a key element in the concept of swirling jet combustion of pulverized solid fuels [21, 21–23]. By introduction of proper recirculation, intense mixing and combustion may be achieved along with good flame stability [24]. The velocity gradients in the quarl zone may become significant [25]. The reversed flow of hot combustion gases raises the temperature in the near burner field facilitating early ignition and close flame attachment [20], as shown in figure 1.2. As the degree of swirl increases, the internal recirculation zone is stimulated and the convective transport of hot combustion gases to the near burner area increases, thus increasing the gas phase temperature.

The primary job of the bluff body, or flame holder, is to attach the flame to the burner. Bluff bodies introduce a strong, however, small recirculation zone downstream of the object, cf. figure 1.1. This intense recirculation zone facilitates an initial mixing of the particle laden primary air and the surrounding combustion air [26].

A comparative investigation [28] of the recirculation zone created from a variety of buners; vaned swirlers, stabilizer disks, and swirling annular jets, showed that the dimensions of the recirculation zone were influenced by primarily four principal factors:

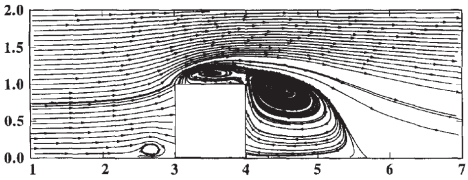

Figure 1.1 Inferred flow around a bluff body in a channel flow. Experiments by: Martinuzzi and Tropea [27].

1. Degree of swirl imparted to the flow
2. Blockage ratio of the flame holder in the stream
3. Divergent walls, provided that separation of the flow from the walls is prevented
4. The shape of the flame holder

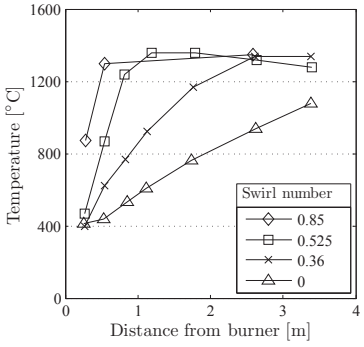

Figure 1.2 Gas temperatures along the axis of pulverized-anthracite flames as a function of the degree of swirl [23].

Although cold flow modeling or experiments will provide insight into the resulting fluid dynamics, changes to the shape and size of the recirculation zones must be expected as the flow is accelerated by combustion reactions [20].

1.1.2 Characterization of Swirling Flows

Swirling flames are stabilized by the introduction of an angular velocity component to all or selected flows in the burner. Thus, the most common method

to characterize a swirling flame is by the relative comparison of the overall angular to axial momentum fluxes, yielding the swirl number, S, [23]:

$$S = \int_0^{\mathrm{d}_0/2} \rho\omega u r^2 \mathrm{d}r \left[d \int_0^{\mathrm{d}_0/2} \rho u^2 r \mathrm{d}r \right]^{-1} \tag{1.1}$$

Swirl, being a fluid dynamic phenomena, is often characterized by describing the dominant forces acting upon the individual fluid elements [29]. The influences of both the fictitus Coriolis force and centrifugal forces are important in the dynamics of swirling flows. Especially the Coriolis force has been shown to play a key role in these kind of flows because of the high degree of rotation and thereby large deflection due to the Coriolis effect.

The Coriolis force acting in the lateral plane (perpendicular plane to the axial flow direction) restricts the radial displacement of fluid elements due to the force unbalance between the local pressure and the centrifugal force as a fluid element travels either inwards or outwards in a rotating flow. Thus fluid elements entering a swirling jet system will experience a low pressure zone in the core and will naturally flow towards it, but will be deflected due to the Coriolis effect. Because different positions in a rotating frame of reference will be observed to have different velocities seen from an inertial frame of reference, a fluid element must be accelerated in order to maintain a straight trajectory so that its velocity changes from point to point by the same magnitude as the relative difference in velocities between the inertial and rotating frame of reference. This effect is proportional to the angular velocity, ω, and to the fluid velocity component in the lateral plane. Hence the Coriolis acceleration, a_C, can be written

$$a_\mathrm{C} \propto \Omega \times v = \frac{\omega r}{\Delta t} \tag{1.2}$$

where v signifies the velocity component of the fluid element, r the radius, and Δt a given interval of time in which the acceleration can be determined.

The extent to which the retarding effect to the radial movement of a fluid element depends on the relative importance of other forces acting on the same fluid element. In inviscid fluid dynamics the most dominant force would typically be inertial forces. Hence, a comparison of the Coriolis acceleration relative to the inertial acceleration, $\mathrm{d}u \times (\mathrm{d}t)^{-1}$, is given by

$$\frac{\text{Coriolis force}}{\text{Inertial force}} = \frac{\omega R}{u} \tag{1.3}$$

where R is the outer radius and U the axial velocity.

Comparing this relation to the commonly used [30–32] expression of the swirl number, S, yields:

$$S = \int_0^{\mathrm{d}_0/2} \rho\omega u r^2 \mathrm{d}r \left[d \int_0^{\mathrm{d}_0/2} \rho u^2 r \mathrm{d}r \right]^{-1} = \frac{\omega R}{2u} \tag{1.4}$$

showing how the use of the swirl number for flow characterization is similar to comparing the relative importance of the Coriolis forces to the inertial forces.

The swirl number, S, is commonly used to classify laboratory or pilot scale flames [21, 33] but are rarely used for industrial scale flames because the required pressure and velocity measurements are difficult to obtain. The understanding of the relative importance of the axial and angular momentum is however directly transferable.

Other forces relevant to suspension fired combustion include; the gravitational pull is in particular important in biomass combustion because of the difficulties of grinding the fuels [10]. It can, however, be utilized to maximize the residence time of the fuel, improving the particle burn-out [34].

1.1.3 Flame Classification

Categorically two types of flames[1] may be generated from a swirling jet burner [35, 36], including flame types 0, 1, and 2. In the first type (type-0), the momentum of the central jet is great enough to pierce through the central recirculation zone created by the swirling motion of the secondary air, as illustrated in figure 1.3a. This is commonly a combination of low swirl or no swirl and/or high primary air velocities and heavy fuel particles. The result is a flame stabilized by external recirculation, facilitating fuel ignition and flame attachment, followed by a longer flame where char burn-out is completed. These flames, referred to as type-0 flames, are typically used in corner fired boilers, where a cooperative positioning of multiple burners stabilizes a central fire ball, ensuring burn-out of particles penetrating the recirculation zone.

The second flame type utilized high degrees of swirl completely or close to completely absorbing the primary jet, resulting in a short flame close to the nozzle exit. This, type-2 flame, produces excellent flame stability for wall firing purposes (single flame stabilization). The internal recirculation zone is the key to generate a stable type-2 flame. A strong internal recirculation zone facilitates significant convective heat transport by hot combustion gases into the burner quarl where the fuel ignites in the close vicinity of the fuel injector [37–39].

Combustion experiments on the same high volatile Scotts Brench coal led to 470–520 pm of NO_x formation using a type-0 flame compared to 900–1000 ppm NO_x formation using a type-2 flame in the same 2 MW IFRF flame [40, 41]. Thus, in addition to flame stability, NO_x considerations are required when deciding for a flame type. Avoiding excessive NO_x formation can, however, be assisted by e.g. air-staging [35].

The transition between flame types 0 and 2 as function of swirl takes place gradually [42, 43] and are referred to as type-1 flames, cf. figure 1.3b [35, 40, 44]. If the forward momentum of the primary air stream is sufficiently

[1] In the discussion of flame types based on aerodynamic properties, the International Flame Research Foundation (IFRF) flame classification system will be adopted [35].

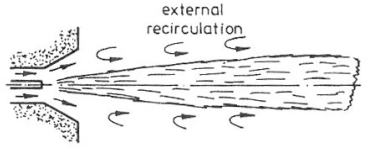

(a) Type-0 flame with no swirl and high axial momentum of the central fuel jet. The flame is stabilized by external recirculation.

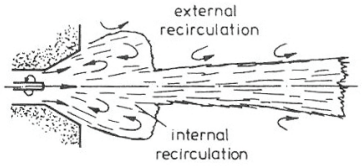

(b) Type-1 flame with low swirl degrees and relatively high axial momentum of the central fuel jet. The flame is a combination of flame type-0 and 2.

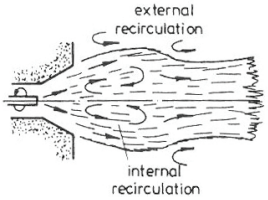

(c) Type-2 flame with high swirl degrees and relatively low axial momentum of the central fuel jet. The central jet does not penetrate the IRZ.

Figure 1.3 Illustration of the three types of swirling flow flames [16, 35].

low, it will immediately be reflected in the radial direction upon contact with the reverse flow created by the toroidal recirculation zone. As the momentum of the central jet exceeds a critical value, it overcomes the opposite force of the reverse flow, deflecting the vortex from the central axis, confining it to the region between the now established central jet and the inside boundary of the flow of combustion air.

It is important to notice; that the flame classification related only to the fluid flow and not to the particle trajectories. For small particles, where the inertial forces are small compared to the drag forces of the fluid acting upon the particle, the particle will readily follow the fluid flow. However, the transition from coal to biomass have had a fundamental influence on the structures of swirl stabilized flames. The lower energy density of biomass compared to coal, leads to higher transport air flows pr. thermal energy unit input, thus increasing the momentum of the typically axial particle laden primary air [45]. The high forward momentum of the dense biomass particles may then cause penetration of a type-2 central internal recirculation zone, while the low density primary air flow is repelled by the strength of the internal recirculation zone. Thus, particle penetration into the center of a type-2 flame, without the flame structure collapses, is possible for biomass combustion [45, 46].

Pilot-scale studies on low and high volatile coals [47] have shown how the flame stability is primarily controlled by the flame aerodynamics and to less extent by the volatile content, while the ignition behavior is determined by the volatile content and the chemical composition of the volatiles [48].

1.2 Thermochemical Conversion of Biomass

The combustion of solid fuel particles can be described as a sequence of processes as outlined in figure 1.4. When a solid fuel particle is exposed to heat, the particle temperature will begin to increase due to heat transport by conduction, convection, and radiation, the ratio of which is dependent on the local environment [49]. The rate at which the particle is heated is central to the combustion process and differs greatly for the type of industrial application, cf. table 1.1.

Table 1.1 An overview of pyrolysis conditions and their related industries [50].

Type	Temperature K	Heating rate $K \cdot s^{-1}$	Application	Ref
Conventional	673–973	10^{-2}–10^{2}	Activated carbon, filter carbon	[51]
Flash	~ 773	10^{2}–10^{3}	Production of bio-oil	[52]
Very fast	< 2000	10^{4}–10^{5}	Gasification and suspension fired combustion	[53]

As the particle is heated any moisture will begin to evaporate, leaving behind a dry particle. The organic matrix will start to decompose as the particle temperature approaches 500 K [54]. The devolatilization occurs rapidly and results in the release of volatiles, which for biomass constitute a significant fraction of the available heating value. The volatiles are oxidized in gaseous homogeneous reactions while the remaining char is oxidized via surface reactions. The rate at which the devolatilization of biomass will occur is a question of chemical kinetic rate control versus internal heat transport [55–57] thus, categorizing the parent fuel into thermally thin and thermally thick particles.

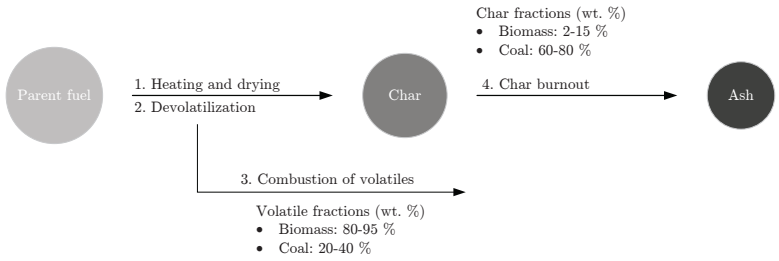

Figure 1.4 Conceptual outline of the combustion sequence.

Figure 1.4 represents the simplest mechanism to describe the combustion of biomass particles. In reality, a number of sub-mechanism will occur. For high temperature combustion one of the more widely accepted mechanisms is illustrated in figure 1.5. The formation of tar is accelerated at higher temperatures [58, 59] and the net rate of tar formation changes as the devolatilization progresses [60–62], potentially influencing on the PF combustion. Thus, for some operating conditions more complex models may be required. An extensive portfolio of devolatilization mechanisms have been proposed through the years. Developed for specific purposes, the complexity and the experimental conditions at which they were derived, vary greatly. Thus, although many models exists, only a few are relevant for PF combustion of biomass. The detailed studies and their relevance to swirl stabilized flames will be introduced in the modeling chapters.

1.2.1 Influence of Temperature

As pyrolysis is the thermal decomposition of the organic structure, the temperature plays a natural important role. The effect of reactor temperature has been studied both experimentally [63, 64] and through modeling [63–65]. The largest impact of temperature is often reported to be the change in the char yield [65–69]. The char yield decreases as a function of increasing temperature.

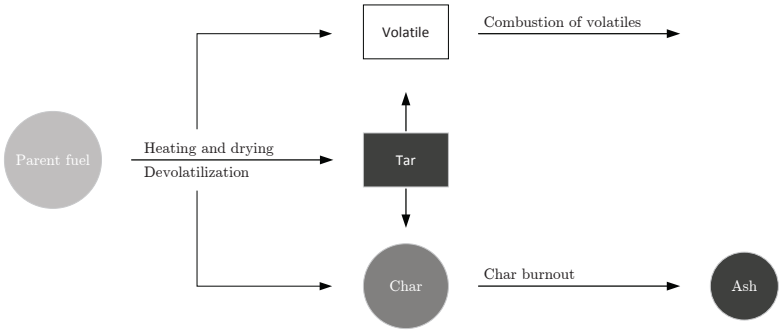

Figure 1.5 Conceptual outline of the combustion sequence including the formation and destruction of tars.

At around 1173 K the char yield stabilizes and any small continued decrements are believed to be caused by the increased auto-gasification processes [70].

Tar formation is promoted at elevated temperatures [71], however, competing with secondary cracking [70] leading to an increase in soot formation. The overall net result of tar is often seen to decrease as a function of temperature [69, 72].

In all cases, the net result of the decrease in char, increase in tar followed by tar cracking, results in higher volatile yields at elevated temperatures [65–70].

1.2.2 Influence of Heating Rate

Utility boilers operate at very high heating rates, cf. table 1.1, and thus investigating intrinsic pyrolysis kinetics at comparable heating rates are of natural interest. However, multiple practical problems have been encountered in the literature, most of which, can be traced to poor temperature control from either the employed apparatus or due to heat transfer limitations determination of the heat of reaction. In general, high heating rates have been related to low activation energies [73, 74] and vice versa for low heating rates [73, 75–82]. This apparently lower activation energy at higher heating rates is believed to stem from the endothermic pyrolysis [54, 83] typically not included in heat balances used to evaluate the particle temperatures. The endothermic reactions occurs fast at high temperatures and thus requires a significant heat input. As a direct consequence of this, volatile release is often reported to take place at higher temperatures than the true particle temperature. Numerical studies have been conducted to illustrate the significance of including the heat of reaction to the overall energy balance [84–86]. Other arguments have been made that applying kinetic parameters from low or high heating rate experiments are without great influence [87]. The problem becomes even more ambiguous

as the literature reports the pyrolysis as both endo- and exothermic, as will be discussed later.

The heating rate has been shown to have significant influence on the char yield [88] being as low as 1–6 wt. % dry and ash free (d.a.f.) during fast pyrolysis (10^4–$10^5\,\mathrm{K \cdot s^{-1}}$) versus 15–17 wt. % d.a.f. at low heating rates (10–20 $\mathrm{K \cdot min^{-1}}$) for pine wood devolatilization in a nitrogen atmosphere. Dall'Ora *et al.* [88] also showed how fast heating rate experiments resulted in melted chars while the fibrous structure of the parent fuel was retained if exposed to low heating rates.

Heating Rates of $10^5\,\mathrm{K \cdot s^{-1}}$: Entrained Flow Reactors

Entrained flow reactors (EFRs), or similar, are widely used in the combustion literature. Heated by burners [89] or electric heaters [70, 88] these reactors can reach the desirable heating rates on the order of 10^4–$10^5\,\mathrm{K \cdot s^{-1}}$. Such studies are however notoriously difficult to carry out for several reasons:

- The actual heating rate of the particles can be difficult to determine.
- The devolatilization occurs fast and particle must therefore be extracted and quenched equally fast from the system.
- Low feeding rates ensures single particle behavior but also induces difficulties in the operation.

Heating Rates of $10^3\,\mathrm{K \cdot s^{-1}}$: Captive Sample Reactors

As an alternative to the entrained flow reactor, grid heating systems also provides the opportunity to exceed the slow heating rates of the standard thermogravimetric analysis (TGA) equipment [90, 91]. Grid heaters, heated mesh, wire mesh, screen heater, etc. collectively known as captive sample reactors, first introduced by Loison and Chauvin [92] in the study of rapid coal pyrolysis, work by applying high currents across a high resistant wire mesh to which the fuel particles are directly exposed. This method allows for accurate control of the temperature ramp and reaction residence time. In addition, there is no movement of the fuel and thus the mass balance is often easier to close. The high slip velocity also limits the contact time between released species and the solid phase, thus minimizing the effects of secondary reactions [91, 93]. The penalty is lower heating rate, typically operating at two–three orders of magnitude below entrained flow reactors [60, 62, 94–96].

In general the captive sample reactors add the benefits of:

- Forced sweep gas configuration: Rapidly removes volatile gases isolating the study of primary devolatilization reactions.
- Well defined temperature programs.

- Well defined residence times.
- Excellent mass balance closure.

1.2.3 Influence of Mineral Matter

Mineral matter, especially alkali and alkali earth species, plays an important role in the utilization of biomasses in the thermal industry for two reasons:

- Release of certain inorganic species lead to downstream undesired effects: E.g. fouling and subsequent accelerated corrosion of internal parts of the boiler installations, deactivation of selective catalytic reduction (SCR) catalysts, degradation of the ash quality, etc.
- The presence of alkali and alkali earth metals have shown to effect the devolatilization and char formation processes.

Investigating heating rates between 1 and $1000\,\mathrm{K}\cdot\mathrm{s}^{-1}$, Okuno *et al.* [97] concluded that the release of alkali and alkali earth metals takes place regardless of the applied heating rate.

The presence of alkali and alkali earth metals, especially potassium, sodium, calcium, and magnesium, have been found to act as catalysts for the decomposition process, favoring char formation [98–101]. The charring effect can be reversible adjusted by leaching or doping with inorganic salts [98]. The effect has been documented to apply regardless of heating rate [102]. Fuel pretreatment with inorganic salts ($MgCl_2$, NaCl, $FeSO_4$, and $ZnCl_2$) have also shown tendencies to change the thermal stability of the organic macro components in parent biomass, making it difficult to apply e.g. superposition modeling [103].

Upon leaching of parent fuels the tar yield has been found to increase at the cost of the gas yield [100].

1.2.4 Evolving Species

Using a simplified decomposition model, greatly simplifies the devolatilization process making the data readily available for computational intensive numerical simulation tools like CFD. In order to be able to simulate the gas-gas combustion using either detailed mechanisms or apparent rates requires some additional insight into the speciation of the evolving volatiles and possibly secondary reactions.

Numerous factors come into play when considering composition and properties of the evolving product classes. Both the reaction conditions, primarily temperature and heating rate, and the particle properties, chemical composition, size, shape, mineral matter, density, moisture content, porosity, etc., has been suggested to influence the pyrolysis process.

Nunn *et al.* [104] used a captive sample reactor to rapidly heat samples of hardwood analyzing the evolving gases and liquids. The tar production was found to peak around 1123 K after which a decrease in tar content was observed, presumably due to secondary cracking of tars to lighter gases. This seems to be the general observation made in the literature [58–62].

Decoupling the pyrolysis process chemically from the main flow has shown simulated absence of significant tar cracking across a wide temperature range [105]. Whilst, disregarding particle-bulk phase interaction and solid phase physical changes greatly reduce computational costs, such an assumption may not represent realistic conditions, especially in the case of biomass where the solid phase is known to undergo significant physical changes during the conversion processes.

The evolving species, or the combination of evolving species, play an important role in CFD simulations using a single model compound to represent the escaping volatile gases. The composition effects both the molecular weight of this net compound and physical properties like the heat capacity. In the coal literature statistical models like the chemical percolation devolatilization (CPD) have been developed and proven as an effective tool to predict the composition of devolatilizing species [106]. However, although the CPD model has been modified to suit biomasses, the b-CPD model [107, 108], the diversity of the biomass fuels prevent such a model to be used as a true generic starting point. As an alternative to the statistical models the literature provides a large number of wire-mesh reactor experiments. These reactors exhibit the high heating rates and the fixed position of the solid sample makes it ideal for closing mass balances. A number of these reactors have been equipped with gas analysis equipment that can be used to estimate the fuel specific composition of devolatilizing gases [93, 95, 109]. This approach will be used for the development of a model fuel in chapter 8.

1.2.5 Enthalpy of Devolatilization

Pyrolysis takes place as bond breakage in the solid structure occurs as the temperature rises. Thus, the net enthalpy formation may possibly influence on the rate of pyrolysis. No general consensus exists in the literature on the change in enthalpy as devolatilization occurs.

Daugaard and Brown [110] investigated a range of samples in an inert atmosphere at elevated temperatures. They found a consistent endothermic trend for pyrolysis in a flow system closing a global heat balance. Havens *et al.* [111] used simultaneous thermal analysis (STA) to relate the mass loss during pyrolysis to the observed thermal response. By separating the heat of decomposition from the specific heat he arrived at an overall endothermic reaction, with a large spread for pine and oak wood.

Rath *et al.* [54] concluded from differential scanning calorimetry (DSC) experiments on wood that the net heat of reaction is composed of two competing

reactions; an endothermic release of volatiles and an exothermic formation of char. An observation of both endo- and exothermic reactions was also found by Broido [112] using differential thermal analysis (DTA) equipment on model compounds; cellulose, ash free cellulose ($x_{\text{ash}} < 0.01\,\text{wt. \%}$), and $KHCO_3$ doped cellulose. The experiments were carried out in both inert and oxidizing atmospheres using small sample sizes. In both atmospheres the reactions were found to be endothermic at temperatures below $\sim 600\,\text{K}$ and exothermic at higher temperatures. Akita and Kase [113] arrived at similar conclusions but did not observe an exothermic contribution in inert atmospheres.

Arseneau [114] found the reaction in inert atmospheres to be purely endothermic for $460\,\mu\text{m}$ (diameter) particles, however, increasing the sample size to $900\,\mu\text{m}$ he observed a net exothermic reaction at temperatures exceeding $623\,\text{K}$.

Using general techniques such as DSC or DTA on model compound devolatilization or larger systems closing global heat balances has lead to confusing results in the literature. The reactions have been described as both exothermic, endothermic, and a combination of the two. The inconsistent conclusions can be attributed to the differences in the experimental conditions; atmospheric condition, sample size, particle size, impurities, etc. If any general trends are to be derived, the results indicate a slightly endothermic nature of the primary pyrolysis whereas the secondary reactions may contribute with either endo- or exothermic reactions, possibly with an exothermic net output [83, 115, 116].

1.2.6 Physical Parameters

Numerous studies have been carried out on the effect of the physical parameters of the particle; size, density, heat capacity, shape, etc. [117–119]. Many of the general conclusions can be related to the above discussions. Most of the investigated parameters can be traced back to either particle temperature, heating rate, or residence time. Large particles posses a larger total heat capacity and thus for a constant heat flux will exhibit lower heating rates and temperatures, and longer residence times. The observed phenomena can be difficult to assign one particular parameter due to the interdependence of the thermal mechanisms. However, as will be discussed in part III, the numerical studies on large particle do provide a lot of information on non-isothermal particle behavior.

Oxy-fuel entrained flow reactor experiments on coals [120] have shown that the devolatilization phase seems to be independent of the bulk phase atmosphere.

CHAPTER 2

Biomass as a Fuel

Biomass is a widely used term for any substance that is derived from plants or animals [121–123]. Plant material is, in its simplest description, a composite material made from a combination of cellulose, hemicellulose, lignin, extractives, and inorganic matter [124]. Thus, large variations occur in both chemical composition and physical structure and appearance. This chapter will briefly introduce the reader to the use of biomass as a fuel for heat and power production. It includes some of the most important physical (page 17) and chemical (page 20) properties which will be briefly presented and discussed in relation to combustion and high temperature processes. A simple method for characterizing oddly shaped fuels will be be presented on page 25. This project includes two model fuels (wood and straw) for its kinetic study. These fuels along with their basic properties will also be presented in this chapter.

2.1 The Physical Properties of Biomass

The physical properties of biomass vary greatly [123, 124] and will indeed influence both the thermochemical conversion and the fluid dynamic properties. This thesis will cover both the conversion of woody fuels and annual crops. The use of annual crops (straws) will however be limited to small scale experimental and modeling at conditions limiting the impact of the physical appearance of the fuel. Hence, this section will be limited to the characterization of woody fuel properties.

2.1.1 Wood Structure

A tree trunk may roughly be divided into outer and inner bark, cambium, sapwood, and heartwood, as illustrated in figure 2.1. Each zone with their own specific physiological functions. The sapwood consists of as much as 90 % dead cells and acts as a transport vein for water and nutrients extracted from the surroundings through the tree roots. Wood growth primarily takes place by cell division in the thin cambium layer, consisting of living cells, between sapwood and inner bark. Growth will also take place to a limited extend in the inner bark, however, the primary function of the inner bark is to facilitate transport of larger molecules; sugars and nutrients [125].

The wood cells are elongated and aligned in the longitudinal direction of the trunk. This causes a natural anisotropy of the woody biomass leading to

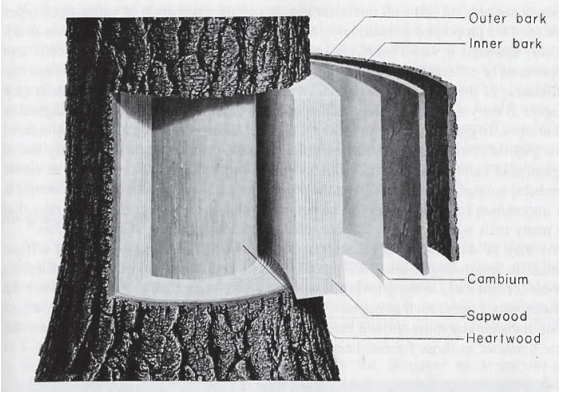

Figure 2.1 An overall view of the wood structure [125].

challenging properties in characterizing biomass from a mathematical point of view. In the case of thermochemical conversion of large biomass, the intra-particular gradients of species and temperature are often subjects for debate in the literature [63, 126, 127]. Such problems can be difficult to solve using the already existing models for simple spherical or non-spherical particle conversion due to the directional properties of e.g. thermal conductivity and gas permeability. The thermal conductivity has been reported as low as 1/3 in the radial and tangential direction of woody biomass while the permeability to gas species can be lowered by as much as a factor of 10^4 [128, 129].

2.1.2 Particle Shape

The shape of any fuel particle surely plays an important role whether one considers the conversion of a single particle under well controlled conditions, a cloud of particles, or simulates trajectories of suspended combustion.

The importance of particle size and shape manifests it self for two primary reasons:

- Thermochemical conversion (chemical kinetics and transport phenomena)
- Fluid dynamic properties (drag and moment of inertia)

Thus, relating to two of the central topics within PF combustion.

Biomass particles are often found to be highly non-spherical [130, 131]. The grinding of fuel prior to injection to the furnace is an important process in suspension fired solid fuel technology. The formulation of the fuel in the mills affects both the aerodynamics and the reactivity by changing the

available surface area. This influences the overall flame stability and combustion efficiency [16]. The finer the grind the more readily the particles are retained in the recirculation zone, and the less its combustion rate is inhibited by transport limitations [132].

The fibrous structure of lignocellulosic biomass makes it difficult to fracture by application of compression forces. Unlike coal, which is a brittle material that is easily crushed, the milling procedure results in flattening rather than crushing of the biomass particles leaving non-spherical particles with aspect ratios exceeding 10 [133]. This results in an increased energy consumption for the fractioning of biomass compared to coal.

Figure 2.2 illustrates the differences in obtained figure 2.2a cumulative particle size distribution and resulting figure 2.2b aspect ratios after 60 min of milling of Norwegian spruce tree shaving dust starting out as a few millimeters thick and a few centimeters in length.

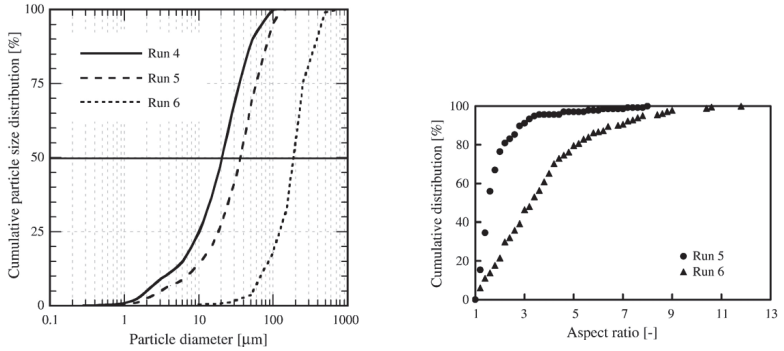

(a) **(b)**

Figure 2.2 Cumulative figure 2.2a size distributions and figure 2.2b aspects ratios after 60 min grinding of Norwegian spruce in vibration mill (run 5) and cutter mill (run 6) [134].

A significant difference between the results from the two preparation methods both in respect to particle distribution and particle aspect ratio, identifies the milling as an important parameter in defining the properties of the particle that are injected to the furnace. Figure 2.3 show SEM-images of a typical particle from the two milling processes. The difference in size is clear, as indicated by the particle size distribution, figure 2.2a, while the more spherical appearance of the vibration mill product is evident, also shown by the aspect ratio distribution in figure 2.2b.

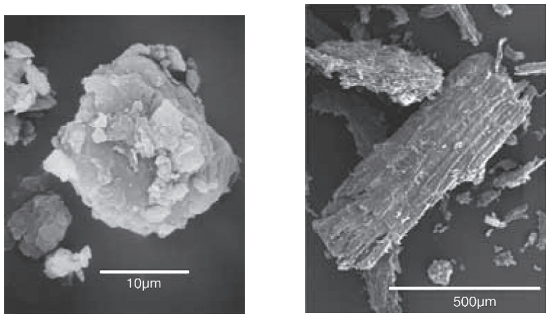

(a) **(b)**

Figure 2.3 SEM-images of particles after 60 min grinding of Norwegian spruce in figure 2.3a vibration mill and figure 2.3b cutter mill [134].

2.1.3 Wood Density and Pelletisation

Because of the open and porous structure of virgin wood two definitions of density should be considered when characterizing fuels. The apparent density, ρ, which is the defined by the external density, and the skeletal or true density, ρ^{s}, which omit the volume of the particle occupied by pores. The apparent and skeletal densities are connected by the particle porosity, φ:

$$\varphi = 1 - \frac{\rho}{\rho^{\mathrm{s}}} \tag{2.1}$$

The porosity of untreated woody fuels is typically around 0.5–0.7 and increasing as the particle is thermally converted [63, 127]. The typical apparent density spans between 500–700 $\mathrm{kg \cdot m^{-3}}$ [127, 135] for most hard and soft woods and between 40 and 150 $\mathrm{kg \cdot m^{-3}}$ for the grass type biomass [136, 137]. This yields skeletal densities of around 1000–1400 $\mathrm{kg \cdot m^{-3}}$. By pelletizing processes the particle porosity can be decreased to essentially zero, resulting in apparent densities close to the skeletal densities and with bulk densities of 700–800 $\mathrm{kg \cdot m^{-3}}$ [138] greatly reducing the costs of storage and transportation. The increase in apparent density is dependent on the compaction pressure [139].

2.2 The Chemical Composition of Biomass

The differences in chemical composition between conventional coal and biomass fuels are distinct. As illustrated in the van Krevelen diagram, figure 2.4, coals consists primarily of carbon, with a typical content between 90 and 95 wt. %. In comparison, agricultural residues and woody materials typically contain

between 40–50 wt. % of carbon and correspondingly more oxygen and hydrogen [15, 140–142]. The differences in the C/H/O-ratios are clearly indicated in figure 2.4. Also the fraction of fixed carbon (char forming carbon) is relevant when comparing coal to biomass, however, also when comparing e.g. woody biomass to agricultural biomass.

Standard laboratory test are used to characterize the stored energy distribution between fixed carbon and volatiles [123]. This distribution directly influences on the heat release mechanism during combustion. Often legacy standards are used from coal characterization and determines the volatile content by the mass loss during heating to a fixed temperature at a pre-set time. The most common standards specify temperatures between 973 and 1273 K and residence times of 7 to 10 min. The amount of fixed carbon is found as the remaining mass, excluding ashes. A general consensus, on the volatile fraction being a function of the peak temperature [89, 143] questions the use of coal standards for biomass characterization. However, no generally applicable standards for biomasses have been agreed upon. Table 2.1 lists typical values of the proximate analysis for different solid fuels.

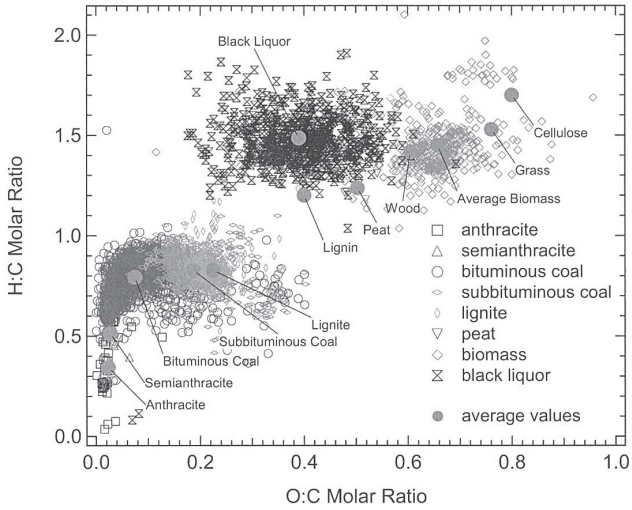

Figure 2.4 A van Krevelen diagram comparing the molar composition of coals and biomass [144].

2.2.1 The Organic Composition of Woody Biomass

By far the largest share of biomass of any kind (woody, aggricultural, etc.) is made up of C, O, and H which is why overviews provided by for example

Table 2.1 Proximate analysis of Danish cereal straws and wood chips [145] compared to common coals. *Data collected from separate source [15, 133, 146].

		Straw		Wood chips		Coal*	
Specie	Unit	Typical	Variation	Typical	Variation	Typical	Variation
Moisture	wt. %	14	8–23	45	20–60	3	2.1–14
LHV	$MJ \cdot kg^{-1}$	18.6	18.0–19.0	19.5	18.5–20.5	30	29–32
Ash	wt. %, dry	4.5	2–7	1.0	0.3–6	10	4–11
Volatiles	wt. %, dry	78	75–81	81	70–85	30	5–40

the van Krevelen diagram, figure 2.4, is of high importance when considering any chemical transformation of biomass material. However, when considering the composition on a macromolecular scale other important similarities will occur. Woody biomass primarily consists of combinations of lignin, cellulose, and hemicellulose [124, 140, 147], cellulose typically constituting just about half of most woody biomasses. The ratio between hemicellulose and lignin then varies from biomass to biomass but can be divided into two sub categories of woody material: Soft wood and hard wood [148] of which soft wood generally has a high lignin to hemicellulose ratio and vice versa for hard woods. Typical macromolecular compositions are listed in table 2.2.

Table 2.2 Macromolecular composition of Scandinavian wood [63].

Component	Unit	Birch	Spruce	Pine
Cellulose	wt. %	40	44	43
Hemi-cellulose		39	27	27
Lignin		21	29	30

Cellulose

Cellulose, figure 2.5, is one of the most abundant organic compounds. It is an unbranched polymer of glucose residues joined by β-1, 4 linkages allowing formation of long straight chains optimal for wood fibre construction. It features a reducing and a non-reducing end as well as a number of hydroxy groups susceptible to chemical reaction, e.g. through pyrolysis and combustion, however, considerably more stable than hemicellulose [140]. Cellulose is often found to form intra- and intermoelcular hydrogen bonds, stiffening the straight chains, resulting in the construction of cellulose fibers of high mechanical strength. Although well structured in its repeating pattern, the size (degree of polymerization) can differ by several hundreds orders of magnitude. It is, however, often found as a high molecular weight polymer [149]. Cellulose decomposes at temperatures around 598–648 K [150, 151] and decomposes into light gases, tars, and char [126].

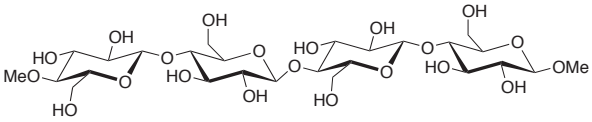

Figure 2.5 Cellulose structure.

Hemi-Cellulose

Hemicellulose is less structured than cellulose. It is an amorphous polysaccharide constructed from xylose, arabinose, galactose, glucose, and mannose (cf. figure 2.6) and thus contains both methyl, carboxyl, and hydroxyl functional groups [126]. Where xylan is the major hemi-cellulose component in secondary cell walls, constituting around 18–25 wt. % of hardwood and herbaceous biomasses. The generally smaller units with a high degree of branching make hemi-cellulose structures more susceptible to chemical degradation known to onset around 498–598 K depending on the building block composition [150–152]. Hemi-cellulose decomposes primarily into light gases [126].

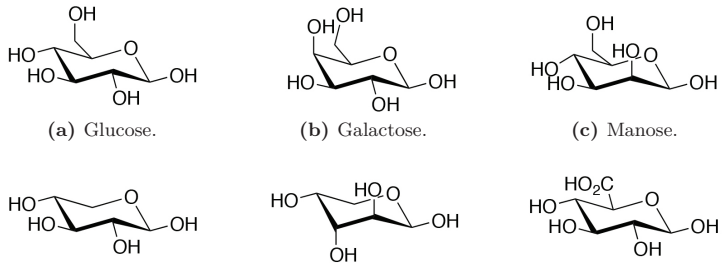

(a) Glucose. **(b)** Galactose. **(c)** Manose.

(d) Xylose. **(e)** Arabinose. **(f)** Gluconic acid.

Figure 2.6 Main hemi-cellulose building blocks [126].

Lignin

Lignin is an amorphous biopolymer. Highly branched and difficult to dehydrate compared to both cellulose and hemicellulose [123, 151]. The three dimensional structure makes lignin an important part in plant structure integrity and although commonly stated that cellulose, hemicellulose, and lignin are strongly intermeshed [148, 149], the lignin is often found outside the cell wall were it functions as an inter-cellular binding agent [124]. Because of the random nature of lignin, the thermal decomposition takes place across a wider temperature range than both cellulose and hemi-cellulose. The thermal de-

composition is taking place at temperatures around 523–773 K [150, 153] and is known to be heavily charring [153].

2.2.2 The Inorganic Composition of Woody Biomass

Table 2.3 illustrates the differences in the chemical composition of straw, wood, and coal. In general biomasses contain more inorganic matter in terms of alkali, earth-alkali, and halogens. For general purpose combustion modeling the inorgnaic content is often lumped together as a single ash pseudo-component. However, the presence of the inorganic elements may indeed influence on the combustion process. Release of inorganic constituents lead to downstream problems with fouling, corrosion, catalyst deactivation, and fly ash quality [146, 154]. But the presence and composition of inorganic elements may also have a more direct influence on the combustion process, shifting the yield ratio between gas, tar, and char yields [155] causing the relative char yield to increase [99]. Other effects include morphology changes [156, 157] causing significant changes to the physical appearance of the fuel; influencing fluid dynamic properties and both internal and external transport properties of the particle.

The role of the inorganic elements during combustion processes are many and the thermal stability of the present species is wide [154, 158, 159] thus general trends can be difficult to deduct.

Table 2.3 Approximate values for different types of solid fuels [145]. *Data collected from separate source [15, 146, 160].

		Wheat		Wood chips		Coal*	
Specie	Unit	Typical	Variation	Typical	Variation	Typical	Variation
H	wt. %, dry	5.9	5.4–6.4	5.8	5.2–6.1	5	3–6
C		47.5	47–48	50	49–52	88	69–93
N		0.7	0.3–1.5	0.3	0.1–0.7	1.5	1–1.8
S		0.15	0.1–0.2	0.05	<0.1	1	0.9–5
Cl		0.4	0.1–1.1	0.02	<0.1	—	0.04–0.17
Si		0.8	0.1–1.5	0.1	<1.0	2.10	—
Al		0.005	<0.03	0.015	<0.1	0.28	—
Fe		0.01	<0.03	0.015	<0.1	—	0.08–0.74
Ca		0.4	0.2–0.5	0.2	0.1–0.9	—	0.62–0.95
Mg		0.07	0.04–0.13	0.04	<0.1	—	0.57–0.78
Na		0.05	<0.3	0.015	<0.1	—	1.52–1.86
K		1.0	0.2–1.9	0.1	0.05–0.4	—	0.02–0.03
P		0.08	0.03–0.2	0.02	<0.1	—	—

Washing the biomass in water or acid will remove the soluble components, typically present as salts [98, 161–163]. Woody biomasses will have a tendency to bind the salts into the organic structure and thus leaching processes will be less effective than if applied to e.g. annual crops. Jenkins *et al.* [141] established how approximately 90 % of the potassium and chlorine content in high ash content fuels are present as water soluble salts.

2.2.3 Water Content

The water content of biomass, woody or agricultural, can be significant and thus impact the early stages of thermochemical conversion of biomass in combustion processes. Water can be present in the form of [150]:

1. Capillary liquid water in the pores.
2. Water vapor in the pores.
3. Hygroscopic (bound) water in the solid structure.

Among which the capillary and vaporous water can be assumed to be in the same potential energy state as it would be outside the biomass and which content to a large degree depends on the porosity of the structure. While the hygroscopic water, attached to hydroxyl sites in the cellulosic structure by hydrogen bonding, requires greater effort to evaporate. The extent of hygroscopic water varies with the macromolecular composition of the ligniocellulosic structure but can for fully saturated fibers exceed 30 wt. %.

2.3 Particle Size and Shape Characterization

Fuel characterization is of great importance in combustion modeling [164]. The particle size and shape influence both the thermal history of the particle and its fluid dynamic properties. Often simple 1D methods like sieving analyses are used to characterize the PSD of biomass samples. These methods, are known to provide results difficult to interpret due to the irregular shapes of the particles [131]. It is desirable to be able to describe the particle appearance using simple and standardized geometries. Based on studies in progress by Trubetskaya [165] a combination of characteristic lengths will be used to describe the typical biomass particle processed for PF combustion. Combining the results of microscopy, laser diffraction, 2D image projection analysis (CAMSIZER®), and sieve analysis, Trubetskaya [165] concluded that the best geometry to describe the oddly shaped biodust particles was a parallelepiped. The width described by the Martin minimum diameter, the thickness by 2/3 of the Martin minimum diameter, and the particle length by the maximum ferret diameter corrected by $\cos(\pi/4)$ as illustrated in figure 2.10. The CAMSIZER®equipment will be used as the base line for particle size characterization throughout the thesis. Comparisons will be made to the corresponding sieve analysis, as this remains to be the most widely used method for size characterization. The CAMSIZER®definitions of the diameters are summarizes in figures 2.7 and 2.8. The minimum chord, x_c, is also presented, cf. figure 2.9, and will be used during the thesis as a comparative measure for the e.g. the sieve analysis.

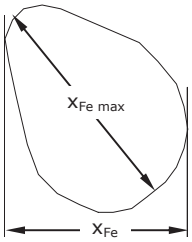

Feret diameter, x_{Fe} Distance between two tangents placed perpendicular to the measurement direction.
Maximum Feret diameter, $x_{\mathrm{Fe,max}}$ Teh greatest distance between two points on the circumference of the particle projection.

Figure 2.7 Illustrative and written definition of x_{Fe} and $x_{\mathrm{Fe,max}}$ [166].

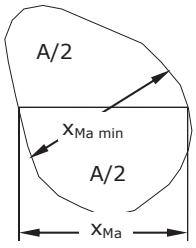

Martin diameter, x_{Ma} Length of the diameter through the centre of area in the measurement direction.
Minimum Martin diameter, $x_{\mathrm{Ma,min}}$ The shortest Martin diameter of all measured Martin diameters of a particle projection.

Figure 2.8 Illustrative and written definition of x_{Ma} and $x_{\mathrm{Ma,min}}$ [166].

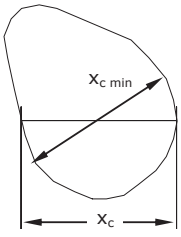

Maximum chord, x_{c} Length of the maximum chord perpendicular to the measurement direction.
Shortest maximum chord, $x_{\mathrm{c,min}}$ The shortest maximum chord of a particle projection measured from all measurement directions.

Figure 2.9 Illustrative and written definition of x_{c} and $x_{\mathrm{c,min}}$ [166].

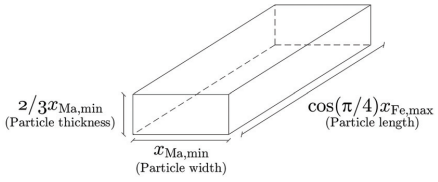

Figure 2.10 Characteristic lengths of a model particle based on the findings of [165] using the Martin minimum and ferret maximum diameters.

For simplicity the particle length can be approximated by an averaged aspect ratio of $9/2$ based on the $x_{\mathrm{Ma,min}}$ diameter, as suggested by Trubetskaya [165] as shown in figure 2.11.

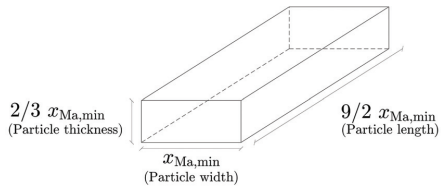

Figure 2.11 Characteristic lengths of a model particle based on the findings of [165] using solely the Martin minimum diameter.

Spherical Particles

Spheres has been widely used throughout the literature to describe the size of fuel particles. The sphere possesses unique mathematical features making it especially appealing as a model geometry used in computational simulations:

- The sphere can be characterized by a single variable, radius.
- The sphere has constant width and constant girth, neglecting the importance of orientation in space.
- All points of a sphere are umbilics (any point on a surface a normal direction is at right angles to the surface) making flux calculations as simple as possible, eliminating changes in any boundary effects.

In addition, the sphere has the largest volume to surface area ratio of any geometrical shape. Hence, approximating particle shapes by spheres without compensating in the physical properties of the fuel will inevitable lead to a conservative estimate of particle conversion in any state of combustion: heating, drying, devolatilization, or burn-out [167].

For the purpose of CFD implementation a single characteristic length, i.e. spherical geometry, is desired. The transformation is illustrated in figure 2.12 and several approaches may be used, as will be discussed later.

2.4 The GREEN Fuels

A selection of different fuels were prepared for laboratory experiments aiming to determine the devolatilization kinetics, cf. part II. Based on two parent fuels: A commercial wood pellet and a miscanthus grown by Aarhus University specifically for the power Generation from REnewable ENergy (GREEN) project.

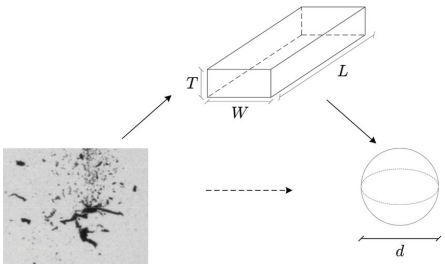

Figure 2.12 Describing oddly shaped particles in a single dimension [165]. The image is a CAMSIZER®2D projection of particles in free fall.

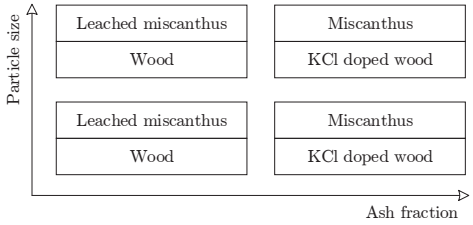

Figure 2.13 Qualitative overview of the parent fuels used in the devolatilization experiments in the EFR. Small/large particle sizes (sieve cut off): 63–90/106–125 μm. Ash content (dry) of wood/KCl-doped wood: $0.2/1.2 \pm 0.2$ wt. %. Ash content (dry) of miscanthus/leached miscanthus: $3.4/0.8 \pm 0.2$ wt. %

2.4.1 Miscanthus

The basic growth data for the crop has been listed in table 2.4 provided by Aarhus University. The harvest is a mix of experimental paired cells, hence, the double fertilizer values. Growth data is important, especially for annual crops, as the use of fertilizer, leaching in the field, etc. have been shown to influence on the properties of the biomass as a fuel [145]. The miscanthus has been supplied by the Department of Agroecology at Aarhus University, Denmark, as part of GREEN WP 1. The fuel is received from Aarhus after chipping and restored in sealed plastic barrels. The fuel has been dried prior to both chemical analysis and fuel storage.

2.4.2 Wood Pellets

The wood pellets are commercial products obtained from DCC Energi, Denmark: Premium Pellets, product no.: 020131, www.DCCenergi.dk. They have a diameter of 6 mm and do not contain any additives. They are extruded under high pressure and moist conditions, re-polymerizing the lignin content

Table 2.4 Basic growth data for the miscanthus fuel.

Variant:	Miscanthus x giganteus
Established:	1994
Harvest frequency:	Annually
Time of harvest:	March 6, 2012
Fertilizer:	0.75 kg N/Ha annually
	150 kg N/Ha annually
Harvest:	No remarks

to work as particle binder.

2.4.3 Fuel Treatment

Selected fuels have been further treated at the DTU Chemical Engineering laboratory facilities for the purpose of mineral enriching or leaching.

Fuel Leaching

Leaching of miscanthus and the wood pellets has been carried out. The objective was to demineralize the samples to as great an extend as possible in water. The approaches are similar, but wood pellets have been leached in ultra pure water while the miscanthus has been leached in deionized water and washed in ultra pure water.

The fuels were leached in 15 litres plastic buckets. The bucket was half filled with fuel (without compression) and completely filled with water (ultra pure or deionized depending on the fuel). The bucket was sealed of by a lid with a center hole. A propeller was inserted through the lid and vigorous stirring was applied. The water was changed every 24 hours until a total of 72 hours was reached. The water was drained and the fuel was washed with ultra pure water on a sieve. Afterwards the fuel was dried at 60 °C until reaching a moisture level below 2 wt. %.

Fuel Doping

Fuel doping was applied to the wood pellets. The objective was to dope the material with KCl to increase the ash level corresponding to energy crops: Aiming for 1.5 wt. % KCl. The 6 mm pellets were cut down in a mill cutter using a 4 mm screen. Using a büchner funnel and a low powered vacuum pump the cut material was found to hold an estimated 110 g of water per 100 g of fuel. A 73.8 mM solution of KCl in ultra pure water was prepared and the material was left to soak briefly. Excess solution was drained by means of a büchner funnel, a low powered vacuum pump, and a fibre glass filter with a 0.75 μm cut-off. The wet cake was left to dry at 60 °C until the moisture content had dropped below 2 wt. %.

2.4.4 Fuel Analysis

All analyses have been conducted according to international standards listed in table 2.5 and the reported expanded uncertainty provides a level of confidence of approximately 95 %.

Table 2.5 Overview of standards used for proximate and ultimate analysis.

Parameter	Standard
Moisture	EN 14774-1 (2009)
Ash	DS/EN 14775 (2009)
Volatiles	DS/EN 145148 (2009)
HHV, LHV	EN 14918 (2010)
C, H, N	CEN/TS 15104 (2011)
Al, Ca, Fe, K, Mg, Na, P, Si, Ti	CEN/TS 15290 (2006)
Cl, S	CEN/TS 15289 (2011)

Proximate Analyses

The proximate analyses are listed in table 2.6 for all fuels. The moisture content data reflect the moisture content of the fuels as received. The fuels have been hot air dried prior to sample preparation for easy grinding. All other results are given on a dry matter basis.

Table 2.6 Proximate analysis of the two parent fuels.

	Unit	Wood	Miscanthus
Moisture	wt. %	4.0	27.0
Ash	wt. % (dry)	0.2	3.4
Volatile		82.4	77.8
HHV	MJ/kg	19.75	14.07
LHV		18.36	12.45

Ultimate Analyses

Table 2.7 summarizes the ultimate analysis data for all four fuels. All data are given on a dry matter basis.

Leaching and Doping of Wood Pellets

Tables 2.8 and 2.9 list the proximate and ultimate analysis for the fuel treatment of wood pellets. Graphical illustrations are presented in figures 2.14 and 2.15.

Table 2.7 Ultimate analysis of the two parent fuels.

	Unit	Wood		Miscanthus	
C	wt. % (dry)	51.5	±0.003	48.5	±1.5
H		6.2	±0.2	6.0	±0.2
N		< 0.20	—	0.45	±0.10
S	ppmw (dry)	70.	±30	650	±70
Cl		160	±20	3000.	±300
Al		32	—	270.	—
Ca		950	±60	1100	—
Fe		26	±5	270	—
K		480	±30	7900	—
Mg		140	±10	540	—
Na		95	±10	340	±30
P		52	±8	740	±60
Si		< 200	—	6200	±600
Ti		< 5.0	—	313	±4

Table 2.8 Fuel analysis of leached wood pellets compared to the original fuels. Reductions are listed based on mass.

		Virgin	Leached	Reduction [%]
Ash	wt. % (dry)	0.2	< 0.1	> 50
Volatiles		82.4	85	−3.16
C	wt. % (dry)	51.5	52.3	−1.55
H		6.2	6.2	0.0
N		< 0.20	< 0.20	n/a
S	ppmw (dry)	70	50	29
Cl		150	< 20	> 86.7
Al		32	13	59
Ca		950	340	64.2
Fe		26	28	−7.7
K		480	49	89.8
Mg		140	21	85.0
Na		95	12	87
P		52	< 20	> 62
Si		< 200	< 200	n/a
Ti		< 5.0	< 5.0	n/a

Table 2.9 Fuel analysis of doped wood pellets compared to the original fuels. Increments are listed based on mass.

		Virgin	Doped	Increase [%]
Ash	wt. % (dry)	0.2	1.2	500
Volatiles		82.4	77.6	−5.83
C	wt. % (dry)	51.5	51.7	0.388
H		6.2	6.2	0
N		< 0.20	< 0.2	n/a
S	ppmw (dry)	70	70	0
Cl		150	4700	3033
Al		32	20	−38
Ca		950	430	−54.7
Fe		26	36	38
K		480	5700	1088
Mg		140	40	−71.4
Na		95	33	−65
P		52	< 20	> −62
Si		< 200	< 200	n/a
Ti		< 5.0	< 5.0	n/a

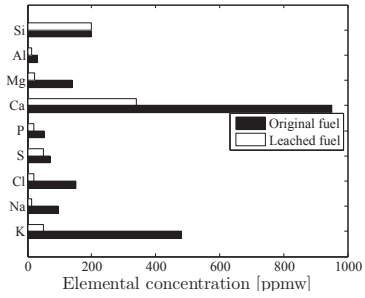

Figure 2.14 Comparison of inorganic content present in the virgin wood pellet fuel and the leached fuel sample.

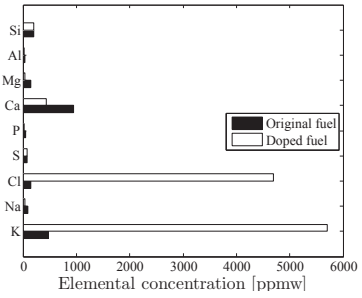

Figure 2.15 Comparison of inorganic content present in the virgin wood pellet fuel and the doped fuel sample.

Leaching of Miscanthus

Table 2.10 lists the proximate and ultimate analysis for the fuel treatment of miscanthus. A graphical illustration is presented in figure 2.14.

Table 2.10 Fuel analysis of leached miscanthus compared to the original fuels. Reductions are listed based on mass.

		Miscanthus	Leached	Reduction
Ash	wt. % (dry)	3.4	0.8	76.47
Volatiles		77.8	85.7	−10.15
C	wt. % (dry)	48.5	49.9	−2.89
H		6	6.1	−1.7
N		0.45	0.31	31.1
S	ppmw (dry)	650	270	58.5
Cl		3000	70	97.7
Al		270	< 10	> 96
Ca		1100	870	20.9
Fe		270	180	33.3
K		7900	330	95.8
Mg		540	330	38.9
Na		340	< 10	< 97.1
P		740	200	73.0
Si		6200	2100	66.1
Ti		13	< 5.0	> 62

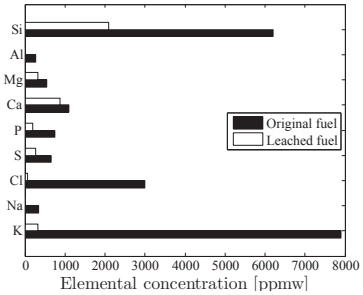

Figure 2.16 Comparison of inorganic content present in the virgin miscanthus fuel and the leached fuel sample.

2.4.5 Parent Fuel Particle Shapes and Sizes

The particle size plays a central role as intrinsic kinetics at PF-combustion relevant reaction conditions can only be studied from thermally thin particles.

Both the miscanthus and the wood samples were cut and sieved into two size fractions using Retsch wire mesh test sieves:

- 63–90 μm
- 106–125 μm

Figures 2.17 and 2.18 show representative scanning electron microscopy (SEM) images of all fuel types included in the present study. A majority of elongated particles can be seen making any conclusion based on the sieve cut off difficult. 2-dimensional image analysis tools have been employed in order to assist the particle size characterization and in an attempt to describe the particle shape.

Characteristic Lengths

Yin *et al.* [168] investigated biomass particles a few hundred microns in diameter concluding that intra-particle gradients of heat and mass to be a secondary issue at most. Thus, although increasing the particle size has been shown to influence conversion to noticeable degree [169, 170], if pretreated carefully to small enough particle sizes such issues can be avoided.

Tables 2.11 and 2.12 summarize a range of characteristic data describing the wood and miscanthus based fuels used in the devolatilization study. All data are based on the CAMSIZER XT®output and takes starting point in a rectangular parallelepiped particle, cf. figure 2.10.

The volume equivalent sphere is the most commonly met method for representing non-spherical particles in numerical systems limited to accommodate 1-dimensional geometries in the discrete phase [168]. However, because of the highly irregular particle shapes of biomass this approximation of fixed volume imposes significant deviations in the volume to surface area (V/A) ratio. This will also increase the equivalent diameter while limiting the surface area exposed for heat exchange, effectively increasing the Biot number further challenging the assumption of an isothermal particle.

The purpose of the present study is to accurately model the particle temperature history as it undergoes fast heating by entraining a pilot flame. Thus, it is desirable to maintain a constant Biot number, i.e. heat transfer rate to the particle relative to the rate at which the heat is transported into the particle. Describing the fuel as spherical particles with the same volume to surface area ratio as the original rectangular parallelepiped shape characterized by the CAMSIZER XT®will satisfy this requirement.

As can be seen from tables 2.11 and 2.12 the diameter for a fixed V/A equivalent sphere correspond well to the minimum Martin diameter, $x_{\mathrm{Ma,min}}$ obtained as a direct output from the CAMSIZER XT®raw data treatment. For simplicity the $x_{\mathrm{Ma,min}}$ diameter will be used to represent the particle diameter of a fixed V/A ratio equivalent sphere.

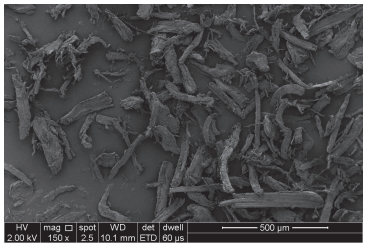

(a) Wood.

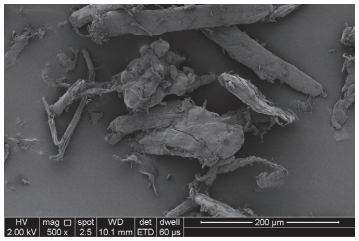

(b) Wood.

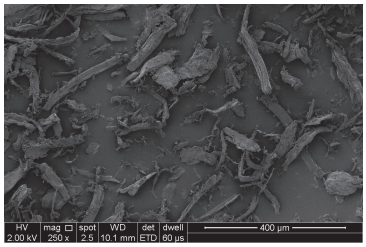

(c) KCl-doped wood.

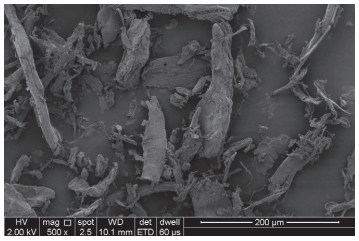

(d) KCl-doped wood.

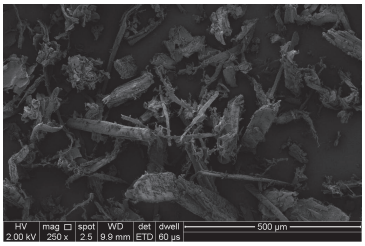

(e) Miscanthus.

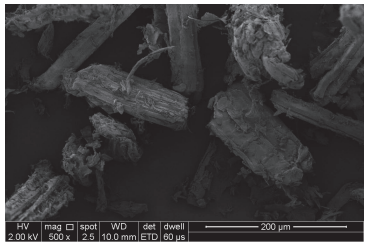

(f) Miscanthus.

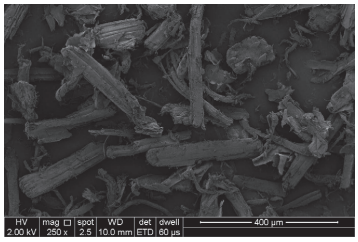

(g) Leached miscanthus.

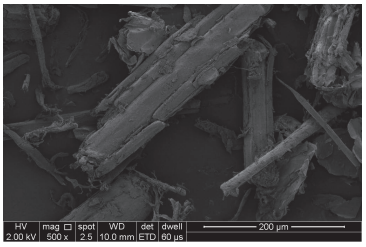

(h) Leached miscanthus.

Figure 2.17 SEM images of the GREEN fuels in the size fraction: 63–90 um.

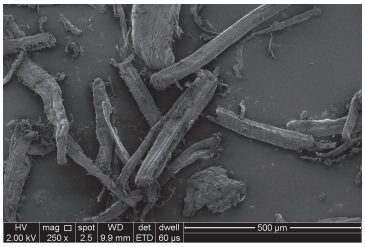

(a) Wood.

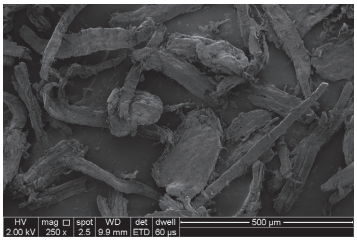

(b) Wood.

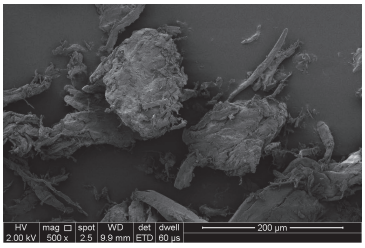

(c) KCl-doped wood.

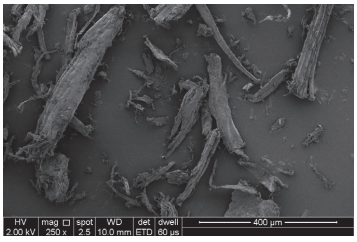

(d) KCl-doped wood.

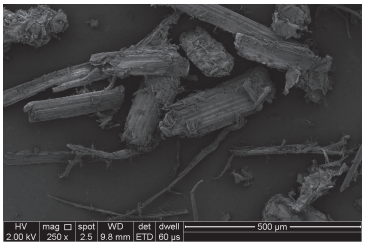

(e) Miscanthus.

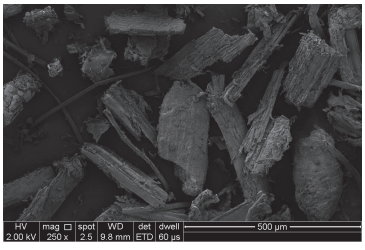

(f) Miscanthus.

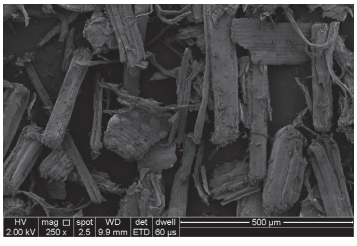

(g) Leached miscanthus.

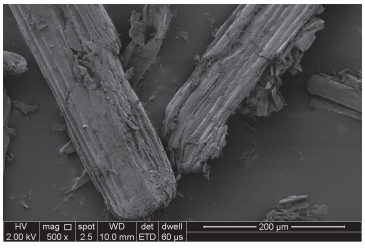

(h) Leached miscanthus.

Figure 2.18 SEM images of the GREEN fuels in the size fraction: 106–125 um.

Table 2.11 Characteristic shape and size data for the woody fuels used for the devolatilization study. $x_{\mathrm{Fe,max}}$: Maximum Feret diameter, $x_{\mathrm{Ma,min}}$: Minimum Martin diameter, V: Calculated volume based on the relevant particle shape, A: Calculated surface area based on the relevant particle shape, d: Diameter, SF: Shape factor $A/A_{\text{rectangular parallelpepied}}$, NC: Number correlation $V/V_{\text{rectangular parallelpepied}}$.

Fuel		Wood		Wood, KCl	
Sieve size cut off μm		63-90	106-125	63-90	106-125
Rectangular Parallelepiped					
$x_{\mathrm{Fe,max}}$	μm	153	294	118	199
$x_{\mathrm{Ma,min}}$	μm	53.6	78.9	45.9	63.2
$2/3x_{\mathrm{Ma,min}}$	μm	35.8	52.6	30.6	42.1
V	$\mu\mathrm{m}^3$	293 804	1 218 414	165 750	528 294
A	$\mu\mathrm{m}^2$	31 224	85 534	20 863	47 135
V/A	μm	0.106	0.070	0.126	0.089
Volume equivalent sphere					
$d_{\mathrm{eq,vol}}$	μm	82.5	133	68.2	100
V	$\mu\mathrm{m}^3$	293 804	1 218 414	165 750	528 294
A	$\mu\mathrm{m}^2$	21 373	55 167	14 592	31 603
V/A	μm	13.7	22.1	11.4	16.7
SF	—	0.68	0.64	0.70	0.67
Parallelepiped thickness equivalent sphere					
$d_{2/3\mathrm{Ma,min}}$	μm	35.8	52.6	30.6	42.1
V	$\mu\mathrm{m}^3$	23 938	76 121	15 007	39 109
A	$\mu\mathrm{m}^2$	4017	8686	2942	5572
V/A	μm	5.96	8.76	5.10	7.02
SF	—	0.13	0.10	0.14	0.12
NC	—	12	16	11	14
Fixed V/A equivalent sphere					
d	μm	56.6	85.7	47.6	67.4
V	$\mu\mathrm{m}^3$	94 959	329 730	56 538	160 429
A	$\mu\mathrm{m}^2$	10 066	23 081	7124	14 278
V/A	μm	0.106	0.0700	0.126	0.0890
SF	—	0.32	0.27	0.34	0.30
NC	—	3.1	3.7	2.9	3.3

Table 2.12 Characteristic shape and size data for the miscanthus fuels used for the devolatilization study. $x_{\mathrm{Fe,max}}$: Maximum Feret diameter, $x_{\mathrm{Ma,min}}$: Minimum Martin diameter, V: Calculated volume based on the relevant particle shape, A: Calculated surface area based on the relevant particle shape, d: Diameter, SF: Shape factor $A/A_{\text{rectangular parallelpepied}}$, NC: Number correlation $V/V_{\text{rectangular parallelpepied}}$.

Fuel		Mischanthus		Miscanthus, leached	
Sieve size cut off μm		63-90	106-125	63-90	106-125
Rectangular Parallelepiped					
$x_{\mathrm{Fe,max}}$	μm	116	297	150	308
$x_{\mathrm{Ma,min}}$	μm	52.7	90.8	58.9	86.0
$2/3x_{\mathrm{Ma,min}}$	μm	35.2	60.6	39.3	57.3
V	$\mu\mathrm{m}^3$	214 836	1 632 954	347 801	1 517 722
A	$\mu\mathrm{m}^2$	24 077	100 889	34 151	98 097
V/A	μm	0.112	0.062	0.098	0.065
Volume equivalent sphere					
$d_{\mathrm{eq,vol}}$	μm	74.3	146	87.3	143
V	$\mu\mathrm{m}^3$	214 836	1 632 954	347 801	1 517 722
A	$\mu\mathrm{m}^2$	17 347	67 060	23 917	63 867
V/A	μm	12.4	24.4	14.5	23.8
SF	—	0.72	0.66	0.70	0.65
Parallelepiped thickness equivalent sphere					
$d_{2/3\mathrm{Ma,min}}$	μm	35.2	60.6	39.3	57.3
V	$\mu\mathrm{m}^3$	22 754	116 265	31 700	98 693
A	$\mu\mathrm{m}^2$	3883	11 520	4844	10 328
V/A	μm	5.86	10.1	6.54	9.56
SF	—	0.16	0.11	0.14	0.11
NC	—	9.4	14	11	15
Fixed V/A equivalent sphere					
d	μm	53.6	96.8	61.2	92.3
V	$\mu\mathrm{m}^3$	80 500	474 545	120 164	411 825
A	$\mu\mathrm{m}^2$	9016	29 422	11 776	26 769
V/A	μm	0.1120	0.0620	0.0980	0.0650
SF	—	0.37	0.29	0.34	0.27
NC	—	2.7	3.4	2.9	3.7

Particle Size Distributions

The characteristic length describing a sphere with similar V/A_{eq}-ratio as the biomass particle can be approximated by the Martin minimum diameter, $d_{\mathrm{Ma,min}}$, as discussed in the work of Trubetskaya [171]. A Rosin-Rammler distribution is used to describe the particle size distribution. The Rosin-Rammler distribution function is given as:

$$Y_{\mathrm{d}} = \exp\left[-\left(\frac{d}{\bar{d}}\right)^{n}\right] \tag{2.2}$$

where $\bar{d}$ and n are the Rosin-Rammler mean diameter and distribution spread. Figure 2.19 shows the CAMSIZER XT®analyses of the GREEN fuels and the fitted Rosin-Rammler distributions. A summary of the distribution parameters is listed in table 2.13.

Table 2.13 Summary of the Rosin-Rammler parameters used to describe the GREEN fuels.

	$\bar{d}$	n	$\bar{d}$	n
	μm	—	μm	—
Size fraction	63–90		106–125	
Wood	53.6	2.41	78.8	2.45
Miscanthus	52.7	2.13	90.8	2.92
Wood KCl	45.9	1.92	63.2	2.00
Miscanthus leached	58.9	2.56	86.0	2.98

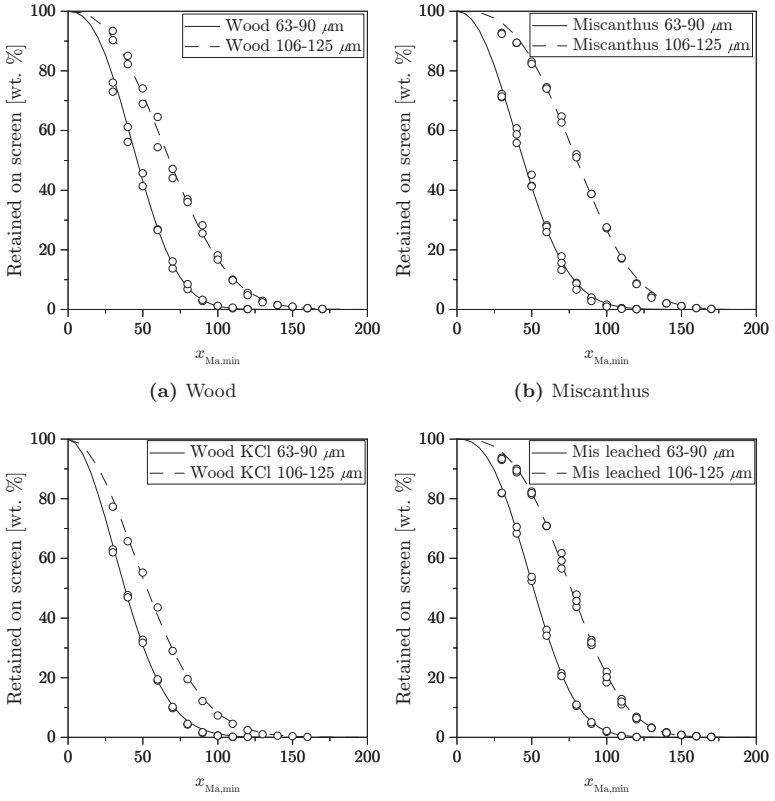

(a) Wood **(b)** Miscanthus

(c) Wood KCl **(d)** Miscanthus leached

Figure 2.19 PSD of the GREEN fuels. The fuels have been analyzed using the CAMSIZER XT©and a Rosin-Rammler distribution has bee fitted to the results. The Martin minimum diameter has been used as the characteristic length.

Part II

Devolatilization of Small Biomass Particles

"Everything should be made as simple as possible, but no simpler"

—Albert Einstein

CHAPTER 3

Introduction and Phenomenological Models

The thermochemical conversion of solid fuels to heat and combustion products includes a series of processes; from thermal degradation of the solid structure to the final oxidation of volatile gases and solid char [172, 173].

The high content of volatile material in biomass fuels makes the devolatilization a central process in the fuel conversion sequence [89, 150]. The majority of heat is released through the combustion of volatiles and thus the major flame characteristics rely on an accurate prediction of the devolatilization.

This chapter will provide a brief introduction to biomass devolatilization and go through some of the efforts on pyrolysis modeling made in the literature.

3.1 Introduction

Solid fuel conversion by thermal processes has been studied for centuries. Being able to utilize combustion processes for the production of heat and power facilitated the industrial revolution and remain to be a central part of today's society [173]. As such, much of the knowledge and tools used to study the thermal conversion of biomass were originally developed for coal combustion. Although the conversion of biomass and coal does share many common features, recall the outline of the general combustion process from chapter 1, the properties of biomass do deviate from those of coal in a number of central ways, as pointed out in chapter 2. Therefore, the transition from coal to biomass requires a renewed effort in particle conversion research. The changes in both chemical and physical properties comprise a series of deviations from conventional coal combustion, potentially affecting the conversion process. Most noticeable is probably the shift in the volatile/char/ash ratios.

Understanding the chemistry and the reaction regimes of biomass thermal conversion have been the subjects of many studies throughout recent decades. A number of reviews are available on the subject [73, 174–178].

A conception of biomass thermally degrading into three main species has been adopted from coal combustion: Gas, tar, and char. These groups of reaction products lump together all species within their respective categories. The ratio between these groups varies with temperature [63–65], chemical composition [69], ash composition [156, 157], heating rate [73, 74]; and thus in turns particle size [117–119, 179], particle shape [63, 180], moisture content [63] to mention a few.

This chapter will focus on the kinetic description of the biomass devolatilization. Oxidation of volatiles constitutes the major heat release in biomass combustion [181]. Thus being able to describe the devolatilization process is an important part of understanding biomass combustion. Carrying out experiments on small particles reduces transport limitations. Hence, effectively reacting under chemical control.

An exhaustive review is scarcely possible due to the number of studies available. Hence, this work will not attempt to report all findings but rather present results from studies using related fuels. In line with the overall objective to link general fuel properties to flame properties, the following review will also focus on general trends applicable across fuel types, experimental set-ups, etc.

3.2 Modeling Isothermal Particle Devolatilization

Pyrolysis, or devolatilization, is the thermochemical decomposition of organic material. Only few studies distinguish the terminology defined as thermal decomposition in reducing and oxidizing environments, respectively. At high heating rates and temperatures the decomposition of biomass takes place rapidly releasing reducing volatiles. In oxidizing conditions the produced volatiles will either be in stoichiometric excess to the available oxygen or convectively displace it. Thus creating a local reducing environment, making the distinction somewhat ambiguous. Interchangeable use of the two terms will be used throughout the thesis, much in line with most of the literature.

3.2.1 Modeling Devolatilization of Biomass

The mathematical description of the devolatilization process of biomass poses difficulties due to the complexity of the biomass structures, the diversity of fuels, and the inhomogeneous nature of biomass, as described in chapter 2.

The devolatilization process is, therefore, usually described by phenomenological models which can vary in complexity, requirements for input parameters, and available data used to validate or evaluate the model. In general, the models can be divided in to three categories:

- Step-wise mechanisms
- Superposition models
- Chemical structure based models

The structural models such as the CPD or the advanced biomass and coal devolatilization (ABCD) models are high in complexity, computationally demanding, and require a comprehensive fuel characterization [182]. Therefore,

they will not be included in this study, which aims for low cost methods to describe particle devolatilization.

The Step-Wise Mechanisms

This is probably the most commonly used category of devolatilization mechanisms. It also covers the widest range of proposals for mechanisms. To maintain an overview, the step-wise mechanisms can be further sub-divided into several categories:

- Global mechanism
- Single step, semi-global mechanism (parallel reactions)
- Multi step, semi-global mechanisms (consecutive reactions)
- Infinite reactions

The first three types of step-wise mechanisms use predefined reactions and require rate expressions to be derived specifically for each reaction. The semi-global mechanisms can be combined to express different degrees of complexity. The latter of the four employ an infinite number of parallel reactions with the kinetics expressed as distributions. This has the advantage of being able to cover a wider span of operational conditions; temperature, heating rate, etc. and does not require the isolation of kinetic expression for individual reactions. Detailed reviews on model studies can be found in the literature [63, 150, 183].

Single n^{th} order reaction The single n^{th} order reaction (SNOR) model is the simplest category of models available. As illustrated in figure 3.1, it reacts the parent fuel to products in a single global reaction.

$$\text{Parent fuel} \xrightarrow{\quad k \quad} \text{Char} + \text{Volatiles}$$

Figure 3.1 The SNOR mechanism.

The reaction can be described as:

$$\frac{\mathrm{d}\chi}{\mathrm{d}t} = k f(\chi) \tag{3.1}$$

where the rate of conversion $\dot{\chi}$ is driven by the available volatile matter, $f(\chi)$, related by the rate constant, k. The rate constant, k, is usually modeled as a function of temperature. The equation of choice in chemical engineering is the Arrhenius expression:

$$k\,(T) = A \exp\left[\frac{-E_{\mathrm{a}}}{RT}\right] \tag{3.2}$$

where the fitting parameters A and E_a are detoned the pre-exponential factor and the activation energy respectively. Although many other expressions can be found [184] most rely on an exponential temperature dependency.

The driving force of the reaction, $f(\chi)$, is usually modeled as:

$$f(\chi) = (\chi^* - \chi)^n \tag{3.3}$$

where χ^* denotes the total amount of available reactant. If the reaction order, n, assumes unity the simplest form of the single step global mechanism arises: The single first order reaction (SFOR):

$$\frac{\mathrm{d}\chi}{\mathrm{d}t} = A \exp\left[\frac{-E_a}{RT}\right](\chi^* - \chi) \tag{3.4}$$

For linear heating profiles, such as the ones found in TGA experiments, equation (3.4) can be linearized into:

$$\ln\left[\frac{-1}{\chi^* - \chi}\frac{\mathrm{d}\chi}{\mathrm{d}t}\right] = \ln[A] - \frac{E_a}{RT} \tag{3.5}$$

knowing that:

$$T(t) = \beta t + T_0 \tag{3.6}$$

expressing the linear relationship between time, t, and temperature, T, with the slope β. This is known as the differential method and is easily applicable to TGA experiments, where a plot of the left hand side of equation (3.5) versus the inverted temperature, should give a straight line with a slope of $-E_a/R$ and intercepting $T^{-1} = 0$ at $\ln[A]$.

However, considering arbitrary temperature histories requires an approximation of the temperature integral arising when (3.4) is integrated:

$$I = \int_0^t A \exp\left[\frac{-E_a}{RT(t')}\right] \mathrm{d}t' \tag{3.7}$$

which has no closed analytical solution [184–187]. This mathematically intractable temperature integral is probably the biggest shortcoming of the Arrhenius expression. Multiple suggestions for solving the integral have been proposed [184, 187–194]. A good approximation to equation (3.7) is important because the temperature integral sums up the cumulative contribution of the rate constant to the overall reaction. This implies that the integral must be adequately solved in order to determine the devolatilization history.

Most frequently met are studies related to linear temperature increments at moderate temperatures [191]. In these systems the temperature of the particle is justifiably believed to assume the temperature of the reactor. In addition, the sample particle sizes are small enough to eliminate heat transport limitations. However, for more practical applications a fully coupled system of

heat transport and chemical reactions implies a much more complex thermal history. A number of numerical approaches have been suggested [189, 190], generally proposing to incorporate the instantaneous local temperature and heating rate provided by a suitable transient transport model. Thus, evaluating the temperature integral recursively. Equation (3.7) can be discretized into:

$$I = \sum_{i=1}^{N} \int_{t_{i-1}}^{t_i} A \exp\left[\frac{-E_\mathrm{a}}{RT\left(t'\right)}\right] \mathrm{d}t' \tag{3.8}$$

where indices 0, i, and N denote time zero, past, and elapsed.

Niksa and Lau [190] evaluates the integrals of equation (3.8) by Laplace's method and arrives at:

$$I = \sum_{i=1}^{N} \frac{AR}{E_\mathrm{a}} \left(\frac{T_{i+1}^2 \exp\left[\frac{-E_\mathrm{a}}{RT_{i+1}}\right]}{\frac{\mathrm{d}T_{i+1}}{\mathrm{d}t}} - \frac{T_i^2 \exp\left[\frac{-E_\mathrm{a}}{RT_i}\right]}{\frac{\mathrm{d}T_i}{\mathrm{d}t}} \right) \tag{3.9}$$

thus, allowing for the evaluation of I if the absolute temperature and the heating rate are known at discrete times.

Braun and Burnham [189] approximate equation (3.8) by linear interpolation of T between discrete times, which for constant temperature[1] can be expressed as:

$$I = \sum_{i=1}^{N} A \exp\left[\frac{E_\mathrm{a}}{RT}\right] \left(t_i - t_{i-1}\right) \tag{3.10}$$

Single step, semi-global mechanisms The two greatest inadequacies of the SNOR model are the inability to describe the formation and destruction of the major product categories: Char, tar, and volatiles, and the difficulties describing larger intervals of temperature and heating rates. This has, among others, been addressed by Chan *et al.* [129], Biagini [182], Shafizadeh [195], Thurner and Mann [196], Font *et al.* [197] who divided the the primary mass loss into the production of the three major product phases, each with their individual rate expression, allowing the competing reactions to appropriately predict the ratios between these categories of products, figure 3.2.

Multiple step, semi-global mechanisms This is by far the largest group of kinetic schemes including suggested mechanisms of a variety of complexities. From an additional activation step [198] to large reactions schemes of multiple reactions and species [199–201]. This section will only cover the most relevant

[1]The assumption of constant temperature, $\Delta T = T_i - T_{i-1} = 0$, can be justified for small time steps.

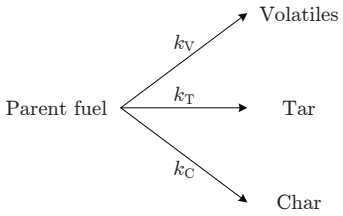

Figure 3.2 Kinetic scheme for the primary pyrolysis of solid fuels [195].

mechanisms for PF combustion, i.e. simplified mechanisms with emphasis on char yield and mass loss rate.

One of the more common models is build on the mechanism presented in figure 3.2 but includes an additional consecutive thermal cracking reaction of the tar [196], satisfying empirical observations of peak concentrations of tar [74], cf. figure 3.3. Alternatively, the SNOR or SFOR model can be coupled directly to a tar cracking mechanisms [202].

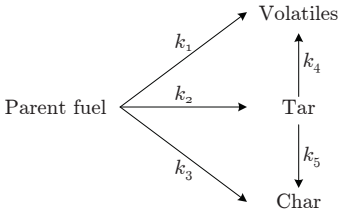

Figure 3.3 Kinetic scheme for the primary and secondary pyrolysis of solid fuels [196].

The Broido-Shafizadeh kinetic scheme [71, 203] modified by Bradbury *et al.* [198] and later by Liden *et al.* [204] includes tar secondary cracking is another widely used model for solid fuel pyrolysis. As see in figure 3.4 this model features not only a secondary tar cracking but also an activation step. From a modeling point of view, this yields the opportunity to tune the model to provide the correct tar yield, however fixed, and include a delay of the process onset through the activation step. The idea of introducing an activation step has been disputed during the years. Antal and Várhegyi [73], Várhegyi *et al.* [205] claimed that better fits to experimental data could be obtained without the activation step.

The Distributed Activation Energy Model The distributed activation energy model (DAEM) [206] model operates under the assumption that the thermal degradation of any fuel takes place through many different reactions

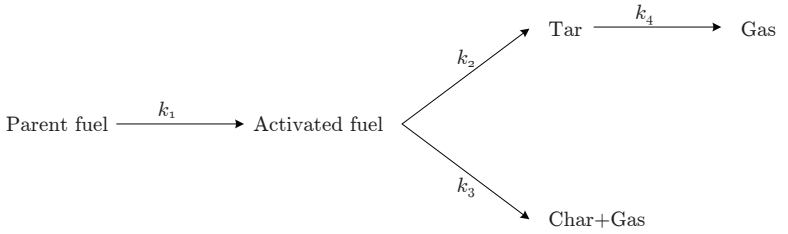

Figure 3.4 The modified Broido-Shafizadeh kinetic scheme for the primary and secondary pyrolysis of solid fuels [198, 204].

governed by the variations in bond strengths within the complex organic structure. It relies on many years of experience with the SFOR model being able to describe the decomposition of a single fuel organic species at a set of given reaction conditions. Thus, reaction i adopts the SFOR kinetic expression, which in its integral form can be written:

$$\chi_i^* - \chi_i = \chi_i^* \exp\left[-\int_0^t k_i \mathrm{d}t'\right] \tag{3.11}$$

Simplifying the task of deriving kinetics for each of the reactions i the rate constant k is assumed to differ only in activation energy, E_a. The distributed activation energy model (DAEM) model assumes that the number of reactions taking place is great enough to describe the change in activation energy as a continuous distribution function, $f(E_\mathrm{a})$. This would allocate available volatile matter to each of the individual reactions i. Thus, the total amount of matter available for release is taken to be a distribution satisfying:

$$\mathrm{d}\chi^* = \chi^* f\left(E_\mathrm{a}\right) \mathrm{d}E_\mathrm{a} \tag{3.12}$$

where

$$\int_0^\infty f\left(E_\mathrm{a}\right) \mathrm{d}E_\mathrm{a} = 1 \tag{3.13}$$

Combining equations (3.11) and (3.12) yields an expression for the global conversion up to time t by integrating equation (3.11) over all values of E_a using equation (3.12):

$$\chi^* - \chi = \chi^* \int_0^\infty \exp\left[-\int_0^t k\left(E_\mathrm{a}, T\left(t'\right)\right) \mathrm{d}t'\right] f\left(E_\mathrm{a}\right) \mathrm{d}E_\mathrm{a} \tag{3.14}$$

or on its differential form:

$$\frac{\mathrm{d}\chi}{\mathrm{d}t} = \chi^* \int_0^\infty k\left(E_\mathrm{a}\right) \exp\left[-\int_0^t k\left(E_\mathrm{a}, T\left(t'\right)\right) \mathrm{d}t'\right] f\left(E_\mathrm{a}\right) \mathrm{d}E_\mathrm{a} \tag{3.15}$$

Multiple proposals for suitable distribution functions have been tested with the gaussian [188–190, 206] and the natural logarithmic [153] distributions among the most popular:

$$f\left(E\mathrm{a}\right) = \frac{1}{\sigma\sqrt{2\pi}} \exp\left[\frac{-\left(E_\mathrm{a} - \bar{E}_\mathrm{a}\right)^2}{2\sigma^2}\right] \tag{3.16}$$

$$f\left(E\mathrm{a}\right) = \frac{1}{\sqrt{2\pi\sigma^2 E_\mathrm{a}^2}} \exp\left[\frac{-\left(\ln\left(E_\mathrm{a}\right) - \mu\right)^2}{2\sigma^2}\right] \tag{3.17}$$

Because the DAEM model is based on equation (3.4), the method also inherits the intractable temperature integral of equation (3.7). However, the approach of solving this integral is the same as in the case of the SFOR modeling and has been the scope of many previous studies [188–190, 192, 193] specifically using the DAEM model.

3.2.2 Thermal Decomposition of Biomass Components

A great number of investigations have taken starting point in the biological macromolecular composition of biomass fuels. This method of studying biomass as a resulting structure of a few main sub-structures; cellulose, hemicellulose, and lignin [124], is one of the most widely used methodologies praised for its simplicity and ability to adapt across the diverse selection of biomass fuels. These three categories of biological macromolecules also make up the model components for kinetic studies of biomass pyrolysis and/or combustion, as will be presented in this section.

In general the three components, cellulose, hemicellulose, and lignin, posses quit different thermal properties, easily identified by e.g. the temperatures at which they will begin to thermally decompose [207], cf. table 3.1. This causes distinct behavior of each component in e.g. thermogravimetric analyses, making it possible to extract kinetic data from each component from both whole biomass and chemically isolated samples [208]. Most of the work conducted in this field using this approach assume that the thermal decomposition of each individual component happens independently of each other. A method which seems reasonable considering the general consensus of the literature authors.

Table 3.1 Decomposition temperatures of ligniocellulosic components [150].

Component	Decomp. temp K
Hemicellulose	498–598
Cellulose	598–648
Lignin	523–773

An overview of the content of each component (cellulose, hemicellulose, and lignin) is shown in figure 3.5. It should, however, be kept in mind that the variations are large even within the same biological species; susceptible to growth conditions, utilization of fertilizer, season of harvest, storage, transport, etc.

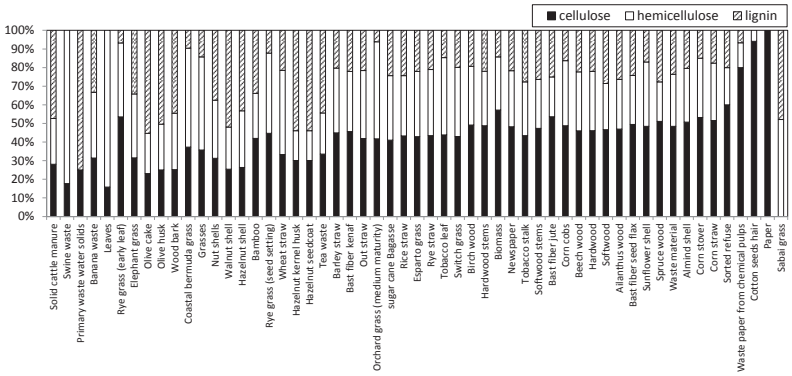

Figure 3.5 Macromolecular composition of different ligniocellulosic materials. Multiple literature sources.

A challenging subject when comparing kinetic properties between different biomasses is the possible catalytic effects of mineral matter [155]. This review of kinetic parameters has not given this matter any particular focus and kinetic data are listed along side each other regardless of its mineral content. This is, however, an obvious subject that requires attention for detailed kinetic analysis, and the subject will be discussed in later sections. However, in this case where a general model is desired and the fuel diversity in the experiments is large, it seems reasonable to analyse all sorts of bio-fuels on equal terms.

Pyrolysis of Cellulose

Cellulose is the most abundant organic macromolecular structure in most biomass material [124] and the effort on kinetic characterization of the thermal degradation of cellulose has been inherently high for decades. The process has been investigated by a great number of laboratories using different techniques and different sources of biomass. An overall image of the kinetic parameters using a global single step model is presented in figure 3.6. This figure, depicting the rate constant, k, as a function of the inverted temperature, shows large variations in the effective rate constant ranging across almost four orders of magnitude. Because the heating rates are similar, the temperature intervals in which the kinetics are valid will also be similar. Therefore, the kinetics are shown in a pre-defined temperature interval, but can only be considered

valid in the temperature intervals given in the specific studies. A trend of generally similar activation energies can however be identified by a broad band spanning across a couple of orders of magnitude in the rate constant. A tight connection between apparent activation energies and pre-exponential factors have been observed, cf. figure 3.7, similar to other studies [83].

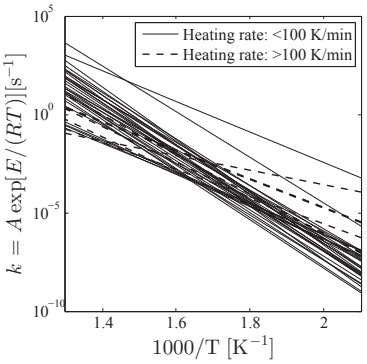

Figure 3.6 Cellulose global one step pyrolysis kinetics. References listed in table 3.4.

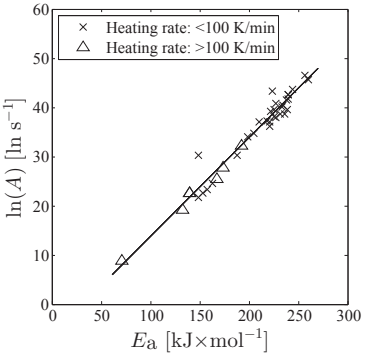

Figure 3.7 Relation between A and E_a for cellulose pyrolysis. References listed in table 3.4.

Milosavljevic *et al.* [83] observed a trend gathering literature data from multiple sources showing that heating rates above $15\,\mathrm{K}\cdot\mathrm{min}^{-1}$ resulted in lower activation energies. This survey adopts the same philosophy as heating rate and final temperature indeed will affect the charring processes [73–82] (char yield, plasticity, etc.). The threshold has however been increased to $100\,\mathrm{K}\cdot\mathrm{min}^{-1}$ as differences at lower heating rate have also been found to be minor in this study. This leads to an average apparent activation energy of 216 and $145\,\mathrm{kJ}\cdot\mathrm{mol}^{-1}$ at heating rates below and above $100\,\mathrm{K}\cdot\mathrm{min}^{-1}$ respectively.

Tables 3.2 and 3.3 summarize the statistics on the data included in figure 3.8 for data obtained under low and high heating rates respectively.

Pyrolysis of Hemicellulose

Significantly less kinetic data is available for thermal degradation of hemicellulose. Most results are derived from whole biomass kinetic studies where a typical derivative thermogravimetric investigation of ligniocellulosic material evidence two distinct peaks in mass loss [73]. A low temperature peak corresponding to the thermal decomposition of hemicellulose and a peak at moderate temperatures (350–500 °C) for cellulose decomposition. Rarely, three peaks may occur, in which case the two low temperature peaks typically can be related to hemicellulose decomposition [82] and not degradation of lignin

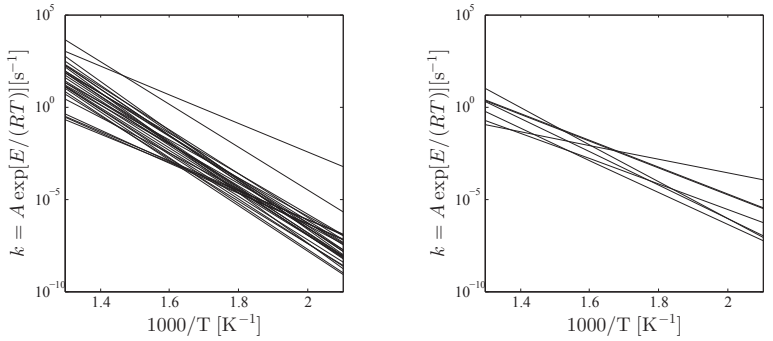

Figure 3.8 Literature comparison of single-reaction first order kinetics for thermal degradation of cellulose at figure 3.8a low ($< 100\,\mathrm{K}\cdot\mathrm{min}^{-1}$) and figure 3.8b high ($> 100\,\mathrm{K}\cdot\mathrm{min}^{-1}$) heating rates. References listed in tables 3.4 and 3.5.

Table 3.2 Summary of the kinetic parameters for global single step models for cellulose pyrolysis kinetics obtained at low heating rates as displayed in figure 3.8a. E_a, std., and A are the apparent activation energy, the standard deviation of E_a, and the pre-exponential factor, respectively.

	E_a $\mathrm{kJ}\cdot\mathrm{mol}^{-1}$	std. $\mathrm{kJ}\cdot\mathrm{mol}^{-1}$	$\log_{10} A$ $\log_{10}\mathrm{s}^{-1}$
Average	216	31.8	18.9
Min	149		9.43
Max	260		20.2

Table 3.3 Summary of the kinetic parameters for global single step models for cellulose pyrolysis kinetics obtained at high heating rates as displayed in figure 3.8b. E_a, std., and A are the apparent activation energy, the standard deviation of E_a, and the pre-exponential factor, respectively.

	E_a $\mathrm{kJ}\cdot\mathrm{mol}^{-1}$	std. $\mathrm{kJ}\cdot\mathrm{mol}^{-1}$	$\log_{10} A$ $\log_{10}\mathrm{s}^{-1}$
Average	145	39.2	13.2
Min	71.0		3.83
Max	192		14.0

Table 3.4 Summary of cellulose pyrolysis kinetic parameters at heating rates below $100\,\mathrm{K}\cdot\mathrm{min}^{-1}$. E_a and A are the apparent activation energy and the pre-exponential factor, respectively.

Heating rate $\mathrm{K}\cdot\mathrm{min}^{-1}$	Temperature °C	E_a $\mathrm{kJ}\cdot\mathrm{mol}^{-1}$	$\log_{10} A$ $\log_{10}\mathrm{s}^{-1}$	Ref.
7	298–341	149	13.1	[77]
10.9	<600	149	9.43	[75]
55	<600	153	9.85	[75]
5.65	<600	158	10.1	[75]
22.4	<600	163	10.7	[75]
—	—	199	14.8	[209]
80	<400	205	15.1	[82]
1–60	<700	210	16.1	[210]
2.16	<600	221	15.7	[75]
2–20	250–450	221	16.1	[73]
40	<358	222	17.0	[78]
0.23–2.4	295–330	223	18.8	[113]
1.25	<330	225	17.2	[81]
3–30	300–500	227	16.5	[80]
1–80	—	227	17.7	[76]
20	—	232	16.8	[73]
10	<400	234	17.6	[82]
10	—	236	16.8	[73]
2–80	—	238	18.0	[73]
10	—	239	17.2	[73]
2	200–400	240	18.5	[211]
10	200–400	240	18.5	[211]
50	200–400	240	18.1	[211]
5	<327	244	19.0	[78]
10	200–410	257	20.2	[212]
0.092–0.93	<327	218	16.2	[213]
5	<720	260	19.8	[214]
20	<720	233	17.4	[214]
40	<720	225	16.6	[214]
80	<720	188	13.2	[214]

Table 3.5 Summary of cellulose pyrolysis kinetic parameters at heating rates above $100\,\mathrm{K}\cdot\mathrm{min}^{-1}$. E_a and A are the apparent activation energy and the pre-exponential factor, respectively.

Heating rate $\mathrm{K}\cdot\mathrm{s}^{-1}$	Temperature °C	E_a $\mathrm{kJ}\cdot\mathrm{mol}^{-1}$	$\log_{10} A$ $\log_{10}\mathrm{s}^{-1}$	Ref.
iso	295–314	174	12.1	[208]
iso	359–370	192	14.0	[215, 216]
iso	257–322	167	11.1	[217]
1000	300–1000	133	8.30	[74]
7–167	250–1000	140	9.83	[90]

as is occasionally interpreted in the literature. Sole hemicellulose studies are most frequently conducted using xylan as model component with fairly good agreement to results derived from whole biomass.

Because of the more complex molecular structure of hemicellulose and indeed the large variations in decomposition properties, fitting first order, single step models to the thermal degradation is obviously a challenge. These physical constraints may solely explain the large variations in kinetic parameters observed in the literature. Figure 3.9 shows the kinetic rate constant following a typical Arrhenius expression as a function of the interved temperature. It is seen how the spread in the absolute value of the rate constant is as large as for the cellulose decomposition but with a much larger variation in apparent activation energy (slope of the curves). It is however worth noticing how the neat correlation between activation energy and pre-exponential factor is maintained, cf. figure 3.10. A wide spread in activation energies is also found for hemicellulose, as summarized in table 3.6.

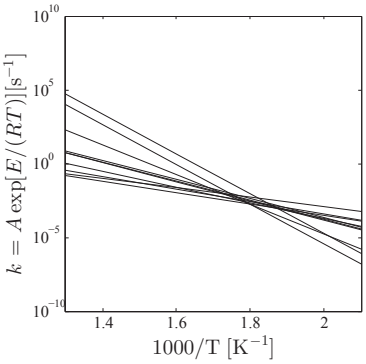

Figure 3.9 Hemi-cellulose global one step pyrolysis kinetics. References listed in table 3.7.

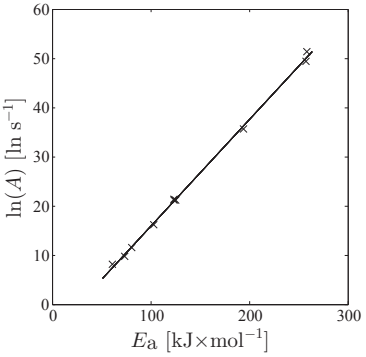

Figure 3.10 Relation between A and E_a for hemi-cellulose pyrolysis. References listed in table 3.7.

Pyrolysis of Lignin

Thermal decomposition of lignin takes place over a large temperature interval and thus is hard to distinguish in thermogravimetric measurements [219, 220] where lignin decomposition will typically occur as a broad peak seen as a slightly curvy baseline [82, 82, 221].

Lignin typically constitutes the lesser part of the three major component making up lignocellulosic material, and thus, also makes up little data in the literature in combustion applicable investigations. As seen from figure 3.11, showing the kinetic rate constant as a function of the inverted temperature, a

Table 3.6 Summary of the kinetic parameters for global single step models for hemicellulose pyrolysis kinetics as displayed in figure 3.9. E_a, std., and A are the apparent activation energy, the standard deviation of E_a, and the pre-exponential factor, respectively.

	E_a $kJ \cdot mol^{-1}$	std. $kJ \cdot mol^{-1}$	$\log_{10} A$ $\log_{10} s^{-1}$
Average	140	72.2	21.3
Min	61.5		3.51
Max	259		22.3

Table 3.7 Summary of hemicellulose pyrolysis kinetic parameters. E_a and A are the apparent activation energy and the pre-exponential factor, respectively.

Heating rate $K \cdot min^{-1}$	Temperature °C	E_a $kJ \cdot mol^{-1}$	$\log_{10} A$ $\log_{10} s^{-1}$	Ref.
10	270-360	124	9.29	[218]
10	270–360	61.5	3.51	[218]
10	270–360	73.8	4.21	[218]
10	270–360	80.7	5.01	[218]
10	270–360	103	7.05	[218]
30	300–500	124	9.16	[80]
5	<720	259	22.3	[214]
20	<720	257	21.4	[214]
40	<720	194	15.5	[214]
80	<720	125	9.21	[214]

large spread is seen in the effective rate constant, apparent activation energy, and pre-exponential factor, cf. figure 3.12 for the latter. An approximate spread of four orders of magnitude in rate constant is observed and with the usual good agreement between apparent activation energy and pre-exponential factor for data fitted using a global, single step degradation model.

In general, lignin pyrolysis has been found to have a lower activation energy than both cellulose and hemicellulose. The data has been summarized in table 3.8.

3.2.3 Thermal Decomposition of Whole Biomass

Biomass decomposition kinetics have been widely studied using whole biomass samples. Some have been described using a global, single step model, as will be discussed in this section, while others use more complex models; ranging from two parallel reaction models, semi-global functional group modeling and statistical link breakage modeling, to highly detailed chemical mechanisms. The choice of model, and more importantly the implied consequences, is a classical trade of between accuracy, diversity, and computational demands.

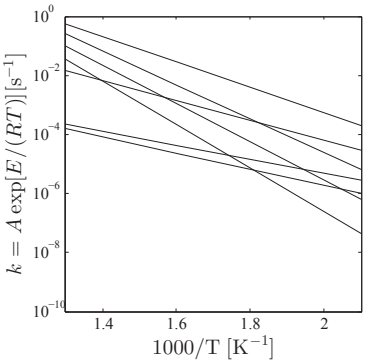

Figure 3.11 Lignin global one step pyrolysis kinetics. References listed in table 3.9.

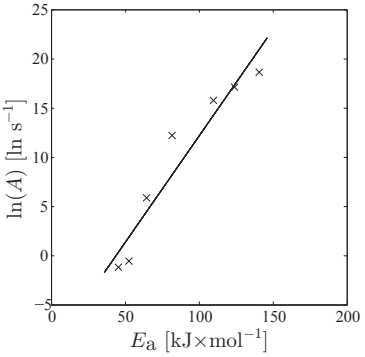

Figure 3.12 Relation between A and E_a for lignin pyrolysis. References listed in table 3.9.

Table 3.8 Summary of the kinetic parameters for global single step models for lignin pyrolysis kinetics as displayed in figure 3.11. E_a, std., and A are the apparent activation energy, the standard deviation of E_a, and the pre-exponential factor, respectively.

	E_a $\mathrm{kJ}\cdot\mathrm{mol}^{-1}$	std. $\mathrm{kJ}\cdot\mathrm{mol}^{-1}$	$\log_{10} A$ $\log_{10}\mathrm{s}^{-1}$
Average	88.6	37.0	7.36
Min	45.8		−0.54
Max	141		8.10

Table 3.9 Summary of lignin pyrolysis kinetic parameters. E_a and A are the apparent activation energy and the pre-exponential factor, respectively.

Heating rate $\mathrm{K}\cdot\mathrm{min}^{-1}$	Temperature °C	E_a $\mathrm{kJ}\cdot\mathrm{mol}^{-1}$	$\log_{10} A$ $\log_{10}\mathrm{s}^{-1}$	Ref.
1000[a]	600–1400	82.0	5.30	[104]
30	300–500	141	8.10	[80]
10	200–410	110	6.86	[212]
5	<720	124	7.44	[214]
20	<720	64.6	2.55	[214]
40	<720	52.6	−0.24	[214]
80	<720	45.8	−0.54	[214]

[a] unit = $\mathrm{K}\cdot\mathrm{s}^{-1}$.

Although for engineering purposes a common approach is to convert parent fuel into: Permanent gasses, oil/tar, and char, or simply into volatiles and char [222], the latter allows a single set of kinetics to describe the process of decomposition.

This author will argue that for generic trend modeling aiming for qualitative results; a global, single step model will be a good starting point for any kind of simulations considering the stochastic spread in fuel composition, reaction conditions, and multiple purposes of such models. Thus, these kind of data will constitute the kinetic review for this chapter.

Like for all of the sub-components; cellulose, hemicellulose, and lignin, the kinetic spread of whole biomass is large. Figure 3.5 shows the kinetic rate constant as a function of the inverted temperature for all of the included studies. Similar to the case of cellulose, the data has been divided into studies using heating rates above and below $100\,\mathrm{K}\cdot\mathrm{min}^{-1}$. A spread of almost 15 orders of magnitude is observed, however, the greater part of the data are present within a five order of magnitude band. Looking at figure 3.14, it is clear how looking at whole biomasses scatters the data when compared to the pure sub-components. There is however, a trend with increasing pre-exponential factor with apparent activation energy, although not as profound as for the sub-components.

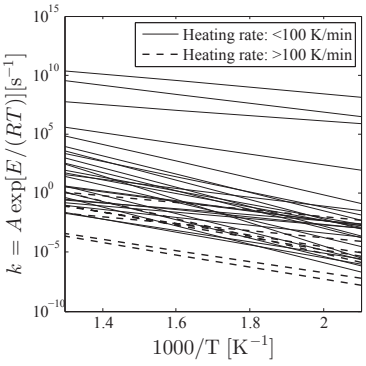

Figure 3.13 Biomass global one step pyrolysis kinetics. References listed in table 3.12.

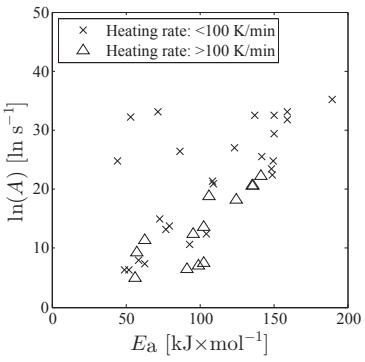

Figure 3.14 Relation between A and E_a for whole biomass pyrolysis. References listed in table 3.12.

One study [223] stands out featuring very high activation energies. These data have been included in figures 3.15 and 3.16 for the purpose of completion. However, they should probably be treated with caution.

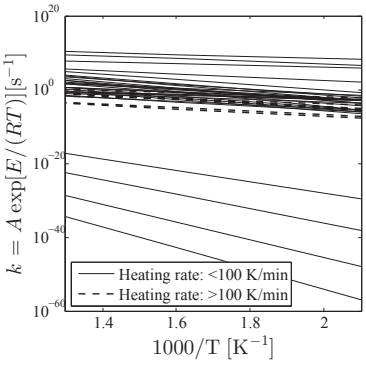

Figure 3.15 Biomass global one step pyrolysis kinetics. References listed in table 3.12.

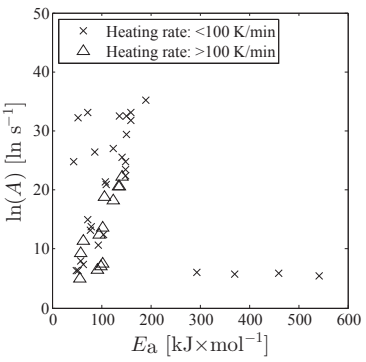

Figure 3.16 Relation between A and E_a for whole biomass pyrolysis. References listed in table 3.12.

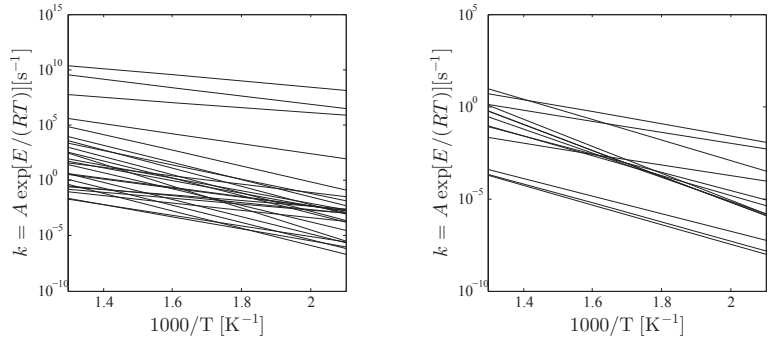

(a) **(b)**

Figure 3.17 Literature comparison of single-reaction first order kinetics for thermal degradation of whole biomass at (a) low ($< 100\,^\circ\mathrm{C}\cdot\mathrm{min}^{-1}$) and (b) high ($> 100\,^\circ\mathrm{C}\cdot\mathrm{min}^{-1}$) heating rates. References listed in table 3.12.

Table 3.10 Summary of the kinetic parameters for global single step models for whole biomass pyrolysis kinetics obtained at low heating rates as displayed in figure 3.17a. E_a, std., and A are the apparent activation energy, the standard deviation of E_a, and the pre-exponential factor, respectively. These data exclude the results of Wilson *et al.* [223].

	E_a $\mathrm{kJ \cdot mol^{-1}}$	std. $\mathrm{kJ \cdot mol^{-1}}$	$\log_{10} A$ $\log_{10} \mathrm{s^{-1}}$
Average	107	42.9	14.06
Min	44.5		2.74
Max	190		15.3

Table 3.11 Summary of the kinetic parameters for global single step models for whole biomass pyrolysis kinetics obtained at high heating rates as displayed in figure 3.17b. E_a, std., and A are the apparent activation energy, the standard deviation of E_a, and the pre-exponential factor, respectively.

	E_a $\mathrm{kJ \cdot mol^{-1}}$	std. $\mathrm{kJ \cdot mol^{-1}}$	$\log_{10} A$ $\log_{10} \mathrm{s^{-1}}$
Average	101	29.0	5.78
Min	56.5		2.13
Max	141		9.64

3.2.4 Thermal Decomposition at High Heating Rates

Although multi-step mechanisms have been used on low heating rate experiments [211, 234, 242] the SFOR or alternatively the SNOR mechanism usually will be able to describe the fuel conversion well. On the contrary, more complex mechanisms are often found for the high heating rate experiments were large temperature and heating rates spans make it difficult for the SFOR to suffice [109, 241, 244–247]. The high heating rate or high peak temperature studies that have been conducted using SFOR kinetics are usually limited to narrow temperature intervals. The short residence times required to carry out kinetic studies at high heating rates make it difficult to derive the necessary temporal resolution of the particle decomposition in the set-ups without an integrated sample scale. Many studies rely on kinetics derived from quantification of the evolving gases. Common for most studies, is the challenges related to estimate the temperature history of the particle. One of the primary advantages of the high heating rate, high temperature experiments is the possibility to derive char yields at conditions similar to PF firing.

Figure 3.18 shows a number of high heating rate studies on various biomasses and coals. The figure shows a wide spread of the pyrolysis kinetics and emphasises the consequences of missing standards within biomass kinetics and the various industry applications. However, the trend relating the activation

Table 3.12 Summary of whole biomass pyrolysis kinetic parameters at heating rates below $100\,\mathrm{K}\cdot\mathrm{min}^{-1}$. E_a and A are the apparent activation energy and the pre-exponential factor, respectively.

Fuel	Heating rate $\mathrm{K}\cdot\mathrm{min}^{-1}$	Temperature °C	E_a $\mathrm{kJ}\cdot\mathrm{mol}^{-1}$	$\log_{10} A$ $\log_{10}\mathrm{s}^{-1}$	Ref.
Wheat grass	5–10	200–425	44.5	10.8	[224]
Sugarcane bagasse	50	25–450	49.0	2.75	[225]
Sugarcane bagasse	50	25–900	52.0	2.74	[225]
Switch grass	5–10	200–425	53.4	14.0	[224]
Wood	—	low	58.5	3.48	[226]
Beech	—	—	62.7	3.18	[227]
Rape straw	5–10	200–425	71.7	14.4	[224]
Oak	5–20	200–400	73.2	6.52	[228]
Pine	20	—	77.0	5.73	[229]
Wood	50	270–600	79.5	6.00	[230]
Reed canary grass	5–10	200–425	86.7	11.5	[224]
Sugarcane bagasse	5–50	195–395	93.2	4.64	[231]
Wood	—	high	105	5.42	[226]
Fir	—	270–340	109	9.28	[232]
Wood chips	5–20	<800	109	9.08	[233]
Pine	—	90–250	123	11.7	[232]
Olive husk	5–20	<800	137	14.1	[233]
Pine seed shells	5–20	<800	142	11.1	[233]
Beech	1000	<435	149	10.2	[234]
Wood	—	110–600	150	10.7	[235]
Pine	—	300–600	150	14.1	[236]
Glucose	5	<720	159	14.4	[214]
Glucose	80	<720	150	12.7	[214]
Xylose	80	<720	160	13.8	[214]
Melezitose	80	<720	190	15.3	[214]
Pine	5–20		149	9.72	[237]
Cashew nut shells	10	180–370	293	2.60	[223]
Coffee husk	10	180–370	371	2.52	[223]
Mill bagasse	10	180–370	461	2.58	[223]
Palm stem	10	180–370	542	2.36	[223]
Corn cob	20	190–280	75	6.27	[238]
Corn stalk	20	189–280	107	9.48	[238]
Olive Pruning	20	189–280	101	8.67	[238]
Olive Kernel	20	171–287	86.7	7.55	[238]
Sunflower residue	20	204–375	26.3	4.38	[238]

Table 3.13 Summary of whole biomass pyrolysis kinetic parameters at heating rates above $100\,\mathrm{K \cdot min^{-1}}$. E_a and A are the apparent activation energy and the pre-exponential factor, respectively.

Fuel	Heating rate $\mathrm{K \cdot min^{-1}}$	Temperature °C	E_a $\mathrm{kJ \cdot mol^{-1}}$	$\log_{10} A$ $\log_{10} \mathrm{s^{-1}}$	Ref.
Beech	1000	<435	141	9.64	[239]
Fir	1000[a]	400–500	56.5	2.13	[240]
Erica Arborea	100–150[a]	400-700	57.5	4.01	[241]
Beech	1000	<435	95.4	5.39	[239]
Beech	1000	<435	103	5.89	[234]
Wood	iso	700–900	91.5	2.80	[242]
Pallet	iso	700–900	99.3	3.06	[242]
Furniture	iso	700–900	103	3.24	[242]
Wood	iso	300–400	107	8.17	[196]
Wood	iso	225–325	125	7.89	[242]
Pallet	iso	225–325	136	8.95	[242]
Furniture	iso	225–325	136	8.96	[242]
Wood	iso	<300	62.8	4.96	[243]

[a] unit = $\mathrm{K \cdot s^{-1}}$.

energy to the pre-exponential factor, cf. figure 3.19, appears well defined.

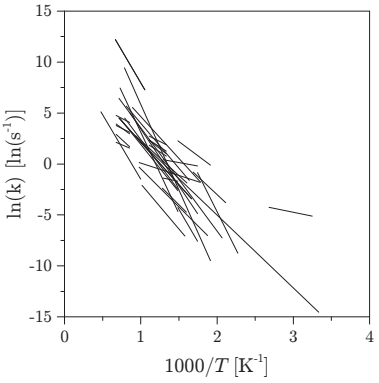

Figure 3.18 Arrhenius plot of high heating rate or high temperature experiments on different biomasses, references listed in table 3.14.

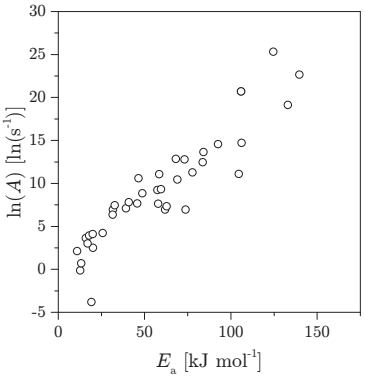

Figure 3.19 SFOR kinetic parameters at high heating rate or temperature for various biomasses and coals, references listed in table 3.14.

Table 3.14 Overview of high heating rate kinetic parameters of various biomasses and coals.

Fuel	Max HR $K \cdot s^{-1}$	Max temp. K	E_a $kJ \cdot mol^{-1}$	$\ln(A)$ $\ln(s^{-1})$	Volatiles wt. %	Ref.
Rapeseed	48	373	12.7	−0.139	73.01	[248]
Rapeseed	48	593	58.5	11.1	73.01	[248]
Rapeseed	48	773	13.3	0.693	73.01	[248]
Beech	100	1123	68.2	12.8	88.80	[249]
Wood	100	1300	106	20.7	95.94	[250]
Erica arberea	150	700	57.5	9.23	82.40	[241]
Corn cob	300	750	20.1	2.51	68.00	[238]
Corn stalk	300	750	62.0	6.96	78.00	[238]
Olive prunings	300	600	11.0	2.12	60.00	[238]
Olive kernels	300	400	46.6	10.6	68.40	[238]
Sunflower residues	300	710	73.8	6.94	67.00	[238]
Beech	500	1237	73.2	12.8	88.51	[249]
Hard wood	1000	1400	69.0	10.4	84.35	[104]
Hard wood	1000	1123	69.0	10.4	92.97	[251]
Cellulose	1000	1100	77.8	11.3	85.00	[58]
Bagasse	1000	900	92.6	14.6	89.50	[94]
Beech	1000	1402	84.1	13.7	87.57	[249]
Wood	1000	947	106	20.7	95.94	[250]
Cellulose	10 000	1000	140	22.6	–	[90]
Bagasse	10 000	1100	59.5	9.31	91.60	[202]
Beech	10 000	1266	83.7	12.5	81.52	[249]
Wheat straw	10 000	900	31.7	6.96	75.95	[252]
Coconut shell	10 000	900	48.7	8.83	69.79	[252]
Rice Husk	10 000	900	39.3	7.08	59.22	[252]
Cotton stalk	10 000	900	40.8	7.80	72.60	[252]
Cellulose	15 000	1100	133	19.1	94.08	[74]
HVB lignin	200 000	1827	105	11.1	63.00	[253]
Black pellet	High	1200	31.5	6.35	88.58	[89]
Straw	High	1200	45.8	7.66	95.13	[89]
Lignin	High	1200	32.8	7.45	83.88	[89]
Palm kernel shell	High	1200	25.8	4.22	84.09	[89]
Softwood pelllet	High	1200	58.0	7.63	94.21	[89]
Beech	Low	505	62.8	7.32	72.00	[227]
Oak	Low	400	106	14.7	70.00	[196]
Spruce	Various	Various	125	25.3	Various	[232]
Coal	12 000	1200	19.2	−3.82	50.00	[254]
Bituminous	3000	1100	16.0	3.64	60.00	[255]
Bituminous	1600	1200	17.0	3.00	33.40	[256]
Bituminous	1600	1200	18.0	3.91	37.10	[256]
Bituminous	1600	1200	20.0	4.09	39.40	[256]

3.3 Summary on the Thermal Decomposition of Biomass and Its Components

Table 3.15 summarizes the averaged values of devolatilization kinetics of the low heating rate literature study. The interdependency of the pre-exponential factor and the activation energy makes it difficult to exactly deduce the relation between one another.

Cellulose being less branched than hemi-cellulose will typically decompose at higher temperatures than hemi-cellulose [73]. This corresponds well to the higher activation energy of cellulose compared to hemi-cellulose. Likewise, will the complex structure of lignin result in a partial thermal stability with a reaction zone stretching across a larger temperature interval. The activation energy of lignin is expected to be low, because the branched parts of the structure will decompose at low temperatures. The pre-exponential factor is significantly lower compared to cellulose and hemi-cellulose, effectively lowering the overall rate of reaction, stretching the temperature interval in which lignin decomposition occurs. Thus, analysing the macromolecular composition of the fuel will provide an initial idea of the fuel reactivity.

Figure 3.20 summarizes table 3.15 in an Arrhenius plot. This clearly shows, how the rate of reaction is different from the the macromolecular components.

Table 3.15 Summary of the kinetic properties of biomass components.

Averaged parameter	Unit	Cellulose	Hemi-cellulose	Lignin	Biomass
E_a	kJ · mol	203	140	88.6	104
$\log_{10} A$	$\log_{10} s^{-1}$	18.8	21.3	7.36	13.9

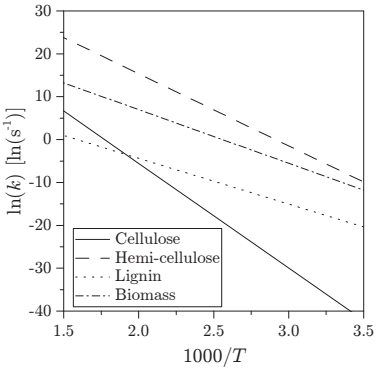

Figure 3.20 Summary on slow heating rate. Arrhenius plot based on averaged values. Sources are listed in

Although the variations in pre-exponential factor and activation energy are considerable, a stringent systematic, known as the kinetic compensation effect [85, 257], appears when comparing the activation energy relative to the pre-exponential factor. From a devolatilization study's point of view this effect causes any change owing to procedural mistakes or changes which causes the activation energy to change to be accompanied by a corresponding change in the pre-exponential factor. The linear behavior of the individual biomass components given in figures 3.7, 3.10 and 3.12 indicates that any sample in each of their respective groups will undergo the same rate of reaction at a characteristic temperature.

The lack of order when comparing data from whole biomasses figures 3.14 and 3.16 expresses the increase in complexity from individual components to biomass. Thus, using the DAEM or similar might be more suitable for complex mixtures. However, evident for all of the presented mathematical models, except maybe the CPD model, is the need for empirical data to fit the models. Thus, opting for the DAEM model or multi-step models may not always be the optimal choice.

As can be seen from the preceding sections the method of individual macromolecular contributions to the devolatilization process is able to provide some systematic connection especially between the Arrhenius kinetic parameters. However, despite the quantity of studies based on thermogravimetric data a systematic classification of parent fuels based on such results is not yet available.

The most pronounced disadvantage of the low heating rate method, is the inability to simulate the reaction environment present in industrial type boilers, particularly in PF combustion, as has been pointed out numerous times in the literature [91, 202, 240, 258, 259]. Modeling biomass devolatilization based on superimposed macromolecular kinetics data obtained at low heating rates do not represent the conversion behavior at PF conditions. As will be seen in the following sections the rate at which the particle is heated will influence on the devolatilization behavior of the fuel, char yield, and char properties. It will, however, provide an initial idea of the expected behavior of the different available models.

CHAPTER 4

Pyrolysis at Low Heating Rate

This chapter presents experimental work conducted as part of the present study in thermogravimetric analysis (TGA) equipment and use the data to derive low heating rate, low temperature kinetics for the devolatilization of different biomasses. The methodology is widely used across the litereature [115, 223–225, 228–230, 233, 237–242] and therefore this chapter makes up a base of reference, relating the GREEN fuels to the general devolatilization literature. The kinetic analysis takes starting point in a woody and an annual crop, representing the two main categories of fuels relevant to the power industry.

4.1 Experimental Analysis

The non-isothermal TGA set-up is among the most widely used types of apparatuses for solid fuel thermal conversion analysis. The main advantage of the method is the well defined temperature history and the precision and convenience of the time resolved mass loss.

4.1.1 Experimental Set-Up

The Netzsch STA 449 F1 STA was used for low heating rate experiments on the full range of fuels presented in section 2.4. Only the TGA features of the STA was used and thus no DSC results have been analyzed due to uncertainties in the thermal lag of the set-up.

The Netzsch STA 409C simultaneous thermal analysis (STA) is a vertical TGA apparatus operating with sample masses typically between 2 and 10 mg. The sample rested in a ⌀6 mm platinum crucible. The with inner wall height was reduced to 1.5 mm to minimize diffusion limitations. Lids were not used. Identical crucibles were used for reference. Typical experimental conditions are listed in table 4.1.

4.1.2 Experimental Procedure

All of the parent fuels were analyzed using the same temperature program, cf. figure 4.1. Samples of $\sim$ 2–6 mg were heated at $2\,\mathrm{K}\cdot\mathrm{min}^{-1}$ to 378 K at which temperature the samples were allowed to dry for 30 min. After drying the samples were heated to 1273 K at heating rates of 2 or $40\,\mathrm{K}\cdot\mathrm{min}^{-1}$. The

Table 4.1 Typical reaction conditions for TGA experiments.

		STA 449 F1	Typical experiment
Sample mass	mg	< 5000	2–10
Heating rate	$K \cdot min^{-1}$	0.001–50	0.5–40
Temperature	K	423–2673	< 1273
TGA resolution	ng	25	
Gas flow	$mL \cdot min^{-1}$ (SATP)	—	100
O_2 in N_2	vol. %	—	0–4

samples were kept at the final temperature for 60 min after which the heating elements were turned off and the reactor allowed to cool to ambient. No active cooling other than the 100 mL (standard ambient temperature and pressure (SATP)) purge flow. All runs were preceded with blanc runs (empty crucibles) in order to correct for the lift forces on the crucibles.

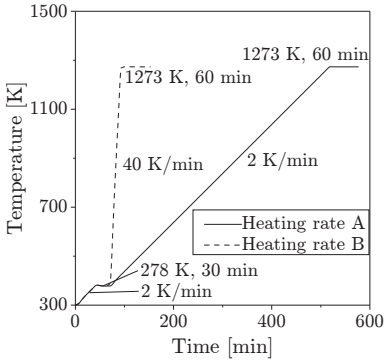

Figure 4.1 TGA temperature program for parent fuel pyrolysis analysis. O_2 in N_2: 0 %.

4.1.3 Repeatability

The repeatability of the TGA experiments was tested using laboratory grade carbon black samples. Burn-out rather than pyrolysis experiments were conducted for the repeatability test in order to test the calibration of the scale. The carbon black samples were heated continuously at $10\,K \cdot min^{-1}$ to 1184 K. The samples were fully combusted in 10 vol. % O_2 in N_2 which were increased to 21 vol. % O_2 in N_2 at the final temperature at which the samples were kept for 60 min. Figure 4.2 shows the temperature program and the mass loss curves of the double determination experiment.

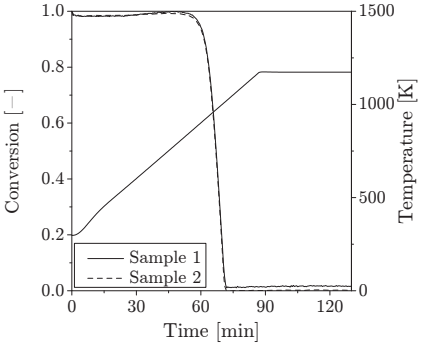

Figure 4.2 Repeatability experiments on carbon black burn out at $10\,\mathrm{K}\cdot\mathrm{min}^{-1}$ in 10 vol. % O_2 in N_2. Sample 1: 1.9 mg, sample 2: 3.4 mg.

Figure 4.2 shows small deviations between the two runs. The mass increase at $t \approx 30$ min suggest slight errors in the correction of the lift forces. At full burn out sample 1 fails to reach full conversion. The deviations were, however, considered to be within acceptable limits. No effects that could be contributed to the size of the sample mass (Sample 1: 1.9 mg, sample 2: 3.4 mg) where observed. The temperature profiles are not fully linear in the beginning of the experiment. This effect is well known and the extend of the problem is proportional to the applied heating rate. The repeatability of the temperature profiles were however close to ideal.

4.1.4 Samples and Sample Pre-Treatment

The samples used for the TGA experiments have already been introduced in details in chapter 2 section 2.4. All fuel samples were prepared in a Retsch ZM100 rotating cutter mill equipped with a 500 μm screen. The samples were subsequently sieved in a Retsch Analytical Sieve Shaker AS200 with a lower and upper cutoff (wire mesh) of 63 and 90 μmm, respectively. Automatic weighing of each crucible and sample was conducted by the Netzsch STA 449 F1 calibrated by a manually weighed reference weight.

4.1.5 Results

The following section will present the slow heating rate devolatilization experiments conducted in the TGA. Comparisons between fuel type, heating rate, and mineral content will be made.

Influence of Heating Rate

The influence of heating rate has been extensively reported in the literature using thermogravimetric analysis apparatuses [63, 64, 153]. The heating rate has been identified as one of the key parameters in biomass pyrolysis influencing the global reaction kinetics [73–82] and the product distribution [88]. A comparison of the four fuels used in this study is given in figure 4.3. The figure shows the mass loss and the normalized time derivative of the mass loss curves for heating rates of 2 and $40\,\mathrm{K}\cdot\mathrm{min}^{-1}$. The sample masses, the maximum time derivative mass loss, and the char yields are listed in table 4.2.

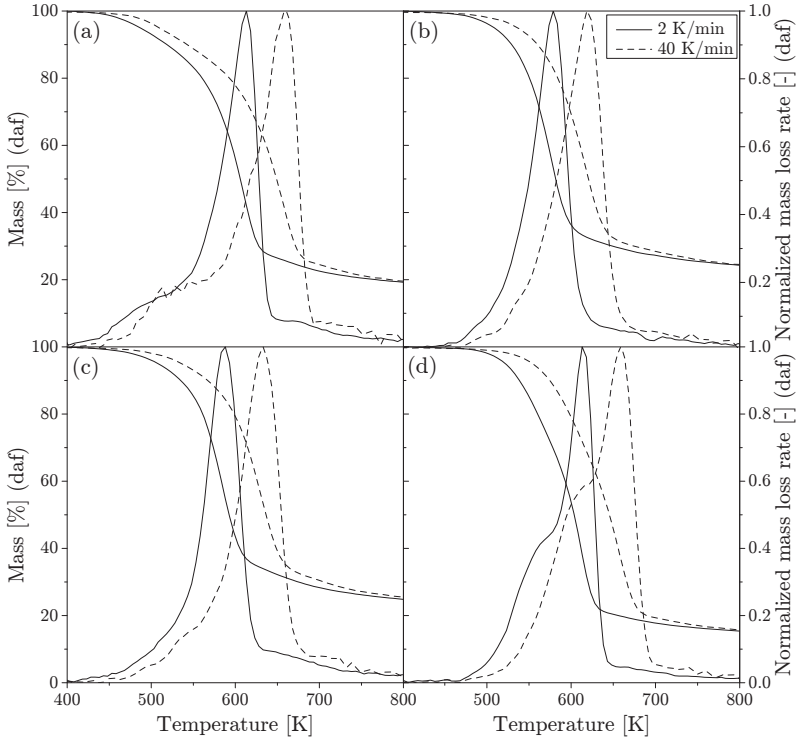

Figure 4.3 The influence of heating rate on the pyrolysis of (a) pine wood, (b) miscanthus, (c) KCl-doped pine wood, and (d) leached miscanthus. Temperature program, cf. figure 4.1. Atmosphere: 100 % N_2. 2–4 mg samples.

Figure 4.3 shows the expected shift in reaction towards higher temperatures as the heating rate is increased. This is in full agreement with other studies in the literature on both model fuels [153] or biomasses [50].

The low temperature, low heating rate char yields have been derived and listed in table 4.2. The char yield is not stabilized during the TGA runs which could either be due to small oxygen leaks in the system or a peak temperature dependence on the char yield. This work aims at utilizing biomass at suspension firing conditions, i.e. high peak temperatures heating rates. It is commonly recognized that the char yield from low temperature or low heating rate experiments are not representative of the char yield obtained at suspension firing conditions [89]. Therefore, the observed declination in the char yield was not further investigated.

It is noticeable how the low ash (figure 4.3 a and d) and the high ash (b and c) samples share common features especially when considering the derivative thermogravimetry (DTG) curves. The low ash samples increase in mass loss faster than their high ash sample counter part at low temperatures, even though the onset of devolatilization seems to be similar for all samples. The effect of the low temperature mass loss is stabilizing before the primary pyrolysis initiate at temperatures around 600 K. The result is a distinct shoulder on the low temperature side of the DTG curve. This shoulder is similar to what has been reported from superposition studies of mixes of cellulose, hemicellulose, and lignin, in which case the shoulder stems from the low temperature onset of the hemicellulose [150].

Table 4.2 Overview of maximum heating rate, DTG_{max}, char yield at 1273 K, and sample masses used in the TGA experiments.

	Heating rate		Wood		Miscanthus	
	$K \cdot min^{-1}$	Pre-treatment	—	Doped	—	Leached
DTG_{max}	2	$\% \cdot s^{-1}$, daf	2.23	2.22	2.41	2.59
	40		45.4	47.6	52.2	48.3
Char yield	2	wt. %, daf	15.3	21.1	18.0	11.6
	40		15.9	21.3	18.3	11.7
Sample mass	2	mg	4.06	3.99	4.24	4.57
	40		3.94	4.70	4.34	4.65

The influence of temperature on the char yields, cf. table 4.2 was left inconclusive as the differences were to small to derive any trends from. The mineral pre-treatment of the samples did however influence the char yields to significant degree. The char yields were evaluated at 1273 K and indicate how low mineral matter significantly reduces the char yield on an ash free basis. This is in line with other studies [153].

4.1.6 Discussion

The influence of heating rate and mineral content has proven to be pronounced. The onset of the primary pyrolysis is shifted towards higher temperatures as the heating rate is increased from 2 to 40 $K \cdot min^{-1}$. The ash

free char yield decreases noticeable when the mineral content is removed from the sample. The effect seems to be reversible as doping of the low ash wood sample resulted in an increase in the char yield. The mineral content also seems to influence the temperature range at which the pyrolysis takes place. For the low ash samples the DTG curve is wider than their high ash counter parts. Likewise, the peak of the primary pyrolysis is shifted towards higher temperatures.

4.2 Kinetic Modeling

This section relates to the experimental results of section 4.1. It will include selected mathematical models reviewed in section 3.2 and apply them to the experimental results.

4.2.1 Modeling of Low Heating Rate Experiments

The low heating rate experiments conducted in the TGA form the general platform for literature comparison of the GREEN fuels. This kind of experimental results is by far the most abundantly represented type of experimental data on thermal degradation of biomass. Hence, the kind of data that most readers will be familiar with and it is recommended to included it as a base of reference in all studies of this nature.

The low heating rate experiments excel in being ideal for model fitting. The low heating rate minimizes transport limitations and the linear temperature profile simplifies the rate expressions.

The formulation of the ideal kinetic model for biomass pyrolysis will naturally depend on the purpose of the study. In this work, we aim to implement pyrolysis kinetics to large numerical models often limited by the computational resources available. It is thus desired to simplify as many of the sub-routines as possible without loosing critical information.

To evaluate the differences between models, this section will apply two of the best known kinetic models:

- Single first order reaction (SFOR)
- Distributed activation energy model (DAEM)

both described to detail in section 3.2. Besides being well known in the devolatilization literature, they represent the very simplest model (the SFOR model) and a more complex model (the DAEM model).

Fitting the SFOR Model

Because of the linear temperature profile the differential methods of the SFOR model can be applied to fit a set of activation energy and pre-exponential

factor to the TGA experimental data. The best fit to the data is found if an individual fit is applied to each heating rate using a method of linear least-square-fit. Fitting a SFOR expression (equation (3.4)) to a set of mass loss data at any given heating rate, could in principle result in a unique set of kinetic constants capable of describing the same reaction at other heating rates. However, the chance for multiple combinations of activation energy and pre-exponential factor all of which are able to satisfy the same data is sizeable. This is known as non-uniqueness in kinetic inverse modeling. The problem can be elucidated by applying heating rate variation analysis as described by Kissinger [260]. The heating rate is quantified by observing the shift in the temperature at which the reaction rate peaks, $T_{k,\max}$, relative to the applied constant heating rate, β:

$$\ln\left(\frac{\beta}{T_{k,\max}^2}\right) = \ln\left(\frac{AR}{E_\mathrm{a}}\right) - \frac{E_\mathrm{a}}{RT_{k,\max}} \tag{4.1}$$

Using equation (4.1) allows one to determine one set of global kinetics applicable to a specific fuel. From figure 4.4 the kinetic constants can be found from the slope and the intercept of the linear regression fit:

$$\text{slope} = \frac{-E_\mathrm{A}}{R} \tag{4.2}$$

$$\text{intercept} = \ln(A) - \ln\left(\frac{E_\mathrm{a}}{R}\right) \tag{4.3}$$

Figure 4.4 shows the resulting Kissinger plot with the kinetic constants listed in table 4.3. Kinetic parameters are determined for all four fuels, each investigated at two heating rates.

The method was found to be easily applicable. The necessary input information is simple to extract from the TGA data and, if carried out consistently, found to be fairly stable. Comparison across experimental set-ups should however be carried out with care, as the method is potentially vulnerable to phenomena like thermal lag (shifting the $T_{\max}$ peak).

Fitting the DAEM Model

The DAEM model, equation (3.12), has been fitted using a natural logarithmic distribution of activation energies, equation (3.17). The fitting of σ, μ, and A is done by minimizing the sum of squared errors, e, as:

$$e = \sum_{i=1}^{N}\left(\chi_i - \left(1 - \int_{E_{\mathrm{a},0}}^{E_{\mathrm{a},1}} \exp\left[-\int_0^{t_i} k\left(T_i\right)\mathrm{d}t\right] f\left(E_\mathrm{a}\right)\mathrm{d}E_\mathrm{a}\right)\right)^2 \tag{4.4}$$

where $E_{\mathrm{a},1}$ and $E_{\mathrm{a},0}$ are the upper and lower boundaries of the numerically expressed activation energies.

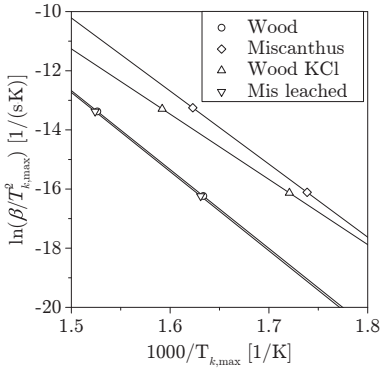

Figure 4.4 Determination of SFOR kinetics using the Kissinger method [260].

Table 4.3 SFOR kinetic constant determined by the Kissinger method [260].

Fuel	β $\mathrm{K \cdot min^{-1}}$	$T_{k,\max}$ K	A $10^{13} \times \mathrm{s^{-1}}$	Ea $\mathrm{kJ \cdot mol^{-1}}$
Wood	2.00	612	1993	222
	40.0	655		
Miscanthus	2.00	575	1120	205
	40.0	616		
Wood KCl	2.00	581	6.66	183
	40.0	628		
Miscanthus leached	2.00	613	2136	223
	40.0	656		

The result of the DAEM parameter fitting is listed in table 4.4 and the distributions of activations energies are illustrated in figure 4.5.

Table 4.4 TGA derived kinetics constants using the DAEM model for heating rates 2 and $40\,\mathrm{K \cdot min^{-1}}$.

Property	Unit		Wood		Miscanthus	
			None	Doped	None	leached
A	$\mathrm{s^{-1}}$	$\times 10^{18}$	23.0	8.135	116	2.664
$\bar{E}_\mathrm{a}$	$\mathrm{kJ \cdot mol^{-1}}$		231	191	230	220
μ			12.35	12.31	12.35	12.30
σ			0.0871	0.0727	0.0646	0.0647

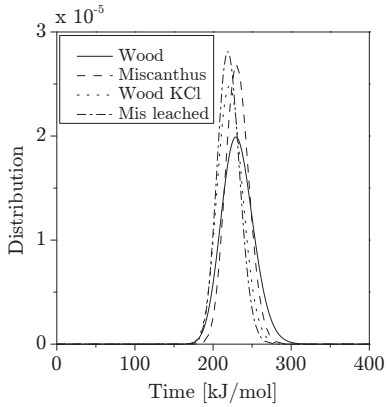

Figure 4.5 The distributions of activation energies used for the DAEM modeling of the TGA experiments.

Model Comparison

The asymmetry of the DTG peaks of the wood and leached miscanthus samples, cf. figure 4.3, is usually caused by the difference in thermal behavior of the various constituents in the specific fuel, i.e. multiple reactions occurring in parallel [153, 234]. Hence, difficulties in fitting a SFOR mechanism is expected. The rate of devolatilization varies as function of temperature and the fit of the differential SFOR model, equation (3.5), depends on a linear correlation between rate of reaction and the inverse temperature. This implies that the fit of the SFOR model to the asymmetric DTG curves will depend on in which temperature interval the fit was carried out. Figure 4.6 shows the logarithmic scale to which the SFOR fit is carried out for wood at the two applied heating rates. The appearance of two distinct reactions zones is especially pronounced for the low heating rate experiment.

Figure 4.7 shows a comparison of the different models fitted to TGA data on wood at heating rates of 2 and $40\,\mathrm{K}\cdot\mathrm{min}^{-1}$. The "SFOR‘" and "Kissinger" methods are both model fits based on the SFOR model. The "SFOR" model is fitted to the specific data of a single heating rate experiment, resulting in two separate sets of kinetic parameters specific to both fuel and heating rate. The "Kissinger" approach is based on a single fit to the data from both heating rates, resulting in a single set of kinetic parameters specific only to the fuel.

As expected the DAEM performs the best, being able to describe the devolatilization process with a single set of model parameters, regardless of heating rate. The heating rate specific SFOR fit also describe the mass loss well. It should be noted that the temperature (horizontal) offset between the SFOR fit and the TGA curve can be shifted by changing the temperature

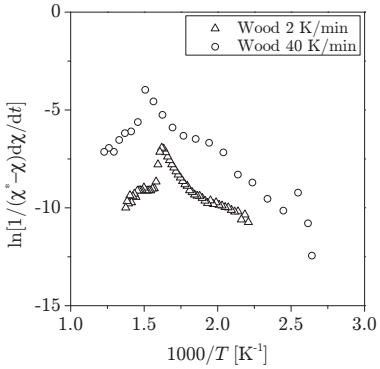

Figure 4.6 The logarithmic fit for wood at 2 and 40 K · min^{-1}.

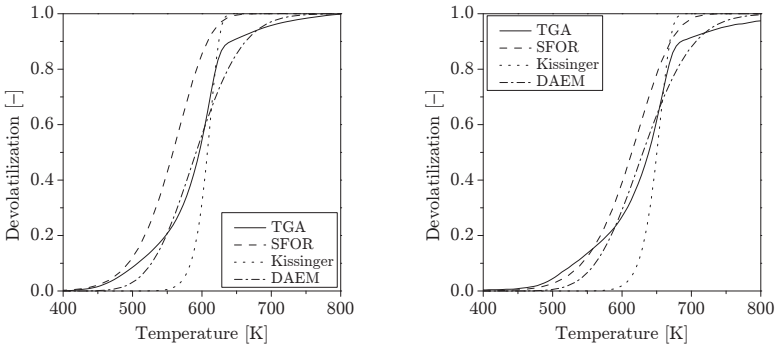

(a) Heating rate: 2 K · min^{-1}. **(b)** Heating rate: 40 K · min^{-1}.

Figure 4.7 Kinetic fit to the wood fuel heated in the TGA at 2 and 40 K · min^{-2}. Comparison of a single heating rate SFOR kinetic, SFOR fit by heating rate variation (Kissinger), and DAEM modeling.

interval in which the SFOR kinetics have been fitted, cf. figure 4.6. The Kissinger fit performs well considering the simplicity of the method. The temperature for maximum mass release is well predicted regardless of the applied heating rate.

Figures 4.8 to 4.10 show the model fit to the KCl doped wood, the miscanthus, and the leached miscanthus samples. It is noticeable when figure 4.7 and figure 4.8 how the heating rate dependent SFOR fit is better for the KCl doped sample. This is due to the symmetric shape of the DTG curves, cf. figure 4.3.

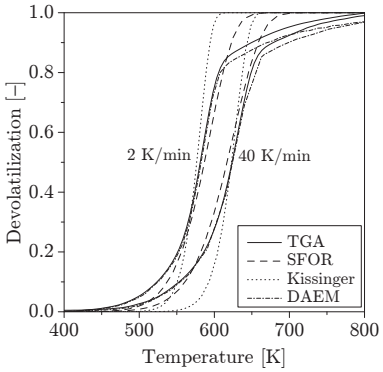

Figure 4.8 The logarithmic fit for the KCl doped wood at 2 and 40 $\mathrm{K} \cdot \mathrm{min}^{-1}$.

The miscanthus samples, cf. figures 4.9 and 4.10, are likewise well predicted by the DAEM model, however, the Kissinger method SFOR model continues to provide reasonable predictions. In general, the DAEM model is the only model that is capable of capturing both the low and the high temperature devolatilization taking place at a low rate.

4.3 Summary

Low heating rate experiments have been carried out in a TGA apparatus. Four fuels based on pine wood and miscanthus have been used to identify the differences in biomass species and the influence of mineral matter on the devolatilization behavior. A reversible effect of the mineral matter was found to increase the char yield and accelerate the mass losses with a lower onset temperature.

Kinetic modeling was applied to the experimental results, and a comparative study of the very simple SFOR and the more complex DAEM model was carried out. The DAEM model is found to be superior to the SFOR model, which struggles to predict the mass losses across heating rates and large tem-

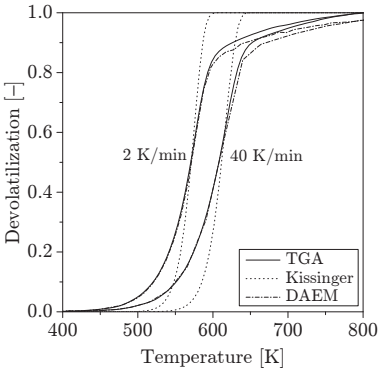

Figure 4.9 The logarithmic fit for the untreated miscanthus sample at 2 and $40\,\mathrm{K}\cdot\mathrm{min}^{-1}$.

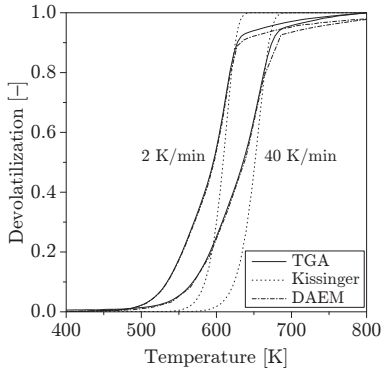

Figure 4.10 The logarithmic fit for the leached miscanthus sample at 2 and $40\,\mathrm{K}\cdot\mathrm{min}^{-1}$.

perature intervals. However, although the low heating rate TGA experiments show an apparent superiority of the DAEM model over the SFOR model the purpose of the project to which the kinetic model is applied should be taken into consideration.

For the purpose of describing the devolatilization of an industrial feed of pulverized wood fed in large quantities to industrial power plants, this author will argue; that the gain in accuracy won by using the DAEM model is easily outweighed by the additional computational cost and the fact that the DAEM model, like the SFOR model, is fuel specific and thus must be fitted for every change in fuel properties. In addition, it can be difficult to assess the implications on the upstream, and often more crude, assumptions like; particle shape. In many scenarios going for the simpler choice of the SFOR could be beneficial despite its apparent struggle to describe the process across different heating rates. An engineering fix to this problem is the scope of part III.

CHAPTER 5

Pyrolysis at High Heating Rate

High heating rate set-ups like entrained flow reactors [70, 89, 261, 262], wire-mesh reactors [92, 99], or similar [72, 263] have been extensively reported in the literature. The set-ups are capable of heating small particles at heating rates on the order of 10^3–$10^5\,\mathrm{K \cdot s^{-1}}$, thereby simulating conditions similar to those expected in suspension fired units. Achieving high heating rates and peak temperatures, typically comes at the cost of the loss of control of particle residence time [262, 264], particle temperature history [68, 252, 265–267], and the ability to close the sample mass balance [268], making it difficult to derive kinetics.

Being able work out the particle residence and temperature history is imperative in order to model the process due to the temperature dependency of the rate expression, cf. equation (3.2). This work employed a laminar entrained flow reactor (LFR) and fully characterized the flow and temperature field by computational fluid dynamics (CFD) simulations. Upon validation of the model, multi-phase flow Euler-Lagrange simulations were carried out extracting the all necessary thermal particle profile.

The combined experimental and numerical approach for the woody fuel has been published in Applied Energy [269] and enclosed in appendix A. The paper covers the general method and the derivation of the devolatilization kinetics of pine wood.

5.1 Experimental Analysis

The experimental part consists of two reactors. The primary set-up including the LFR reactor at Stanford University [270, 271] was used to derive devolatilization kinetics at short residence times and high heating rates and peak temperatures. The bench-scale 15 kW vertical combustor at Clausthal University of Technology [164, 272] was used to evaluate the kinetics in a larger scale.

5.1.1 Laminar Entrained Flow Reactor

This section presents the LFR reactor set-up, the operational conditions, and the experimental procedures. The results are presented along side the numerical modeling output in section 5.4.

The Experimental Set-Up

The LFR, figure 5.1, is a laboratory scale reactor heated by an understoichiometric, non-premixed CH_4/H_2 pilot flame diluted in N_2 and stabilized by a honeycomb like flat flame burner configuration (759 fuel inlets and 2200 oxidizer inlets). The oxidizer was a mixture of O_2 and N_2. It has been used in previous studies to obtain partially reacted coal and biomass chars at high temperatures and heating rates [270, 271]. The solid fuel was pneumatically transported to the reactor by a carrier flow of nitrogen at ambient temperature. The solid fuel feed rate was sufficiently low (10–20 $mg \cdot h^{-1}$) to study single particle behavior. The entrance point of the solid fuel feed was elevated slightly above the honeycomb burner, to match the height of the pilot flame, cf. figure 5.3. Semi-transparent quartz walls confined the reactor domain from the flat flame burner and 455 mm downstream, cf. figure 5.1. The reactor vented directly to the surroundings.

The particle collection system consisted of a quadruple concentric probe, cf. figure 5.1. Particles were collected through the inner tube. The particles where quenched by a flow of helium gas transported to the tip of the probe through the inner concentric channel. Water cooling was applied through the outer two channels, cooling the outside of the probe to temperatures below the water dew point. Velocity measurements of the gas extraction was not possible and thus true iso-kinetic conditions for the particle collection could not be achieved. However, observing the shape of the burning volatile gases the suction was assessed to be sufficiently high for all particles to be safely collected.

The particles were separated from the extractive gas flow on a simple silicon filter or low cut off membrane. The separation was carried out at slightly above ambient temperatures.

Operational Conditions

Two temperature conditions were used to characterize the biomass devolatilization. The temperature was adjusted by changing the composition of the pilot-flame feed. Table 5.1 lists the molar fractions of the inlet and post flame gases. The post flame composition and adiabatic flame temperature were calculated using CHEMKIN.

The temperature profile along the center axis of the reactor was characterized by un-shielded thermocouple measurements, manually corrected for radiation bias.

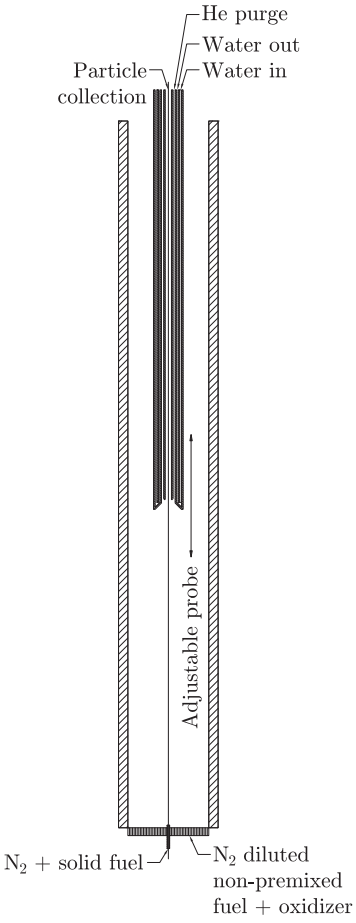

Figure 5.1 A cross sectional sketch of the LFR. Total length of the combustion chamber: 455 mm. Internal reactor width: 55 mm.

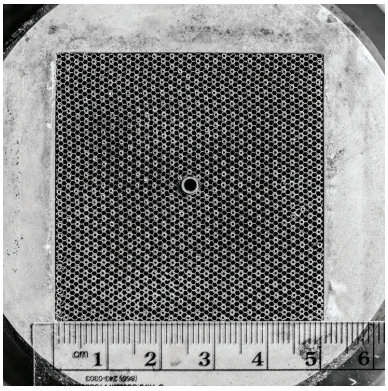

Figure 5.2 The honeycomb structure of the LFR flat flame burner. The solid fuel injection nozzle is seen in the center of the burner. The scale is shown in cm (5×5 cm).

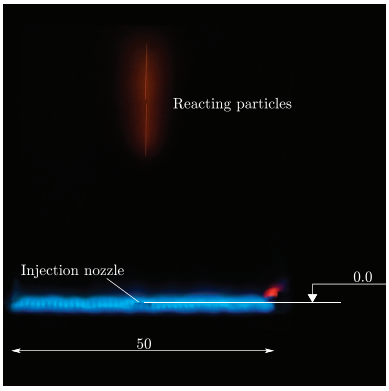

Figure 5.3 Sideview of the LFR. Level 0.0 indicate the injection point of the solid fuel. Scales are indicated in mm. Pulverized wood 106–125 μm in flame 2 conditions.

Table 5.1 Mole fractions and the total molar flow, F_{tot}, of the reactor set-up before and after combustion. Post flame composition is based on adiabatic equilibrium calculations.

Inlet	Flame 1	Flame 2	Post flame	Flame 1	Flame 2
CH_4	0.040	0.033	CO	0.021	0.021
O_2	0.109	0.087	CO_2	0.020	0.013
H_2	0.127	0.158	H_2O	0.163	0.130
N_2 (pilot)	0.675	0.602	H_2	0.050	0.099
N_2 (carrier)	0.049	0.120	O_2	0.000	0.000
			N_2	0.746	0.736
F_{tot} [mol $\cdot$ s^{-1}]	0.0382	0.0416		0.0371	0.0407
Adiabatic flame temperature [K]				1667	1406

Fuel Preparation

All GREEN fuels were tested in the LFR set-up. The fuels were divided into two size categories by wire-mesh sieving.

- 63–90 μm
- 106–125 μm

The resulting particle size distributions have been discussed and derived in section 2.4 on page 39, figure 2.19 and table 2.13.

Experimental

The experimental procedure includes variations in fuel and particle residence time, i.e. height adjustment of the collection probe. A typical experiment would include 5–6 probe positions injecting ~ 100 mg of fuel at each position. Because of the low char and ash content of the parent fuels the experiments were often repeated until a suitable amount of char had been collected. This could imply feeding up to 7 g of fuel at a single probe position. Table 5.2 lists the experimental matrix.

Table 5.2 A short overview of the LFR experimental matrix. "• •" indicates double determination.

Fuel	Size μm	Flame 1 $T_{ad} = 1667$ K	Flame 2 $T_{ad} = 1405$ K
Wood	63–90	•	
	106–125	• •	•
Miscanhus	63–90	•	
	106–125	•	
Wood KCl	63–90	•	
	106–125	•	•
Miscanthus leached	63–90	•	
	106–125	•	

Determination of the degree of Conversion

The degree of conversion in e.g. a TGA apparatus is continuously monitored by the integrated micro-balance. The LFR relies on the extraction of particles at discrete locations along the flow direction of the reactor. In order to determine the degree of conversion of the collected partially or fully reacted samples, one would need to compare them to the parent fuel. The conversion can be calculated in a number of ways. The most obvious would be to close the overall particle mass balance [64, 170], i.e.:

$$\chi = \frac{m}{m_0} \tag{5.1}$$

where m and m_0 are the current and initial mass of the sample respectively. This method assumes that no mass fails to enter the system, is accumulated in the system, or escapes the system by passing the particle collection system. The reactor was heated by a CH_4/H_2 pilot flame and thus water condensation was taking place to noticeable degree as the particles and the bulk gas were quenched in the collection probe. This resulted in char sticking to the side of the probe and further downstream of the collection system. Additionally, unburned fuel was clearly visible in the feeding system after each run. Such phenomena directly influence on the mass balance calculation, cf. equation (5.1).

Alternatively the conversion can be determined by closing an ash balance [252, 252, 264] in its simple form:

$$\chi = 1 - \frac{m_{\text{ash}}}{m_{\text{ash0}}} \tag{5.2}$$

where m_{ash} and m_{ash0} indicate the weight of the ash fraction of the reacted and parent fuel. alternatively, the mass balance can be closed, on a dry an ash free basis, as:

$$m_0 x_{\text{ash0}} = m x_{\text{ash}} = m_{\text{ash}} \tag{5.3}$$

where x_{ash0} and x_{ash} are the mass fractions of ash in the parent fuel and the sample respectively. This can be rearranged by substituting expressions for m and m_{ash} in terms of m_0, into:

$$\chi = \frac{x_{\text{ash0}} - x_{\text{ash}}}{x_{\text{ash}}\,(x_{\text{ash0}} - 1)} \tag{5.4}$$

This method disregards any loss of sample in the reactor because it is based on a local mass balance including only the ash. Although, advantageous over the overall mass balance method, the ash tracer method does assume a thermally stable ash phase, i.e. complete retention of all ash species. The volatility of especially alkali [146, 156–158, 273–278], alkaline earth [154, 158], halogens [158, 159, 163, 273, 277, 279, 280], and P and S [156, 273, 274, 277, 281–283] has been extensively reported in the literature. Concluding that the thermal conditions during either pyrolysis, devolatilization, or combustion will induce a release of inorganic matter at temperatures as low as 700–800 K. Biomass is typically rich in all of the above and therefore difficulties may arise when trying to close the mass balance.

To avoid the errors introduced to equation (5.4) a similar approach can be used, closing the mass balance over just a single or a group of chemically alike elements. For high ash content material Si would be a preferred tracer due to its abundance and thermal stability [284]. However, for the Si lean

wood fuel used in this study the uncertainties on the chemical analyses would exceed the advantage of the method. For coal studies Ti is commonly used, however, not suitable for biomass material which is lean in Ti. For this study the conversion has been calculated based on a Ca-mass balance:

$$\chi = \frac{x_{\mathrm{Ca}} - x_{\mathrm{Ca0}}}{x_{\mathrm{Ca}}\,(1 - x_{\mathrm{ash0}})} \tag{5.5}$$

This method also relies on the assumption of a non-volatile ash phase. However, the sensitivity towards ash volatility is limited for low ash fuels such as the ones used in this study. It also relies on the full retention of Ca in the solid phase. Conflicting findings in the literature on the volatility of Ca lead one to conclude that the release of Ca during devolatilization conditions is fuel specific [97, 154, 158, 285].

To validate the method a series of fixed bed reactor (FBR) experiments have been carried out at pyrolysis conditions. The FBR is a slow heating rate method and therefore it does not directly compare to the high heating rate LFR experiments. However, the peak temperatures reaches 1423 K and thus the thermodynamic equilibria are comparable.

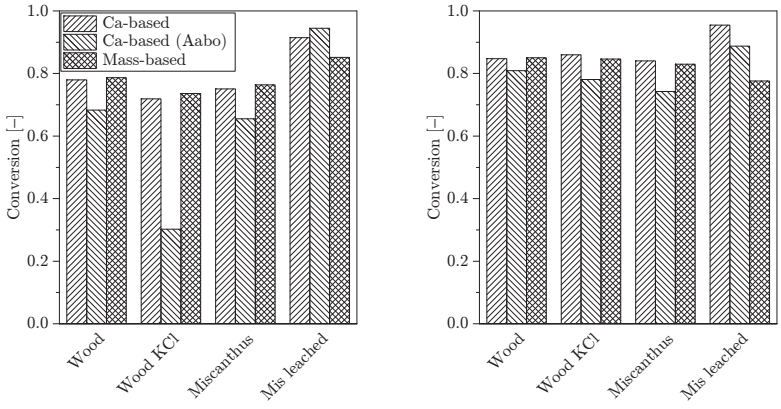

(a) 873 K. **(b)** 1423 K.

Figure 5.4 Experimental comparison of the mass and Ca-based conversion methods. Experiments are carried out in a fixed bed reactor in 100 % N_2. The Ca-analysis follows CEN/TS15290(2006). The Caanalysis from Aabo is carried out on 10 mg samples and do not follow international standards.

Figure 5.4 shows how the calculation of the pyrolysis conversion by Ca-tracing corresponds well to the weight based conversion. The weight based conversion of figure 5.4b has been corrected for complete sublimation of KCl as suggested by Johansen *et al.* [273].

The low feed rates of solid fuels used in the LFR results in only small amounts of char; on the order of mg. Thus, standardized methods of analysis can not be applied, e.g. CEN/TS15290(2006), which requires approximately 100 mg of sample. A cooperation with Åbo Academy University has made it possible to analyze for Ca on the LFR samples. The comparative results are presented in figure 5.4, showing a convincing agreement between Åbo's method and the international standard. Only one sample stood out, "wood KCl", but was not investigated further due to resources and an overall good accordance.

5.1.2 Vertical Solid Fuel Combustor

This section presents the 15 kW vertical combustor set-up [286], the operational conditions, and the experimental procedures. The results are presented along side the numerical modeling output in section 5.6.2.

The Experimental Set-Up

The reactor was electrically heated (< 35 kW) with a solid fuel thermal input of 15 kW. It consisted of a high temperature radiative section: 2 m long and 0.3 m in diameter. The radiative section was lined with refractory material and heated by four individual electrical heating elements to compensate for heat losses. A 1.8 m water cooled convective section followed the radiative section. All measurements were carried out in the radiative section. Process control was based on feedback controlling from gas composition measurements in the convective section.

Intrusive probe measurements were performed along the centerline of the flame: Gas phase temperature by un-shielded thermocouple measurements manually corrected for radiation bias and extractive gas sampling for gas species quantification: CO, CO_2, O_2, NO_x, and SO_2. The reactor was accessible through four view ports positioned 0.55, 1.18, 1.81, and 2.49 m downstream of the quarl, denoted P1–4, respectively, cf. figure 5.5.

Operational Conditions

The reactor was operated at an oxygen surplus corresponding to $\lambda = 1.2$ at a nominal solid fuel input of 15 kW. The flow velocity of the carrier gas at the outlet to the quarl was fixed to $30\,\mathrm{m} \cdot \mathrm{s}^{-1}$ and the remaining combustion air was channelled through the secondary air annulus. The fuel was pneumatically transported by the primary air at ambient temperature. It entered the quarl through an annulus concentrically centred in the quarl. In the quarl the solid fuel and transport air were mixed with the preheated (523 K) combustion air injected through an outer annulus. The furnace was operated with an air split (primary air/total air) of 0.3, at a total flow rate corresponding to around

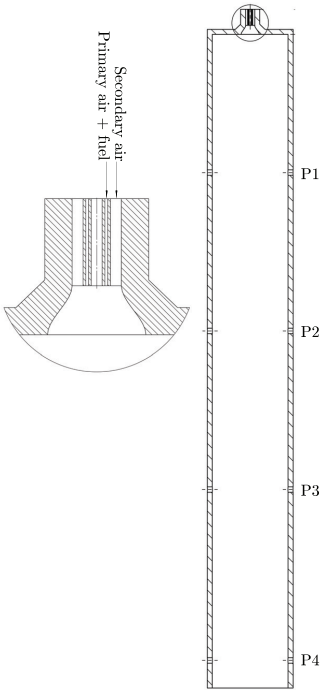

Figure 5.5 Schematic of the 15 kW vertical combustor.

3.5 vol. % (dry) O_2 in the exhaust. The reactor walls were electrically heated to 1423 K. Table 5.3 summarizes the flow settings of the reactor.

Only the wood fuel was burned in the 15 kW vertical combustor. Due to the high feed rate only the large size fraction given in table 2.13 was used.

Table 5.3 Flow setting of the 15 kW vertical combustor.

Parameter	Unit	Flow	Temperature
Biomass	$kg \cdot h^{-1}$	2.94	298
Carrier air		6.47	298
Combustion air		14.7	523

5.2 Numerical Analysis

CFD simulations of both the LFR and the 15 kW furnace have been carried out. The LFR simulations have been used to derive particle temperature and residence time histories, a requirement for the derivation of the devolatilization kinetics. The primary function of the bench-scale set-up is to evaluate the performance of the derived kinetics at higher fuel loads.

5.2.1 Laminar Entrained Flow Reactor

This section presents the CFD set-up of the LFR reactor used for the high heating rate experiments of small particles. It will include the numerical configuration, inlet and boundary conditions, as well as validation material. The particle conversion results are presented along with the experimental results in section 5.4.

Geometry and Mesh

The rectangular prism shaped LFR measures $50 \times 50 \times 455$ mm (width, depth, length) and is made from semi-transparent quartz walls in the entirety of the reactor length. The numerical model is presented in figure 5.6 and represents one quarter of the base plane, extending to the entire domain through two symmetry planes. The CFD domain begins at the flame front, i.e. levelled with the solid fuel injection nozzle. The solid fuel feed is extended upstream to allow the solid fuel particles to adjust to the carrier flow. The main reactor is modeled 255 mm downstream. The entire domain consists of 1 205 213 cells primarily made from hexahedral elements, except from in the mixing zone where the tetrahedal mesh ensures a smooth cell growth extending from the injection nozzle in both radial and axial direction.

In order to reduce the cell count, enhanced wall treatment (EWT) modeling was used allowing for relaxation of the near wall discretization requirements ($y^+ < 3$).

Inlet and Boundary Conditions

The LFR is constructed from two separate inlets: (1) Pilot flame and (2) solid fuel and carrier gas. The pilot flame inlet is positioned at the level of the solid fuel nozzle outlet and thus represents the flame front. The non-premixed pilot flame is assumed to be fully reacted (thermodynamic equilibrium) and assume the adiabatic flame temperature, cf. table 5.1. The gas, of the post-flame composition, is injected with an uniform velocity profile and the rate controlled by closing the mass balance according to table 5.1.

The solid fuel and carrier gas inlet is given as an uniform mass-flow inlet. The particles are injected from the center of each of the 14 faces making up the quarter of the symmetry plane feed tube, cf. figure 5.7.

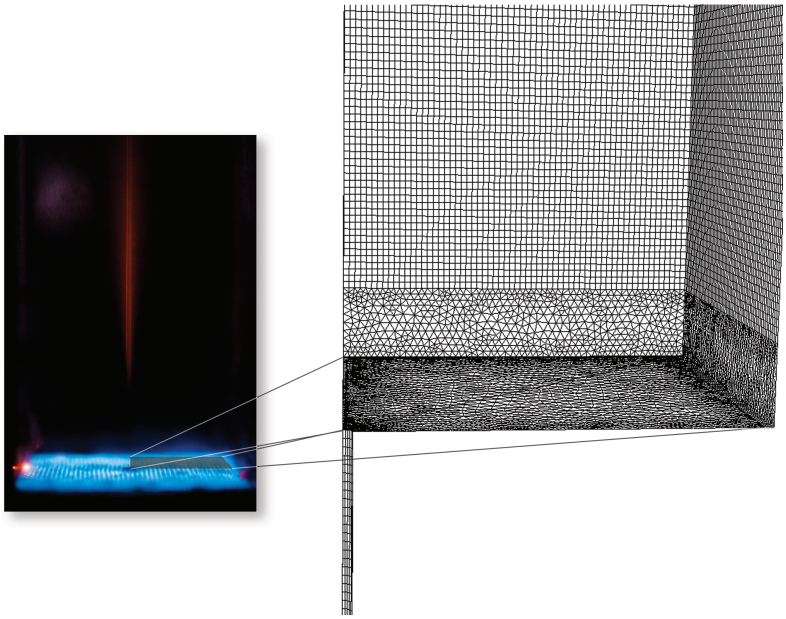

Figure 5.6 Illustration of (right) part of the computational domain relating it to (left) the experimental set-up.

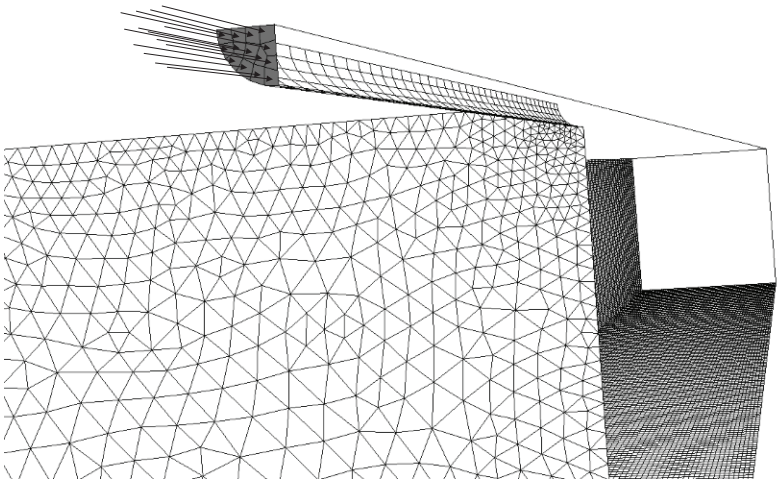

Figure 5.7 Schematic illustration of the particle inlet.

The outlet is set to zero gauge pressure with a radiation temperature corresponding to ambient conditions.

The semi-transparent walls are modeled as no-slip boundaries reflecting colliding particles. The thermal properties of the wall boundaries are adopted from previous work on quartz material [287–289]. The conductive heat transport is calculated by specifying a temperature dependent thermal conductivity with a free stream temperature of 300 K. The radiative contribution to the heat loss is controlled by the internal, ε_i and external emissivity, ε_e, both assuming the value of $\varepsilon_\mathrm{i} = \varepsilon_\mathrm{e} = 0.57$ with an external radiation temperature of 300 K.

Model Configuration

The model set-up is summarized in tables 5.4 to 5.6. For a detailed explanation of the specific models, the reader is referred to the FLUENT®Theory Guide [290].

Reactor Characterization and Model Validation

The LFR simulations have been validated against gas phase temperature measurements of the reactor running without solid fuel input. The measurements have been carried out by an unshielded thermocouple traversing along the centeraxis of the reactor. The measurements have been manually corrected for radiation bias.

Table 5.4 An overview of the sub-routines used in the LFR simulations.

Property	Model	Further specification
Turbulens	RSM	Linear pressure-strain
Wall treatment	EWT*	
Radiation	DO	
	Particle radiation interaction	
Species model	Species transport	vol, O_2, CO_2, CO, H_2O, N_2
	2-step oxidation	
Turbulence-chemistry	Finite-rate/eddy-dissipation	
Discrete phase	DPM	
	Saffman lift force	
	Pressure gradient force	
	Stochastic tracking	DRW
	Diameter distribution	Rosin-Rammler

* Scalable wall functions are used for the 15 kW combustor simulations.

Table 5.5 An overview of the physical properties of the continuous phase.

Property	Unit	Value or method
Density	$\mathrm{kg \cdot m^{-3}}$	Incompressible ideal gas
Specific heat	$\mathrm{J\,(kg \cdot K)^{-1}}$	Mixing law
Thermal conductivity	$\mathrm{J\,(s \cdot m \cdot K)^{-1}}$	Ideal gas mixing law
Viscosity	$\mathrm{kg\,(m \cdot s)^{-1}}$	Ideal gas mixing law
Absorption coeffcient	$\mathrm{m^{-1}}$	0.8
Scattering coefficient	$\mathrm{m^{-1}}$	0.8

The comparisons of the radiation corrected thermocouple measurements and the corresponding CFD simulations are shown in figure 5.8 for both flames 1 and 2. Simulation results showing the gas phase temperature at a 1 and 2 mm offset represent the physical space occupied by the thermocouple.

Figure 5.9 shows the temperature and velocity field in the mixing zone of the LFR. Figure 5.9a clearly shows how the temperature changes along the radial direction. Thus, the temperature profile used to validate the thermocouple measurements in figure 5.8 ideally is a volumetric integration of the space that thermocouple thread occupies. However, considering the accuracy of the measurements the method using discrete lines will suffice.

The bulk domain of the reactor is well within the laminar flow region [291] ($Re = 372$ and $Re = 459$ for flame 1 and 2 conditions), cf. table 5.7. However, the flow velocity of the carrier gas transporting the solid fuel particles is almost one order of magnitude higher than the bulk flow average velocity, cf. figure 5.9b. This yields slip velocities of 7–9 $\mathrm{m \cdot s^{-1}}$ between the carrier gas exiting the injection nozzle and the bulk flow. This causes local turbulent conditions in the vicinity of the injection nozzle. The overall laminar flow properties is however maintained. Figure 5.11 shows the stream lines of the

Table 5.6 An overview of the boundary conditions for the LFR simulations.

Paramter	Unit	Flame 1	Flame 2
Carrier gas			
Mass flow rate	$kg \cdot s^{-1}$	1.67×10^{-6}	
Direction	—	Face normal	
Turbulent intensity	%	1	
Hydraulic diameter	mm	1.1	
Temperature	K	300	
Emissivity	—	1	
Species	vol. % N2	100	
Pilot flame			
Mass flow rate	$kg \cdot s^{-1}$	235.5×10^{-6}	247.8×10^{-6}
Direction	—	Face normal	
Turbulent intensity	%	1	
Hydraulic diameter	mm	31	
Temperature	K	1667	1405
Emissivity	—	1	
Species	vol. $\%N_2$	Table 5.1	
Discrete phase			
Mass flow	$kg \cdot s^{-1}$	6.9×10^{-9}	
Velocity	$m \cdot s^{-1}$	6.3	
Temperature	$kg \cdot s^{-1}$	300	
Number of diameters	—	30	
Direction	—	Face normal	
Drag law shape factor	—	0.68	

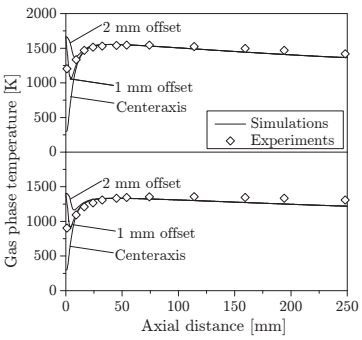

(a) Full length of the computational domain.

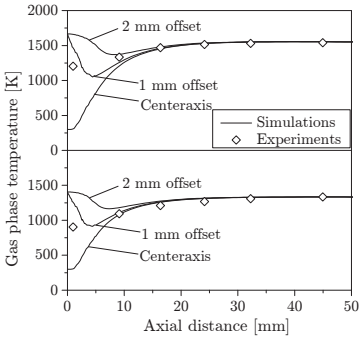

(b) Close-up.

Figure 5.8 Comarison of radiation corrected thermocouple measurements and CFD simulations of the LFR. (Above) Flame 1, (below) flame 2. The offset (radial) corresponds to the physical dimensions of the width of the thermocouple.

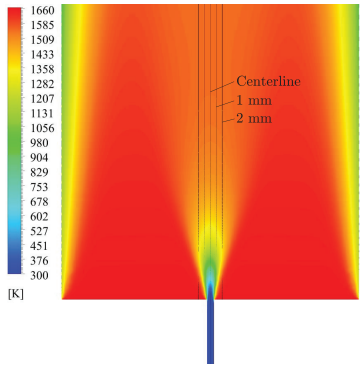

(a) Gas phase temperature.

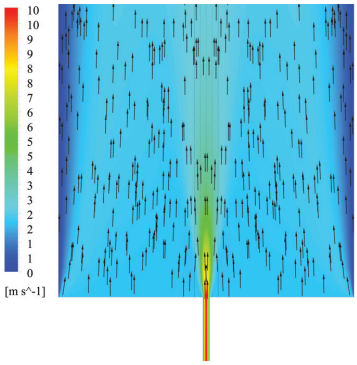

(b) Velocity field. Colors indicate absolute magnitude and arrows indicate direction.

Figure 5.9 Temperature and velocity fields in the mixing zone of the LFR. Flame 1 conditions.

LFR seeded from the pilot flame and carrier gas inlet separately. Only little radial dispersion can be observed. Figure 5.10 likewise shows the characteristic growth of both the thermal and viscous boundary layer along the no-slip walls.

Table 5.7 Average bulk flow properties. All properties evaluated at the adiabatic flame temperature.

Property	Unit	Flame 1	Flame 2
Flow	$\mathrm{L \cdot s^{-1}}$	5.07	4.70
Velocity	$\mathrm{m \cdot s^{-1}}$	1.88	1.74
Viscosity	$\mathrm{Pa \cdot s \times 10^{-5}}$	6.05	5.39
Density	$\mathrm{kg \cdot m^{-3}}$	0.20	0.24
Reynolds number	—	372	459

5.2.2 Vertical Solid Fuel Combustor

This section presents the CFD set-up of the 15 kW vertical combustor. It will include the numerical configuration, and inlet and boundary conditions. The particle conversion results are presented along with the experimental results in section 5.6.2.

Geometry and Mesh

The vertical combustor was modeled in 2D axisymmetry using a fully structured grid of 72 694 cells with a maximum aspect ratio of 4.96 and minimum

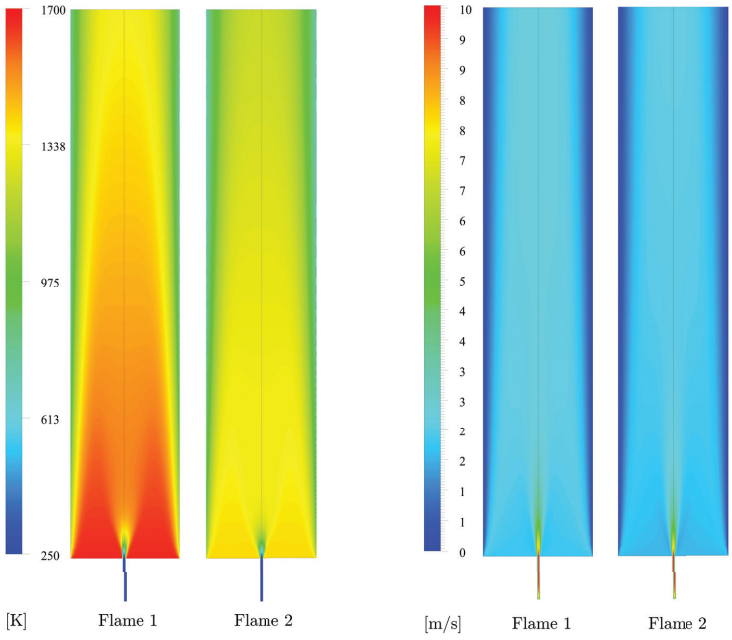

(a) Gas phase temperature. **(b)** Velocity field.

Figure 5.10 Full profile LFR temperature and velocity field along the symmetry plane. Flame 1 conditions.

orthogonality of 0.79. The fuel properties were identical to the fuel used in the LFR. Only the large size fraction shown in table 2.13 was used for the bench-scale experiments. Figure 5.12 shows the mesh around the quarl area.

Model Configuration, and Inlet and Boundary Conditions

Many sub-routines and parameters were kept in line with the LFR simulations, i.e., the DO model, finite-rate/eddy-dissipation were used for the radiation modeling and volumetric reactions. Thus, the tables of sub-routines and physical properties of the continuous phase are identical to tables 5.4 and 5.5 except that the turbulence was modeled using the realizable k-ε-model and the influence of the walls was modeled using scalable wall function in order to further relax the cell count requirements.

The inlet and boundary conditions are summarized in tables 5.8 and 5.9 respectively.

Table 5.8 An overview of the boundary conditions for the 15 kW vertical combustor simulations.

Paramter	Unit	Value
Carrier air		
Mass flow rate	$kg \cdot s^{-1}$	1.759×10^{-3}
Direction	—	Face normal
Turbulent intensity	%	5
Hydraulic diameter	mm	4
Temperature	K	300
Emissivity	—	1
Species	vol. $\%O_2$ in N_2	21
Secondary air		
Mass flow rate	$kg \cdot s^{-1}$	4.083×10^{-3}
Direction	—	Face normal
Turbulent intensity	%	5
Hydraulic diameter	mm	16
Temperature	K	525
Emissivity	—	1
Species	vol. $\%O_2$ in N_2	21
Discrete phase		
Mass flow	$kg \cdot s^{-1}$	817×10^{-6}
Velocity	$m \cdot s^{-1}$	30
Temperature	$kg \cdot s^{-1}$	300
Number of diameters	—	30
Direction	—	Face normal
Drag law shape factor	—	0.68

Table 5.9 An overview of the boundary conditions for the 15 kW vertical combustor simulations.

Paramter	Unit	Value
PA and SA walls		
Shear condition	—	No slip
Thermal condition	—	Adiabatic
Emissivity	—	0.85
discrete phase model (DPM) type	—	Reflect
Quarl and top walls		
Shear condition	—	No slip
Thermal condition	—	Adiabatic
Emissivity	—	0.85
DPM type	—	Reflect
Reactor walls		
Shear condition	—	No slip
Thermal condition	K	1423
Emissivity	—	0.85
DPM type	—	Reflect

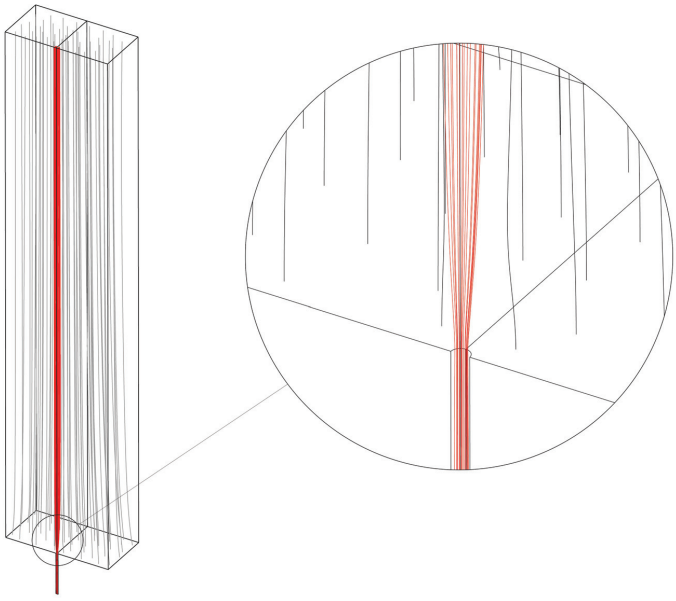

Figure 5.11 Streamlines seeded from (gray) the pilot flame inlet (red) the solid fuel inlet.

5.3 Methodology

The latter two sections presented the experimental and numerical set-up of the LFR reactor. This study work to combine the experimental data on particle partial conversion with the information on time and temperature history derived from the CFD simulations. This will provide the information needed to fit any of the kinetic models described in chapter 3.

This section will briefly outline the employed algorithm used to derive the kinetic parameters for devolatilization at very fast heating rates, cf. table 1.1.

The SFOR model is chosen for its simplicity (i.e. low computational costs) and the possibility for direct implementation to most commercial CFD codes as discussed in chapter 4.

Deriving devolatilization kinetics by combining the experimental and numerical set-ups is an iterative process. To evaluate the SFOR expression both the particle temperature, time, and mass history are required. All being interdependent on one another.

All of the work presented in this entire part (part II) relies on the common assumption that the employed particles are all small enough to be considered isothermal, i.e. neglecting all transport phenomena inside the particle. Thus,

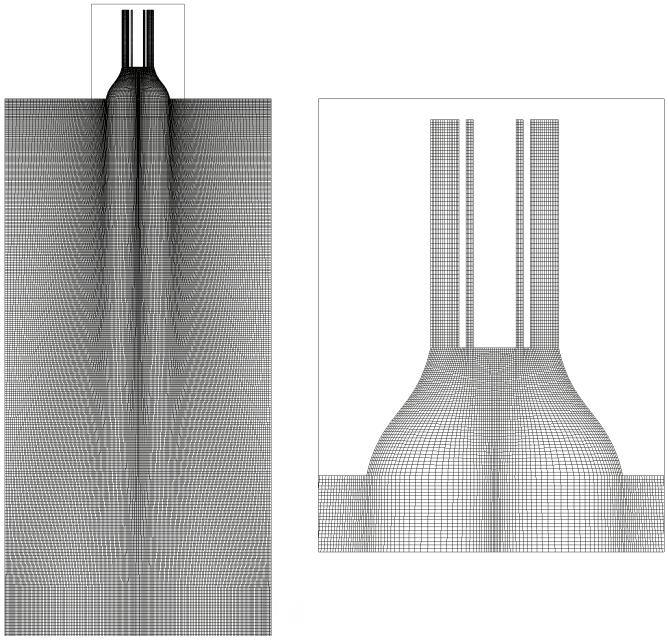

Figure 5.12 Mesh close to the quarl of the 15 kW vertical combustor.

the particle temperature can be calculated from a simple heat balance:

$$m_{\mathrm{p}} c_p \frac{\mathrm{d}T_{\mathrm{p}}}{\mathrm{d}t} = A_{\mathrm{p}} q_{\mathrm{ext}} \tag{5.6}$$

where m_{p}, c_p, A_{p}, and T_{p} are the mass, specific heat, surface area, and temperature of the particle. The external heat flux to the particle is denoted by q_{ext}. The time derived particle temperature is a direct function of the particle mass and heat capacity, which in terms are functions of pyrolysis conversion (for shrinking or swelling particles, the surface area, A_{p}, would likewise be a function of conversion). Thus coupling the particle temperature to the particle conversion and vice versa. The influence on the residence time relates to the interaction with the surrounding fluid as the particle properties change, i.e. changes in; moment of inertia, gravitational pull, drag forces, etc.

This work employs a two step algorithm to derive the kinetic parameters summarized in figures 5.13 and 5.14.

The initialization step, cf. figure 5.13, introduces inert particles to the CFD set-up deriving the particle temperature and residence time history. Combined with the experimentally obtained particle conversions a set of SFOR

kinetic parameters are determined and fed to the iterative algorithm, cf. figure 5.14.

The kinetic parameters derived on the basis of the temperature history of the inert particle simulations are used as a starting point for devolatilization simulations according to figure 5.14. Enabling reacting particles will imply a new particle temperature history that can be used to fit updated devolatilization kinetics. The cycle is repeated until the simulated conversions cohere with those obtained from the experiments.

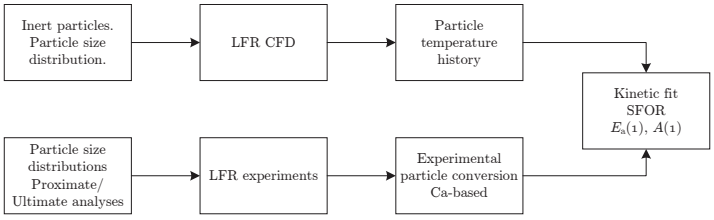

Figure 5.13 Initialization step of the kinetic fit algorithm.

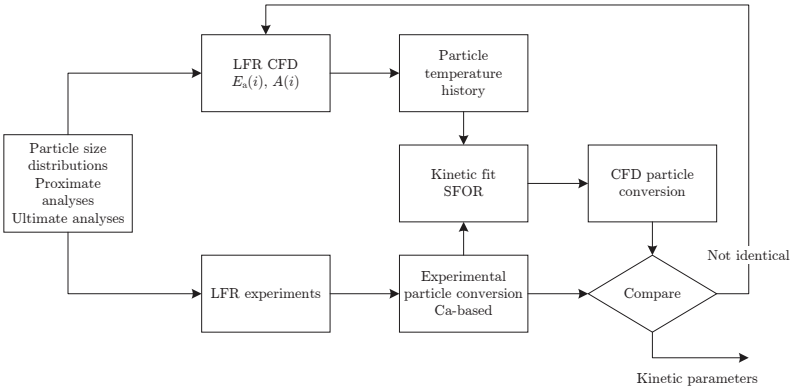

Figure 5.14 Iterative step of the kinetic fit algorithm.

5.4 Results

This section presents the results obtained from the laminar entrained flow reactor (LFR). It will combine the results from the CFD simulations with the experimental data.

5.4.1 Particle Trajectories

Because the LFR is not uniform in neither temperature or velocity field, the particle trajectories will affect both particle temperature history and residence time — both needed in order to derive devolatilization kinetics. Figure 5.15 shows an example of particle trajectories burning wood fuel at flame 1 and 2 conditions. The laminar bulk flow keeps the particles in a narrow path at the center of the reactor. However, some radial dispersion does occur. The particles are kept along the centerline as they heat up and it is not until the devolatilization initiates that the radial dispersion can be seen (the onset of devolatilization is indicated as a volume rendering of the mass fraction of volatile components in the gas phase).

This radial spread of the particles raises two concerns: (1) How does it influence the particle residence time? (2) How does it influence the particle temperature history?

As some of the particles are reflected away from the centerline their effective covered distance increases at the same time as the velocity decreases, cf. figure 5.9b. This effectively increases the particle residence time evaluated at discrete points measured as axial distances from the injection nozzle, i.e. particle collection points. This effect implies that as particles are collected experimentally at fixed points in space each particle will potentially posses its own temperature and residence time history.

To relate discrete points in space to particle property history a number of virtual planes are introduced to the CFD simulations. The plane normal follows the flow direction and are placed as indicated by the levels in figure 5.16.

Particle properties are then extracted at each of these planes, corresponding to the experimental particle collection. Figure 5.17 illustrates how the particles pass the planes. It also shows that even though the thermal boundary layer continuously grows as a function of axial distance from the inlet, the particles stay in a hot core all the way to the end of the computational domain.

When collecting particle information at discrete planes in space the resulting data summary is a distribution of the given property. Figures 5.18 and 5.19 give an overview of the resulting distributions of temperature and time, respectively.

Figures 5.18b and 5.19b show the particle temperature and residence time distributions at flame condition 1 when feeding inert particles and compare them to the distributions when devolatilization is allowed to occur. As expected only slight changes can be seen in the residence time distributions. However, when comparing the particle temperature distributions a significant increase in the discrete dispersion occurs. This can be attributed to the phenomena discussed in section 5.3.

In general, the spread in temperature distributions at low residence times is noticeable, spreading across several hundred kelvin. This could in prin-

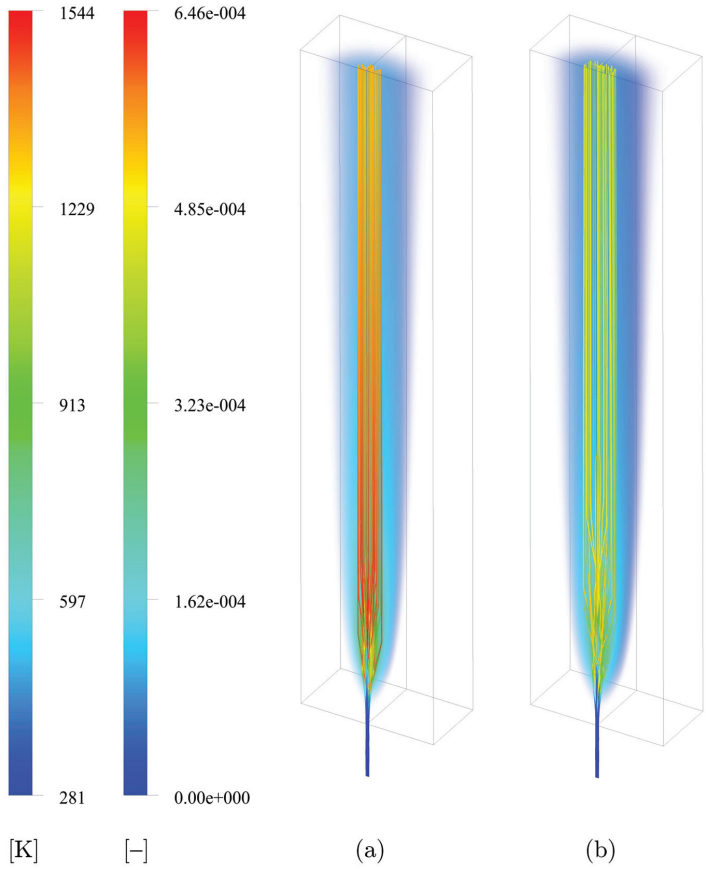

Figure 5.15 Particle trajectories colored by particle temperature. Volume rendering of the mass fraction of volatiles in the gas phase. (a) Flame 1 conditions (b) flame 2 conditions. Fuel: Wood 106–125 μm.

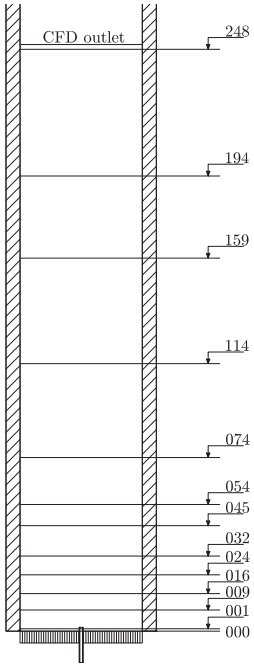

Figure 5.16 A schematic illustration of the LFR. The levels indicate the discrete planes at which information of simulated particle residence time, temperature, and conversion has been evaluated at. All units in mm.

ciple introduce difficulties when trying to fit an Arrhenius rate expression, notoriously sensitive to the temperatures.

Averaged Values of Temporal Data

Averaged values of particle temperature and residence times are computed for each discrete plane in space. This simplifies the process of fitting kinetic data. Being aware of the introduction of a statistical error, more complex modeling could consider to use the distributions of temperature and particle residence time directly. However, this is found be beyond the scope of this project.

Figure 5.20 shows the resulting particle mean temperatures as a function of the averaged particle mean residence times, derived from the CFD simulations. The figure presents both the temperature heating profile of the inert particle, cf. figure 5.13, and the temperature history as devolatilization is allowed to occur, cf. figure 5.14. The distinct difference in the shape of the temperature profile between inert and reacting particles illustrates the importance of the

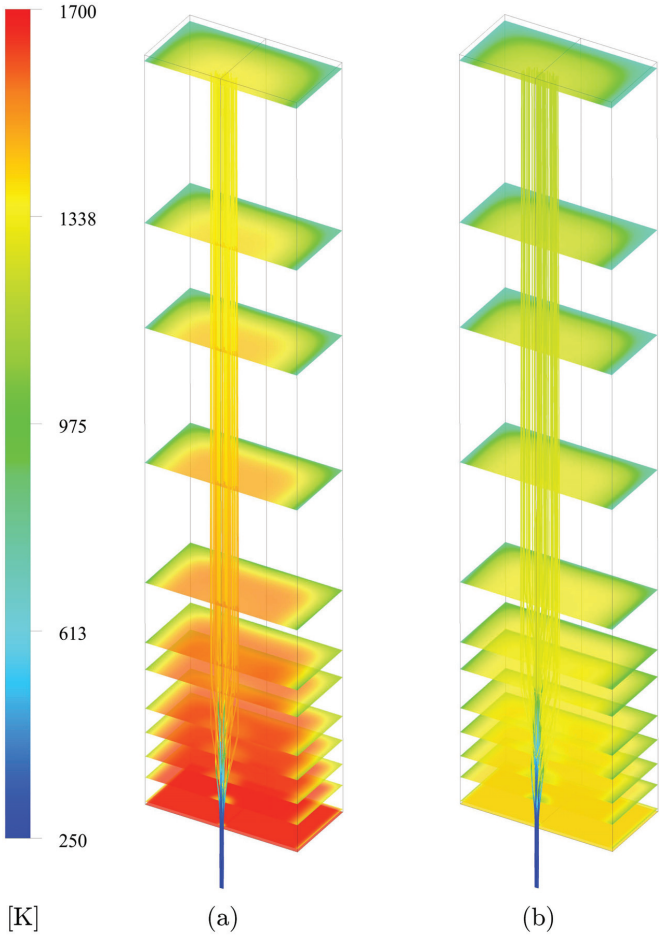

Figure 5.17 Particle trajectories colored by particle temperature. The virtual planes indicate the simulations extraction points of particle information. The planes are colored by gas phase temperature. (a) Flame 1 conditions (b) flame 2 conditions.

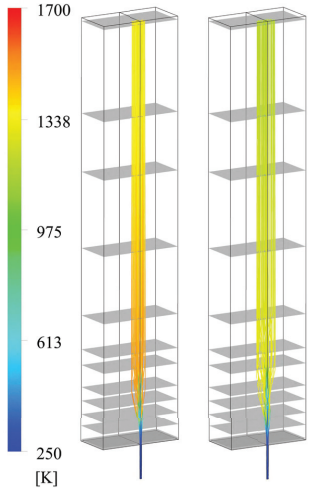

(a) (Left) Flame condition 1 (right) Flame condition 2. Colored by particle temperature.

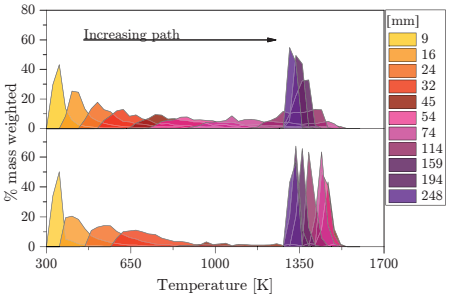

(b) Flame condition 1. (Above) Inert particles (below) Devolatilizing particles.

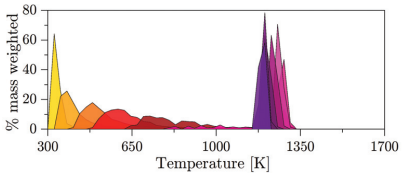

(c) Flame condition 2. Devolatilizing particles.

Figure 5.18 Particle temperature distributions for flame condition 1 and 2. Fuel: wood 106–125 μm. Each histogram corresponds to particle information collected at discrete planes in space. All histograms are mass averaged and divide the selected variable span in 50 bins.

temperature-conversion coupling. The increase in the size of the error bars is evidence of the increasing spread of the particle temperature histograms as seen in figures 5.18 and 5.19.

The development of the temperature profiles of the first and second iteration of devolatilization kinetic fit, cf. figure 5.14, are close to identical. This is caused by the comparable time scales for particle devolatilization and heat-up.

5.4.2 Release of Volatile Matter

The experimental matrix listed in table 5.2 includes particle extraction at several fixed points along the center axis of the LFR. These axial distances have been translated to average particle residence times using the CFD simulation results for each fuel and flame condition.

Due to resources only the parent fuels (untreated wood and miscanthus) have been analyzed using the Ca-tracer methods. Therefore, the following data presentation will be carried out based on the mass balances obtained from all experiments.

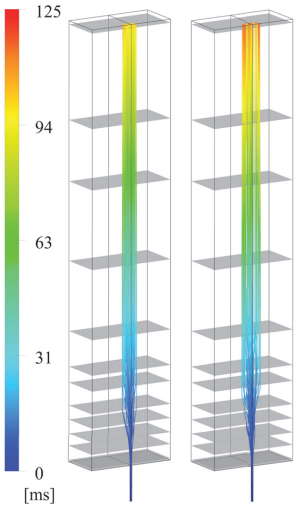

(a) (Left) Flame condition 1 (right) Flame condition 2. Colored by particle residence time.

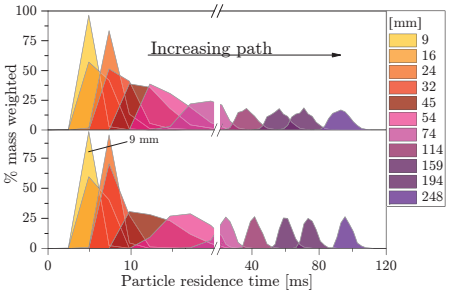

(b) Flame condition 1. (Above) Inert particles (below) Devolatilizing particles.

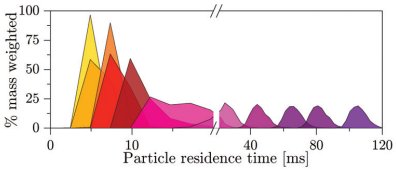

(c) Flame condition 2. Devolatilizing particles.

Figure 5.19 Particle residence distributions for flame condition 1 and 2. Fuel: wood 106–125 μm. Each histogram corresponds to particle information collected at discrete planes in space. All histograms are mass averaged and divide the selected variable span in 50 bins. The histograms are indications of distributions in discrete variable intervals. The semi-continuous representation is made for simplicity.

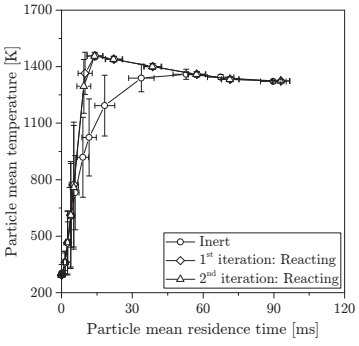

(a) Flame condition 1.

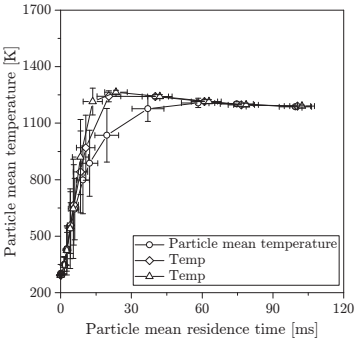

(b) Flame condition 2.

Figure 5.20 Averaged values of the computed particle temperatures and residence times. Error bars indicate standard deviations. Fuel: Wood 106–125 μm.

Repeatability

The LFR experiments were carried out in two sittings spanning across two years. A repeatability test was carried out on wood fuel at flame condition 1. Figure 5.21 presents the result of the repeatability experiment.

An offset corresponding to 0.05 in conversion can be seen, however, taking the uncertainty of the experiments and the following mass based conversion calculations into account, this is considered well within expectations.

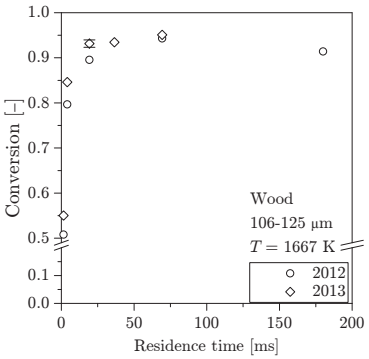

Figure 5.21 Repeatability experiment at flame condition 1 burning wood fuel 106–125 μm. The legends indicate the year of the experiment.

Influence of Particle Size

The influence of particle size have been investigated by comparing the conversion profiles of two size fractions (63–90 μm and 106–125 μm) at flame condition 1 for all four fuels. The experimental series has been designed on the assumption of isothermal particles. Thus, only slight differences in the conversion profiles are expected.

Figure 5.22 presents the conversion profiles of all four fuels. As expected only slight differences are seen between the two size fractions. For the woody fuels, the larger particles indicate slightly slower reaction times in the very beginning of the process, cf. figures 5.22a and 5.22c.

Influence of Peak Temperature

The temperature conditions of the bulk gas directly influence on the thermal driving force on the local particle heat balance. Thus, it is expected to influence to a noticeable degree, especially in the initial phase of the devolatilization. Figure 5.23 shows the comparison between the woody fuels devolatilizing in flame conditions 1 and 2.

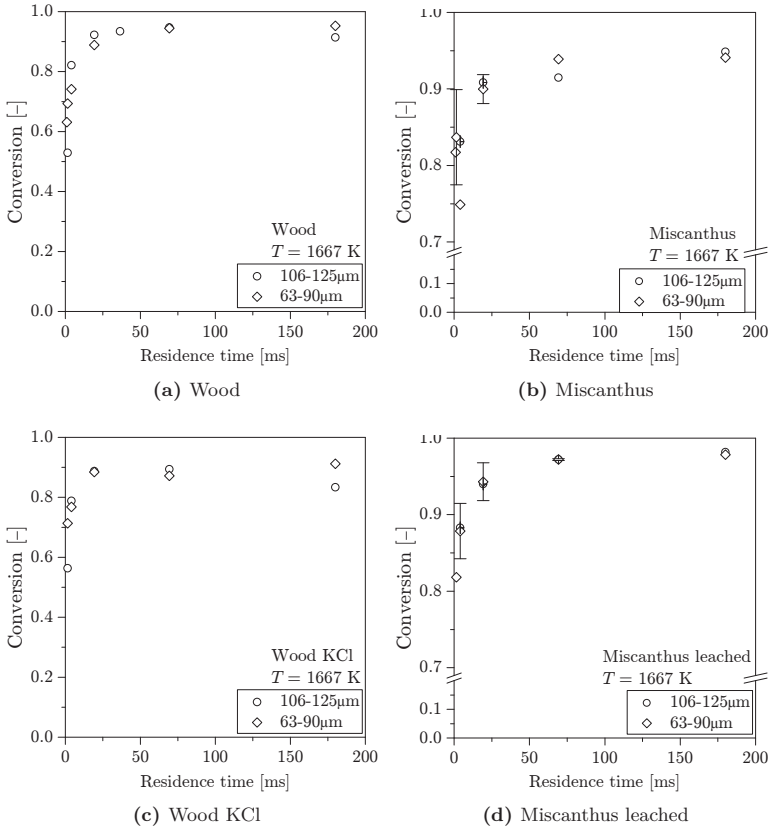

(a) Wood **(b)** Miscanthus

(c) Wood KCl **(d)** Miscanthus leached

Figure 5.22 The influence of particle size of all four fuels at flame condition 1. Error bars indicate standard deviation of multi-determination runs.

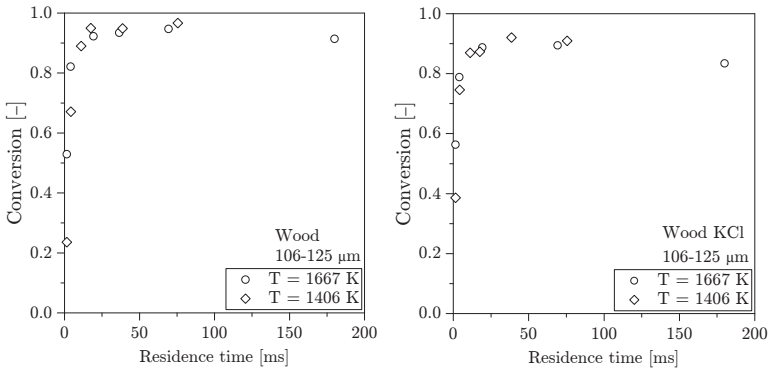

(a) Wood **(b)** Wood KCl

Figure 5.23 The influence of peak temperature on woody fuels.

The differences at low residence times are significantly more pronounced than e.g. the influence of particle size. All particles will, however, reach high degrees of conversion within the first 50 ms.

Influence of Mineral Content

Figure 5.24 presents the comparisons of the influence of mineral matter, i.e. fuel pre-treatment. The influence of the mineral matter on the final degree of conversion appears clear-cut. A full chemical analysis of the chars were not possible due to the low amounts of char and the available resources. Thus, determining whether the lower conversion is due to an increased ash fraction or a char promoting catalytic effect of the ash phase can not be determined. The temperatures are well beyond the sublimation temperature of e.g. KCl [156, 158, 273, 274, 277, 292], however, the residence times are potentially short enough for release kinetics to be the limiting factor.

For the wood based fuels, cf. figures 5.24a and 5.24b, the addition of KCl results in faster conversion in the beginning of the process compared to the un-treated wood. The opposite effect is seen for miscanthus.

Differences in Conversion Calculations

The conversion results presented in figures 5.21 to 5.24 are all calculated by closing the global mass balance, i.e. comparing the collected particle mass to the initial mass of fuel fed to the reactor. As discussed in section 5.1.1 mass losses in the system and the potential volatile ash phase could bias such calculations. This section will compare the mass balance method to

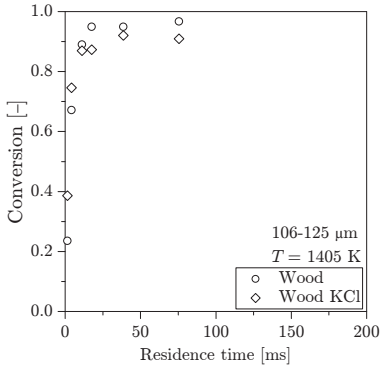

(a) $T = 1405\,\mathrm{K}$

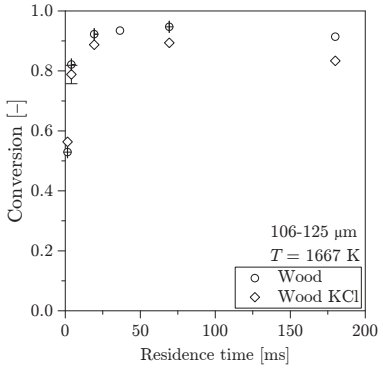

(b) $T = 1667\,\mathrm{K}$

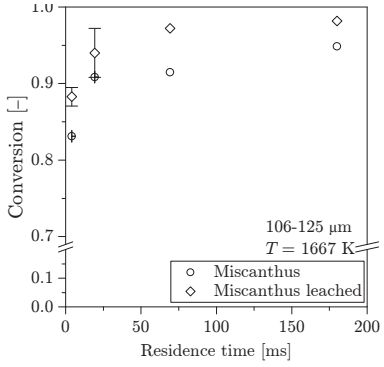

(c) $T = 1667\,\mathrm{K}$

Figure 5.24 The influence of mineral content on the devolatilization.

the elemental tracer method. Figure 5.25 shows the direct comparison of the mass and calcium based conversion. Significant differences are present, most pronounced close to the injection nozzle. The calcium volatility at low temperatures is considered negligible and thus the calcium based conversion calculations at low residence times are considered reliable. Both methods converge to the approximate same level of full conversion.

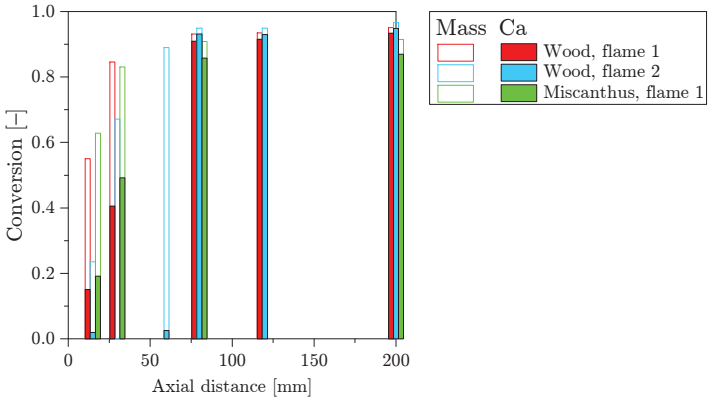

Figure 5.25 Comparison of the mass and Ca based conversion methods.

5.4.3 Morphogenic Development during Pyrolysis

The development in particle size, shape, and appearance is of interest for both a fluid dynamics and a chemical reactions point of view. Because of the high volatile fraction in biomasses most of the mass leaves the particle during the pyrolysis. In addition, the ash phase may undergo significant phase transitions during particle heating. One of many mechanisms has been proposed by Chen *et al.* [293] and summarized in table 5.10.

This section presents empirical observations as the particles undergo partial and full devolatilization.

Parent Fuels

Figure 5.26 shows SEM images of the parent fuels in the size fraction 106–125 μm depicted on the same scale. The samples are evidently needle shaped and although the upper cut-off was specified to 125 μm by sieve size, the longest dimension exceeds it by up to five times. Both the pine wood and miscanthus fuel, as well as their mineral treated derivatives, exhibit these noticeable aspect ratios. In general, the particles appear well defined and only the KCl doped wood seems slightly frayed. Among the needle shaped

Table 5.10 Phase changes of aluminosilicates at rising temperatures. Data obtained from [293].

Temperature [K]	Phase change
273–773	$2\,SiO_2 \cdot Al_2O_3 \cdot 2\,H_2O$ (kaolinite) $\longrightarrow$ $2\,SiO_2 \cdot Al_2O_3 + 2\,H_2O$ (metakaolinite)
~ 1253	$2\,SiO_2 \cdot Al_2O_3$ (metakaolinite) $\longrightarrow$ $SiAl_2O_4$ (spinel) $+ SiO_2$ (amorphous)
or	$2\,SiO_2 \cdot Al_2O_3$ (metakaolinite) $\longrightarrow$ Al_2O_3 ($\gamma-$alumina) $+ SiO_2$ (amorphous)
>1373	$SiAl_2O_4$ (spinel) $+ SiO_2$ (amorphous) $\longrightarrow$ $\frac{1}{3}\,(_3Al_2O_3 \cdot 2\,SiO_2)$ (mullite) $+ \frac{4}{3}\,SiO_2$ (amorphous)
>1573	$4\,SiO_2$ (amorphous) $\longrightarrow 4\,SiO_2$ (cristobalite) Mullite remains stable at $T > 1200\,^\circ C$
>1773	$4\,SiO_2$ (cristobalite) $\longrightarrow 4\,SiO_2$ (amorphous)

particles, which by far constitute the majority of the particles, a number of lower aspect ratio particles are present. This is the case for all four fuels but is expressed best from figure 5.26b.

Partial and Full Devolatilization

The char fractions extracted from the LFR were examined using SEM. Figure 5.27 presents the morphogenic development as the particles undergo devolatilization. The conversions are obtained experimentally and calculated based on the Ca-balance. Ca-based conversion has only been carried out for wood and miscanthus, thus, no conversion profile is given for the KCl doped wood. The time scales derived from the CFD simulations. The morphology of the leached miscanthus is discussed separately below.

Common for all of the fuels is a significant change to the shape of the particles as they undergo pyrolysis. As seen in figure 5.26, all of the fuels are needle shaped in their virgin state. However, they quickly assume close to spherical shapes as the degree of conversion approaches 1, cf. figure 5.27. The leached miscanthus seems to retain some of the structure of the parent fuel and thus exhibit less tendency to transform, cf. figure 5.28. This could be due to the low content of inorganic material other than silicon. The absence of inorganic elements prohibits the formation of eutectic compounds of low melting points, e.g. incorporation of Ca or K in the silicon phase [141, 156, 177, 294]. Figure 5.29 shows spot elemental analysis by SEM coupled with energy-dispersive x-ray spectroscopy (EDX). The areas that looks like they have transformed through a melted phase (smooth surface) are rich in both Ca and K, in addition to the Si. The melting point of the $xK_2O \cdot yCaO{\cdot}zSiO_2$ system may be as low as 990 K [295] whereas the melting point of SiO_2 is

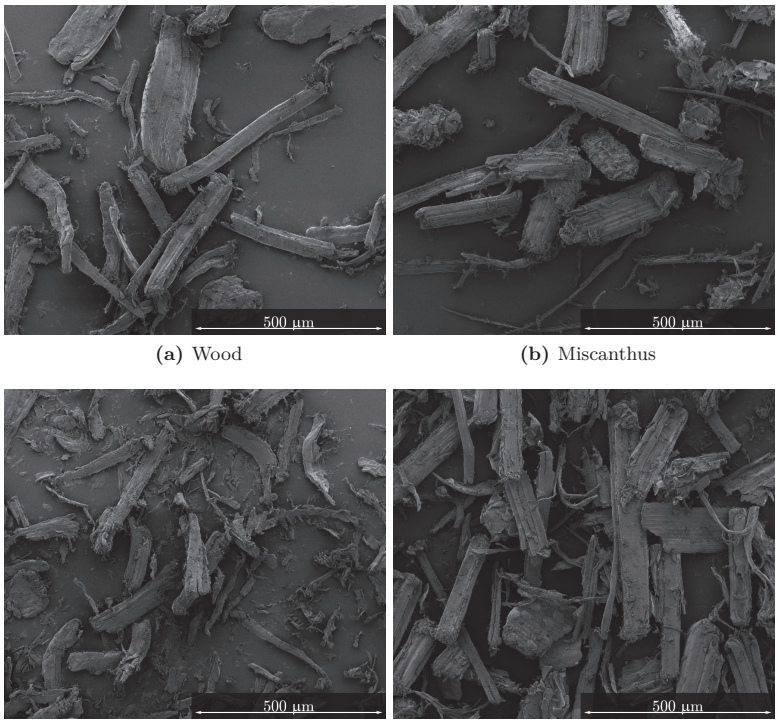

(a) Wood **(b)** Miscanthus

(c) Wood KCl **(d)** Miscanthus leached

Figure 5.26 SEM of the parent fuels. All depicted images are in the size fraction 106–125 μm and presented in same scale.

around 1900 K. The frayed areas contains almost pure Si (SiO_2) and thus less prone to transform through a melted state. This is the main difference between the leached miscanthus fuel and all of the other fuels.

The wood fuel is, if compared to the miscanthus on an absolute basis, lean in inorganic components like K, Na, Ca, etc. However, the wood particles seem retain their structural shape less well than the leached miscanthus. An indication as to why is present in the ultimate analysis of the parent fuels, cf. tables 2.7 and 2.10. Although low in the absolute concentration of components that will lower the ash melting point, the K/Si-ratio of the wood is >2.4 compared to the leached miscanthus with a K/Si-ratio of 0.15. The trend remains the same if taking other eutectic forming components into account. Thus the structure retaining Si is far in abundance in the sample of leached miscanthus and thus the fuel is more prone to retained its structural integrity

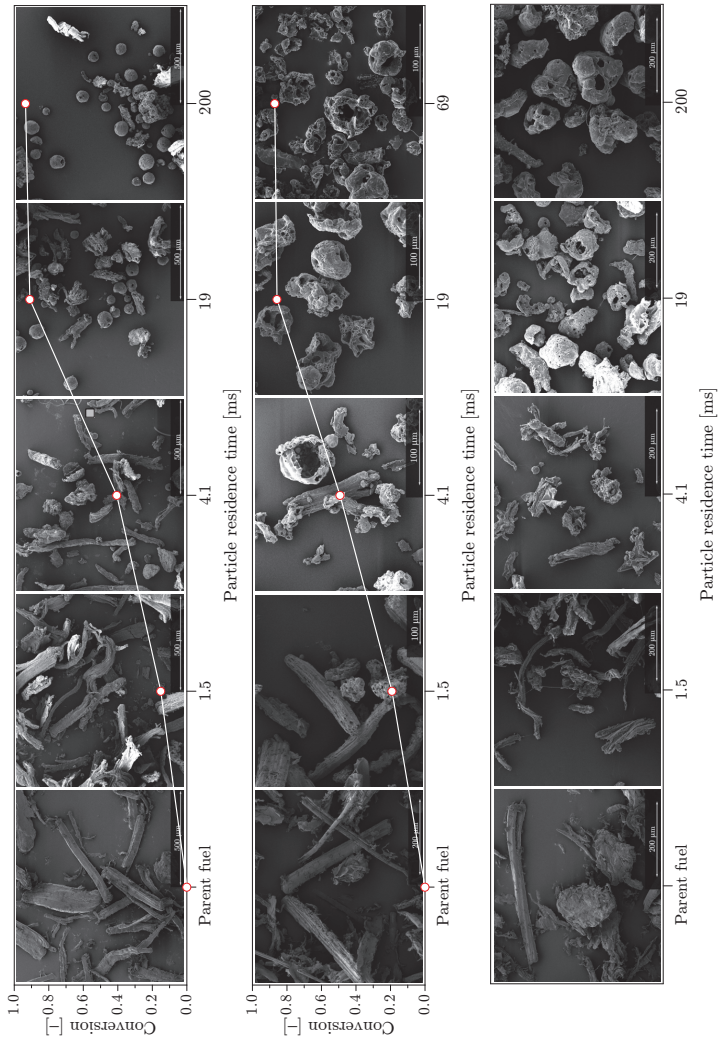

(a) Wood **(b)** Miscanthus **(c)** Wood KCl

Figure 5.27 Morphogenic development of the fuels as they undergo devolatilization in the LFR. Residence times are obtained from averaged values of the CFD simulations.

during thermal decomposition, compared to the wood fuel. Doping the wood with KCl further increases the K/Si ratio, thus potentially explaining the earlier and more severe phase shifts observed and presented in figure 5.27.

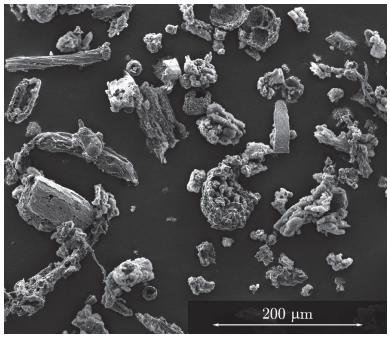

Figure 5.28 SEM image of fully devolatilized leached miscanthus.

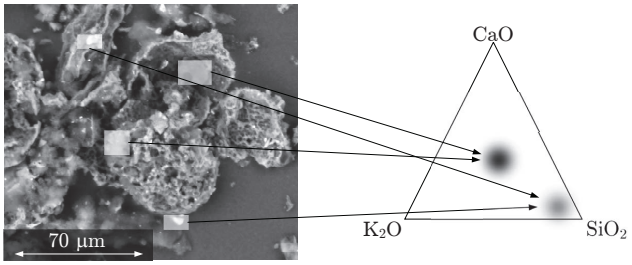

Figure 5.29 SEM-EDX analysis of fully devolatilized leached miscanthus image of fully devolatilized leached miscanthus. The melting point of the $xK_2O \cdot yCaO \cdot zSiO_2$ system may be as low as 990 K [295].

The fully devolatilized char samples, cf. figure 5.30, are dominated by spherical particles with large central cavities.

5.5 Kinetic Modeling

The algorithm summarized in figures 5.13 and 5.14 is used to generate a set of SFOR kinetics describing the devolatilization of the four fuels. This section will use the wood fuel as a case study and summarize the kinetic parameter for all fuels in the next section.

The best fit for both flame condition 1 and 2 is obtained using SFOR kinetics [296] with a pre-exponential factor and an activation energy of $18\,939\,s^{-1}$

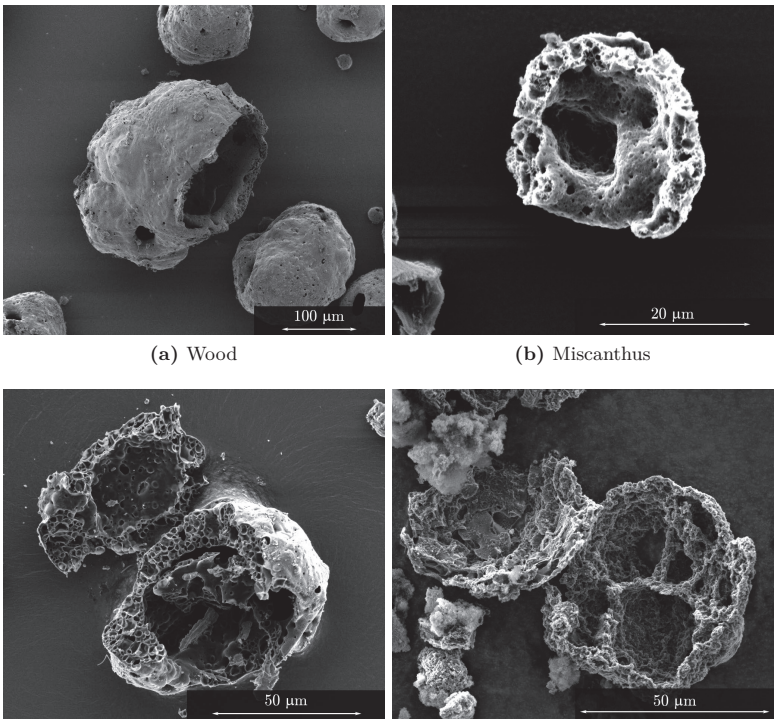

(a) Wood **(b)** Miscanthus

(c) Wood KCl **(d)** Miscanthus leached

Figure 5.30 SEM images of fully devolatilized particles.

and 21 305 J · mol^{-1}, respectively. The volatile yield was found to be 92 and 94 wt. % (dry) at flame conditions 1 and 2, respectively.

Figure 5.31 shows the fit between experimental results and the CFD simulation results. The fast devolatilization is captured well by the simulations. However, fitting a single set of SFOR kinetics to multiple temperature conditions, and thereby multiple heating rates, will never yield a perfect fit to all of the experimental results at the same time. This corresponds to the situation of the TGA as discussed in section 4.2.

During the experiments, the devolatilizing particles were surrounded by a red glow from burning volatiles. This is the main empirical indication of the ongoing devolatilization and can be compared to the simulated mass loss of the particles. Figure 5.32 shows a good agreement between the onset of the simulated particle mass loss, cf. figure 5.32a, and the observed appearance of the red glowing burning volatiles, cf. figure 5.32b.

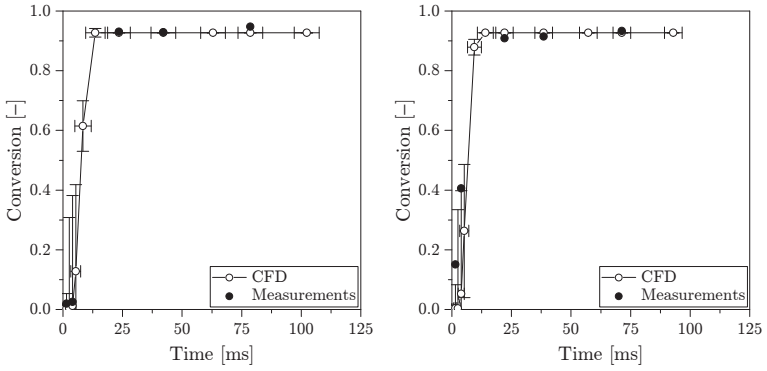

(a) Flame condition 1. **(b)** Flame condition 2.

Figure 5.31 Comparison between the measurements and CFD simulations. The errorbars: standard deviation indicating the spread of the particle temperature and residence time distributions obtained from the CFD simulations.

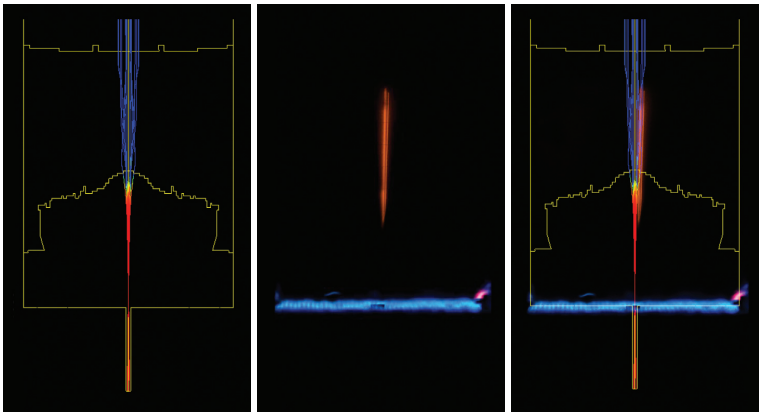

(a) Simulation. **(b)** Experiment. **(c)** Combined.

Figure 5.32 A comparison of the simulated particle devolatilization and the observed reacting particles. Color scale: Particle mass, red: Initial mass, blue: Fully devolatilized.

5.6 Discussion

This section includes a number of comparisons of kinetic expressions. All comparison will be based on the untreated wood fuel.

5.6.1 Literature Comparison

Figure 5.33 compares the conversion curves as function of particle temperature for the low heating rate TGA experiments and the high heating rate LFR predictions. The tendency of shifting the conversion curve to the right as the heating rate increases is apparent. This of course influences the small isothermal particles, but becomes even more important when modeling larger non-isothermal particles as they potentially experiences large variations in both temperature and heating rate as conversion progresses.

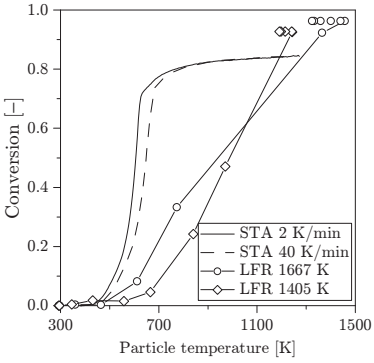

Figure 5.33 Comparison between low heating rate TGA and high heating rate LFR experiments.

When deriving high heating rate devolatilization kinetics, three levels of assumptions are often met in the literature:

- The particles assume the nominal temperature of the reactor set-up.
- The particles follow the gas phase temperature.
- The particle temperature history has been calculated on the basis of a simple heat balance with static boundary conditions.

Figures 5.34 and 5.35 compare kinetic devolatilization data across selected literature studies. The comparison has been made based on the temperature history predictions from the current work. It compares the current results to the work of Simone *et al.* [264] who likewise based their kinetic derivation on

CFD generated temperature histories, the work of Bonvicini *et al.* [89] who evalutated the global kinetics at the nominal temperature of the reactor, and the slow heating rate TGA classic approach.

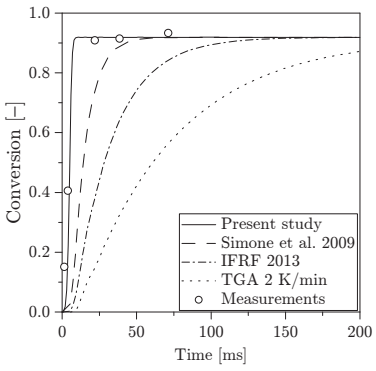

Figure 5.34 Comparison of the current work to literature data on devolatilization kinetics obtained using different levels of assumptions.

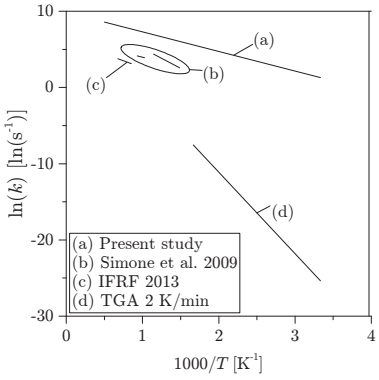

Figure 5.35 Comparison of the results of (a) the current work [269], (b) Simone *et al.* [264], (c) Bonvicini *et al.* [89], and (d) TGA, current work.

Simone *et al.* [264] determined a set of SFOR kinetics for the devolatilization of cacao shells using a laboratory scale drop tube furnace. The experiments were assisted by CFD generated particle temperature histories, however, at relatively low nominal temperatures (673–1073 K) and with broad size distributions (90–150 μm). The conversions were based on the ash tracer method, justified by the low nominal temperatures, thus leading to increased likelihood of a non-volatile ash phase. Simone *et al.* [264] concluded that a single set of kinetic parameters struggled to describe the devolatilization process to a satisfying degree when spanning large temperature intervals. Instead they employed a two-zone system applying different kinetics for low and high temperatures respectively, with the shift in kinetic regime taking place between 873 and 973 K.

The most common approach to the determination of kinetics using high heating rate set-ups has recently been applied by Bonvicini *et al.* [89] studying the pyrolysis of a range of biomasses, including a softwood, presumably comparable to the fuel used in this study (based on ash and high temperature volatile fractions and the ultimate analysis). In the study it was assumed that the particles follow the nominal temperature of the reactor. The method is expected to result in an artificially slow set of kinetics to compensate for the assumed instant heat up of the particles. The effect is in agreement with the comparison in figure 5.34.

Although the conditions are significantly different from suspension firing conditions, low heating rate thermogravimetric methods of biomass fuels are often used and thus compile the most comprehensive information base on fuel pyrolysis characteristics across fuels and reaction conditions. However, no consensus on how to interpret these results for application to high heating rate processes seems to exist.

It is noticeable how the kinetics, for the high heating rate studies, become gradually slower as the assumptions increase in coarseness, figure 5.34. This is reasonable if considering the approximation of Bonvicini *et al.* [89] evaluating the global kinetics at the nominal temperature of the reactor. Because the heat up of the particles has been neglected, the determined kinetics are slower and thereby account for the particle heating (and mixing) in the original experiments.

In line with literature reports the activation energy of the corresponding TGA derived kinetics for the parent fuel is significantly higher than the fitted data from the high heating rate experiments. This results in a considerably slower occurrence of the pyrolysis reaction when applied to the high heating rate temperature history, figure 5.34. This emphasizes the need for high temperature data if reliable devolatilization kinetics are to be used for pulverised fuel fired boilers.

5.6.2 Bench-Scale Evaluation

The devolatilization kinetics derived in the preceding section is applied to CFD modeling of the 15 kW bench scale reactor. With a solid fuel feed rate of $2.9\,\mathrm{kg}\cdot\mathrm{h}^{-1}$ it allows for the evaluation of the combustion process at higher particle bulk densities.

Reactor Characterization

Figures 5.36 and 5.37 give an overview of the primary properties of the reactor. The un-swirled primary air and secondary air result in a jet like flame structure. The fast kinetics results in a short but intense reaction zone. The reacting particles are stabilized along the centeraxis by the large toroidal recirculation zone. All reactions are taking place in the first half of the reactor.

Results

Figures 5.38 to 5.40 summarize the comparison between measurements along the center axis of the 15 kW vertical combustor and the model simulations. Key parameters: Gas phase temperature, O_2, CO, and CO_2 concentrations are used to characterize the combustion process, data which is available from both simulations and measurements. Further more the influence of devolatilization kinetics is studied by comparing the simulation results to calculations using devolatilization kinetics obtained by alternative methods; using the TGA

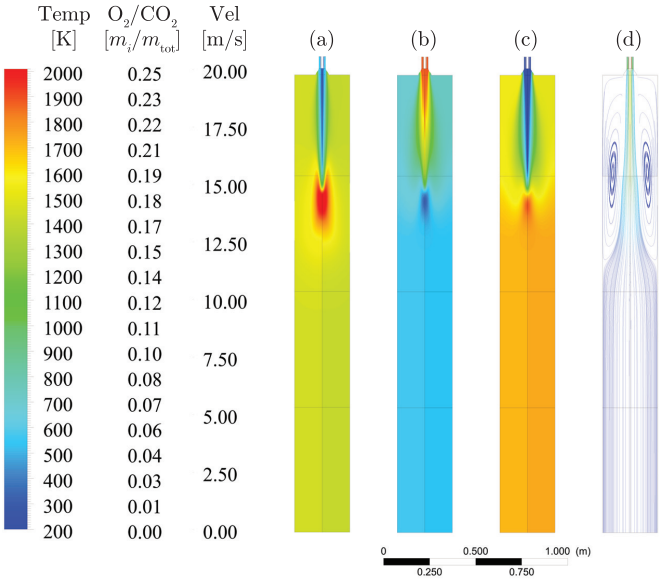

Figure 5.36 Central contour plots of the 15 kW vertical combustor. (a) Temperature, (b) O_2 concentration, (c) CO_2 concentration, (d) overall streamlines.

kinetics derived from section 4.2 and selected literature data [89]. The literature data has been selected based on the method used to derive the kinetic parameters. Bonvicini *et al.* [89] use the common assumption that the particles assume the reactor temperature. This results in slower kinetics as it will compensate for the particle heat up.

The jet like flame penetrates approximately half a meter (around sampling port P1) before the particles reach the decomposition temperature. Figure 5.38 describes the temperature level well. However, the gas phase temperature has already reached post combustion temperatures at the first measurement port. Thus making it difficult, solely based on the gas phase temperature results, to evaluate whether the CFD calculations are in fact capable of predicting the correct onset of the devolatilization. The gas phase temperature peak predicted by the CFD simulation correspond well to previous experiments in the vertical combustion [297].

Comparing the O_2 and CO_2 measurements to the CFD predictions yield a better insight to the onset of the devolatilization. Figure 5.39 indicate ongoing reactions at measurement port P1. The CFD predictions correspond well to the observed O_2 and CO_2 levels. Comparing it to the slower kinetics derived from the TGA or the literature data shows a significant delay in the

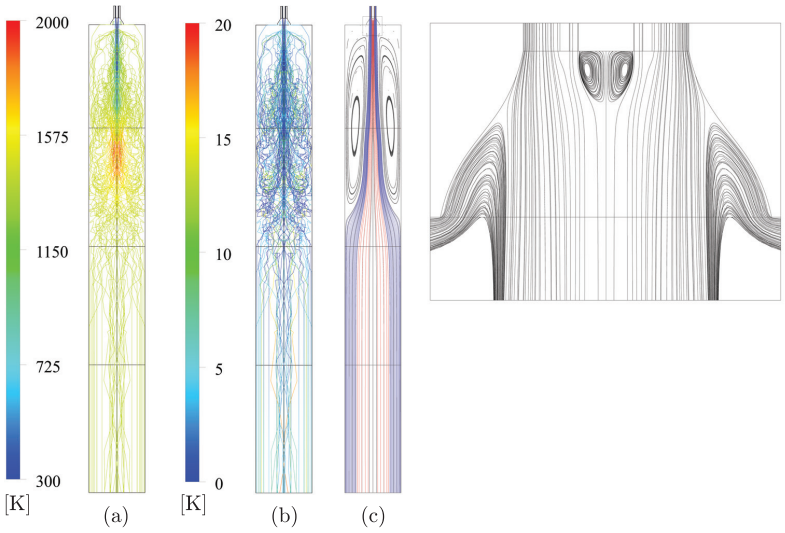

Figure 5.37 (a) Particle tracks residence time, (b) particle tracks temperatureParticle tracks, and (c) streamlines of the 15 kW vertical combustor (red) primary air, (blue) secondary air, (black) recirculation zones.

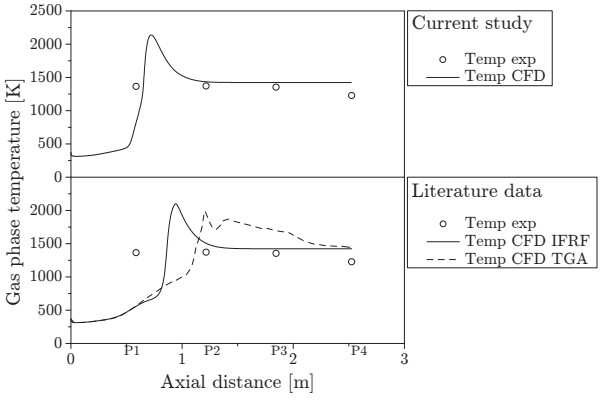

Figure 5.38 Comparison between CFD results and gas phase temperature measurements. (Above) Current study and (below) comparison to TGA data and Bonvicini *et al.* [89]. The indications P*i* refers to the ports as defined in figure 5.41.

consumption and production of O_2 and CO_2, respectively.

The appearance of CO is often used as an indication of ignition in gas-phase kinetic studies. The disagreement between the CFD predictions and the measurements of CO are believed to stem from the simplified two-step volatile oxidation mechanism. The appearance of the CO peak in the axial direction does however correspond to the expected onset of the ignition.

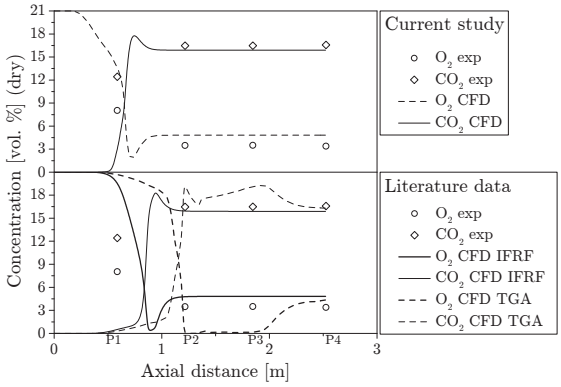

Figure 5.39 Comparison between CFD results and gas phase measurements. (Above) Current study and (below) comparison to TGA data and Bonvicini *et al.* [89]. The indications P*i* refers to the ports as defined in figure 5.41.

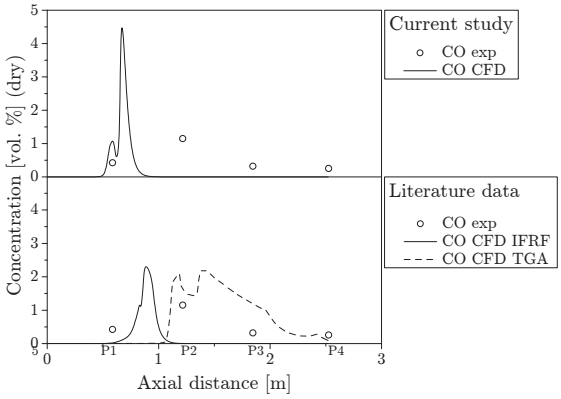

Figure 5.40 Comparison between CFD results and gas phase measurements. (Above) Current study and (below) comparison to TGA data and Bonvicini *et al.* [89]. The indications P*i* refers to the ports as defined in figure 5.41.

In general, a slight delay in ignition is indicated from both the gas phase

temperature (figure 5.38), and the O_2 and CO_2 predictions (figure 5.39). However, large gradients occur in both the axial and radial direction, as indicated by the contour plots in figure 5.36. Such gradient make point-to-point comparison between computational predictions and experimental measurements notoriously difficult as small deviations from either method may lead to a slight offset and thus a large absolute difference. The simulations is inherently influenced by assumptions such as uniformly shaped particles, influencing the multiphase aerodynamics, the simplified chemistry, influencing the chemical source term distribution, etc. The experimental methods are influenced by practical issues like wear and tear on the equipment, introducing asymmetries, large tolerances on the flow control, not ideally continuous fuel feed, etc.

The char and ash samples collected from the reactor has been analyzed by SEM and a chronological overview is presented in figure 5.41. The samples were collected along the centerline and shows a clear development of the particle morphology much in line with the findings of the LFR study.

5.7 Summary

In this chapter a method has been developed and applied for characterizing the devolatilization process of four fuels at heating rates ($\mathcal{O}10^4$–$10^5\,\mathrm{K\cdot K}$) and peak temperatures (1405–1667 K) relevant to PF suspension fired combustion.

Detailed particle temperature and residence time histories have been calculated using CFD simulation of the specific set-up. The simulations are coupled to the experimental results by iteratively updating the devolatilization kinetics.

Table 5.11 summarizes the final SFOR kinetics of all tested fuels. The resulting kinetics are found to be significantly faster than those previously reported in the literature. The influence of the fast kinetics has been evaluated in a 15 kW vertical furnace at higher fuel loads. The slower kinetics found in the literature results in a significant ignition delay, compared to the experimental bench-scale data. Implementing the fast kinetics, derived in the present work, yield good agreement between simulations and experimental measurements.

Table 5.11 A summary of the derived SFOR devolatilization kinetics.

	A $\times 10^3\,\mathrm{s}^{-1}$	E_a $\mathrm{J\cdot mol}^{-1}$
Wood	18.9	21 305
Miscanthus	20.5	17 891
Wood KCl	14.8	14 350
Miscanthus leached	13.7	13 511

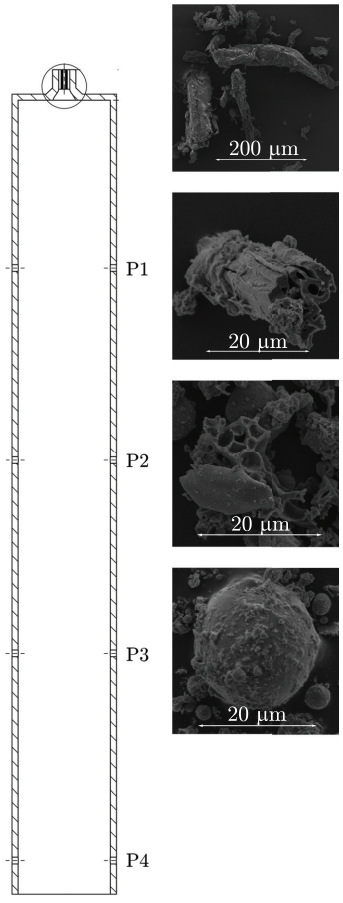

Figure 5.41 SEM images of char and ash samples collected from the 15 kW reactor.

As will be discussed in part III the existence of thermally thin particle for conditions relevant to suspension fired condition can be questioned. However, the physical consequences may justify the application of these simplified models.

Part III

Devolatilization of Larger Biomass Particles

"A man who dares to waste one hour of time

has not discovered the value of life"

—Charles Darwin

CHAPTER 6

Introduction and Existing Literature

Part II described the devolatilization of particles small enough for the internal heat gradient to be insignificant and the conversion controlled by chemical kinetics. This part will characterize and mathematically describe the behavior of larger and transport limited particles as they undergo thermal decomposition; starting with the introduction of intraparticle transport phenomena and existing literature. The part will be concluded with a study aiming to simplify the mathematical description of the multi-dimensional phenomenon of thermally thick particle conversion. An isothermal approach has been developed, making heat transport corrected calculations readily implementable to commercial CFD solvers with minimal computational requirements, thus reducing the turn-over time of complex reacting multiphase flow calculations.

6.1 Introduction

When a particle is exposed to pyrolysis or combustion conditions it will undergo a series of processes commonly described as heating, drying, devolatilization, and char burn-out. The heat-up of the particle largely defines the ignition delay [49]. Particle drying is an endothermic process that has been shown to cause a measurable temperature plateau around 373 K [298, 299], thus consuming most of the energy transported to the local point at the edge of the heat front. The thermal degradation of the organic structure takes place at higher temperatures, and the char burn-out is often limited by the gas composition of the surrounding gas or hindered by a convective mass flux leaving the particle as a result of increasing temperature and the phase transition originating from the drying and devolatilization processes. Hence, the processes of drying and devolatilization can be assumed to take place in series for thermally thin particles, cf. figure 6.1a. However, for thermally thick particles all stages can in principle co-exist due to the span of temperatures inside the particle, cf. figure 6.1b.

6.1.1 Basic Mechanisms of Fuel Pyrolysis

When a thermally thick particle is exposed to an external heat flux at pyrolysis conditions a number of interdependent processes take place. The complexity is outlined in figure 6.2, sketching out the mass transport, heat transport,

(a) Sequential devolatilization of a thermally thin particle.

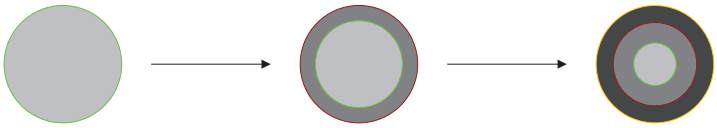

(b) Parallel devolatilization of a thermally thick particle.

Figure 6.1 Principled differences between devolatilization of a thermally thin and thick particle. Char burn-out is not considered in this sketch.

and reactions as they take place in the different co-existing zones inside the particle.

The external heat flux will induce a heat front propagating from the surface towards the center. The temperature at radial distance r will continue to increase to around 373 K where it will stagnate until all water has been evaporated. Water evaporation takes place at the heating front and all through the drying zone. Any water contained below the fiber saturation point (FSP) (essentially all water in PF relevant fuels) will be chemically bound to the solid structure and thus energy will be diverted to a desorption reaction directly followed by the evaporation. As water is evaporated, it is transported to the surface of the particle by diffusion or convection.

As time proceeds, the local moisture content at radial distance r will reach depletion and the temperature will continue to rise. As the temperature rises, the thermal decomposition of the organic structure will accelerate leading to the release of volatile components and formation of char. This pyrolysis zone propagates behind the drying zone towards the center of the particle leaving behind a shell of char.

The co-existence of the drying, devolatilization, and char zones imply that the evaporated water travels through the moderate temperature pyrolysis zone. In this zone, the water vapor meets the primary pyrolysis products leading to potential secondary reactions of either endo- or exothermic nature. In addition, the devolatilization process it self may be endothermic. A sufficient drop in temperature would lead to condensation of the heavier pyrolysis products, tars, and possibly water vapor.

Primary pyrolysis products, not re-condensing or reacting with water vapor , will be transported together with the remaining water vapor to the high temperature char layer. Again, secondary reactions may occur accelerated by the elevated temperatures. Cracking of tar to lighter gases and char occurs in

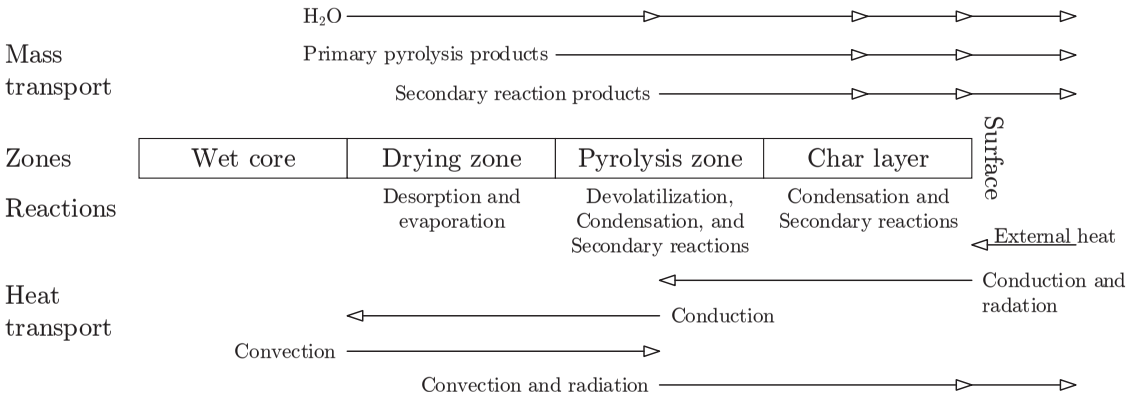

Figure 6.2 Schematic diagram of the thermal degradation of a non-isothermal particle.

the gas phase while char gasification by either water or oxygenated pyrolysis products takes place from the exposed surface.

From a modeling point of view, the sequential nature of the devolatilizing thermally thick particle implies a fundamental difference from the smaller particles. The sequential approach may be modeled as independent processes only linked by a continuation in the particle temperature, as illustrated in figure 6.1a. The parallel approach necessary in order to describe the pyrolysis of larger particles can be illustrated as in figure 6.1b.

6.1.2 Thermal Thickness of a Particle

The relevance of developing a non-isothermal model for application in the PF combustion industry turns on the existence of transport limitation in the relevant particle sizes. This section does preliminary analysis on a typical woody fuel establishing the relevance of a non-isothermal model.

One of the most widely used methods to categorize a particle as being thermally thin or thermally thick is by assessing the Biot number[1], Bi. For inert particles the transition from the iso-thermal to the non-isothermal regime occurs at $Bi = 0.1$. However, for transient models where the thermophysical properties change as function of temperature and solid composition, the problem becomes somewhat more ambiguous.

Bryden *et al.* [300] used a Biot number analysis based on the parent fuel properties and correlated the output to their transient model for solid fuel thermal degradation. They found that a Biot number of 0.2 indicates the transition from the thermally thin to the thermally thick regime, as recommended by Borman and Ragland [301]. They included the contribution from external radiation by assuming a particle surface temperature equal to that of the bulk. Knowing that this would overestimate the radiative heat transfer, they corrected the total heat transfer coefficient by dividing it by a factor of 2. The resulting output was estimated to be within 25 % accuracy.

However, because the contribution from external radiation depends on the particle surface temperature to the power of 4, this term will change significantly as the particle undergoes heat up from ambient to the final temperature. In addition, the contribution from radiation for smaller particles will be small compared to the influence of convective heat transport.

A conventional Biot number analysis is illustrated in figure 6.3. It shows how the requirement of $Bi \ll 1$ will never be satisfied for conditions relevant to suspension fired combustion, even for very small particle sizes. The implication is that on dimensionless time scales, the temperature gradients inside a particle cannot be neglected, regardless of particle size.

[1] $Bi = \frac{h d_p}{2\lambda} = \frac{\text{Heat transport to the particle}}{\text{Heat transport through the particle}}$

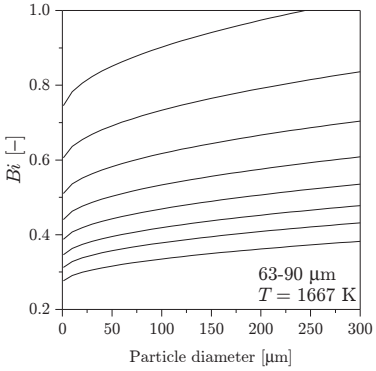

Figure 6.3 A Biot number ($Bi = hd_p/(2\lambda)$) of a biomass particle analysis based on the physical properties listed in table 7.3. The heat transfer coefficient, h, is calculated on averaged values of gas properties at temperatures between 1400 and 1700 K and at a slip velocity of $2\,\mathrm{m}\cdot\mathrm{s}^{-1}$. The temperatures indicate particle temperatures.

6.2 Existing Literature

Non-isothermal modeling related to pulverized fuel (PF) combustion has only recently become interesting as the transition from coal to biomass feedstock introduced much larger particles to the combustion facilities. However, it has been the focus of numerous studies in related technologies; grate firing units, fluidized bed combustors, wildfire simulations [302], fire protection [299], wood-stoves, and similar technologies utilizing solid particles of a certain size; pellets, chips, logs, etc. As a result, a number of studies on non-isothermal models exists in the literature. However, the focus of the studies and the conditions at which the models or experiments are derived from or carried out in are likewise diverse. Carrying out an exhausting literature review on non-isothermal models is far beyond the scope of this study and thus this section will outline the main features of only a few selected studies.

One of the earliest models developed by Bamford *et al.* [303] was based on a 1-dimensional thermal conduction transport mechanism and validated against core temperatures of a 2–4 cm thick wooden slab. The width of the slab was sufficiently large to avoid boundary effects from multiple dimensions. The heating rates obtained were limited and it was possible to describe the decomposition by a single first order Arrhenius type rate expression. The heat of thermal decomposition was modeled as exothermic.

A similar 1-dimensional thermal model was developed by Roberts and Clough [227] using cylindrical samples. They conducted decomposition experiments at low temperatures ($< 700\,\mathrm{K}$) in an inert atmospheres. They acquired time resolved mass loss data and temperature measurements in six

radial positions measured by thermocouple. This was used to fit a SFOR mechanism with an exothermic latent heat. They observed core temperatures exceeding the surface temperatures and concluded that it stemmed from secondary exothermic reactions. However, they did not implement this into their model. Exothermic reactions resulting in core temperatures exceeding those of the furnace was also observed by Tinney [304] who also studied the blowing effect of escaping volatiles by measuring the pressure inside the particle.

In 1971 Panton and Rittmann [305] developed a shrinking core model by adapting thermophysical properties from existing literature: Density and thermal conductivity. No experimental work was related to the model and thus the thermal decomposition was based on literature data, using cellulose as a model compound. Using a two competing reaction scheme, this work was one of the earliest attempts of implementing more complex reaction schemes in a full heat transport based model.

The most detailed single particle models couple multiphase transport of heat and mass with volumetric gas-phase reactions, cracking reactions, and multiple competing multi-step reactions for the pyrolysis process. Kung [306] introduced a model including both heat and mass transport, modeling the decomposition of the organic matrix by a SFOR mechanism; including heat of reaction, however, not taking secondary reactions into account. A further study on the secondary reactions [307] showed an apparent endothermic nature of the primary reactions — contradicting the common conception since the earliest experiments by Bamford *et al.* [303]. In general, no real consensus can be established on the thermal properties of the pyrolysis [54].

Di Blasi [308] studied the rate of flame spread in a two-dimensional transport model including energy, momentum, and mass. He found that concerning flame spread the transition from thermally thin to thermally thick particles varies greatly with fuel type.

The limitations of the SFOR mechanism were addressed by Kansa *et al.* [309] who developed a complex model based on the advances of Kung [306]. In addition, the anisotropic nature of the wood structure was included and the radiative contribution to internal heat transport was taken into account. The mass transport of gaseous species inside the particles was calculated by closing Darcy's momentum equation.

Chan *et al.* [129] did a large experimental and modeling based study on 1 cm cylindrical biomass particles. They implemented a complex multi-step reaction scheme taking both water evaporation and the formation of gas, char, and tar into account. By introducing a fully coupled reaction scheme and experimental quantification of escaping gases, they were able to predict the product yields of gases, char, and tar.

Di Blasi and Russo [310] included the effect of secondary reactions in the form of tar cracking. Modeled by first order Arrhenius expressions, this mechanism remains as one of the most widely used to this day.

Lu *et al.* [170] developed a single particle one-dimensional model taking

heat and mass transfer into account and including both drying, devolatilization, and char burn-out. They found the non-isothermal model to significantly deviate from the corresponding isothermal model for particles exceeding a few hundred microns in diameter. This resulted in longer reaction times. Similarly Grønli and Melaaen [115] developed a single particle model for large particles (2–3 cm) and found that the addition of secondary cracking reactions is necessary in order to capture the ratio between gas, tar, and char for variations in the heating conditions. They concluded that the density, temperature, pressure, and moisture profiles were affected by the applied external heat flux. Mehrabian *et al.* [87] addressed the heating rate regime for different industrial purposes, using a one dimensional transport model to evaluate the effect of heating rate, validated against the experimental results of Lu *et al.* [170].

Bharadwaj *et al.* [311] carried out a mathematical investigation on the influence of particle internal heat and mass transport and concluded that the drying and devolatilization was controlled by heat transport alone.

Johansen *et al.* [269] showed through high heating rate experiments of particles less than 125 μm in diameter that the time scale for particle heat-up is comparable to that of complete devolatilization, extending even further for larger particles.

Wagenaar *et al.* [236] combined the classic slow heating rate thermogravimetric methods with flash pyrolysis drop tube experiments. They were able to derive a single set of kinetic parameters capable of describing the pyrolysis of both set-ups at temperatures below 873 K.

The internal temperature gradients in biomass particles have been proposed to also affect particle burn-out [312]. However, this study will limit the particle modeling to the devolatilization as this process will impact to the largest degree on the flame stability and contribute indirectly to the largest heat release.

6.3 Summary on Literature Review

During the years, a number of models describing the thermal degradation of thermally thick biomass particles have been developed; a few of which have been discussed in the above. The complexity of the models has increased as the understanding of the processes has improved and computational power became readily available. A number of assumptions have been applied to the modeling process. A few of the most central assumptions have been listed in table 6.1. The progress in model development is illustrated in table 6.2 listing selected works and the employed assumptions.

Direct quantitative comparison between the models is not feasible due to the differences in model objectives. The implementation of sub-routines do, however, yield a good insight into the effect of each assumption. This know-how will be applied in the next chapter, developing a particle model for a

devolatilization study of non-isothermal particles at conditions relevant to PF combustion.

Table 6.1 An overview of common assumptions used in model development.

Legend	Assumption
A1	Thermal equilibrium across phases
A2	No mass transport by diffusion
A3	No secondary reactions
A4	Fixed char yield
A5	Isotropic particle structure
A6	Single first order reaction
A7	No radiative heat transport
A8	No convective heat transport inside the particle
A9	Constant thermophysical properties

Table 6.2 An overview of central assumptions in model development. Selected models.

Reference	Year	A1	A2	A3	A4	A5	A6	A7	A8	A9
Bamford *et al.* [303]	1946	•	•	•	•	•	•	•	•	•
Roberts and Clough [227]	1963	•	•	•	•	•	•	•	•	•
Panton and Rittmann [305]	1971	•	•	•	•	•		•	•	
Kung [306]	1972	•	•	•	•	•	•	•		
Kansa *et al.* [309]	1977	•	•	•	•		•			
Chan *et al.* [129]	1985	•	•	•						
Di Blasi and Russo [310]	1993	•	•							
Grønli and Melaaen [115]	2000	•								
Lu *et al.* [170]	2008	•								

CHAPTER 7

Modeling Heat Transfer Controlled Particle Devolatilization

In the preceding part the devolatilization of thermally thin particles was discussed, i.e. particle conversion limited by chemical kinetics rather than transport limitations. This chapter aims to evaluate the effect of heat transport on the total time required for devolatilization of biomass particles. It will present a 1-dimensional, non-isothermal model, predicting the drying and devolatilization of biomass particles.

7.1 Modeling Methods

This section will introduce different methods for modeling the individual phenomena occurring during non-isothermal particle drying and devolatilization.

7.1.1 Particle Drying

Water is typically present in biomasses in noticeable quantities. Ranging from 40–60 wt. % in fresh wood [313], to 30–35 wt. % in naturally dried wood [314], to up to 10 wt. % in industrially dried pellets [315].

Biomass moisture is present in two forms: Bound and free water [316]. Bound water is adsorbed in the cell walls whereas free water flows freely in the particles pores. Free water is only present if the water content exceeds the fiber saturation point (FSP), Y_{fsp}. The FSP has been estimated [317] as:

$$Y_{\mathrm{fsp}} = \left(Y^0_{\mathrm{fsp}} + 0.298\right) - \frac{T}{1000} \tag{7.1}$$

where Y^0_{fsp} is a reference value and can be assumed to be $Y^0_{\mathrm{fsp}} = 0.3$ for wood. For high temperatures, the FSP becomes infeasibly low and thus the minimum value of the FSP is commonly set to $Y_{\mathrm{fsp}} = 0.2$.

For suspension fired applications the moisture content will rarely exceed the FSP.

The distinguishing between water types is important for combustion purposes because of the differences in the energy levels. Gas phase water has the highest energy level, followed by free water, and bound water with the lowest energy level. The free water is basically at the same energy level as normal water and thus the heat required to evaporate is the same as the heat

of evaporation of normal water. Bound water is adsorped in the cell wall and must be desorped which releases the water as free water. Hence, the energy required to evaporate free and bound water is:

$$\Delta_{\text{vap}}H_{\text{free}} = \Delta_{\text{l}}H \quad , \quad Y \geq Y_{\text{fsp}} \tag{7.2}$$

$$\Delta_{\text{vap}}H_{\text{bound}} = \Delta_{\text{l}}H + \Delta_{\text{ds}}H \quad , \quad Y < Y_{\text{fsp}} \tag{7.3}$$

$$\tag{7.4}$$

where the heat of water evaporation and desorption are denoted by $\Delta_{\text{l}}H$ and $\Delta_{\text{ds}}H$, respectively.

The heat of evaporation was estimated by Ražnjević [318] as:

$$\Delta_{\text{l}}H = 3179 - 2.5T \qquad \left[\text{J} \cdot \text{kg}^{-1}\right] \tag{7.5}$$

while the heat of desorption has been estimated by Stanish *et al.* [316] to vary quadratically with the content of bound water:

$$\Delta_{\text{ds}}H = 0.4\Delta_{\text{l}}H \left(1 - \frac{Y_{\text{bound}}}{Y_{\text{fsp}}}\right)^2 \qquad \left[\text{J} \cdot \text{kg}^{-1}\right] \tag{7.6}$$

Y_{bound} being the fraction of bound water.

Modeling Particle Drying

Particle drying is generally described by one of three methods:

- Thermal models
- Kinetic models
- Equilibrium models

The thermal models, or heat sink models, are widely used due to their simplicity [319–325] and rely on the premise that moisture evaporation takes place at a fixed temperature. All supplied heat is used to vaporize water until exhaustion, hence the name; heat sink model.

The model does not account for phase equilibrium and introduces moisture evaporation to particle conversion as an infinitely thin reaction front separating the wet core from the dry outer parts of the particle. The model is typically implemented as either a shrinking core type model or by applying conditional formatting when solving the energy balance.

The kinetic models [129, 300, 302, 326, 327] are both efficient and easily implemented to the typical numerical models. The drying process is controlled

by a rate expression that can be coupled directly to the existing kinetic scheme. Contrary to the thermal models which modeled the drying as a propagating front, the kinetic models introduce a drying zone. This allows the model to adjust for the different types of water, i.e. the release of bound and free moisture, respectively. It also allows for re-condensation of evaporated water by introducing reversible reactions rate expressions.

The equilibrium models are based on the premise that the water is in equilibrium across all present phases [63, 314, 316, 328], i.e. the partial pressure of water vapour is fixed by the saturation pressure. The equilibrium models rely not only on the heat balance to solve the equations of state, but also on the mass balances. This requires significantly more information on the particle and the development of particle properties as it undergoes thermal conversion.

7.1.2 Particle Devolatilization

The models considered for particle devolatilization of the larger particles are the same as for the small particles, cf. chapter 3.

7.1.3 Thermophysical Properties

One of the primary implications of transiting from thermally thin to thermally thick particles is the variation in particle properties as the reaction zones progresses through the particle.

Thermal Conductivity

The anisotropic nature of fibrous material has been reported to play a significant influence on the thermal conductivity [317, 318]. Maclean [329] reported the thermal conductivity in the tangential and longitudinal direction to be 0.5–0.9 and 1.75–2.25 times that in the radial direction. Commonly the terms parallel and perpendicular direction refer to the heat flow going along or across the fibers with an approximate 2:1 ratio, as seen in figure 7.1b.

The effective thermal conductivity, λ_{eff} is commonly found as the sum of the contribution from all contributing transfer mechanisms including radiation, λ_{r}:

$$\lambda_{\text{eff}} = \lambda_{\text{cond}} + \lambda_{\text{r}} + \lambda_{\text{g}} \tag{7.7}$$

where λ_{g} is the contribution from the gas inside the particle pores. The thermal conductivity of char is often significantly lower than that of virgin biomass material [63, 115, 332–334] and thus the net thermal conductivity of the solid matrix can be considered as a function of the conversion.

It is important to note that although thermal conductivity is lower for char than virgin wood, the contribution from the radiative term becomes increasingly important as the temperature rises. Brown [335] reported an

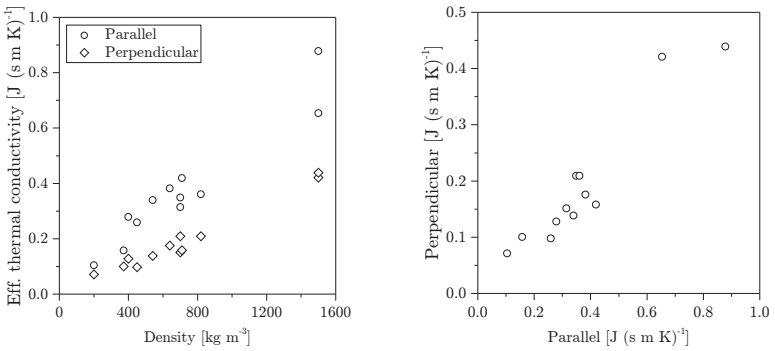

(a) Function of density. **(b)** Influence of direction.

Figure 7.1 The influence of density and direction on the effective thermal conductivity. All measurements are carried out at ambient conditions. References: [318, 330, 331].

effective thermal conductivity of char at 873 K, almost twice the value of the corresponding virgin wood.

Radiative heat transfer in the pore structure of a particle is often treated analogous to Knudsen diffusion [63], i.e. property transport scaling with an effective pathway. Hottel and Sarofim [336] developed a generic expression for radiative thermal conductivity in porous media:

$$\lambda_\mathrm{r} = A\Lambda\sigma T^3 \tag{7.8}$$

where A is a model constant and Λ is the photon mean free path. Table 7.1 lists a number of literature values for the model constant and the mean free path.

Table 7.1 Literature overview of model parameters for radiative heat transfer in porous media. d_por: pore diameter, ε: emissivity, φ_g: porosity, d_fiber: fiber diameter.

A	Λ	Reference.
—	m	
16/3	d_por	[336]
4.5	$d_\mathrm{fiber}\varepsilon\,(1-\varphi_\mathrm{g})^{-1}$	[337]
4	$\varphi_\mathrm{g}\varepsilon d_\mathrm{por}\,(1-\varphi_\mathrm{g})^{-1}$	[305]
4.5	$3\varepsilon d_\mathrm{fiber}\varphi_\mathrm{g}^{-1}$	[129]
16/3	$d_\mathrm{fiber}\,(\ln(\varphi_\mathrm{g}))^{-1}$	[338]
1	$d_\mathrm{por}\varepsilon^{-1}$	[339]

The cubed temperature dependency of the radiative contribution to the

effective thermal conductivity will indeed shift the weight of the individual transport mechanisms as the temperature increases. The solid matrix conduction is often modeled as a linear relation between temperature and thermal conductivity. Koufopanos *et al.* [333] developed an empirical expression for the thermal conductivity of both virgin, λ_f, wood and char, λ_c:

$$\lambda_f = 0.13 + 3 \times 10^{-4} (T - 273) \qquad \left[\mathrm{J} \cdot (\mathrm{m} \ \cdot \mathrm{K} \cdot \mathrm{s})^{-1}\right] \tag{7.9}$$

$$\lambda_c = 0.08 - (T - 273) \times 10^{-4} \qquad \left[\mathrm{J} \cdot (\mathrm{m} \ \cdot \mathrm{K} \cdot \mathrm{s})^{-1}\right] \tag{7.10}$$

The method of Koufopanos *et al.* [333] has been widely adopted throughout the literature [340, 341]. It is worth noting the different signs of the slopes for the temperature dependency of fuel and char.

Other more complex models have been developed taking the water content into account [170]:

$$\lambda_f = \left(0.129 - 4.9 \times 10^{-2} Y\right) \left(1 + (2.05 + 4Y) \times 10^{-3} (T - 273)\right) (0.986 + 2.695Y) \qquad \left[\mathrm{J} \cdot (\mathrm{m} \ \cdot \mathrm{K} \cdot \mathrm{s})^{-1}\right] \tag{7.11}$$

Other methods include density based function [129] or constant values which are especially widely used for the char conductivities [64, 170, 332, 342].

Specific Heat Capacity

While the effective thermal conductivity relates temperature differences to the heat flux, the specific heat capacity dictates the amount of heat absorbed per mass unit of particle. This makes the specific heat capacity of the particle at any given location and any given time a central parameter in a thermal model like the one developed in this work.

The thermal degradation of biomass initiates at low temperatures starting with hemi-cellulose around 500 K [150]. Thus, the importance of knowing the temperature dependency of the virgin fuel heat capacity at elevated temperature becomes less important. For this reason, many studies use constant values for the specific heat capacities of the parent fuel. In some instances even for the chars. A few selected values are listed in table 7.2.

Most temperature dependent relations have been empirically fitted and extrapolated [63, 333, 345]. Merrick [346] adopted the Einstein model relating the specific heat capacity of coal and coke to the atomic weight of a fuel specific model compound. This approach has since been modified and used for biomass purposes [64, 170].

Table 7.2 Heat capacity of wood and char.

Wood $\mathrm{J\,(kg \cdot K)^{-1}}$	Char $\mathrm{J\,(kg \cdot K)^{-1}}$	Reference
1380	670	[307]
1500	1100	[310]
1670	1000	[343]
1950	1350	[325]
2300	—	[303]
2300	710	[309]
2510	1050	[129]
1670	—	[344]

$$c_p = \frac{1000R}{MW}\left(g\left(z_1\left(T\right)\right) + 2g\left(z_2\left(T\right)\right)\right) \qquad \left[\mathrm{J \cdot (kg \cdot K)^{-1}}\right] \tag{7.12}$$

where

$$g\left(z\right) = \frac{z_i^2 \exp\left[z_i\right]}{\left(\exp\left[z_i\right] - 1\right)^2} \tag{7.13}$$

and

$$z_1 = 380T^{-1} \qquad z_2 = 1800T^{-1} \tag{7.14}$$

where the constants of equation (7.14) are referred to as the Einstein characteristic temperatures and are used to fit the model [346]. The molar weight, MW, of equation (7.12) is commonly set to:

$$MW_{\mathrm{f}} = 7.72\,\mathrm{g \cdot mol^{-1}} \tag{7.15}$$

$$MW_{\mathrm{f}} = 11.3\,\mathrm{g \cdot mol^{-1}} \tag{7.16}$$

Figure 7.2 compares selected expressions for the specific heat capacity of virgin wood and char. The spread of the expressions is considerable and the linear expressions assume unrealistic values at high temperatures.

7.1.4 A Mathematical Model for Drying and Devolatilization

In the following a mathematical model for the drying and devolatilization of wood will be developed based on the methods described in the above. The central premise for the model is the assumption that the devolatilization of non-isothermal particles is controlled dominantly by heat transport.

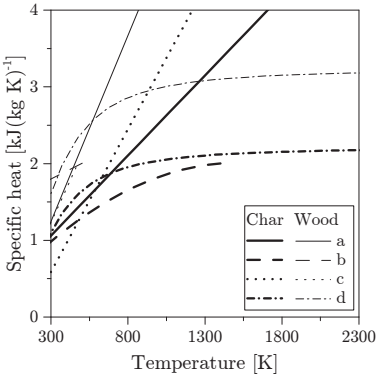

Figure 7.2 Selected expressions for the specific heat capacity of virgin wood and chars. a: Koufopanos *et al.* [333], b: Grøli [63], c: Koch [345], and d: Merrick [346].

7.1.5 Fundamental Assumptions

The modeling is based on the following assumptions:

1. The model is solved in one dimension
2. Only primary pyrolysis takes place
3. The heat of pyrolysis sums to zero
4. No convective heat transport takes place inside the particle
5. There are no mass diffusion limitations
6. The particles are spherical
7. Only the reactor walls contribute to the radiative external heat flux

Governing Equations

The drying of the particles is described by a kinetic model [302]:

$$\dot{w} = k_Y \left(Y^* - Y\left(t\right)\right) \rho_{\mathrm{w}} \tag{7.17}$$

where $\dot{w}$ is the rate of water evaporation, and Y^* and Y are the water content of the virgin fuel and the released amount of water at time t. The rate constant, k, is expressed as:

$$k_Y = A_Y T^{1/2} \exp\left[\frac{-E_{\mathrm{a},Y}}{RT_{\mathrm{p}}}\right] \tag{7.18}$$

where A_Y and $E_{a,Y}$ are the pre-exponential factor and the activation energy for the water evaporation model and T_p and R are the local particle temperature and the universal gas constant.

The devolatilization is solely driven by the thermal breakdown of the organic structure and is described by a single global reaction:

$$\text{parent fuel} \xrightarrow{k} \text{solid} + \text{volatiles} \tag{7.19}$$

As such, only the primary pyrolysis [347, 348] is taken into account neglecting any secondary reactions[204, 349].

The rate of reaction is described by a single first order reaction (SFOR):

$$\frac{\mathrm{d}V(t)}{\mathrm{d}t} = k\left(V^* - V(t)\right) \tag{7.20}$$

where V and V^* are the fraction of volatile matter released and the ultimate fraction of volatile matter respectively. V^* has been obtained experimentally in entrained flow reactors to yield the true high temperature, high heating rate value which is known to deviate significantly from low temperature, low heating rate experiments often used in fuel characterization standards [89].

The rate constant, k, obeys an Arrhenius type expression:

$$k = A \exp\left[\frac{-E_a}{RT_p}\right] \tag{7.21}$$

where A and E_a are the pre-exponential factor and the activation energy respectively, for the pyrolysis step while R and T_p denote the universal gas constant and the local temperature of the solid.

The heat balance accommodates the intra-particular heat transport limitations coupled with a transport model for the external heat flux. If a quasi-steady-state is considered and the heat transport described by Fourier's law, then

$$c_p \rho \frac{\partial T(t,r)}{\partial t} = \frac{2\lambda}{r}\frac{\partial T(t,r)}{\partial r} + \lambda \frac{\partial^2 T(t,r)}{\partial r^2} - \dot{w}\Delta_{vap}H \tag{7.22}$$

describes the heat transport through the particle where c_p, ρ, and λ are the specific heat capacity, density, and thermal conductivity of the solid phase, respectively.

The initial condition is given by the particle temperature at time zero, T_0:

$$T(0,r) = T_0 \tag{7.23}$$

The boundary conditions are defined as adiabatic behavior at the particle center, and the heat flux from the surrounding to the particle, q_{ext}, given by the total contribution from a convective flux, q_c, and a radiative flux, q_r. This yields the spatial boundaries of the particles as:

$$\lambda \left.\frac{\partial T}{\partial r}\right|_{r=0} = 0 \tag{7.24}$$

$$\lambda \left.\frac{\partial T}{\partial r}\right|_{r=R} = q_{\text{ext}} \tag{7.25}$$

7.1.6 Algebraic Equations

In addition to the governing equation describing the energy balance of the system, a number of algebraic equations must be defined in order to describe the transport properties of the transient system.

Heat of Evaporation of Water

Because the model aims at describing particles used for suspension fired boilers, only bound water is taken into consideration. The moisture content of the fuels used for these purposes is assumed not to exceed the fiber saturation point.

The energy needed to evaporate bound water, $\Delta_{\text{vap}}H$, is found as the sum of the heat of desorption of the bound water, $\Delta_{\text{ds}}H$, and the subsequent evaporation of liquid water, $\Delta_{\text{l}}H$:

$$\Delta_{\text{vap}}H = \Delta_{\text{l}}H + \Delta_{\text{ds}}H \tag{7.26}$$

Particle Material Properties

Each of the material specific properties, c_p, ρ, and λ changes linearly with conversion, χ, [115] as:

$$\xi_i\left(\chi_i\right) = \chi_i \xi_{\text{a}} + \left(1-\chi_i\right)\xi_{\text{b}} \tag{7.27}$$

where index i indicates the discretization in the radial direction. The radiative contribution is introduced through an effective thermal conductivity, λ_{eff}, found as the sum of conduction in the solid, λ_{s}, and gas phase, λ_{g}, as well as the radiative, λ_{r}, contribution:

$$\lambda_{\text{eff}} = \lambda_{\text{g}} + \lambda_{\text{s}} + \lambda_{\text{r}} \tag{7.28}$$

The intraparticular heat transport by radiation, λ_{r}, is correlated from previous studies [310] and is proportional to the cubed particle temperature, thus, especially important at elevated temperatures [335]:

$$\lambda_{\text{r}} = \frac{\left(\chi d_{\text{pore,c}} + \left(1-\chi\right) d_{\text{pore,f}}\right)\sigma T_{\text{p}}^3}{\varepsilon} \tag{7.29}$$

Here d_{pore} denotes the pore diameter of the char and parent fuel respectively. ε is the particle emissivity and σ is the Stefan-Boltzmann constant.

External Transport

The radiative heat flux to the particle, q_r, is given by the Stefan-Boltzmann law [291], while the convective heat transport is driven by the temperature difference between the bulk gas temperature, T_g, and particle surface temperature, $T_\mathrm{p}|_{r=R}$, correlated by the heat transfer coefficient, h, which is calculated for a spherical particle based on the flow conditions [350]:

$$h = \frac{\lambda Nu}{2R} = \frac{\lambda \left(2 + 0.6 Re^{\frac{1}{2}} Pr^{\frac{1}{3}}\right)}{d_\mathrm{p}} \tag{7.30}$$

$$Re = \frac{d_\mathrm{p} v_\mathrm{g} \rho_\mathrm{g}}{\mu_\mathrm{g}} \tag{7.31}$$

$$Pr = \frac{c_{p,\mathrm{g}} \mu_\mathrm{g}}{\lambda_\mathrm{g}} \tag{7.32}$$

where Nu, Re, and Pr denote the Nusselt, Reynold, and Prandtl number, respectively. The slip velocity between gas and particle is denoted v_g. The gas density, ρ_g, specific heat capacity, $c_{p,\mathrm{g}}$, viscocity, μ_g, and thermal conductivity, λ_g, are empirically correlated to the temperature [351].

The net contribution of heat, q_ext, used in equation (7.25) can then be expressed by:

$$q_\mathrm{ext} = h \left(T_\mathrm{g} - T_\mathrm{p}|_{r=R}\right) + \varepsilon\sigma \left(T_\mathrm{w}^4 - T_\mathrm{p}^4\big|_{r=R}\right) \tag{7.33}$$

where T_w is the temperature of a radiating wall, assumed to be equally visible from all angles.

Shrinking

A 20 % reduction in particle size was observed during devolatilization experiments of wood particles [352]. This is assumed to primarily affect the external heat transport to the particle. Thus, the effect is taken into account by correcting the external heat transport: The convective contribution is corrected by correlating the heat transport coefficient, h, to the reduction in particle diameter as function of conversion. The radiative contribution is reduced through a factor scaling with the reduction in surface area. A linear correlation between mass averaged conversion and particle size reduction is assumed.

Particle Properties

The particle is described as a sphere and correlated to experimental data from literature of non-spherical particles by using a fixed V/A-ratio in order to balance the external heat flux and particle heat capacity. The thermophysical data used in the model is listed in table 7.3.

Table 7.3 Thermophysical properties used in the model.

Symbol	Unit	Description	Expression	Ref
$c_{p,\mathrm{f}}$	$\mathrm{J}\cdot(\mathrm{kg}\cdot\mathrm{K})^{-1}$	Specific heat capacity	$\frac{1000R}{7.72}\left(g\left(z_1\left(T\right)\right)+2g\left(z_2\left(T\right)\right)\right)$	[115, 346]
$c_{p,\mathrm{c}}$			$\frac{1000R}{11.3}\left(g\left(z_1\left(T\right)\right)+2g\left(z_2\left(T\right)\right)\right)$	[346]
			$g=\frac{z_i^2\exp^{z_i}}{\left(\exp^{z_i}-1\right)^2}$	
			$z_1=380/T,\ z_2=1800/T$	
$c_{p,\mathrm{g}}$	$\mathrm{J}\cdot(\mathrm{mol}\cdot\mathrm{K})^{-1}$		$31.2-14.6\times10^{-3}T+32.9\times10^{-6}T^2$ $-20.9\times10^{-9}T^3+4.36\times10^{-12}T^4$	[351]
λ_{f}	$\mathrm{J}\cdot(\mathrm{m}\cdot\mathrm{K}\cdot\mathrm{s})^{-1}$	Thermal conductivity	$0.13+3\times10^{-4}(T-273), T\leq1006\,\mathrm{K}$ $0.3, T>1006\,\mathrm{K}$	[63, 115, 333]
λ_{c}			$0.08-(T-273)\times10^{-4}, T\leq943\,\mathrm{K}$ $0.013, T>943\,\mathrm{K}$	[333, 334]
λ_{g}			0.0258	[63]
λ_{r}		*	$d_{\mathrm{pore}}\sigma T_{\mathrm{p}}^3/\varepsilon$	[310]
λ_{eff}		*	$(1-\chi)\lambda_{\mathrm{f}}+\chi\lambda_{\mathrm{c}}+\lambda_{\mathrm{g}}\varphi+\lambda_{\mathrm{r}}$	[63, 115]
$\lambda_{\mathrm{g\ ext}}$			$-1.72\times10^{-4}+1.03\times10^{-4}T-5.67\times10^{-8}T^2+2.68\times10^{-11}T^3-4.92\times$ $10^{-15}T^4$	[351]
μ	$\mathrm{Pa}\cdot\mathrm{s}$	Viscosity	$3.98\times10^{-7}+7.24\times10^{-8}T-4.81\times10^{-11}T^2+2.28\times10^{-14}T^3-4.20\times$ $10^{-18}T^4$	[351]
$d_{\mathrm{por,f}}$	m	Pore diameter	3.2×10^{-6}	[115]
$d_{\mathrm{por,c}}$			10^{-4}	[115]
ε	—	Particle emissivity	0.85	
σ	$\mathrm{J}\cdot(\mathrm{m}^2\cdot\mathrm{K}^4\cdot\mathrm{s})^{-1}$	Stenfan-Boltzmann	5.6704×10^{-8}	[353]
ρ_{f}	$\mathrm{kg}\cdot\mathrm{m}^{-1}$	Density (Wood/pellet)	700/1180	[127]
ρ_{c}			$\rho_{\mathrm{f}}\times(1-vol)$	
ρ_{g}			$362.65T^{-1.006}$	[351]
$\Delta_{\mathrm{l}}H$	$\mathrm{J}\cdot\mathrm{kg}^{-1}$	Heat of evaporation	$(3179.0-2.5T)\,1000$	[318]
$\Delta_{\mathrm{ds}}H$		Heat of desorption	$400\Delta_{\mathrm{l}}H\left(1-\frac{Y}{Y_{\mathrm{fsb}}}\right)^2$	[316]
Y_{fsb}	—	Fibre saturation point	$0.598-0.001T$	[317]

* In this study the porosity, φ, has been assumed to vary linearly with the conversion, χ.

Drying and Devolatilization Kinetics

Because of the low moisture content (<10 wt. %) in fuels used for suspension fired combustion purposes, all of the inherent water is treated as bound water. The release of bound water is controlled by a kinetic expression derived by Chan *et al.* [129] who determined the kinetic parameters as listed in table 7.4.

The devolatilization kinetics will in this work need to cover both a wide range of temperatures (300–1850 K) and heating rates (10–$10^5\,\mathrm{K}\cdot\mathrm{s}^{-1}$). This is notoriously difficult using a global mechanism such as the one employed in equation (7.19) [236]. This challenge motivated the development of the distributed activation energy model (DAEM); however, even for these infinite parallel reaction models, the validation material often stem from low heating rate thermogravimetric experiments [188, 354, 355].

The devolatilization kinetics needed to evaluate equation (7.19) at high heating rates are obtained from previous work on high heating rate, high temperature experiments on biomass devolatilization [269]. That work was aimed at developing devolatilization SFOR kinetics for isothermal particles at conditions similar to suspension firing. These results ($E_{\mathrm{a},1} = 21\,305\,\mathrm{J}\cdot\mathrm{mol}^{-1}$, $A_1 = 18.9\times10^3\mathrm{s}^{-1}$) will in this work be employed as intrinsic kinetics which coupled with the heat transport model will yield a conversion rate for non-isothermal particles.

For low heating rates, i.e. larger particles, the kinetics derived by Wagenaar *et al.* [236] have been used. They used a two step mechanism: One primary pyrolysis step with three competing reactions forming gas, tar, and char followed by a consecutive step cracking the tar to gas, cf. figure 7.3. These kinetic data have previously been used with success for larger particles of around 11 mm in diameter [170].

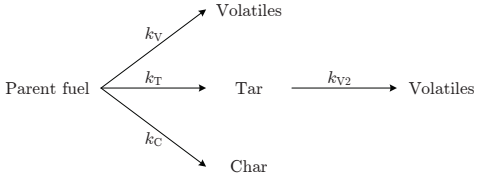

Figure 7.3 Two-step semi-global reaction mechanism [236].

Because equation (7.19) assumes that the char yield is independent of the devolatilization conditions, the net devolatilization rate constant can be found as:

$$k_2 = k_{\mathrm{V}} + \min\left(k_{\mathrm{T}}; k_{\mathrm{V2}}\right) \tag{7.34}$$

The resulting rate constant can be expressed with an Arrhenius type equation with the kinetic constant listed in table 7.4 ($E_{\mathrm{a},2}$ and A_2).

Table 7.4 Kinetic parameters used for the 1D non-isothermal particle modeling.

Parameter	Unit	Constant	Reference
High temperature kinetics			
A_1	s^{-1}	18.9×10^3	[269]
$E_{a,1}$	$kJ \cdot mol^{-1}$	21.305	
Low temperature kinetics			
A_V	s^{-1}	1.11×10^{11}	[236]
$E_{a,V}$	$kJ \cdot mol^{-1}$	177	
A_T	s^{-1}	9.28×10^9	[236]
$E_{a,T}$	$kJ \cdot mol^{-1}$	149	
A_{V2}	s^{-1}	4.28×10^6	[236]
$E_{a,V2}$	$kJ \cdot mol^{-1}$	108	
Water evaporation			
A_Y	$s^{-1} \cdot K^{-1/2}$	4.4×10^6	[129]
$E_{a,Y}$	$kJ \cdot mol^{-1}$	88	

The model adopts the approach of Simone *et al.* [264] introducing a critical temperature separating the high from the low temperature pyrolysis kinetics. The separation is necessary in order for the SFOR mechanism to remain valid in the entire temperature interval. A critical temperature of around 800 K matches the typical reported shift in first order kinetics [251, 264] as illustrated in figure 7.4. The large particles (11 mm) experience heating rates on the order of $10\,K \cdot s^{-1}$ [170], while the small particles ($\sim 100\,\mu m$) are heated much faster on the order of $10^5\,K \cdot s^{-1}$ [269]. Thus, the influence of each reaction constant is as a function of particle diameter.

Numerical Solution

The system consists of a partial differential equation describing the energy conservation, a set of non-linear equations describing the boundary conditions, and a set of algebraic equations describing the thermophysical properties.

The system has been solved numerically using Matlab® R2014b by means of finite differences. The 1-dimensional particle is discretizised by finite volume, reducing the energy balance to a set of ordinary differential equations, in which any information is stored in the cell centers. The boundary conditions are introduced by extending the numerical domain by ghost cells.

The number of cells scales with the particle size. The scaling factor has been determined by grid sensitivity testing. The time steps are adaptive and chosen automatically on the basis of the solution.

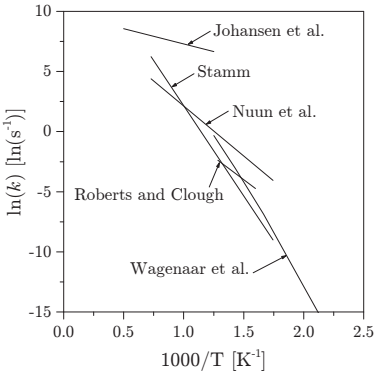

Figure 7.4 Kinetic data for the devolatiliszation of different biomasses Roberts and Clough [227], Stamm [232], Wagenaar *et al.* [236], Nunn *et al.* [251], Johansen *et al.* [269]. The rate constant for Wagenaar *et al.* [236] is the net rate given by equation (7.34).

7.2 Non-Isothermal Model Validation

The model is validated against data from three different studies, each presenting devolatilization data of woody fuel at different particle sizes and different heating rates. An overview of the key characteristics of the validation material is given in table 7.5.

Table 7.5 Overview of the set-ups used for validation data.

#	Set-up	Particle size mm	Heating rate $K \cdot s^{-1}$	Temperature K	Ref.
A	Entrained flow reactor	0.063–0.090	10^5	1405–1667	[269]
B	Single particle combustor	1.79–5.8	10^2–10^3	1480–1831	[179, 356]
C	Single particle combustor	10.9	30	1050–1267	[170]

7.2.1 Small Particles, Validation Set-Up A

Set-up A consists of the LFR reactor previously introduced in part II. It is a laminar flow reactor operating at high peak temperatures (1405–1667 K) and the particles experience heating rates on the order of $10^5\,K \cdot s^{-1}$. The reactor was operated at laminar bulk flow conditions with an understoichiometric CH_4/H_2-flame [269]. The solid fuel feed rate was kept at 10–20 $mg \cdot h^{-1}$ ensuring single particle conditions. Particles were collected at different residence times by a movable probe. The work provided time resolved devolatilization

profiles and computational fluid dynamics (CFD) determined particle temperature and residence time data. These experiments assume isothermal particle behavior. Figure 7.5 shows a comparison between measurements and results for the 1D model at 1405 and 1667 K.

In figure 7.5 the 1D model results are compared to the experimental data. The 1D model uses a temperature dependent combination of low heating rate kinetics (Wagenaar *et al.* [236]) below 800 K and high heating rates kinetics (Johansen *et al.* [269]). The effect of using only the kinetic data from Johansen *et al.* [269] or only the kinetics from Wagenaar *et al.* [236] are shown in figure 7.5 and compared with the model using the combined kinetics.

The comparison shows how the kinetics obtained, partially using slow heating rate TGA equipment (Wagenaar *et al.* [236]), over predicts the devolatilization time of the small particles. Contrary, the kinetics derived at high heating rates (Johansen *et al.* [269]) capture the high temperature experiment well. The combined kinetic expression used in this work predicts slightly higher reaction times than the experimental data, however, the agreement is still found to be reasonable, considering the time scales.

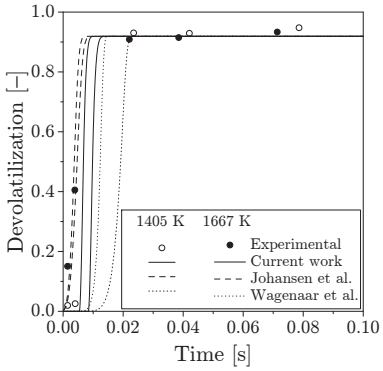

Figure 7.5 Comparison of the 1D model to the laminar entrained flow reactor devolatilization experiments. The devolatilization profiles obtained by using kinetic data obtained by Wagenaar *et al.* [236], Johansen *et al.* [269] is also compared to the kinetics derived in this work. A single particle diameter of 78.9 μm has been used for the simulations corresponding to the Rosin-Rammler mean diameter of the experiments. The illustrated conversion is the mass averaged conversion.

7.2.2 Medium Size Particles, Validation Set-Up B

Set-up B is a single particle combustor heated by a non-premixed gas flame. The particle is rapidly exposed to the hot environment and the devolatilization and char burn-out processes are analysed by visual methods.

The measured devolatilization compile the work of Jensen [356] and Jepsen [179]. They worked on devolatilization experiments using cubic wood particles. The particle sizes range from 1.79–5.8 mm (corresponding spherical diameter) and the temperature interval from 1458 to 1831 K. The reactor is a convective single particle reactor heated by a flat flame burner. The particle is introduced to the burner fixed on a platinum wire and shielded by a removable ceramic tube. A high speed camera (65 Hz) captures the devolatilization and combustion phases through a view port in the side of the reactor. The set-up has previously been used in other work and a detailed description can be found elsewhere [352].

Figure 7.6 compares the observed residence time required for complete devolatilization (including heating and drying) to the model results. The devolatilization time has been defined in the experimental work as the time from which the particle is exposed to the hot reactor and to the point where a flame is no longer visible around the particle. In the 1D model the time for complete devolatilization has been defined as the time when 95 % of the original volatile matter has left the particle.

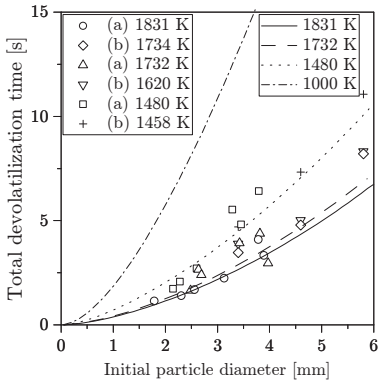

Figure 7.6 Comparison between measured single wood particle devolatilization times and the corresponding simulations using the 1D model. The devolatilization times includes particle heat up, drying, and devolatilization. Experimental data: [179, 356].

The model is able to predict the net devolatilization times well. The model will in general slightly underpredict the required residence times. The results are, however, well within the uncertainty of the experimental material.

7.2.3 Large Particles, Validation Set-Up C

The set-up is based on the same principles as set-up B but includes a scale which allows for time resolved analysis of the mass loss during devolatilization

and char burn-out.

The experiments include single particle pyrolysis of large biomass particles of 10.9 mm. The data is obtained from the work of Lu *et al.* [170] and include temporal data of mass loss as well as surface and center particle temperatures. The mass loss is obtained by a micro scale, the surface temperature by two-line thermometry, and the center temperature by thermocouple measurements. Figures 7.7 and 7.8 show the comparison of the 1D model results to the experimental data. The model is able to predict both the conversion profile and the surface temperature well. The conversion (drying and devolatilization) is predicted to initiate slightly later than the measured data and reach completion slightly before the measured data. The particle core temperature is significantly under estimated at low degrees of conversion. This is, however, believed to originate from experimental deviations, e.g. by heat conduction through the thermocouple itself.

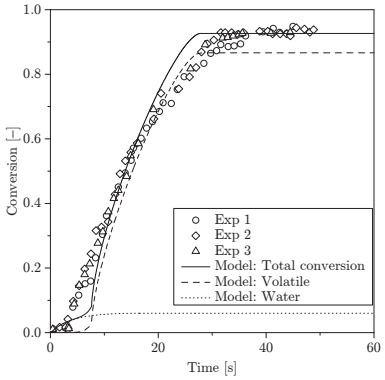

Figure 7.7 Conversion comparison between single particle measurements and the 1D model. $T_g = 1050\,\mathrm{K}$, $T_w = 1276\,\mathrm{K}$, $d_p = 10.9\,\mathrm{mm}$.

7.3 Sensitivity Analysis

The mathematical model derived and validated in the preceding sections describes the transient drying and devolatilization of a particle resolved in a single dimension. It relies to extent on input acquired from the literature. Such input includes drying and devolatilization mechanisms and mathematical description, kinetic data, thermophysical properties, etc. The uncertainties of many of these parameters are high. This section aims to test the model and assess the sensitivity towards selected parameters. The sensitivity tests will be performed by variations in a single parameter at a time, while maintaining

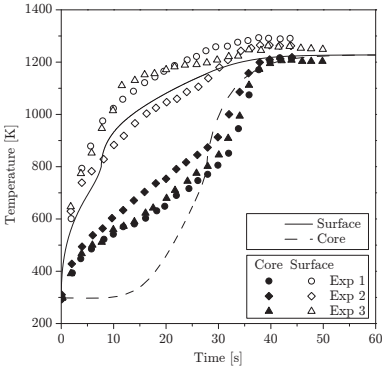

Figure 7.8 Comparison between single particle temperature measurements and the 1D model. $T_g = 1050\,\mathrm{K}$, $T_w = 1276\,\mathrm{K}$, $d_p = 10.9\,\mathrm{mm}$.

the rest at reference values. The reference values correspond to those listed in table 7.3.

The sensitivity analysis has been categorized into three main categories

- Internal heat transport properties
- External heat transport properties
- Reaction properties

The internal heat transport properties will focus on the thermophysical properties and transfer models. This relates primarily to the fuel characterization. The external heat transport properties will include the effect of the boundary conditions. This corresponds to subjecting particles to different combustion environments. The reaction properties, i.e. the drying and devolatilization properties, will include an analysis on the effect of the two phenomena occuring in parallel as well as the sensitivity towards the kinetics them self.

7.3.1 Reference Cases and Evaluation Parameters

Three reference cases have been established to quantify the effect of the imposed parameter variations. Since the primary objective of this study is to ensure an accurate release of volatiles at a given set of reaction conditions, the parameter variations will be evaluated solely on the net devolatilization time, i.e. the time required to release 95 wt. % of the available volatiles.

The reference cases will consist of three particle diameters with fixed boundary conditions corresponding to the experiments at 1831 K in figure 7.6.

The particle diameters correspond to the mean diameters of the characteristic particle bins defined in section 8.3.1.

The fuel composition is based on a fuel sample from AMV during the second full-scale campaign. The proximate analysis is given in table 7.6.

Table 7.6 The proximate analysis used for the sensitivity test. The volatile yield has been corrected to high temperatures by a high temperature yield factor of 1.14, based on the LFR results.

Species	Unit	Value
Moisture	wt. %	4.10
Volatiles		90.8
Char		4.32
Ash		0.800

The comparison to the reference values will be given on both an absolute and a relative scale as:

$$\text{response value} = \text{new value} - \text{reference value} \tag{7.35}$$

$$\text{response relative}\,\% = \frac{\text{new value} - \text{reference value}}{\text{reference value}} 100\,\% \tag{7.36}$$

Table 7.7 lists the reference values for the three particle sizes denoted: d_p (89), d_p (490), and d_p (1603), respectively.

Table 7.7 Reference values for the sensitivity test.

	Unit	d_p (89)	d_p (490)	d_p (1603)
Reference	ms	14.4	251	1708

7.3.2 Internal Heat Transport Properties

The internal heat transport properties include a number of empirical correlations acquired from the literature. As discussed in section 7.1.3, a number of different methods describing the various phenomena exist. Most of the methods are derived from empirical data and thus may be specific to the conditions or to the fuel used in the relevant study.

The absolute and relative values for the sensitivity tests **S1**–**S8c** are shown in table 7.9.

The effect of internal radiation has previously been reported as a significant contributor to the heat transfer inside the particle at elevated temperatures. **S1** compares the net devolatilization time without the internal contribution

Table 7.8 Overview of the parameter variations for internal heat transport property impact evaluation. Prime indicates sensitivity test values or expressions.

Test	Variation	Comment
Thermal conductivity		
S1	$\lambda'_{\text{eff}} = (1-\chi)\,\lambda_{\text{f}} + \chi\lambda_{\text{c}} + \lambda_{\text{g}}\varphi$	No radiation
S2	$\epsilon'_{\text{i}} = 0.5$	Reduced internal emissivity
S3	$\lambda'_{\text{eff}} = (1-\chi)\,\lambda_{\text{f}} + \chi\lambda_{\text{c}} + \lambda_{\text{r}}\varphi$	No gas conduction
S4a	$\lambda'_{\text{f}} = \lambda_{\text{f}} \times 1.2$	20 % increase in fuel conductivity
S4b	$\lambda'_{\text{f}} = \lambda_{\text{f}} \times 0.8$	20 % decrease in fuel conductivity
S5a	$\lambda'_{\text{c}} = \lambda_{\text{c}} \times 1.2$	20 % increase in char conductivity
S5b	$\lambda'_{\text{c}} = \lambda_{\text{c}} \times 0.8$	20 % decrease in char conductivity
Total heat capacity		
S6a	$c'_{\text{c,f}} = c_{\text{P}} \times 1.2$	20 % increase in fuel specific heat
S6b	$c'_{\text{c,f}} = c_{\text{P,f}} \times 0.8$	20 % decrease in fuel specific heat
S7a	$c'_{\text{c,c}} = c_{\text{P,c}} \times 1.2$	20 % increase in char specific heat
S7b	$c'_{\text{c,c}} = c_{\text{P,c}} \times 0.8$	20 % decrease in char specific heat
S8a	$\rho'_{\text{f}} = \rho_{\text{f}} \times 1.2$	20 % increase in fuel density
S8b	$\rho'_{\text{f}} = \rho_{\text{f}} \times 0.8$	20 % decrease in fuel density
S8c	$\rho'_{\text{f}} = \rho_{\text{f}} \times 0.5$	50 % decrease in fuel density

Table 7.9 The absolute and relative results of the sensitivity test for the internal heat transfer parameters.

	d_{p} (89)		d_{p} (490)		d_{p} (1603)	
	ms	%	ms	%	ms	%
Reference	14.4	—	250.6	—	1708	—
Thermal conductivity						
S1	14.5	0.7	248	−1.2	1698	−0.54
S2	14.3	−0.7	247	−1.5	1655	−3.1
S3	14.4	0.0	250.6	0.0	1708	0.0
S4a	14	−2.8	242	−3.4	1605	−6.0
S4b	14.8	2.8	265	5.8	1885	10
S5a	14.4	0.0	250	−0.24	1709	0.076
S5b	14.4	0.0	251	0.040	1706	−0.064
Total heat capacity						
S6a	16.6	15	297	19	2024	19
S6b	12.0	−17	204	−19	1388	−19
S7a	14.5	0.69	253	0.88	1725	1.0
S7b	14.2	−1.4	249	−0.80	1688	−1.1
S8a	16.7	16	299	19	2043	20
S8b	11.9	−17	202	−19	1371	−20
S8c	8.10	−44	129	−49	863.8	−49

from radiation. **S2** presents the results with decreased internal emissivity, as has been reported for surface emissivity of coal char [318]. Intuitively, the required residence time for complete devolatilization should increase if the effective thermal conductivity is decreased. However, for the specific reaction conditions investigated here, the problem becomes somewhat more ambiguous. Because the very fast devolatilization initiates at relatively low temperatures, the solid conduction will remain the dominating mechanism of heat transfer for most of the time.

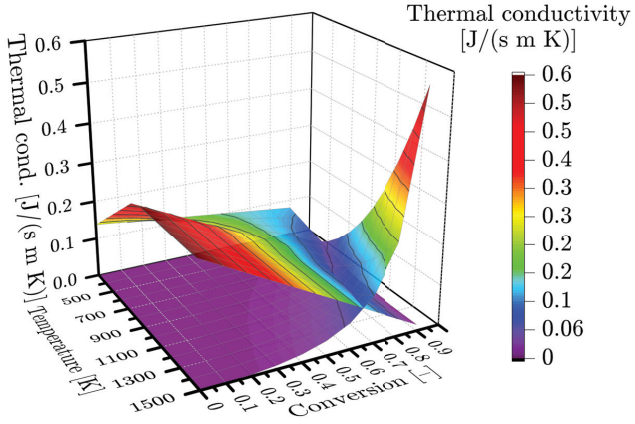

Figure 7.9 The relative contribution of radiation and conduction to the effective solid thermal conductivity inside a biomass particle.

Figure 7.9 illustrates the relative contributions of solid conduction and radiation as functions of particle temperature and conversion. From this figure it is apparent that the radiative contribution becomes dominant at high levels of conversion and at temperatures exceeding $\sim 1000\,\mathrm{K}$. The radiative contribution to the internal heat transfer is thus expected to contribute primarily to the heat transport through the char layer. Contrary, the solid conduction is expected to decrease significantly, as the devolatilization approaches 100 %, i.e. forming an insulating char layer. These effects especially influence on the surface temperature, as seen in the comparison in figure 7.10a.

The increase in the surface temperature increases the driving force for the solid matrix heat conduction which for temperatures below approximately 1000 K remains the dominant mode of heat transport.

The counterintuitive result of neglecting the internal radiation is a result of the very fast devolatilization kinetics used at temperatures above 800 K. This ensures that the devolatilization takes place in a temperature regime where the solid matrix conduction is still the dominating heat transfer mechanism. If the critical temperature for the shift between low and high temperature de-

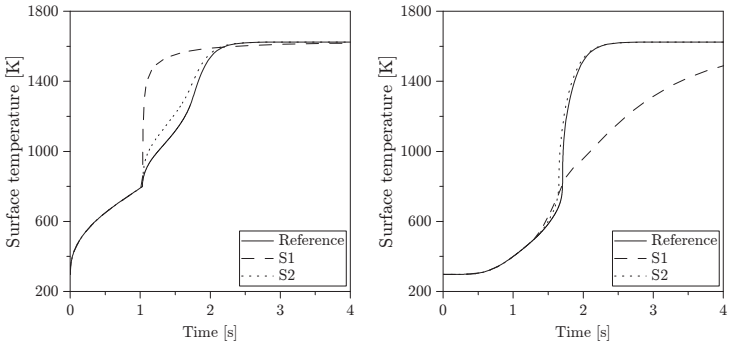

(a) Surface temperature. **(b)** Core temperature.

Figure 7.10 Influence of internal radiation on particle temperatures for a 1603 μm particle.

volatilization kinetics was to be increased, the result would be in line with that of Lu [64]. The contribution from gas conduction (**S3**) is likewise negligible.

As already discussed, the devolatilization takes place in the conduction dominated temperature regime. Therefore, it is also to be expected that changes to the solid matrix thermal conductivity (**S4a**–**S5b**) influence the result. As seen from table 7.9, it is primarily the thermal properties of the virgin wood that influence the net devolatilization time. The seemingly negligible influence of the changes to the thermal conductivity of the char, could stem from the increased contribution from internal radiation. As soon as the matrix reaches the critical temperature, it will devolatilize fast. This will significantly decrease the available heat capacity in the char matrix and thus induce rapid heat-up, increasing the significance of the radiative mechanism.

The parameter variations **S1**–**S5b** concern the heat transport properties of the particle. The parameter variations **S6a**–**S8c** investigate the influence of available heat capacity. The net heat capacity is assumed to be a linear function of conversion. The specific heat of the parent fuel and the char is primary parameters in a heat balanced model, it is however, difficult to derive consistent data from the literature, cf. e.g. figure 7.2. These difficulties are linked to the fact that the sample changes as it is exposed to heat. The importance of the specific heat appears clear when considering the response values for sensitivity test **S6a** and **S6b**; a relative response of ±15–19 % induced by a 20 % change in specific heat of the virgin fuel. The impact of specific heat of the char (**S7a** and **S7b**) is less important and has been calculated to influence only to negligible degree.

Changing the virgin fuel density (**S8a**–**S8c**) will effectively change the available heat capacity, thus a response similar to **S6a**–**S7b** can be expected.

The total heat capacity scales linearly with the particle density and thus corresponds to a change in the specific heat of the fuel and char at the same time. The close correlation between density and heat capacity becomes apparent when comparing the response values of test **S8a** and **S8b** to those of **S6a** and **S6b**. The results compare well emphasizing the importance of a good characterization of the thermophysical properties of the fuel.

7.3.3 External Heat Transport Properties

The thermal model builds on the assumption of quasi-steady-state between external and internal heat transport. The negligible influence of the thermal conductivities, discussed in the above, could indicate an external heat transport limited problem at the specific conditions. An overview of the sensitivity tests for external heat transport properties is listed in table 7.10. The absolute and relative values for the sensitivity tests **S9**–**S12** are shown in table 7.11.

Table 7.10 Overview of the parameter variations for external heat transport property impact evaluation. Prime indicates sensitivity test values or expressions.

Test	Variation	Comment
Transfer mechanisms		
S9	$T_w = 500\,\mathrm{K}$	Small radiative contribution
S10	$T_g = 1000\,\mathrm{K}$	Small convective contribution
S11	$h' = h \times 0.2$	Simulated blowing effect
S12	shrinking = 0	No shrinking

Table 7.11 The absolute and relative results of the sensitivity test for the external heat transfer parameters.

	d_p (89)		d_p (490)		d_p (1603)	
	ms	%	ms	%	ms	%
Reference	14.4	—	250.6	—	1708	—
Transfer mechanisms						
S9	15.0	4.2	315	26	2747	61
S10	42.4	194	536	114	2612	53
S11	44.1	206	562	124	2647	55
S12	14.4	0.0	250	−0.24	1695	−0.76

S9 studies the influence of decreased external radiation temperature. As expected, the influence increases with particle size. A reduction of 1000 K in the radiation temperature increases the required time for complete devolatilization of a 1603 μm particle by 16 %. The effect is especially relevant to the near burner field in a PF fired facility. In the quarl area the particle cloud density is high, thus the chance of particles shielding each other will be

large. In addition, the wall temperatures (typically 600–800 K) will define the radiation temperature.

A relatively larger influence on the small particles is predicted if the influence of external radiation is increased relative to convective heat transport (**S10**). Reducing the gas phase temperature by 831 K increases the required residence time for complete devolatilization of a 89 μm particle by almost 200 %. The absolute increase is however only 28 ms emphasizing the importance of taking time scales into account when analyzing the relative response values.

The blowing is caused by the rapid expansion of gases inside the particle as the devolatilization process occurs. This results in a jet of gases leaving the particle and disrupting convective heat transport. The phenomena can be difficult to model as the volatiles leave the particle through discrete channels. Therefore, the effect may not be even across the entire surface. The blowing effect is in this case modeled by correcting the heat transfer number, h, by a blowing factor running from zero to unity (effectively corrections are made to the Nu-number [357]). Lu [64] reported blowing factors reaching 0.1 in the initial phase of the devolatilization. **S11** investigates the influence with a blowing factor of 0.2 which increases the required time for complete devolatilization corresponding to a decrease in the gas phase temperature similar to **S10**. The influence scales with particle size similar to **S10** because of the effective reduction in convective heat transport.

The influence of shrinking (**S12**) is negligible. It should however be kept in mind that the shrinking effect only takes scaling of the external heat transport into account. Changes in the density and internal structure of the particle could influence on the overall process [358], however, insufficient data have been acquired to cover such a study.

7.3.4 Reaction Properties

The drying process is potentially important for the ignition. It is also one of the areas where the sequential approach of FLUENT®could result in noticeable differences from a stand-alone model where drying, devolatilization, and potentially char burn-out are allowed to take place in parallel. **S13** studies the influence of the heat of evaporation. This indicates no significant influence of the heat of evaporation. Only a slight increase in required residence time was observed when increasing the content of moisture (**S14**).

The sensitivity of the critical temperature, separating the high temperature kinetics from the low temperature kinetics (**S15a** and **S15b**), influences the required devolatilization time significantly. A change in 100 K induces relative changes of between 15 and 23 % in the response values. This stems from the large differences in the nominal value of the rate constants at the critical temperature.

Table 7.12 Overview of the parameter variations for reaction impact evaluation. Prime indicates sensitivity test values or expressions.

Test	Variation	Comment
Thermal conductivity		
S13	$\Delta_{\mathrm{vap}} H' = 0$	No heat of evaporation
S14	$Y^{*,\prime} = 0.1$	Increased water content
Devolatilization		
S15a	$T_{\mathrm{c}}' = 700\,\mathrm{K}$	Lower critical temperature
S15b	$T_{\mathrm{c}}' = 900\,\mathrm{K}$	Higher critical temperature
S16a	$E_{\mathrm{a},1}' = E_{\mathrm{a},1} \times 1.05$	5 % increase in $E_{\mathrm{a},1}$
S16b	$E_{\mathrm{a},1}' = E_{\mathrm{a},1} \times 1.2$	20 % increase in $E_{\mathrm{a},1}$
S16c	$E_{\mathrm{a},1}' = E_{\mathrm{a},1} \times 0.95$	5 % decrease in $E_{\mathrm{a},1}$
S16d	$E_{\mathrm{a},1}' = E_{\mathrm{a},1} \times 0.8$	20 % decrease in $E_{\mathrm{a},1}$
S16e	$E_{\mathrm{a},2}' = E_{\mathrm{a},2} \times 1.05$	5 % increase in $E_{\mathrm{a},2}$
S16f	$E_{\mathrm{a},2}' = E_{\mathrm{a},2} \times 1.2$	20 % increase in $E_{\mathrm{a},2}$
S16g	$E_{\mathrm{a},2}' = E_{\mathrm{a},2} \times 0.95$	5 % decrease in $E_{\mathrm{a},2}$
S16h	$E_{\mathrm{a},2}' = E_{\mathrm{a},2} \times 0.8$	20 % decrease in $E_{\mathrm{a},2}$
S17a	$A_1' = A_1 \times 1.05$	5 % increase in A_1
S17b	$A_1' = A_1 \times 1.2$	20 % increase in A_1
S17c	$A_1' = A_1 \times 0.95$	5 % decrease in A_1
S17d	$A_1' = A_1 \times 0.8$	20 % decrease in A_1
S17e	$A_2' = A_2 \times 1.05$	5 % increase in A_2
S17f	$A_2' = A_2 \times 1.2$	20 % increase in A_2
S17g	$A_2' = A_2 \times 0.95$	5 % decrease in A_2
S17h	$A_2' = A_2 \times 0.8$	20 % decrease in A_2

S16a–**S16h** investigate the impact to the net devolatilization time of the activation energies. The high temperature kinetics (**S16a**–**S16d**) influences the small particles to a larger extend than the larger particles. This is reasonable, considering the temperature regime in which the kinetics are active. Due to the slower heating rate of the larger particles, a larger share of the overall devolatilization will take place in the low temperature regime and vice versa for the small particles. The result adjusting the low temperature kinetics (**S16e**–**S16h**) is consistent and shows a greater influence on the larger particles.

In general, the devolatilization time is less sensitive to changes in the activation energies (**17a**–**17h**). But the trends that do appear are consistent with the pattern emerging from adjusting the activation energies (**16a**–**16h**).

7.3.5 Discussion on the Sensitivity Analysis

The build-up of temperature in the outer layer of the particle, when the internal radiation is neglected (**S1**), did not induce an apparent difference in the net devolatilization time when compared to the reference. The effect was balanced by the solid matrix heat conduction which for low to moderate temperature remains the dominant mode of transport. The reference case is, how-

Table 7.13 The absolute and relative results of the sensitivity test for the reaction mechanisms.

	d_p (89)		d_p (490)		d_p (1603)	
	ms	%	ms	%	ms	%
Reference	14.4	—	250.6	—	1708	—
Drying						
S13	14.3	−0.69	250	−0.24	1708	0.0
S14	14.6	1.4	251	0.28	1713	0.32
Devolatilization						
S15a	17.1	19	309	23	2027	19
S15b	12.2	−15	194	−22	1341	−21
S16a	14.6	1.4	252	0.40	1710	0.12
S16b	15.6	8.3	256	2.00	1717	0.53
S16c	14.1	−2.08	250	−0.40	1706	−0.11
S16d	13.4	−6.94	247	−1.48	1701	−0.36
S16e	14.3	−0.69	251	0.16	1719	0.67
S16f	14.4	0.00	251	0.32	1725	1.05
S16g	14.4	0.00	250	−0.32	1684	−1.39
S16h	14.2	−1.39	229	−8.78	1471	−13.86
S17a	14.3	−0.69	250	−0.08	1707	−0.03
S17b	14	−2.78	249	−0.52	1705	−0.13
S17c	14.4	0.00	251	0.12	1708	0.04
S17d	14.9	3.47	252	0.68	1711	0.19
S17e	14.3	−0.69	251	0.08	1707	−0.06
S17f	14.4	0.00	251	0.00	1711	0.19
S17g	14.4	0.00	251	0.04	1708	0.05
S17h	14.4	0.00	251	0.04	1711	0.18

ever, simulating an external radiation temperature (1500 K) close to the gas phase temperature (1831 K). If the external radiation temperature was to be decreased (**S9**), the net devoaltilization time significanly increased, especially for the larger particles. This is expected because the particle temperature relatively fast exceeds that of the external radiation temperature, reversing the radiative heat flux. The mechanism is enhanced if the internal radiation is neglected, increasing the surface temperature and therefore the temperature difference between the particle surface and the radiation background.

When assessing the response values, the absolute time scales should be kept in mind. The time required for a small particle (89 μm) to fully devolatilize is two orders of magnitude smaller than the time required for a large (1603 μm) particle to devolatilize. Hence, large relative changes to the small particles may in fact be insignificant when compared to the larger particles dominating the flame.

The influence of the choice of critical temperature (separating the low temperature kinetics from the high temperature kinetics, **S15a** and **S15b**) is an inherent consequence of the discontinuous rate constant. By employing multiple kinetic rate constants, the model attempts to compensate for the inability

of a single SFOR mechanism to take heat rate effects into account. The discontinuous nature of the model can be avoided if a proper blending function is implemented. In order to develop and tune such a function, additional validation material would be required.

In general, the available heat capacity at time t, effectively, will control the property gradients in time $t + 1$. Because a substantial quantity fraction of the particle initial matter is devolatilized, the reduction in heat capacity is significant. The reduction in mass, and thus heat capacity, accelerates the particle heat-up and thus the rate of devolatilization. This self-stimulating mechanism was also found to be of importance when analyzing small particles in the LFR, cf. section 5.4.

7.4 Summary

A transient, one dimensional model has been constructed. The model includes heat transport coupled to a drying and a devolatilization model.

The model has been evaluated using three different set-ups resulting in three significantly different reaction environments. The model perform well across the following main parameters:

- Particle sizes: $63\,\mu$m to $1.1\,$cm
- Peak gas phase temperatures: $1080\,$K to $1831\,$K
- Average particle heating rate: $30\,\mathrm{K}\cdot\mathrm{s}^{-1}$ to $10^5\,\mathrm{K}\cdot\mathrm{s}^{-1}$
- Particle inital moisture content: ~ 0 to $9\,$wt. %
- Particle densities: 580 to $1180\,\mathrm{kg}\cdot\mathrm{m}^{-3}$

It seems that the release of volatile matter can be well predicted solely from a heat transport model coupled to a simple SFOR devolatilization mechanism.

The application of the model to improve the performance of larger CFD simulations follows in chapter 8.

CHAPTER 8

A Model Fuel for CFD Implementation

Part I discussed the diversity of properties among the selection of available biomass fuels. This chapter narrows the selection of fuels to wood fuels and takes the results from the previous chapters into account to generate a generic model fuel for easy implementation to CFD. A summary of this chapter has been published in Energy [359] and enclosed in appendix B.

8.1 Introduction

There are many CFD solvers available on the market capable of solving multiphase, reacting flows. This project has been based on ANSYS®FLUENT®and thus the formulation of a model fuel will be fitted to the options and limitations offered by this particular software.

FLUENT®approaches dilute particle laden flows using an Euler-Lagrangian approach. The fluid flow is described by solving the Navier-Stokes equation in a fixed frame of reference [290]. The trajectories of the dispersed phase is then tracked based by integrating the force balance on the particle, in a Lagrangian frame of reference[360]:

$$m_{\mathrm{p}} \frac{\mathrm{d}\vec{u}_{\mathrm{p}}}{\mathrm{d}t} = \sum \vec{F}_i \tag{8.1}$$

where m_{p} and $\vec{u}_{\mathrm{p}}$ are the particle mass and particle velocity vector, t is time and F_i sums up the forces acting upon the particle. The primary forces are due to the drag force, $\vec{F}_{\mathrm{drag}}$, and the gravitational pull, $\vec{F}_{\mathrm{g}}$. A number of additional phenomena can be taken into account, including: The Saffman's lift force, bouyancy effects, pressure gradients, virtual mass force (acceleration of surrounding fluid), and thermophoretic force.

The discrete phase model (DPM) model allows for exchange of mass, momentum, and energy with the fluid phase. The phase interaction is categorized into two: One-way coupling in which the fluid flow acts upon the particle, but the effect of the discrete phase on the continuum is not included. Or a two-way coupling, where the exchange is allowed to occur in both directions. Particle-particle interactions are not included in the standard DPM model, justified by the dilute particle laden flows.

Thus, in order to solve the multiphase system, a number of input parameters is required for the discrete phase. This chapter aims to summarize some of the central parameters needed for accurate discrete phase behavior.

8.2 Case Study: AMV1 (2014)

The diversity of biomass makes it difficult to derive generic data on particle properties, as discussed in chapter 2. This relates not only to the rate of devolatilization, cf. chapters 4 and 5, the selection of thermophysical properties or phenomenological models, cf. chapters 3 and 7, but also to the physical appearance of the particles. To resemble a typical fuel used for PF combustion a case study is carried out, characterizing the chemical composition and the particle size distribution of the fuel used during the full-scale campaign at Amager power station (AMV) unit 1 in 2014. This case study will constitute the basis for the following construction of a model fuel for CFD implementation.

8.2.1 Particle Size Distribution

The PSD is a central parameter in PF combustion as the particle size dictates the reaction regime and thus the rate of release of volatiles. It will naturally likewise influence on the fluid dynamics.

During the full-scale campaign, three types of fuel samples were acquired:

- Un-crushed pellets
- Dust samples extracted by static probing
- Dust samples extracted by rotor probing

The pellet samples are extracted from the buffer tank feeding the mill. All dust samples were acquired from a horizontal transport tube between the mill and the burner. The static probing was carried out by inserting a tube connected to a vacuum cleaner. The mouth of the tube was angled towards the flow of particles and positioned approximately on the centerline. The rotor probe is designed to minimize collection bias. It collects particles through a rotating probe with its normal direction aligned with the direction of the flow. Particles are collected at two different diameters, thus effectively collecting particles through two concentric circles.

Analysis Equipment

Because of the oddly shaped particles of biomass, no obvious method for particle size characterization is apparent. This case study includes the results of three different analyses:

- Sieve analysis
- Particle image projection
  - Sympatec QICPIC®

– Retsch CAMSIZER®

Figure 8.1 compares the applied methods. Unfortunately, a direct comparison between the two image based analysis methods using the same characteristic size was not possible. The QICPIC®is depicted using the diameter of a volume equivalent sphere, while the CAMSIZER®results are shown using the Martin minimum diameter, on the recommendation of Trubetskaya [165].

Figure 8.1a shows the variations in particle size across all three measurement days. Each day is depicted by four repetitive measurements on the same sample batch using the Sympatec QICPIC®apparatus. This shows good repeatability of the QICPIC®method and only small deviations in the PSD across the three days. Day 1 deviates the most with a larger fraction of small particles.

When comparing the methods, cf. figures 8.1b to 8.1d, the trends appear consistent. The QICPIC®method indicates a larger fraction of smaller particles, followed by the sieve analysis and the CAMSIZER®method. For an in depth methodological analysis of the CAMSIZER®, comparison to alternative characterization methods, and the choice of particle characteristic lengths, the reader is referred to the work of Trubetskaya [165] who provides detailed documentation and discussions on particle size and shape.

Influence of Sampling Method

Collection bias has been evaluated using conventional sieve tower analysis. Three sampling methods are compared:

- Dust from manually crushed pellets collected before the mill
- Dust collected after the mill by static probing
- Dust collected after the mill by iso-kinetic probing

The isokinetic probing is carried out using a rotor probe equivalent to the one presented in figure 8.2. By rotating the probes perpendicular to the direction of flow, the apparatus minimizes collection bias caused by uneven distribution of particles in the tube. By adjusting the suction velocity, iso-kinetic sampling is obtained thus avoiding collection bias due to mass/momentum phenomena.

Figure 8.3 compares the measurement methods across the entire campaign. The comparison is made on the Rosin-Rammler mean diameter and spread. A clear trend appears when comparing the mean diameters: The static probing indicates the smallest mean diameters, followed by the rotor probe and finally the pellets. This can be rationally explained. The pellets are expected to yield the largest particle size. Although the roller mill is not designed to further grind the particles, some degree of particle crushing must be expected. Thus,

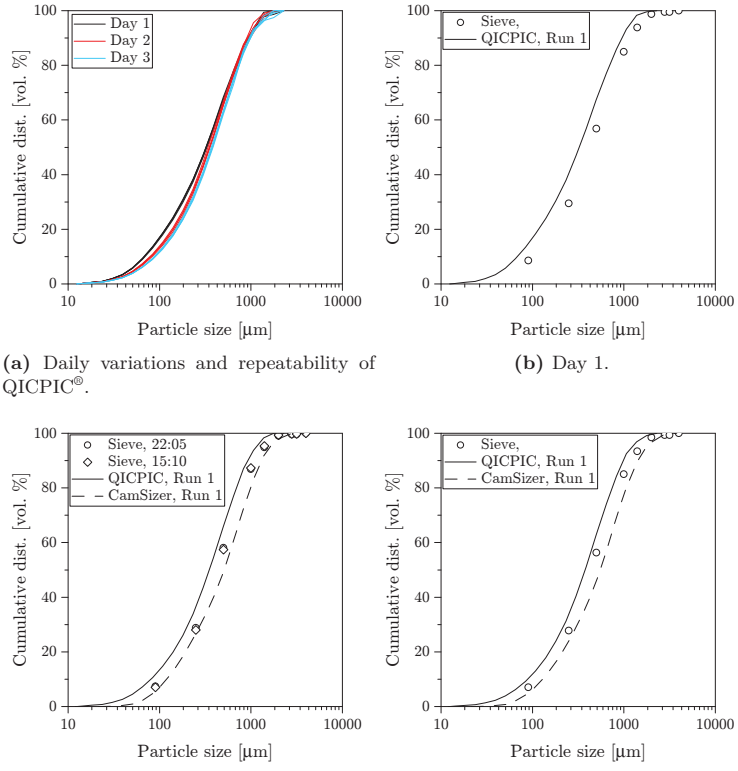

(a) Daily variations and repeatability of QICPIC®.

(b) Day 1.

(c) Day 2.

(d) Day 3.

Figure 8.1 Comparison of PSD characterization methods. Particle size is defined as: Sieve: The mesh size, QICPIC®: The diameter of a sphere with the same volume, CAMSIZER®: The Martin minimum diameter.

Figure 8.2 Illustration of the rotor probe used for isokinetic dust sampling. Illustration has been modified from [361].

resulting in larger particles upstream of the mill. The static probing is sucking with a fixed compressor output, i.e. anisokinetic sampling. The suction velocity is expected to exceed the velocity of the particle flow. The pressure difference induced by the different flow velocities will have a greater impact on lighter particles, resulting in a collection bias towards smaller particles. The differences are significant and the difference between the smallest and largest mean diameters is around 300 μm.

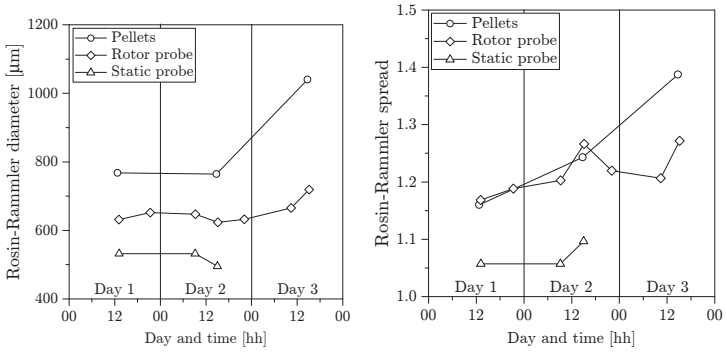

(a) Rosin-Rammler mean diameter. **(b)** Rosin-Rammler spread.

Figure 8.3 Comparison of collection methods based on the Rosin-Rammler distribution.

Summary on Particle Size Distribution

To provide a concrete description of the particle sizes, a single sample has been selected to represent the particles used at Amager power station. Figure 8.1a indicates that the variation in particle sizes are small.

The CAMSIZER®results from day #2 have been chosen using the Martin minimum diameter as the characteristic length. The Rosin-Rammler fit is presented in figure 8.4.

8.2.2 Proximate and Ultimate Analysis

Table 8.1 lists the proximate analyses from dust samples extracted during the second full-scale campaign at AMV. The average values are recommended as fuel composition values in future calculations.

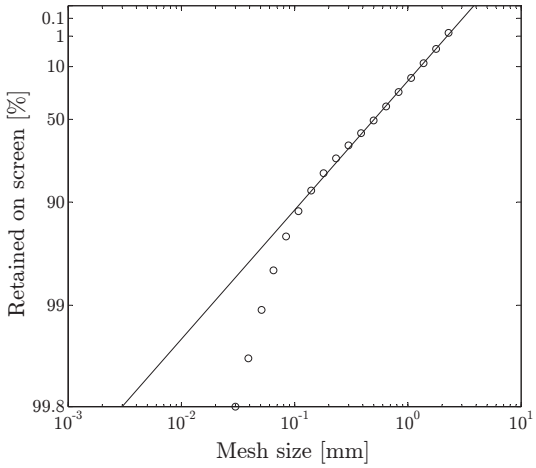

Figure 8.4 Rosin-Rammler fit to AMV dust using CAMSIZER®data from day #2 of the second full-scale campaign: $\bar{d} = 670.8\,\mu$m, $n = 1.277$. The Martin minimum diameter has been used as the characteristic length.

Table 8.1 Proximate analysis from the second full-scale campaign at AMV.

Property	Unit	Dust sample			Average		
		#1	#2	#3			
HHV	$\mathrm{MJ \cdot kg^{-1}}$	19.37	19.33	19.29	19	±	0.0
Moisture	wt. % (wet)	3.9	4.9	3.5	4.1	±	0.7
Ash		0.90	0.70	0.80	0.80	±	0.1
Volatiles		80	79	80	80	±	0.6
C	wt. % (d.a.f.)	50.7	50.7	50.2	50.5	±	0.3
H		6.26	6.34	6.16	6.25	±	0.1
N		0.202	0.201	0.202	0.202	±	0.0
O		42.9	42.8	43.5	43.1	±	0.4

8.3 Effective Devolatilization Kinetics

The devolatilization models available in FLUENT®offers only a few inherent options for modeling particle devolatilization: Constant rate, SFOR, two competing SFORs (Kobayashi *et al.* [253]), and the CPD-model (coal based), of which the latter will not be used in this work. The following brief presentation of inherent FLUENT®devolatilization models will be based on FLUENT®nomenclature and might deviate from the rest of the thesis.

The constant rate model assumes that volatiles are released at a constant rate, characterized by a single parameter, A_0:

$$-\frac{\mathrm{d}m_\mathrm{p}}{\mathrm{d}t} = A_0 f_{\mathrm{v},0}\,(1 - f_{\mathrm{w},0})\,m_{\mathrm{p},0} \tag{8.2}$$

where m_p is the mass of the particle at time t and $m_{\mathrm{p},0}$, $f_{\mathrm{v},0}$, and $f_{\mathrm{w},0}$ are the initial mass of the particle, and initial fraction of volatiles and moisture, respectively. A_0 is the rate constant.

The single kinetic rate model assumes the rate of devolatilization to be first order on the amount of remaining volatiles:

$$-\frac{\mathrm{d}m_\mathrm{p}}{\mathrm{d}t} = k\left[m_\mathrm{p} - (1 - f_{\mathrm{v},0})\,(1 - f_{\mathrm{w},0})\,m_{\mathrm{p},0}\right] \tag{8.3}$$

where the rate constant, k, is expressed as an Arrhenius type equation:

$$k = A_1 \exp\left[\frac{-E}{RT}\right] \tag{8.4}$$

where A_1 and E are the fitting parameters, pre-exponential factor and activation energy, R is the gas constant, and T the temperature.

The Kobayashi model includes two rate expression similar to equation (8.4). The kinetic parameters are tuned to provide limiting rates at different temperature intervals. The model does however require additional yield factors for the blending of the independent reactions, and thus, the model becomes more difficult to tune.

The conversion profiles presented in chapter 7 clearly show how the constant rate model is not a feasible option to describe the particle pyrolysis. Experiences from chapter 4 indicate that a SFOR mechanism will struggle to describe the large span of temperatures and heating rates expected for PF combustion using biomass fuels. Applying a single set of SFOR kinetics to describe all particle sizes will result in wrong predictions of the release of volatiles. There is currently no way of correcting for such bias when using the intrinsic FLUENT®models.

This section provides a method for correcting the kinetic parameters for thermal transport limitations. The thermal history of a particle is dependent on the particle size. Thus, a set of unique SFOR kinetics are necessary to each particle of different size, resulting in the need for an infinite number of

kinetic parameters for a continuous PSD. To simplify matters, this work will lump together related particle sizes into particle bins and use a single set of SFOR kinetics to describe the average expected behavior of each respective particle size category. The heat transport corrected kinetics are derived from the following algorithm:

1. The non-isothermal 1D model, combining heat transfer, water release, and devolatilization is used to generate conversion profiles of a specific particle size at a given temperature.

2. The conversion profile (from step 1) is superimposed on an isothermal devolatilization model (equation (8.5)) and the corresponding particle temperature history is calculated.

3. The combination of the non-isothermal conversion profile (step 1) and the isothermal temperature history (step 2) is used to derive a set of apparent devolatilization kinetics corrected for heat transport limitations.

The isothermal model used to derive heat transport corrected devolatilization kinetics shares all of the thermophysical data with the non-isothermal model, cf. table 7.3. The temperature history is computed by solving a heat balance:

$$m_\mathrm{p} c_p \frac{\mathrm{d}T_\mathrm{p}}{\mathrm{d}t} = hA_\mathrm{p}\left(T_\mathrm{g} - T_\mathrm{p}\right) + \varepsilon_\mathrm{p} A_\mathrm{p} \sigma \left(T_\mathrm{w}^4 - T_\mathrm{p}^4\right) \tag{8.5}$$

where m_p, c_p, ε_p, and A_p are the mass, specific heat, emissivity, and surface area of the particle. T_p, T_g, and T_w are the particle, bulk gas, and radiation temperatures, respectively. σ and h are the Stefan-Boltzmann constant and the gas phase heat transfer number.

8.3.1 Characteristic Particle Size Bins

The discretization of the PSD into suitable particle size bins has been made on the basis of the non-isothermal modeling results.

By analyzing the radial conversion and temperature profiles of the particles, three distinct categories can be defined, cf. figure 8.5:

1. Small particles, cf. figure 8.5a: Nearly isothermal particles. The internal heat transport occurs fast and as a result, the core of the particle reaches elevated temperatures before the outer part of the particle is fully devolatilized. The heat up is fast, thus the devolatilization process is primarily controlled by the high temperature devolatilization kinetics.

2. Medium size particles, cf. figure 8.5b: The particle size is sufficiently large as to introduce non-negligible temperature gradients. However, the heat transport still occurs relatively fast. Thus, as the outer part

of the particle reaches full devolatilization, the temperature of the core has risen sufficiently to initiate devolatilization. The relative increase in internal thermal resistance compared to small particles results in a primary share of the conversion taking place in the high temperature kinetic regime.

3. Large particles, cf. figure 8.5c: The internal heat transport is significantly slower compared to the smaller particle sizes. As a result, an unreacted core remains even as the outer part of the particle reaches full conversion. The heat propagates slowly through the particles resulting in a broad reaction zone controlled by the low temperature kinetics. This is directly followed by a narrow shell of high temperature kinetics.

The transition between the three categories of particle sizes can be defined on a conceptual basis as described in table 8.2.

Table 8.2 Definitions of the transitions between the three particle size categories. T_p is the local particle temperature, T_c is the threshold temperature separating low and high temperature devolatilization kinetics, r is the normalized radial distance going from center to surface, χ is the local devolatilization conversion, and $|_t$ denotes a given time step.

Transition	Description	Mathematical description
–Small	From zero length to the critical particle diameter where the outer part of the particle reaches full conversion before the core reaches the critical temperature threshold separating low from high temperature kinetics.	$T_\mathrm{p} > T_\mathrm{c} \quad r \in [0;1]$ $\wedge$ $\chi < 1 \quad r \in [0;1]$
Small–medium	From small particles to where the outer shell reaches full conversion before devolatilization has begun at the core.	$T_\mathrm{p} < T_\mathrm{c} \quad r \in [0;r_1]$ $\wedge$ $T_\mathrm{p} > T_\mathrm{c} \quad r \in]r_1;1]$ $\wedge$ $\chi < 1 \quad r \in [0;r_1]$
Medium–	From medium particles and up.	

Figure 8.6 shows the transition diameters as function of the gas temperature. The critical diameters vary only slightly with temperature. For a generically applicable discretization of a given size distribution, the mean values are used to define the small, medium, and large particles.

8.3.2 Conversion Profiles for Characteristic Particle Sizes

Following the particle sizes, defined in figure 8.6, conversion profiles are calculated for a single particle size representing the different particle size bins.

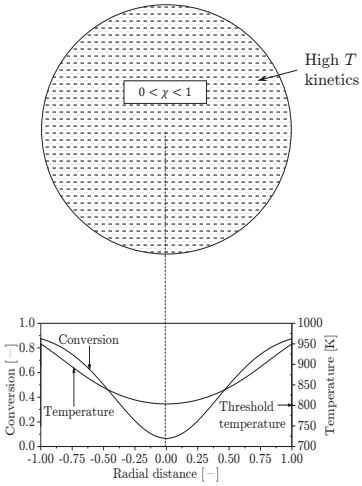

(a) Small particle.

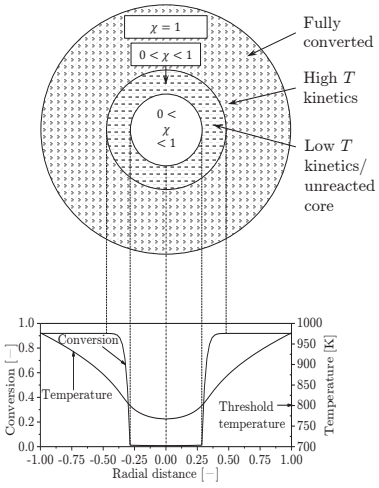

(b) Medium particle.

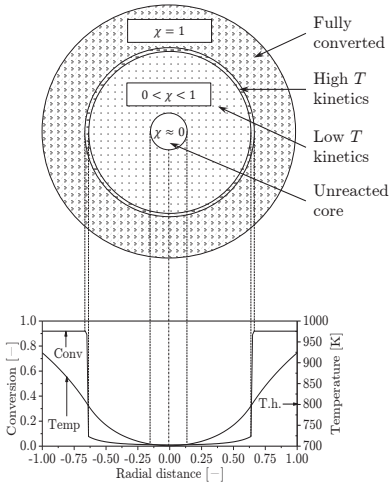

(c) Large particle.

Figure 8.5 Definition of the three characteristic particle sizes. Figure 8.5a: small particles: The entire particle is being converted in the high temperature kinetic regime. Figure 8.5b: medium particles: The outer part of the particle reaches full conversion before the temperature in the center exceeds the critical threshold separating low from high temperature pyrolysis kinetics. Figure 8.5c: large particles: The heat transport through the particle is slow. Thus, the outer part will reach full conversion while the core is still unreacted. The heat front propagates slowly, leaving only a thin shell of high temperature kinetics, while a large part of the particle is converted in the low temperature kinetics regime. The calculations are carried out with $T_g = 1405\,\mathrm{K}$ and $T_w = 1000\,\mathrm{K}$, and particle properties given in table 8.4.

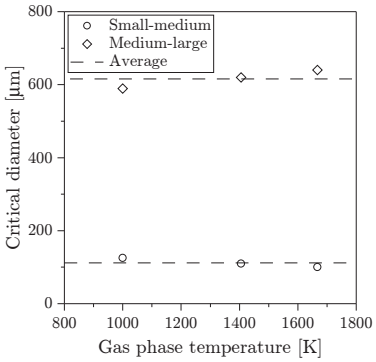

Figure 8.6 The critical particle diameters satisfying the conditions given in table 8.2. The average values are used as a generic measure for particle size classification. Average values: small-medium 112 μm, medium-large 616 μm.

The characteristic particle diameter is chosen as the diameter equivalent to half of the net volume of the corresponding size bin. The average particle diameter for the large particle bin is calculated using 2 mm as the largest particle diameter. This corresponds to the typical 95 % quantile for pulverized biomass combustion [362]. The transition from small to medium particles at 112 μm corresponds reasonably well with previous studies on single dimensional non-isothermal modeling [168], concluding that the internal heat transport limitations for particles less than a few hundred microns is secondary at most.

Table 8.3 Effective particle diameter for each particle bin. Heat transport corrected devolatilization kinetics specific to the class size.

Size bin	Interval μm	Diameter μm	A s^{-1}	Ea $kJ \cdot mol^{-1}$
Small	0–112	89	8.56×10^{10}	171.8
Medium	112–616	490	3.99×10^{9}	162.3
Large	616–2000	1603	2.62×10^{6}	118.7

In figure 8.7 the resulting heat transport corrected kinetics are compared to the literature values of Wagenaar *et al.* [236], Johansen *et al.* [269]. The ANSYS®FLUENT®default values for wood devolatilization ($E_a = 74\,kJ{\cdot}mol^{-1}$ and $A = 312 \times 10^3\,s^{-1}$) is also represented and will be used as a literature reference in the following comparison of kinetics, cf. figures 8.8 and 8.10. Figure 8.7 clearly shows why the combination of the low (Wagenaar *et al.* [236]) and the high (Johansen *et al.* [269]) temperature kinetics is necessary in order

to describe the devolatilization across different heating rates. The differences in the rate of devolatilization are significant, especially at low temperatures. Although the non-isothermal model uses a combination of the low and high temperature kinetics, the resulting rate constants for the isothermal corrections are even slower than the low temperature kinetics at low temperatures. This stresses the importance of the time and temperature history.

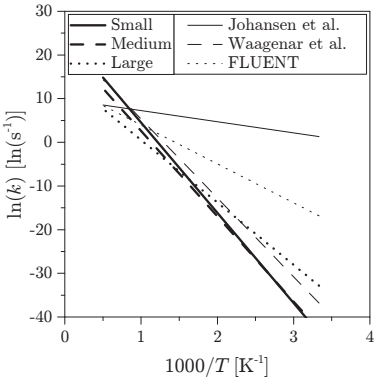

Figure 8.7 The resulting kinetics for the heat transport corrected characteristic particles sizes. Compared to the literature values of Wagenaar *et al.* [236], Wagenaar *et al.* [236], and the FLUENT®default values for wood devolatilization.

The fuel properties used for the calculations are listed in table 8.4. Since the work aims to facilitate large numerical simulations of pulverized biomass fired boilers, the density is chosen as that of a typical wood pellet [127]. To simplify data interpretation, the calculations have been carried out on dry particles. The high temperature volatile yield (HTVY) is FLUENT®terminology for the ratio between volatile yields at high and low temperatures. This factor is particularly useful as most volatile standards used in proximate fuel analyses specify the volatile yield at temperatures below 1000 K. However, the volatile yield is often found to be significantly higher at higher temperatures [89]. The HTVY was derived on the basis of the high temperature LFR experiments on wood fuels compared to the corresponding proximate analysis following DS/EN14775(2009).

Figures 8.8 and 8.10 present a model comparison of devolatilization profiles for two gas phase temperatures at each of the characteristic particle size classes. The figures compare the results of the non-isothermal model, the isothermal model using FLUENT®default values, and the isothermal model using heat transport corrected devolatilization kinetics, as seen in table 8.3.

Figure 8.8 presents the results from the small particle size ($d_\mathrm{p} = 89\,\mu$m). It shows a longer devolatilization time using the default FLUENT®values,

Table 8.4 Particle characterization for the model fuel.

Parameter	Unit	Value	Reference
Moisture	wt. %	0.0	
Volatiles		91.9	[269]
Char		7.90	[269]
Ash		0.200	[269]
Density	$kg \cdot m^3$	1180	[127]
HTVY	—	1.4	[269]

increasing the required residence time for complete devolatilization by around 30 %.

This trend is reversed for the medium and large particle classes, cf. figures 8.9 and 8.10. The isothermal model using the uncorrected kinetics underpredicts the required time for devolatilization, most pronounced for larger particles. The heat transport corrected kinetics used in the isothermal model is capable of predicting approximately the same time for complete devolatilization as the non-isothermal model.

The discontinuous behavior of the conversion profile produced by the non-isothermal model is a consequence of using two sets of kinetics for different temperature intervals. Thus, the conversion levels amongst the model are different for low degrees of conversion.

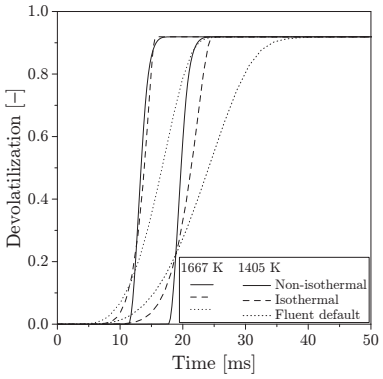

Figure 8.8 Small particles: $d_p = 89\,\mu m$. Comparison between the non-isothermal and the isothermal model using the heat transport corrected devolatilization kinetics and the default FLUENT®values.

The non-isothermal model has been developed based on time resolved conversion data for very small particles ($< 200\,\mu m$) and large particles of 10.9 mm. The model performance for particles within this interval has been evaluated

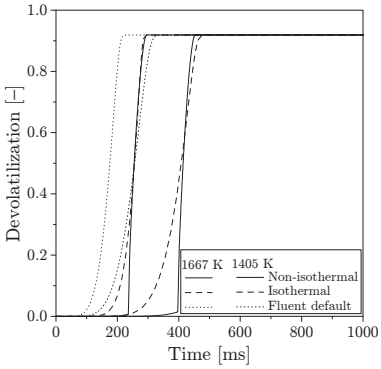

Figure 8.9 Medium particles: $d_p = 489.9\,\mu$m. Comparison between the non-isothermal and the isothermal model using the heat transport corrected devolatilization kinetics and the default FLUENT®values.

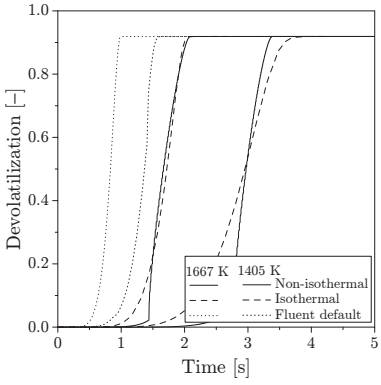

Figure 8.10 Large particles: $d_p = 1603\,\mu$m. Comparison between the non-isothermal and the isothermal model using the heat transport corrected devolatilization kinetics and the default FLUENT®values.

based on the total devolatilization time, and a critical temperature at which the rate constant changes from low to high temperature kinetics has been assigned. Thus, the time dependent release of the volatiles may not be accurately predicted by the model. This could be improved by introducing a blending option based on multiple parallel reactions [190] or alternatively by an implementation of a more detailed devolatilization mechanism, e.g. the DAEM [188, 189]. The computational penalty should however be kept in mind [184].

8.3.3 Direct Comparison to the Isothermal Model

Figure 8.11 illustrates the direct comparison between the predicted total devolatilization time using the non-isothermal model and the isothermal model with and without the heat transport correction in the devolatilization kinetics. A noticeable better fit is achieved by applying the heat transport corrected devolatilization kinetics in the appropriate size categories.

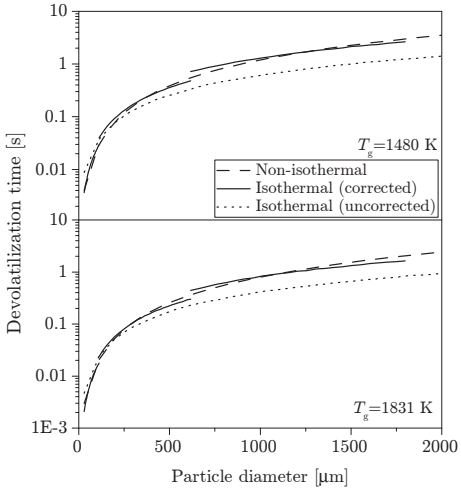

Figure 8.11 A direct comparison on the predicted total devolatilization time between the non-isothermal and isothermal model using heat transport corrected and uncorrected devolatilization kinetics as a function of initial particle diameter. Temperatures indicate gas phase temperatures.

8.4 Evolving Gases

The speciation of the volatile component released during particle devolatilization influence the calculations through the subsequent homogeneous gas phase

oxidation. A generalized two-step mechanism is commonly used to oxidize the "volatile" species [363] and has been found to predict the reactions reasonably well [168]:

$$C_nH_m + \left(\frac{n}{2} + \frac{m}{4}\right) O_2 \longrightarrow nCO + \frac{m}{2}H_2O \tag{8.6}$$

$$CO + \frac{1}{2}O_2 \longrightarrow CO_2 \tag{8.7}$$

By definition the primary pyrolysis covers the conversion of virgin fuel to the respective products, depending on the selected mechanism, cf. page 44. The simplest representation of the primary pyrolysis in a large temperature span is probably presented by transforming virgin fuel into volatiles, tar, and char [197]. This sort of single-stage semi-global reaction model is extensively reported in the literature [104, 230, 240, 364–369] with consistent trends for the behavior of volatiles, tar, and char formation. At moderate temperatures, tar and volatiles evolve at comparable rates. Increasing the temperature will typically favor the production of tar. As the temperature increases, the tar production is challenged by the secondary cracking of tar into gas and char, as suggested by Di Blasi [117]. This occurrence of a local maximum in the rate of tar production takes place around 800–850 K and is indeed relevant for pulverized fuel combustion conditions [222].

Additionally Hajaligol *et al.* [369] suggested the net production of tar to be dependent on heating rate. At low heating rates below 100 K/s no maximum in the rate of tar production is observed. Rather a constant value was found. This is believed to be the case when the residence time of the tars is not sufficiently long for reaching a temperature sufficiently high for secondary reactions to occur.

This work aims to lump together all evolving species in the gas phase and characterize the thermophysical properties as a single component. This will ease the implementation of the data into commercial CFD codes like ANSYS® FLUENT®. It also aims to use the work at suspension firing conditions which reaches both high temperatures and heating rates. Thus, the net volatile component, expressed as "vol", will be including both the gaseous product of the primary pyrolysis and the secondary cracking of tar. This essentially reduces the two stage wood pyrolysis model proposed by Di Blasi [117] to a single step global mechanism, cf. figure 8.12.

The composition of the evolving gases relies on a great number of parameters. First of all will the macromolecular composition of the parent fuel influence on the evolving gases. The temperatures at which cellulose, hemicellulose, and lignin is thermally degraded varies [150]. The different C:O and C:H ratios influence directly on the volatile compounds, thus making the devolatilization characteristics unique to a fuel. However, in general the pyrolysis gas will be dominated by CO followed by CO_2 and H_2O [370, 370].

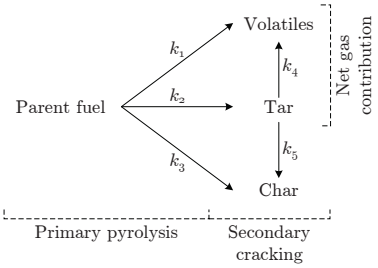

Figure 8.12 The net contribution to the gaseous volatile model component.

Combined CO, CO_2, and H_2O commonly make up around 80 wt. % of the net release and with only slight variations in the ratios. Therefore, a generically applicable model compound can be justified to represent the volatile species.

The model compound denoted "vol" is based on the work of Nunn *et al.* [251] who analyzed the release of eight species from a hardwood. The pyrolysis was carried out using a captive sample reactor capable of heating pulverized fuel (45–88 μm) at $1000\,\mathrm{K}\cdot\mathrm{s}^{-1}$. This does not compare to the heating rates of suspension fired boilers, however, based on the work of Hajaligol *et al.* [369] it should be sufficient to stabilize the product yields, i.e. facilitate tar cracking at low residence times. In addition, Nunn *et al.* [251] analyzed the pyrolysis process at high peak temperatures which is believed to be important for the product yield ratios [369].

Table 8.5 Composition of evolving gases [251] at high peak temperatures $\sim 1400\,\mathrm{K}$ and heating rates on the order of $10^3\,\mathrm{K}\cdot\mathrm{s}^{-1}$.

Species	MW $\mathrm{g}\cdot\mathrm{mol}^{-1}$	wt. %	MW_m $\mathrm{g}\cdot\mathrm{mol}^{-1}$
H_2O	18.0	0.15	2.7
CO	28.0	0.50	14
CO_2	44.0	0.18	7.8
CH_4	16.0	0.06	1.0
C_2H_6	30.1	0.01	0.15
C_2H_4	28.1	0.03	1.0
C_3H_6	42.1	0.01	0.54
CH_2O	30.0	0.06	1.8
Vol			29

* Value not stable at peak temperature $< 1500\,\mathrm{K}$. Value evaluated at 1400 K.

Table 8.5 lists the composition of the volatile gases. The concentration of most of the products: CO, CO_2, H_2O, C_3H_6, and CH_2O stabilizes at peak

temperatures exceeding $\sim 900\,\mathrm{K}$. The concentration of CH_4 and C_2H_4 continues to increase, however, at a reduced rate. This can probably be explained by the occurence of tar cracking reactions known to initiate at around that temperature. In the interest of simplification, the composition has been evaluated at a peak temperature of 1400 K which corresponds well with what can be expected at suspension firing conditions.

Thermophysical Data of Evolving Gases

The individual compounds, cf. table 8.5, are assumed to behave as ideal gasses. Thus, the thermophysical data for the net volatile, "vol", component is a sum of the mass-weighted individual properties, MW_m. Tables 8.5 to 8.7 list selected thermophysical properties of the individual volatile species and the resulting net "vol" species.

Table 8.6 Specific heat capacities of selected gas compounds. "Vol" indicates the resulting specific heat for a composition of evolving gases given by table 8.5. $c_{\mathrm{P},i} = a_1T^4 + a_2T^3 + a_3T^2 + a_4T + a_5\ \left[\mathrm{J\,(kg\,K)^{-1}}\right]$.

Species	$a_1 \times 10^{12}$	$a_2 \times 10^{9}$	$a_3 \times 10^{6}$	$a_4 \times 10^{3}$	a_5	T K	Ref
H_2O	4.84	−38.5	−8.24	740	1612	273–4000	[370]
CO	15.9	−96.1	138	139	982	273–3000	[370]
CO_2	−31.5	274	−899	1390	508	273–3000	[370]
CH_4	141.2	−682	159	3820	1086	273–3000	[370]
C_2H_6	39.2	−29.5	−1200	4340	488	100–3000	[371]
C_2H_4	93.9	−455	113	2190	649	50–3000	[372]
C_3H_6	60.5	23.9	−2250	7330	854	50–3000	[372]
C_2HO	103	−603	863	569	891	50–3000	[372]
Vol	21.8	−96.9	−61.8	877	976		

8.5 Summary

This chapter has systematically constructed a model fuel for direct and easy implementation into FLUENT®. The model fuel includes a particle size distribution based on a case study, heat transport corrected kinetics for wood fuel, and characterization of the leaving species.

A method has been developed that increases the accuracy of the time dependent volatile release for particle sizes relevant for suspension fired combustion $< 2\,\mathrm{mm}$. The method makes it possible to simulate heat transport limited pyrolysis in zero dimensions using a set of corrected single first order reaction kinetics. This allows one to carry out multiphase fluid dynamics cal-

Table 8.7 Standard state enthalpy and entropy of evolving gases. Reference temperature: $T_0 = 298.15\,\mathrm{K}$. "Vol" indicates the resulting specific heat for a composition of evolving gases given by table 8.5. Averaged values are used if multiple references.

Species	H^0 $\mathrm{kJ \cdot mol^{-1}}$	S^0 $\mathrm{J \cdot mol^{-1}}$	Ref
H_2O	−743.8	188.8	[370, 372, 373]
CO	−141.0	197.7	[370, 372, 373]
CO_2	−203.1	213.8	[370, 372, 373]
CH_4	−190.1	187.5	[370, 372, 374]
C_2H_6	−84.16	229.6	[375–377]
C_2H_4	52.49	219.3	[372, 375, 376]
C_3H_6	20.41	238.0	[375, 378, 379]
CH_2O	−112.3	219.0	[372, 380]
Vol	−233.6	201.3	

culations (CFD) without having to implement computational heavy single or multi-dimensional calculations of the discrete phase.

Comparison of the modeling approach to the existing method shows that using uncorrected pyrolysis kinetics will overestimate the total pyrolysis time of small particles (89 μm) by 50–80 %. For larger particles (1603 μm) the uncorrected pyrolysis kinetics will lead to a predicted devolatilization time of under half of that predicted by the 1-dimensional model.

The method for heat transport, correcting the devolatilization kinetics, is easily implemented into most CFD commercial codes. It avoids the requirement for computational demanding multidimensional computations of the discrete phase while still providing a more accurate prediction of the time resolved release of volatiles.

Table 8.8 lists the effective particle size distribution classes formulated for direct implementation into FLUENT®. Table 8.9 lists the corresponding SFOR devolatilization kinetics for each characteristic size class. The effective devolatilization rates are compared to the literature values from which they were constructed; Wagenaar *et al.* [236], Johansen *et al.* [269] and to the FLUENT®default values, in figure 8.13. The method is applied to the PSD obtained from the AMV campaign and the results illustrated in figure 8.14.

Table 8.8 Particle size characterization of the model fuel.

Injection	$\bar{d}$ μm	n —	$d_{\min}$ μm	$d_{\max}$ μm	Fraction wt. %	Mass flow $\mathrm{g \cdot s^{-1}}$
Small	670.6	1.277	30.8	112	9.68	177.4
Medium	—〃—		112	616	49.6	908.3
Large	—〃—		616	1799	40.8	747.3

Table 8.9 Kinetic values for the devolatilization of the model fuel.

Injection	A	Ea
	s^{-1}	$kJ \cdot mol^{-1}$
Small	8.56×10^{10}	171.8
Medium	3.99×10^{9}	162.3
Large	2.62×10^{6}	118.7

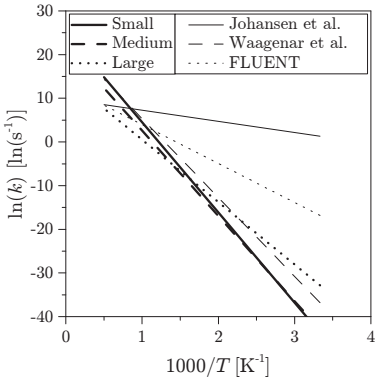

Figure 8.13 Kinetic comparison of the model fuel to literature values [236, 269].

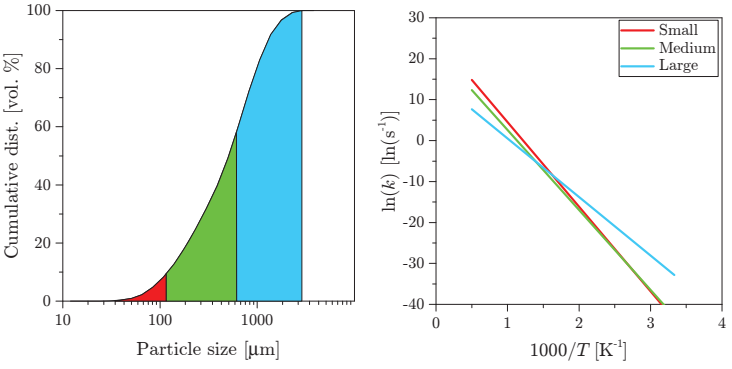

(a) PSD.

(b) Heat transport corrected devolatilization rates.

Figure 8.14 The PSD from the AMV campaign day #2 divided into the characteristic particle bins (with no upper cap) and the corresponding heat transport corrected SFOR devolatilization rates.

Part IV

Full-Scale Measurements

"If I have seen further it is by standing

on the shoulders of Giants"

—Isaac Newton

CHAPTER 9

Full-Scale Measurements

Three full-scale campaigns have been carried out during the duration of this project, two of which will be presented in this thesis. The two campaigns have been carried out at Amager power station unit 1 (AMV1) and Herning power station (HEV) respectively, representing two different front wall mounted 100 % biodust burners. The main focus of the campaigns were to develop a method for fast flame mapping, focusing on the near burner zone. Being able to swiftly characterize a flame allows for direct comparison of flame responses to multiple operational conditions. The near burner field is of central importance to the flame stability [39].

The results of the full-scale campaign serve two purposes. They provide an experienced based insight into what kind of flame response that can be expected from changes to the operational conditions and they provide evaluation material for CFD simulations.

9.1 Preface

The full-scale campaigns carried out in the GREEN research center are the result of a large collaborative work between GREEN partners. The instrumentation has been developed by senior scientist Sønnik Clausen, senior scientist Alexander Fateev, and technician Karsten L. Nielsen from DTU Chemical Engineering. The measurements are carried out by senior scientist Sønnik Clausen, senior scientist Alexander Fateev, technician Karsten L. Nielsen, and PhD student Joakim M. Johansen in collaboration with the power stations and engineers from DONG Energy and Vattenfall.

The planning, execution, analysis, and reporting was coordinated by PhD student Joakim M. Johansen and the entire process included all interested parties from the GREEN WP3.

9.2 Introduction

The reported results from full-scale measurements are scarce in the literature [6, 7, 9–11, 381–384], providing only little material for e.g. model evaluation or development of experimental equipment or methods. Full-scale facilities are often unique in design, especially when it comes to testing new technologies. therefore, it is difficult to compare experimental conclusions across campaigns.

To help the interpretation of the full-scale flame measurements it may be more reasonable to compare the qualitative trends to scaled down experiments, e.g. the IFRF flames [19, 25, 36, 37, 41, 44, 57, 385–387]. These flames represent the characteristic flame types that can be obtained by manipulating the flow field.

The effect of scale is important, not only to the design of scaled test rigs, but many of the concepts can be transferred directly into the operation of full-scale equipment. In general two types of scaling criteria are considered when downscaling into pilot-scale: Constant velocity scaling and mixing time scaling [31]. In constant velocity scaling the velocities and momentums of all flows are maintained constant with the scale reduction:

$$Q = \rho U D^2 \tag{9.1}$$

where Q, U, and D are the burner throughput, characteristic burner velocity, and the characteristic burner diameter. While ρ characterizes the fluid density. From this relation if follows that the burner diameter scales with the square root of the throughput:

$$D \propto \sqrt{Q} \tag{9.2}$$

and the burner dimensions scales with the burner throughput as:

$$\frac{Q_0}{Q_1} = \left(\frac{D_0}{D_1}\right)^2 \tag{9.3}$$

where indices 0 and 1 indicate baseline and scaled dimension.

Contrary, the velocities are allowed to scale with the burner diameter in such a way that the ratio between the burner diameter, D, and the burner velocity, U, remains constant and proportional to the macro-mixing time scale, τ_m:

$$\tau_\mathrm{m} \propto \frac{D}{Q} = \text{constant} \tag{9.4}$$

Thus:

$$Q = \rho U D^2 \propto \rho D^3 \tag{9.5}$$

Thus, the burner diameter scales linearly with the burner velocity or the cube root of the burner throughput when using the constant mixing time criteria:

$$D \propto U \propto \sqrt[3]{Q} \tag{9.6}$$

And:

$$\frac{Q_0}{Q_1} = \left(\frac{D_0}{D_1}\right)^3 = \frac{U_0}{U_1} \tag{9.7}$$

For the interpretation of the specific literature results on scaled down burners, the specific scaling criteria is of less importance as they do not represent the baseline burners employed in this work and thus is used solely on a qualitative basis. Nevertheless, the consequence of the choice of scaling criteria should be kept in mind, as the resulting flame properties may change significantly [388].

9.3 Instrumentation and Analytical Equipment

Table 9.1 An overview of the applied analytical techniques.

Parameter	Method	AMV	HEV
Centerline measurements			
Temperature	FTIR	•	•
Temperature	Suction pyrometry		•
Gas concentration[1]	IR/UV	•	•
Gas concentration[2]	Paramagnetic	•	•
Sideview port activities			
High speed IR imaging		•	•
VIS imaging		•	•

[1] H_2O, CO, CO_2, CH_4, C_2H_2.
[2] O_2.

Quantitative measurements using extractive gas methods and fourier transform infrared spectroscopy (FTIR) fiber optics are sampled simultaneously at discrete points in space and may thus be directly compared. Care should be taken when evaluating the FTIR temperature measurements. The signal is based on radiation from CO_2 and a critical lower limit of 5 vol. % of CO_2 is required in order to obtain reliable measurements. Thus, FTIR-based temperature readings close to the burner mouth may deviate from the actual gas temperature due to low concentrations of CO_2. This was only the case at AMV. The critical limit is clearly indicated on all graphical presentations of FTIR temperature measurements throughout the report.

9.3.1 Water Cooled Probe

A water cooled multi-purpose probe has been used as the primary analytical tool during both the Amager and Herning power station campaigns. Two different probes have been developed and commissioned specifically for these campaigns. The main differences are the probe lengths which are listed in table 9.2.

Probe measurements are conducted in the near-burner field entering the boiler through the center-pipe of the burner; replacing the oil-lance. This

Table 9.2 Probe dimensions and effective penetration depths of the employed probes

Parameter	Unit	AMV	HEV
Total probe length	m	5.0	8.4[1]
Effective penetration	m	2.1	4.0
Probe diameter	mm	60	80

[1] The probe is assembled from two parts to achieve the total length.

limits the effective penetration depths, but allows for fast and accurate positioning of the probe along the centerline. Figures 9.1a to 9.1d show the installation of the 5.0 m probe at AMV.

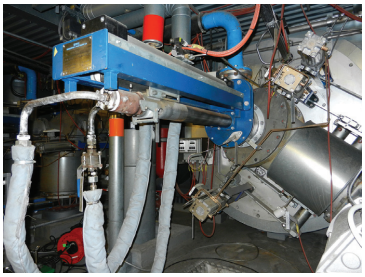

(a) The rear of burner 11 with the oil lance installed.

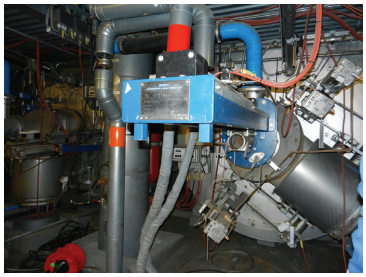

(b) The rear of burner 11 with the oil-lance dismounted.

(c) Partially inserted probe. The probe is resting in the oil-lance insertion tube without additional balancing.

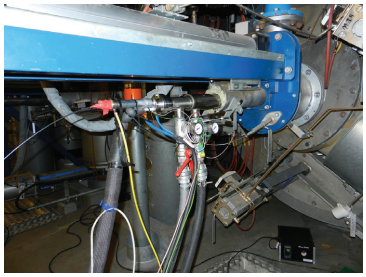

(d) Fully inserted probe. The probe is resting in the oil-lance insertion tube.

Figure 9.1 Probe installation at AMV.

Figure 9.2 shows a cross section of the AMV burner with the fully inserted 5.0 m probe. Probe and burner has been drawn to scale. The progression of

the probe could be followed using IR-imaging from a view port positioned on the side of the boiler. These images showed no apparent bending of the probe, cf. figure 9.3, and the exact position was determined by markings on the probe entering the back of the burner, ensuring the same traversing pattern in all mappings.

The probes are designed to make simultaneous gas extractive and in-situ optical gas temperature measurements. The installed fiber-optics connected FTIR as well as heated teflon piping connected to parallel ultraviolet (UV) and IR cells and an oxygen cell. A conceptual sketch illustrating the functionalities of both probes is shown in figure 9.4.

A cross sectional view of the probes are shown in figure 9.5 while a front view is shown in figure 9.6.

9.3.2 FTIR Fiber-Optic Gas Temperature Measurements

In-situ gas temperature gas measurements were conducted by use of a Bomem 155 FTIR-spectrometer mounted with an InSb liquid N_2 cooled detector. A CaF_2 lens mounted on the probe tip collected the radiation from the flame and hot flue gas and transferred it to the spectrometer by an optical fiber. All optical components were purged with the use of a Balston purge generator. The purge is also used to keep the lens on the front of the probe cleaned.

Because the temperature measurements rely on CO_2 radiation, the exact coordinates in space depend on the optical density of the local environment. Thus, temperature measurements using the FTIR method may extend as much as 15 cm ahead of the tip of the probe, cf. figure 9.8.

9.3.3 Extractive Gas Sampling

Extractive gas sampling is usually the “standard” method in combustion measurements. Combination of gas extractive and in-situ optical gas temperature methods in the project is used to get the most comprehensive information about the processes taking place locally in a complex flame.

Extractive Gas Sampling Line and Movable Gas Measurement Bench

Two 50 cm gas cells for simultaneous UV and IR absorption measurements, a paramagnetic O_2-analyzer, calibrated mass-flow controllers, a pressure gauge, a cooler, and a pump were used in order to make gas measurements and control pressure and gas flow during measurements. The data acquisition system continuously recorded the main sampling parameters such as sampling gas flow, gas temperature, pressure in the UV/IR gas cells and oxygen concentration. The temperature in the gas sampling line (from the probe to the two gas cells) was maintained above 150 °C by electronically controlled electric heaters. The suction line in the probe was also heated to around 150 °C. A Bomem MB100

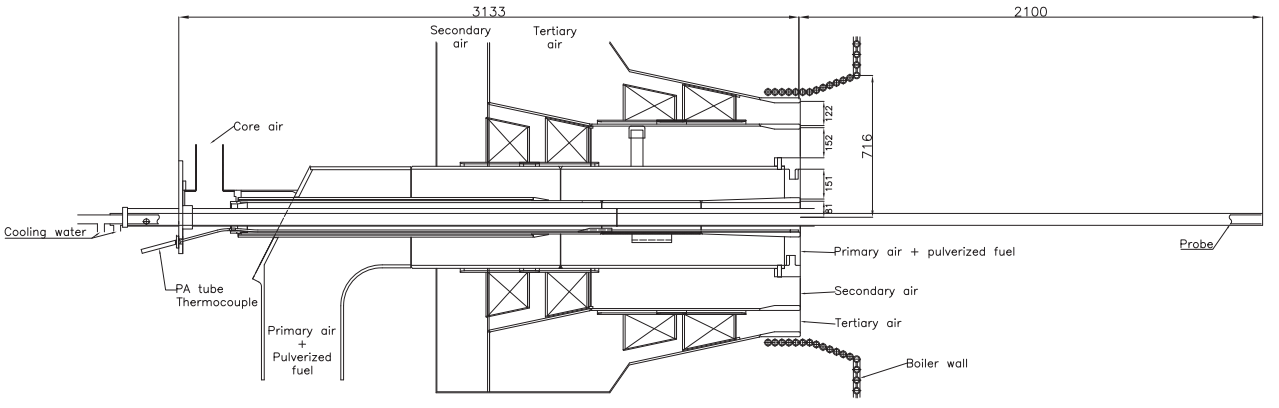

Figure 9.2 Cross section of the AMV burner with fully inserted 5.0 m probe. The drawing has been simplified for illustrative purposes. The drawing is made to scale.

Figure 9.3 Burner with fully inserted probe. The water cooled probe is easily seen by the IR-imaging.

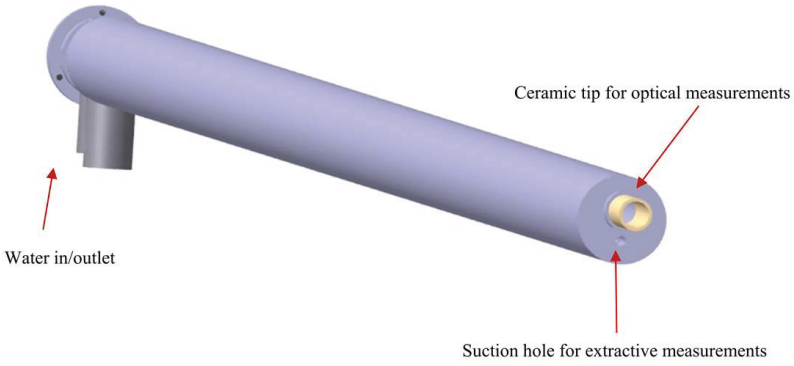

Figure 9.4 Conceptual CAD drawing of the probe illustrating the position of the optical inlet and the opening for extractive measurements.

FTIR spectrometer with a built in IR light source and external deuterated triglycine sulfate (DTGS) detector was used for IR-absorption measurements. For UV-absorption measurements a highly-stable D2-lamp was utilized as a light source. UV-absorption spectra were carried out with an Acton 0.5 m spectrometer equipped with an UV enhanced charge-coupled device (CCD) camera.

In the measurement campaign UV-spectroscopy has been used for measurements of SO_2 and NO, whereas IR-absorption spectroscopy is used for measurements of H_2O, CO_2, CO, light hydrocarbons (e.g. CH_4, C_2H_2, etc.), and SO_2. A general view of the moveable gas measurement bench is shown in figure 9.10.

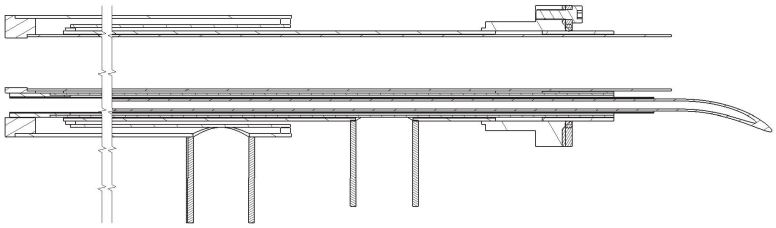

(a) Single part 5.0 m probe.

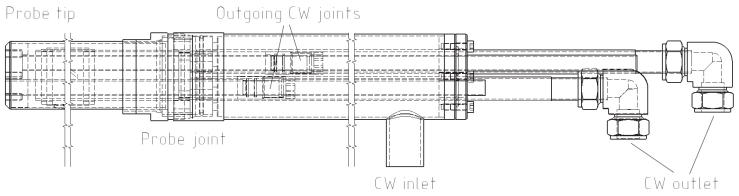

(b) Two part 8.4 m probe.

Figure 9.5 Cross sectional sketches of the probes.

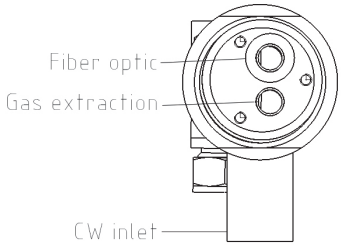

Figure 9.6 Front view sketch of the two-part 8.4 m probe. The construction of the single part 5.0 m probe is similar. CW = cooling water.

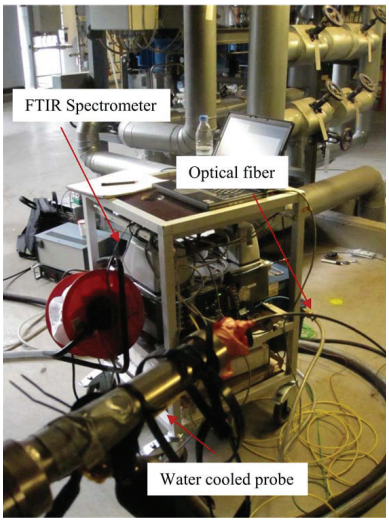

Figure 9.7 An overview of the FTIR-bench used for in-situ gas temperature measurements.

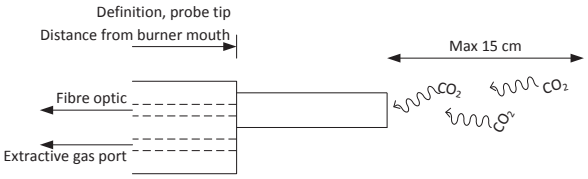

Figure 9.8 A side view sketch of the probe tip. The ceramic tip measuring between 10 and 15 cm in length.

9.3.4 Uncertainties

Uncertainties in the gas extractive measurements are mainly depended on the quality of databases used in gas concentrations calculations (e.g. HITRAN or HITEMP). There are minor deviations ($< 1\,\%$) between HITRAN-based calculations and reference (e.g. $N_2 + H_2O$) measurements in the gas cell of the movable gas measurement bench.

Uncertainties in the in-situ optical gas temperature measurements are mainly caused by the stability of the optical system (e.g. ambient temperature variations or possible contamination of optical components). The stability of the optical system shown in the measurements was generally such that uncertainties in the gas temperature calcualtions were less than 8 K.

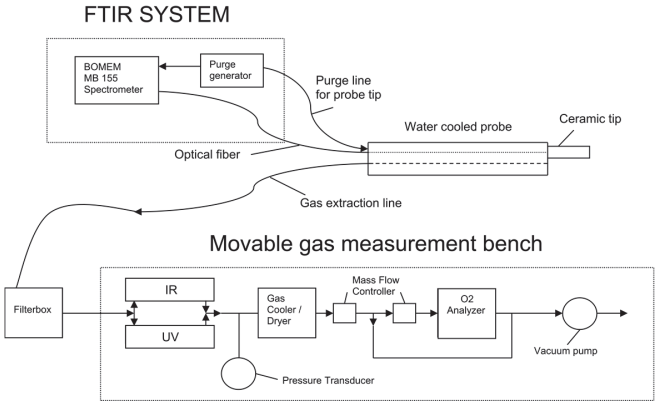

Figure 9.9 Diagram of the gas sampling and IR system.

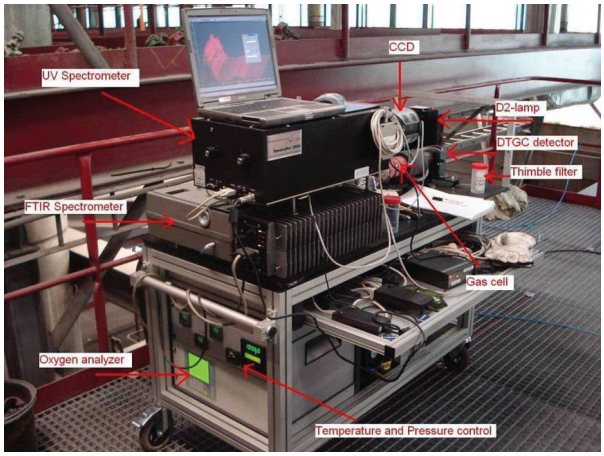

Figure 9.10 Overview of the movable gas measurement bench.

9.3.5 Suction Pyrometry

Suction pyrometry with a single radiation shield was performed on a few selected settings: reference and reduced tertiary air swirl. However, the temperature in the near burner field was found to quickly raise above 1300 °C (thresh hold of the thermocouple used). In addition, the gas analysis revealed CO_2 concentrations far in excess of the 5 vol. % necessary for the FTIR analysis to produce reliable gas temperature results, rendering the suction pyrometry measurements redundant.

9.3.6 Optical Diagnostics

Video and IR imaging is conducted through the side view port located directly adjacent to the burner position. VIS imaging allows for excellent assessment of flame attachment/detachment while IR imaging shows the progression of the cool fuel particles and the mixing or lack of mixing of fuel and combustion air in the near-burner field.

Amagerværket Unit 1

Near Burner Investigation

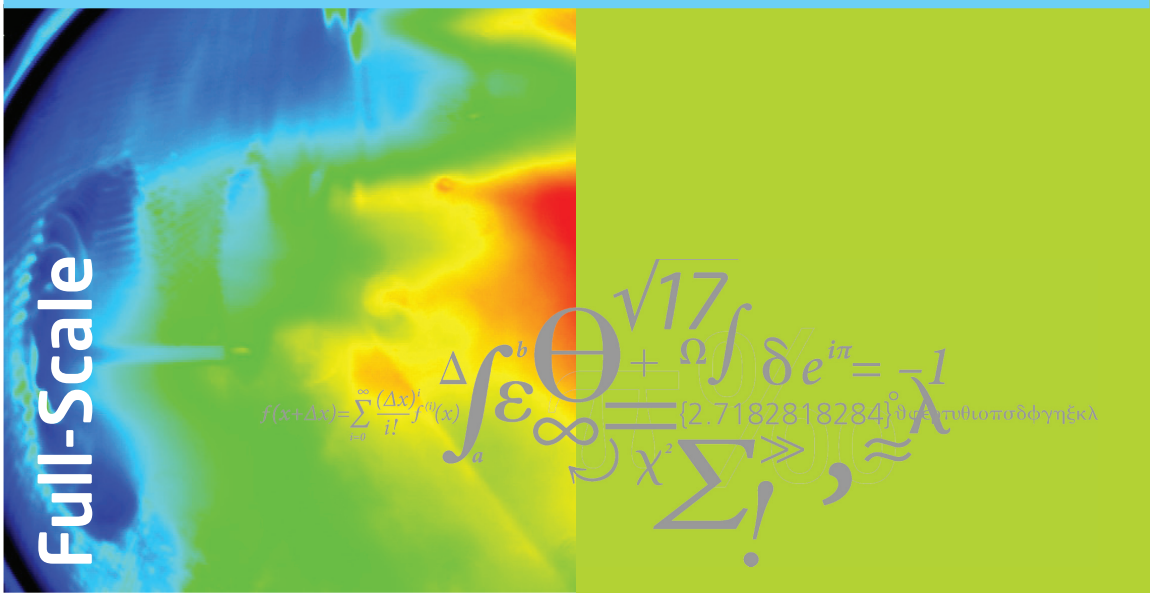

Week 9, 2012

DTU Chemical Engineering
Department of Chemical and Biochemical Engineering

Abstract

This report is written as a part of the power Generation from REnewable ENergy (GREEN) research project funded by the Danish Council for Strategic Research. It covers the experimental results of a full-scale campaign conducted at Amager power station unit 1 (AMV1) biomass fired suspension boiler owned and operated by Vattenfall. The campaign ran over two and a half days in week 9, 2012 and includes both optical and extractive probe measurements on burner 11 firing primarily milled wood pellets.

AMV is newly (2004) renovated and commissioned as a multi-fuel unit capable of firing coal, wood, straw, and oil with a total thermal output of 318 MW producing both district heating and electricity.

The current campaign focuses on near-burner measurements on a single burner running in steady-state using wood fuel. The operational conditions are changed systematically and with as large amplitude as possible, aiming to investigate the flame response to changes in selected process parameters. Ten different operational conditions have been mapped during the campaign including a stable reference repeated at the beginning and end of each experimental day. Changes in process parameters include: In- and decrease in secondary air flow rates, in- and decrease in the ratio between secondary and tertiary swirl, reduced secondary and tertiary air (individually adjusted), in- and decrease in the primary air flow rate, and changes to the mill classifier settings.

A water cooled probe was employed directly on the centerline of the flame entering the furnace through the core tube of the burner, replacing the oil lance. The probe was used to obtain gas extractive samples through a heated suction tube for gas species analysis by parallel UV/IR-cells and subsequent O_2-paramagnetic analyzer. In addition, a fiber optic wire fed an optical signal for temperature measurements based on CO_2-radiation. With an effective probe penetration depth of 2.1 m each flame was mapped using between 10 and 20 points along the centerline.

Flame observation by video and high speed IR-imaging was performed from a view port perpendicular to the fuel flow direction in the vertical plane. IR-images gave good indications of the entraining particle cloud behavior and surface temperature while flame attachment could be evaluated by imaging in the visible spectrum.

Close to all operational conditions gave rise to large variations of the flame properties. This was quantified as changes in both temperature, oxygen, combustion and pyrolysis products concentration profiles. The position of the pyrolysis front seems to be one of the key changes influenced by the investigated parameters. The relative response in the pyrolysis and gasification products was also found to be more profound compared to the gas phase temperature, oxygen profile, and combustion products.

Table of Contents

Introduction

Amager power station unit 1 (AMV1) was originally designed for pulverized coal combustion but decommissioned for major renovation in 2004. Today AMV1 has been recommissioned as a multi-fuel unit capable of firing with oil, and pulverized coal and biomass at 100 % load.

This project will aim to do coarse flame mapping of selected parameters during a range of systematically altered burner operational conditions; swirl, flow rates, flow distributions, etc., during dedicated biodust combustion. Such measurements will provide data scarce in literature on how to relate flame response to operating conditions useful in e.g. CFD simulations evaluation.

By performing coarse measurements the data sampling time per operational condition is decreased significantly compared to previous full-scale campaigns [389]. Thus, the number of operational conditions that can be tested in a given time period is increased correspondingly.

This test campaign comprise the first of three campaigns at AMV and HEV. Thus, besides from providing data for model evaluation and general plant performance it will also serve to: 1. test the measurement equipment build specifically for this purpose and 2. test the method of coarse flame mapping and entering through the back of the burner, optimizing the starting point for the following campaigns.

The work makes up a central part of the GREEN project's WP3 which primary objective is to elucidate the relation between fuel properties and flame properties through full-scale campaigns and CFD calculations.

CHAPTER 10A

Plant and Burner Description

AMV was owned by Vattenfall at the time of the first measurement campaign (currently owned and operated by HOFOR). Vattefall is a partner in the GREEN research project. The in-flame measurements were conducted by a measurement team from DTU Chemical Engineering while the plant operation and parameter changes were carried out by Vattenfall staff. An effort was made to maintain as stable operational conditions as possible throughout the campaign. Parameter changes were only applied to the specific burner and/or the corresponding gallery, depending on the parameter, e.g. classifier changes affects the entire gallery 10 while swirl settings only affects burner #11.

In the following a brief description of the plant and the measurement equipment and techniques will be given.

10A.1 Plant and Burner Description

The experiments were conducted on Amager power station unit 1 (AMV1), burner 11. A multi fuel Burmeister and Wain Energy (BWE) burner capable of firing 27, 30, 35, or 44 MW_{th} of straw-dust, wood-dust, oil, and coal, respectively. It is fed from a central roller-mill feeding all burners on level 10 (burner 11, 12, 13, 14). Figure 10A.1 shows a top view of the boiler with the view ports used for data acquisition and general orientation.

The burner is a concentric construction with the oil lance in the center tube and primary air and dust feed in the second concentric pass followed directly by secondary and tertiary air. Adjustable swirlers are installed in both the secondary and tertiary air channels. A cross section of the burner is presented in figure 10A.2.

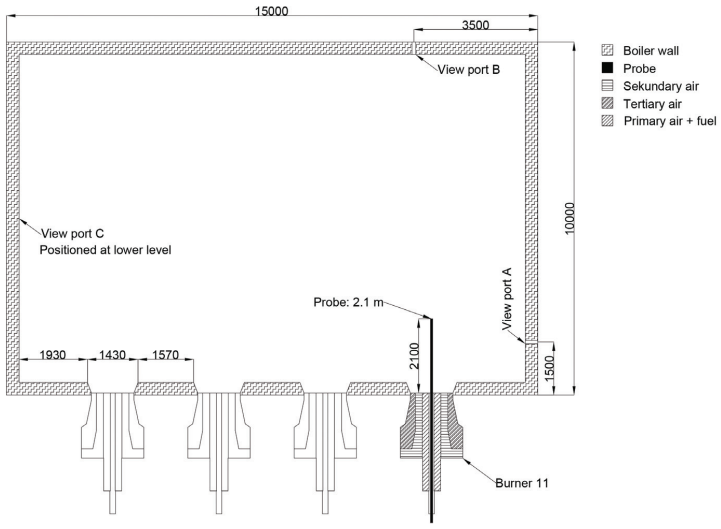

Figure 10A.1 Top view of AMV1 level 10 including view ports used in this campaign. The drawing is drawn to scale and all measures are given in mm unless otherwise specified.

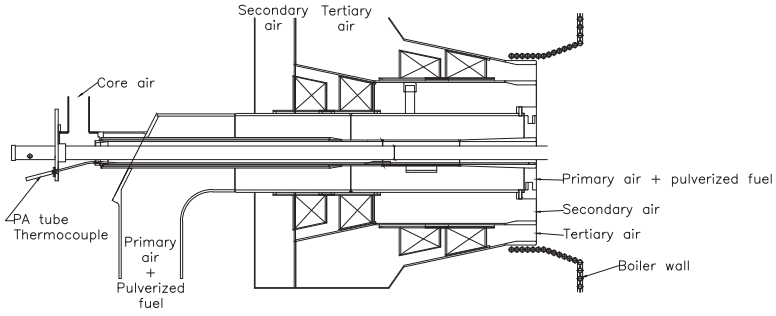

Figure 10A.2 Cross section of the burner. The drawing has been simplified has been simplified for illustrative purposes. The drawing is made to scale.

CHAPTER 10B

Experimental Matrix and Fuels

The campaign stretched across two full days of measurements, excluding half a day for equipment installation and pilot experiments. Throughout the report test day #0, #1, and #2 will be used to refer to the pilot day and the two measurement days, respectively. The measurement campaign included 10 burner settings including a reference setting which was repeated at the beginning and end of each experimental day in order to identify any unintended drift in the operation of the plant.

10B.1 Adjusted Parameters

The experimental test involved adjustments to the below listed process parameters:

- Secondary air (SA)
- Air split (AS)
- Secondary air (SA) swirl
- Tertiary air (TA) swirl
- Primary air (PA)
- Fuel particle size distribution (adjustment of classifier rotational speed)

Table 10B.1 presents the experimental matrix including the relative change in each parameter, the absolute value, and the reference value for operation. The experiments are listed in chronological order.

10B.2 Logged Power Plant Settings

A number of data were collected from the power plant log system. The logged data included in this report are listed in table 10B.2 and represents central parameters for systems with direct (e.g. fuel flow to burner #11) or (possible) indirect (e.g. air flow to neighbouring burner(s)) influence on the flame properties of the investigated burner. Selected time resolved data sets are presented in appendix C. Averaged values off key operational conditions are listed in table 10B.3. Table 10B.4 lists the same settings as table 10B.3 explaining the physical meaning of each setting.

Table 10B.1 Experimental matrix for AMV1 campaign #1, week 9, 2012. Absolute values of all burner parameters are presented in table 10B.3.

Exp #	Date dd-mm-yyyy	Time hh:mm	Parameter	Setting Change [%]	Abs	Ref	Unit
1	29-02-2012	09:55	Reference	—	—	—	—
2		13:36	SA	20	9.4	7.8	kg/s
3		14:33	SA	−16.7	6.5	7.8	kg/s
4		16:00	Air-split*	−38	31	50	—
5		17:31	Reference	—	—	—	—
6		18:31	Air-split*	12	56	50	—
7	01-03-2012	09:23	Reference	—	—	—	—
8		10:05	SA swirl**	−20	80	100	%
9		12:43	TA swirl**	−20	80	100	%
10		14:49	PA	−5.3	14.2	15	kg/s
11		16:05	Classifier***	−20.7	15.23	19.20	%
12		16:57	PA	6.7	16	15	kg/s
13		17:50	Reference	—	—	—	—

* The air-split, AS, is defined as $AS = \frac{SA}{(SA+TA)}$
** The percentage refers to the physical position of the swirler.
*** The percentage refers to the fractional rotational speed of the classifier.

10B.3 Fuels

The fuels used for the campaign are primarily wood pellets mixed with minor fractions of what seemed to be straw pellets. The fuels were taken from different silos during the three experimental days and the exact composition, and how the composition was changing, is unknown. By visual inspection of the pellets in the buffer tank leading to the mill a change in composition seems to be taking place from experimental day #1 to #2 as illustrated in figure 10B.1.

(a) Pellet sample from test day #1. **(b)** Pellet sample from test day #2.

Figure 10B.1 Comparison of the pellet feed taken from the buffer tank before the mill. The dark pellets with larger diameter in figure 10B.1b is believed to be straw pellets (one of these pellets has been marked with a red ring).

Table 10B.2 List of the logged data included in this report.

Signal Tag	Designation	Unit
01 HFB10FF001___XQ01	BRAENDSTOF FLOW MOELLE 10	kg/s
01 HHE11FF001___XQ01	STOEVFLOW BR.ROER 11	kg/s
01 HHE12FF001___XQ01	STOEVFLOW BR.ROER 12	kg/s
01 HHE13FF001___XQ01	STOEVFLOW BR.ROER 13	kg/s
01 HHE14FF001___XQ01	STOEVFLOW BR.ROER 14	kg/s
01 HFC10CE214___XQ01	KW MOELLE 10	kW
01 HFC10CP001___XQ01	DIF.TRYK OVER MALEBORDMOELLE 10	mbar
01 HFC10CS001___XQ01	OMDR. SIGTE MOELLE 10	%
01 HFE13FF001___XQ01	FLOW PA BLAESER MOELLE 10	kg/s
01 HHL11FF001___XQ01	FLOW FORBR.LUFT BRD.11	kg/s
01 HHL11FF002___XQ01	FLOW SEK.LUFT BRD.11	kg/s
01 HHL12FF001___XQ01	FLOW FORBR.LUFT BRD.12	kg/s
01 HHL12FF002___XQ01	FLOW SEK.LUFT BRD.12	kg/s
01 HHL21FF001___XQ01	FLOW FORBR.LUFT BRD.21	kg/s
01 HHL21FF002___XQ01	FLOW SEK.LUFT BRD.21	kg/s
01 HHA11AA001___XQ01	TA TURBULATOR BRAENDER 11	%
01 HHA11AA002___XQ01	SA TURBULATOR BRAENDER 11	%
01 HHA11CR001A___XQ01	IR FLMDET BRAENDER 11	%
01 HHA11CT001___XQ01	TEMP.SA MUNDSTYKKE BR.11	°C
01 HHA11CT002___XQ01	TEMP.KERNEROER MUNDST.BR.11	°C
01 HHE11CT001___XQ01	TEMP. KULSTOEV BRAENDERD.10	°C
01 CJD00DU290___XR01	AKTIVE BLOKLASTSIGNAL	%
01 HHA12CR001A___XQ01	IR FLMDET BRAENDER 12	%
01 HHA21CR001A___XQ01	IR FLMDET BRAENDER 21	%
01 HNA31CQ901___XQ01	O2 EFT. KEDEL LUFO SYD	%
01 HNA41CQ901___XQ01	O2 EFT. KEDEL LUFO NORD	%
01 HNA50CQ004___ZQ05	NOx ROEGGAS EFT.KEDEL 6%ILT	mg/Nm3
01 HFC10CT901___XQ01	TEMP. OVER SIGTE MOELLE 10	°C
01 HFE14CT001___XQ01	TEMP. MOELLE 10 INDLOEB	°C
01 HHE11FS001___XQ01	LUFTHASTIGHED BR.ROER 11	m/s
01 HHE12FS001___XQ01	LUFTHASTIGHED BR.ROER 12	m/s
01 HHE13FS001___XQ01	LUFTHASTIGHED BR.ROER 13	m/s
01 HHE14FS001___XQ01	LUFTHASTIGHED BR.ROER 14	m/s
01 HFE14CT001___XQ01	TEMP. MOELLE 10 INDLOEB	°C
01 HHL11CT001___XQ01	TEMP. FORBR.LUFT BRD.11	°C

Table 10B.3 Key numbers of operational conditions, all runs. Scheduled deviations from reference values are highlighted in bold. All numbers are averaged in time. For time resolved data refer to appendix C.

Setting Experiment #	Unit	Ref #1 1	Ref #2 5	Ref #3 7	Ref #4 13	SA(+) 2	SA(−) 3	AS(−) 4	AS(+) 6	SA swirl(−) 8	TA swirl(−) 9	PA(−) 10	PA(+) 12	Classifier(−) 11
Fuel flow M10	kg/s	7.52	7.51	7.49	7.50	7.49	7.52	7.49	7.49	7.49	7.52	7.50	7.51	7.51
Dust flow Br.11 pipe*	kg/s	2.52	2.55	2.43	2.48	2.61	2.52	2.60	2.61	2.53	2.44	2.46	2.68	2.72
Dust flow Br.12 pipe*	kg/s	2.52	2.53	2.41	2.17	2.49	2.47	2.47	2.46	2.33	2.27	2.13	2.35	1.96
Dust flow Br.13 pipe*	kg/s	2.21	2.20	2.06	2.18	2.22	2.20	2.25	2.21	2.17	2.16	2.21	2.30	2.35
Dust flow Br.14 pipe*	kg/s	2.28	2.40	2.32	1.89	2.30	2.27	2.27	2.28	1.94	1.87	2.30	1.61	1.48
PA flow M10	kg/s	15.03	14.97	14.99	14.95	15.00	15.01	14.97	15.02	15.04	15.04	**14.23**	**16.00**	15.01
Combust. air flow Br.11	kg/s	7.77	8.05	7.77	7.32	**9.39**	**5.98**	8.06	8.07	7.71	7.62	7.67	7.24	7.56
SA flow Br.11	kg/s	3.85	4.05	3.88	3.70	**4.66**	**2.97**	**2.51**	**4.52**	3.81	3.77	3.84	3.60	3.74
Combust. air flow Br.12	kg/s	7.74	7.56	7.73	7.36	7.66	7.50	7.57	7.59	7.66	7.64	7.68	7.22	7.54
SA flow Br.12	kg/s	3.86	3.75	3.88	3.70	3.78	3.78	3.73	3.76	3.81	3.79	3.83	3.62	3.76
Combust- air flow Br.21	kg/s	6.63	6.49	6.65	6.35	6.57	6.48	6.55	6.54	6.63	6.46	6.55	6.42	6.35
SA flow Br.21	kg/s	3.80	3.88	3.83	4.01	3.89	3.92	3.93	3.91	3.84	3.95	3.91	4.02	4.00
Air speed Br.11 pipe	m/s	32.5	32.6	32.3	32.4	32.5	32.7	32.4	32.7	32.4	32.6	**30.4**	**34.5**	34.2
Air speed Br.12 pipe	m/s	32.8	32.7	31.8	31.8	32.9	32.8	33.1	33.0	32.1	31.7	31.6	33.6	32.0
Air speed Br.13 pipe	m/s	25.4	26.3	25.1	24.7	25.2	25.4	25.3	25.3	24.2	24.5	25.4	25.0	25.3
Air speed Br.14 pipe	m/s	30.2	30.1	29.9	31.2	30.4	30.3	30.4	30.5	31.3	31.3	28.8	34.3	30.4
Temp. combust. air Br.11	°C	327	330	324	328	329	327	331	331	326	327	328	328	327
Temp. Br.11 mouth	°C	484	496	476	497	478	497	484	490	458	470	499	483	503
Temp. core tube Br.11	°C	232	248	235	249	249	217	237	243	206	211	269	235	262
Temp. dust pipe Br.11	°C	51	52	51	54	51	52	52	52	52	53	52	55	53
TA turbulator Br.11	%	99.6	99.7	99.6	99.3	99.7	99.7	99.7	99.7	98.2	**80.4**	99.3	99.3	99.3
SA turbulator Br.11	%	99.7	99.7	99.7	99.3	99.7	99.7	99.7	99.7	**82.0**	99.1	99.3	99.3	99.3
Frequency M10	rpm	19.2	19.2	19.2	19.2	19.2	19.2	19.2	19.2	19.2	19.2	19.2	19.2	**15.2**
IR flame detector Br.11	%	104	104	104	104	104	104	104	104	104	104	104	104	104

* The dust flows to the individual burners on gallery #10 are measured by Promecon and are understood as relative data.

Table 10B.4 Explanation of the designations used in table 10B.3.

Designation	Unit	Explanation
Fuel flow M10	kg/s	Flow of pellets to mill #10 supplying all four burners at level #10.
Dust flow Br.11 pipe	kg/s	Flow of dust in the PA channel to burner #11.
Dust flow Br.12 pipe	kg/s	Flow of dust in the PA channel to burner #12.
Dust flow Br.13 pipe	kg/s	Flow of dust in the PA channel to burner #13.
Dust flow Br.14 pipe	kg/s	Flow of dust in the PA channel to burner #14.
PA flow M10	kg/s	PA flow through mill #10 supplying all four burners at level #10.
Combust. air flow Br.11	kg/s	Flow of combustion air ($SA+TA$) to burner #11.
SA flow Br.11	kg/s	Flow of SA to burner #11.
Combust. air flow Br.12	kg/s	Flow of combustion air ($SA+TA$) to burner #12.
SA flow Br.12	kg/s	Flow of SA to burner #12.
Combust- air flow Br.21	kg/s	Flow of combustion air ($SA+TA$) to burner #21.
SA flow Br.21	kg/s	Flow of SA to burner #21.
Air speed Br.11 pipe	m/s	Speed of PA through burner #11.
Air speed Br.12 pipe	m/s	Speed of PA through burner #12.
Air speed Br.13 pipe	m/s	Speed of PA through burner #13.
Air speed Br.14 pipe	m/s	Speed of PA through burner #14.
Temp. combust. air Br.11	°C	Temperature of the combustion air (SA and TA) to burner #11.
Temp. Br.11 mouth	°C	Temperature at the burner mouth of burner #11.
TA turbulator Br.11	%	Turbulator setting in the tertiary channel. % of the physical position.
SA turbulator Br.11	%	Turbulator setting in the secondary channel. % of the physical position.
Frequency M10	rpm	Rotational speed of the classifier above mill 10.
IR flame detector Br.11	%	Flame detector signal.

Changes in the temperature and O_2-concentration profiles for the reference settings show different behavior from test day #1 to #2, cf. figure 10C.3. This could stem from the changes in fuel feed and hence, a raw fuel analyses will be presented in the following. However, difficulties in maintaining constant process parameter values on test day #2 is believed to constitute the major cause for the deviations in flame behavior observed during reference run #4 (exp #13) on test day #2.

10B.3.1 Particle Size Distributions

Dust samples have been collected by a rotor-sampler, previously introduced on page 165. The samples are collected directly from the feeder tube to burner #11 from a view port in a horizontal pipe section. Samples were retrieved according to table 10B.5. Only samples analyzed and used in this report have been given a sample ID in table 10B.5.

Image based particle characterization methods, Retsch Technology CAMSIZER®, are used to evaluate the particle size distribution of selected dust

Table 10B.5 Time table for dust sampling from feeder tube to burner #11.

Exp #	Sample ID	Date dd-mm-yyyy	Time hh:mm	Setting	Value %
3		29-02-2012	15 : 15	SA	−16.7
4			16 : 40	AS	+38
5	dust #1		17 : 45	Ref	—
7	dust #2	01-03-2012	09 : 30	Ref #3	−20
8			10 : 15	SA swirl	−20
8			12 : 00	SA swirl	−20
9			13 : 15	TA swirl	−20
10	dust #3		15 : 30	PA	−5.3
11			16 : 20	Classifier	−20.7
11	dust #4		16 : 40	Classifier	−20.7
13	dust #5		17 : 15	PA	+6.7

samples. Each run has been submitted to double determination and the averaged frequency distributions are presented in figure 10B.2. A statistical overview is listed in table 10B.6 presenting the d_{10}, d_{50}, and d_{90} values for all five analyzed dust samples based on volume. Two different lengths are used for comparison: $x_{\mathrm{Ma,min}}$ and $x_{\mathrm{c,min}}$ defined as illustrated in figures 2.8 and 2.9 on page 26. No significant changes between the analyzed samples can be identified. It is noticeable that the change in classifier frequency (exp #11) did not seem to affect the resulting particle size distribution (dust #4).

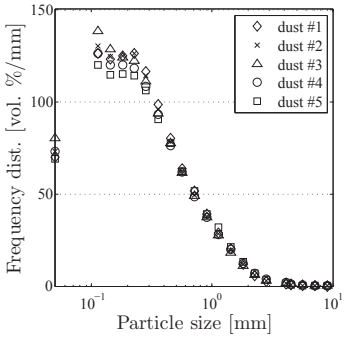

Figure 10B.2 Comparison of particle size distributions analyzed by CAMSIZER®technology. Particle sizes are based on a minimum particle diameter.

The CAMSIZER®equipment delivered by Retsch Technology fits the analysis results as shown in figure 10B.3. It is not possible to retrieve the algorithm used for the function fit carried out by the CAMSIZER®software.

Comparing the discrete particle size results illustrated in figure 10B.2 with

Table 10B.6 Size distribution statistics based on CAMSIZER®results for the selected five dust samples. Two different lengths are used for comparison: $x_{\mathrm{Ma,min}}$ and $x_{\mathrm{c,min}}$. All results are based on volume distributions.

Exp #	Sample ID	$x_{\mathrm{Ma,min}}$ [mm]			$x_{\mathrm{c,min}}$ [mm]		
		d_{10}	d_{50}	d_{90}	d_{10}	d_{50}	d_{90}
5	dust #1	0.094	0.381	1.330	0.124	0.505	1.688
7	dust #2	0.091	0.377	1.374	0.121	0.507	1.789
10	dust #3	0.087	0.377	1.391	0.114	0.503	1.877
11	dust #4	0.092	0.397	1.478	0.121	0.532	1.945
13	dust #5	0.095	0.424	1.468	0.126	0.553	1.823

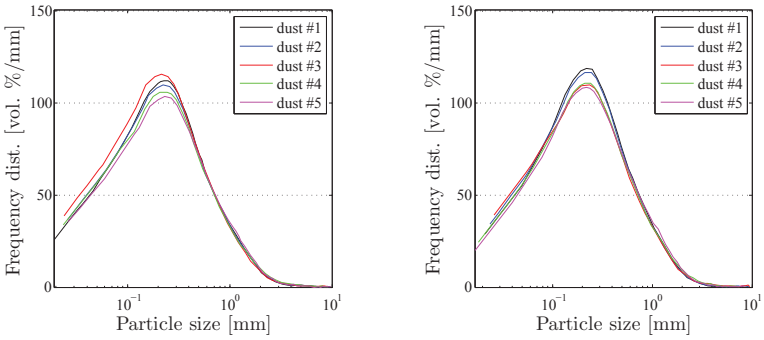

(a) First run. **(b)** Second run.

Figure 10B.3 Particle size frequency distributions for AMV dust samples with CAMSIZER®function fit.

the functions fitted by the CAMSIZER®software shows how the Retsch algorithm struggles to fit the data at particle sizes between 0.1 and 1 mm, critical for the fuels used in this campaign. A direct comparison is shown in figure 10B.4a.

Applying a log normal probability density function defined as:

$$f\left(x;\mu,\sigma\right) = \frac{1}{x\sigma\sqrt{2\pi}} \exp\left[\frac{-\ln\left(x-\mu\right)^2}{2\sigma^2}\right] \tag{10B.1}$$

where μ and σ signifies the mean and standard deviation of the minimum diameter of the particle's natural logarithm. This yields a better fit to the discrete data points in the critical interval, cf. figure 10B.4b.

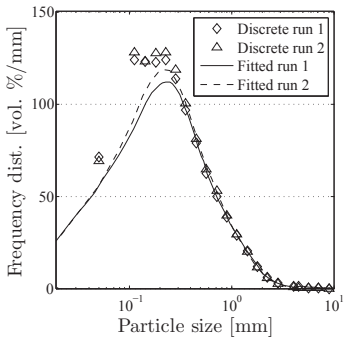

(a) CAMSIZER®frequency distribution fits for dust sample 1. All results are based on particles minimum diameter and fitted by the CAMSIZER®software developed by Retsch Technology.

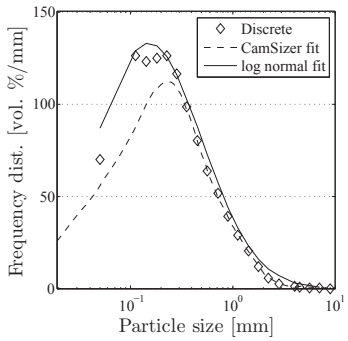

(b) Log normal probability density function fit for CAMSIZER®discrete results compared to the Retsch Technology algorithm.

Figure 10B.4 Particle size frequency distributions for AMV dust samples with CAMSIZER®function fit.

Evaluation of the CAMSIZER®Method

The use of the CAMSIZER®technology is a relatively new method and the lack of experience call for extra attention to result validation. For every CAMSIZER®run a series of pictures are taken and stored for evaluation. The pictures in figures 10B.5 and 10B.6 illustrate two consecutive shots of dust particles passing the foto cell. The pictures clearly show how a cloud of "agglomerated" particles breaks apart as it travels in space. Because the CAMSIZER®analyses the projected image it is of great importance that the particles travel as individual particles in a plane parallel to the photo cells, i.e. do not overlap. This is apparent when comparing to an other run of the same sample, illustrated in figure 10B.7, where a dense particle cloud is clearly passing the photo cell without breaking up. The results are distinct when compared to the run illustrated by figures 10B.5 and 10B.6, cf. figure 10B.7, showing the cumulative size distribution, figure 10B.8a, and the frequency distribution, figure 10B.8b.

Hence, the feeding procedure should be followed very carefully when using the CAMSIZER®equipment for particle size distribution.

10B.3.2 Particle Size Distribution by Sieving

Sieve analysis was performed on a single selected sample for comparison with the CAMSIZER®method. Dust #4 was used for comparing the results of

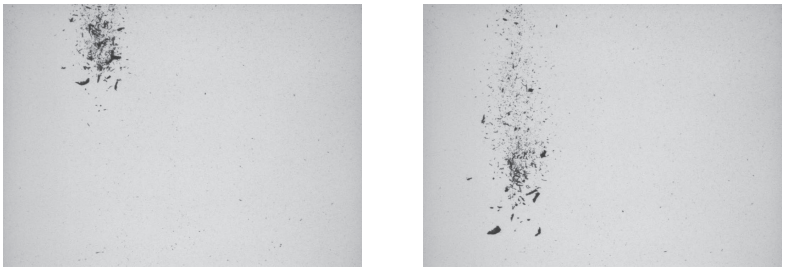

(a) First frame. **(b)** Second frame.

Figure 10B.5 CAMSIZER®pictures of particle cloud breaking up as it travels through the foto cell. Sample: AMV-dust-1.

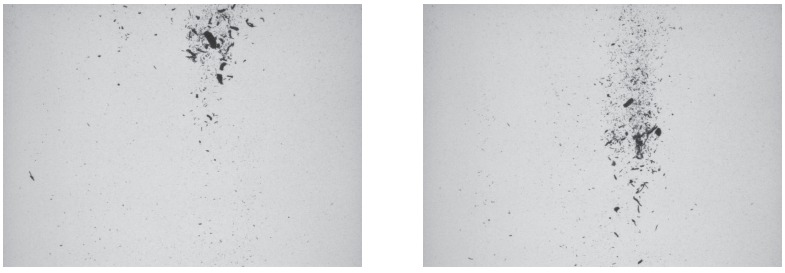

(a) First frame. **(b)** Second frame.

Figure 10B.6 CAMSIZER®pictures of particle cloud breaking up as it travels through the foto cell. Sample: AMV-dust-1.

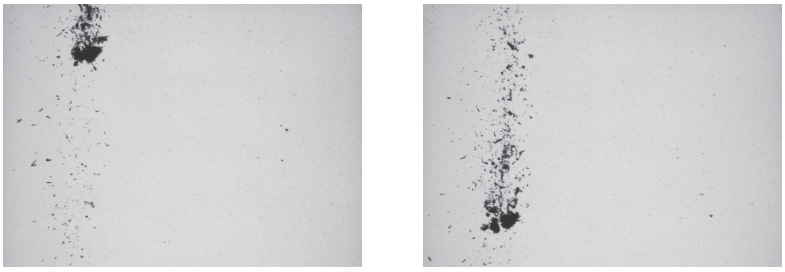

(a) First frame. **(b)** Second frame.

Figure 10B.7 CAMSIZER®pictures of particle cloud penetrating the photo cell. Sample: AMV-dust-1.

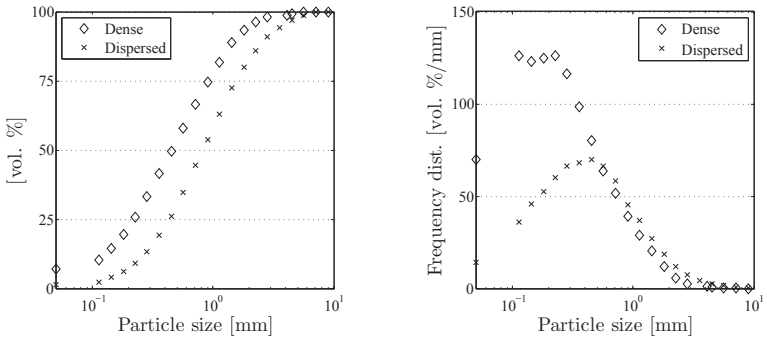

(a) Cumulative size distribution. **(b)** Frequency distribution.

Figure 10B.8 Comparison of size distribution obtained from the CAMSIZER®equipment. Dense curves are derived from the run illustrated by figure 10B.7 and dispersed from figures 10B.5 and 10B.6. All distribution are based on the minimum diameter of the particles outlined by a 2D projection.

the CAMSIZER®to the more well known sieving method. The particle size distribution was carried out at DONG Energy Powers laboratory at Ensted power plant. Double determination was performed using sieves of the sizes: 0.0, 0.25, 0.5, 1.0, 1.4, 2.0, 2.8, and 3.15 mm in a Retsch AS450 sieve tower for 15 min at an amplitude of 1.0 mm/g.

Figure 10B.9 shows a direct comparison between the CAMSIZER®results and the averaged sieve analysis (double determination). The CAMSIZER®suggest a smaller amount of smaller particles compared to the sieve tower analysis.

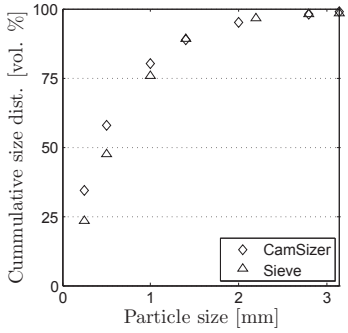

Figure 10B.9 Comparison of the particle size distribution of dust #4 using the CAMSIZER®equipment and traditional sieve towers.

10B.3.3 Proximate Analysis

Aiming to trace any changes in the feed stock fuel blend (e.g. increasing fraction of straw compared to wood) a series of proximate analyses have been conducted on the dust samples collected from the burner feed tube. The samples have been analyzed at DONG Energy laboratory at Ensted power station, Aabenraa. However, the ash fraction in the wood pellet fuel is so low and the ash determining procedure includes multiple transfers of sample. Hence, a large statistical deviation is inherent in the method making it difficult to evaluate on the results with such small expected differences between the samples, cf. table 10B.7.

Table 10B.7 Proximate analysis results for selected dust samples collected at AMV1. All results are based on double determination except the volatile analysis. Deviations are based on statiscal data from the method. The analysis follows standard: DS/EN14775:2009.

Date dd-mm	Time hh:mm	Exp* #	Ash wt. %	Dev. ±	Volatile wt. %	Dev. ±	HHV MJ/kg	Dev. ±	LHV MJ/kg
29-02	15:15	3	1.31	0.20	82.2	1.6	20.07	0.12	18.76
	17:45	5	1.07	0.20	82.8	1.7	20.10	0.12	18.78
01-03	09:30	7	1.32	0.20	82.4	1.6	20.14	0.12	18.83
	15:30	10	1.30	0.20	82.3	1.6	20.15	0.12	18.84
	16:40	11	1.07	0.20	82.4	1.6	20.17	0.12	18.86
	17:45	13	1.32	0.20	82.5	1.7	20.18	0.12	18.86

* Experimental number during which the sample has been extracted.

Attempting to minimize the deviation related to the standard proximate analysis approach, selected dust samples were divided using a Retsch PT-1000 rotary divider into fractions of approximately 20 g. One of these fractions were then processed at 18 000 rpm in a cutter mill equipped with a 120 μm screen. $\sim$5 mg of the cutted fuel where then transferred to an alumina crucible and analysed using a Netzsch STA 449/F1 and burned out at a final temperature of 900 °C in 21 vol. % O_2 for 30 min. The resulting data are presented together with the standard proximate analysis in figure 10B.10. The data show an offset towards higher ash fractions when analysing the fuel in the TGA apparatus. Double determination of a selected sample has been performed without quantifiable differences. No clear conclusion can be drawn from either of the proximate analyses with respect to a possible shift in the fuel composition. However, all results indicates only minor changes in fuel properties.

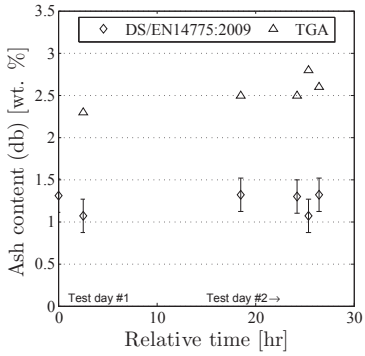

Figure 10B.10 Comparison of proximate analysis results using DS/EN14775:2009 and TGA approach. Relative time = 0 correspond to the onset of the first measurement on February 29 at 10:15.

CHAPTER 10C

Results

This chapter presents the experimental results for each of the investigated operating conditions. Time schedules are connected to each experiment as all supplementary material, e.g. video material, pellet and dust samples, etc. are identified by date and time. Each experiment is also assigned an experiment ID (Exp #) as defined in table 10B.3.

10C.1 Reference Setting

Four reference measurements have been conducted — in the beginning and end of each test day (#1 and #2). The time schedule is presented in table 10C.1.

Table 10C.1 Time schedule for the reference measurements at the beginning and end of each test day.

Exp #	Name	Date dd-mm-yyyy	Begin hh:mm	End hh:mm	Comment
1	Ref #1	29-02-2012	09:55	12:10	125 mm steps, double determination[a]
5	Ref #2		17:21	18:31	250 mm steps
7	Ref #3	01-03-2012	09:23	10:00	250 mm steps
13	Ref #4		17:50	18:50	250 mm steps

[a] Double determination performed at selected positions only.

10C.1.1 Power Plant Settings

A set of stable operating parameters were chosen for reference settings. Table 10C.2 lists the average values and corresponding standard deviation for a number of key process parameters during all four reference runs. In general, stable conditions are maintained for all key parameters. The maximum deviation for the parameters listed in table 10C.2 is below 10 %.

All plant data listed in table 10B.2 are presented in time dependent graphs in appendix C. In general, the operating conditions during all four reference runs are stable and assume close to identical quantities. However, in the following a few examples on differences are presented.

Figure 10C.1 illustrates an offset in the combustion air flow rate in the time intervals corresponding to reference flames #1–4. The measurements are logged every minute and the presented data represent the operating conditions

Table 10C.2 Selected averaged values for reference process parameters and their standard deviations. For designation explanation please refer to table 10B.2.

Designation	Unit	Ref #1		Ref #2		Ref #3		Ref #4		Max deviation
		Avg	σ	Avg	σ	Avg	σ	Avg	σ	%
Stoevflow br.roer 11	kg/s	2.52	0.101	2.55	0.0925	2.43	0.0974	2.48	0.0866	4.7
Flow forbr.luft brd.11	kg/s	7.77	0.0198	8.05	0.00837	7.77	0.0243	7.32	0.0370	9.1
Flow sek.luft brd.11	kg/s	3.84	0.0179	4.05	0.0122	3.88	0.0128	3.70	0.0292	8.6
TA turbulator broender 11	%	99.6	0.00660	99.7	0.00585	99.6	0.00580	99.3	0.0074	0.6
SA turbulator broender 11	%	99.7	0.00512	99.7	0.00757	99.7	0.00760	99.3	0.0089	0.4
Temp.SA mundstykke br.11	°C	483	2.51	496	0.789	476	0.920	497	1.15	4.2
Temp.kerneroer mundst.br.11	°C	232	4.04	248	5.40	235	7.60	249	9.92	6.8
Temp. Kulstoev braenderd.10	°C	50.8	0.165	51.7	0.0148	51.0	0.101	54.0	0.341	5.9
Lufthastighed br.roer11	m/s	32.5	0.394	32.6	0.333	32.3	0.303	32.4	0.442	0.9
Temp. Forbr.luft brd.11	°C	327	0.287	330	0.0652	324	0.123	328	0.125	1.8

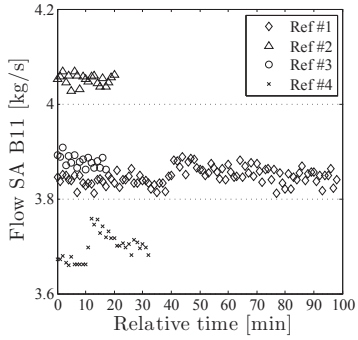

(a) SA flow rate.

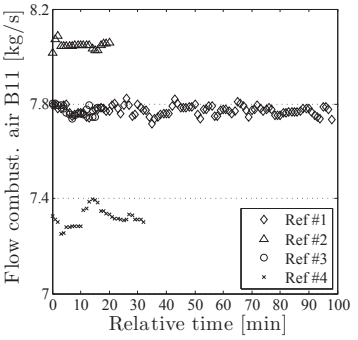

(b) Total combustion air ($SA + TA$) flow rate.

Figure 10C.1 Differences in the feed of combustion air during reference run #1–4 to burner #11.

during the time period across which the temperature and extractive probe measurements are averaged. The similarities in offset in secondary air and total combustion air suggest that the change primarily affects the secondary air flow. As will be shown in sections 10C.2 and 10C.4 the secondary air flow tends to influence strongly on the flame properties.

10C.1.2 Temperature and Oxygen Concentrations

Figure 10C.2a illustrates the temperature and O_2-profile for reference flame #1. For simplicity only one reference run has been included. The error bars indicate time resolved standard deviations between 100–200 K for the temperature measurements. Figure 10C.2b presents time resolved standard deviations at specific positions along the centerline. The shapes of the temperature and the O_2-profiles respectively compliment each other well.

All four reference runs are presented in figure 10C.3. There is good consistency between both reference runs carried out during test day #1. Reference runs #3 and #4 deviate slightly compared to reference run #1 and #2. Especially reference run #4 is showing a cooler flame $\sim$ 100 K as the probe progresses past 1 m. Correspondingly, a higher oxygen level has been observed, even though the plant logging system indicated a lower supply of combustion air during the last measurement, cf. figure C.8 on page page 405.

10C.1.3 Gas Probe Analysis

Gas extraction was performed through the entraining probe. An excess of cooling water efficiently quenched the sample gas after which it was analysed

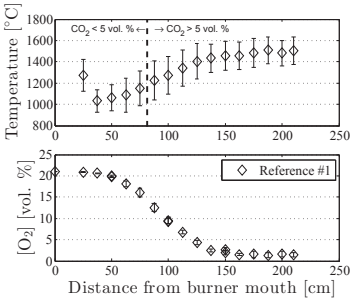

(a) Reference #1 with double resolution in space. Temperature measurements to the left of the dashed bar are considered unreliable due to the low CO_2 concentration.

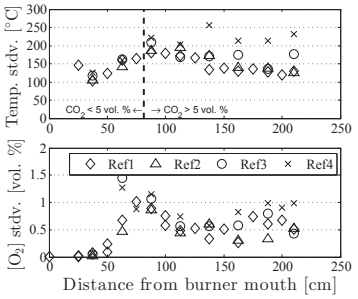

(b) Time resolved standard deviations for (top) the optical temperature and (bottom) the O_2-concentration measurements for each reference flame.

Figure 10C.2 Gas temperature and O_2-concentrations for reference run #1, errorbars signifies time resolved standard deviation. Figure 10C.2b comparison of standard deviations for measured temperature and O_2-concentrations for the four reference runs.

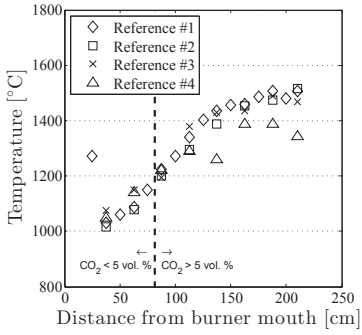

(a) Gas temperatures measurements. Temperature measurements to the left of the dashed bar are considered unreliable due to the low CO_2 concentration.

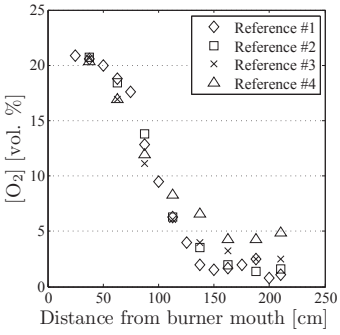

(b) O_2-concentration measurements.

Figure 10C.3 Gas temperature and O_2-concentration measurements for reference runs #1–4. Time resolved standard deviations are found in figure 10C.2b for specific intrusion depths.

by means of an IR and UV spectrometer. Figure 10C.4 presents both carbon combustion products and biomass pyrolysis products as function of distance from the burner mouth.

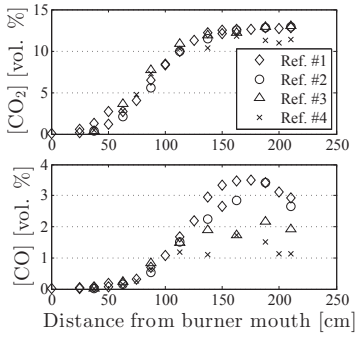

(a) Carbon combustion products given on a dry basis.

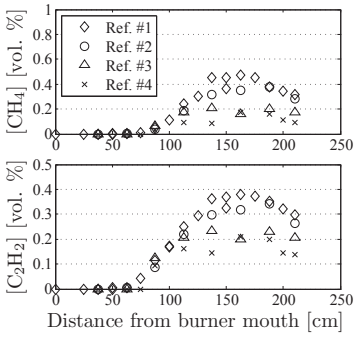

(b) Pyrolysis product concentrations given on a dry basis.

Figure 10C.4 Gas analysis for all reference runs depicting both (a) primary carbon combustion products and (b) pyrolysis products. All concentrations are given on a dry basis.

The CO_2-level follows the same pattern as the temperature curve and reaches around 14 vol. % at approximately 1.5 m from the burner mouth after which it levels out. This agrees well with the observed depletion of available O_2, cf. figure 10C.3b.

The general qualitative tendencies of the main pyrolysis products: CO, CH_4, and C_2H_2 are almost the same, indicating a distinct mixing pattern of all four flames. The production of all three species increases with temperature until a local maximum is reached, approximately simultaneous with the depletion of oxygen and thereby the release of reaction heat. A differential analysis of figures 10C.4a and 10C.4b shows how the local maximum of CO is found further from the burner mouth than both CH_4 and C_2H_2 which peaks at approximately 1.6 m from the burner mouth. This indicates how the destruction of light hydrocarbons could contributes to the production of CO to noticeable degree and thus elongate the reducing zone.

As was the case for the temperature and oxygen measurements, reference runs #3 and #4 (test day #1) deviate from reference runs #1 and #2 (test day #2). Less CO is produced on test day #2 while the same CO_2 levels can be detected. The same trend, with an almost identical pattern, is seen for the primary pyrolysis products: CH_4 and C_2H_2.

The contribution of CO relative to CO_2 is shown in figure 10C.5. This effectively shows the oxidative or reducing conditions of the local environment,

showing large quantities of CO around 1.6 m from the burner mouth.

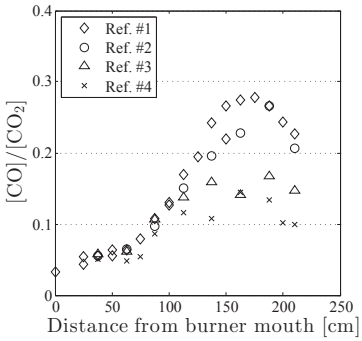

Figure 10C.5 The relative CO/CO_2 levels during reference runs #1–4 indicating the oxidative properties along the centerline.

No direct correlation between the differences in pyrolysis products and neither local temperature nor O_2-concentration have been found.

Time Resolved Standard Deviations

The measurements for both the optical temperature readings and the extractive gas analyses are resolved in time to average the flame fluctuations. Standard deviations reported in this work therefore refers to physical fluctuations in time and not to the precision of the used equipment. These time resolved standard deviations are for the temperature and O_2-measurements illustrated in figure 10C.2b. The corresponding time resolved standard deviations for the extractive gas measurements are illustrated for the reference runs in figure 10C.6.

10C.1.4 Optical Observations

Differences in the reference flames where also observed by video imaging. Figure 10C.7a illustrates a representative image of reference flame #1 showing close flame attachment to the burner quarl. While reference flame #4, figure 10C.7b clearly detaches, stabilizing a flame approximately 1 m from the burner mouth. Examining video sequences of reference flame #1 and #4 yields detachment fractions of 0 and 30 % respectively. Meaning, that during a 15 s video sequence of reference flame #1, (ID: 1120.avi), not a single occurrence of flame detachment was observed. Similarly, a 16 s video sequence of reference flame #4 has been examined, (ID: 1854.avi), clear flame detachment could be observed approximately 30 % of the time.

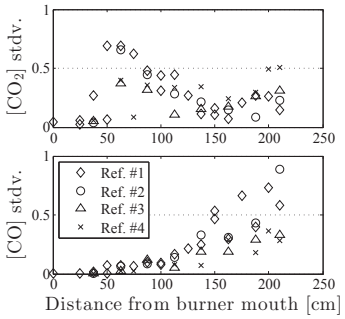

(a) Units in (vol %).

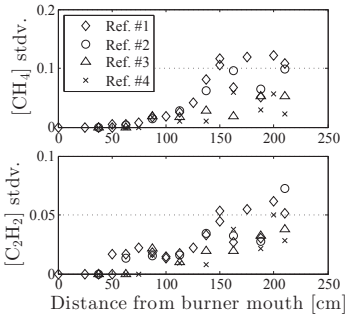

(b) Units in (vol. %).

Figure 10C.6 Time resolved standard deviations for all reference runs. All concentrations are given on a dry basis.

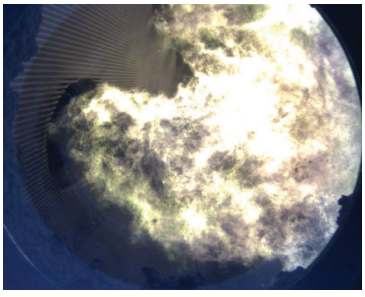

(a) Reference #1. (File: 1120.avi (00:11)). Good flame attachment.

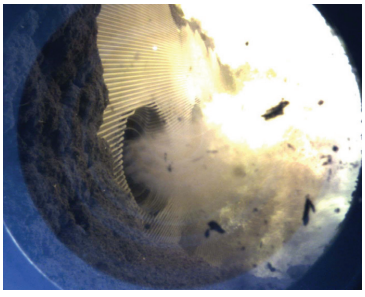

(b) Reference #4. (File: 1154 (00:07)). Clear flame lift.

Figure 10C.7 Video image of reference flame #1 (a) and #4 (b). Stable flame and good flame attachment is observed in flame #1 while clear flame detachment is observed in flame #4.

Temporal Resolution of Optical Measurements

The infrared measurements are recorded at an average frame rate of 94 Hz. The number of frames over a short period of time may vary due to limited buffer capacity of the connected laptop. In most cases the frame rate is sufficiently rapid to capture the dynamics of the large scale development in both gas and solid phase flows. This includes gas phase fluctuations in any direction on the observed plane and particle cloud trajectory tracking in the near burner field. An image sequence of $\sim$ 12 ms showing reference flame #1 is shown in figure 10C.8 to provide an overview of the temporal resolution of the high speed infra-red imaging employed in the current study. In this sequence, the cold particle clouds, in blue colors, can be easily followed as they emerge from the burner mouth and entrain into the furnace.

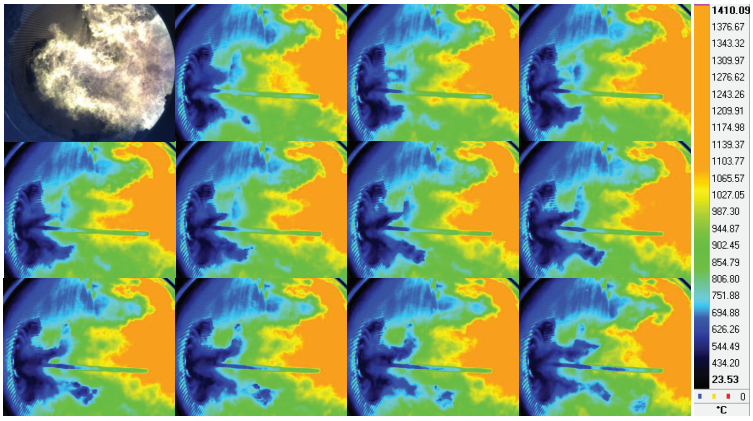

Figure 10C.8 IR imaging sequence showing the adequacy of temporal resolution for particle cloud progression.

For flame lift identification optical analysis in the visible spectrum has proven the most effective. These video sequences are recorded by CCD cameras at lower frame rates; averaging around 20.8 Hz. However, still sufficiently fast to capture the fluctuating behavior of an unstable flame attachment, i.e. where flame lift and flame (re)-attachment is observed multiple times in rapid succession. Such behavior is seen in reference flame #4 and an image sequence is presented in figure 10C.9. Good flame attachment is seen at 01:02 detaching from frame 01:04 to 01:07 and reattaching from frame 01:10 to 01:12, given in seconds:frame number. I.e. at an average frame rate of 20.82 Hz in the given sequence flame detachment and reattachment is achieved within $\sim$ 400 ms.

Another type of flame detachment has also been observed from the same flame. Approximately five seconds later than the video sequence illustrated in

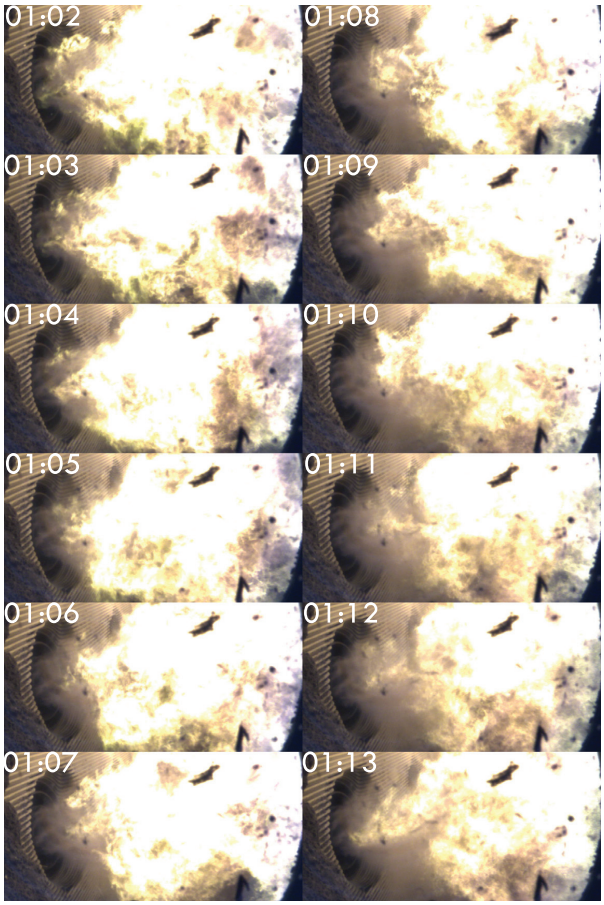

Figure 10C.9 Oscillating flame attachment/detachment. AMV1 reference flame #4 (File: 1854.avi). Time stamps indicate seconds:frame taken at an average frequency of 20.82 Hz. Total time: 528 ms.

figure 10C.9 was captured a strong flame detachment was observed. This is illustrated in figure 10C.10. At frame 06:09 a clearly lifted flame is stabilized approximately 1 m from the burner mouth. This lifted flame is stabilized for another 5 s before the flame reattaches close to the burner quarl, as illustrated in figure 10C.11.

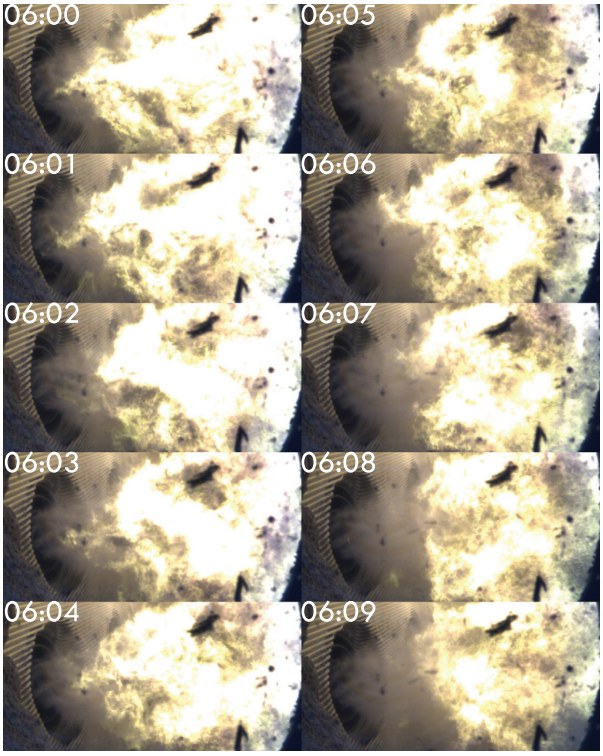

Figure 10C.10 Strong flame detachment. AMV1 reference flame #4 (File: 1854.avi). Time stamps indicate seconds:frame taken at an average frequency of 20.82 Hz. Total time: 432 ms.

10C.1.5 Particle Cloud Velocity

The IR high speed imaging made it possible to estimate the entrance velocity of the larger particle clouds. The IR-camera recorded at a frame rate of 94 Hz. The probe inserted 75 cm into the flame is used as a distance reference in the flame. The velocity estimates for reference run #1 are listed in table 10C.3. An example of particle cloud tracing is giving in figure 10C.12.

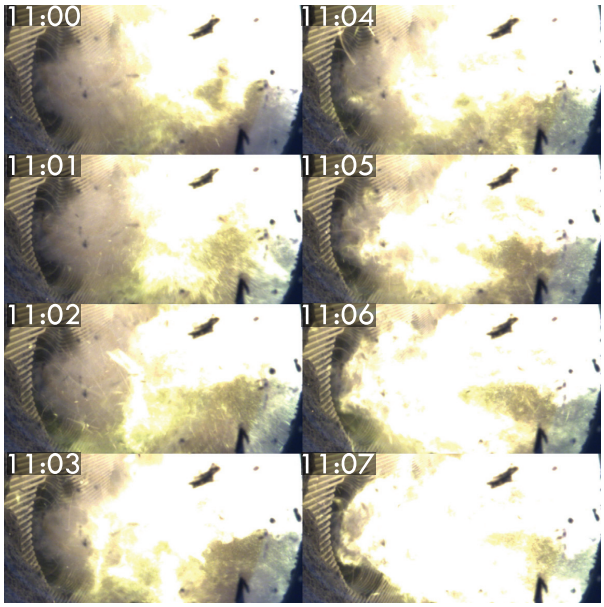

Figure 10C.11 Reattachment of lifted flame. AMV1 reference flame #4. (File: 1854.avi). Time stamps indicate seconds:frame taken at an average frequency of 20.82 Hz. Total time: 336 ms.

It should be kept in mind that the particles may only be distinguished from the gas radiation as long as they are significantly colder than the surrounding gas phase. It is likely that the particles in the boundary of the particle cloud are sufficiently exposed to convective, conductive, and heat transport by radiation that they will disappear in thermal background and thus the particle cloud velocity calculated from the IR images will represent an effective cold particle cloud entraining velocity rather than the true velocity of the individual particles.

10C.1.6 Particle Cloud Temperature and Flame Penetration

The IR-imaging recorded from the side view-port can be used to estimate particle cloud surface temperatures assuming a known grey body behavior of the particle cloud and complete IR-radiation shielding in the target area. It should however be kept in mind that quantitative conclusions should only be drawn with caution. For qualitative assessment and comparison the method is considered valid.

Figure 10C.13 shows a comparison between the minimum detected tem-

Table 10C.3 Particle cloud velocity estimations from high speed IR imaging at 94 Hz over a distance of 75 cm (ID: AMV129feb06.ptw).

IR-ID	Frame	Metric time [s]	Velocity [m/s]
AMV29feb06	4–9	17.183–17.247	5.5
AMV29feb06	263–272	20.385–20.502	6.4
AMV29feb06	550–559	27.832–28.013	4.1
AMV29feb06	609–618	28.810–28.981	4.4
AMV29feb06	632–641	29.225–29.406	4.1
AMV29feb06	909–918	37.225–37.481	2.9
Average			4.6
Standard deviation			1.3

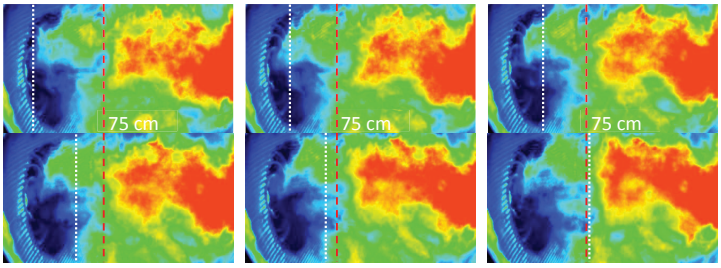

Figure 10C.12 Particle cloud tracing for velocity estimations in reference flame. (ID: AMV29feb06.pwt) frame 4–9. The red dashed line indicate the position of the probe penetrating 75 cm into the flame. The white line indicates the front of the entraining cold particle cloud. The color scale goes from cold (blue) to red (hot) and is only valid for regions of high particle density, cf. section 10C.1.6.

perature along vertical lines in fixed positions in space for both reference flames #1 and #4 sampled across 1000 images taken at a frequency of 94 Hz. It is clear that the minimum detected temperatures, originating from the cold surfaces of particles penetrating the flame, are lower for reference flame #4 compared to the same data obtained from reference flame #1. This indicates that the cold particles are penetrating further into the boiler, presumably introducing a more unstable flame which, possibly, could contribute to the more oscillating flame behavior observed during test day #2.

Averaging the signal from the same IR-image sequences yields the temperature mappings illustrated in figure 10C.14. Both maps are shown on the same color scale. Figures 10C.14a and 10C.14b are slightly blurred due to the hand-held camera method. Both maps are averaged across 1000 images sampled with a frequency of 94 Hz, i.e. just over 10 s. It is clear that the near burner cold region stretches further into the boiler in reference flame #4, figure 10C.14b. IR-imaging of reference flame #2 and #3 was not acquired.

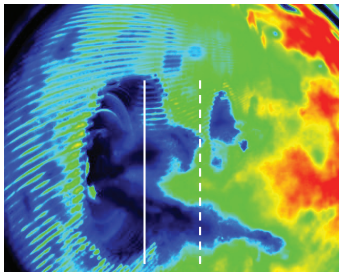

(a) IR image of burner #11 with a particle cloud penetrating into the boiler. (Image ID: AMV1mar26.ptw, frame: 608).

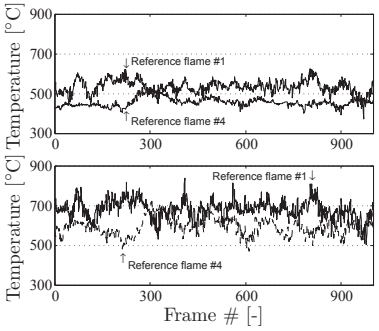

(b) Minimum temperatures detected along vertical lines from IR-thermometry. (upper) closest (lower) furthest from the burner.

Figure 10C.13 Comparison of minimum temperature IR-thermometry between reference flame #1 and 4. (b) reports the minimum temperature detected in both space, along the vertical lines illustrated in (a), and time, across a 1000 IR-images sampled at a rate of 94 images/s.

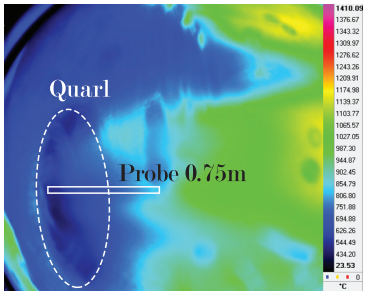

(a) Reference flame #1. (Sequence ID: AMV29feb06.ptw).

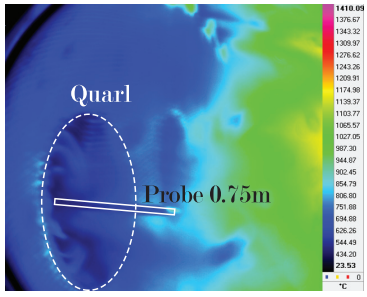

(b) Reference flame #4. (Sequence ID: AMV1mar25.ptw).

Figure 10C.14 Averaged temperature maps for (a) reference flame #1 and (b) #4. The images are averaged over 1000 frames sampled at a rate of 94 Hz.

10C.2 Secondary air Flow

The secondary air flow has been both in- and decreased relative to the reference configuration according to table 10B.1. The time schedule is listed in table 10C.4. The affected channels are hatched black in figure 10C.15.

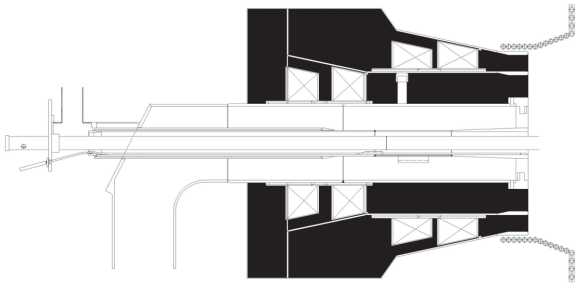

Figure 10C.15 Burner sketch: The SA and TA channels are hatched in black to illustrate the area affected by the change in secondary air flow. The burner sketch has been modified for illustrative purposes.

Table 10C.4 Time schedule for secondary air flow runs and operational deviations from reference values.

Exp #	Date dd-mm-yyyy	Begin hh:mm	End hh:mm	Setting kg/s	Reference kg/s
2	29-02-2012	13:36	14:33	4.66	3.87
3		14:33	16:00	2.97	3.87

The flow rate of the combustion air flow is changed independent from the primary air and with compensating in the combustion air air split to maintain constant tertiary air flow.

10C.2.1 Probe Measurement Results

The development in the flow of secondary air to burner #11 is illustratively presented in appendix C figures C.7 and C.8. The flow of tertiary air is not measured but can be calculated by closing the mass balance over the total combustion air flow and the flow of secondary air. Both flows are stabilized before the measurements were carried out. The resulting changes in the stoichiometric conditions are illustrated in figure 10C.16 showing the development in the λ-value calculated using $CH_{1.8}O_{0.5}N_{0.2}$ as an equivalent composition for biomass [390]. This results in an air-to-fuel ratio below unity for experiment #3, low combustion air flow rate. However, no noticeable differences in

either the pyrolysis gas production, oxygen concentration, or temperature profile have been observed. A decrease in the air supply in the internal recirculation zone is expected to increase the fraction of pyrolysis gases, assuming that the radiation and convective transport of heat from further away is still sufficient to maintain the temperature profile. Likewise, a lower O_2-concentration is expected due to the limited fuel rich conditions, i.e. any O_2 present would be expected to react.

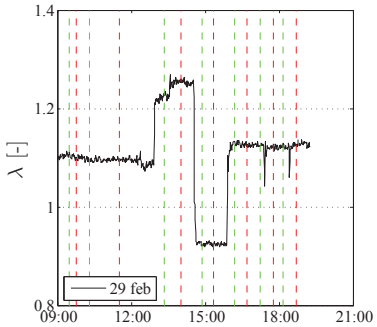

Figure 10C.16 Development in the λ-value during test day #1. Green and red lines indicate the start and end of measurements.

Figure 10C.17 presents the temperature and approximate O_2-concentration for the SA runs compared to a reference. No major differences in gas temperature or O_2-concentration have been observed. The similar shape and absolute values of the O_2-profile suggest that the internal recirculation zone is strong enough to maintain convective transport of O_2 to the near burner field even though the combustion air flow rate is lowered by 16.7 % on a mass basis.

Considering the pyrolysis and combustion products presented as function of distance from the burner mouth in figure 10C.18 indicate significant changes in the flame dynamics as the combustion air flow is increased. Increasing the combustion air flow decreases the absolute concentration of CO, CH_4, and C_2H_2 in the far-burner field, distinguishing from the reference flame at distances greater than approximately 1 m from the burner mouth. All concentration profiles follows the same path in the near-burner field (< 1 m from the burner mouth).

10C.2.2 Particle Cloud Flame Penetration

Thermal imaging of the flame undergoing changes in the flow rate of the combustion air is interesting due to the expected changes in the near burner mixing pattern. Figure 10C.19a shows the burner operating under high combustion air flow and a strong internal recirculation zone is therefore to be

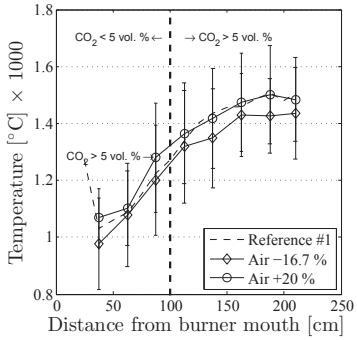

(a) Temperature measurements. Error bars indicate time resolved standard deviations. Temperature measurements to the left of the dashed bar are considered unreliable due to the low CO_2 concentration.

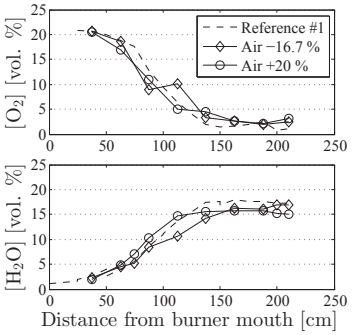

(b) O_2 and H_2O-concentrations. O_2 is given on a dry and H_2O on a wet basis.

Figure 10C.17 Gas temperatures and O_2 and H_2O-concentration measurements for changes in the combustion air flow rate and compared to reference flame. The legend numerics indicate the changes in combustion air mass flow.

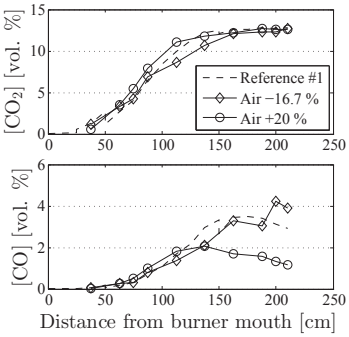

(a) Carbon combustion products given on a dry basis.

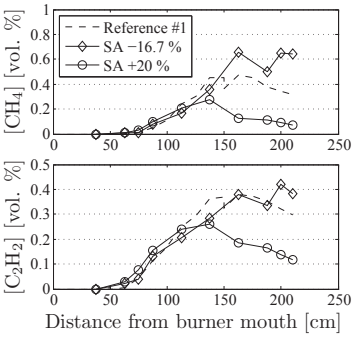

(b) Pyrolysis product concentrations given on a dry basis.

Figure 10C.18 CO_2 and relative CO-concentrations and light hydrocarbon-concentration measurements for changes in the SA flow rate and compared to reference flame. The legend numerics indicate the changes in SA mass flow.

expected, convectively supplying heat to the core jet. Contrary, a weaker internal recirculation zone is expected in the case of lower combustion air flow, cf. figure 10C.19b. A fuel richer stoichiometry and less convective transport close to the burner mouth is expected to give rise to a better penetration of cold particles into the furnace.

These trends are both indicated by the thermal images of the in- and decrease in the combustion air flow as shown in figure 10C.19. Figure 10C.19a shows a small low temperature zone appearing only in the very vicinity of the burner quarl and actual particles clouds are difficult to identify. Contrary, the low temperature area extends slightly further into the furnace when decreasing the flow of combustion air, as seen in figure 10C.19b.

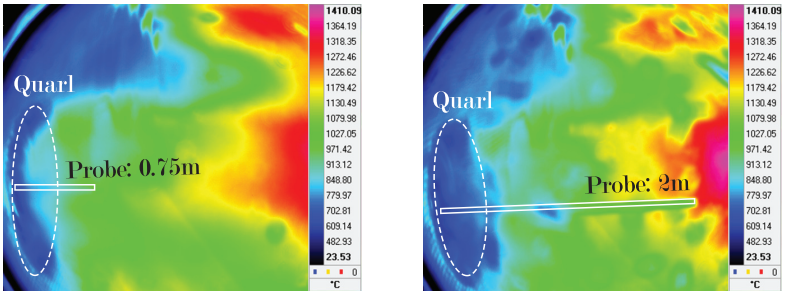

(a) Increased combustion air flow. **(b)** Reduced combustion air flow.

Figure 10C.19 Thermal imaging of burner #11 at (a) increased and (b) reduced combustion air flow rate respectively. The color scale is in °C and may only be considered valid for dense particle clouds, i.e. closest to the burner mouth.

10C.3 SA/TA Air-Split

The air split is defined as $SA/(SA+TA)$ (secondary air flow to total combustion air flow on a mass flow basis). The air-split has been both in- and decreased, according to table 10B.1. Table 10C.5 lists the time schedule for the air-split runs.

Table 10C.5 Time schedule for air split (AS) runs. Where AS = SA/ (SA + TA).

Exp #	Date dd-mm-yyyy	Begin hh:mm	End hh:mm	SA kg/s	SA+TA kg/s	AS —	Ref. AS —
4	29-02-2012	16:00	17:21	2.51	8.06	0.31	0.50
6		18:31	19:29	4.52	8.07	0.56	0.50

Variations in the air split have been carried out with an overall constant flow rate of combustion air (SA+TA). Thus, a decrease in air split implies a decrease in the secondary air flow rate together with a corresponding increase in tertiary air on a mass based flow rate. The affected channels are hatched black in figure 10C.20.

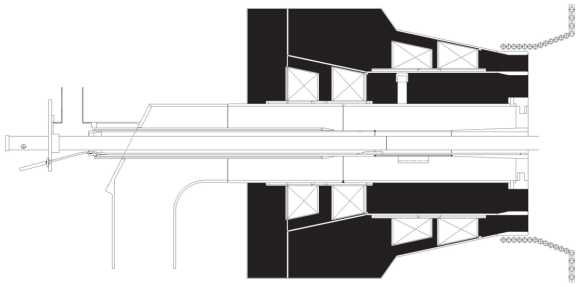

Figure 10C.20 Burner sketch: The SA and TA channels are hatched in black to illustrate the area affected by the change in AS. The burner sketch has been modified for illustrative purposes.

10C.3.1 Probe Measurement Results

Figure 10C.21 illustrates the total flow of combustion air, the secondary air flow, and the corresponding air-split value during the experimental time. Steady levels of all flows are achieved before measurements are carried out. Figures C.7 and C.8 in appendix C show the same information during the entirety of the campaign.

Increasing the air-split seems to stabilize the flame closer to the burner mouth; higher temperatures and lower O_2-concentrations, cf. figure 10C.22. While decreasing the air-split significantly decreases the temperature in the near burner field with a corresponding increase in O_2-concentration. Interestingly, video imaging shows close flame attachment at all time for the decrease in air-split while an increase in air-split causes slight and brief, however, frequent flame lift; cf. figure 10C.23. IR-imaging also shows a tendency for increased fuel roping during high air-split operation, i.e. cold particles penetrating further into the flame.

Changing the air split introduces alternative behavior of all pyrolysis or combustion products compared to the reference flame, as presented in figure 10C.24. Decreasing the air split reduces both the CO and the CO_2 production along the center-line of the flame. Reaching the same concentration of CO_2 at an approximate 180 cm from the burner mouth which would suggest either a poor burn-out or a shift in the position of the combustion zones.

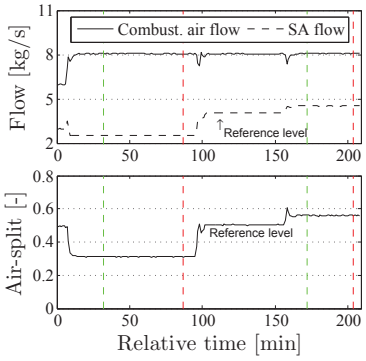

Figure 10C.21 Air flows (upper) and AS (lower) during AS changes. Green and red dashed lines indicate the beginning and end of each measurement period.

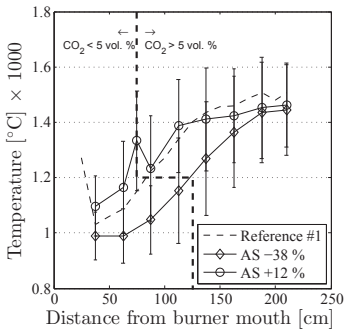

(a) Temperature measurements. Error bars indicate time resolved standard deviations. Temperature measurements to the left of the dashed bar are considered unreliable due to the low CO_2 concentration.

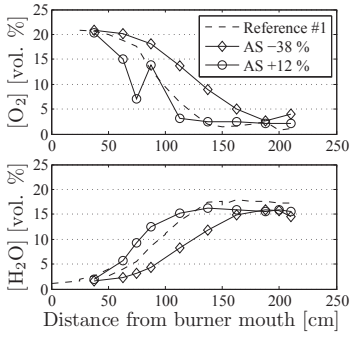

(b) O_2 and H_2O-concentrations. O_2 is given on a dry basis and H_2O on a wet basis.

Figure 10C.22 Gas temperatures and O_2 and H_2O-concentration measurements for changes in the AS settings and compared to reference flame. The legend numerics indicate the change in AS.

(a) Low AS. (File: 1717.avi). Good flame attachment.

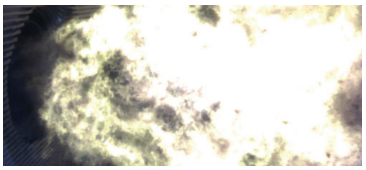

(b) High AS. (File: 1929.avi (00:06)). Slight flame lift.

Figure 10C.23 Video image of reference flame #1 (a) and #4 (b). Stable flame and good flame attachment is observed in flame #1 while clear flame detachment is observed in flame #4.

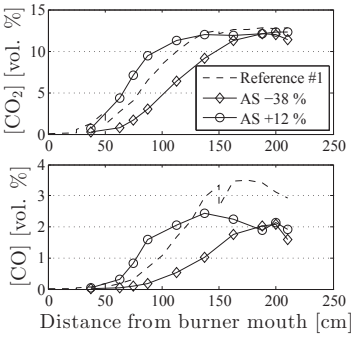

(a) Carbon combustion products given on a dry basis.

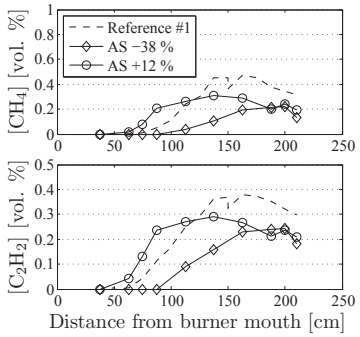

(b) Pyrolysis product concentrations given on a dry basis.

Figure 10C.24 (a) CO_2 and relative CO-concentrations and (b) light hydrocarbon-concentration measurements for changes in the AS and compared to reference flame. The legend numerics indicate the changes in AS.

Increasing the relative rotational momentum of the tertiary air flow could potentially broaden the internal recirculation zone diluting the pyrolysis and combustion products along the center-line probe. In an other scenario, decreasing the effect of the secondary air flow could cause the primary air to better penetrate the internal recirculation zone and prolong the combustion zone beyond the reach of the probe. It is, however, noticeable how all concentration measurements stabilizes at the same value at approximately the same position in space.

10C.3.2 Particle Cloud Flame Penetration

Like for the, in section 10C.2.2 discussed, importance of the influence of the near burner mixing pattern when changing the secondary air flow rate, similar behavior is expected when changing the ratio between the secondary and the tertiary air flow, i.e. the air split. Increasing the air split increases the ratio between secondary and tertiary air flow rate. From figures 10C.25a and 10C.25b only slight differences can be identified. Indications of a slightly better particle penetration is seen when increasing the air split, i.e. increasing the flow of secondary air and correspondingly lowering the flow of tertiary air.

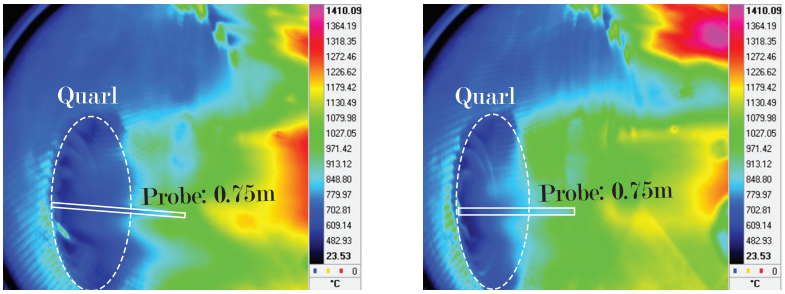

(a) Increased air split. **(b)** Reduced air split.

Figure 10C.25 Thermal imaging of burner #11 at (a) increased and (b) reduced AS respectively. The color scale is in °C and may only be considered valid for dense particle clouds, i.e. closest to the burner mouth.

10C.4 SA Swirl

Normal operation at AMV1 takes place with 100 % swirl on both secondary and tertiary air. In this series the swirl on the secondary air is decreased to 80 %, meaning that the swirler position is adjusted to 80 % by linear actuators. Figure C.11 in appendix C shows the turbulator setting in the secondary air channel during the campaign.

Table 10C.6 Time schedule for the SA-swirl run. The percentage refers to the physical position of the turbulators in the SA channel.

Exp #	Date dd-mm-yyyy	Begin hh:mm	End hh:mm	Setting %	Reference %	Comments
8	01-03-2012	10:05	11:30	82.0	99.7	Increased sampling time

Changing the secondary air swirl is carried out by moving the turbulators positioned in the secondary air channel back and forth to let more and less air pass without being swirled, respectively.

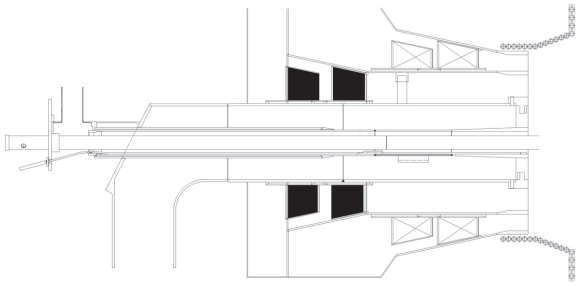

Figure 10C.26 Burner sketch: The SA turbulators are hatched in black to illustrate the area affected by the change in SA swirl. The burner sketch has been modified for illustrative purposes.

10C.4.1 Probe Measurement Results

Because the fuel composition, presumably, was changing during day #2 all data obtained during this day will be compared to both reference data from the morning and the evening.

Decreasing the secondary air swirl significantly decreases the stability of the flame. This is clearly seen by video observations, cf. figure 10C.23a, where flame detachment of approximately 75 cm is observed. Because of the unstable flame, the sampling time for the temperature and gas-analyses has been increased.

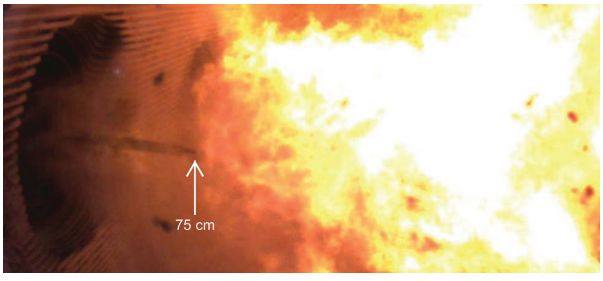

Figure 10C.27 Video imaging of low SA-swirl flame (ID: 1115.avi (00:02)). The tip of the probe is 75 cm inside the boiler.

As seen in figure 10C.28a a generally lower temperature profile has been observed in the entire measurement space. This corresponds to the video observations of an unstable flame as the secondary air swirl is reduced.

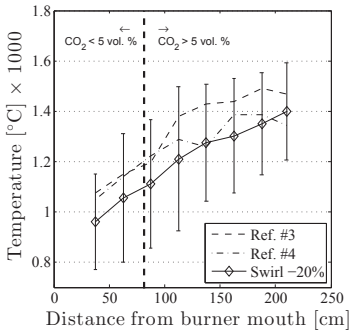

(a) Temperature measurements. Error bars indicate time resolved standard deviations. Temperature measurements to the left of the dashed bar are considered unreliable due to the low CO_2 concentration.

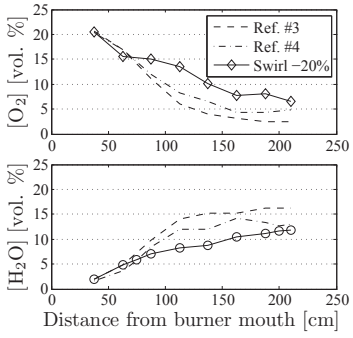

(b) O_2 and H_2O-concentrations. O_2 is given on a dry and H_2O on a wet basis.

Figure 10C.28 Gas temperatures and O_2 and H_2O-concentration measurements for changes in the SA swirl settings and compared to reference flame. The legend numerics indicate the position of the swirler.

The shapes of the combustion and pyrolysis product profiles, figures 10C.29a and 10C.29b respectively, are different from both the reference run but also from most of the other tested settings. The CO_2-curve does not level out within the reach of the probe and the CO-profile does not exhibit the characteristic peak around 1 m from the burner mouth. Likewise the presence of the major pyrolysis products: CH_4 and C_2H_2, figure 10C.29b, is nearly non existing. This is in agreement with the temperature and O_2-profiles. A lower temperature, slowing down the pyrolysis, and an overall high O_2-concentration consuming any released volatiles. This could cause for speculations of poor burn-out or potentially a significantly delayed pyrolysis front.

10C.4.2 Particle Cloud Flame Penetration

Decreasing the secondary air swirl decreases the swirl number, i.e. the relative axial momentum. This is also reflected in the IR imaging of the particle cloud leaving the burner. When comparing the IR image from the flame with reduced secondary air swirl, figure 10C.30a, with a reference flame, figure 10C.30b, the cold areas are entraining further into the furnace in the case of reduced swirl. Also seen as lower temperatures throughout the flame in fig-

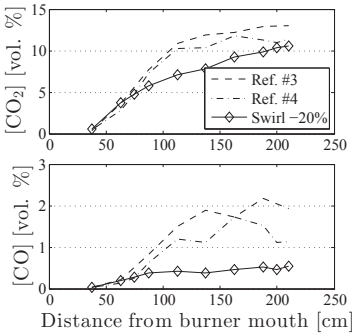

(a) Carbon combustion products given on a dry basis.

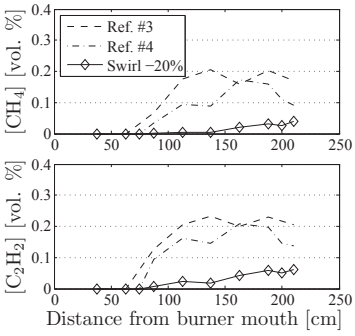

(b) Pyrolysis product concentrations given on a dry basis.

Figure 10C.29 CO_2 and relative CO-concentrations and light hydrocarbon concentration measurements for changes in the SA swirl settings and compared to reference flame. The legend numerics indicate the changes in swirler position.

ure 10C.28 and lower production of both pyrolysis and combustion products, cf. figure 10C.29.

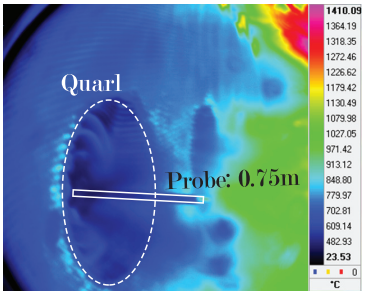

(a) Reduced SA swirl.

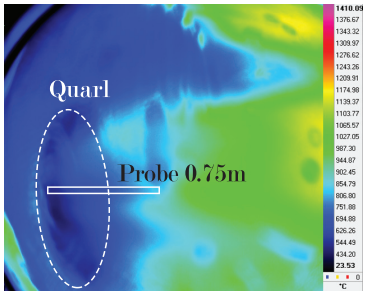

(b) Reference flame #1.

Figure 10C.30 Thermal imaging of burner #11 at (a) reduced SA swirl and (b) Reference flame 1. The color scale is in °C and may only be considered valid for dense particle clouds, i.e. closest to the burner mouth.

10C.5 TA Swirl

The flame was evidently sensitive to variations in the secondary air swirl settings. This series describes the flame response to a tertiary air swirl decrease

of the same magnitude as for the secondary air swirl change (again a swirl setting of 80 % refers to the position of the swirler not and the scaling with the resulting fluid flow is unknown). Figure C.12 in appendix C shows the turbulator setting in the tertiary air channel during the campaign.

Table 10C.7 Time schedule for the TA-swirl run. The percentage refers to the physical position of the turbulators in the TA channel.

Exp #	Date dd-mm-yyyy	Begin hh:mm	End hh:mm	Setting %	Reference %
9	01-03-2012	12:43	14:01	80.4	99.7

Changing the tertiary air swirl is carried out by moving the turbulators positioned in the tertiary air channel back and forth to let more and less air pass without being swirled, respectively.

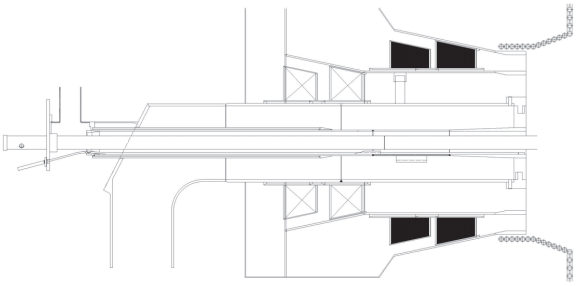

Figure 10C.31 Burner sketch: The TA turbulators are hatched in black to illustrate the area affected by the change in TA swirl. The burner sketch has been modified for illustrative purposes.

10C.5.1 Probe Measurement Results

When decreasing the tertiary air swirl the flame temperature and oxygen consumption is stabilized close to the burner mouth, following the progression of the reference flames. At farther distances ($> 100\,\mathrm{m}$) lower temperatures are seen compared to the reference runs. Considering the comparison between the infrared image of the reference flame and the tertiary air swirl reduced flame, cf. figure 10C.33, a clear difference in the particle path can be seen. The reference flame spreads the particles in the radial directions, while the TA swirl reduced flame features a dense oblong core of particles. Observing the flame with video camera shows a vaguely attached flame which appears narrow in the vicinity of the quarl.

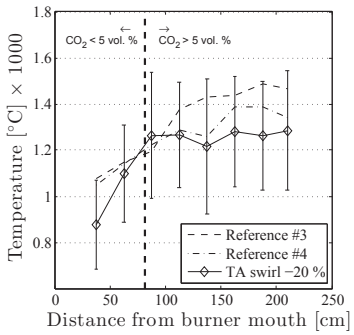

(a) Temperature measurements. Error bars indicate time resolved standard deviations. Temperature measurements to the left of the dashed bar are considered unreliable due to the low CO_2 concentration.

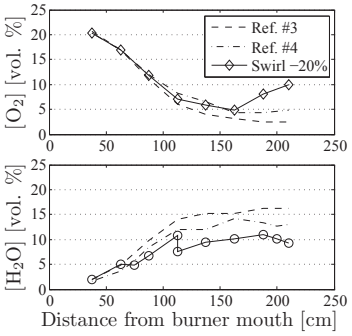

(b) O_2 and H_2O-concentrations. O_2 is given on a dry and H_2O is given on a wet basis.

Figure 10C.32 Gas temperatures and O_2 and H_2O- concentration measurements for changes in the TA swirl settings and compared to reference flame. The legend numerics indicate the position of the swirler.

Figure 10C.33 (left) IR imaging of the reference flame: (ID: AMV1mar25 frame 136). Good radial spread of the particles. (right) IR image of the TA reduced flame: ID AMV1mar9 frame 75. Dense, narrow, and long core of particles .

As for the temperature and O_2-concentrations, the pyrolysis and combustion product profiles follow the same path as the reference flame in the near-burner field ($< 1\,\mathrm{m}$), cf. figure 10C.34. As the temperature profile levels out so does the production of additional pyrolysis gases: CO, CH_4, and C_2H_2.

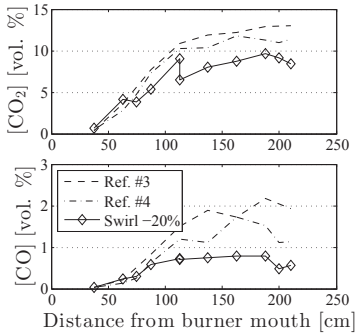

(a) Carbon combustion products given on a dry basis.

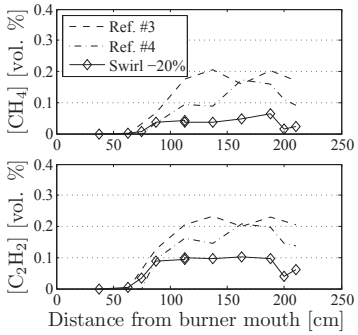

(b) Pyrolysis product concentrations given on a dry basis.

Figure 10C.34 CO_2 and relative CO-concentrations and light hydrocarbon concentration measurements for changes in the TA swirl settings and compared to reference flame. The legend numerics indicate the changes in swirler position.

10C.5.2 Particle Cloud Flame Penetration

As was the case for the reduced secondary air swirl flame, cf. section 10C.4, the reduction in overall swirl number when reducing the degree of tertiary air swirl, cf. figure 10C.35a, implies a deeper penetration of cold particles into the furnace when comparing to a reference flame, figure 10C.35b. The spread of particles looks more disperse when reducing the degree of tertiary air swirl compared to secondary air swirl, comparing figures 10C.30a and 10C.35a respectively.

10C.6 PA Flow

Decrease and increase in the primary air flow has been conducted according to table 10B.1. The time schedule for the primary air flow experiments is listed in table 10C.8. The de- and increase experiments are not conducted in direct sequence. Changes to the classifier frequency are carried out in between.

The primary air flow rate is changed centrally at the mill. The flow rates listed in table 10C.8 are measured at the mill and constitute the total amount of primary air delivered to burner level #10. Thus, the flow rate of primary

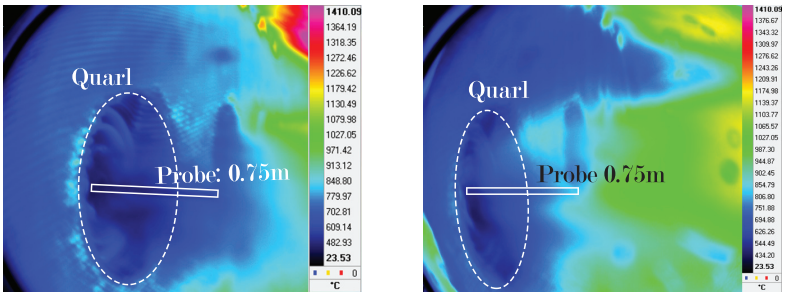

(a) Reduced tertiary air swirl. **(b)** Reference flame #1.

Figure 10C.35 Thermal imaging of burner #11 at (a) reduced TA swirl and (b) Reference flame 1. The color scale is in °C and may only be considered valid for dense particle clouds, i.e. closest to the burner mouth.

Table 10C.8 Time schedule for PA flow runs. The listed flow rates are measured at the mill and constitute the total amount of primary air delivered to burner level 10. The approximate PA flow rate to burner #11 is 1/4 of the listed values.

Exp #	Date dd-mm-yyyy	Begin hh:mm	End hh:mm	Setting kg/s	Reference kg/s
10	01-03-2012	14:49	15:39	14.23	14.97
12		16:57	17:50	16.00	14.97

air specifically to burner #11 is estimated as 1/4 of the listed values. The primary air tube is hatched black in figure 10C.36 to illustrate the affected areas in the burner.

10C.6.1 Probe Measurement Results

The change in primary air flow rate gave rise to a number of deviations in other operating parameters, with respect to the reference values. All burners on each individual level are fed by the same mill. The primary air is assumed to distribute evenly:

Decreasing the primary air flow in burner #11 therefore means to decrease the primary air flow to Mill #10. This is illustrated in figure 10C.37a. As the primary air flow to Mill #10 is decreased the pressure drop across the mill increases, cf. figure 10C.38, presumably due to a beginning fuel build-up. Interestingly, the plant data shows how the dust flow to burner #11 maintains a steady value.

Returning to reference values at approximately 16:05 for the classifier changes, both the values of the air speed in burner #11 and the dust flow

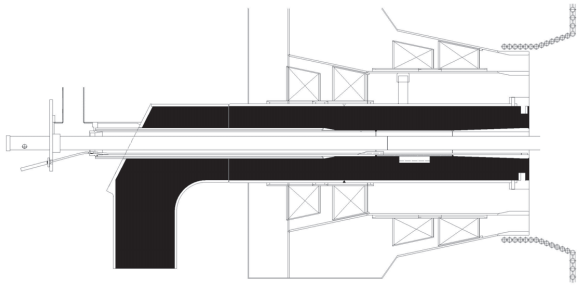

Figure 10C.36 Burner sketch: The PA channelis hatched in black to illustrate the area affected by the change in PA flow rate. The burner sketch has been modified for illustrative purposes.

to burner #11 overshoots the reference values. This is compensated by a corresponding drop in burner #14 in both air speed and dust mass flow rate.

Increasing the primary air flow induces a corresponding compensation in total combustion air as illustrated in figure 10C.37 by a close to constant total air flow. However, as seen from figure 10C.37b, the total air flow gradually decreases during test day #2 and with a constant fuel flow, this leads to a gradual decrease in the stoichiometric conditions.

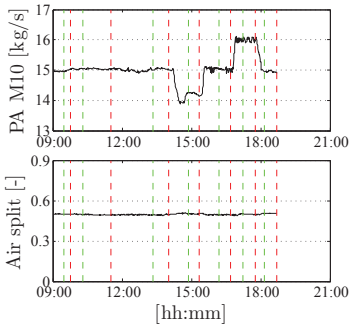

(a) primary air mass flow and air split.

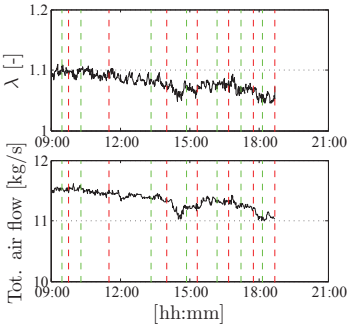

(b) λ-values and total combustion air.

Figure 10C.37 Presentation of key parameters during test day #2. The λ-values are calculated using $CH_{1.8}O_{0.5}$ as an equivalent composition for biomass.

Decreasing the primary air flow by 5 % (on a mass basis) significantly changes the shape of both the temperature and O_2-profile. Visual inspection shows no signs of flame lift and IR-images show a good mixing of particles. For high primary air flows, the O_2 and temperature profiles follow the ref-

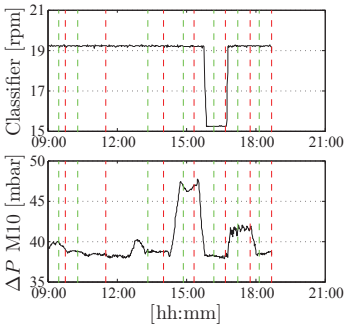

Figure 10C.38 Classifier frequency and pressure drop across M10 during test day #2.

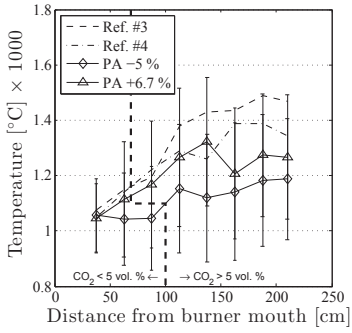

(a) Temperature measurements. Error bars indicate time resolved standard deviations. Temperature measurements to the left of the dashed bar are considered unreliable due to the low CO_2 concentration.

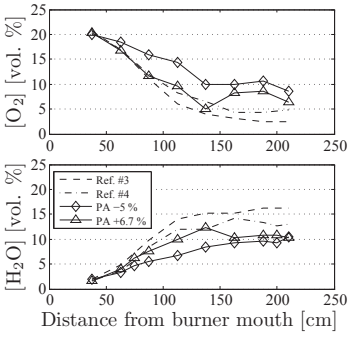

(b) O_2 and H_2O-concentrations. O_2 is given on a dry and H_2O is given on a wet basis.

Figure 10C.39 Gas temperatures and O_2 and H_2O- concentration measurements for changes in the PA flow rate and compared to reference flame. The legend numerics indicate the change in PA flow rate on a mass basis.

erence curves in the near burner region. Further away from the burner the temperature levels of earlier than the references.

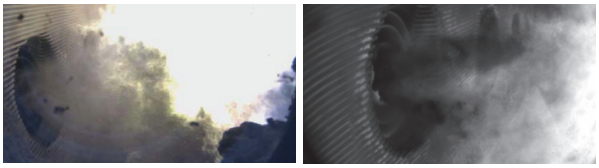

Figure 10C.40 Optical observations of the PA flow increased flame (left) (video image: ID: 1716.avi) shows flame detachment. (right) IR image shows high velocity jet of cold particles reaching far into the flame.

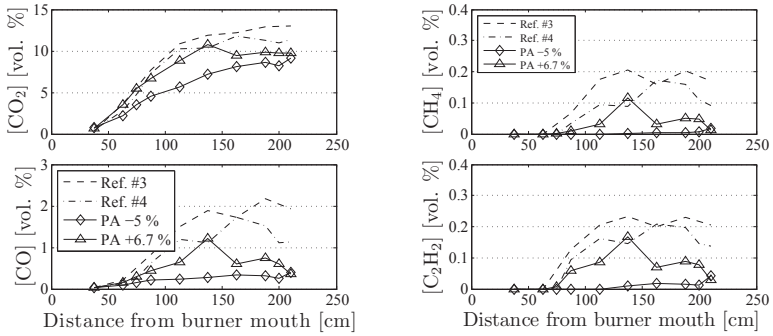

(a) Carbon combustion products given on a dry basis.

(b) Pyrolysis product concentrations given on a dry basis.

Figure 10C.41 CO_2 and relative CO-concentrations and light hydrocarbon concentration measurements for changes in the PA flow rate and compared to reference flame. The legend numerics indicate the changes in PA flow rate on a mass basis.

At increased primary air flow rate all pyrolysis and combustion product concentration profiles follows the reference flames in the near burner field. Peaks in both CO, CH_4, and C_2H_2 are found around 1.4 m from the burner mouth after which the concentrations decrease rapidly to values below the corresponding reference flame measurements. Visual inspection shows flame detachment and IR-images show high velocity jets of cold particles being injected far into the flame, cf. figure 10C.40.

Decreasing the primary air flow exhibit the same pyrolysis and combustion product concentration properties as the increase in secondary air flow rate, i.e. effectively increasing the swirl number, cf. figure 10C.18.

10C.6.2 Particle Cloud Velocity

High speed IR imaging of the flame enables for particle cloud velocity estimations. The IR camera records at a frame rate of 94 Hz. The probe inserted 75 cm into the flame is used as a length reference in the flame. Estimation of the particle cloud velocity has not been possible for the low velocity primary air run due to; 1. very good radial mixing of particles and combustion air and 2. very close flame attachment "drowning" the particles in the thermal image. Compared to the velocity estimations for the reference setting, cf. table 10C.3, the average particle cloud velocity is higher at increased primary air flow.

Table 10C.9 Particle cloud velocity estimations from high speed IR imaging at 94 Hz over a distance of 75 cm (ID: AMV101mar22.ptw).

IR-ID	Frame	Metric time [s]	Velocity [m/s]	Reference [m/s]
AMV101mar22	615–624	55.241–55.337	7.8	
AMV101mar22	697–705	56.114–56.199	8.8	
AMV101mar22	773–781	56-922–57-007	8.8	
AMV101mar22	850–858	57.795–57.880	8.8	
Average			8.6	4.4
Standard deviation			0.50	1.3

10C.6.3 Particle Cloud Flame Penetration

Increasing the primary air flow rate increases the axial momentum of the fuel particles making them more likely to penetrate the internal recirculation zone created by the unchanged flow of combustion air. This is well indicated by the IR images showing the averaged thermal signal in figures 10C.42a and 10C.42b for increased and decreased primary air flow, respectively. For increased primary air flow, figure 10C.42a, the cold areas extends beyond 75 cm into the furnace, while at decreased primary air flows, figure 10C.42b, almost no cold particle clouds are observed on an average.

10C.7 Classifier (Particle Size Distribution)

Changing the rotational speed of the classifier above the mill changes the particle size distribution.

10C.7.1 Probe Measurement Results

Both the temperature and the O_2-curve follows the progression of the reference samples. This is also the case for the gas analysis. The direct impact of the change in classifier frequency on the particle size distribution, as discussed in section 10B.3.1, is seemingly very small.

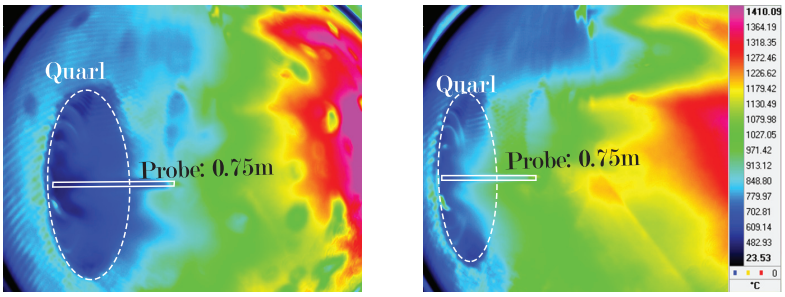

(a) Increased primary air. **(b)** Reduced primary air.

Figure 10C.42 Thermal imaging of burner #11 at (a) increased and (b) reduced PA respectively. The color scale is in °C and may only be considered valid for dense particle clouds, i.e. closest to the burner mouth.

Table 10C.10 Time schedule for classifier run. Below the rotational frequencies of the classifier are listed.

Exp #	Date dd-mm-yyyy	Begin hh:mm	End hh:mm	Setting rpm	Reference rpm
11	01-03-2012	16:05	16:57	15.2	19.2

10C.7.2 Particle Cloud Flame Penetration

No real differences have been observed in the particle size distributions, cf. figures 10B.3 and 10B.3b, in addition similar temperature and chemical species concentrations profiles have been measured between reference runs and after changes to the classifier rotational speed, cf. figures 10C.43 and 10C.43. Thus, similar particle cloud penetration is also expected. Similar trends are observed from the IR-imaging, cf. figure 10C.45a, when compared to Reference flame #1, cf. figure 10C.45b. A dense cold particle cloud with a good spread in the vicinity of the burner is observed and no deep entrainment of cold particles into the furnace.

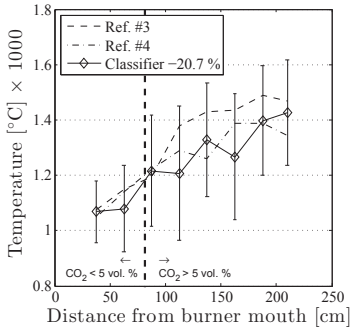

(a) Temperature measurements. Error bars indicate time resolved standard deviations. Temperature measurements to the left of the dashed bar are considered unreliable due to the low CO_2 concentration.

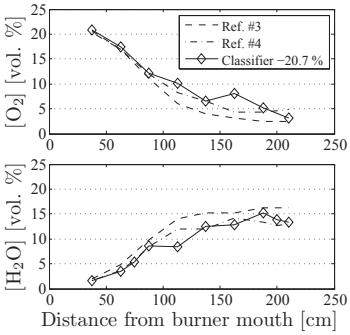

(b) O_2 and H_2O-concentrations. O_2 is given on a dry and H_2O is given on a wet basis.

Figure 10C.43 Classifier frequency changes (a) gas temperatures and (b) O_2 and H_2O- concentration measurements for changes in the rotational speed of the classifier compared to reference flame. The legend numerics indicate the change in classifier frequency.

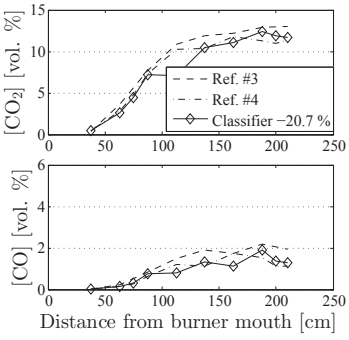

(a) Carbon combustion products given on a dry basis.

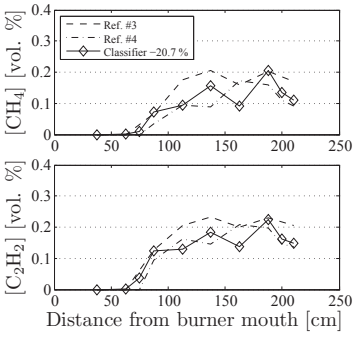

(b) Pyrolysis product concentrations given on a dry basis.

Figure 10C.44 CO_2 and relative CO-concentrations and light hydrocarbon concentration measurements for changes in the classifier rotational speed and compared to reference flame. The legend numerics indicate the change in classifier frequency.

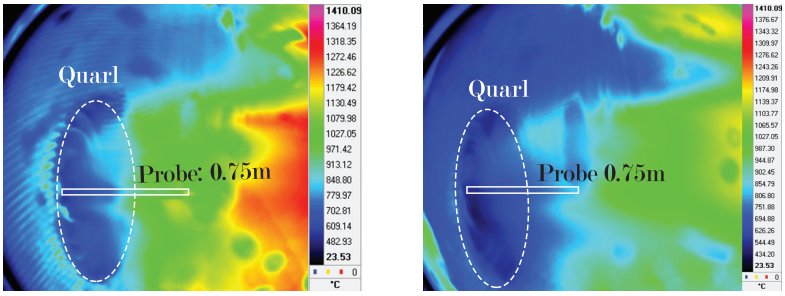

(a) Reduced classifier frequency. **(b)** Reference flame #1.

Figure 10C.45 Thermal imaging of burner #11 at figure 10C.45a reduced classifier frequency and (b) Reference flame 1. The color scale is in °C and may only be considered valid for dense particle clouds, i.e. closest to the burner mouth.

CHAPTER 10D

Results Discussion

In the previous chapter all results are presented and to some extend discussed as observed. This chapter will briefly discuss the results and, when possible, compare them to expectations from theory and literature.

The following discussion is based on a mechanistic understanding of the flame. However, at the time of the analysis, no finished numerical model existed to support the interpretations. The discussions are therefore subject to some degree of speculations. In the moment of writing, new numerical models have been developed, supporting the hypotheses that the following discussions have been based upon.

10D.1 Fuel Variations

Changes in the fuel blend (wood/straw pellets) have been observed by visual inspection of the pellet feed to the mill. By manually inspecting the pellets, cf. figure 10B.1 on page 208, it is believed that the share of straw pellets increases from test day #1 to #2. This change in fuel composition has, however, not been identifiable in either particle sizing or proximate fuel analysis including ash and volatile content. The apparent increase in straw pellet share is therefore believed not to influence the combustion process to significant degree and the fuel blend has been treated as being homogeneous in composition. Care CAMSIZER®however be taken when interpreting the particle size distribution analyses from the CAMSIZER®equipment since the limited experience with this method might bias the result evaluation. However, fairly good corresponance between a CAMSIZER®analysis and a corresponding sieve tower analysis has been demonstrated in section 10B.3.2.

10D.2 Changes in the Reference Flame

Changes in the reference flames have been observed both by visual means and by evaluation of the temperature and gas species analyses. A more unstable flame is found as times progresses. Especially reference flame #4 seems to detach frequently. This could result from an apparent change in the fuel composition, as discussed above. Increasing the share of straw would be expected to influence on the particle size distribution, influencing on the ignition of the fuel particles. Such a change in fuel composition has, however, not been

identifiable by the analysis methods applied (proximate and particle size distribution), as discussed above. In addition to the fuel issues, a decrease in the λ-value has been observed during test day #2, cf. figure 10C.37b, continuously decreasing from 1.1 to around 1.05 across a nine hour time span. This is caused by a decrease in the combustion air as seen in figure 10C.1 comparing the total amount of supplied combustion air and the flow of secondary air specifically for the four reference runs. In general for the two reference runs on test day #2 lower concentrations of pyrolysis products have been observed, cf. figure 10C.4, approximately reducing the CO and C_2H_2 peak values by half and the CH_4 by two thirds. Characterizing the pyrolysis front by the first derivative peak of CO also suggest a flame, on average, closer attached to the burner mouth during test day #2.

For reference run #3 a temperature profile is observed matching both runs from test day #1, figure 10C.3a. Likewise the oxygen profile, figure 10C.3b, matches both reference run #1 and #2. This could indicate better mixing of combustion air with the primary jet taking place close to the burner mouth. No indications in either primary, secondary, or tertiary air flow rates explain such behavior, cf. figures C.2, C.7 and C.8, respectively.

A generally lower temperature profile measured in reference flame #4, compared to the other reference runs, could explain a slower release of pyrolysis product and consumption of oxygen. IR-imaging also suggest a qualitatively consistent lower particle cloud temperature as the particles enters the furnace, cf. figure 10C.13b.

10D.3 Individual Parameter Changes

The systematic parameter study gave rise to a number of flame responses quantified by the probe measurements and assessed by the visual instrumentation. The following will briefly discuss the individual parameter changes.

10D.3.1 Secondary Air Flow Rate

The flame response to the change in secondary air at constant air split is primarily found in the axial development of the CO and unburned hydro carbons (UBC). Maintaining the same air split and flow of primary air leads to a fuel leaner flame when increasing the supplied quantities of combustion air, while also increasing the overall swirl number due to the gain in rotational momentum. Lower quantities of CO and UBC are found at distances $> 140\,\text{cm}$ from the burner mouth. This corresponds to the expected response as the stoichiometric conditions are changed towards fuel leaner conditions.

Decreasing the combustion air flow rate makes the conditions richer in fuel and the flame responds with a slightly higher level of CH_4 at distances $> 140\,\text{cm}$ from the burner mouth. Also corresponding to previous full-scale

co-firing experiences [7] were significantly lower burn-out were achieved when decreasing the air to fuel ratio.

Since the CO and the UBC profiles all start to deviate from the reference flame measurements at the same distance from the burner mouth, this gives a good indication at which effective distance from the burner mouth such an in- or decrease in the secondary air influences on the centerline values.

Interestingly, it seems like both an increase and a decrease in the swirl number could cause a local peak in the pyrolysis gases at distances approximately 140 cm from the burner mouth. Increasing the combustion air flow rate under constant primary air flow will effectively increase the relative rotational momentum of the flame. During the primary air flow rate changes, as will be discussed in section 10D.3.5, an increase in the primary air flow rate, an effective decrease in swirl number, leads to the same phenomena of a local peak in the pyrolysis products. Adjusting the primary air flow rate will, however, also change the inlet speed of the fuel particles, etc. in addition to altering the overall swirl number.

10D.3.2 SA/TA Air-Split

Changing the air split gives rise to a significant flame response. Maintaining the stoichiometric conditions in the flame, changing the air split essentially means to change the velocities of the combustion airs with a constant mass flow rate. Increasing the air split, defined as air split over total combustion air, will locally increase the swirl number close to the centerline, potentially creating a strong internal recirculation zone close to the burner mouth. This is well reflected in all data obtained, cf. figures 10C.22 and 10C.24.

Contrary, decreasing the air split will increase the effect of the axial momentum of the primary jet along the centerline. Limited mixing is captured well in the O_2 and temperature profiles for decreased air split, figures 10C.22a and 10C.22b.

10D.3.3 Secondary Swirl

Decreasing the secondary swirl is expected to elongate the flame and offset the internal recirculation zone further into the boiler [33]. Also shifting towards a more fuel penetrating burner configuration, reduced swirl number, pushes the CO level in the radial direction [31] investigated in a 2.5 MW_{th} test furnace, IFRF furnace no. 1. The effect should be qualitatively comparable to a decrease in air split and possibly to an increase in primary air, both effectively decreasing the rotational momentum close to the centerline relative to the axial momentum. When comparing figures 10C.28 and 10C.29 showing the temperature and gas concentration profiles of the reduced secondary air swirl flame with the corresponding graphs for air split changes, figures 10C.22 and 10C.24, similar trends can be found, as expected. Lower temperatures

and production of pyrolysis/combustion products with a slow consumption of oxygen.

10D.3.4 Tertiary Swirl

At constant stoichiometric conditions, a decrease in the tertiary air swirl will decrease the overall swirl number of the flame. However, because the flow rate of the secondary air is maintained, the mixing and ignition pattern in the near burner field is not expected to be influenced to a significant degree. Further from the burner mouth, similar effects are expected, comparable to a decrement in the secondary air swirl or e.g. increasing air split, however, in both cases to a less pronounced degree, due to the fact that all measured data have been collected along the centerline where the effect of the secondary air shields the traversing probe from changes in the tertiary air flow. All expectations are reflected to a good degree in the obtained data, cf. figures 10C.32 and 10C.34.

10D.3.5 Primary Air Flow Rate

Changes in the primary air flow rate yield significant changes to all monitored values. Increasing the flow rate, and thereby the air speed, of the primary air will intuitively increase the penetration depth of the fuel particles (λ is kept constant, decreasing the swirl-number adding to the effect). An increase in the CO level along the centerline corresponds to findings in the semi-industrial scale IFRF facilities [391] where the position of the centertube is used to control the penetration depth of the fuel particles. However, the opposite effect on the development of both the temperature, water, CO_2, and O_2 profiles is observed. A significant decrease in temperature is observed at all positions when decreasing the primary air flow with a qualitative corresponding positive offset in the O_2 concentrations and drops in H_2O, CO, and CO_2 levels. When decreasing the primary air flow local peaks of pyrolysis products: CO, CH_4, and C_2H_2 are detected consistently around 140 cm from the burner mouth, cf. figure 10C.41. These local maximums corresponds to a local minimum in the O_2 concentration, cf. figure 10C.39b. This indicates a critical limit where mixing between the primary air jet and the swirling combustion air is taking place.

10D.3.6 Classifier Frequency

Changing the rotational speed of the classifier should effectively change the particle size distribution of the dust transported to the burner. This could however not be seen, to significant degree, in the CAMSIZER®analyses conducted on the dust samples, cf. figures 10B.2 and 10B.3. No changes are observed in the pressure drop across the classifier, cf. figure 10C.38, which would be expected to change when cut-off value is changed.

10D.3.7 Characteristics Profiles

From an ignition and flame stabilization point of view, certain flame properties play central roles. Besides flow fields, which are not characterized in this campaign, the gas temperature, the particle temperature, and the oxidative properties of the gas at discrete points in space are all parameters that influence on the flame.

This section will summarize and directly compare measurement results at either fixed distances from the burner mouth or report locations for selected threshold values. In this way, an overview of the flame responses can be established for quick comparison.

The gas analysis results show that especially the pyrolysis products, CO, CH_4, C_2H_2, are sensitive to the applied changes in process parameters. Figure 10D.1 illustrates the positions of the peak concentrations for all tested operational settings.

Although a distinct CH_4 peak is hard to identify in most of the operational settings, figure 10D.1 shows how the pyrolysis gas concentrations peak relatively far from the burner mouth: 1.5–2.0 meters.

Considering the position of the CO/CO_2-ratio peak gives a good qualitative overview of the oxidizing properties of the current flame. When assessing the peak positions given in figure 10D.1a setting by setting it reacts to an extend to expectations: Increasing the air split (AS), i.e. increasing the relative flow of secondary to tertiary air, intuitively strengthen the internal recirculation zone (IRZ) and thus pulls the flame closer to the quarl, while a corresponding decrease in air split will weaken the internal recirculation zone and thus the momentum of the primary jet is expected to enlongate the flame and push away the pyrolysis gas peak. These effects are both indicated by figure 10D.1a, showing the CO/CO_2 peaks closer and further away from the burner mouth, respectively.

Likewise, an increase in secondary air at constant tertiary air will increase the strength of the internal recirculation zone while also increase the oxygen-excess and thus is expected to cause a decrease in the concentration of pyrolysis gases, primarily CH_4, cf. figure 10D.1b. Contrary, decreasing the secondary air is expected to pull the flame closer to the quarl, as seen on figure 10D.1a.

When decreasing swirl, either secondary or tertiary air swirl, the internal recirculation zone is weakened and the presence of a CO peak is no longer found, cf. figure 10D.1a.

Figure 10D.2 summarizes the flame responses by showing the position at which a thresh hold value for figure 10D.2a the gas phase temperature and figure 10D.2b the local O_2-concentration is reached.

The gas phase temperature is a key feature when evaluating the flame response. Figure 10D.2a indicate at which distance from the burner mouth a gas phase temperature of 1400 °C is reached. Again, tendencies can be identified corresponding to expectations:

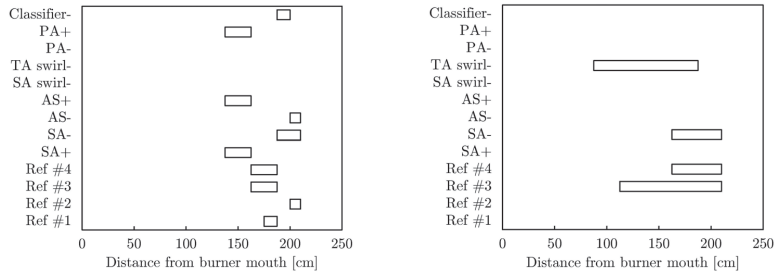

(a) CO/CO_2-ratio peak. **(b)** CH_4 peak.

Figure 10D.1 Illustrating the peak positions of the pyrolysis products (a) CO and (b) CH_4 as a function of distance from the burner mouth. If no bar is present a peak cannot be identified.

Comparing the in- and decrease in air split result in the temperature to exceed 1400 °C closer and further away from the burner mouth, respectively. This corresponds well to the expected strengthening and weakening of the internal recirculation zone, i.e. drawing more and less hot combustion gas back towards the quarl, respectively. Similar results, however, less profound is seen for the in- and decrease in secondary air.

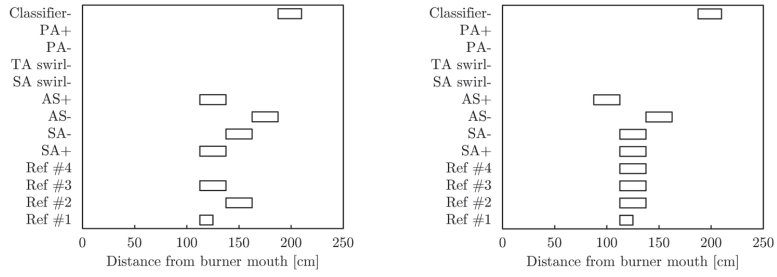

(a) Identifies the position at which the gas phase temperature exceeds 1400 °C.

(b) Identifies the position at which the O_2 concentrations decreases below 5 vol. %.

Figure 10D.2 Summarizes characteristic lengths for temperature and O_2-concentrations at all tested operational conditions. If no bar is presented the thresh hold value has not been reached.

Conclusions

During the week 9, 2012 campaign at Amager power station unit 1 (AMV1) the following parameters where adjusted and the flame response measured using the centreline traversing probe developed to the purpose:

- Secondary air: 20 % increase and 16.7 % decrease (mass flow rate)
- Air-split: 12 % increase and 38 % decrease (mass flow rate/mass flow rate)
- Secondary air swirl: 20 % decrease (swirler position)
- Tertiary air swirl: 20 % decrease (swirler position)
- Primary air flow: 6.7 % increase and 5.3 % decrease (mass flow rate)
- Particle size distribution through classifier adjustment: −20.7 % decrease (classifier frequency)

The flame was mapped using a water cooled probe traversing along the axial centreline of the flame, entering the boiler through the oil lance entrance of the burner. The probe was used for:

- Gas composition measurements using extractive gas methods connected to FTIR, UV spectrometer and a paramagnetic oxygen analyzer for optical gas temperature and light combustion gas analysis.

Optical observations were made through a view port located on the side of the boiler:

- IR high speed imaging was used to track particle cloud movement as cold particles entered the furnace
- Video imaging was used to observe the general shape of the flame and phenomena like flame lift and attachment

Four reference runs have been conducted during two test days; one in the beginning and end of each day. Significant differences have been observed especially when analyzing the pyrolysis products: CO, CH_4, C_2H_2, but also differences, however less pronounced, are seen in both temperature and oxygen

concentrations. This is attributed to changes in fuel composition, where a larger share of straw pellets are found when inspecting the pellet feed to the mill during test day #2. This change has, however, not been identifiable by either particle size distributions of the dust feed to the burner nor from proximate analysis of the dust. Another explanation could be changes in the stoichiometric conditions going towards a more fuel rich flame as test day #2 progresses.

Comparing the parameter study flame responses to the reference measurement closest in time;

Significant changes in the flame response have been observed when:

- Increasing the SA mass flow (+20 %)
- Decreasing the AS (−38 %)
- Decreasing the SA swirl (−20 %)
- Decreasing the PA mass flow (−5.3 %)

Less pronounced but still obvious changes in flame response have been observed when:

- Increasing the AS (+12 %)
- Decreasing the TA swirl (−20 %)
- Increasing the PA mass flow (6.7 %)

Little or no flame response has been observed when

- Decreasing the SA mass flow (−16.7 %)
- Decreasing the classifier frequency (−20.7 %)

Besides providing much needed full-scale data this campaign also served to approve the method of course flame mapping as well as to test the equipment specially developed for this campaign. Both objective have been proven with success in this work.

This report is written in the GREEN research project (power Generation from REnewable Energy) and covers the experimental results from the near-burner full-scale campaign at Amagerværket Unit 1 (AMV1) carried out in week 9, 2012.
A single low-NOx multifuel burner is investigated across two and a half days firing primarily wood pellets. Flame mapping is conducted during large amplitude parameter changes using both optical and extractive probe methods.

DTU Chemical Engineering
Department of Chemical and Biochemical Engineering
Technical University of Denmark

Søltofts Plads
Bygning 229
2800 Kgs. Lyngby
Tlf. 45 25 28 00
Fax 45 88 22 58
E-mail kt@kt.dtu.dk
Web www.kt.dtu.dk

Herningværket

Flame Response Characterization

Week 49, 2012

DTU Chemical Engineering
Department of Chemical and Biochemical Engineering

Abstract

This report is written in the power Generation from REnewable ENergy (GREEN) project and presents the measurement results from the full scale campaign conducted at Herning power station (HEV) across four days (three test days) in week 49, 2012.

The campaign is built around intrusive probe measurements entering the quarl and boiler domain through the center of the burner, replacing the oil-lance. The probe is equipped with a heated tube for extractive gas composition measurements; O_2, CO_2, H_2O, CO, CH_4, C_2H_2, and C_2H_4 and fibre optics for radiation derived gas phase temperature readings. With an effective penetration depth of four meters, the probe was able to penetrate the full length of the flame.

Optical access was obtained from view ports in side of the boiler and from the back wall. Video sequences in both the visible spectrum (VIS) and infrared (IR) spectrum was acquired at all operational conditions.

A parameter screening was performed on the first day making subjective assessments of the flame response to changes in the operational conditions using primarily optical observations, creating a base for the further development of a full experimental matrix. This includes: Changes to the particle size distribution (PSD), reducing the tertiary air (TA) swirl, lowering the air split (AS), reducing the primary air (PA) temperature, and decreasing the load. These experiments have been carried out across two consecutive test days with reference runs conducted at the beginning of each day.

All parameters other than the variable in focus has been maintained as close to reference values as possible in order to minimize the influence of secondary parameters in the flame response.

The flame can in general be characterized as highly swirled with strong recirculation zones and high convective flux of heat and combustion products to the near burner field. Changes to the flow field was found to impact the flame response to the greatest extent, expect for the load decrement, which in terms also can be classified as flow field changes. Reduction in the primary air temperature and increasing particle size distribution was found to incur only minor responses (in the investigated interval).

Table of Contents

CHAPTER 11A

Plant and Burner Description

The experiments are conducted at Herning power station (HEV), a newly renovated combined heat and power (CHP) plant firing 100 % biomass fuel. It combines both grate and suspension firing making it very flexible with respect to fuel sources and with a relatively high efficiency. It consists of a grate contributing with approximately 60 % of the thermal load, four identical multi-fuel burners distributed on two levels, and two gas burners on the upper level.

11A.1 Plant and Burner Description

This campaign will carry out experiments on burner 31 located on the upper multi-fuel burner level, below the gas burner level, cf. figure 11A.1. Burner 31 is a multi fuel BWE unit capable of firing straw-dust, wood-dust, and gas. Each burner is fed from its own disc mill making it possible to operate the burners independently of each other.

A top view of gallery 30 is shown in figure 11A.2. The drawing is drawn to scale but the indicated dimensions are only approximative. This figure shows how the two-part probe is capable of reaching almost half way through the boiler.

The burner is of a quintuple concentric construction. The center tube was originally used for the oil-lance. This is no longer available, but during the campaign the center tube has been used to insert the probe. The second concentric register is used for gas firing. Third concentric register is used for primary air, carrying air and fuel dust. The primary air and the carrying air (including dust) is mixed up-stream of the burner mouth and both channels are swirled by fixed turbulators just before mixing. The fourth and fifth concentric registers are used for secondary and tertiary air respectively. Adjustable swirlers are installed in both channels. The flow of air to the secondary and tertiary air channels are split after the air pre-heater (APH) and thus, enters the boiler at the same temperature.

A cross section of the burner is presented in figure 11A.3.

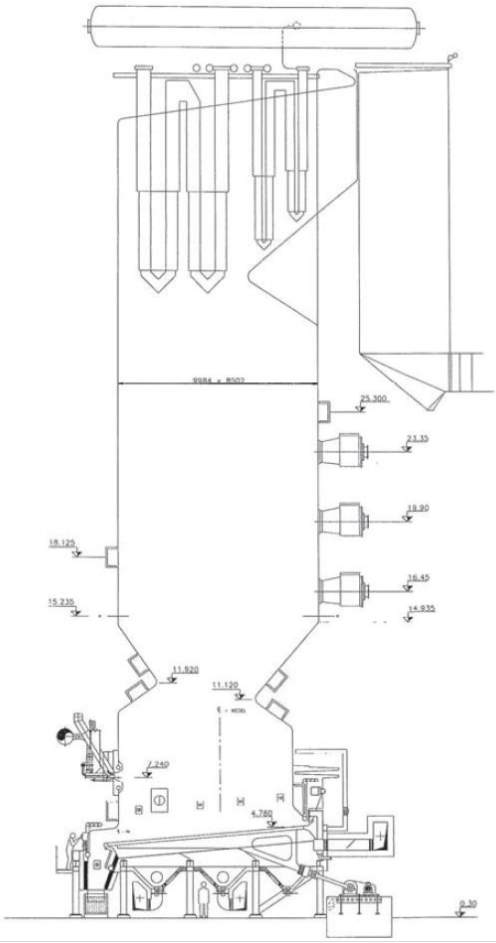

Figure 11A.1 Side view sketch of the HEV boiler. Burner #31 is installed on the middle burner level.

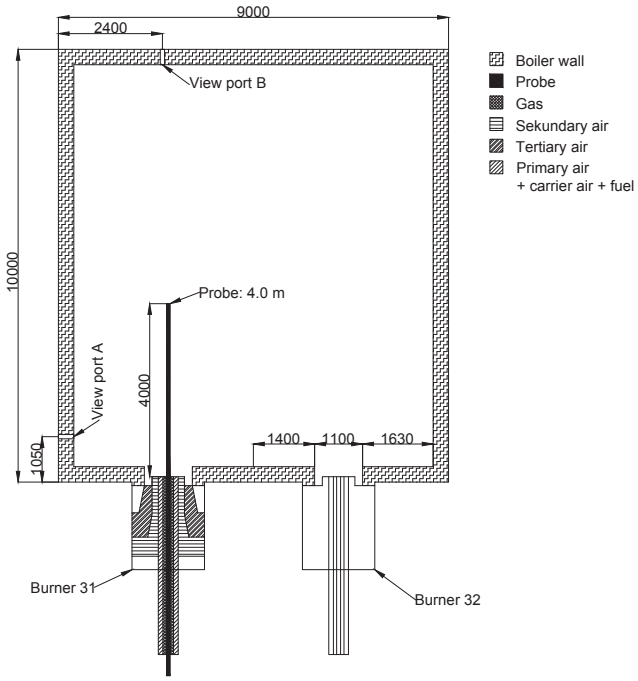

Figure 11A.2 Top view of HEV gallery 30. The drawing is drawn to scale, but indicated length scales are only approximative. Units are given in milimeters unless otherwise indicated.

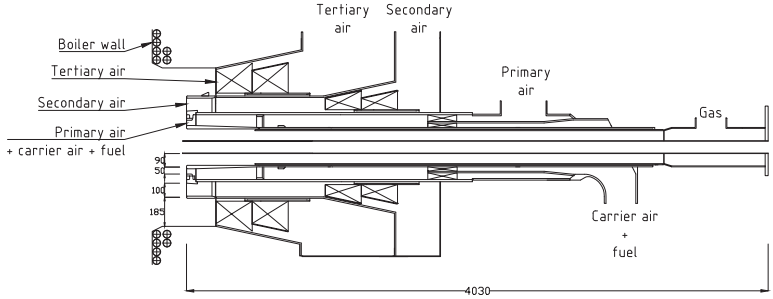

Figure 11A.3 Cross section of the burner. The drawing has been simplified has been simplified for illustrative purposes. The drawing is made to scale.

CHAPTER 11B

Experimental Schedule and Fuels

This campaign stretches across three test days including one pilot day and two regular test days denoted test day #0, and test day #1 and #2, respectively. This chapter will summarize the overall schedule and include the fuel analysis results. For detailed explanations of the individual settings please refer to the respective result presentations in the following chapters.

11B.1 Experimental Schedule

The test campaign is divided into two main parts:

1. A parameter screening focusing on subjective assessment of the flame response to large changes in the operational conditions.

2. A detailed quantitative analysis of the flame response to selected operational conditions.

The operational conditions selected for detailed mapping is based on the results of the parameter screening. Thus the progress of the experimental campaign can be outlined as shown in figure 11B.1.

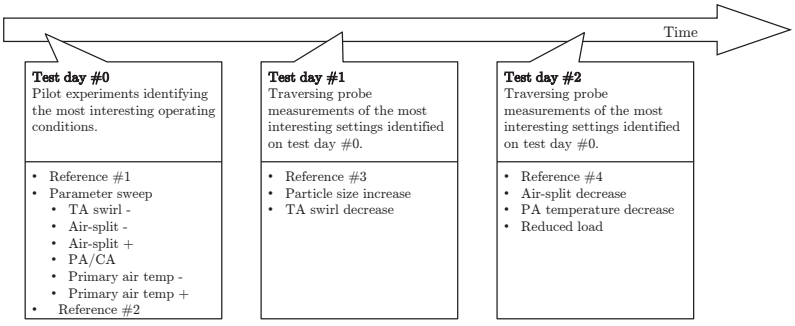

Figure 11B.1 Outline of the experimental schedule.

Figure 11B.1 lists the parameters analyzed during the entirety of the full-scale campaign. For detailed information on quantified parameter values

please refer to chapters 11C and 11D for screening and detailed mappings respectively.

11B.2 Fuels

This section summarizes all data collected up-stream of the furnace. This primarily includes chemical analysis and particle size distributions of the fuel pellets and dust.

11B.2.1 Collection of Samples

Fuel samples were collected just before and just after the disc mill. Pellet samples were collected via a high powered vacuum pump from the buffer tank directly above the mill, cf. figure 11B.2.

Figure 11B.2 The mill setup at HEV.

All collected dust samples are listed in table 11B.1 and can be identified and related to operational conditions by date and time. All samples have been analysed at Enstedværket Laboratory, Aabenraa, Denmark for proximate analysis and particle size distributions by both sieve analysis and by using CAMSIZER®equipment (projected imaging).

Wood pellet samples are collected on a daily basis as listed in table 11B.2. A single wood chip sample is collected from up stream of the grate. Complete chemical analysis (ultimate and proximate) has been conducted on pellet sample #2.

Table 11B.1 Collected dust samples.

#	Date dd-mm-yyyy	Time hh:mm	Disc space* mm	Comments
1	04-12-2012	11:35	1.32	
2	05-12-2012	13:20	1.32	Big sample
3	05-12-2012	17:05	2.0	
4	05-12-2012	18:35	2.0	
5	05-12-2012	20:08	1.36	
6	06-12-2012	11:25	1.36	
7	06-12-2012	18:10	1.36	Low load

* Refers to the spacing between the discs in the disc mill grinding the fuel pellets to dust.

Table 11B.2 Collected wood pellets and chip samples.

#	Date dd-mm-yyyy	Time hh:mm	Comments
1	04-12-2012	11:45	
2	05-12-2012	13:15	Complete chemical analysis
3	06-12-2012	11:35	
4	06-12-2012	13:20	Wood chip sample

11B.2.2 Chemical Analysis

Proximate analyses have been conducted on all samples listed in table 11B.1.

Table 11B.3 Proximate analysis results for the dust samples collected at HEV.

#	Date dd-mm-yyyy	Time hh:mm	Moisture wt. %(wet)	Ash wt. %(dry)	Volatiles wt. %(dry)	Fixed C wt. %(dry)
1	04-12-2012	11:35	6.8 ± 0.2	1.2 ± 0.2	81.6 ± 1.6	17.2
2	05-12-2012	13:20	6.8 ± 0.2	0.8 ± 0.2	83.3 ± 1.7	15.9
3	05-12-2012	17:05	6.8 ± 0.2	0.8 ± 0.2	83.1 ± 1.7	16.1
4	05-12-2012	18:35	6.9 ± 0.2	0.9 ± 0.2	82.7 ± 1.7	16.4
5	05-12-2012	20:08	6.9 ± 0.2	0.9 ± 0.2	83.0 ± 1.7	16.1
6	06-12-2012	11:25	6.8 ± 0.2	1.2 ± 0.2	82.1 ± 1.6	16.8
7	06-12-2012	18:10	6.9 ± 0.2	1.3 ± 0.2	81.9 ± 1.6	16.9

As seen from table 11B.3 and figure 11B.3 only small fluctuations are observed in fuel composition during the entire campaign. Indications of slightly better quality (lower ash and fixed carbon content and higher volatile fraction) fuels during test day #2.

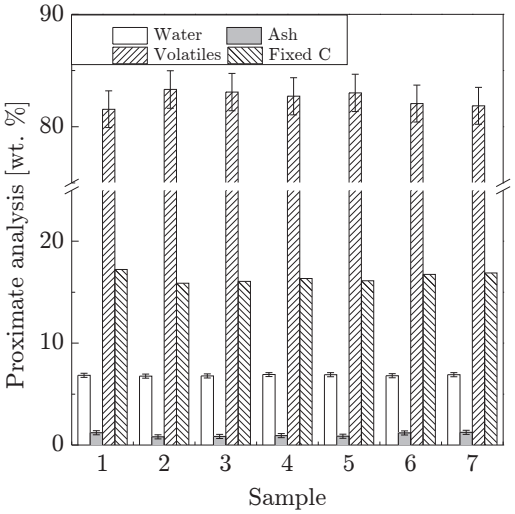

Figure 11B.3 Proximate analysis results of the HEV fuels.

11B.2.3 Particle Size Distribution

Dust samples have been collected by vacuum cleaner from a horizontal pipe positioned directly downstream the mill, cf. figure 11B.2. A rectangular mouthpiece was mounted on the suction tube and inserted into the dust pipe, thus minimizing biasing in one dimension. Samples were retrieved according to table 11B.1 and the dust sample ID assigned in this table will be used to refer to the individual results.

All dust samples (#1–7) have been analyzed employing both standard sieve tower methods (DS/EN 15149-2:2010) as well as by CAMSIZER®characterization. Because of the differences between the two methods and the lack of standards for the optical particle shape and size characterization, comparison between the measurements results will be presented for each fuel in the following.

The CAMSIZER®data are presented as function of the Martin minimum diameter, $x_{\mathrm{Ma,min}}$, cf. figure 2.8 on page 26. Whereas the size categories for the sieve tower analysis are strictly defined by the mesh size.

As can be seen from figures 11B.4 and 11B.6, the trends between the CAMSIZER®and the sieve tower method appear consistent. In general, the sieve tower analysis under predicts the fraction of smaller particles, relative to the CAMSIZER®results. Vice versa for the larger particles. However, considering the differences between the two methods and in particular the complexity of the post processing, then the data appear similar within reasonable limits.

Figure 11B.7 compares the CAMSIZER®data for all seven dust samples.

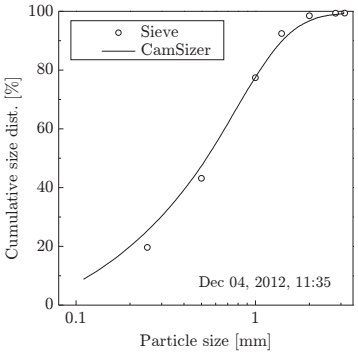

Figure 11B.4 PSD data from test day #0. Dust #1.

All samples lie within a relatively narrow band. The dark blue and green lines (05-12-2013 17:05 and 05-12-2013 18:35) samples are taken during increased particle size operation, i.e. the mill settings have been changed. Thus, shifting the cumulative distribution curve to towards larger particles, as expected.

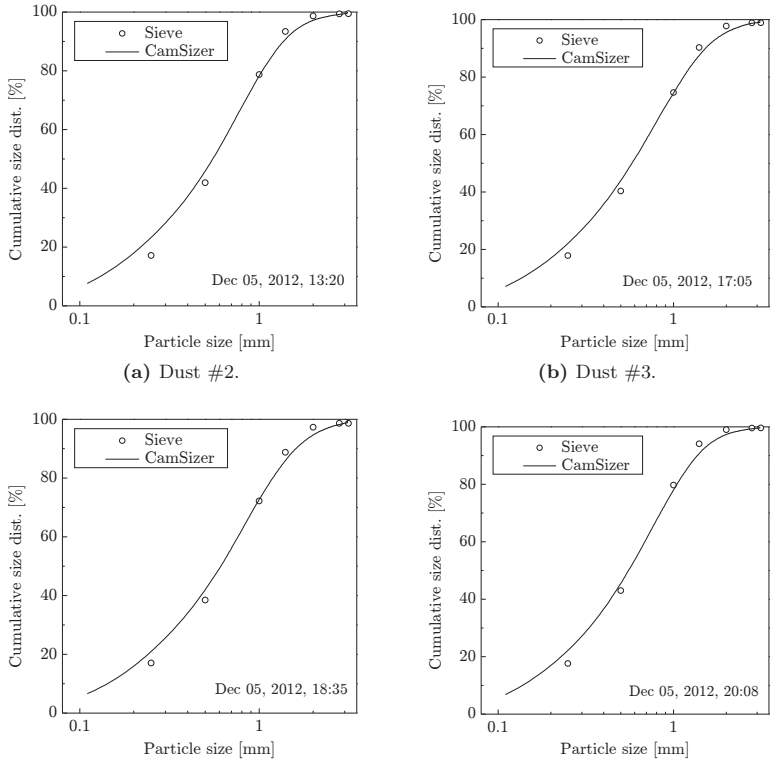

(a) Dust #2. **(b)** Dust #3.

(c) Dust #4. **(d)** Dust #5.

Figure 11B.5 PSD data from test day #1.

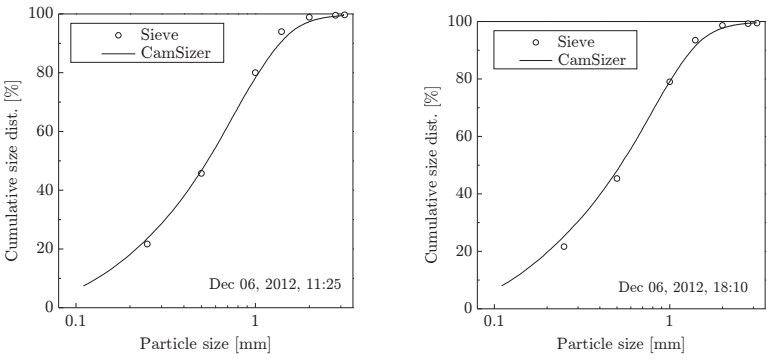

(a) Dust #6. **(b)** Dust #7.

Figure 11B.6 PSD data from test day #2.

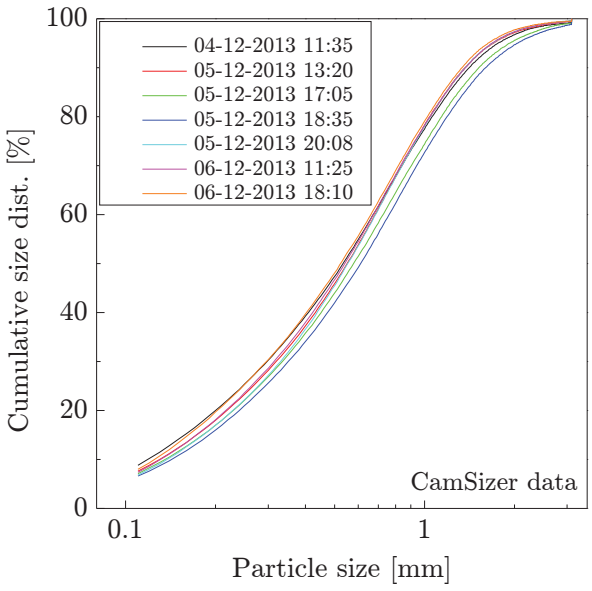

Figure 11B.7 Direct comparison of all particle size data from the CAMSIZER®based on the $x_{\mathrm{Ma,min}}$ diameter.

CHAPTER 11C

Parameter Screening

The aim of this campaign is to investigate the flame response while systematically introducing a step disturbance to selected operational parameters. It is desirable to investigate the operational conditions leading to a significant flame response within the measured flame properties: Chemical species concentrations, gas phase temperature, and/or optical observations. To ensure a quantifiable flame response to the investigated operating conditions a series of pilot experiments were carried out during which three extractive probe measurements and both VIS and IR observations were acquired per setting. This will constitute the basis for the construction of an extended experimental matrix for more detailed flame characterization.

Except for the O_2-concentration, of which readings could be acquired continuously, none of the other gas concentration measurements could be evaluated on the site. Hence, the design of the experimental matrix for the following test days are solely based on O_2-readings and subjective judgement from the optical observations.

This chapter outlines the results of this initial parameter screening.

11C.1 Selected Operational Conditions

A total of eight screening experiments were carried out including one complete reference run with a spatial discretization of 25 cm and two double determination analyses. All other screening experiments included three measurement points at 75, 225, and 350 cm from the burner mouth as well as both IR and video imaging.

Table 11C.1 lists the experimental matrix for the screening experiments including the relative change in the specific parameter, and its absolute and reference setting.

11C.2 Extractive Probe Measurements

Gas concentration measurements were conducted using extractive gas sampling through the probe. In the following the main pyrolysis and combustion products will be presented as well as the oxygen level. Gas probing was conducted at $x/D = 0.7$, 2.1, and 3.2, corresponding to 75, 225, and 350 cm from the burner mouth.

Table 11C.1 Overview of the screening experiments.

Exp #	Time hh:mm	Parameter	Setting Change [%]	Abs	Ref	Unit
01	11:53	Reference*	—	—	—	—
02	16:16	TA swirl	−61	35	90	%
03	16:49	AS**	−67	5	15	—
04	17:21	AS**	100	30	15	—
05	18:02	PA/CA		0.45		—
06	18:50	PA temp	−28	137	190	°C
07	19:38	PA temp	37	260	190	°C
08	20:38	Reference	—	—	—	—

* Complete reference run with a 25 cm spatial discretization.
** The air split, AS, is defined as $AS = \frac{SA}{TA}$

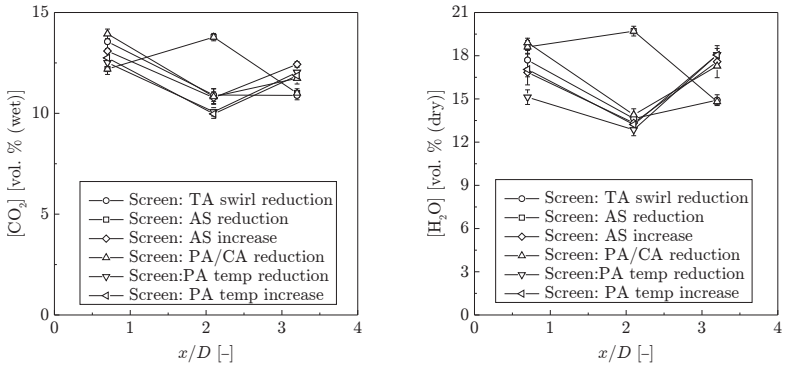

(a) CO_2-concentration screening. **(b)** H_2O-concentration screening.

Figure 11C.1 Direct comparison of combustion products at multiple operational conditions.

Figure 11C.1 shows a direct comparison of the combustion products CO_2 and H_2O for all screened operational conditions. Similar trends appear for most runs: Air split increase, PA/carrier air (CA) reduction, primary air temperature in- and decrease. They all seem to reach a local minimum for $x/D \in]0.7; 2.1[$. A reduction in the tertiary air swirl (○) lead to a stable level after an overall concentration reduction from $x/D = 0.7$ to 2.1. Reducing the air split, i.e. reducing the flow of SA while correspondingly increasing the tertiary air flow, inverts the trend, thus resulting in a local maximum. It is interesting to see, how the reduction in tertiary air swirl, by changing the resulting angle of the velocity vector, results in the same level of combustion products (both CO_2 and H_2O) as reducing the air split. Because the concen-

trations at $x/D = 3.2$ are not equal for all operational conditions, it implies that the operational condition influences the local environment even at 350 cm from the burner mouth.

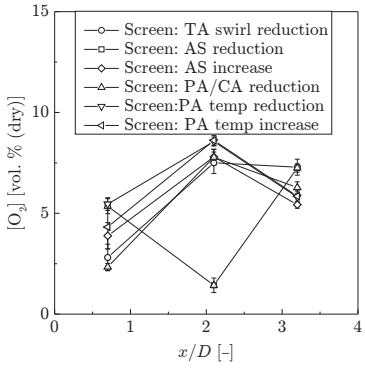

Figure 11C.2 Direct comparison of local O_2-concentrations at multiple operational conditions.

The opposite trends appears when observing the local O_2-concentrations, cf. figure 11C.2, indicating mixing as the limiting factor for reaction.

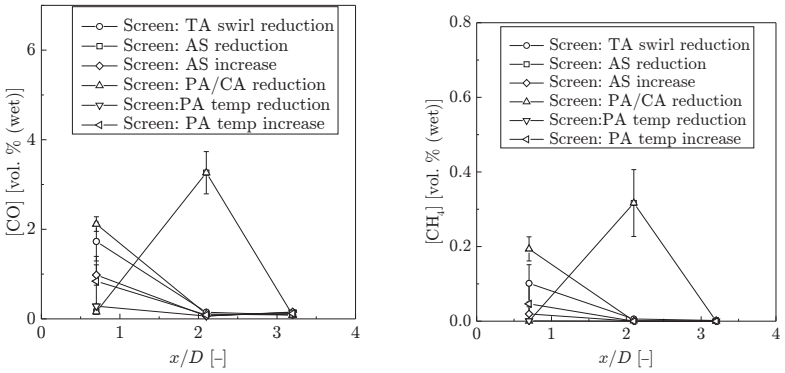

(a) CO-concentration screening. **(b)** H_2O-concentration screening.

Figure 11C.3 Direct comparison of pyrolysis products at multiple operational conditions.

The development of the pyrolysis gas concentration profiles differs from both the combustion products and the oxygen presented in figures 11C.1 and 11C.2 as they do not pass through local extremes, except for when reducing the air split. Also the differences are more pronounced in the near

burner field. Where for example a net reduction in the temperature of the particle laden flow results in only trace amounts of pyrolysis gases (both for the PA/CA reduction and the direct decrease in primary air temperature). The absence of pyrolysis gases in the near burner field during reduced air split operation indicate how the devolatilization zone has been separated from the burner nozzle and stabilized further down stream.

It is noticeable how the reduction in TA swirl results both in the highest concentration of pyrolysis and combustion products as well as oxygen concentration. Whether or not this can be attributed to general time bias can not be determined from the data in hand.

11C.3 Optical Observations

In this section, the image material in both the VIS and IR spectrum is presented. The material is presented across settings to facilitate direct and easy comparison.

11C.3.1 Observations in the VIS

Figure 11C.4 compares images in the VIS for all screened operational conditions. In general, all flames are short, wide, and well attached to the burner quarl. Direct changes to the flow field, by altering the swirl levels, are found to impact the flame shape and flame stability to the greatest extent.

A subjective appraisal of similar flames and observed stability, links a narrower and longer flame to more unstable operation. I.e. figure 11C.4c indicates an unstable flame as the base of the flame in the quarl area is noticably narrower and the over all flame shape more elongated compared to e.g. the reference flame in figures 11C.4a and 11C.4b.

11C.3.2 Optical Observations in the IR Spectrum

The IR images are a great help when comparing operational conditions of particle laden flows. The cold particle clouds, and in some cases ropes, of particles entraining the hot combustion gases can be followed as dark shadow in the IR images shown in figures 11C.5 and 11C.6. Thus, making evaluation of mixing patterns and particle dispersion possible.

Figure 11C.5 shows averaged images of all screened operational conditions. Averaging across 10 s. Distinct ropes of particles are visible in the illustrated scenarios. Based on the number of ropes appearing they presumably originate from the fixed swirlers in the primary air and carrier air tubes rather than from the teeth at the burner exit.

From the averaged images it appears clearly how cold particles are penetrating the quarl section under all operational conditions. Changing the swirl

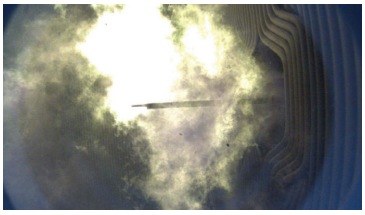

(a) Exp #01, reference.

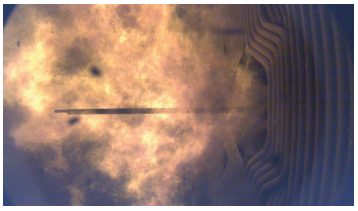

(b) Exp #08, reference.

(c) Exp #02, reduced TA swirl.

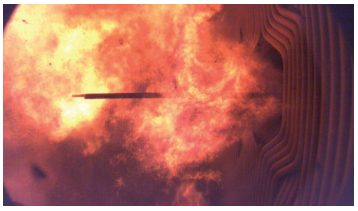

(d) Exp #03, reduced AS.

(e) Exp #04, increased AS.

(f) Exp #05, PA/CA.

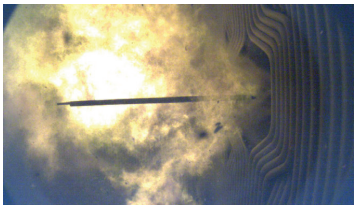

(g) Exp #06, reduced PA temperature.

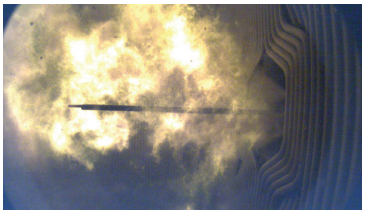

(h) Exp #07, increased PA temperature.

Figure 11C.4 Overview of all screening experiments.

number seems to have some effect on the particle cloud direction which appears to be more axial in the case of low swirl number, i.e. high (relative) axial to tangential momentum. On the contrary the radial dispersion of particles appears good in the reference flame featuring high swirl numbers. A visible difference can also be seen when increasing the primary air temperature where the particles appears to be heating up faster, i.e. disappearing as a dark shadow.

Looking at instantaneous images in the IR spectrum, cf. figure 11C.6 some of the effects can be observed to an even greater extent. I.e., by reducing the tertiary air swirl, cf. figure 11C.6c, large clouds of cold particles are now allowed to penetrate far into the burner in an almost horizontal trajectory.

11C.4 Summary

The visual observations (in the VIS) gave a good first impression of the flame. At stable operation the flame appears well attached and only small fluctuations are seen. Of course the system is highly turbulent but the difference between operating a stable flame, e.g. the reference flame, and an unsteady flame, e.g. the reduced tertiary air swirl flame, can be easily recognized. The characteristics of the particle roping, visualized in the IR spectrum, is perhaps the best indication linking the operational conditions to the observed flame response during stable and unstable operation respectively. Following this train of thought the flame becomes unstable as function of roping angle and penetration depth. I.e., the less radially dispersed the particle cloud, the less stable a flame. However, fixating on such observations as the sole causation for flame instability is most likely incorrect as the gas concentration data indicate shifts in pyrolysis and combustion zones, independent from apparent particle trajectories making gas phase mixing properties just as important.

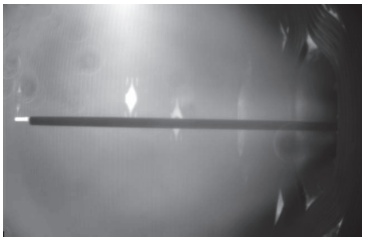

(a) Exp #01, reference.

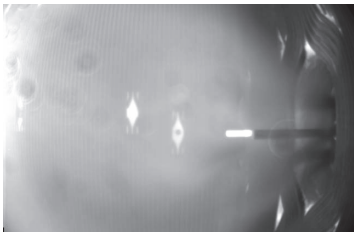

(b) Exp #08, reference.

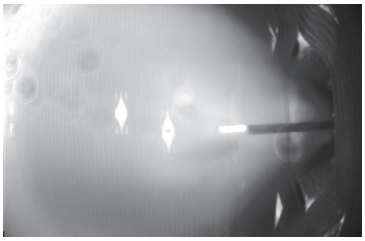

(c) Exp #02, reduced TA swirl.

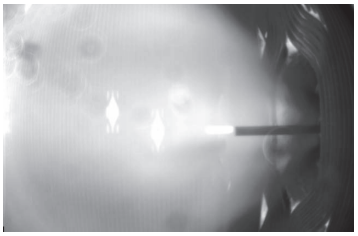

(d) Exp #03, reduced AS.

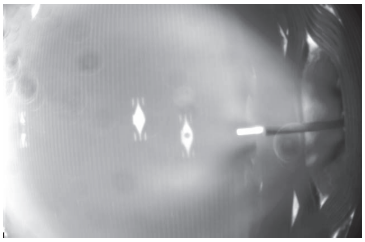

(e) Exp #04, increased AS.

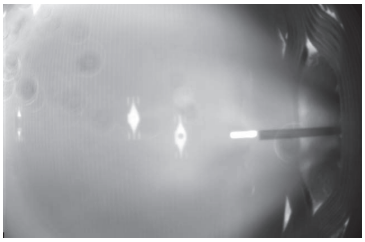

(f) Exp #05, PA/CA.

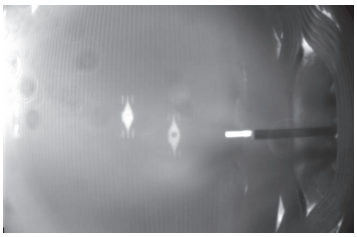

(g) Exp #06, reduced PA temperature.

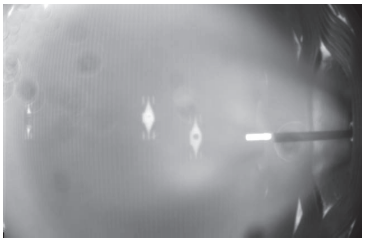

(h) Exp #07, increased PA temperature.

Figure 11C.5 Overview of all screening experiments. The IR images are averaged across 1024 frames and presented on the same intensity scale. The probe is inserted 200 cm in (a) and 75 cm in (b) to (h).

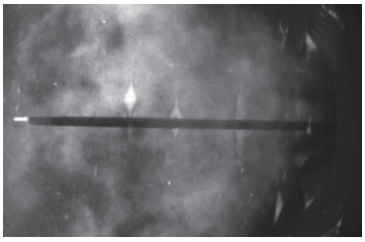

(a) Exp #01, reference.

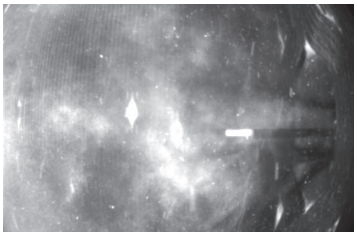

(b) Exp #08, reference.

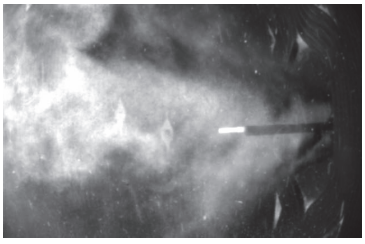

(c) Exp #02, reduced TA swirl.

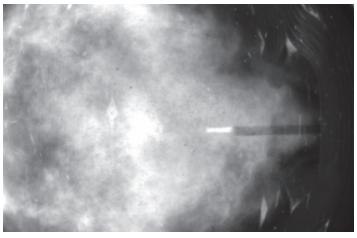

(d) Exp #03, reduced AS.

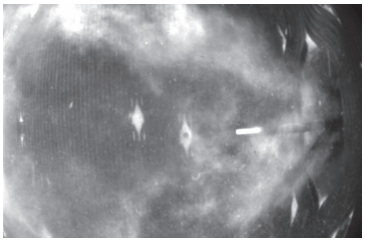

(e) Exp #04, increased AS.

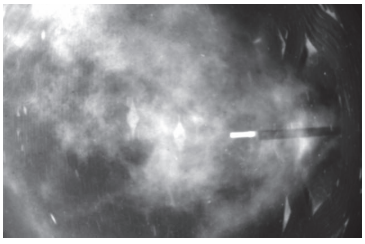

(f) Exp #05, PA/CA.

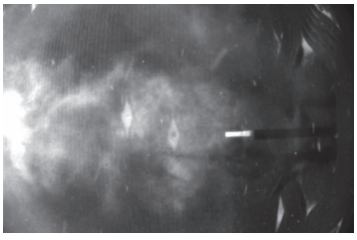

(g) Exp #06, reduced PA temperature.

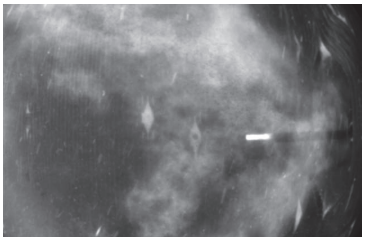

(h) Exp #07, increased PA temperature.

Figure 11C.6 Overview of all screening experiments. All images are presented on the same intensity scale. The probe is inserted 75 cm in (a) and 200 cm in (b) to (h).

CHAPTER 11D

Results

Based on the results from the parameter screening, a number of operational conditions were selected for further investigation. These include a higher spatial resolution in the probe measurements (extractive gas analysis and optical gas phase temperature measurements) and video imaging in the IR and VIS spectrum. Suction pyrometry measurements are also attempted on selected runs but were found to be redundant due to favorable conditions for reliable optical measurements (high CO_2-concentrations).

Time schedules are presented along side every experiment and all supplementary material, e.g. video material, pellet and dust samples, etc. are identified by date and time stamps. Each experiment is also assigned an experiment ID (Exp #) as defined in table 11D.1.

All temperature and concentration data are presented on the same scale for easy and direct comparison unless otherwise stated.

11D.1 Experimental Matrix

A total of seven experiments were conducted with full flame characterization, including two reference runs (#3 and #4) in the beginning of each of the two test days. The time reference and value of the adjusted parameter is presented in table 11D.1.

Table 11D.1 Experimental matrix for single parameter changes. All other conditions are fixed.

Exp #	Date dd-mm-yyyy	Time hh:mm		Setting Change [%]	Abs	Ref	Unit
1	05-12-2012	14:33	Reference #3	—	—	—	—
2		17:23	Disc*	35	2.0	1.3	mm
3		19:55	TA swirl**	−100	45	90	%
4	06-12-2012	09:50	Reference #4	—	—	—	—
5		12:02	Air-split	50	0.3	0.15	—
6		15:19	PA temp	40	150	210	°C
7		17:34	Load***	−33	4.8	6.4	tons/h

* The distance refers to the disc offset in the mill.
** The percentage refers to the physical position of the swirler.
*** Total pellet feed to all six burners.

11D.2 Detailed Operational Conditions

Multiple operational parameters are monitored during the campaign. A summary of the most important parameters (flow data, mill settings, et.c) are listed in table 11D.2 and represents time averaged values during the sampling times listed in the schedules presented in the beginning of each of the sections presenting results.

11D.3 Reference Runs

A set of operational conditions have been selected as a reference state. These settings correspond to typical settings during normal operation at full load. I.e. the flame should be stable and the results repeatable. Reference flame #1, #3, and #4 are all fully mapped with good spatial resolution in both optical and extractive methods. The optical fiber used to measure gas phase temperature during reference flame #1 was found to be faulty and hence only gas phase concentration measurements are available for this flame. Reference flame #2 is characterized according to the screening method.

Video material from view port A, cf. figure 11A.2, is available for all runs.

11D.3.1 Optical Observations

The flame is observed in the visual spectrum using video equipment from the side view port (port A, cf. figure 11A.2). Figure 11D.1 shows the flame with and without the probe inserted. No changes in the flame shape are observed, giving confidence that the probe does not interrupt the flow field to significant degree.

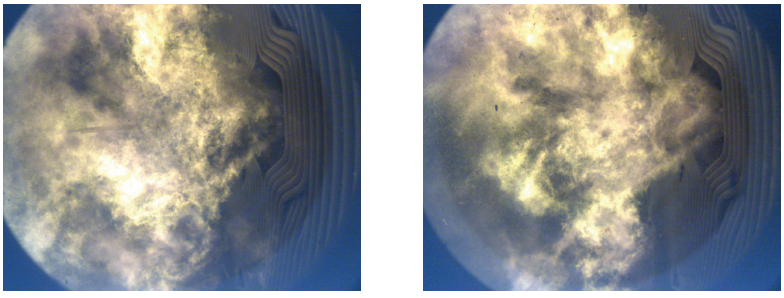

(a) ID: HEV1608: 00:02. **(b)** ID: HEV1618: 00:05.

Figure 11D.1 Video images of reference flame #3. (a) with and (b) without inserted probe. The probe is inserted 225 cm.

Table 11D.2 Summary of averaged operational conditions.

Setting		Ref #3	Mill	TA	Ref #4	AS	PA temp	Load
Exp #		1	2	3	4	5	6	7
Pellet flow	kg/s	1.78	1.78	1.78	1.78	1.78	1.78	**1.31**
CA flow	kg/s	0.916	0.912	0.910	0.900	0.900	0.901	0.902
PA air flow	kg/s	0.352	0.351	0.353	0.353	0.351	0.345	0.353
Combustion air flow	kg/s	10.61	10.61	10.58	10.66	10.65	10.59	**8.936**
Air split	%	15.0	15.0	15.0	15.0	**30.0**	15.0	16.2
SA swirl	%	60.9	60.9	60.9	60.9	60.9	60.9	60.9
TA swirl	%	90.4	90.4	**45.4**	90.5	90.5	90.5	90.5
Carrier air temp	°C	27	27	27	27	27	27	27
PA temp	°C	209	209	208	210	210	**154**	209
combustion air temp	°C	307	307	304	307	309	307	306
Mill disc distance	mm	1.36	1.94	1.38	1.38	1.38	1.38	1.38
Mill power		47.58	41.41	46.92	47.80	47.68	47.85	**42.98**

The reference flame is generally observed to be stable and with a characteristic shape as shown in figure 11D.2. A sharply defined conical shape emerges from the quarl zone and breaks up, significantly expanding in diameter after approximately 1 m.

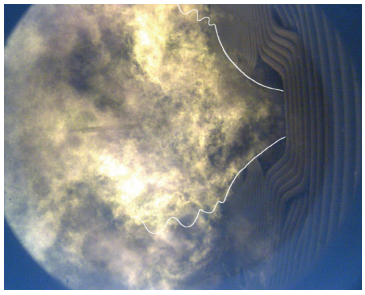

Figure 11D.2 Illustration of the characteristic reference flame shape (ID: HEV1608: 00:02).

IR imaging, figures 11D.3 and 11D.4, clearly show the conical trajectories of the entraining particles, appearing as dark trails in figure 11D.3 and blue colors in figure 11D.4. Both images are captured with the same camera but presented in different color schemes for clarity. Figure 11D.3 is a single frame, i.e. the momentanous situation, whereas figure 11D.4 illustrates averaged values across 1024 frames captured at a 94 Hz frequency.

The IR radiation intensity has been translated to a temperature scale by a grey body calibration. This temperature scale should be considered as estimated values, but can be used e.g. to estimate surface temperatures of thick particle clouds like the ones emerging from the quarl zone.

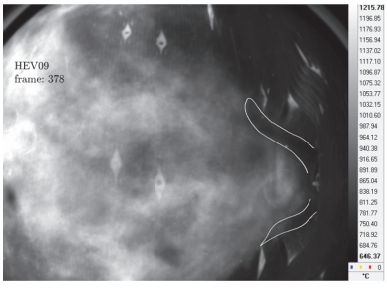

Figure 11D.3 Instant IR image of reference flame #3 (ID: HEV09, frame: 378).

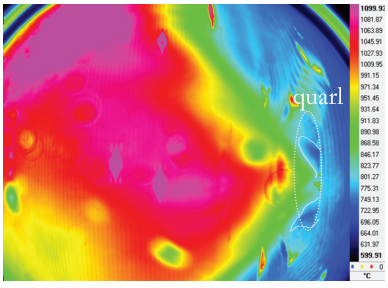

Figure 11D.4 IR image of reference flame #3, averaged across 10 seconds.

The averaged IR images, cf. figure 11D.4, show how the cold particles spread out from the quarl zone and are quickly heated. A large recirculation zone ensures convective transport of hot gases in the center of the flame.

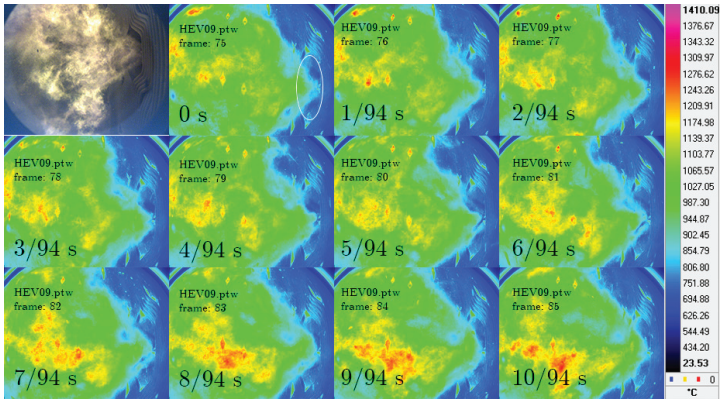

Figure 11D.5 IR image series of particles entraining the quarl. Reference flame #3.

Figure 11D.5 shows a chronological sequence of IR images (94 Hz). A stable and even supply of particles can be seen across the series. Roping is observed but cold particles are not allowed to penetrate the internal recirculation zone.

In the interest of assessing any day-to-day drift in the operational conditions, corresponding images of reference flame #4 are presented in the following.

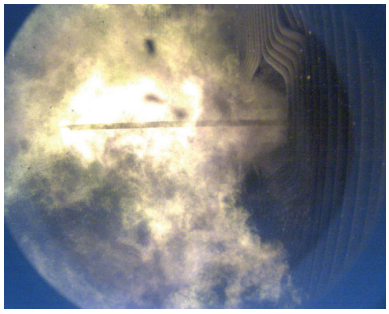

Figure 11D.6 VIS image of reference flame #4. Probe inserted 225 cm (ID: HEV1033 22:06).

The conical shape of the flame base is also seen in reference flame #4, cf. figure 11D.6, after which the flame expands in width.

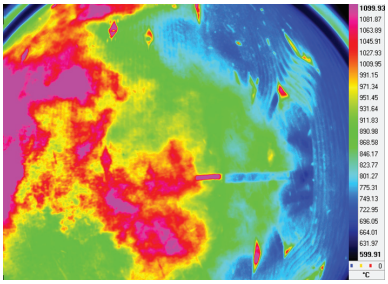

Figure 11D.7 Instant IR image of reference flame #4. Probe insertion 75 cm (ID: HEV18, frame: 562).

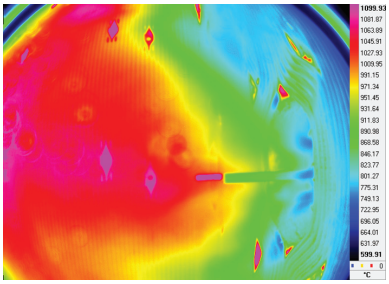

Figure 11D.8 IR image of reference flame #4, averaged across 10 seconds. Probe insertion 75 cm.

Figures 11D.7 and 11D.8 show an instantaneous image and an averaged IR image of reference flame #4 respectively. The same trends are seen in reference flame #4 as in #3. Distinct roping is observed from figure 11D.7, however, this could also be found in reference flame #3. Using the inserted probe as a length reference the degree of cold particle entrainment can be assessed. The probe is inserted 75 cm or 0.54 quarl diameters and thus it can be seen how the cold particles barely enters the quarl zone before they are heated and drowns in the thermal signal from the hot combustion gases.

11D.4 Particle Size Distribution

The burners are fed by individual disc mills making adjustments to the particle size distribution fed to burner #31 convenient and with close to immediate responses. The reference operating conditions used a mill disc spacing of 1.3 mm. Increasing the mill disc spacing is expected to effectively increase the particle size distribution. A 35 % increase in disc spacing yields an absolute distance of 2.0 mm.

Table 11D.3 Time schedule for changes in the particle size distribution of the fuel by changing the spacing between the disc in the mill feeding burner #31.

Date dd-mm-yyyy	Begin hh:mm	End hh:mm	Setting mm	Reference mm
05-12-2012	17:23	18:51	2.0	1.3

11D.4.1 Measured Particle Size Distributions

The effect on the particle size distribution when increasing the mill disc spacing has been analysed by both CAMSIZER®and sieve tower analysis. The results, comparing dust collected during reference conditions (1.3 mm) and after the changes to the mill setting (2.0 mm) is shown in figure 11D.9. Both the CAMSIZER®and the sieve tower results indicate a slightly higher fraction of larger particles after the changes have been made to the mill. However, the resulting increment in the particle size distribution is surprisingly low considering the 35 % increase in disc spacing. For a comparative study between the CAMSIZER®and the sieve tower method, please refer to the full fuel analysis, section 11B.2.3.

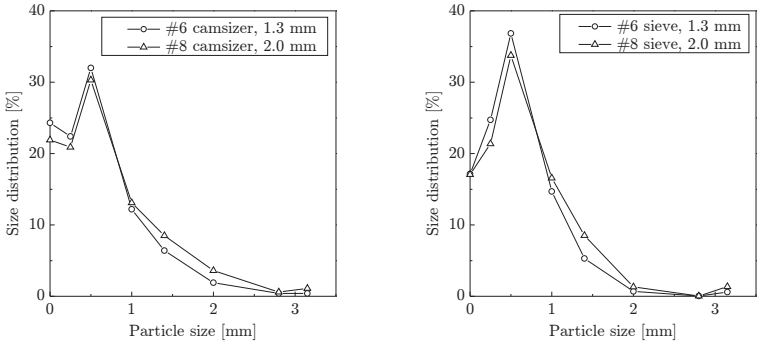

(a) CAMSIZER®. **(b)** Sieve.

Figure 11D.9 PSD comparison during changes to the mill spacing. (a) shows the CAMSIZER®results, (b) shows the corresponding sieve tower analysis.

Dust samples are collected before, during, and after the changes to the mill are in effect. Table 11D.4 compares the d_{10}, d_{50}, and d_{90} values for dust samples #6, 7, 8, and 9. The apparent change in particle size distribution is well expressed in resulting analysis data. Especially when comparing the d_{90} values. This also shows how the disc mill configuration makes it possible to introduce changes to the particle feed at short response times.

11D.4.2 Probe Measurement Results

An increase in the particle size distribution is expected to destabilize the flame due to slower heating and thereby ignition of the individual particles. In the probe measurements, this is seen as a general decrease ($\sim$ 200 K) in gas phase temperature in the far field area, as illustrated in figure 11D.10. It is noticeable how the temperature of the large particle flame is higher closest

Table 11D.4 Comparison of PSD data before, during, and after changes to the mill setting. All samples are collected on the fifth of December 2012.

Samples #	Time hh:mm	Mill spacing mm	d_{10} mm	d_{50} mm	d_{90} mm
6	13:20	1.3	0.120	0.541	1.355
7	17:05	2.0	0.126	0.569	1.510
8	18:35	2.0	0.133	0.601	1.591
9	20:08	1.3	0.128	0.544	1.356

to the burner mouth, decreasing below the reference temperature at distances $x/D >\sim 1$. Small temperature differences ($< 50\,\mathrm{K}$) close to the burner mouth suggest that the increase in particle size distribution affects the flame to a greater degree down stream of the near burner field.

The O_2-concentrations are obtained manually on site due to a data fall out in the logging system, thus, the missing error-bars in figure 11D.11. However, manual readings have been found to coincide well with the averaged logged data and thus may be used as good estimates of the actual O_2-concentration, although some margin of error must be expected. Figure 11D.11 shows how the O_2-level is higher than the reference flame throughout the flame length, corresponds well with a lower gas phase temperature. Although the reasonable explanation would be a slower heat up of the particle, thus delaying the release of volatiles available for oxidation. As will be presented next, this also corresponds to the development of the pyrolysis gas profiles.

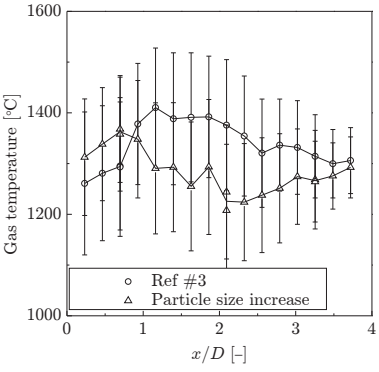

Figure 11D.10 Gas phase temperatures at (○) increased PSD compared to (△) reference flame #3.

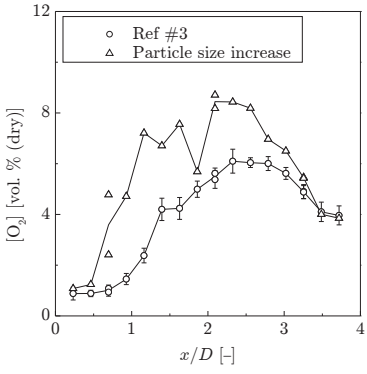

Figure 11D.11 O_2-concentrations profiles at (○) increased PSD and (△) reference flame #3. Readings are obtained manually.

Observing the development of the major combustion products, CO_2 and H_2O, similar conclusions can be drawn, cf. figure 11D.12. However, the level of combustion products are generally lower in the entire length of the flame. Both the concentration of CO_2 and H_2O start at similar or close to similar levels as was observed in reference flame #3, but both immediately decrease to levels well below the reference level, contrary to the gas phase temperature. This could indicate that the rate of local combustion is indeed decreased, even though the local gas phase temperature has increased.

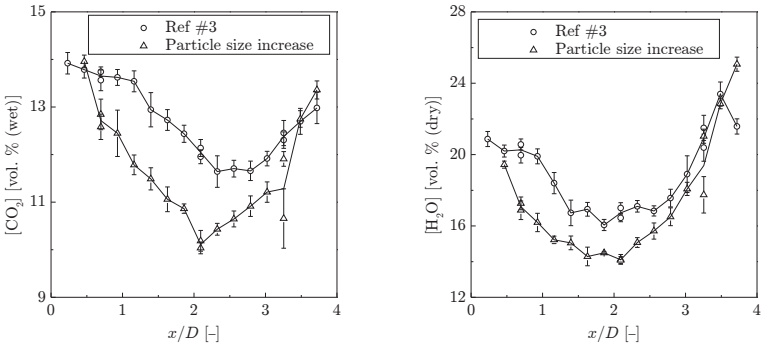

(a) CO_2-concentrations profiles. **(b)** H_2O-concentration profiles.

Figure 11D.12 Gas concentration profiles of the major combustion products at (○) increased PSD and (△) reference flame #3.

Looking at the primary pyrolysis gas concentrations, CO and CH_4, obvious differences emerge between the reference flame and the large particle flame. Starting at concentrations close to reference levels, both the concentration of CO and CH_4 quickly decreases to negligible levels, cf. figure 11D.13. This happens at $x/D > 0.7$. Since the overall stoichiometric conditions remain unchanged the sudden decrease in pyrolysis gases is a good indication for slow release of volatiles allowing for instantaneous oxidation once leaving the devolatilizing particle.

The same trends can be observed when looking at the larger pyrolysis products, cf. figure 11D.14.

As both the local O_2-concentrations, primary combustion and pyrolysis products suggest that combustion is taking place to a lower degree, on a mole to mole basis, as the mass flow of fuel and air is kept constant. Alternatively taking place in other zones than along the center axis. The gas phase temperature, primary pyrolysis and combustion products concentrations curves reaches the same level as the reference curve when the probe is fully inserted, indicating complete penetration of the flame. Thus, if the reaction zones were to change it would occur in the radial direction. Increasing the mass of each

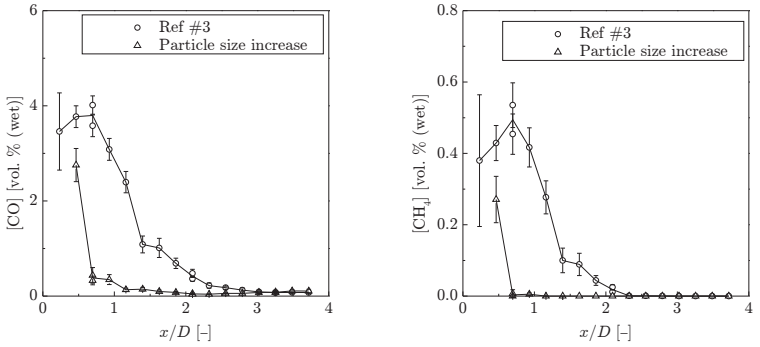

(a) CO-concentrations profiles. **(b)** CH_4-concentration profiles.

Figure 11D.13 Gas concentration profiles of the major pyrolysis products at (○) increased PSD and (△) reference flame #3.

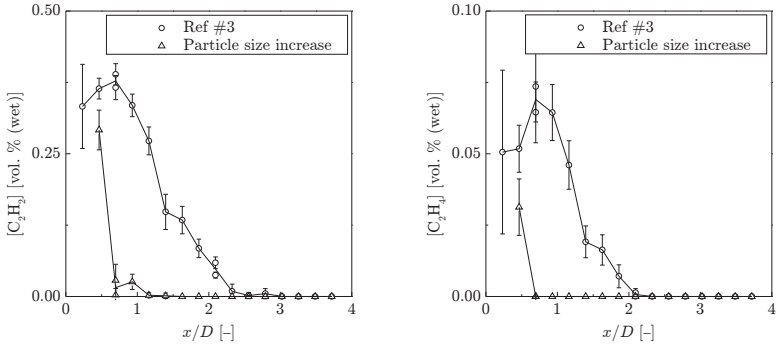

(a) C_2H_2-concentrations profiles. **(b)** C_2H_4-concentration profiles.

Figure 11D.14 Gas concentration profiles of the pyrolysis products at (○) increased PSD and (△) reference flame #3.

individual fuel particle will increase the relative momentum of each particle and thus making them less likely to radially disperse, compared to the reference flame. In the following section, the optical observation will also suggest a more narrow flame shape with more distinct particle cloud ropes entraining the center part of the flame. In summary, poor carbon burn-out could be a potential problem at these operating conditions.

11D.4.3 Optical Observations

A slightly longer conical shape can be seen at the base of the flame, when comparing the flame using larger particles with reference flame #3, cf. figure 11D.15. Both flames attach well to the burner nozzle and ignition does not seem to be a problem. The turbulent zone of the flame, emerging from the conical base after approximately 1 m seem to be more confined. Be aware that the soot radiation in the bottom of figure 11D.15a originates from the burner on the lower level at the opposite wall, this area has been hatched in green.

Both pictures in figure 11D.15 are shown with the probe inserted 225 cm. It is clearly seen how increasing the particle size distribution decreases the opacity of the flame in the VIS spectrum.

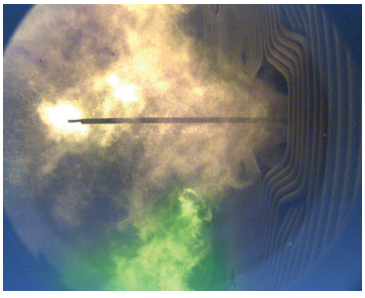

(a) Particle size increase, exp #2.

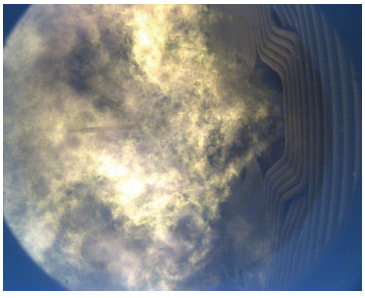

(b) Reference flame #3, exp #1.

Figure 11D.15 Comparison of (a) increased PSD flame and (b) reference flame #3.

Analyzing the flame in the IR spectrum reveals more distinct differences between the increased particle size distribution flame and the reference flame. On average, cf. figure 11D.16, the particles manage to entrain further into the boiler before heating up. The particles still spread radially probably due to the quarl action, however, a greater concentration of particles is observed closer to the centerline. This could indicate the effect of the increase in moment of inertia due to the increased individual particle masses making them less prone to be affected by pressure differences induced by quarl and swirling flows.

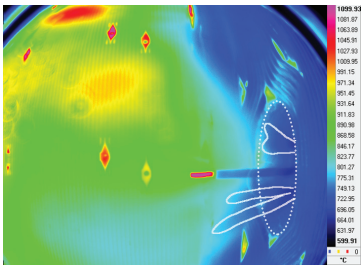

(a) Particle size increase, exp #2.

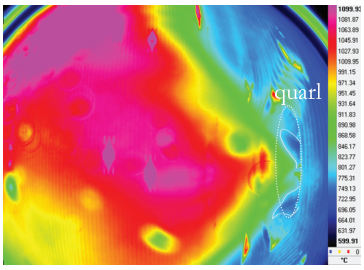

(b) Reference flame #3, exp #1.

Figure 11D.16 Comparison of (a) increased PSD flame and (b) reference flame #3. The probe is inserted 75 cm.

Looking at a single frame from the IR sequences distinct roping can be seen, cf. figure 11D.17 in the quarl area and from figure 11D.18 it is clear how cold clouds of particles penetrate far into the boiler room, especially in the bottom half of the quarl.

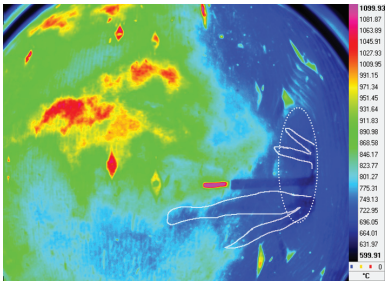

Figure 11D.17 Roping from the increased PSD flame (ID: HEV11 frame 813).

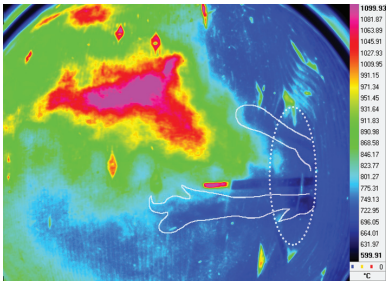

Figure 11D.18 Cold particles entraining deep into the boiler of the increased PSD flame (ID: HEV11 frame 819).

11D.5 TA Swirl

Reducing swirl of the tertiary air is managed by shifting the axial position of the swirlers in the conical tertiary air channel. Thereby letting more or less air bypass the angled swirlers, in- or decreasing the overall swirl number, respectively. The time schedule for the tertiary air swirl change is listed in table 11D.5.

Because the burner is operated at a low-air split, i.e. most of the combustion air is supplied through the tertiary air, reducing the tertiary air swirl is

expected to affect the overall swirl number to a significant degree.

Table 11D.5 Time schedule for changes in the TA swirl.

Date dd-mm-yyyy	Begin hh:mm	End hh:mm	Setting %	Reference %
05-12-2012	19:55	21:28	90	45

Reducing the swirl number of the flame is expected to affect the flame stability. The general recirculation is weakened and the convective transport of hot gases to near burner field reduced. This is expected to delay ignition and elongate the flame.

Figure 11D.19 presents the gas phase temperatures. A generally lower gas phase temperature is the first indication of a less stable flame. Even though, the temperature profile in the near burner field ($x/D < 1$) develops similar to the reference flame, it is noticeable how both the average flame temperature and the peak temperature are both significantly lower ($\sim 150\,\mathrm{K}$).

Noticing the 100 K temperature difference at $x/D \approx 4$ indicates that the change of tertiary air swirl setting affects the flame properties in the entire flame length. All other settings have led to similar temperatures at $x/D \approx 4$, which is believed to be an indication of the probe reaching through the flame, measuring the overall conditions of the boiler. Reducing the swirl number shift the flame characteristics towards more jet like behavior, of which a longer flame can be expected, as indicated by the temperature profile and the O_2-profile, figures 11D.19 and 11D.20.

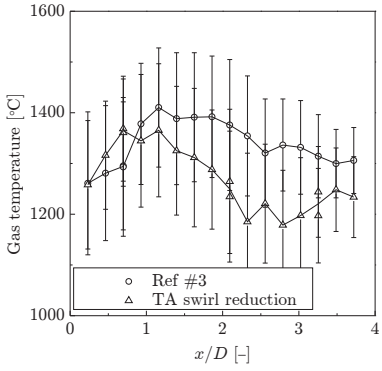

Figure 11D.19 Gas phase temperatures at (○) reduced TA swirl compared to (△) reference flame #3.

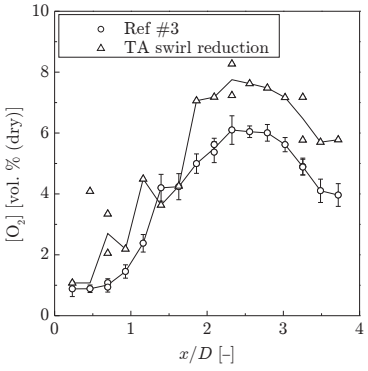

Figure 11D.20 O_2-concentrations profiles at (○) reduced TA swirl and (△) reference flame #3.

The similar near burner temperatures and primary combustion products, cf. figure 11D.21 does indicate an intact internal recirculation zone, probably stabilized by the secondary air flow, shielding the near burner core from the changes to the tertiary air flow. Lower levels of primary combustion products, CO_2 and H_2O, at $x/D \approx 4$ again indicates an elongated flame.

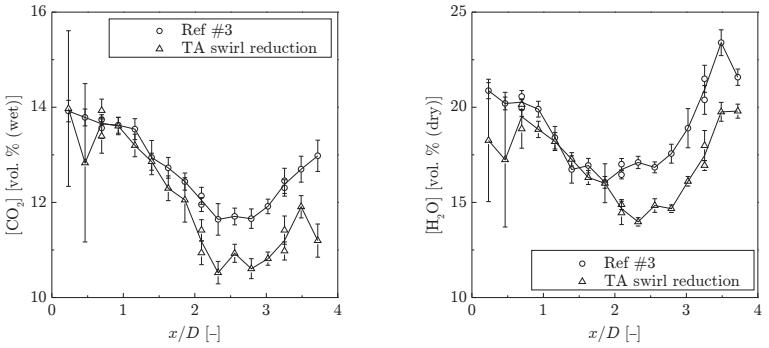

(a) CO_2-concentrations profiles. **(b)** H_2O-concentration profiles.

Figure 11D.21 Gas concentration profiles of the major combustion products at (○) reduced TA swirl and (△) reference flame #3.

The pyrolysis gas release profiles (figures 11D.22 and 11D.23) do indeed indicate observable differences in the devolatilization dynamics. A decrease in pyrolysis gas concentrations can either be caused by slower release of volatiles or a faster consumption, primarily due to higher concentrations of oxygen, cf. figure 11D.20. Because a reduction in the tertiary air swirl reduces the strength of the internal recirculation zone, and thereby limits convective transport of hot gas to the core of the flame, the lower concentrations of pyrolysis gases can be assumed to be caused by a slower release of products.

For all observed pyrolysis gases, figures 11D.22 and 11D.23, the concentration profiles are consistent with the development of the corresponding reference profiles at $x/D > 1.5$. The combination of low gas phase temperatures, figure 11D.19, high oxygen concentrations, figure 11D.20, and low combustion product profiles, figure 11D.21, are all indications of reduced devolatilization rates in the near burner field.

11D.5.1 Optical Observations

As indicated by the temperature profile and the pyrolysis products concentrations profiles described above, limiting the swirling motion of the TA induces noticeable responses in the flame behavior. This is supported by the optical characterization.

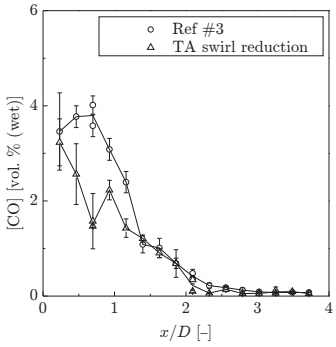

(a) CO-concentrations profiles.

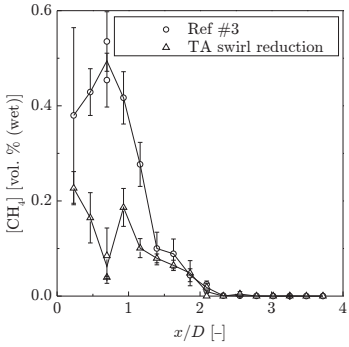

(b) CH_4-concentration profiles.

Figure 11D.22 Gas concentration profiles of the major pyrolysis products at (○) reduced TA swirl and (△) reference flame #3.

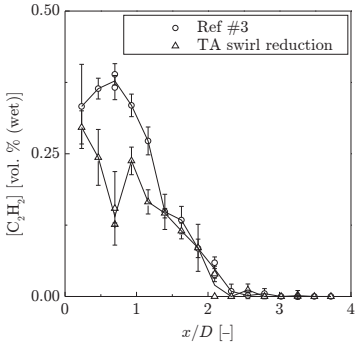

(a) C_2H_2-concentrations profiles.

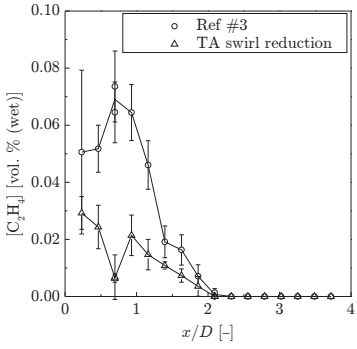

(b) C_2H_4-concentration profiles.

Figure 11D.23 Gas concentration profiles of the pyrolysis products at (○) reduced TA swirl and (△) reference flame #3.

The shape of the flame appears more narrow and longer than the reference flame, cf. figure 11D.24, which can be expected as a results of the destabilized recirculation zones.

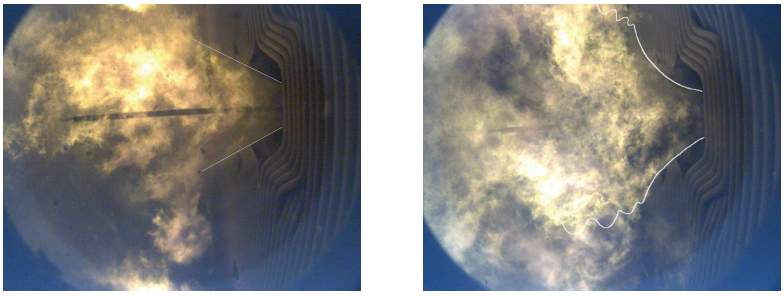

(a) Reduced TA swirl, exp #3. **(b)** Reference flame #3, exp #1.

Figure 11D.24 Comparison of (a) reduced TA swirl flame and (b) reference flame #3.

Using soot radiation in the VIS spectrum as an indicator for ignition, then frequent flame lift has been observed, e.g. figure 11D.25. The ignition zone during flame detachments stabilizes in the transition zone from the conically shaped jet in the quarl area to the more turbulent down stream region, cf. figure 11D.25. This could indicate a shift in the position of a centralized external recirculation zone struggling to supply the near burner field with convective heat during reduced TA swirl operation.

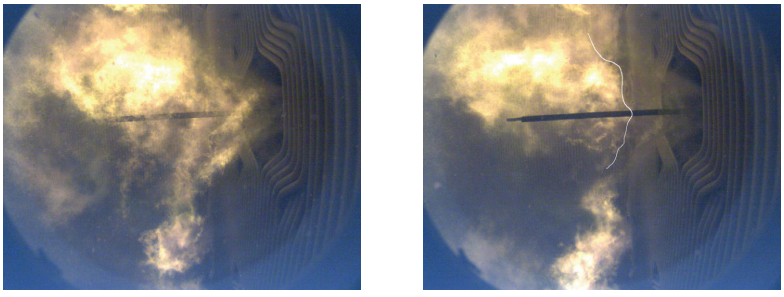

(a) Attahced flame, exp #3. **(b)** Flame lift, exp #3.

Figure 11D.25 Illustration of an (a) attached and a (b) lifted flame during reduced TA operation.

A reduction in the degree of TA swirl results in significantly colder signals in the IR spectrum. I.e., cold particles are allowed to penetrate far ($> 2\,\mathrm{m}$)

into the boiler through the bottom half of the burner, cf. figure 11D.26a.

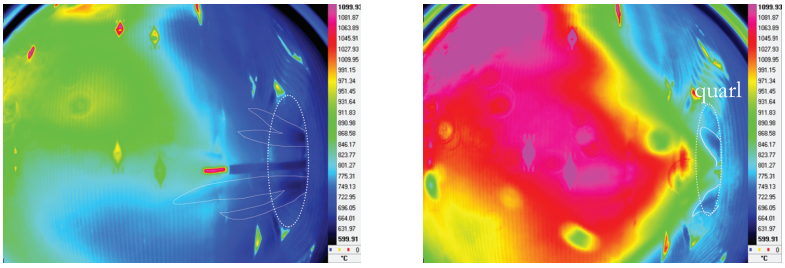

(a) Reduced TA swirl, exp #3. **(b)** Reference flame #3, exp #1.

Figure 11D.26 Comparison of (a) reduced TA swirl flame and (b) reference flame #3. The probe is inserted 75 cm.

Distinct roping and cold particles entraining far into the boiler have already been seen from the averaged IR image, cf. figure 11D.26a. However, examining instant situation, i.e. single IR frames, shows the severity of particle entrainment. Considering figure 11D.27 it is clear how the hot zone is pushed away from the burner and cold particles are allowed to entrain deep into the boiler. Whether such behavior can be directly linked to the occurrences of flame lift observed in the VIS spectrum is unknown, as the IR imaging and the VIS video are not synchronized. However, the frequency and durations of these events match to a convincing degree.

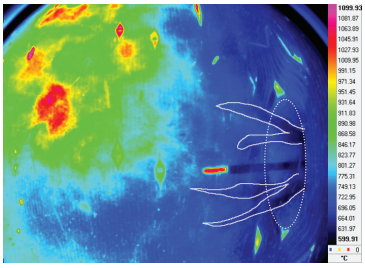

Figure 11D.27 IR image of the reduced TA swirl flame showing severe cold particle roping and deep entrainment (ID: HEV15.ptw frame: 408).

11D.6 Air-Split

The air split (AS) is defined as the ratio between secondary and tertiary air:

$$AS = SA/TA \tag{11D.1}$$

on a flow basis. All combustion air is supplied from the same register. Increasing the air split will increase the flow of secondary relative to tertiary air and thus change the flow dynamics.

Table 11D.6 Time schedule for changes in the AS.

Date dd-mm-yyyy	Begin hh:mm	End hh:mm	Setting %	Reference %
06-12-2012	12:02	13:29	30	15

The swirler settings in both the secondary and tertiary air channels are maintained at reference values, i.e. 60 and 90 % for the secondary and the tertiary air respectively. However, it should be kept in mind that the position of the swirlers can not be directly translated to swirlnumbers and thus this study should not be used to evaluate the effect of swirl in staged combustion but rather the effect of relative speed at which the combustion air enters the quarl in staged combustion.

Because the secondary air enters the quarl directly adjacent to the particle laden primary air the properties of the secondary air flow will presumably have a larger direct effect on the flame ignition. Both the gas phase temperature profile and the O_2-concentration profile show similar qualitative behavior between the reference flame (#4) and the increased air split flame. Increasing the air speed of the secondary air caused a local increase in O_2 and slightly lower gas phase temperatures, cf. figures 11D.28 and 11D.29. A relative increase in the influence of convective transport from the external environment to the centerline is also suggested by a general dilution of the combustion products, cf. figure 11D.30.

Lower pyrolysis gas concentration was also observed corresponding well to a general dilution effect of the stronger IRZ and the more readily available O_2. In general though, the pyrolysis products concentrations are low on test day #2 when comparing reference flame #3 and #4.

11D.6.1 Optical Observations

Increasing the air split, i.e. increasing the flow of secondary air and correspondingly decreasing the flow of tertiary air, narrows and elongates the flame. The characteristic outward bending of the reference flame, can no longer be recognized. It indicates that the velocity and angle of the secondary

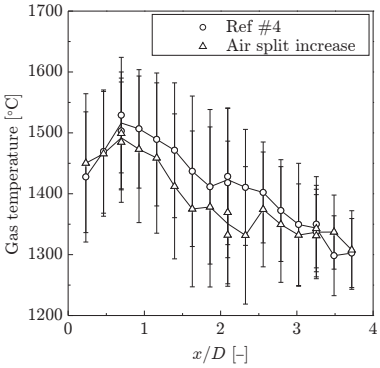

Figure 11D.28 Gas phase temperatures at (△) increased AS compared to (○) reference flame #4.

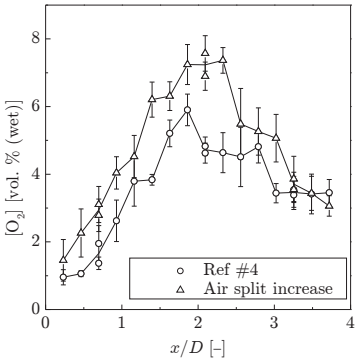

Figure 11D.29 O_2-concentrations profiles at (△) increased AS compared to (○) reference flame #4.

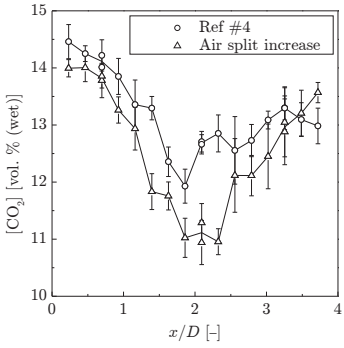

(a) CO_2-concentrations profiles.

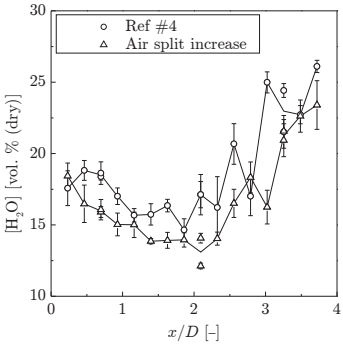

(b) H_2O-concentration profiles.

Figure 11D.30 Gas concentration profiles of the major combustion products at (△) increased AS and (○) reference flame #4.

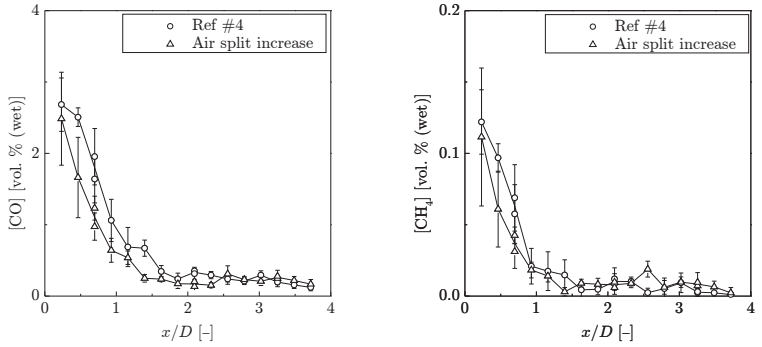

(a) CO-concentrations profiles. **(b)** CH_4-concentration profiles.

Figure 11D.31 Gas concentration profiles of the major pyrolysis products at (△) increased AS and (○) reference flame #4.

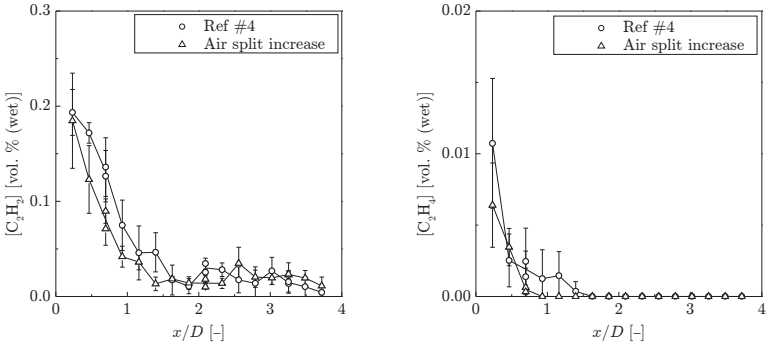

(a) C_2H_2-concentrations profiles. **(b)** C_2H_4-concentration profiles.

Figure 11D.32 Gas concentration profiles of the pyrolysis products at (△) increased AS and (○) reference flame #4.

air adds to the jet flame like behavior. This would also mean that the tertiary air potentially plays a significant role in the overall shape of the flame.

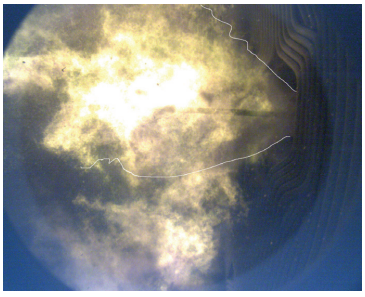

(a) Increased AS, exp #5.

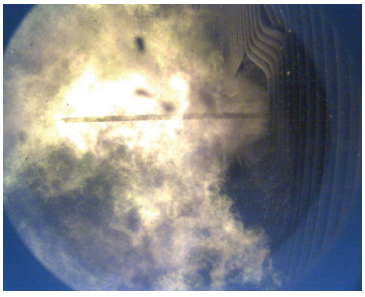

(b) Reference flame #4, exp #4.

Figure 11D.33 Comparison of (a) increased AS flame and (b) reference flame #4.

Figure 11D.34 illustrates the averaged flame in the IR spectrum. It appears clear how ropes of cold particles manage to penetrate further into the boiler when compared to the reference flame. This agrees well with the observations made in figure 11D.33. Generally lower temperatures in the near burner field also indicate a weakened circulation zone.

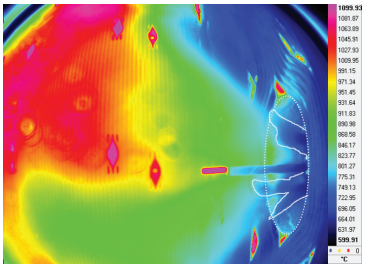

(a) Increased AS, exp #5.

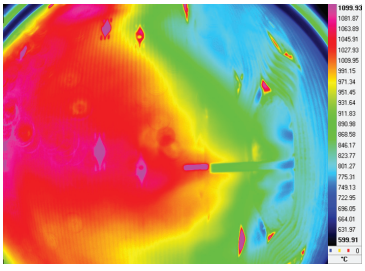

(b) Reference flame #4, exp #4.

Figure 11D.34 Comparison of (a) increased AS flame and (b) reference flame #4. The probe is inserted 75 cm.

This can also be seen if analyzing an instant shot of the increased air split flame, cf. figure 11D.35. With a lower radial dispersion of the particles compared to the reference flame, the resulting flame shape is expected to be longer and more narrow.

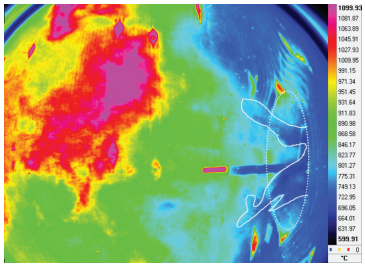

Figure 11D.35 IR image of the increased AS flame (ID: HEV23.ptw frame: 570).

11D.7 PA Temperature

The primary air is fed to the burner and mixed with the particle laden carrier air 1672 mm from the burner mouth. By preheating the primary air flow the particles will enter the furnace at elevated temperature while avoiding explosion hazards in the mills and conveying systems. Table 11D.7 list the time schedule for the changes to the primary air temperature.

Table 11D.7 Time schedule for changes in the PA temperature.

Date dd-mm-yyyy	Begin hh:mm	End hh:mm	Setting °C	Reference °C
06-12-2012	15:19	16:39	150	210

Both the primary and the carrier air flows are swirled before mixing after which they enter the boiler through the first concentric inlet, as seen in figure 11D.36.

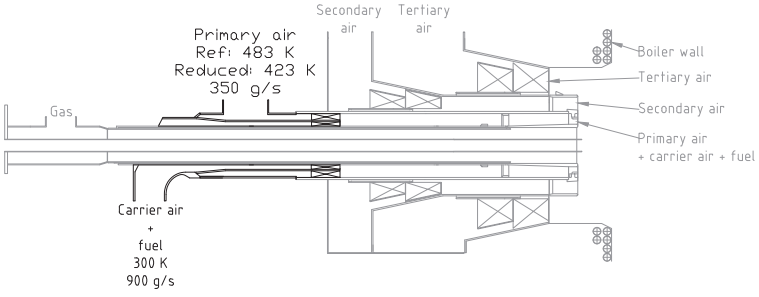

Figure 11D.36 Cross section of the HEV burner, highlighting the PA/CA/particle system.

Because the primary air flow is small compared to the carrier air flow, the flow and temperature ratio between the two flows should be considered in order to estimate the net impact of the temperature change. The flows and the respective temperatures are listed in table 11D.8 based on averaged values from the exact period. Assuming a constant specific heat capacity for air of $1.0076\,\mathrm{kJ}\cdot(\mathrm{kg}\cdot\mathrm{K})^{-1}$ and an averaged literature specific heat capacity for wood of $1.7\,\mathrm{kJ}\cdot(\mathrm{kg}\cdot\mathrm{K})^{-1}$, the flows and temperatures add up to net post-mix temperatures as listed in table 11D.9.

Table 11D.8 Flows and temperatures during reduced PA temperature runs.

	Flow kg/s	Reduced PA temp °C	Reference °C
PA	0.35	150	210
CA	0.90	27.5	27.5
Pellet	1.78	27.5	27.5

Table 11D.9 Net temperature of the mixed PA and CA flows. Effective impact of reducing the PA temperature with and without the influence of pellet heat capacity.

	Reduced PA temp °C	Reference °C
With pellet	38	43
Without pellet	62	79

Thus, only small differences are observed when taking the heat capacity of the woody fuel particles into account, reducing the post-mix system (gas and solid in thermal equilibrium) by 5 K from 43 to 38 °C when reducing the primary air temperature from 210 to 150 °C.

The small net impact on the mixed flow temperature leads to only negligible differences in the measured flame properties: gas phase temperature and O_2-level, cf. figures 11D.37 and 11D.38.

Likewise, the progress of the combustion products concentration profiles appear similar to the reference flame, cf. figure 11D.39.

Indications of a slightly lower concentration of pyrolysis gases in the close vicinity of the burner mouth can be seen in figures 11D.40 and 11D.41 which could stem from the reduction in the air and particle temperatures fed to the burner.

11D.7.1 Optical Observations

Reducing the primary air temperature does not change the apparent flame shape. Although influencing, it seems resonable that a gas flow temperature

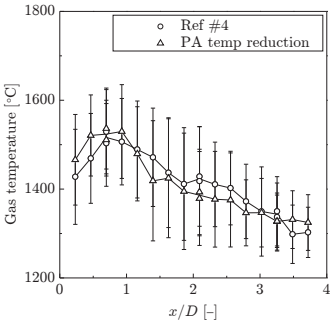

Figure 11D.37 Gas phase temperatures at (○) reduced PA temperature compared to (△) reference flame #4.

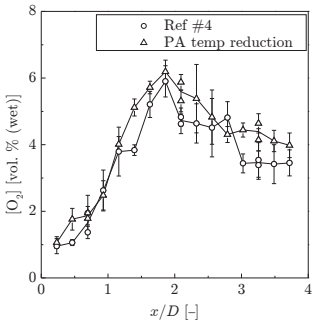

Figure 11D.38 O_2-concentrations profiles at (○) reduced PA temperature compared to (△) reference flame #4.

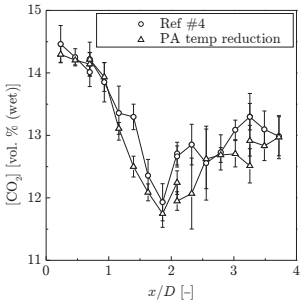

(a) CO_2-concentrations profiles.

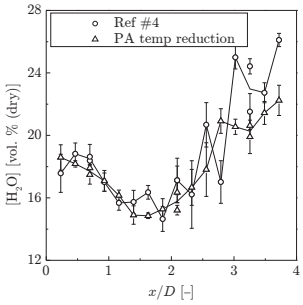

(b) H_2O-concentration profiles.

Figure 11D.39 Gas concentration profiles of the major combustion products at (○) reduced PA temperature and (△) reference flame #4.

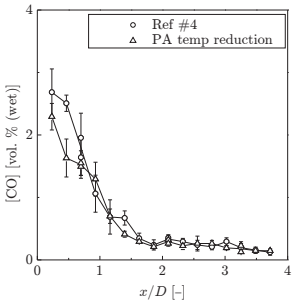

(a) CO-concentrations profiles.

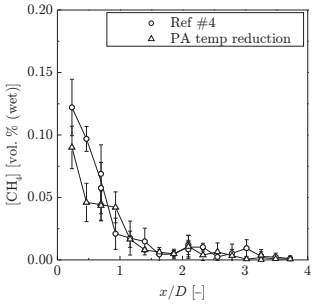

(b) CH_4-concentration profiles.

Figure 11D.40 Gas concentration profiles of the major pyrolysis products at (○) reduced PA temperature and (△) reference flame #4.

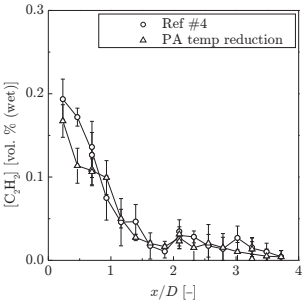

(a) C_2H_2-concentrations profiles.

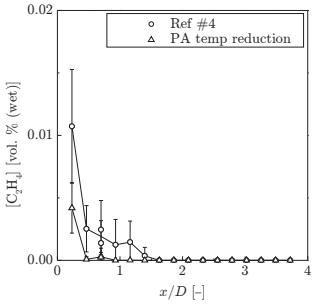

(b) C_2H_4-concentration profiles.

Figure 11D.41 Gas concentration profiles of the pyrolysis products at (○) reduced PA temperature and (△) reference flame #4.

reduction of just 40 K on 3 wt. % of the total air flow (excluding reactions in all phases) will not impact significantly on the resulting flow field.

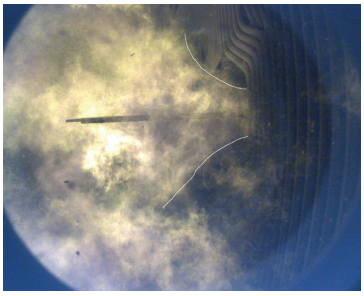

(a) Reduced PA temperature reduction, exp #6.

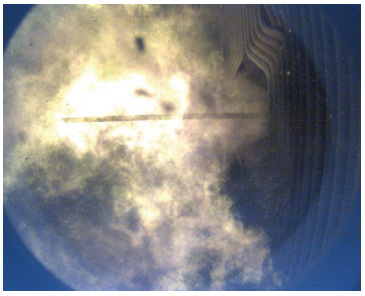

(b) Reference flame #4, exp #4.

Figure 11D.42 Comparison of (a) reduced PA temperature flame and (b) reference flame #4.

The same trends appear when observing the flame in the IR spectrum. Low penetration depth of the cold particles, cf. figure 11D.43 and with good radial dispersion, cf. figure 11D.44

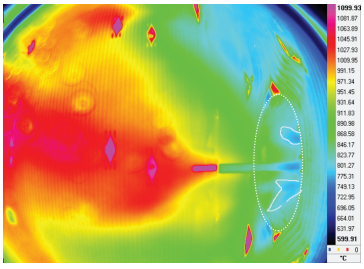

(a) Reduced PA temperature, exp #6.

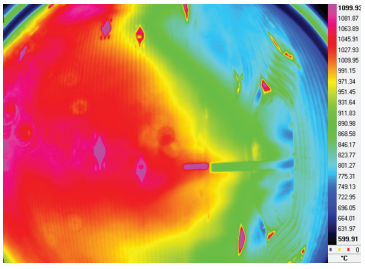

(b) Reference flame #4, exp #4.

Figure 11D.43 Comparison of (a) reduced PA temperature flame and (b) reference flame #4. The probe is inserted 75 cm.

11D.8 Load

Reducing the load by 33 % from 6.4 to 4.7 tonnes/hour (1.78 to 1.31 kg/s), yields noticeable impact on the observed flame properties. Because changing the fuel flow also require an adjustment of the air flows, a more detailed

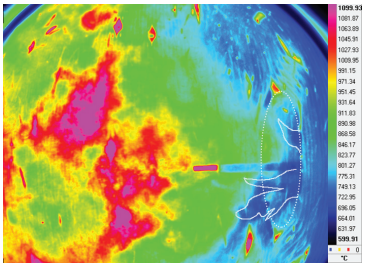

Figure 11D.44 IR image of the reduced PA temperature flame (ID: HEV24.ptw frame: 166).

walk through of the plant operational conditions will be given in this section, focusing only on the operational conditions during reduced load operation.

Table 11D.10 lists the time schedule for the reduced load experiment.

Table 11D.10 Time schedule for changes in the PA temperature.

Date dd-mm-yyyy	Begin hh:mm	End hh:mm	Setting tons/h	Reference tons/h
06-12-2012	17:34	19:09	4.8	6.4

11D.8.1 Operational Conditions at Reduced Load

Key numbers at reduced load operation are listed in table 11D.11 and compared to reference flame #4. The pellet flow is adjusted and the reduction in fuel is compensated by a reduced flow of combustion air, while both primary and carrier air flows are maintained at reference values.

The effects of the multiparameter changes carried out to stabilize the reduced load flame have been calculated and presented in table 11D.12. Because the adjustment in supplied air is only carried out by reducing the flow of combustion air, the stoichiometric conditions in the PA/CA channel changes by 14 % compared to the reference case. Note, that although a reduction in the supplied amount of air has been done the overall stoichiometric conditions still increases towards overall fuel leaner conditions. An increment of 29 % in λ-value has been calculated, corresponding to an oxygen excess of 4.93 vol. % (wet) compared to 2.63 vol. % (wet) in the reference case.

The combustion air exit velocity, estimated from the cross sectional area of the secondary and tertiary air channels when entering the quarl, both decreases as a result of the decrement in flow and maintained air split. Without knowing the effect of the swirlers, conclusions on the effect on the swirl number can be difficult.

Table 11D.11 Key parameters during reduced load operation.

Experiment #		Ref #4 4	Load 7	Change Absolute	Change Relative
Pellet flow	kg/s	1.78	1.31	−0.464	−35.3
CA flow	kg/s	0.900	0.902	0.00	0.288
PA air flow	kg/s	0.353	0.353	0.00	−0.0283
Combustion air flow	kg/s	10.66	8.936	−1.724	−19.29
Air split	%	15.0	16.2	1.18	7.32
SA swirl	%	60.9	60.9	0.00	0.00
TA swirl	%	90.5	90.5	0.00	0.00
Carrier air temp	°C	27	27	0.00	0.00
PA temp	°C	210	209	−1.00	−0.478
Combustion air temp	°C	307	306	−1.00	−0.327
Mill disc distance	mm	1.38	1.38	0.00	0.00
Mill power		47.80	42.98	−4.82	−11.2

Table 11D.12 Stoichiometric and key flow boundary conditions during reduced load.

Experiment #		Ref #4 4	Load 7	Change Absolute	Change Relative
λ (overall)	—	1.16	1.35	0.19	14.1
λ (PA+CA)	—	0.120	0.170	0.0500	29.4
O2 excess	% wet	2.63	4.93	2.30	46.7
SA exit vel	m/s	10.2	9.21	−0.990	−10.7
TA exit vel	m/s	23.9	19.7	−4.18	−21.2
CA+PA exit vel	m/s	14.2	14.2	0.0100	0.0706

11D.8.2 Probe Measurement Results

Please note, that since a reduction in load, has made more significant changes to the observed flame properties than seen from any of the other operational conditions, the ranges of the axes on the probe measurement result figures have been re-scaled.

Reducing the load has, throughout the reach of the probe, lowered the center axis gas phase temperature, cf. figure 11D.45. The maximum temperature is observed at the very nozzle of the burner where the temperature is comparable to the reference case. During the following 1.5 burner diameters the gas phase temperature decreases by approximately 200 K, yielding temperature differences between the reduced load flame and the reference case of up to ~ 300 K. At just short of 1.5 burner diameters the gas phase temperature reaches a local minimum after which the temperature increases slightly to bulk flow temperatures. At 3.5 burner diameters the temperature of the reduced load flame and reference flame #4 are comparable and presumably close to boiler environment level.

The O_2-level, cf. figure 11D.46, is higher throughout the flame. Because the stoichiometric conditions in the PA/CA channel has increased by close to 30 % and the overall λ-value by 14 %, the shift in O_2-level is expected to be apparent al the way from the burner mouth. Contrary to the gas phase temperature profile, the O_2-profile develops according to the same trend as observed for the reference flame, although shifted towards fuel leaner conditions. The oxygen level peaks at around 2 burner diameters from the burner mouth, as was the case for the reference flame. The peak concentration however, increases from approximately 6 vol. % (wet) to just over 11 vol. % when changing from reference conditions to reduced load. The similarities in trends of the O_2-profiles could suggest similar mixing mechanisms with combustion air. The differences in local O_2-availability is apparent throughout the entire length of the flame.

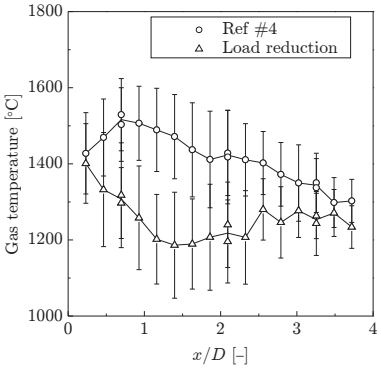

Figure 11D.45 Gas phase temperatures at (○) reduced load compared to (△) reference flame #4.

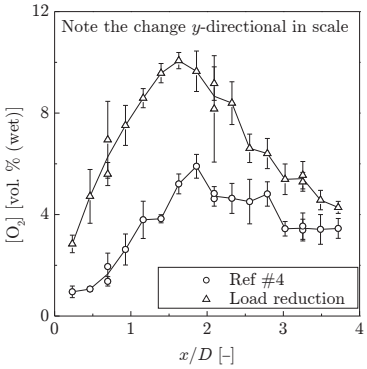

Figure 11D.46 O_2-concentrations profiles at (○) reduced load compared to (△) reference flame #4.

As was seen for the O_2-concentration profile, similar trends between the reference flame and reduced load flame in the development of the CO_2-profile have been observed.

Although oxygen is readily available, cf. figure 11D.46, and the temperatures elevated, cf. figure 11D.45, the local CO_2-concentration in the vicinity of the burner is significantly lower than the reference flame. In general, the concentrations of both primary combustion products, CO_2 and H_2O, are significantly lower within the first three burner diameters. The CO_2-level reaches reference quantities at four burner diameters.

The pyrolysis gas profiles appears to follow the trends observed from the reference flame. Even though the O_2-concentrations are high, noticeable quantities of both CO, CH_4, C_2H_2 and C_2H_4 can be observed. With the exception

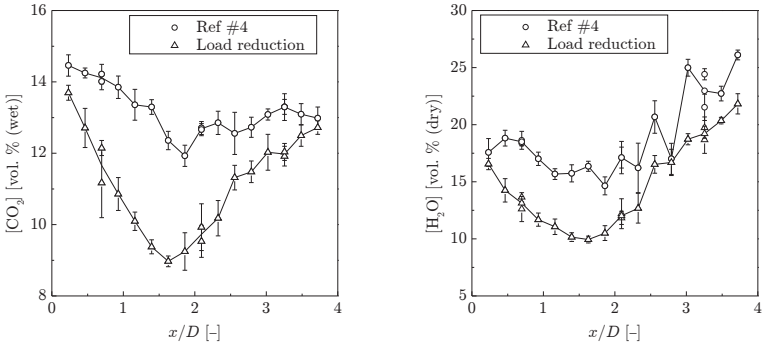

(a) CO_2-concentrations profiles. **(b)** H_2O-concentration profiles.

Figure 11D.47 Gas concentration profiles of the major combustion products at (○) reduced load and (△) reference flame #4.

of C_2H_2 the remaining pyrolysis gases follows the same trend as the reference flame, but with an approximate 50 % reduction in volumetric concentration.

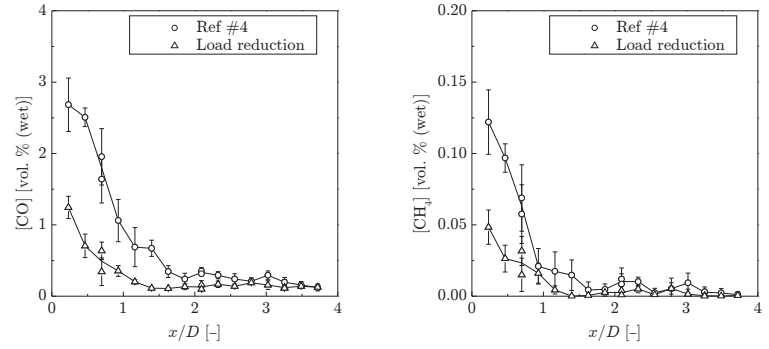

(a) CO-concentrations profiles. **(b)** CH_4-concentration profiles.

Figure 11D.48 Gas concentration profiles of the major pyrolysis products at (○) reduced load and (△) reference flame #4.

11D.8.3 Optical Observations

When reducing the load (reduction in dust flow and corresponding reduction in air flow to maintain overall constant stoichiometric conditions) the flame becomes unstable, fluctuating and frequently lifting. Figure 11D.50a shows

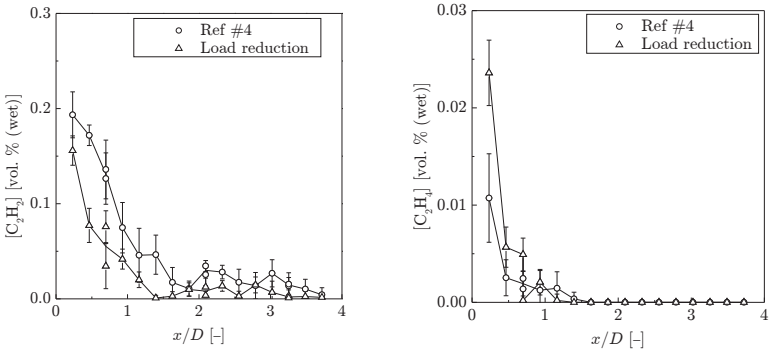

(a) C_2H_2-concentrations profiles. **(b)** C_2H_4-concentration profiles.

Figure 11D.49 Gas concentration profiles of the pyrolysis products at (○) reduced load and (△) reference flame #4.

how the flame is lifting from the burner mouth and the flame boundaries are less defined compared to the reference flame, cf. figure 11D.50b.

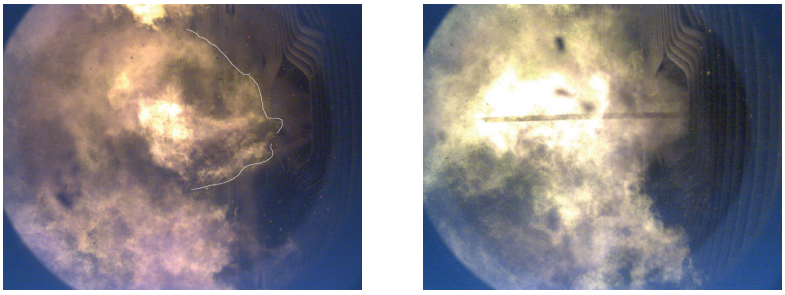

(a) Reduced load, exp #7. **(b)** Reference flame #4, exp #4.

Figure 11D.50 Comparison of (a) reduced load flame and (b) reference flame #4.

Figure 11D.51 shows two consecutive frames (at 24 Hz). From this it appears clear how dynamic the flame behavior appears during reduced load operation.

Extensive entrainment of cold particles are observed by the IR camera, cf. figure 11D.52a. Distinctive ropes of particles can be identified and a bias towards the bottom of the burner can be identified. As neither the flow of primary nor carrier air has been reduced, cf. table 11D.11, it serves to illustrate how important an impact the combustion air has on the resulting flow field in the quarl zone.

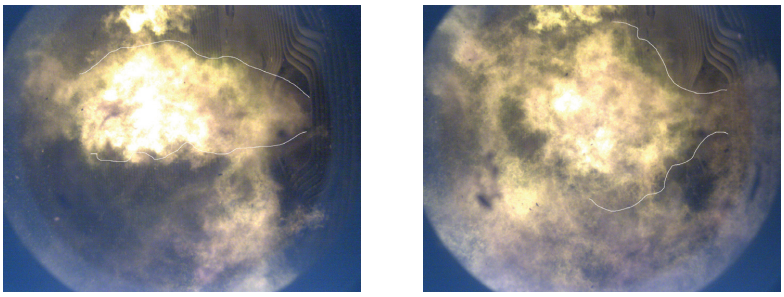

(a) Reduced load, $t = t_1$. **(b)** Reduced load, $t = t_1 + 1/24\,\mathrm{s}$.

Figure 11D.51 Flame shape development at reduced load operation.

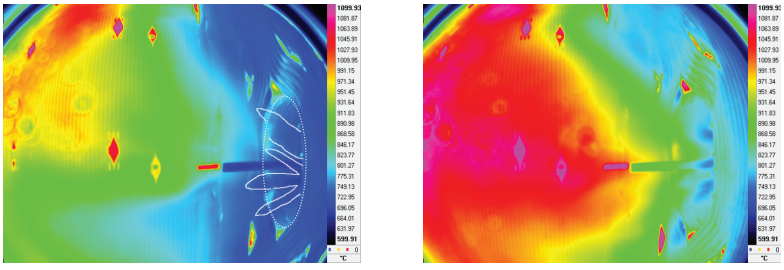

(a) Reduced load, exp #7. **(b)** Reference flame #4, exp #4.

Figure 11D.52 Comparison of (a) reduced load flame and (b) reference flame #4. The probe is inserted 75 cm.

Figure 11D.53 shows an instant shot of the burner operating at reduced load. It can clearly be seen how a dense rope of cold particles penetrate far into the boiler. Using the probe as a reference of distance (inserted 75 cm into the boiler) an approximate penetration depth of $\sim 1.2\,\mathrm{m}$ can be estimated. Although particle ropes do emerge from the top part of the burner, none have been observed with the same penetration depth nor density as the one illustrated in figure 11D.53.

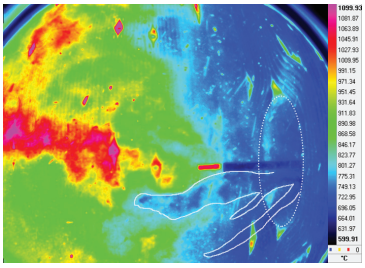

Figure 11D.53 IR image of the reduced load flame (ID: HEV26.ptw frame: 918).

CHAPTER 11E

Discussions and Conclusions

Chapter 11D presented the measurement results and to some extent discussed the acquired data. This chapter will further discuss the results and when possible compare them to expectations.

11E.1 The Reference Flame

Preliminary CFD simulations (the model provided by DONG Energy) have been carried out on the full burner geometry with the swirlers in both the secondary and the tertiary channel in the fully forward position. This will most likely increase the significance of the recirculation zones. Due to the complexity and the known susceptibility towards hysteresis and potentially multiple stable operation conditions it can be difficult to assess the differences in impact of the swirler positions. The following discussion takes starting point in the assumption that the observed flame share a common overall flow field structure with the simulation data.

Simplifying the flow field output divides the vertical center plane into two major recirculation zones: A large central internal recirculation zone (IRZ) and an external recirculation zone (ERZ) between the boiler wall and the combustion air.

The swirling and particle laden PA flow, entering the furnace through the third concentric circle at a radius of 150–220 mm or 0.14–0.20 burner diameters, creates a dense recirculation zone attaching the flame to burner. This bluff-body induced recirculation zone facilitates the initial mixing between combustion air and the particle laden primary air flow and attaches the flame to the burner. The bluff-body recirculation zones have been omitted in the illustrations in order to simplify the sketching. Whether an actual recirculation zone is established downstream of the flame holder has been questioned in scaled cold flow experiments [387], however, preliminary cold flow CFD simulations support the existence of a strong but small recirculation zone of high turbulence. The secondary and tertiary air flows, entering the burner through the outer consecutive concentric channels, enter the quarl zone at high velocity and quickly merges to a single flow. At the point of entrance to the slow moving bulk gas in the furnace the combustion air is angled outwards creating recirculation zones in the low pressure areas on both the in- and external side of the combustion air flow.

These primary flow field properties are outlined in figure 11E.1, approximately drawn to scale.

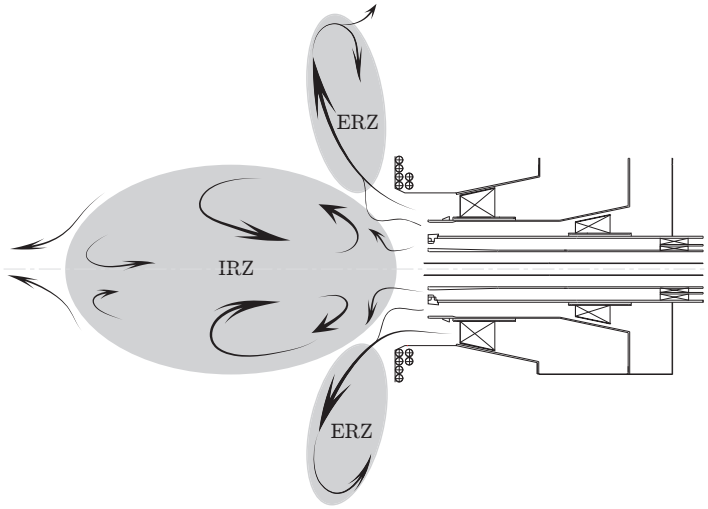

Figure 11E.1 Approximated flow field during reference operation based on preliminary CFD calculations and the measurement results.

The flame shape observed during the campaign corresponds well to these flow field estimations. A distinct concave shape can be easily identified, cf. figures 11D.2 and 11D.6. The turbulent zone following the well defined base of the flame indicates the presence of recirculating behavior, corresponding well to the flow field predictions. The fact that the flame is well attached and performs stably and with good ignition also indicate the presence of a strong internal recirculation zone facilitating the convective transport of hot combustion processes to the near burner field.

The operating conditions for the reference flame has been found to be stable and gas concentrations, flame shapes, and temperatures have been reproducible to an acceptable degree considering the turbulent conditions in swirl stabilized combustion.

11E.2 Parameter Variations

With starting point in the basic flame shape and simplified and zone divided flow properties of the reference flame, each operating condition will be discussed in the following.

Outlines of the main flow field properties are sketched out under each individual walk through of flame responses. These sketches take starting point in the reference operating conditions. The impact of operational changes are based on a mechanistic understanding supported by the full set of data from the results chapter.

11E.2.1 Increase in Particle Size Distribution

The main features of the flame operated under increased particle size distribution can be summarized as follows (reference flame #3 is used for reference):

- Generally lower gas phase temperatures at $x/D > 1$
- Higher local concentrations of O_2 in the entirety of the flame
- Pyrolysis gases are only present in the very near burner field
- Local concentrations of combustion products are generally lower
- The flame shape appears more narrow
- More defined particle ropes penetrating further into the furnace can be identified following trajectories close to the center axis

The effect of the increased particle size distribution has been tentatively sketched out in figure 11E.2 taking starting point in the preliminary CFD calculations used to generate the reference sketch, cf. figure 11E.1.

Increasing the particle size distribution will in terms increase the mass and thereby the momentum of the individual particles. This makes the particles more prompt to penetrate internal recirculation zone and interfere with the stability of the internal recirculation zone. The internal recirculation zone is stabilized by the low pressure zone in the core of the flame and the high velocity flow of the secondary and tertiary air. However, if mass is allowed to penetrate the internal recirculation zone, taking on flame type-0 properties, this internal recirculation zone will destabilize due to: 1. counter flow from the center jet and 2. a pressure increase in the core of the flame due to the flow of the center jet. The more narrow flame shape could indicate a collapse of this internal recirculation zone.

The lower temperatures and combustion product concentrations combined with high oxygen concentration indicate poor mixing properties of this flame. Which, especially along the center line, would be expected for a flame type-2 to 0 transition.

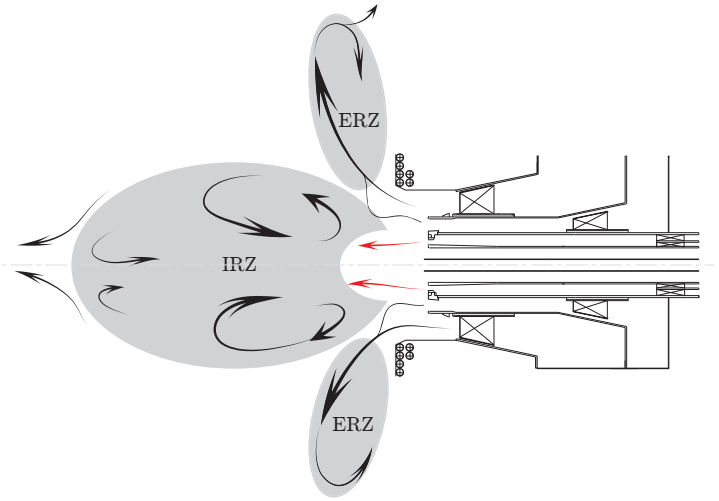

Figure 11E.2 Approximated flow field during increased PSD operation. Axial momentum increase illustrated by red arrows.

11E.2.2 Decreased TA Swirl

The flame response when decreasing the degree tertiary air swirl relative to reference flame #3 can be summarized as follows:

- Generally lower gas phase temperatures at $x/D > 1$
- Generally higher O_2-concentrations in the far burner field
- Generally lower concentrations of combustion products in the far burner field
- Significantly lower concentrations of pyrolysis gases in the near burner field
- A more narrow flame loosing the concave shape of the reference flame
- Flame lift and particle roping

Figure 11E.3 outlines the main flow field properties of the reduced tertiary air swirl operation.

Because the burner is operated at a highly skewed combustion air ratio ($AS = 0.15$) then changing the degree of swirl in the tertiary air flow will to a large extend define the swirling properties of the flame. Noticeable differences

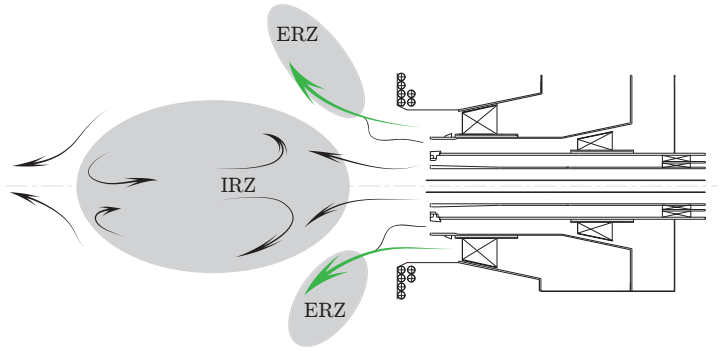

Figure 11E.3 Approximated flow field during reduced TA swirl operation based on preliminary CFD calculations. The reduced influence of TA swirl is illustrated by green arrows.

to the reference flame have indeed been observed. Both with respect to visual observations (flame shape, particle cloud trajectories, and overall stability) and when quantifying the in flame properties (temperature and gas species composition).

Decreasing the swirl increases the axial velocity component and thereby the axial momentum relative to the tangential. This destabilizes both the internal and the external recirculation zone which can be immediately identified from the flame shape loosing its concave shape to a more funnel shaped base. Comparable (to the reference flame) temperatures and combustion product concentrations in the vicinity of the burner indicates that the flameholder induced flame attachment is maintained. In fact, similar properties for temperature and combustion products can be found as far as two burner diameters downstream of the nozzle, indicating a continued presence of a strong internal recirculation zone.

The decrement in pyrolysis gases in the near burner field does however indicate some influence on the flame core and does support the significance of convective transport of primarily heat from the primary mixing zones to the ignition zones of the flame. Insufficient availability of easily combustible pyrolysis gases is prime to be the cause of the flame instabilities observed as flame lifts.

11E.2.3 Increase in AS

The effect of the air split on the flame properties can be summarized as follows:

- Slightly lower gas phase temperatures

- Slightly higher O_2 concentrations
- Slightly lower local concentrations of pyrolysis and combustion products
- Uniform tendencies for all quantified parameters
- Slightly more narrow flame taking on a convex shape

Two scenarios can emanate from changing the ratio between secondary and tertiary air flows. Because the trajectory of the combustion air is largely determined by the pressure difference between the high velocity swirling combustion air and the low pressure zones on either side, the net effect will depend on how this change in ratio will effect the relative magnitude of the pressure differences to either side of the combustion air, cf. figure 11E.4.

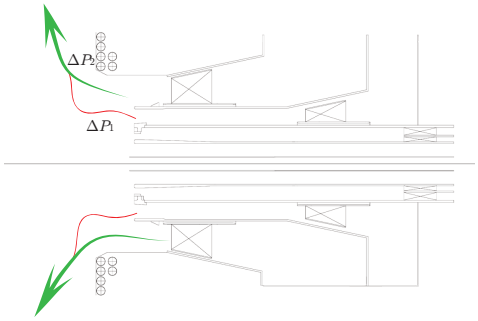

Figure 11E.4 Illustration of the impact of changes in the AS on the pressure differences.

In case of a relative greater pressure difference on the internal side of combustion air stream, this will strengthen the internal recirculation zone zone, narrowing the flame shape, cf. figure 11E.5.

Contrary, if the pressure changes favor strengthening of the external recirculation zone on the outside of the combustion air streams it will result in a scenario sketched out in figure 11E.6.

11E.2.4 Reduced PA Temperature

Reducing the primary air temperature did in short lead to the following flame responses:

- No noticeable differences in gas phase temperature, combustion products, flame shape, or thermographic image

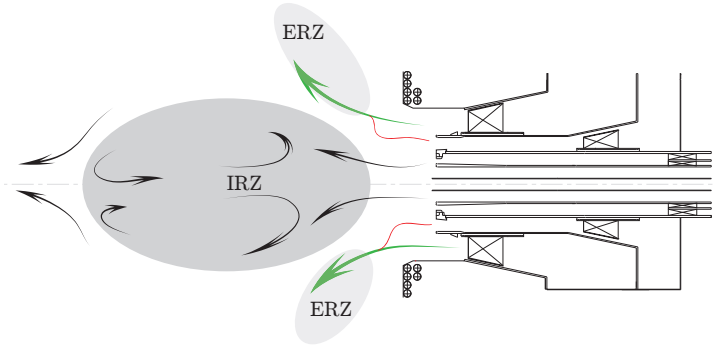

Figure 11E.5 Approximated flow field during increased AS operation. Strengthening the ERZ2.

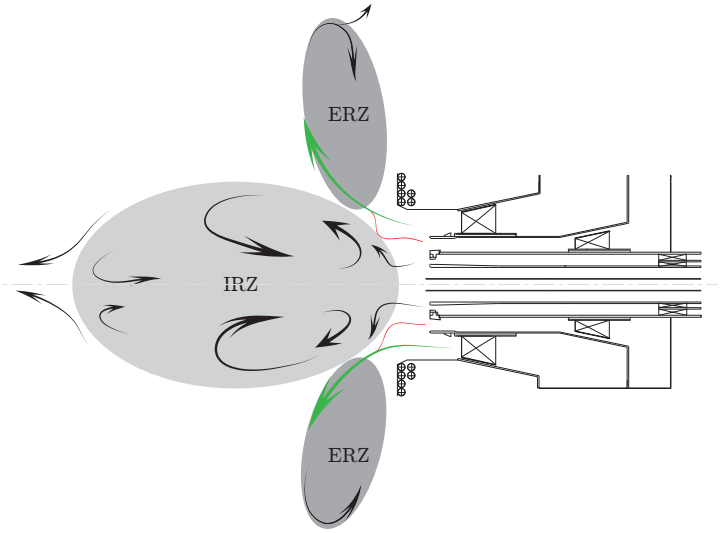

Figure 11E.6 Approximated flow field during increased AS operation. Strengthening the ERZ1.

- Slightly lower concentrations of pyrolysis gases in the very vicinity of the burner mouth

Decreasing the temperature of the primary air decreases the volumetric flow and thus the entry velocity of the particle laden primary and carrier air air. However, the effective temperature reduction has been estimated to be very low: $\sim 5\,^{\circ}\mathrm{C}$, if taking the heat capacity of the particles into account. This will not cause a significant change in the overall swirl number and thus the similar flame characteristics are expectable. Because of the small change in the effective temperature, no significant changes to the thermal processes are expected either.

11E.2.5 Reduced Load

Multiple parameters are changed during reduced load operation in order to balance out the smaller input of mass. Hence, the results are difficult to compare as both thermal and flow field dynamics are changed with significant margins compared to the reference settings. However, the following summarizes the observed flame responses to reduced load operation:

- Similar temperature at attachment point
- Lower gas phase temperature down stream of the flameholder
- Significantly higher O_2 levels throughout the flame
- Significantly less pyrolysis and combustion products
- Unstable flame: Flame detachments and rapidly changes in the flame shape
- A generally more narrow flame
- Long and dense particle ropes penetrating far into the boiler along the center axis

Because the reduced load operation requires changes to multiple of the primary parameters, the relative impact of each of the changes can be difficult to assess. An attempt has been presented in figure 11E.7.

Measurements along the center axis may not be the best way to evaluate the flame response to reduced load operations. Because the particle laden flow primarily acts as carrier flow, most of the air compensation is carried out through the combustion air channels. This raises the available amount of O_2 relative to the reduced amount of particles in the PA/CA flow and could explain some of the O_2 surplus in the near burner field. Overall the stoichiometric conditions changes from $\lambda = 1.16$ to 1.35, while the stoichiometric conditions locally in the PA/CA flow increases from $\lambda = 0.12$ to 0.17.

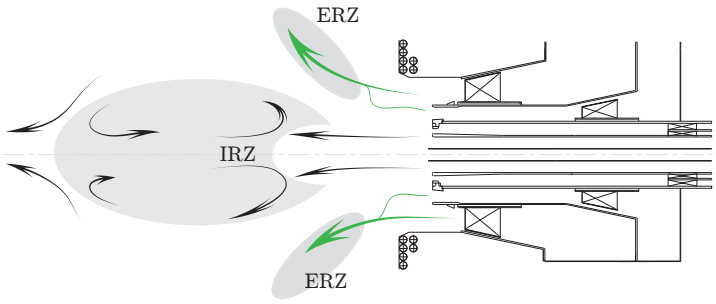

Figure 11E.7 Approximated flow field during reduced load operation.

It is noticeable how even though the entry velocity of the SA and TA decreases with 11 and 21 % respectively, the influence of these swirling flows impacts at the same axial distance, $x/D \approx 2$, as during reference operation. This influence is identified by the peak position of O_2 and combustion products and the elimination of pyrolysis gases indicating the introduction of external gas/gas mixing.

The more narrow flame shape can be expected from the low velocity outer swirling flows weakening the internal recirculation zone.

This report is written in the GREEN research project (power Generation from REnewable Energy) and covers the experimental results from the flame response characterization full-scale campaign at Herningværket (HEV) carried out in week 49, 2012.
A single low-NOx multifuel burner is investigated across four days firing wood pellets. Flame mapping is conducted during large amplitude parameter in the operational conditions using both optical and extractive probe methods.

DTU Chemical Engineering
Department of Chemical and Biochemical Engineering
Technical University of Denmark

Søltofts Plads
Bygning 229
2800 Kgs. Lyngby
Tlf. 45 25 28 00
Fax 45 88 22 58
E-mail kt@kt.dtu.dk
Web www.kt.dtu.dk

CHAPTER 12

Summary on the Full-Scale Measurements

The burners installed at Amager and Herning power station respectively share a number of common features but categorically on the resulting flame. This particular situation constitutes an interesting starting point in a study on flame response characterization. This chapter will go through a comparative presentation of the two burners and discuss the resulting flames on a conceptual basis, taking starting point in the results from the full-scale campaigns.

12.1 Burners and Flame Types

Both burners are low-NO_x burners using adjustable vein swirlers in both the secondary and tertiary air channels. They both feature the same type of tooth-based flame holder on the outer wall of the primary air channel (the AMV flame holder is combining teeth and cavities). The thermal throughput are comparable (within 5–10 %) and thus the total throughputs of air are likewise comparable. However, the cross sectional areas of the flow channels and the distributions of air are significantly different. Table 12.1 summarizes the flow conditions at the burner mouth and at reference operating conditions (tables 10C.2 and 11D.2).

A primary difference is the magnitude of the velocities in the primary and tertiary air channels. The PA flows are in both cases operated at relatively low swirl. In the case of Amager power station almost pure axial velocity vectors are observed due to an installation of support legs (supporting the core tube) downstream of the primary air swirler. These support legs are plate shaped and installed in parallel to the center axis, effectively killing the swirl induced by the primary air swirlers.

As discussed in chapter 1 the forward momentum of the particle laden primary air is of central importance to the resulting flame type [38]. The centerline measurements support a hypothesis of two different flame types. Figure 12.1 compares the gas phase temperatures, O_2, CO, and CO_2-concentration measurements along the centerline of the Amager power station and HEV burners.

Analyzing the results of figure 12.1 all of the global trends can be rationally explained. The two burners result in two inherently different flames. The penetration of a cold, cf. figure 12.1a, and oxygen rich, cf. figure 12.1b, zone from the AMV results suggest a penetration of the internal recirculation zone by the cold and particle laden primary air jet. The flame attachment close to

Table 12.1 Comparison of the flow conditions at the burner outlet in operating at reference conditions as defined in tables 10C.2 and 11D.2.

Parameter	Channel	Unit	AMV	HEV
Temperature	PA	K	323	343
	SA		600	580
	TA		600	580
Cross sectional area	PA*	m^2	0.15	0.09
	SA		0.34	0.17
	TA		0.35	0.52
Flow rate	PA	$m^3 \cdot s^{-1}$	3.5	1.2
	SA		6.6	2.3
	TA		6.6	15
Linear velocity	PA	$m \cdot s^{-1}$	23	14
	SA		19	14
	TA		19	29

* The cross sectional area of the PA is calculated disregarding the flameholders.

the burner, but with a tendency to occasionally stabilize further downstream, suggests the presence of a toroidal internal recirculation zone surrounding the central jet and facilitate ignition in the shear layer between the primary and secondary air. This matches the expected behavior, considering the high linear velocity of the primary air, cf. table 12.1, and the flow straightening effect of the support legs installed downstream of the primary air swirler. This results in a high axial momentum of the particle laden primary air flow, which is further increased by the acceleration of the PA jet at the burner mouth. The swirling motion of the combustion air stabilizes the toroidal internal recirculation zone off the centeraxis.

Conversely, the close to depleted oxygen level in the very near burner field of the Herning power station burner, cf. figure 12.1b, suggests a closely attached flame, governed by a strong internal recirculation zone. Flame instabilities due to changes in the operating conditions were significantly more difficult to provoke than compared to the Amager power station burner, resulting in a very stable flame. The macro mixing seemed to be the main stability determining feature of the Herning power station flame, the flame being especially sensitive to changes in the tertiary air flow.

The measurements suggest the Amager power station burner to produce a IFRF type-1 flame and the Herning power station burner to produce a type-2 flame, as illustrated in figure 12.2. Flame type interpretation are assisted by literature studies on scaled burners [31, 37, 44, 391].

The type-1 flame (AMV): The establishment of a toroidal recirculation zone enclosing the penetrating central jet, cf. figure 12.2a, creates an important mixing zone off the centerline and thus invisible to the centerline probe

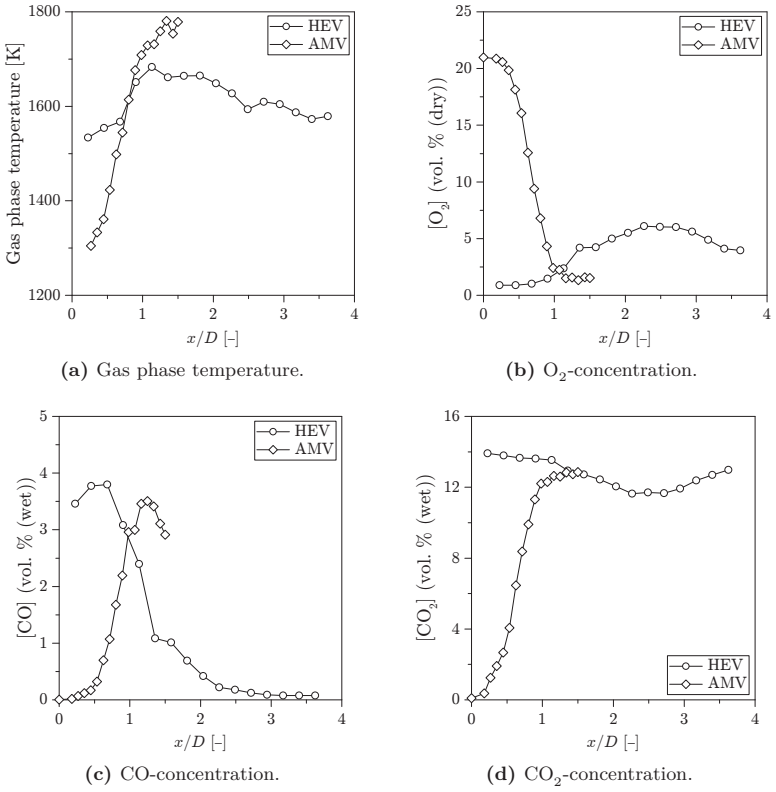

(a) Gas phase temperature. **(b)** O_2-concentration.

(c) CO-concentration. **(d)** CO_2-concentration.

Figure 12.1 Comparison between AMV and HEV centerline measurements. Both burners operating at reference conditions.

measurements. The core jet penetrates the flame thus giving rise to the low temperatures and high oxygen concentrations until it is mixed with hot combustion gases further downstream.

The type-2 flame (HEV): The forward momentum of the particle laden primary air is smaller than the AMV primary jet due to the lower velocity and smaller mass flow, cf. table 12.1. The swirling motion of the combustion air creates an internal recirculation zone sufficiently strong to reflect the primary air jet and establish a central internal recirculation zone transporting hot combustion gases well into the center of the quarl [392]. Because the centerline probe penetrates through the central internal recirculation zone the measurements shows high temperatures and post combustion gas composition already in the quarl area.

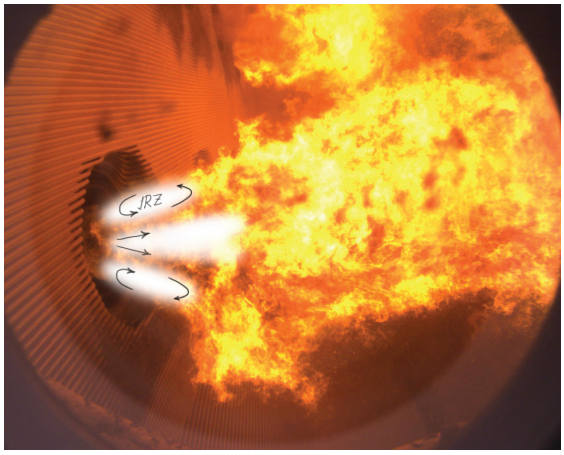

(a) AMV reference flame, IFRF type-1 flow field.

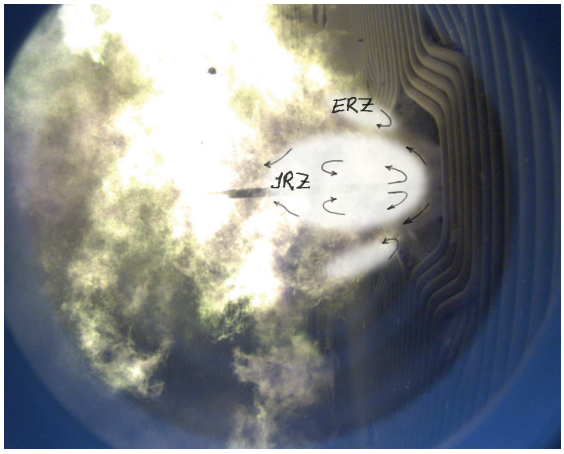

(b) HEV reference flame, IFRF type-2 flow field.

Figure 12.2 Suggested flow fields based on the centerline measurements and the flame shapes.

12.2 Discussions on Flame Optimization

Being able to describe the flame-type and outline the position of the internal and external recirculation zones as well as the temperature fields and oxidizing conditions, yields an optimal starting point for decision making regarding flame optimization.

The manipulation of the flow field pattern can be achieved by a multitude of changes, including geometric factors such as the quarl angle and length and the fuel injector position, flow criteria such as the degree of swirl and flow ratios, etc. [24, 36, 385, 386, 393]. Both the AMV and the HEV burners have shown potential for good flame stability and further optimization of the everyday operation could potentially be achieved by changes to the inlet conditions [393].

The AMV flame assumes a characteristic flame type-1 in which the primary air penetrates the internal recirculation zone and in general do not mix with the secondary air for several quarl diameters [41, 43]. The resulting flame is often long and although potentially NO_x efficient, the particle burnout and flame stability may be undesirable. The separated flows also calls for caution when choosing a suitable method for turbulence closure in Reynold averaged Navier-Stokes (RANS) simulations, as distinct differences have been observed in direct comparison between lower and higher order turbulence modeling [394] with the standard k-ϵ model generally intensifying the ignition zone [32, 394]. The axial and high velocity primary air flow may well lead to particle trajectories similar to path 1 in figure 12.5. With poor mixing between primary and secondary air the devolatilization will not begin until further down stream, and the stability of the flame relies on the decentralized internal recirculation zone being able to transport volatile gases and hot combustion products all the way to the burner mouth and optimally fully connecting to the flame holder wake. The three dimensional features of the flame holder would potentially contribute to an effective mixing between secondary and primary air flow and divert particles to devolatilize in the resulting oxygen lean zone in the wake of the bluff body flame holder. The effect might, however, be limited by the flow straightening effect of the support legs installed downstream of the primary air swirlers, killing off the radial momentum of the particles and primary air fluid [32, 395]. The presumably low swirl number caused by the high axial momentum of the PA particle laden jet, is probably the main cause of the observed flame lift phenomena at high load operation [396].

A more desirable flow pattern would be to divert the particles into the wake of the flame holder, resulting in direct devolatilization in the quarl area, path 2 in figure 12.3. Deflecting the trajectory of the primary air jet is probably obtained with the greatest effect by altering the primary air settings and not adjusting the swirl induced by the combustion air [393]. Depending on the focus of flow field changes or particle trajectories, such modifications could be carried out by inducing radial momentum to the particles, e.g. by re-

establishing the primary air swirl. Alternatively, the shape of the internal recirculation zone could be modified by altering the axial momentum of the primary air jet, i.e. decreasing the flow rate, or apply changes to the air split [397]. Care should be taken, not to overcompensate, as the production of NO_x could increase as a consequence of the particles entraining into the main combustion air stream [398, 399].

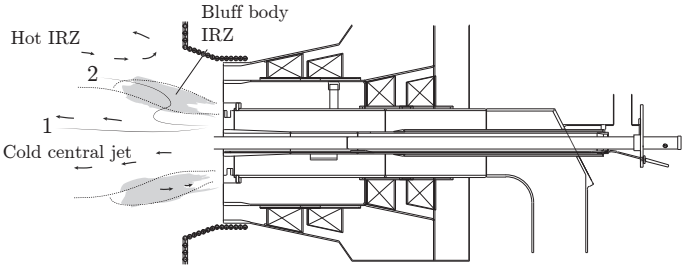

Figure 12.3 Particle trajectories through a decentralized IRZ.

The Herning power station showed excellent flame stability. While no NO_x figures were included in this study the air staged low NO_x burner results in flame structures that potentially could result in high NO_x production. Comparing the IR and VIS imaging, cf. figures 12.4a and 12.4b, gives an approximate idea of the particle trajectories through the flame. The images have been merged in figure 12.4c. This shows how the strength of the central internal recirculation zone deflects the entraining particles around the oxygen lean flame center, following particle trajectory 1 in figure 12.5. It is desirable to devolatilize the fresh particles in the oxygen lean center of the internal recirculation zone for two reasons: 1) It will limit the initial formation of thermal NO_x [19, 392] and 2) make it easier to define the mixing properties of the staged air because all major species will be in the gas phase. Experiences from annulus concentric co-firing of coal and biomass shows that ignition of the larger biomass particles could be stabilized by firing smaller coal particles in an outer annulus, providing the heat necessary for the biomass to devolatilize [400]. This effect can potentially be simulated using the centripetal force induced by the primary air swirl [32], while still maintaining a sufficient forward momentum for the larger particles to penetrate the internal recirculation zone [168] where significant particle slip has been observed [401] thus allowing for the separation of fluid and particle trajectories.

The observed flame stability of the Herning power station burner leaves an excellent starting point for particle trajectory optimization, aiming for trajectories similar to path 2 or 3 in figure 12.5. Increasing the likelihood of

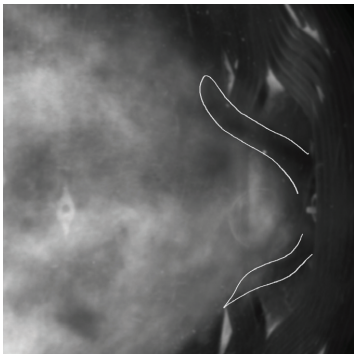

(a) IR imaging of entraining particles.

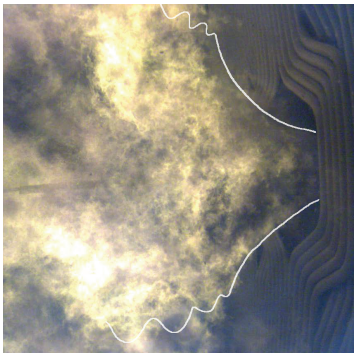

(b) VIS imaging of the flame shape.

(c) Combined IR and VIS imaging.

Figure 12.4 Comparison of IR and VIS imaging of the HEV reference flame #3.

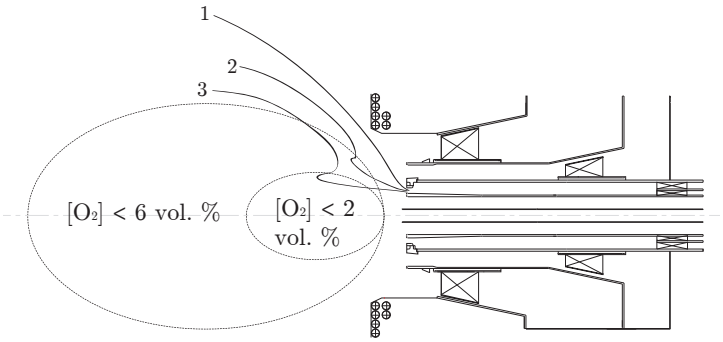

Figure 12.5 Particle trajectories through a central IRZ.

the particles to entrain into the internal recirculation zone without making the IRZ collapse can be achieved by a number of changes to the either the burner operating conditions or the burner geometry [395, 400]. Aiming to increase the axial momentum of the particles while reducing the radial motion as the particles leaves the burner, while maintaining the high swirl of the tertiary air flow could potentially lead to a more desirable low NO_x flame. Reducing the swirl of the primary air flow would both increase the axial momentum and reduce the radial motion, while minimizing the pressure loss inside the burner. Alternatively the flow ratio between primary and combustion air could be changed. However, based on the experiences from the Amager power station burner, a stable balance might be difficult to achieve.

The AMV and HEV burners share an overall construction and the principles of low NO_x flames through air staging. The flow settings encourage two different flame stabilization flow patterns. Although both flames depend on a toroidal internal recirculation zone to define the macro mixing capabilities of the flame, the mechanisms are widely different. The operating conditions of one flame can be adjusted to take on desirable properties of the the other, but a continuous transition between the AMV and HEV is not possible due to the reverted flow direction of the toroidal recirculation zone.

12.3 Summary

The measurements on the two full-scale flames at AMV and HEV have provided unique data on flame response behavior to changes in operational conditions. A method for fast flame mapping was developed and successfully commissioned, allowing for a systematic parameter study to be carried out.

The sampling of fuel dust and pellets links the fundamental studies on particle thermochemical processes and fuel characterization directly to the observed flame behavior. The information can be used to identify and define the most important parameters that can be further investigated by numerical studies or scaled experiments.

The two flames represent textbook flame types and thus the parametric study can be used on a qualitative basis to evaluate the versatility of numerical studies on similar burners, providing much needed full-scale data to the literature [402].

Part V

Recapitulations and Conclusions

"Life is the art of drawing sufficient conclusions

from insufficient premises"

—Samuel Butler

Conclusions

This thesis aims to contribute to a scientific basis for the development of the next generation of biodust burners. It contains experimental work in lab-, pilot-, and full-scale as well as engineering modeling on single particle devolatilization at operating conditions and using particle sizes relevant to PF combustion. The work aims to ease the implementation into commercial CFD softwares which have also been used to assist the experimental and modeling work.

Engineering Particle Devolatilization

Laboratory scale entrained flow experiments were carried out on pine wood and miscanthus fuels with two different mineral contents processed to particle sizes below 125 μm and introduced to the reactor in dilute mass flows. Short residence times and effective sample quenching allowed for the collection of partially devolatilized particles. Accurate conversion determination was obtained by selective element tracing. Particle temperature and residence time histories were derived from CFD simulations coupled to the experimental results through an iterative update of the devolatilization kinetics. The results indicate noticeable faster devolatilization kinetics at the applied heating rate (10^4–$10^5\,\mathrm{K \cdot s^{-1}}$) and peak temperatures (1405–1667 K) than previously reported in the literature. This is a result that can be ascribed to the improved characterization of the particle property histories. The devolatilization of pine wood particles could be described by a SFOR mechanism and an Arrhenius type rate expression with a pre-exponential factor of $A = 18.9 \times 10^3\,\mathrm{s^{-1}}$ and an activation energy of $E_\mathrm{a} = 21\,305\,\mathrm{J \cdot mol^{-1}}$. The derived kinetics were validated by comparing CFD calculations to experimental results from a 15 kW furnace. The fast devolatilization kinetics resulted in good predictions of fuel ignition, while kinetics derived at low heating rates resulted in a significant ignition delay.

Slow heating rate TGA experiments were carried out on the same pine wood and miscanthus fuels at heating rates of 2 and $40\,\mathrm{K \cdot min^{-1}}$. Different phenomenological models were employed to shed light on the heating rate versatility of the available devolatilization models. In accordance with the general literature the SFOR mechanism struggled to describe the devolatilization process across different heating rates, while more complex models such as the DAEM were found to be superior.

An initial Biot number evaluation showed how biomass particles would never assume thermally thin properties, and thus isothermal modeling will appear insufficient for biodust combustion simulations. However, the absolute time scales should be kept in mind, as large relative deviations of the devolatilization rate of small particles were found to be insignificant on an absolute scale. A thermal analysis was conducted on single particles using a one-dimensional heat transport model coupled to a drying and a devolatilization model and validated against experimental data for particle sizes of 63–125 μm, 2–6 mm, and 10.9 mm. A combined thermal and kinetic model was found to be sufficient to describe the devolatilization process. Two sets of kinetics, active at high and low temperatures respectively, were necessary in order to describe the devolatilization using the SFOR model.

A method to implement heat transport corrected SFOR kinetics for isothermal particle calculations was developed as a part of the current study. This will ease the implementation into the commercial CFD code ANSYS®FLUENT® (version 15.07) and eliminate the need for implementation of user specified and computational demanding heat transport modeling of the particle phase. The method is based on discrete particle size intervals, each with their own specific set of apparent devolatilization kinetics based on the simulation results of the stand-alone single particle devolatilization model. The implementation into FLUENT®can be achieved by the inherent discrete phase functions and adds no additional strain to the computational requirements.

The standard FLUENT®devolatilization kinetics using the inherent isothermal particle approach and the SFOR model resulted in slightly slower devolatilization of a 89 μm particle when compared to simulations using the heat transport corrected kinetics. This could imply overall ignition delay and predictions of flame instabilities, as the primary function of the small particles is to ensure early ignition close to the burner mouth. Contrary, significant over prediction of the rate of devolatilization emerged when comparing to the results for pyrolysis of larger particles. The delay for 95 % devolatilization of a 1.6 mm particle was found to be on the order of seconds when comparing the default FLUENT®kinetics to the present work. This would not only affect the chemical source term distribution in the computational domain but also the momentum balance and thus particle modulation and trajectories [384, 403].

Full-Scale Biodust Combustion

Three full-scale campaigns were carried out during the project, two of which have been reported in this thesis. The campaigns covered in-flame measurements at Amager and Herning power station. The flame responses to changes in the operational conditions were quantified using rapid flame mapping by intrusive probing and non-intrusive optical observations in the infrared (IR) and visible spectrum (VIS). The method of fast flame mapping was proven

successful and allowed to map the response for several operating conditions.

Two fundamentally different flames were produced by the two burners. The properties of them can be rationally explained by analyzing the air flows of the two otherwise similar burners. With an equal air flow through the primary, secondary, and tertiary air channels, the AMV burner produced a type-1 flame[1]. The high momentum of the particle laden primary air flow penetrated the internal recirculation zone, which was easily recognized by the centeraxis probe measurements.

The Herning power station flame was found to assume the characteristics of a type-2 flame. The large internal recirculation zone stretched well into the quarl area and gave rise to high temperatures and post combustion gas compositions immediately after entering the quarl from the burner. In general, the HEV flame was very stable and with a clearly defined conical flame shape at the base of the flame. Primarily stabilized by the high velocity tertiary air, flame instabilities could be provoked by reducing the swirl. IR images showed how the entraining particles were deflected by the internal recirculation zone and thus entered the presumed oxygen rich shear layer between primary air and combustion air.

[1] IFRF flame classification system [38].

Work in Progress and Suggestions to Further Development

The current work is constructed from multiple sub-components, supplementing each other. This part will describe the on-going work, which has not been included in this thesis, and makes suggestions to further work based on the experiences from the current project.

Engineering Models

The devolatilization model developed in this work relies on two sets of kinetics dominant in each of their respective temperature intervals. The transition from low to high temperature kinetics is introduced to the model as a discontinuous step change, thus giving rise to a discontinues behavior of the mass loss curve. Two potential implications may occur from such an approach: Discontinuities in numerical simulations may result in convergence difficulties, and the discontinuous kinetic profile will most likely result in an infeasible mass loss curve for particles devolatilizing across both temperature intervals. Thus, although the total devolatilization time may be well predicted, the accumulated volatile release curve may not assume the correct shape.

The individual devolatilization kinetics were validated against experimental data for small particles ($< 125\,\mu$m) and large particles ($> 2\,$mm). Given the observed heating and devolatilization time scales, the critical particle diameter interval, in which substantial devolatilization will occur under both low and high temperature kinetics, will occur in between the $125\,\mu$m to $2\,$mm interval. In this particle size interval no relevant validation data exist to our knowledge. This prevents the application of more complex models like the DAEM which has shown excellent potential for the low heating rate experiments. It also prevents the application of a scientifically justified blending function, employed to avoid discontinuities in the global kinetic expression.

Experiments evaluating the time dependent mass loss of particles in the size range $125\,\mu$m to $2\,$mm at operating conditions relevant to PF combustion are of central importance to the further development of more accurate devolatilization models. Preferably, particle temperature measurements should be included for single or multidimensional transport modeling validation.

This thesis has been focusing on the near burner field and the thermochem-

ical processes that affect this region. Flame stability and ignition properties are of great importance to the daily operation of the existing burners, and the understanding of the field is fundamental to the development of improved technology. However, many processes taking place in a boiler are to some extent coupled, and thus the post devolatilization processes should not be neglected. The topic of burnout and the ability to predict the level of carbon in ash remain to be a key evaluation point for solid fuel efficiency. The heat release from biomass is primarily emerging from homogeneous gas phase combustion of volatiles. To accommodate this the flow patterns and air-staging mechanisms will to extent focus on gas-gas mixing properties rather than particle residence time optimization. Therefore, a further understanding of the char properties for fuels undergoing high heating rate and high temperature devolatilization would be of natural interest as the conditions may be different from conventional coal studies [404, 405]. The work conducted on particle devolatilization during this study also includes an extensive char reactivity study of wood, miscanthus, KCl doped wood, and mineral leached miscanthus. It follows the development in char reactivity, morphology, and size distribution as the particles undergo partial devolatilization at high heating rates. A continuation of this work would complete the model fuel characterization in regards to the thermochemical processes.

Full-Scale Measurements

The two full-scale campaigns reported in this thesis are primarily based on fast flame mapping by center axis probe measurements. This provides useful information to the understanding of the resulting flame dynamics. However, as swirling flows are three-dimensional flows and key features like air-staging take place in the radial direction, additional measurements in the horizontal and vertical plane would contribute greatly to the further interpretation of flame responses to changes in the operating conditions. During week 12 of 2014 a third full-scale campaign was carried out at AMV1. This campaign focused on a detailed mapping of a single reference flame. Effort was put into making the operational conditions as similar as possible to those for the reference flame of the first AMV campaign. In addition to the optical observations and the center axis probe measurements the four day campaign also included horizontal and vertical plane probe traversing at three different axial positions. Each traverse included optical temperature measurements and extractive gas sampling, similar to the center line measuremetns. Two dimensional laser doppler anemometry (LDA) velocity measurements were conducted both with and without particle seeding (fly ash or laboratory grade glass beads) of the combustion air registers. Particle extractions were carried out. In-flame UV spectrometry was applied for OH radical quantification. Preliminary raw data analysis shows promising potential for using such data as evaluation material

for e.g. CFD simulations.

Literature surveys and the full-scale measurements suggest the particle trajectories to play a significant role in the flame properties. For future full-scale campaigns it is suggested to do a high resolution and high frequency optical study on the particle flow interaction with the flame holder.

Bibliography

[1] *Chicago Manual of Style*. The University of Chicago Press, Chicago, 16th edition, 2010.

[2] Turabian, K. L. *A Manual for Writers of Research Papers, Theses, and Dissertations: Chicago Style for Students and Researchers*. The University of Chicago Press, Chicago, 8th edition, 2013.

[3] Pachauri, R. K. and Meyer, L. *IPCC Fifth Assessment Synthesis Report*. Technical report, Intergovernmental Panel on Climate Change, 2014.

[4] Basu, P.; Butler, J.; and Leon, M. A. *Renew. Energy* 2011. 36 (1), 282–288.

[5] *Tillægsaftale mellem regeringen, centrum-demokraterne, det konservative folkeparti, venstre og socialistisk folkeparti til biomasseaftalen af 14. juni 1993*. 1997.

[6] Pedersen, L. S.; Nielsen, H. P.; Kiil, S.; Hansen, L. A.; Dam-Johansen, K.; Kildsig, F.; Christensen, J.; and Jespersen, P. P. *Fuel* 1996. 75 (13), 1584–1590.

[7] Wieck-Hansen, K.; Overgaard, P.; and Larsen, O. H. *Biomass Bioenergy* 2000. 19, 395–409.

[8] Wu, H. *Co-Combustion of Fossil Fuels and Waste*. Phd thesis, Technical University of Denmark, 2011.

[9] Beutler, J.; Clausen, S.; Fateev, A.; Hvid, S. L.; Kær, S.; and Baxter, L. In *Coal Rising to New Challenges - Clear. Clean Coal*. 2010 .

[10] Saastamoinen, J.; Aho, M.; Moilanen, A.; Sørensen, L. H.; Clausen, S.; and Berg, M. *Biomass Bioenergy* 2010. 34, 728–736.

[11] Zuwala, J. and Sciazko, M. *Biomass Bioenergy* 2010. 34 (8), 1165–1174.

[12] *2030 Framework for Climate and Energy Policies*. 2015.

[13] Regeringen. *Vores Energi*. Technical Report November, Danish Ministry of Climate, Energy and Building, 2011.

[14] Koza, D. and Shuang, M. *Power Eng.* 2011. 115 (5), 60–68.

[15] Jensen, A. D. and Glarborg, P. *Combustion and High Temperature Processes*. Technical University of Denmark, β edition, 2009.

[16] Beér, J. M.; Chomiak, J.; and Smoot, L. D. *Prog. Energy Combust. Sci.* 1984. 10 (2), 177–208.

[17] Xu, M.; Shen, C.; and Yuan, J. *Energy Fuels* 2000. 14 (3), 533–538.

[18] Lockwood, F. C. and Mahmud, T. *Combust. Sci. Technol.* 1989. 66, 319–328.

[19] Phelan, W. J. and Flament, G. *The Reduction of NOx Emissions by Staged Combustion for a Range of Diverse Coals Fired under Boiler Simulated Conditions.* Technical report, International Flame Research Foundation, Velsen-Noord, 1983.

[20] Syred, N.; Chigier, N. A.; and Beér, J. M. *Proc. Combust. Inst.* 1971. 13 (i), 617–624.

[21] Syred, N. and Béer, J. M. *Combust. Flame* 1974. 23.

[22] Fay, G. C. *Ceram. Bull.* 1978. 57 (5), 500–502.

[23] Beér, J. M. and Chigíer, N. A. *J. Inst. Fuel* 1969. 42 (347), 443–450.

[24] Jing, J.; Li, Z.; Zhu, Q.; Chen, Z.; Wang, L.; and Chen, L. *Energy* 2011. 36, 258–267.

[25] Weber, R.; Dugué, J.; Sayre, A.; Peters, A. A. F.; and Visser, B. M. *Measurements and Computations of Quarl Zone Flow Field and Chemistry in a Swirling Pulverized Coal Flame.* Technical report, International Flame Research Foundation, Velsen-Noord, 1992.

[26] Hardalupas, Y.; Liu, C. H.; and Whitelaw, J. H. *Combust. Sci. Technol.* 1994. 97, 157–191.

[27] Martinuzzi, R. and Tropea, C. *J. Fluids Eng.* 1993. 115, 85–92.

[28] Chigier, N. A. and Gilbert, J. L. *J. Inst. Fuel* 1968. 41 (326), 105–112.

[29] Mahmud, T.; Wall, T. F.; and Truelove, J. S. In *Eight Australas. FLuid Mech. Conf.*. Newcastle, 1983 pages 1B.10–1B.13.

[30] Zhengqi, L.; Rui, S.; Lizhe, C.; Zhixin, W.; Shaohua, W.; and Yukun, Q. *Fuel* 2002. 81 (6), 829–835.

[31] Smart, J. P.; Morgan, D. J.; and Roberts, P. A. *Proc. Combust. Inst.* 1992. 24, 1365–1372.

[32] Orfanoudakis, N.; Hatziapostolou, A.; Krallis, K.; K. Sardi; Vlachakis, N.; Mavromatis, A.; and Tsoukalas, V. D. *J. Comput. Methods Sci. Eng.* 2007. 7, 3–19.

[33] Costa, M.; Costen, P.; Lockwood, F. C.; and Mahmid, T. *Proc. Combust. Inst.* 1990. pages 973–980.

[34] Backreedy, R. I.; Fletcher, L. M.; Jones, J. M.; Ma, L.; Pourkashanian, M.; and Williams, A. *Proc. Combust. Inst.* 2005. 30 (Pt. 2), 2955–2964.

[35] Smart, J. P. and Weber, R. *J. Inst. Energy* 1989. 62 (453), 237–245.

[36] Hagiwara, A.; Bortz, S.; and Weber, R. *Theoretical and Experimental Studies on Isothermal, Expanding Swirling Flows with Application to Swirl Burner Design.* Technical report, International Flame Research Foundation, Velsen-Noord, 1986.

[37] Visser, B. M. and Weber, R. *Predictions of Near Burer Zone Properties of Six Swirling Pulverized Coal Flames.* Technical report, International Flame Research Foundation, Velsen-Noord, 1990.

[38] Smart, J. P. and Weber, R. *J. Inst. Energy* 1989. 62 (453), 237–245.

[39] Lockwood, F. C. and Mahmud, T. *Proc. Combust. Inst.* 1988. pages 165–173.

[40] Weber, R.; Peters, A. A. F.; Breithaupt, P. P.; and Visser, B. M. *J. Fluids Eng.* 1995. 117, 289–297.

[41] Weber, R.; Smart, J. P.; and Phelan, W. J. *NOx Reduction with Coal Firing by Application of Both Internal Air Staging and Fuel Rich Precombustors.* Technical report, International Flame Research Foundation, Velsen-Noord, 1987.

[42] Godoy, S.; Hirji, M.; and Lookwood, L. C. *J. Inst. Energy* 1986. 59, 38–44.

[43] Chigier, N. A. and Beér, J. M. *J. Basic Eng.* 1964. pages 797–804.

[44] Smart, J. and Weber, R. *NOx Reduction and Burnout Optimisation using Aerodynamic Air Staging and Air Staged Precombustors.* Technical report, International Flame Research Foundation, Velsen-Noord, 1987.

[45] Damstedt, B.; Pederson, J. M.; Hansen, D.; Knighton, T.; Jones, J.; Christensen, C.; Baxter, L.; and Tree, D. *Proc. Combust. Inst.* 2007. 31 II, 2813–2820.

[46] Ballester, J.; Barroso, J.; Cerecedo, L. M.; and Ichaso, R. *Combust. Flame* 2005. 141 (x), 204–215.

[47] Truelove, J. S. and Holcombe, D. *Proc. Combust. Inst.* 1990. pages 963–971.

[48] Wolanski, P. and Wójcicki, S. *Proc. Combust. Inst.* 1975. 15, 1295–1302.

[49] Yan, W. and Yu, X. *Heat Transf. Eng.* 1999. 20 (4), 45–51.

[50] Dall'Ora, M. *Reactivity and Burnout of Wood Fuels.* Phd thesis, Technical University of Denmark, 2011.

[51] Biagini, E.; Fantozzi, C.; and Tognotti, L. *Combust. Sci. Technol.* 2004. 176 (5-6), 685–703.

[52] Bridgwater, A. V. *J. Anal. Appl. Pyrolysis* 1999. 51 (1-2), 3–22.

[53] Chen, Y.; Charpenay, S.; Jensen, A.; Wo, M. A.; and Serio, M. A. *Proc. Combust. Inst.* 1998. pages 1327–1334.

[54] Rath, J.; Wolfinger, M. G.; Steiner, G.; Krammer, G.; Barontini, F.; and Cozzani, V. *Fuel* 2003. 82, 81–91.

[55] Zielinski, E. *Fuel* 1967. 46 (4), 329 – 340.

[56] Bryden, K. M. and Hagge, M. J. *Fuel* 2003. 82 (13), 1633–1644.

[57] Phelan, W. J. and Bortz, S. *The Effect of Pulverized Fuel Burner Design Parameters on Flame Characteristics Affecting Emissions NOx and Char Burnout.* Technical report, International Flame Research Foundation, Velsen-Noord, 1986.

[58] Hajaligol, M. R.; Howard, J. B.; and Peters, W. A. *Combust. Flame* 1993. 95 (1), 47–60.

[59] Guell, A. J.; Li, C. Z.; Herod, A. A.; Güell, A.; Stokes, B.; Hancock, P.; and Kandiyot, R. *Biomass Bioenergy* 1993. 5 (2), 155–171.

[60] Fraga, A.-R.; Gaines, A. F.; and Kandiyoti, R. *Fuel* 1991. 70 (7), 803–809.

[61] Chen, J. C.; Castagnoli, C.; and Niksa, S. *Energy Fuels* 1992. 6 (3), 264–271.

[62] Hoekstra, E.; van Swaaij, W. P.; Kersten, S. R.; and Hogendoorn, K. J. *Chem. Eng. J.* 2012. 191, 45–58.

[63] Grøli, M. G. *A Theoretical and Experimental Study of the Thermal Degradation of Biomass.* Phd thesis, The Norwegian University of Science and Technology, 1996.

[64] Lu, H. *Experimental and Modeling Investigations of Biomass Particle Combustion.* Phd thesis, Brigham Young University, 2006.

[65] Miller, R. *Combust. Sci. Technol.* 1996. 119 (1-6), 331 – 373.

[66] Septien, S.; Valin, S.; Dupont, C.; Peyrot, M.; and Salvador, S. *Fuel* 2012. 97, 202–210.

[67] Zhang, Y.; Kajitani, S.; Ashizawa, M.; and Miura, K. *Energy Fuels* 2006. 20 (8), 2705–2712.

[68] Sun, S.; Tian, H.; Zhao, Y.; Sun, R.; and Zhou, H. *Bioresour. Technol.* 2010. 101 (10), 3678–84.

[69] Zanzi, R.; Sjöström, K.; and Björnbom, E. *Biomass Bioenergy* 2002. 23, 357–366.

[70] Qin, K. *Entrained Flow Gasification of Biomass.* Phd thesis, Technical University of Denmark, 2012.

[71] Shafizadeh, F. *J. Anal. Appl. Pyrolysis* 1982. 3, 283–305.

[72] Zanzi, R.; Sjöström, K.; and Björnbom, E. *Fuel* 1996. 75 (5), 545–550.

[73] Antal, M. J. J. and Várhegyi, G. *Ind. Eng. Chem. Res.* 1995. 34 (3), 703–717.

[74] Hajaligol, M. R.; Howard, J. B.; Longwell, J. P.; and Peters, W. A. *Ind. Eng. Chem. Process Des. Dev.* 1982. 21 (3), 457–465.

[75] Antal, M. J. J.; Friedmand, H. L.; and Rogers, F. E. *Combust. Sci. Technol.* 1980. 21, 141–152.

[76] Bilbao, R.; Arauzo, J.; and Millera, A. *Thermochim. Acta* 1987. 120, 121–131.

[77] Fairbridge, C.; Ross, R. A.; and Sood, S. P. *J. Appl. Polym. Sci.* 1978. 22, 497–510.

[78] Grønli, M.; Antal, M. J.; and Várhegyi, G. *Ind. Eng. Chem. Res.* 1999. 38, 2238–2244.

[79] Akita, K. and Kase, M. *J. Polym. Sci. Part A-1 Polym. Chem.* 1967. 5 (4), 833–848.

[80] Min, K. *Combust. Flame* 1977. 30, 285–294.

[81] Bilbao, R.; Arauzo, J.; and Millera, A. *Thermochim. Acta* 1987. 120, 133–141.

[82] Várhegyi, G. and Antal, M. J. J. *Energy Fuels* 1989. 3 (3), 329–335.

[83] Milosavljevic, I.; Oja, V.; and Suuberg, E. M. *Ind. Eng. Chem. Res.* 1996. 35 (3), 653–662.

[84] Kothari, V. and Antal Jr., M. J. *Fuel* 1985. 64 (11), 1487–1494.

[85] Narayan, R. and Antal, M. J. J. *Ind. Eng. Chem. Res.* 1996. 35, 1711–1721.

[86] Simmons, G. M. and Gentry, M. *J. Anal. Appl. Pyrolysis* 1986. 10 (2), 117–127.

[87] Mehrabian, R.; Scharler, R.; and Obernberger, I. *Fuel* 2012. 93, 567–575.

[88] Dall'Ora, M.; Jensen, P. A.; and Jensen, A. D. *Energy Fuels* 2008. 22 (5), 2955–2962.

[89] Bonvicini, G.; Coraggio, G.; and Faleni, M. *Biofuels Devolatilization and Char Combustion Characterization with the IPFR.* Technical Report December, International Flame Research Foundation, 2013.

[90] Lewellen, P.; Peters, W.; and Howard, J. *Proc. Combust. Inst.* 1977. 16 (1), 1471–1480.

[91] Prins, M. J.; Lindén, J.; Li, Z. S.; Bastiaans, R. J. M.; van Oijen, J. A.; Aldén, M.; and Goey, L. P. H. *Energy Fuels* 2009. 23 (6), 993–1006.

[92] Loison, R. and Chauvin, R. *Chim. Ind.* 1964. 91 (3), 269–275.

[93] Sepman, A. and de Goey, L. *Biomass Bioenergy* 2011. 35 (7), 2903–2909.

[94] Drummond, A.-R. F. and Drummond, I. W. *Ind. Eng. Chem. Res.* 1996. 35 (4), 1263–1268.

[95] Hoekstra, E.; Van Swaaij, W. P.; Kersten, S. R.; and Hogendoorn, K. J. *Chem. Eng. J.* 2012. 187, 172–184.

[96] Peacocke, G.; Madrali, E.; Li, C.-Z.; Güell, A.; Wu, F.; Kandiyoti, R.; and Bridgwater, A. *Biomass Bioenergy* 1994. 7 (1), 155–167.

[97] Okuno, T.; Sonoyama, N.; Hayashi, J.-I.; Li, C.-Z.; Sathe, C.; and Chiba, T. *Energy Fuels* 2005. 19 (5), 2164–2171.

[98] Jensen, A.; Dam-Johansen, K.; Wo, M. A.; and Serio, M. A. *Energy Fuels* 1998. 12 (5), 929–938.

[99] Nik-Azar, M.; Hajaligol, M. M. R.; Sohrabi, M.; and Dabir, B. *Fuel Process. Technol.* 1997. 51 (1-2), 7.

[100] Raveendran, K.; Ganesh, A.; and Khilart, K. C. *Fuel* 1995. 74 (12), 1812–1822.

[101] Jones, J.; Darvell, L.; Bridgeman, T.; Pourkashanian, M.; and Williams, A. *Proc. Combust. Inst.* 2007. 31 (2), 1955–1963.

[102] Darvell, L. I.; Hrycko, P.; Jones, J. M.; Nowakowski, D. J.; and Pourkashanian, M. *World Renew. Energy Congr.* 2005. pages 584–589.

[103] Várhegyi, G.; Antal, M. J. J.; Szekely, T.; Till, F.; Jakab, E.; and Szabo, P. *Energy Fuels* 1988. 2 (3), 273–277.

[104] Nunn, T. R.; Howard, J. B.; Longwell, J. P.; and Peters, W. A. *Ind. Eng. Chem. Res.* 1985. 24, 844–852.

[105] Bliek, A. *AIChE J.* 1985. 31 (10), 1666 – 1681.

[106] Grant, D. M.; Pugmire, R. J.; Fletcher, T. H.; and Kerstein, A. R. *Energy Fuels* 1989. 3 (2), 175–186.

[107] Lewis, A. D. and Fletcher, T. H. *Energy Fuels* 2013. 27 (2), 942–953.

[108] Fletcher, T. H.; Pond, H. R.; Webster, J.; Wooters, J.; and Baxter, L. L. *Energy Fuels* 2012. 26 (6), 3381–3387.

[109] Damartzis, T.; Kostoglou, M.; and Zabaniotou, A. *Int. J. Chem. React. Eng.* 2009. 7 (1), 1–27.

[110] Daugaard, D. E. and Brown, R. C. *Energy Fuels* 2003. 17 (4), 934–939.

[111] Havens, J. A.; Hashemie, H. T.; and Brown, L. E. *Combust. Sci. Technol.* 1972. 5 (3), 91–98.

[112] Broido, A. *Pyrodynamics* 1966. 4 (3), 243 – 251.

[113] Akita, K. and Kase, M. *J. Appl. Polym. Sci.* 1967. 5, 833–848.

[114] Arseneau, D. F. *Can. J. Chem.* 1961. 39, 1915–1919.

[115] Grønli, M. G. and Melaaen, M. C. *Energy Fuels* 2000. 14 (4), 791–800.

[116] Milosavljevic, I. *Ind. Eng. Chem. Res.* 1995. 34 (4), 1081 – 1091.

[117] Di Blasi, C. *Chem. Eng. Sci.* 1996. 51 (7), 1121–1132.

[118] Di Blasi, C. *Ind. Eng. Chem. Res.* 1996. 35 (1), 37–46.

[119] Di Blasi, C. *Fuel* 1997. 76 (10), 957–964.

[120] Brix, J.; Jensen, P. A.; and Jensen, A. D. *Fuel* 2010. 89 (11), 3373–3380.

[121] Kroschwitz, J. I., editor. *Kirk Othmers Encyclopedia of Chemical Technology*, volume 3, pages 683–707. John Wiley & Sons, inc., online edition, 2010.

[122] Agency, I. E. *Bioenergy Project Development & Biomass Supply.* Technical report, IEA Bioenergy, 2007.

[123] McKendry, P. *Bioresour. Technol.* 2002. 82 (1), 37–46.

[124] Marschner, H. *Mineral Nutrition of Higher Plants.* Academic Press, 2nd edition, 2002.

[125] Kramer, P. J. and Kozlowsi, T. T. *Physiology of Woody Plants.* 1979.

[126] Saleh, S. B. *Torrefaction of Biomass for Power Production.* Phd thesis, Technical University of Denmark, 2013.

[127] Obernberger, I. and Thek, G. *Biomass Bioenergy* 2004. 27 (6), 653–669.

[128] Chan, R. W.-c.; Kelbon, M.; and Krieger-Brockett, B. *Ind. Eng. Chem. Res.* 1988. 27, 2261–2275.

[129] Chan, W.-C. R.; Kelbon, M.; and Krieger, B. B. *Fuel* 1985. 64 (11), 1505–1513.

[130] Yang, Y. B.; Sharifi, V. N.; Swithenbank, J.; Ma, L.; Darvell, L. I.; Jones, J. M.; Pourkashanian, M.; and Williams, A. *Energy Fuels* 2008. 22 (1), 306–316.

[131] Gil, M.; Teruel, E.; and Arauzo, I. *Fuel* 2014. 116, 328–340.

[132] Godoy, S.; Hirji, K.; Lockwood, F. C.; and Miller, J. *Combust. Sci. Technol.* 1986. 44 (5-6), 319–335.

[133] Mandø, M.; Rosendahl, L.; Yin, C.; and Sørensen, H. *Fuel* 2010. 89 (10), 3051–3062.

[134] Kobayashi, N.; Guilin, P.; Kobayashi, J.; Hatano, S.; Itaya, Y.; and Mori, S. *Powder Technol.* 2008. 180 (3), 272–283.

[135] Simpson, W. and TenWolde, A. *Physical Properties and Moisture Relations of Wood*, volume 72. United States Department of Agriculture, Madison, centennial edition, 2010.

[136] Adapa, P. K. *Powder Handl. Process.* 2002. 14 (4), 252 – 300.

[137] Larsson, S. H.; Thyrel, M.; Geladi, P.; and Lestander, T. a. *Bioresour. Technol.* 2008. 99, 7176–7182.

[138] Sokhansanj, S. and Turhollow, a. F. *Appl. Eng. Agric.* 2004. 20 (4), 495–499.

[139] Stelte, W.; Holm, J. K.; Sanadi, A. R.; Barsberg, S.; Ahrenfeldt, J.; and Henriksen, U. B. *Fuel* 2011. 90 (11), 3285–3290.

[140] Zhang, L.; Xu, C.; and Champagne, P. *Energy Convers. Manag.* 2010. 51 (5), 969–982.

[141] Jenkins, B. M.; Baxter, L. L.; Miles Jr., T. R.; and Miles, T. R. *Fuel Process. Technol.* 1998. 54, 17–46.

[142] Hurt, R. H. *Proc. Combust. Inst.* 1998. 27 (2), 2887–2904.

[143] Li, J.; Bonvicini, G.; Tognotti, L.; Yang, W.; and Blasiak, W. *Fuel* 2014. 122, 261–269.

[144] Baxter, L. L. and Lu, H. *Mechanisms and Rates of Aspherical, Large Particle Conversion in Suspension*, 2011.

[145] Sander, B. *Biomass Bioenergy* 1997. 12 (3), 177–183.

[146] Frandsen, F. J. *Ash Formation, Deposition and Corrosion When Utilizing Straw for Heat and Power Production.* Doctoral thesis, Technical University of Denmark, Kgs. Lyngby, 2001.

[147] Abbasi, T.; Abbasi, S.; and Abassi, S. A. *Renew. Sustain. Energy Rev.* 2010. 14 (3), 919–937.

[148] Saidur, R.; Abdelaziz, E.; Demirbas, A.; Hossain, M.; and Mekhilef, S. *Renew. Sustain. Energy Rev.* 2011. 15 (5), 2262–2289.

[149] Tumuluru, J. S.; Sokhansanj, S.; Hess, J. R.; Wright, C. T.; and Boardman, R. D. *Ind. Biotechnol.* 2011. 7 (5), 384–401.

[150] Di Blasi, C. *Prog. Energy Combust. Sci.* 2008. 34 (1), 47–90.

[151] Mohan, D.; Pittman, C. U.; and Steele, P. H. *Energy Fuels* 2006. 20 (3), 848–889.

[152] Demirbas, A. *Energy Sources, Part A Recover. Util. Environ. Eff.* 2009. 31 (13), 1186–1193.

[153] Stenseng, M. *Pyrolysis and Combustion of Biomass.* Phd thesis, Technical University of Denmark, 2001.

[154] Johansen, J. M. *Release of Inorganic Matter during Combustion of Biomass.* Master's thesis, Technical University of Denmark, 2011.

[155] Müller-Hagedorn, M.; Bockhorn, H.; Krebs, L.; and Müller, U. *Proc. Combust. Inst.* 2002. 29, 399–406.

[156] van Lith, S. C.; Jensen, P. A.; Frandsen, F. J.; and Glarborg, P. *Energy Fuels* 2008. 22 (6), 1598–1609.

[157] Novakovic, A.; van Lith, S. C.; Frandsen, F. J.; Jensen, P. A.; and Holgersen, L. B. *Energy Fuels* 2009. 23 (7), 3423–3428.

[158] Knudsen, J. N. and Nygaard Knudsen, J. *Volatilization of Inorganic Matter during Combustion of Annual Biomass*. Phd thesis, Technical University of Denmark, 2004.

[159] van Lith, S. C. *Release of Inorganic Elements during Wood-Firing on a Grate*. Phd thesis, Technical University of Denmark, 2005.

[160] Telfer, M. A. and Zhang, D. K. *Energy Fuels* 1998. 12 (6), 1135–1141.

[161] Christensen, K. A.; Stenholm, M.; and Livbjerg, H. *J. Aerosol Sci.* 1998. 29 (4), 421–444.

[162] Jenkins, B. M.; Bakker, R. R.; and Wei, J. B. *Biomass Bioenergy* 1996. 10 (4), 177–200.

[163] Bjoerkman, E. and Stroemberg, B. *Energy Fuels* 1997. 11 (5), 1026–1032.

[164] Weber, R.; Mancini, M.; Schaffel-Mancini, N.; and Kupka, T. *Fuel Process. Technol.* 2013. 105, 113–128.

[165] Trubetskaya, A. *Report on biomass Characterization Study*. Technical report, Technical University of Denmark, Kongens Lyngby, 2013.

[166] Retsch. *Operating Instructions / Manual Particle Size Analysis System CAMSIZER and CAMSIZER XT*. Retsch Technology, Retsch Technology GmbH, Retsch-Allee 1–5, 42781 Haan, Germany.

[167] Levenspiel, O. *Chemical Reactor Omnibook*. OSU Book Stores, Inc., Corvallis, Oregon, 1993.

[168] Yin, C.; Kær, S. K.; Rosendahl, L.; and Hvid, S. L. *Bioresour. Technol.* 2010. 101 (11), 4169–4178.

[169] Johansson, R.; Thunman, H.; and Leckner, B. *Combust. Flame* 2007. 149 (1-2), 49–62.

[170] Lu, H.; Robert, W.; Peirce, G.; Ripa, B.; and Baxter, L. L. *Energy Fuels* 2008. 22 (4), 2826–2839.

[171] Trubetskaya, A. *Single Biomass Particle Combustino and Fuel Characterization*. Phd thesis, Technical University of Denmark, 2015.

[172] Turns, S. R. *An Introduction to Combustion Concepts and Applications*. McGraw-Hill Higher Education, 2nd edition, 2006.

[173] Warnatz, J.; Maas, U.; and Dibble, R. W. *Combustion Physical and Chemical Fundamentals, Modeling and Simulation, Experiments, Pollutant Formation*. Springer-Verlag Berlin Heidelberg, Heidelberg, Karlsruhe, Berkeley, 4th edition, 2006.

[174] Milne, T. *Sol. Energy Res. Inst.* 1979. pages II/95A–II/131.

[175] Antal Jr., M. In K. Böer and J. Duffie, editors, *Adv. Sol. Energy SE - 3*, pages 61–111. Springer New York, 1985.

[176] Antal Jr., M. In K. Böer and J. Duffie, editors, *Adv. Sol. Energy SE - 4*, pages 175–255. Springer US, 1985.

[177] Vassilev, S. V.; Baxter, D.; and Vassileva, C. G. *Fuel* 2013. 112, 391–449.

[178] Smooti, L. D. *Prog. Energy Combust. Sci.* 1997. 23, 203–232.

[179] Jepsen, M. S. *Pyrolysis of Large Biomass Particles in a single Particle Combustion Reactor*. Master's thesis, The Technical University of Denmark, 2014.

[180] Momeni, M. *Fundamental Study of Single Biomass Particle Combustion*. Phd thesis, Aalborg University, 2012.

[181] Bolyos, E.; Lawrence, D.; and Nordin, A. In *3rd Int. Dispos. Conf.*, volume 32. 2003 pages 27–33.

[182] Biagini, E. *Review of Solid Fuels Combustion Models for the Determination of Reactivity Parameter*. Technical report, International Flame Research Foundation, Livorno, 2010.

[183] Prakash, N. and Karunanithi, T. *J. Appl. Sci. Res.* 2008. 4 (12), 1627–1636.

[184] Flynn, J. H. *Thermochim. Acta* 1997. 300, 83–92.

[185] Conesa, J. A.; Marcilla, A.; Caballero, J. A.; and Font, R. *J. Anal. Appl. Pyrolysis* 2001. 58-59, 617–633.

[186] Mehmet, Y. and Roche, R. S. *J. Appl. Polym. Sci.* 1976. 20, 1955–1965.

[187] Gyulai, G. and Greenhow, E. J. *Thermochim. Acta* 1973. 6, 239–244.

[188] Cai, J.; He, F.; and Yao, F. *J. Math. Chem.* 2007. 42 (4), 949–956.

[189] Braun, R. L. and Burnham, A. K. *Energy Fuels* 1987. 1 (2), 153–161.

[190] Niksa, S. and Lau, C. W. *Combust. Flame* 1993. 94 (3), 293–307.

[191] Carrasco, F. *Thermochim. Acta* 1993. 213, 115–134.

[192] Miura, K. and Maki, T. *Energy Fuels* 1998. 12 (5), 864–869.

[193] Cai, J.; Yao, F.; Yi, W.; and He, F. *AIChE J.* 2006. 52 (4), 1554–1557.

[194] Cai, J.; Yao, F.; Yi, W.; and He, F. *AIChE J.* 2006. 52 (7), 2656.

[195] Shafizadeh, F. *Abstr. Pap. Am. Chem. Soc.* 1976. 172 (SEP3).

[196] Thurner, F. and Mann, U. *Ind. Eng. Chem. Process Des. Dev.* 1981. 20, 482–488.

[197] Font, R.; Marcilla, A.; Verdii, E.; and Devesa, J. *Ind. Eng. Chem. Res.* 1990. 29, 1846–1855.

[198] Bradbury, A. G. W.; Sakai, Y.; and Shafizadeh, F. *J. Appl. Polym. Sci.* 1979. 23, 3271–3280.

[199] Byrne. *J. Appl. Chem.* 1966. 16, 81–88.

[200] Piskorz, J.; Radlein, D.; and Scott, D. S. *J. Anal. Appl. Pyrolysis* 1986. 9, 121–137.

[201] Órfao, J. J. M. and Figueiredo, J. L. *Thermochim. Acta* 2001. 380, 67–78.

[202] Stubington, J. F. and Aiman, S. *Energy Fuels* 1994. 8 (1), 194–203.

[203] Shafizadeh, F. and Bradbury, a. G. W. *J Appl Polym Sci* 1979. 23, 1431–1442.

[204] Liden, A. G.; Berruti, F.; and Scott, D. S. *Chem. Eng. Commun.* 1988. 65, 207 – 221.

[205] Várhegyi, G.; Jakab, E.; and Antal, M. J. *Energy Fuels* 1995. 36 (10), 119.

[206] Anthony, D.; Howard, J.; Hottel, H.; and Meissner, H. *Proc. Combust. Inst.* 1975. 15 (1), 1303–1317.

[207] Miller, R. S. and Bellan, J. *Cobmustion Sci. Technol.* 1997. 126 (1-6), 97–137.

[208] Ward, S. and Braslaw, J. *Combust. Flame* 1985. 61 (3), 261–269.

[209] Lin, Y.-C.; Cho, J.; Tompsett, G. a.; Westmoreland, P. R.; and Huber, G. W. *J. Phys. Chem. C* 2009. 113 (46), 20 097–20 107.

[210] Fisher, T.; Hajaligol, M.; Waymack, B.; and Kellogg, D. *J. Anal. Appl. Pyrolysis* 2002. 62 (2), 331–349.

[211] Várhegyi, G.; Antal, M. J. J.; Jakab, E.; and Szabó, P. *J. Anal. Appl. Pyrolysis* 1997. 42, 73–87.

[212] Font, R.; Marcilla, A.; Verdti, E.; and Devesa, J. *J. Anal. Appl. Pyrolysis* 1991. 21, 249–264.

[213] Milosavljevict, I. and Suuberg, E. M. *Ind. Eng. Chem. Res.* 1995. 34, 1081–1091.

[214] Williams, P. T. and Gesler, S. *J. Inst. Energy* 1992. 65 (465), 192 – 200.

[215] Kim, S. and Eom, Y. *Korean J. Chem. Eng.* 2006. 23 (3), 409–414.

[216] Alves, S. S. and Figueiredo, J. L. *J. Anal. Appl. Pyrolysis* 1989. 15, 347–355.

[217] Pyrolysis, A. and Engenharia, F. D. *J. Anal. Appl. Pyrolysisl* 1988. 13, 123–134.

[218] Cozzani, V.; Lucchesi, A.; and Stoppato, G. *Can. J. Chem. Eng.* 1997. 75, 127–133.

[219] Evans, R. J. and Milne, T. A. *Energy Fuels* 1987. 1 (2), 123–137.

[220] Milne, T. A. and Evans, R. J. *Energy Fuels* 1987. 1 (4), 311–319.

[221] Faixb, O.; Jakab, E.; Till, F.; and Szekely, T. *Wood Sci. Technol.* 1988. 22 (4), 323–334.

[222] Di Colomba, B. *Prog. Energy Combust. Sci.* 1993. 19, 71–104.

[223] Wilson, L.; Yang, W.; Blasiak, W.; John, G. R.; and Mhilu, C. F. *Energy Convers. Manag.* 2011. 52 (1), 191–198.

[224] Greenhalf, C.; Nowakowski, D.; Bridgwater, A.; Titiloye, J.; Yates, N.; Riche, A.; and Shield, I. *Ind. Crops Prod.* 2012. 36 (1), 449–459.

[225] Bonelli, P. R.; Buonomo, E. L.; and Cukierman, A. L. *Energy Sources, Part A Recover. Util. Environ. Eff.* 2007. 29 (8), 731–740.

[226] Brink, D. L. and Massoudi, M. S. *J. Fire Flammabl.* 1978. 9, 176–188.

[227] Roberts, A. F. and Clough, G. *Proc. Combust. Inst.* 1963. 9 (1), 158–166.

[228] Cordero, T.; García, F.; and Rodríguez, J. J. *Thermochim. Acta* 1989. 149, 225–237.

[229] Gómez, C. J.; Várhegyi, G.; and Puigjaner, L. *Ind. Eng. Chem. Res.* 2005. 44, 6650–6660.

[230] Murty Kanury, A. *Combust. Flame* 1972. 18 (1), 75–83.

[231] Aiman, S. and Stubington, J. F. *Biomass Bioenergy* 1993. 5 (2), 113–120.

[232] Stamm, A. J. *Ind. Eng. Chem.* 1956. 48 (3), 413–417.

[233] Senneca, O. *Fuel Process. Technol.* 2007. 88 (1), 87–97.

[234] Branca, C.; Albano, A.; and Di Blasi, C. *Thermochim. Acta* 2005. 429 (2), 133–141.

[235] Browne, F. L. and Tang, W. K. *Effect of Various Chemicals on Thermogravimetric Analysis of Pinderosa Pine.* Technical report, Forest Products Laboratory U.S. Department of Agriculture Forest Service, Madison, 1963.

[236] Wagenaar, B. M.; Prins, W.; and van Swaaij, W. P. M. *Fuel Process. Technol.* 1993. 36, 291–298.

[237] Yan, W.; Islam, S.; Coronella, C. J.; and Va, V. R. *Environ. Prog. Sustain. Energy* 2012. 31 (2), 200–204.

[238] Zabaniotou, A.; Ioannidou, O.; Antonakou, E.; and Lappas, A. *Int. J. Hydrogen Energy* 2008. 33 (10), 2433–2444.

[239] Di Blasi, C. and Branca, C. *Ind. Eng. Chem. Res.* 2001. 40 (23), 5547–5556.

[240] Samolada, M. and Vasalos, I. *Fuel* 1991. 70 (7), 883–889.

[241] Zabaniotou, A. A.; Gogotsis, D.; and Karabelas, A. J. *J. Anal. Appl. Pyrolysis* 1994. 29, 73–87.

[242] Reina, J.; Velo, E.; and Puigjaner, L. *Ind. Eng. Chem. Res.* 1998. 37 (11), 4290–4295.

[243] Roberts, A. F. *Combust. Flame* 1970. 14, 261–272.

[244] Nelson, P. F.; Smith, I. W.; Tyler, R. J.; and Mackies, J. C. *Energy Fuels* 2006. 2 (9), 391–400.

[245] Wiktorsson, L.-P. and Wanzl, W. *Fuel* 2000. 79 (6), 701–716.

[246] Zabaniotou, A. and Damartzis, T. *J. Anal. Appl. Pyrolysis* 2007. 80 (1), 187–194.

[247] Suuberg, E. M.; Peters, W. A.; and Howard, J. B. *Ind. Eng. Chem. Process Des. Dev.* 1978. 17 (1), 37–46.

[248] Zabaniotou, A.; Ioannidou, O.; and Skoulou, V. *Fuel* 2008. 87 (8-9), 1492–1502.

[249] Nik-Azar, M.; Hajaligol, M. M. R.; Sohrabi, M.; and Dabir, B. *Fuel Sci. Technol. Int.* 1996. 14 (4), 479–502.

[250] Guo, J. *Pyrolysis of Wood Powder and Gasification of Wood-Derived Char*. Ph.D. thesis, Technische Universiteit Eindhoven, 2004.

[251] Nunn, T. R.; Howard, J. B.; Longwell, J. P.; and Peters, W. A. *Ind. Eng. Chem. Process Des. Dev.* 1985. 24, 836–844.

[252] Shuangning, X.; Zhihe, L.; Baoming, L.; Weiming, Y.; and Xueyuan, B. *Fuel* 2006. 85 (5-6), 664–670.

[253] Kobayashi, H.; Howard, J.; and Sarofim, A. *Proc. Combust. Inst.* 1977. 16 (1), 411–425.

[254] Anthony, D. B.; Howard, J. B.; Meissner, H. P.; and Hottel, H. C. *Rev. Sci. Instrum.* 1974. 45 (8), 992.

[255] Desypris, J.; Murdoch, P.; and Williams, A. *Fuel* 1982. 61 (9), 807–816.

[256] Johnson, G. R.; Murdoch, P.; and Williams, A. *Fuel* 1988. 67 (6), 834–842.

[257] Zsakó, J. *J. Therm. Anal.* 1976. 9, 101–108.

[258] Stangeby, P. C.; Sears, P. L.; Strangeby, P. C.; and Sears, P. L. *Fuel* 1981. 60 (2), 131–135.

[259] Miller, R. S. and Bellan, J. *Combust. Sci. Technol.* 2010. 126 (1-6), 37–41.

[260] Kissinger, H. E. *J. Res. Natl. Bur. Stand. (1934)*. 1956. 57 (4), 217–221.

[261] Karlström, O.; Brink, A.; Hupa, M.; and Tognotti, L. *Combust. Flame* 2011. 158, 2056–2063.

[262] Jiménez, S.; Remacha, P.; Ballesteros, J. C.; Giménez, A.; and Ballester, J. *Combust. Flame* 2008. 152, 588–603.

[263] Cetin, E.; Moghtaderi, B.; Gupta, R.; and Wall, T. F. *Fuel* 2004. 83, 2139–2150.

[264] Simone, M.; Biagini, E.; Galletti, C.; and Tognotti, L. *Fuel* 2009. 88 (10), 1818–1827.

[265] Jamaluddin, A.; Truelove, J.; and Wall, T. *Combust. Flame* 1986. 63 (3), 329–337.

[266] Solomon, P. R.; Serio, M. A.; Carangelo, R. M.; and Markham, J. R. *Fuel* 1986. 65 (2), 182–194.

[267] Fletcher, T. H. *Combust. Flame* 1989. 78, 223–236.

[268] Ballantyne, T. R.; Ashman, P. J.; and Mullinger, P. J. *Fuel* 2005. 84 (14-15), 1980–1985.

[269] Johansen, J. M.; Gadsbøll, R.; Thomsen, J.; Jensen, P. A.; Glarborg, P.; De Martini, N.; Ek, P.; Mancini, M.; Weber, R.; and Mitchell, R. E. *Applied Energy* 2016. 162, 245–256.

[270] Campbell, P. A.; Mitchell, R. E.; and Ma, L. *Proc. Combust. Inst.* 2002. 29 (1), 519–526.

[271] Ma, L. and Mitchell, R. *Combust. Flame* 2009. 156 (1), 37–50.

[272] Kupka, T.; Zajac, K.; and Weber, R. *Energy Fuels* 2009. 23 (7), 3429–3436.

[273] Johansen, J. M.; Jakobsen, J. G.; Frandsen, F. J.; and Glarborg, P. *Energy Fuels* 2011. 25 (11), 4961–4971.

[274] Nygaard Knudsen, J.; Jensen, P. A.; and Dam-Johansen, K. *Energy Fuels* 2004. 18 (5), 1385–1399.

[275] Srinivasachar, S.; Helble, J. J.; Ham, D. O.; and Domazetis, G. *Prog. Energy Combust. Sci.* 1990. 16 (4), 303–309.

[276] Davidsson, K. O.; Stojkova, B. J.; and Pettersson, J. B. C. *Energy Fuels* 2002. 16 (5), 1033–1039.

[277] Johansen, J. M.; Aho, M.; Paakkinen, K.; Taipale, R.; Egsgaard, H.; Jakobsen, J. G.; Frandsen, F. J.; and Glarborg, P. *Proc. Combust. Inst.* 2013. 34 (2), 2363–2372.

[278] Dayton, D. C. and Milne, T. A. *Prepr. Pap. - Am. Chem. Soc. Div. Fuel Chem.* 1995. 40 (3), 758–762.

[279] Davidsson, K. O.; Korsgren, J. G.; Pettersson, J. B. C.; and Jaglid, U. *Fuel* 2001. 81 (2), 137–142.

[280] Davidsson, K. O.; Pettersson, J. B. C.; and Nilsson, R. *Fuel* 2001. 81 (3), 259–262.

[281] Dayton, D. C.; Jenkins, B. M.; Turn, S. Q.; Bakker, R. R.; Williams, R. B.; Belle-Oudry, D.; and Hill, L. M. *Energy Fuels* 1999. 13 (4), 860–870.

[282] Dayton, D. C.; French, R. J.; and Milne, T. A. *Energy Fuels* 1995. 9 (5), 855–865.

[283] Knudsen, J. N.; Jensen, P. A.; Lin, W.; Frandsen, F. J.; and Dam-Johansen, K. *Energy Fuels* 2004. 18 (3), 810–819.

[284] Lewis, A. D. *Sawdust Pyrolysis and Petroleum Coke CO2 Gasification at High Heating Rates.* Master's thesis, Brigham Young University, 2011.

[285] Frandsen, F. J. and Moiraghi, L. *Residual Ash Formation from Wood-Firing on a Grate.* Technical report, Technical University of Denmark, Kongens Lyngby, 2005.

[286] Kupka, T.; Mancini, M.; Irmer, M.; and Weber, R. *Fuel* 2008. 87, 2824–2837.

[287] Sergeev, O. A.; Shashkov, A. G.; and Umanskii, A. S. *J. Eng. Phys.* 1982. 43 (6), 1375–1383.

[288] Abdulagatov, I.; Emirov, S.; Tsomaeva, T.; Gairbekov, K.; Askerov, S.; and Magomedova, N. *J. Phys. Chem. Solids* 2000. 61 (5), 779–787.

[289] Gardon, R. *J. Am. Ceram. Soc.* 1954. 69 (d).

[290] ANSYS. *ANSYS Fluent Theory Guide.* ANSYS, Inc., Canonsburg, r15.0 edition, 2013.

[291] Bird, R. B.; Steward, W. E.; and Lightfoot, E. N. *Transport Phenomena.* John Wiley & Sons, Inc., New York, 2nd edition, 2007.

[292] van Lith, S. C.; Alonso-Ramírez, V.; Jensen, P. a.; Frandsen, F. J.; and Glarborg, P. *Energy Fuels* 2006. 20, 964–978.

[293] Chen, C. Y.; Lan, G. S.; and Tuan, W. H. *Ceram. Int.* 2000. 26, 715–720.

[294] Doshi, V.; Vuthalura, H. B.; Korbee, R.; and Kiel, J. H. A. *Fuel Process. Technol.* 2009. 90, 1148–1156.

[295] Shapiro, L. M. and Brannock, W. W. *Rapid Analysis of Silicate, Carbonate and Phosphate Rocks.* United States Government Printing Office, Washington, 1962.

[296] Várhegyi, G. *Thermochim. Acta* 1979. 28, 367–376.

[297] Weber, R.; Poyraz, Y.; Beckmann, A. M.; and Brinker, S. *Proc. Combust. Inst.* 2015. 35, 2749–2758.

[298] White, R. *Wood Fiber* 1981. 13 (1), 17 – 38.

[299] Fredlund, B. *A Model for Heat and Mass Transfer in Timber Structures during Fire.* Phd thesis, Lund University, 1988.

[300] Bryden, K. M.; Ragland, K. W.; and Rutland, C. J. *Biomass Bioenergy* 2002. 22 (1), 41–53.

[301] Borman, G. L. and Ragland, K. W. *Combustion Engineering.* McGraw-Hill, 1998.

[302] Benkoussas, B.; Consalvi, J.-L.; Porterie, B.; Sardoy, N.; and Loraud, J.-C. *Int. J. Therm. Sci.* 2007. 46 (4), 319–327.

[303] Bamford, C. H.; Crank, J.; and Malan, D. H. *Proc. Camb. Philol. Soc.* 1946. 42, 166–182.

[304] Tinney, E. R. *Proc. Combust. Inst.* 1965. 10, 925–930.

[305] Panton, R. L. and Rittmann, J. G. *Proc. Combust. Inst.* 1971. 13 (1), 881–891.

[306] Kung, H.-C. *Combust. Flame* 1972. 18, 185–195.

[307] Kung, H.-C. and Kalelkar, A. S. *Combust. Flame* 1973. 20 (1), 91–103.

[308] Di Blasi, C. *Combust. Flame* 1994. 97, 225–239.

[309] Kansa, E. J.; Perlee, H. E.; and Chaiken, R. F. *Combust. Flame* 1977. 29, 311–324.

[310] Di Blasi, C. and Russo, G. *Adv. Thermochem. Biomass Convers.* 1993. 2, 906–921.

[311] Bharadwaj, A.; Baxter, L. L.; and Robinson, A. L. *Energy Fuels* 2004. 18 (4), 1021–1031.

[312] Gera, D.; Mathur, M. P.; Freeman, M. C.; and Robinson, A. *Energy Fuels* 2002. 16 (6), 1523–1532.

[313] Brammer, J. G. and Bridgwater, A. V. *Renew. Sustain. energy Rev.* 1999. 3, 243–289.

[314] Bellais, M. *Modelling of Pyrolysis of Large Wood Particles.* Phd thesis, Royal Institute of Technology, 2009.

[315] Ståhl, M.; Granström, K.; Berghel, J.; and Renström, R. *Biomass Bioenergy* 2004. 27 (2004), 621–628.

[316] Stanish, M. A.; Schajer, G. S.; and Kayihan, F. *AIChE J.* 1986. 32 (8), 1301–1311.

[317] Siau, J. F. *Transport Processes in Wood*. Springer series in wood science. Springer-Verlag, 1984.

[318] Ražnjević, K. *Handbook of Thermodynamic Tables and Charts*. Hemisphere Pub. Corp., 1976.

[319] Saastamoinen, J. and Richard, J.-R. *Combust. Flame* 1996. 106, 288–300.

[320] Diego, L. F. D.; Garcı, F.; Abad, A.; and Gaya, P. *Ind. Eng. Chem. Res.* 2002. 41, 3642–3650.

[321] Janssens, M. L. *Fire Mater.* 2004. 28 (April 2002), 199–207.

[322] Agarwal, P. K.; Genetti, W. E.; and Lee, Y. Y. *Chem. Eng. Sci.* 1986. 41 (9), 2373–2383.

[323] Bilbao, R.; Mastral, J. F.; Lana, J. a.; Ceamanos, J.; Aldea, M. E.; and Betŕn, M. *J. Anal. Appl. Pyrolysis* 2002. 62, 63–82.

[324] Bilbao, R.; Mastral, J. F.; Ceamanos, J.; and Aldea, M. E. *J. Anal. Appl. Pyrolysis* 1996. 36, 81–97.

[325] Alves, S. and Figueiredo, J. *Chem. Eng. Sci.* 1989. 44 (12), 2861–2869.

[326] Peters, B.; Schröder, E.; Bruch, C.; and Nussbaumer, T. *Biomass Bioenergy* 2002. 23, 291–306.

[327] Shrestha, D. and Cramer, S. *Fire Mater.* 1994. 18, 211–220.

[328] Wurzenberger, J. C.; Wallner, S.; Raupenstrauch, H.; and Khinast, J. G. *AIChE J.* 2002. 48 (10), 2398–2411.

[329] Maclean, J. *Mech. Eng.* 1941. 63 (10), 734 – 735.

[330] Chan, R. W.-C. *Analysis of Chemical and Physical Processes during the Pyrolysis of Large Biomass Pellets*. Phd thesis, University of Washington, 1983.

[331] Maku, T. *Studies on the Heat Conductin In Wood*. Technical report, Kyoto University, Kyoto, 1927.

[332] Lee, C. K. *Proc. Combust. Inst.* 1976. pages 1459 – 1470.

[333] Koufopanos, C. A.; Papayannakos, N.; Maschio, G.; and Lucchesi, A. *Can. J. Chem. Eng.* 1991. 69, 907–915.

[334] Zhang, X.; Dukhan, A.; Kantorovich, I. I.; and Bar-Ziv, E. *Combust. Flame* 1998. 113, 519–531.

[335] Brown, L. E. *An Experimental and Analytical Study of Wood Pyrolysis*. Phd thesis, University of Oklahoma, 1972.

[336] Hottel, H. C. and Sarofim, A. F. *Radiative Transfer*. McGraw-Hill, Michigan, 1967.

[337] Birkebak, R. C. and Ozil, E. In J. P. Hartnett; T. F. Irvine; E. Pfender; and E. M. Sparrow, editors, *Stud. Heat Transf.*, pages 409–418. McGraw-Hill, 1979.

[338] Curtis, L. J. and Miller, D. J. *Ind. Eng. Chem. Res.* 1988. 27, 1775–1783.

[339] Bridgwater, A., editor. *Advances in Thermochemical Biomass Conversion*. Springer, 1993.

[340] Babu, B. V. and Chaurasia, A. S. *Energy Convers. Manag.* 2004. 45 (9-10), 1297–1327.

[341] Babu, B. and Chaurasia, A. *Chem. Eng. Sci.* 2004. 59 (10), 1999–2012.

[342] Ouelhazi, N.; Arnaud, G.; and Fohr, J. P. *Transp. Porous Media* 1992. 7, 39–61.

[343] Pyle, D. L. and Zaror, C. A. *Chem. Eng. Sci.* 1984. 39 (1), 147–158.

[344] Lin, Y.-C.; Cho, J.; Tompsett, G. A.; Westmoreland, P. R.; and Huber, G. W. *J. Phys. Chem. C* 2009. 113 (46), 20 097–20 107.

[345] Koch, P. *Wood Sci.* 1969. 1 (4), 203–214.

[346] Merrick, D. *Fuel* 1983. 62, 540–546.

[347] Janse, A.; Westerhout, R.; and Prins, W. *Chem. Eng. Process. Process Intensif.* 2000. 39 (3), 239–252.

[348] Blasi, C. D. and Di Blasi, C. *Combust. Sci. Technol.* 1993. 90 (5-6), 315–340.

[349] Boroson, M. L.; Howard, J. B.; Longwell, J. P.; and Peters, W. a. *AIChE J.* 1989. 35 (1), 120–128.

[350] Richter, A. and Nikrityuk, P. a. *Int. J. Heat Mass Transf.* 2012. 55 (4), 1343–1354.

[351] Perry, R. *Perry's Chemical Engineers' Handbook*. McGraw-Hill, 2007.

[352] Momeni, M.; Yin, C.; Kær, S. K.; Hansen, T. B.; Jensen, P. A.; and Glarborg, P. *Energy Fuels* 2013. 27 (1), 507–514.

[353] Lide, D. R. and Haynes, W. M., editors. *Handbook of Chemistry and Physics*. CRC Press, Boca Raton, Florida, 90th edition, 2010.

[354] Miura, K. *Energy Fuels* 1995. 9 (2), 302–307.

[355] Sonobe, T. and Worasuwannarak, N. *Fuel* 2008. 87 (3), 414–421.

[356] Jensen, P. *Combustion and Modeling of Alternative Fuels*. Master's thesis, The Technical University of Denmark, 2011.

[357] Truelove, J. S. *Proc. Combust. Inst.* 1986. pages 275–284.

[358] Brix, J.; Jensen, P. A.; and Jensen, A. D. *Fuel* 2011. 90, 2224–2239.

[359] Johansen, J. M.; Jensen, P. A.; Glarborg, P.; Mancini, M.; Weber, R.; and Mitchell, R. E. *Energy* 2016. 95, 279–290.

[360] ANSYS. In *ANSYS Fluent Theory Guid.*, chapter 16, pages 373–464. SAS IP, Inc., Canonsberug, release 15 edition, 2013.

[361] UK, G. G. *Greenbank Advanced Instrumentation & Measurement*. 2015.

[362] Savolainen, K. *Appl. Energy* 2003. 74, 369–381.

[363] Ye, T. H.; Azevedo, J.; Costa, M.; and Semiao, V. *Combust. Sci. Technol.* 2004. 176, 2071–2104.

[364] Scott, D. S.; Piskorz, J.; Bergougnou, M. A.; Graham, R.; and Overends, R. P. *Ind. Eng. Chem. Res.* 1988. 27, 8–15.

[365] BIatridis, B. and Gavalas, G. R. *Ind. Eng. Chem. Prod. Res. Dev.* 1979. 18 (2), 127–130.

[366] Avni, E.; Coughlin, R. W.; and Solomont, P. R. *Fuel* 1985. 64, 1495–1501.

[367] Funazukurl, T.; Hudgins, R. R.; and Silveston, P. L. *Ind. Eng. Chem. Process Des. Dev.* 1986. 25, 172–181.

[368] Jegers, H. E. and Kleln, M. T. *Ind. Eng. Chem. Process Des. Dev.* 1985. 24, 173–183.

[369] Hajaligol, M. R.; Howard, J. B.; Longwell, J. P.; and Peters, W. a. *Ind. Eng. Chem. Process Des. Dev.* 1982. 21 (3), 457–465.

[370] Thunman, H.; Niklasson, F.; Johnsson, F.; and Leckner, B. *Energy Fuels* 2001. 15, 1488–1497.

[371] Gurvich, L. V.; Veyts, I. V.; and Alcock, C. B. *Thermodynamic Properties of Individual Substances*. Hemisphere Pub. Corp., New York, 4th edition, 1989.

[372] Linstrom, P. J. and Mallard, W. G., editors. *NIST Chemistry WebBook, NIST Standard Reference Database Number 69*. National Institute of Standards and Technology, Gaithersburg MD, 20899, 2015.

[373] Cox, J. D.; Wagman, D. D.; and Medvedev, V. A. *CODATA Key Values for Thermodynamics*. Hemisphere Pub. Corp., New York, 1st edition, 1989.

[374] Colwell, J. H.; Gill, E. K.; and Morrison, J. a. *J. Chem. Phys.* 1963. 39 (3), 635–653.

[375] Barin, I. *Thermochemical Data of Pure Substances. Vol 1. Ag-Kr*. VCH Verlagsgesellschaft mbH, Weinheim D-69451, 3rd edition, 1995.

[376] Manion, J. a. *J. Phys. Chem. Ref. Data* 2002. 31 (1), 123.

[377] Pittam, D. A. and Pilcher, G. *J. Chem. Soc. Faraday Trans. 1 Phys. Chem. Condens. Phases* 1972. 68 (12), 2224–2229.

[378] Furuyama, S.; Golden, D. M.; Benson, S. W.; and Hs, I. *J. Chem. Thermodyn.* 1969. 1 (4), 363–375.

[379] Lacher, J. R.; Walden, C. H.; Lea, K. R.; and Park, J. D. *J. Am. Chem. Soc.* 1950. 72, 331–333.

[380] Fletcher, R. A. and Pilcher, G. *Trans. Faraday Soc.* 1970. 66 (4), 794–799.

[381] Butler, B. W. and Webb, B. W. *Energy Fuels* 1999. 7 (6), 835–841.

[382] Zheng, C.; Liu, Z.; Duan, X.; and Mi, J. *Proc. Combust. Inst.* 2002. 29, 811–818.

[383] Gao, H. and Chui, E. H. In *Int. Pittsburgh Coal Conf.*. 2004 .

[384] Mando, M.; Rosendahl, L.; Yin, C.; and Sorensen, H. *Fuel* 2010. 89 (10), 3051–3062.

[385] Beér, J. M. and Chigier, N. A. *Swirling Jet Flames from an Annular Burner*. Technical report, International Flame Research Foundation, 1963.

[386] Fricker, N. and Leuckel, W. *Flow and Mixing in Gas Flames with Swirl in the Annular Air Stream.* Technical report, International Flame Research Foundation, 1969.

[387] Schmid, C.; Bortz, S.; and Weber, R. *Further Experimental Studies on Isothermal, Expanding Swirling Flows with Application to Swirl Burner Design.* Technical report, International Flame Research Foundation, Velsen-Noord, 1987.

[388] Truelove, J. A. and Williams, R. G. *Proc. Combust. Inst.* 1988. pages 155–164.

[389] Clausen, S.; Fateev, A.; Hviid, S. L.; Beutler, J.; and Evseev, V. *Combustion Zone Investigation in Fuel Flexible Suspension Fired Boilers, Experimental.* Technical report, RIS DTU, 2011.

[390] Nielsen, J.; Villadsen, J.; and Liden, G. *Bioreaction Engineering Principles.* Kluwer Academic, 2nd edition, 2002.

[391] Visser, B. M.; Smart, J. P.; van de Kamp, W. L.; and Weber, R. *Proc. Combust. Inst.* 1990. pages 949–955.

[392] Abbas, T.; Costen, P.; Hassan, M. a.; and Lockwood, F. C. *Combust. Sci. Technol.* 1993. 93 (August 2011), 73–90.

[393] Hagiwara, A. and Bortz, S. *Studies on the Near Field Aerodynamics of Swirl Burners.* Technical report, International Flame Research Foundation, Velsen-Noord, 1984.

[394] Weber, R.; Visser, B.; and Boysan, F. *Int. J. Heat Fluid Flow* 1990. 11, 225–235.

[395] Truelove, J. S. *Proc. Combust. Inst.* 1984. page 523.

[396] Godoy, S.; Hirji, J.; Ismail, M.; and Lockwood, F. C. *J. Inst. Energy* 1986. 59 (438), 38–44.

[397] Li, Z. Q.; Sun, R.; Wan, Z. X.; Sun, S. Z.; Wu, U. S.; and Chen, L. Z. *Combust. Sci. Technol.* 2003. 175, 1979–2014.

[398] Spiniti, J. P.; Pershing, D. W.; Brouwer, J.; and Heap, M. P. *Combust. Sci. Technol.* 1997. 126, 1–21.

[399] Milosavljevic, V. D.; Taylor, A. M. K. P.; and Whitelaw, J. H. *Proc. Combust. Inst.* 1990. pages 957–962.

[400] Abbas, T.; Costen, P.; Kandamby, N. H.; Lockwood, F. C.; and Ou, J. J. *Combust. Flame* 1994. 99, 617–625.

[401] Ui, R. W. J. D. U. C.; Sayre, A.; and Visser, B. M. *Proc. Combust. Inst.* 1992. pages 1373–1380.

[402] Stopford, P. J. *Appl. Math. Model.* 2002. 26 (2), 351–374.

[403] Papadikis, K.; Gu, S.; Bridgwater, A. V.; and Gerhauser, H. *Fuel Process. Technol.* 2009. 90 (4), 504–512.

[404] Godoy, S.; Hassan, M. A.; Ismail, M. A.; and Lockwood, F. C. *Combust. Sci. Technol.* 1991. 80, 137–150.

[405] Mithcell, R. E.; Ma, L.; and Kim, B. *Combust. Flame* 2007. 151, 426.

Appendices

APPENDIX A

Publication A

Devolatilization Kinetics of Woody Biomass at Short Residence Times and High Heating Rates and Peak Temperatures

Joakim M. Johansen[a], Rasmus Gadsbøll[a], Jesper Thomsen[a], Peter A. Jensen[a], Peter Glarborg[a], Paul Ek[b], Nikolai De Martini[b], Marco Mancini[c], Roman Weber[c], Reginald Mitchell[d]

[a]Technical University of Denmark, Department of Chemical and Biochemical Engineering, Lyngby Campus, 2800 Kgs. Lyngby, Denmark

[b]Aabo Akademi University, Process Chemistry Centre, 20500 Turku, Finland

[c]Technical University of Clausthal, Institute of Energy Processes Engineering and Fuel Technology, 38678 Clausthal-Zellerfeld, Germany

[d]Stanford University, Department of Mechanical Engineering, 94305 California, United States of America

Published in Applied Energy [269]
Applied Energy 162 (2016) 245–256

Applied Energy 162 (2016) 245–256

Contents lists available at ScienceDirect

Applied Energy

journal homepage: www.elsevier.com/locate/apenergy

Devolatilization kinetics of woody biomass at short residence times and high heating rates and peak temperatures

Joakim M. Johansen [a,*], Rasmus Gadsbøll [a], Jesper Thomsen [a], Peter A. Jensen [a], Peter Glarborg [a], Paul Ek [b], Nikolai De Martini [b], Marco Mancini [c], Roman Weber [c], Reginald E. Mitchell [d]

[a] Technical University of Denmark, Department of Chemical and Biochemical Engineering, Lyngby Campus, 2800 Kgs. Lyngby, Denmark
[b] Aabo Akademi University, Process Chemistry Centre, 20500 Turku, Finland
[c] Technical University of Clausthal, Institute of Energy Processes Engineering and Fuel Technology, 38678 Clausthal-Zellerfeld, Germany
[d] Stanford University, Department of Mechanical Engineering, 94305 CA, United States

HIGHLIGHTS

- High peak temperature (1405–1667 K) and heating rate (10^5 K s^{-1}) devolatilization.
- CFD aided particle history tracking.
- Significantly faster devolatilization kinetics than suggested in the literature.
- Shown to significantly change the predicted ignition distance in pilot scale.
- Partial conversion experiments with residence times below 0.1 s.

ARTICLE INFO

Article history:
Received 8 May 2015
Received in revised form 2 September 2015
Accepted 26 September 2015

Keywords:
Biomass conversion
Devolatilization
High heating rate
Kinetics
High temperature
Low residence time

ABSTRACT

This work combines experimental and computational fluid dynamics (CFD) results to derive global kinetics for biomass (pine wood) devolatilization during heating rates on the order of 10^5 K s^{-1}, bulk flow peak temperatures between 1405 and 1667 K, and particle residence times below 0.1 s. Experiments were conducted on a laboratory laminar entrained flow reactor (LFR) using solid fuel feed rates on the order of 10–20 mg h^{-1}. Employing a simple single step first order (SFOR) mechanism with an Arrhenius type rate expression, the best fit of the pyrolysis kinetics was found to be: $A = 18.9 \times 10^3$ s^{-1}, $E_a = 21\,305$ J mol^{-1}. The accuracy of the derived global kinetics was supported by comparing predictions to experimental results from a 15 kW furnace. The work emphasizes the importance of characterizing the temperature history of the biomass particles when deriving pyrolysis kinetics. The present results indicate faster kinetics than found in the literature, leading to predicted residence times required for full conversion one order of magnitude lower than when compared to thermogravimetric analysis (TGA) derived kinetics.

1. Introduction

Pulverized biomass combustion is of interest in both the academic community and for industrial application. The ability to achieve high thermal throughputs and high electrical and thermal efficiencies makes the technology appealing in the replacement of fossil fuel based facilities.

Biomass being primarily cellulose, hemicellulose, and lignin is less thermally stable than coal due to the high number of readily breakable bonds compared to the more complex coal structures. This results in high quantities of volatile matter which changes the ignition and primary heat release mechanisms compared to coal.

Being able to describe the devolatilization process is important in biomass combustion modeling due to the high content of volatile matter. Devolatilization and pyrolysis studies have been extensively reported in the literature for low heating rates between 5 and 80 K min^{-1} and long residence times using simple global first order models [1–14]. Only a few studies attempt to determine devolatilization kinetics at higher heating rates, i.e. on the order of $>$ 100 K s^{-1} [15,16], using variations of thermogravimetric apparatuses. Extrapolation of the low heating rate studies to pulverized fuel firing, characterized by high heating rates and temperatures, is

* Corresponding author.
E-mail address: jjoha@kt.dtu.dk (J.M. Johansen).
URL: http://www.kt.dtu.dk (J.M. Johansen).

http://dx.doi.org/10.1016/j.apenergy.2015.09.091
0306-2619/

difficult due to the changes in devolatilization kinetics with heating rate [17–19]. Also the ratio between tar, char, and gases is known to be influenced by the temperature [18,20].

Alternative equipment such as captive sample set-ups [21–23] allow for experimens to be carried out at higher heating rates, typically on the order of 1000 K s^{-1}. However, the thermal inertia of the heating elements in these kind of set-ups makes it difficult to study partial conversion for small particles.

In general; achieving high heating rates and peak temperatures, typically come at the cost of the loss of control of particle residence time [24,25], particle temperature history [26–30], and the ability to close the sample mass balance [31], making it difficult to derive kinetics.

A number of studies using high heating rate and/or high temperature together with short residence times have been published. However, many of these rely on one of the following assumptions: (1) the particle temperature equals the adiabatic flame temperature or the temperature of the isothermal reactor wall [26]; (2) the particle temperature follows the gas phase temperature [27], or (3) the particle temperature is calculated from a simple heat balance based on the properties of the parent fuel and assumptions on the expected particle trajectory [28]. Experimentally determined particle temperatures would be preferable, but difficulties in covering the entire temperature range have been reported as a limitation [29].

One concern often encountered is the lack of a sufficiently accurate model of the bulk flow, which is necessary in order to describe the reaction environment to which the entraining particles are subjected [32,33]. The short residence times required for biomass devolatilization make it difficult to examine the dynamics of the process. The development of the bulk flow and the conversion of the fuel particles are strongly coupled processes, thus, being able to mathematically describe and relate both phases are of equal importance to pyrolysis modeling [34].

Brown et al. [33] employed a laminar entrained flow reactor, thus achieving peak heating rates on the order of 10^4 K s^{-1}. The particle and gas flow was simulated by CFD thus significantly improving the energy balance comparing to similar studies. However, the particle modeling it self was decoupled and processed in a separate procedure using the information on particle temperature and time from the CFD results. They also concluded how particles around 50 μm are well within the kinetically limiting regime and thus accurate predictions on the pyrolysis will in terms influence on e.g. full-scale flame simulations.

Simone et al. [24] conducted a detailed CFD aided investigation on the devolatilization of cacao shells using a drop tube furnace at peak temperatures of 873–1073 K. Applying a first order single step mechanism, they concluded that a single set of kinetic parameters struggled to describe the pyrolysis adequately, even at the relatively low peak temperatures. To accommodate the observed model deviations from the experimental results, they divided the kinetic model into a low and high temperature regime, each with its own set of kinetic parameters.

The objective of this work was to determine wood pyrolysis kinetics at high heating rates aided by computational fluid dynamic simulations of the particle property histories (temperature, mass loss, and residence time). Combining simulation results with high temperature, high heating rate experiments at low residence times (partial devolatilization) allows for the derivation of devolatilization kinetics. This study includes the following work:

- Employment of a laboratory scale laminar flow reactor heated by an understoichiometric CH_4/H_2-pilot flame with heating rates on the order of 10^5 K s^{-1} and peak temperatures of 1405–1667 K at residence times below 0.1 s.
- Introduction of dilute solid particle feed, effectively studying single particle behavior.
- Determination of the local conditions in the laminar flow reactor by the use of computational fluid dynamics (CFD) simulations, thereby providing detailed temperature histories of the particles.
- Evaluation of the derived devolatilization kinetics using measurements and CFD simuluation results of a 15 kW furnace.

2. Fuel characterization and experimental

The same fuel (pine wood) was used throughout the study. This section presents the fuel characterization and the experimental set-ups.

2.1. The fuel

In this study, the main emphasis has been on low ash content woody fuels. This represents the type of fuel that is commonly used for suspension fired combustion with 100% biomass, i.e. high quality fuels without bark and soil containments. The fuel was a commercial wood pellet made from Norwegian pine. Proximate and ultimate analyses are presented in Table 1. The volatile fraction is based on the DS/EN15148:09 standard. This or similar standards are widely used [35]. It is, however, commonly recognized that the low heating rates and low temperatures used in the standard do not provide a true measure of the extent of pyrolysis taking place at higher heating rates and temperatures [35]. To determine a more accurate measure of the volatile fraction representative of suspension fired boiler conditions, we calculate the values based on a solid phase tracer method.

The wood pellets were crushed and subsequently treated in a rotating cutter mill with laboratory accuracy screens attached for specific size classification. The resulting wood dust was analyzed by two dimensional image analysis using a Netzsch CamSizer XT. The obtained particle size distributions (PSD) are shown in Fig. 1.

As is common for many biomass fuels, the particles were characterized by high aspect ratios. This study aims to incorporate the derived kinetics into larger CFD systems. It is therefore desirable to be able to describe the particles in a single dimension. Selected methods describing characteristic lengths of oddly shaped

Table 1
Proximate and ultimate analysis of the parent pine wood fuel. Fuel treatment prior to analysis has been carried out according to CEN/TS 14780:05.

Species	Method	Unit		
HHV	EN 14918:10	MJ kg^{-1}, dry	20.58	±0.12
LVH	EN 14918:10		19.23	–
Moisture	EN 14774-1:09	wt.%, dry	4.0	–
Ash	DS/EN 14775:09	wt.%, dry	0.2	±0.2
Volatiles[a]	DS/EN 15148:09		82.4	±1.6
C	CEN/TS 15104:11	wt.%, dry	51.1	±1.5
H			6.2	±0.2
N			<0.20	–
S	CEN/TS 151289:11	mg kg^{-1}, dry	60	±30
Cl	CEN/TS 15289:11		160	±20
Ca	CEN/TS 15290:06		950	±60
Mg			140	±10
K			480	±30
Na			95	±10
P			52	±8
Si			<200	–
Al			32	–
Fe			26	±5
Ti			<5.0	–

[a] The volatile determination has been carried out according to current standards. The result is not true for high temperature, high heating rate application [35].

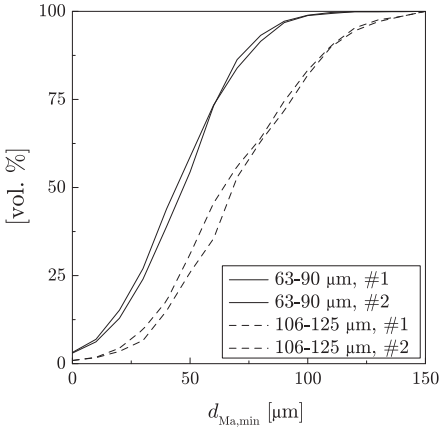

Fig. 1. Particle size distribution double determination data for the two particle sizes of woody fuel used in this study. All data are based on 2D particle projection image analysis (CamSizer XT) using the Martin minimum diameter.

particles are presented in Table 2. For the purpose of this study, the ratio between total heat capacity of the particle and heat transported to the particle is the most important factor. Thus, approximating the particle as a sphere with a fixed volume to surface area ratio makes it possible to describe the particles using only a single characteristic length while still being able to describe a realistic heat up of the particle.

The characteristic length describing a sphere with similar V/A_{eq}-ratio as the wood particle can be approximated by the Martin minimum diameter, $d_{\mathrm{Ma,min}}$, as discussed in the work of Trubetskaya [36]. The $d_{\mathrm{Ma,min}}$ denotes the minimum length of the area bisector. Fig. 1 shows the double determination PSD of the two particle size fractions used in this work, using the $d_{\mathrm{Ma,min}}$ as the characteristic length. Table 3 summarizes the profiles shown in Fig. 1 and provides theRosin–Rammler parameters used in this study to describe the PSD. TheRosin–Rammler distribution function is given as:

$$Y_{\mathrm{d}} = \exp\left[-\left(\frac{d}{\bar{d}}\right)^{n}\right] \tag{1}$$

where $\bar{d}$ and n are the Rosin–Rammler mean diameter and distribution spread given in Table 3.

Additional thermophysical data used in all CFD simulations are presented in Table 4.

2.2. The experimental set-ups

In the following the two experimental set-ups, a laminar flow reactor and a 15 kW solid fuel reactor will be described. Detailed CFD calculations were carried out, characterizing both of the set-ups. This was done in order to describe the property history (temperature, conversion, residence time, etc.) of the wood particles in the reactor. The 15 kW combustor was used to evaluate the performance of the derived kinetic parameters at larger scales and higher particle cloud densities.

2.2.1. Laboratory-scale: laminar flow reactor

A schematic of the laminar entrained flow reactor (LFR) at Stanford University is shown in Fig. 4. The LFR aimed to simulate single particle conversion with a solid fuel feed rate on the order of 10–20 mg h^{-1}. It was heated by an under-stoichiometric, non-premixed, CH_4/H_2 pilot flame. The inlet- and post-flame composition and the adiabatic thermodynamic equilibrium of the pilot flame are shown in Table 5. The fuel particles were suspended in a nitrogen carrier flow and introduced to the reactor at ambient temperature just downstream of the pilot flame front. The reactor has been used in previous studies to obtain partially reacted coal and biomass chars produced at high temperatures and heating rates [37,38].

Particles were collected by an adjustable probe, applying water cooling and helium gas for efficient particle quenching. Since the particle trajectories deviated only slightly from the centerline due to the laminar flow conditions in the bulk flow and the suction velocity of the probe exceeded the velocity of the bulk flow, we can assume that all, or nearly all, particles in the system were collected through the probe. The partially or fully converted particles were then collected on a silicon filter or a low cut-off membrane at temperatures slightly above ambient.

2.2.2. 15 kW vertical solid fuel combustor

The vertical combustor, shown in Fig. 5, has previously been used in experimental studies [39] and characterized by modeling [40]. It is described in detail within these publications.

The reactor was electrically heated (< 35 kW) with a solid fuel thermal input of 15 kW. It consisted of a high temperature radiative section: 2 m long and 0.3 m in diameter. The radiative section was lined with refractory material and heated by four individual electrical heating elements to compensate for heat losses. A 1.8 m water cooled convective section followed the radiative section. All measurements were carried out in the radiative section. Process control was based on feedback controlling from gas composition measurements in the convective section; aiming for an O_2 level of 3.5 vol.% and stable levels of CO and CO_2.

The fuel was pneumatically transported by the primary air at ambient temperature. It entered the quarl through an annulus centered in the axial quarl. In the quarl the solid fuel and transport air was mixed with the preheated (523 K) combustion air injected through an outer annulus. The furnace was operated at an excess air ratio of $\lambda = 1.2$ with an air split (primary air/total air) of 0.3, corresponding to around 3.5 vol.% (dry) O_2 in the exhaust. The reactor walls were electrically heated to 1423 K.

Intrusive probe measurements were performed along the centerline of the flame: Gas phase temperature by un-shielded

Table 2
Comparison of different methods to characterize oddly shaped particles in a single dimension. *d*: diameter, *V*: volume, *A*: surface area, *SF*: shape factor (A/A_{original}), *NC*: number correlation (V/V_{original}), eq: equivalent.

	d_{eq}	V	A	V/A	SF	NC
	m × 10^{-6}	m^3 × 10^{-14}	m^2 × 10^{-8}	m × 10^{-6}	–	–
Parallelepiped	153/53.6/35.8	29	3.1	9.4		
V_{eq} sphere	82.5	29	2.1	13.7	0.684	1.00
Parallelepiped thickness eq sphere	35.8	2.4	0.4	5.96	0.129	12.3
Fixed V/A_{eq} sphere	56.6	9.5	1.1	0.106	0.322	3.09

Table 3
Particle size distribution characteristics. Double determination data and average values. RR: Rosin–Rammler. All data are based on 2D particle projection image analysis (CamSizer XT) using the Martin minimum diameter.

Particle size (μm)	RR $\bar{d}$	RR n
63–90	53.6	2.41
106–125	78.8	2.45

Table 4
Thermophysical data used in all CFD simulations.

Property	Unit	Value	Ref.
Specific heat capacity	J (kg K)$^{-1}$	1680	[50]
Density	kg m^{-3}	1180	[51]

Table 5
Mole fractions and the total molar flow, F_{tot}, of the reactor set-up before and after combustion. Post flame composition is based on adiabatic equilibrium calculations.

Inlet	Flame 1	Flame 2	Post flame	Flame 1	Flame 2
CH_4	0.040	0.033	CO	0.021	0.021
O_2	0.109	0.087	CO_2	0.020	0.013
H_2	0.127	0.158	H_2O	0.163	0.130
N_2 (pilot)	0.675	0.602	H_2	0.050	0.099
N_2 (carrier)	0.049	0.120	O_2	0.000	0.000
			N_2	0.746	0.736
F_{tot} (mol s^{-1})	0.0382	0.0416		0.0371	0.0407
Adiabatic flame temperature (K)				1667	1406

thermocouple measurements manually corrected for radiation bias and extractive gas sampling for gas species quantification: CO, CO_2, O_2, NO_x, and SO_2. The reactor was accessible by four view ports positioned 0.55, 1.18, 1.81, and 2.49 m downstream of the quarl, denoted P1–4, respectively, cf. Fig. 5.

2.3. Particle conversion

When deriving devolatilization kinetics, a reliable method to determine the degree of conversion of the collected particles is equally important as being able to determine the particle time and temperature history. Determining particle conversion may be difficult for any of the following reasons: (1) failing to collect particles at isokinetic conditions leaves the experimental results vulnerable to collection bias; (2) failing to take into account the volatility of biomass ash may cause offsets in the observed conversion, and (3) failing to close the mass balance due to mass losses in the system. No real consensus on a robust method seems to be available in the literature.

The low ash fraction and the high volatility of some of the inorganic species, such as alkali metals and halides [41,42], make it difficult to use ash as a tracer. To circumvent bias from the release of volatile ash components, we use calcium as a tracer, calculating the particle conversion as:

$$\chi = \frac{w_{Ca} - w_{Ca,0}}{w_{Ca}\left(1 - w_{ash,0}\right)} \tag{2}$$

where w_{Ca} and $w_{Ca,0}$ are the weight fractions of Ca in the reacted sample and the parent fuel respectively, and $w_{ash,0}$ is the weight fraction of ash in the parent fuel. This method relies on the assumption of a non-volatile ash phase; however, the sensitivity towards ash volatility is limited for low ash fuels such as the one used in this study. The sensitivity towards the Ca content in the parent fuel is manageable and justified by the precision of the analytical methods used in the ultimate analysis, cf. Table 1. Conflicting findings in the literature on the volatility of Ca lead one to conclude that the release of Ca during devolatilization conditions is fuel specific [43–45]. In this study we assume complete calcium retention and argue that a full characterization of the Ca-release behavior lies beyond the scope of this work. Although no clear consensus on the thermal stability of the ash phase Ca can be drawn from the literature, it is undoubtedly the best candidate among any of the trace elements available [43].

3. Numerical approach

Modeling was used to provide the particle temperature history for the high heating rate experiments. All simulations have been carried out using ANSYS Fluent 15.0.7.

3.1. Laminar flow reactor

The CFD model describes the LFR from the inlet of the fuel particles and 0.25 m downstream. The full length of the reactor has not been modeled in order to reduce the computational requirements. This was found to be sufficient as full devolatilization of the particles happened well within the first 0.25 m of the reactor. The pilot flame was assumed to be in thermodynamic equilibrium and at the adiabatic flame temperature. The gas-phase composition of the pilot flame inlet was based on thermodynamic equilibrium calculations. The solid fuel injection nozzle was modeled upstream in order for the particles to adjust to the flow velocity.

The reactor has a rectangular prism shape and was modeled using a 3D model with two symmetry planes to describe the entire domain. It was discretized in 1.2 million cells. The model has been grid independency tested with ±50% cells. The grid was unstructured in the mixing zone between the pilot flame and entraining particles, whilst being structured in the remaining domain.

Two issues call for careful attention when simulating the temperature and flow field of the LFR: (1) the mixing behavior of the pilot flame (at adiabatic flame temperature) and the entraining carrier flow of nitrogen (at ambient temperature) and (2) the semi-transparent quartz walls combined with the high concentrations of radiating H_2O and CO_2.

Although the Reynolds number of the bulk flow in the reactor was within the laminar range, the carrier gas flow rate needs to be significantly higher in order to fluidize the fuel particles. This causes slip velocities of ~ 5 m s^{-1} between the bulk flow of combustion products from the pilot flame and the carrier gas at which point a pure laminar flow can no longer be justified. To properly resolve the mixing behavior at the point of particle entrainment, the Reynolds stress model (RSM) was employed. In order to reduce the cell count, enhanced wall treatment (EWT) modeling was used allowing for relaxation of the near wall discretization requirements ($y^+ < 3$).

Radiation was modeled by the discrete ordinates model with an angular discretization of 4×4, 3×3 and with 5 energy iterations per radiation iteration and a particle surface emissivity of $\varepsilon = 0.85$ [46].

The pyrolysis was model using a single step:

$$\text{particle} \xrightarrow[\text{phase transition}]{k_{devol}} \text{vol} \tag{3}$$

and the gas-phase reactions were modeled using a two-step oxidation mechanism:

$$\text{vol} + aO_2 \xrightarrow{k_1} bCO + cH_2O \tag{4}$$

$$CO + \frac{1}{2}O_2 \xrightarrow{k_2} CO_2 \tag{5}$$

The volumetric reactions were described by the finite-rate/eddy-dissipation model.

The discrete phase was tracked in a Lagrangian reference frame and allowed for matter and energy (convectively and by radiation) to be exchanged with the continuous phase. Stochastic particle tracking was carried out by the discrete random walk model, and the odd-shape of the particles were taken into account by introducing a shape factor, corresponding to the relative surface area of the corresponding volumetric sphere (0.68), into the non-spherical drag law.

3.2. The 15 kW vertical combustor

The vertical combustor was modeled in 2D axisymmetry using a fully structured grid of 72 694 cells with a maximum aspect ratio of 4.96 and minimum orthogonality of 0.79. The fuel properties were identical to the fuel used in the LFR. Only the large size fraction shown in Table 3 was used for the bench-scale experiments. Many sub-routines and parameters were kept in line with the LFR simulations, i.e., the DO model, finite-rate/eddy-dissipation were used for the radiation, wall function, and volumetric reactions. The turbulence was modeled using the realizable k–ϵ-model and the influence of the walls was modeled using scalable wall function in order to further relax the cell count requirements.

4. Methodology

The current work includes two experimental set-ups and the corresponding numerical models. The combination of numerical simulations with experimental results made it possible to evaluate partially converted particles using detailed temperature histories. To give the reader an overview of the connections between each element, this section outlines the combined experimental and modeling approach taken to derive devolatilization kinetics.

The kinetic parameters describing the apparent devolatilization process in the LFR were derived in two consecutive steps: (1) An initiation step introducing non-reacting particles to the CFD model, thereby obtaining an initial particle temperature history. The experimental time resolved devolatilization conversion profiles were subsequently used to fit an initial set of single step first order reaction (SFOR) kinetic parameters, Fig. 2. (2) An iterative approach, cf. Fig. 3, used for the calculation of updated temperature histories using reacting particles. The new temperature history resulted in updated devolatilization kinetics. The method was repeated until the derived kinetic parameters converged upon a stable solution.

The LFR derived kinetics were applied to make CFD calculations on a 15 kW bench-scale furnace, and the results were compared with in-flame measurements. Contrary to the dilute particle mass

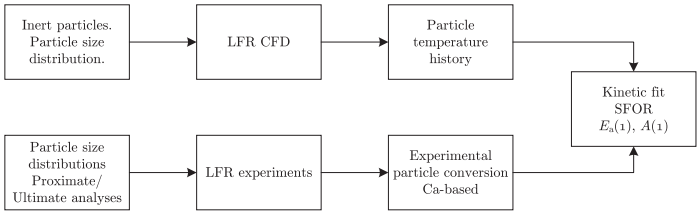

Fig. 2. Method, initiation step: Phase 1. Parallel LFR experiments and CFD simulations using inert particles. The simulated particle temperature history and the measured particle conversion is used to evaluate preliminary SFOR kinetics.

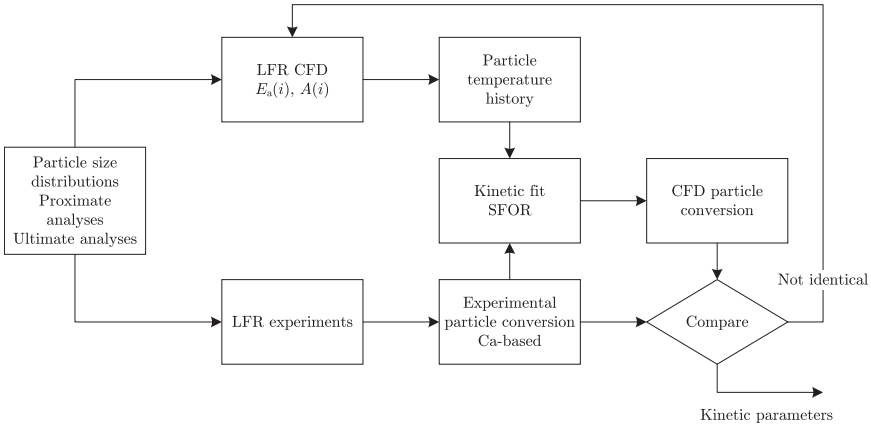

Fig. 3. Method: Phase 2. Iterating the kinetic parameters using reacting particles evaluating the model by comparing simulated and measured conversions.

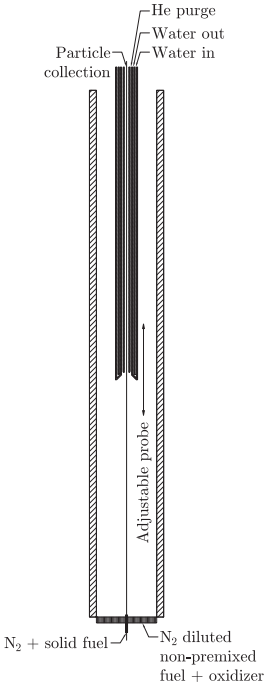

Fig. 4. The 500 mW laminar entrained flow reactor. Total length of the main combustion chamber: 0.455 m. Internal reactor width: = 0.055 m.

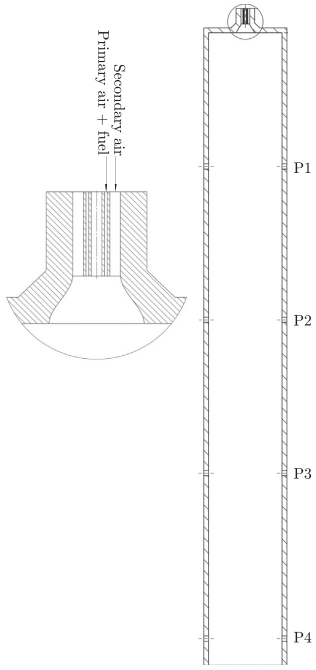

Fig. 5. The 15 kW solid fuel reactor. Total length of the main combustion chamber: 2 m. $D = 0.3$ m. Quarl diameter and length: 36 mm.

flows in the LFR, the 15 kW combustor introduced both larger geometries, denser particle flows, and made it possible to evaluate the devolatilization kinetics for a complete flame.

5. Results

5.1. LFR model validation

The validity of the CFD model of the LFR has been evaluated by comparing predictions with temperature measurements. Radiation corrected thermocouple measurements were conducted along the centerline of the reactor.

Fig. 6 shows a comparison of simulated gas phase temperatures and the corresponding measurements. The comparisons are made without entraining particles but with the carrier gas on. The simulated gas phase temperatures are shown along the centerline and at 1 and 2 mm radial offset. This has been done to show the effect of the physical size of the thermocouple. It shows large radial temperature gradients in the vicinity of the fuel injection nozzle (axialdistance = 0). Such gradients can potentially influence the temperature history of entraining particles, giving rise to extended spread of the particle residence time and temperature histograms at axial distances.

5.2. Particle temperature and residence time

Figs. 7 and 8 show the predicted particle temperature and residence time histograms at given positions along the flow direction of the LFR. The figures compare the histograms of inert particles to reacting (devolatilizing) particles, showing significant differences in the particle temperatures. The spread in particle temperature occurs primarily close to the particle injection. The spread in particle residence time is smaller but increases further downstream of the injection point.

In order to simplify the process, the mean values of both particle residence times and temperatures are used for the kinetic fit. This introduces some statistical error to the analysis. For more complex modeling, one could consider to use the distributions directly in the kinetic fit. However, to do this additional particle size characterization is required.

Fig. 9 summarizes the temperature and residence time histories for inert and reacting particles in terms of mean values and corresponding standard deviations. A distinct difference can be seen in the particle temperature profile between inert and pyrolyzing particles regardless of the bulk phase temperature. The increase in the size of the error bars is evidence of the increasing spread of the particle temperature histograms as seen in Fig. 7.

The difference between inert and reacting particle temperature history can be rationally explained. The model calculates the particle temperature by solving a simple heat balance:

$$m_p c_p \frac{dT_p}{dt} = hA_p(T_\infty - T_p) + \epsilon_p A_p \sigma\left(T_R^4 - T_p^4\right) \quad (6)$$

m_p, c_p, T_p, A_p, and ϵ_p being the mass, specific heat, temperature, surface area, and emissivity of the particle respectively. h is the heat transfer coefficient, T_∞ and T_R are the gas phase temperature and the temperature of any surface to which the particle radiates, and σ is the Stefan–Boltzmann constant. The heat of pyrolysis was set

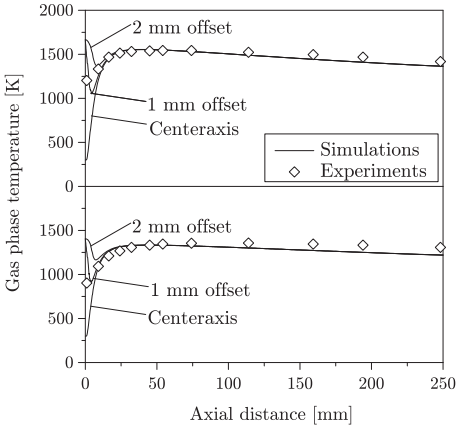

Fig. 6. Simulated and measured gas phase temperature. (above) $T_{ad} = 1667$ K, (below) $T_{ad} = 1405$ K. Simulated data shown along the centerline and at a 1 and 2 mm radial offset to show the effect of the physical size of the thermocouple.

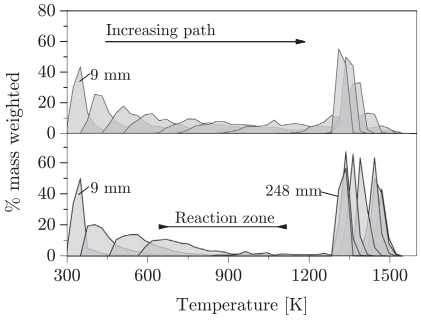

Fig. 7. Simulation results of the particle temperature distributions along the axial distance of the LFR. (Above) inert particles, phase 1, (below) reacting particles, phase 2.

to zero as any contribution from reactions can be assumed negligible compared to transport of heat from the surroundings [47,48].

Considering a particle being heated according to Eq. (6): The heat up time will largely be a function of the particle heat capacity. If the particle is devolatilizing, mass will be released thus reducing the available heat capacity at time t, accelerating the further heat up. Contrary, for a non-reacting particle all mass will be retained significantly increasing the net heat capacity for the duration of the process. This mechanism of diminishing heat capacity might seem trivial, however, it is fundamental and it is often found to be neglected.

Fig. 9 also shows how only small differences in the mean particle temperatures are found between the first and second iteration of reacting particles, i.e. the particle heat up seems to be relatively insensitive to the applied pyrolysis kinetics.

5.3. Particle conversion and kinetic fit

A simple SFOR mechanism is used to describe the experimental observations:

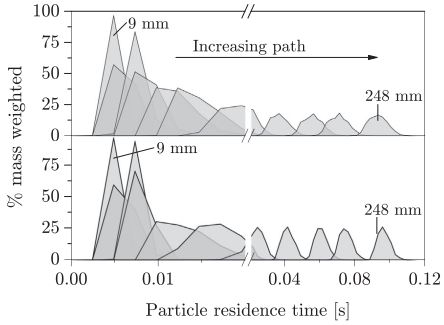

Fig. 8. Simulation results of the particle residence time distributions along the axial distance of the LFR. (Above) inert particles, phase 1, (below) reacting particles, phase 2.

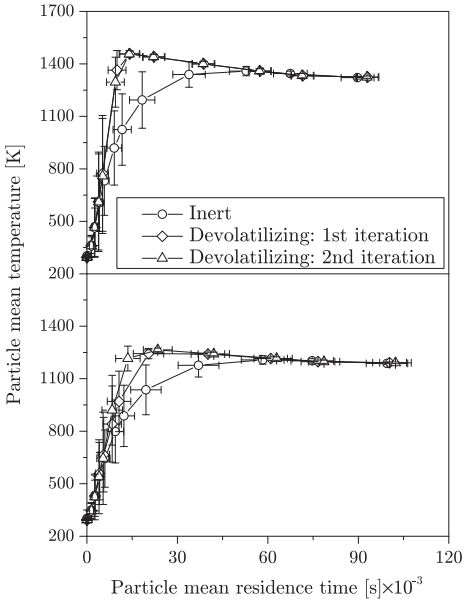

Fig. 9. Simulation results of the particle mean residence time and mean temperature. (Above) $T_{ad} = 1667$ K, (below) $T_{ad} = 1405$ K. Error bars indicate standard deviations based on 2100 tracked particles.

$$\frac{dV(t)}{dt} = A \exp\left[\frac{-E_a}{RT(t)}\right](V^* - V(t)) \quad (7)$$

where V is the released volatile matter and V^* is the high heating rate, high temperature volatile content, fixed as a constant in this study.

A best fit for both the high and low temperature run is obtained using SFOR kinetics with a pre-exponential factor and an activation energy of $A = 18.9 \times 10^3$ 1 s^{-1} and $E_a = 21\,305$ J mol^{-1}. The volatile yield was found to be 92 and 94 wt.% (dry) at 1405 and 1667 K respectively.

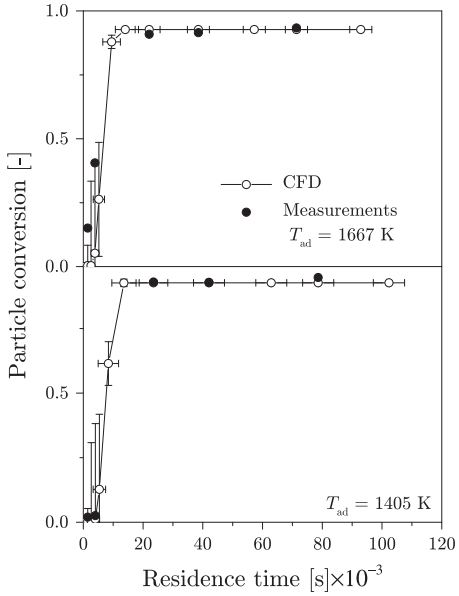

Fig. 10. Comparison of particle conversion measurements with the CFD-results using the derived SFOR kinetic parameters and a fixed ash level. The measured particle conversions are based on Ca-tracing, and the residence times are calculated using the CFD model. Error bars indicate standard deviations based on 2100 tracked particles.

Using the proposed SFOR kinetics together with the average particle time dependent temperatures illustrated in Fig. 9, Eq. (7) is used to evaluate the expected average particle conversion.

Fig. 10 shows the fit between modeled and experimentally obtained particle conversions. The CFD data points correspond to the particle properties at fixed distances downstream of the injection nozzle. The errorbars on the predictions stem from the simulated distributions in particle (vertical) temperature and (horizontal) residence time. The simple SFOR mechanism and the fitted data predict the fast devolatilization well. The slight delay when reducing the reactor temperature agrees well with the model results.

5.4. Bench-scale simulations

The apparent devolatilization kinetics derived in the LFR are applied in the CFD model of the 15 kW combustor. While the solid fuel flow rate of the LFR was sufficiently dilute to study single particle behavior, the 15 kW set-up uses higher particle feed rates (2.9 kg h^{-1}), thus allowing for evaluation of the model performance in particle cloud conditions while still being applicable in a small scale reactor with well defined boundary conditions.

Fig. 11 presents selected contours (gas phase temperature, O_2 and CO_2 concentrations, and streamlines) of the 15 kW furnace employing the derived devolatilization kinetics. The jet like flame penetrates half a meter (around sampling port P1, cf. Fig. 5) before the particles react. The fast devolatilization kinetics and surplus of oxygen ($\lambda = 1.2$) result in a short and intense reaction zone. Peak temperatures reach 2100–2200 K.

Fig. 12 compares measured and predicted gas phase temperatures. The shape of the simulated temperature profile, peaking between P1 and P2, corresponds well to previous experiments

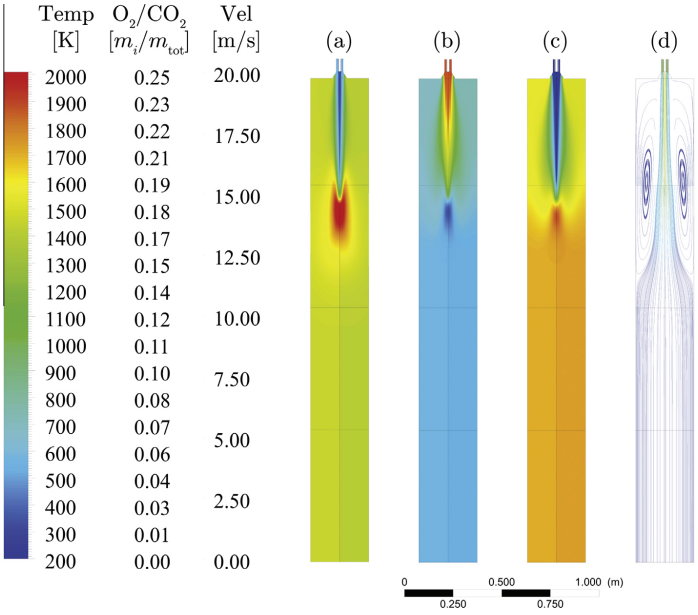

Fig. 11. Contour plots of the 15 kW furnace using the kinetic input from the LFR. (a) Gas phase temperature. (b) O_2-concentration (mass fraction). (c) CO_2-concentration (mass fraction). (d) Streamlines colored by gas velocity. (For interpretation of the references to color in this figure legend, the reader is referred to the web version of this article.)

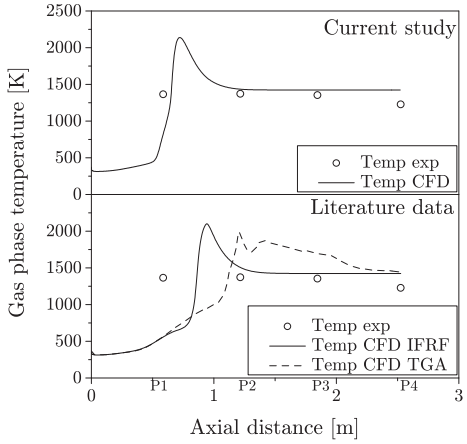

Fig. 12. Comparison of gas phase centerline temperature measurements and CFD simulations results from the 15 kW combustor. Measurements and simulations results presented along the axial symmetry axis. Simulation results using the devolatilization kinetics from the (above) current study and (below) literature data [35] and TGA.

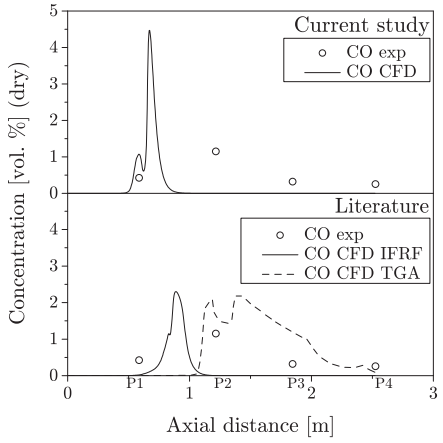

Fig. 14. Comparison of the centerline CO concentration measurements and CFD simulations results from the 15 kW combustor. Measurements and simulations results presented along the axial symmetry axis. Simulation results using the devolatilization kinetics from the (above) current study and (below) literature data [35] and TGA.

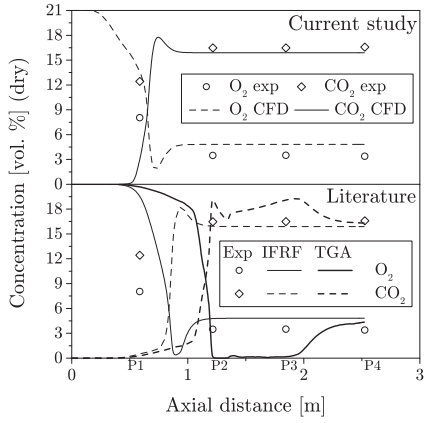

Fig. 13. Comparison of centerline O_2 and CO_2 measurements and simulated data. Measurements and simulations results presented along the axial symmetry axis. Simulation results using the devolatilization kinetics from the (above) current study and (below) literature data [35] and TGA.

conducted in the furnace at similar conditions [49]. However, because the gas phase has already reached high temperatures at P1, it is difficult to assess whether the developed devolatilization kinetics capture the ignition process to a satisfying degree.

Figs. 13 and 14 provide a stronger comparison between the measurements and the predictions. At P1 the devolatilization is still taking place resulting in only partial consumption of the O_2 and corresponding production of CO_2, cf. Fig. 13. These levels match the simulation outputs well.

The appearance of CO is often used as an indication for ignition in gas-phase kinetics studies. The qualitative agreement between the observed and modeled CO peak gives, together with the CO_2 and O_2 results, confidence in the perfomance of the derived devolatilization kinetics. The discrepant in Fig. 14 between the simulated and measured CO levels does not necessarily arise from inaccurate devolatilization kinetics. It is rather a result of the simplified mechanism from solid particle to fully oxidized combustion products, cf. reactions (3)–(5). To further investigate the coupling, or decoupling, between particle mass loss and the development in CO in the gas phase, a transient study including in-situ gas phase measurements would be required. Such a study lies beyond the scope of this work.

The correct prediction of the CO peak adds confidence to the accuracy of the derived devolatilization kinetics used in combinations with these simple reaction mechanisms suitable for numerical simulations.

Figs. 12–14 also include CFD simulation results using the devolatilization kinetics derived by Bonvicini et al. [35]. They show how the simulation results indeed are sensitive towards the applied devolatilization kinetics. The slower kinetics delays the occurrence of the predicted reaction zone.

6. Discussion

The results presented in this work emphasize key points to be taken into consideration when studying devolatilization of biomass at suspension firing conditions, i.e. high heating rates, high temperatures, and short residence times:

1. The fluid flow should be accurately characterized. The statistical results on solid particle trajectories and property history given in Figs. 7 and 8 emphasize the need for a detailed characterization of the reactor as well as the path of the entraining particles, even for experiments carried out in small scale laboratory facilities.
2. The fuel should be properly characterized. Because of the similar time scales for particle heat up and complete devolatilization, effort must be put into characterizing size distributions, particle densities, and heat capacities.

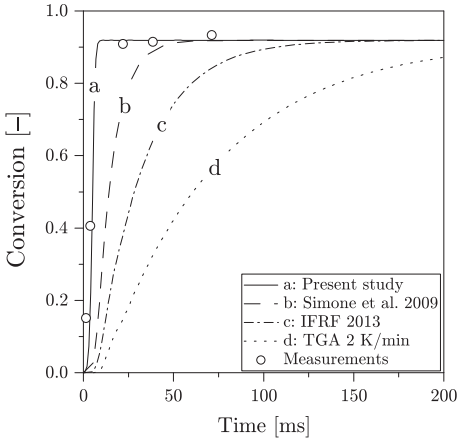

Fig. 15. Comparison of the results of the present study, literature data, and slow heating rate results. Simone et al. [24] and Bonvicini et al. [35].

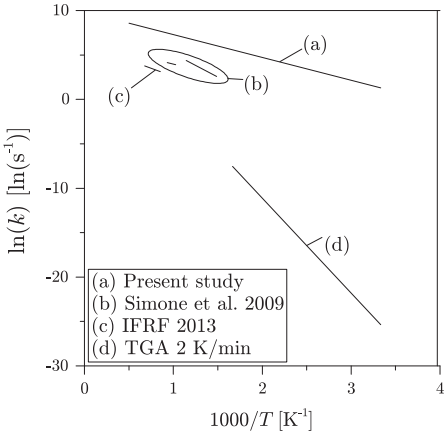

Fig. 16. Comparison of the kinetic data used for the discussion [24,35].

The current work shows how the particle heating profile is comparative in time to the devolatilization progress. This implies an inherent sensitivity towards the description of the particle heat-up. For entrained flow set-ups where the solid particles are introduced to the reactor in a cold fluid flow, large temperature gradients will inevitably occur in the mixing zone, thus, influencing the particle temperature history as has been demonstrated in Fig. 7. By resolving the fluid flow using CFD more detailed information on the actual particle behavior and temperatures can be obtained.

6.1. Particle trajectories and residence time history

The particle conversion at specific heights along the center axis of the LFR has been achieved by collecting char and ash samples and separating the solid from the gas by simple filtering. Exact adjustments to the suction velocity were not possible, i.e. ideal isokinetic conditions could not be established. However, by observing the shape of the flame, it was assumed that the gas velocity in the suction probe well exceeded that of the bulk flow. Hence, all particles can safely be assumed to be collected by the probe.

The particle devolatilization conversion profiles should ideally be presented as a function of particle residence time. This will allow for direct time derivative analysis and an easy kinetic fit. However, because of the velocity gradients near the injection nozzle it can be difficult to correlate the axial distance travelled to the residence time. This effect has been demonstrated in Fig. 8. Using the axial distance travelled, i.e. the distance from the nozzle to the probe makes it difficult to compare time dependent conversion data across experimental rigs and even across different studies.

In order to obtain time resolved data, one would need to characterize the particle entrainment by optical methods [29] or obtain the required profiles through calculations. Multi-phase fluid dynamics calculations allow for predictions on the particle trajectories. This will link both particle conversion (through experimental sampling) and particle temperature history (through modeling) to the particle residence time, making it possible to derive more accurate kinetics.

6.2. Comparison to literature data

Fig. 15 compares predictions with kinetic devolatilization data across selected literature studies. The specific kinetic data is given in Table 6. The comparison has been made based on the temperature history predictions from the current work. Rate constants are taken from (a) the current work (b) the work of Simone et al. [24] who have also based their kinetic derivation on CFD generated temperature histories, (c) Bonvicini et al. [35] who evaluated the global kinetics at the nominal temperature of the reactor, and (d) slow heating rate TGA experiments on the fuel used in this work. The kinetic data are summarized in the Arrhenius plot in Fig. 16.

Simone et al. [24] determined a set of SFOR kinetics for the devolatilization of cacao shells using a laboratory scale drop tube furnace. The experiments were assisted by CFD generated particle temperature histories, however, at relatively low nominal temperatures (673–1073 K) and with broad size distributions (90–150 μm). The conversions were based on the ash tracer method, justified by the low nominal temperatures, reducing the likelihood of a volatile ash phase. Simone et al. [24] concluded that a single set of kinetic parameters could not describe the devolatilization process to a satisfying degree when spanning large temperature intervals. Instead they employed a two-zone system applying different kinetics for low and high temperatures respectively, with the shift in kinetic regime taking place between 873 and 973 K.

Table 6
Summary of the kinetic values used for the comparison of devolatilization, cf. Fig. 15.

		Current study a	Simone et al. [24] b	IFRF 2013 c	TGA 2 k min^{-1} d
A	(s^{-1})	18939	33300/625	571	29400
E_a	(J mol^{-1})	21305	43900/20400	31510	88930

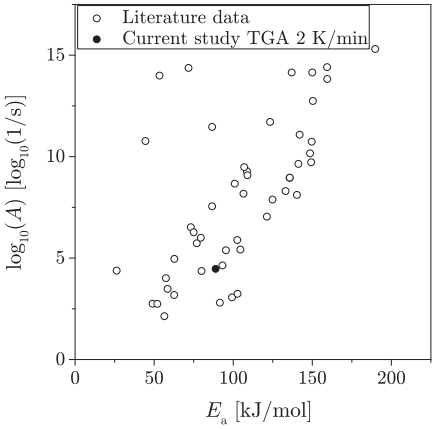

Fig. 17. Literature comparison of TGA experiments on biomass fuels at heating rates below 100 K s^{-1}. Literature sources: [1–7,9–16,52–54].

Bonvicini et al. [35] studied the pyrolysis of a range of biomasses, including a softwood, presumably comparable to the fuel used in this study (based on ash and high temperature volatile fractions and the ultimate analysis). In the study it was assumed that the particles follow the nominal temperature of the reactor, as discussed above. The method may result in an artificially slow set of kinetics to compensate for the assumed instant heat up of the particles. The effect is in agreement with the comparison in Fig. 15.

Although the conditions are significantly different from suspension firing conditions, slowly heated thermogravimetric methods of biomass fuels are often used. TGA data thus form the most comprehensive information base on fuel pyrolysis characteristics across fuels and reaction conditions. However, no consensus on how to interpret these results seems to exist.

Fig. 16 shows how the devolatilization kinetics become gradually slower as the degree of simplifications increases. The influence on the particle conversion profiles are shown in Fig. 15. This illustrates how especially kinetics derived from slow heating rate TGA experiments or on the assumption of particles assuming the nominal reactor temperature will result in an over prediction of the required residence time for complete devolatilization.

In line with literature reports, cf. Fig. 17, the activation energy of the corresponding TGA derived kinetics for the parent fuel is significantly higher than the fitted data from the high heating rate experiments. This results in a considerably slower pyrolysis reaction when applied to the high heating rate temperature history, cf. Fig. 15. This emphasizes the need for high temperature data if reliable devolatilization kinetics are to be used for pulverized fuel fired boilers.

7. Conclusions

This work describes the devolatilization of pine wood particles small enough to be considered isothermal. Experimental work on a laminar flow reactor resulted in partially reacted particles undergoing heating rates on the order of 10^5 K s^{-1} and peak temperatures of 1405 and 1667 K. The particle temperature history was derived using CFD simulations. Employing a single step first order mechanism with an Arrhenius type rate expression, a best fit of the pyrolysis kinetics was found to be: $A = 18.9 \times 10^3$ s^{-1}, $E_a = 21\,305$ J mol^{-1}.

The derived kinetic parameters have been evaluated in a bench-scale set-up with a nominal thermal input of solid fuel of 15 kW. CFD predictions show good quantitative agreement has been reached for major combustion species as well as the bulk flow temperatures.

Our work emphasizes the sensitivity on heating rate when using a single step first order mechanism to describe the pyrolysis process. The importance of being able to describe the particle trajectories has been demonstrated. It clearly points out the difference in pyrolysis behavior if kinetic data is derived without estimating the temperature history. Consequently, when comparing the derived devolatilization kinetics of the present study to literature data, a set of significantly faster kinetics emerges.

Acknowledgement

This work is part of the Power Generation from Renewable Energy (GREEN) Research Centre funded by the Danish Council for Strategic Research who are gratefully acknowledged.

References

[1] Greenhalf C, Nowakowski D, Bridgwater A, Titiloye J, Yates N, Riche A, et al. Thermochemical characterisation of straws and high yielding perennial grasses. Ind Crops Prod 2012;36(1):449–59.
[2] Bonelli PR, Buonomo EL, Cukierman AL. Pyrolysis of sugarcane bagasse and co-pyrolysis with an Argentinean subbituminous coal energy sources, Part A: Recover. Util Environ Eff 2007;29(8):731–40.
[3] Cordero T, García F, Rodríguez JJ. A kinetic study of holm oak wood pyrolysis from dynamic and isothermal TG experiments. Thermochim Acta 1989;149:225–37.
[4] Gómez CJ, Várhegyi G, Puigjaner L. Slow pyrolysis of woody residues and an herbaceous biomass crop: a kinetic study. Ind Eng Chem Res 2005;44:6650–60.
[5] Murty Kanury A. Thermal decomposition kinetics of wood pyrolysis. Combust Flame 1972;18(1):75–83.
[6] Senneca O. Kinetics of pyrolysis, combustion and gasification of three biomass fuels. Fuel Process Technol 2007;88(1):87–97.
[7] Yan W, Islam S, Coronella CJ, Va VR. Pyrolysis kinetics of raw/hydrothermally carbonized lignocellulosic biomass. Environ Prog Sustain Energy 2012;31(2):200–4.
[8] Wilson L, Yang W, Blasiak W, John GR, Mhilu CF. Thermal characterization of tropical biomass feedstocks. Energy Convers Manag 2011;52(1):191–8.
[9] Di Blasi C, Branca C. Kinetics of primary product formation from wood pyrolysis. Ind Eng Chem Res 2001;40(23):5547–56.
[10] Samolada M, Vasalos I. A kinetic approach to the flash pyrolysis of biomass in a fluidized bed reactor. Fuel 1991;70(7):883–9.
[11] Zabaniotou AA, Gogotsis D, Karabelas AJ. Product composition and kinetics of flash pyrolysis of *Erica arboreu* (biomass). J Anal Appl Pyrolysis 1994;29:73–87.
[12] Reina J, Velo E, Puigjaner L. Kinetic study of the pyrolysis of waste wood. Ind Eng Chem Res 1998;37(11):4290–5.
[13] Zabaniotou A, Ioannidou O, Antonakou E, Lappas A. Experimental study of pyrolysis for potential energy, hydrogen and carbon material production from lignocellulosic biomass. Int J Hydrogen Energy 2008;33(10):2433–44.
[14] Grønli MG, Melaaen MC. Mathematical model for wood pyrolysis comparison of experimental measurements with model predictions. Energy Fuels 2000;14(4):791–800.
[15] Branca C, Albano A, Di Blasi C. Critical evaluation of global mechanisms of wood devolatilization. Thermochim Acta 2005;429(2):133–41.
[16] Wagenaar BM, Prins W, van Swaaij WPM. Flash pyrolysis kinetics of pine wood. Fuel Process Technol 1993;36:291–8.
[17] Wiktorsson L-P, Wanzl W. Kinetic parameters for coal pyrolysis at low and high heating rates — a comparison of data from different laboratory equipment. Fuel 2000;79(6):701–16.
[18] Nik-Azar M, Hajaligol MMR, Sohrabi M, Dabir B. Effects of heating rate and particle size on the products yields from rapid pyrolysis of beech wood. Fuel Sci Technol Int 1996;14(4):479–502.
[19] Di Blasi C. Kinetic and heat transfer control in the slow and flash pyrolysis of solids. Ind Eng Chem Res 1996;35(1):37–46.
[20] Gibbins JR, Kandiyoti R. The effect of variations in time-temperature history on product distribution from coal pyrolysis. Fuel 1989;68(7):895–903.
[21] Lewellen P, Peters W, Howard J. Cellulose pyrolysis kinetics and char formation mechanism. Proc Combust Inst 1977;16(1):1471–80.
[22] Cai H-Y, Güell A, Dugwell D, Kandiyoti R. Heteroatom distribution in pyrolysis products as a function of heating rate and pressure. Fuel 1993;72(3):321–7.

[23] Fraga A-R, Gaines AF, Kandiyoti R. Characterization of biomass pyrolysis tars produced in the relative absence of extraparticle secondary reactions. Fuel 1991;70(7):803–9.
[24] Simone M, Biagini E, Galletti C, Tognotti L. Evaluation of global biomass devolatilization kinetics in a drop tube reactor with CFD aided experiments. Fuel 2009;88(10):1818–27.
[25] Jiménez S, Remacha P, Ballesteros JC, Giménez A, Ballester J. Kinetics of devolatilization and oxidation of a pulverized biomass in an entrained flow reactor under realistic combustion conditions. Combust Flame 2008;152:588–603. http://dx.doi.org/10.1016/j.combustflame.2007.10.001.
[26] Shuangning X, Zhihe L, Baoming L, Weiming Y, Xueyuan B. Devolatilization characteristics of biomass at flash heating rate. Fuel 2006;85(5–6):664–70.
[27] Jamaluddin A, Truelove J, Wall T. Devolatilization of bituminous coals at medium to high heating rates. Combust Flame 1986;63(3):329–37.
[28] Solomon PR, Serio Ma, Carangelo RM, Markham JR. Very rapid coal pyrolysis. Fuel 1986;65(2):182–94.
[29] Fletcher TH. Time-resolved particle temperature and mass loss measurements of a bituminous coal during devolatilization. Combust Flame 1989;78:223–36.
[30] Sun S, Tian H, Zhao Y, Sun R, Zhou H. Experimental and numerical study of biomass flash pyrolysis in an entrained flow reactor. Bioresour Technol 2010;101(10):3678–84. http://dx.doi.org/10.1016/j.biortech.2009.12.092. URL http://www.ncbi.nlm.nih.gov/pubmed/20074938.
[31] Ballantyne TR, Ashman PJ, Mullinger PJ. A new method for determining the conversion of low-ash coals using synthetic ash as a tracer. Fuel 2005;84(14–15):1980–5. http://dx.doi.org/10.1016/j.fuel.2005.04.012. URL http://linkinghub.elsevier.com/retrieve/pii/S0016236105001523.
[32] Hallett LH. Flow and particle flow reactor heating in an entrained. Fuel 1987;66:607–11.
[33] Brown AL, Dayton DC, Nimlos MR, Daily JW. Design and characterization of an entrained flow reactor for the study of biomass pyrolysis chemistry at high heating rates. Energy Fuels 2001;15(5):1276–85.
[34] Papadikis K, Gu S, Bridgwater AV, Gerhauser H. Application of CFD to model fast pyrolysis of biomass. Fuel Process Technol 2009;90(4):504–12. http://dx.doi.org/10.1016/j.fuproc.2009.01.010. <http://linkinghub.elsevier.com/retrieve/pii/S0378382009000162>.
[35] Bonvicini G, Coraggio G, Faleni M. Biofuels devolatilization and char combustion characterization with the IPFR. Tech. rep. December, International Flame Research Foundation; 2013.
[36] Trubetskaya A. Single biomass particle combustino and fuel characterization. PhD thesis, Technical University of Denmark.
[37] Campbell PA, Mitchell RE, Ma L. Characterization of coal char and biomass char reactivities to oxygen. Proc Combust Inst 2002;29(1):519–26.
[38] Ma L, Mitchell R. Modeling char oxidation behavior under zone II burning conditions at elevated pressures. Combust Flame 2009;156(1):37–50.
[39] Kupka T, Zajc K, Weber R. Effect of fuel type and deposition surface temperature on the growth and structure of an ash deposit collected during co-firing of coal with sewage sludge and sawdust. Energy Fuels 2009;23(7):3429–36.
[40] Weber R, Mancini M, Schaffel-Mancini N, Kupka T. On predicting the ash behaviour using computational fluid dynamics. Fuel Process Technol 2013;105:113–28.
[41] Johansen JM, Jakobsen JG, Frandsen FJ, Glarborg P. Release of K, Cl, and S during pyrolysis and combustion of high-chlorine biomass. Energy Fuels 2011;25(11):4961–71.
[42] Johansen JM, Aho M, Paakkinen K, Taipale R, Egsgaard H, Jakobsen JG, Frandsen FJ, Glarborg P. Release of K, Cl, and S during combustion and co-combustion with wood of high-chlorine biomass in bench and pilot scale fuel beds. Proc Combust Inst 2013;34(2):2363–72.
[43] Okuno T, Sonoyama N, Hayashi J-I, Li C-Z, Sathe C, Chiba T. Primary release of alkali and alkaline earth metallic species during the pyrolysis of pulverized biomass. Energy Fuels 2005;19(5):2164–71.
[44] Johansen JM. Release of inorganic matter during combustion of biomass. Master's thesis, Technical University of Denmark; 2011.
[45] Knudsen JN. Volatilization of inorganic matter during combustion of annual biomass. PhD thesis, Technical University of Denmark; 2004.
[46] Lu H, Robert W, Peirce G, Ripa B, Baxter LL. Comprehensive study of biomass particle combustion. Energy Fuels 2008;22(4):2826–39. http://dx.doi.org/10.1021/ef800006z. URL http://pubs.acs.org/doi/abs/10.1021/ef800006z.
[47] Daugaard DE, Brown RC. Enthalpy for pyrolysis for several types of biomass. Energy Fuels 2003;17(4):934–9.
[48] Rath J, Wolfinger MG, Steiner G, Krammer G, Barontini F, Cozzani V. Heat of wood pyrolysis. Fuel 2003;82:81–91.
[49] Weber R, Poyraz Y, Beckmann AM, Brinker S. Combustion of biomass in jet flames. Proc Combust Inst 2015;35(3):2749–58.
[50] Pyle DL, Zaror CA. Heat transfer and kinetics in the low temperature pyrolysis of solids. Chem Eng Sci 1984;39(1):147–58.
[51] Obernberger I, Thek G. Physical characterisation and chemical composition of densified biomass fuels with regard to their combustion behaviour. Biomass Bioenergy 2004;27(6):653–69.
[52] Aiman S, Stubington JF. The pyrolysis kinetics of bagasse at low heating rates. Biomass Bioenergy 1993;5(2):113–20.
[53] Thurner F, Mann U. Kinetic investigation of wood pyrolysis. Ind Eng Chem Process Des Dev 1981;20:482–8.
[54] Roberts AF. A review of kinetics data for the pyrolysis of wood and related substances. Combust Flame 1970;14:261–72.

APPENDIX B

Publication B

Extension of Apparent Devolatilization Kinetics from Thermally Thin to Thermally Thick Particles in Zero Dimensions

Joakim M. Johansen[a], Peter A. Jensen[a], Peter Glarborg[a], Marco Mancini[b], Roman Weber[b], Reginald Mitchell[c]

[a]Technical University of Denmark, Department of Chemical and Biochemical Engineering, Lyngby Campus, 2800 Kgs. Lyngby, Denmark

[b]Clausthal University of Technology, Institute of Energy Processes Engineering and Fuel Technology, 38678 Clausthal-Zellerfeld, Germany

[c]Stanford University, Department of Mechanical Engineering, 94305 California, United States of America

Published in Energy [359]
Energy 95 (2016) 279–290

Energy 95 (2016) 279–290

Contents lists available at ScienceDirect

Energy

journal homepage: www.elsevier.com/locate/energy

Extension of apparent devolatilization kinetics from thermally thin to thermally thick particles in zero dimensions for woody biomass

Joakim M. Johansen [a, *, 1], Peter A. Jensen [a], Peter Glarborg [a, **], Marco Mancini [c], Roman Weber [c], Reginald E. Mitchell [b]

[a] Technical University of Denmark, Department of Chemical and Biochemical Engineering, Lyngby Campus, 2800, Kgs. Lyngby, Denmark
[b] Stanford University, Department of Mechanical Engineering, 94305, California, USA
[c] Clausthal University of Technology, Institute of Energy Processes Engineering and Fuel Technology, 38678, Clausthal-Zellerfeld, Germany

ARTICLE INFO

Article history:
Received 1 July 2015
Received in revised form
20 October 2015
Accepted 3 November 2015
Available online xxx

Keywords:
Devolatilization kinetics
Pyrolysis
Biomass
Computational fluid dynamics (CFD)
Non-isothermal
High heating rate

ABSTRACT

This work aims to provide an accurate and simple model, predicting the time dependent devolatilization of woody biomass at conditions (T_{gas} < 2000 K) and particle sizes (<2 mm) relevant to suspension fired boilers. The zero dimensional model is developed from reference calculations with a one-dimensional heat transport model coupled with a drying and a devolatilization model. The model output has been used to generate pyrolysis kinetics corrected for non-isothermal effects, i.e. intraparticle heat transport limitations. Analysis of the modeling results indicate that heat transport corrections of even small particles are necessary. The current work divides a given particle size distribution into suitable size categories based on their internal heat transport properties. The devolatilization is described by size category specific rate constants based on a single first order reaction mechanism. This approach allows for significantly more accurate devolatilization predictions of any particle size distribution to be described by simple kinetic mechanisms and isothermal particle heat balances. Such an approach is easily implemented into most commercial CFD (computational fluid dynamics) codes without adding any additional strain to the computational requirements.

1. Introduction

The number of studies on thermal degradation of biomass material is extensive. The application covers a wide range of fields from wildfire simulations, fire protection, stoves, to utility boilers. Thus, the condition at which the models or experiments are developed or carried out at are very diverse. As a result quite a few biomass particle conversion models exist sharing common features while developed for different purposes. The most detailed single particle devolatilization models couple multiphase transport of heat and mass with volumetric gas-phase reactions, cracking reactions, and multiple competing multi-step reactions.

Hong et al. [1] developed a single particle one-dimensional model taking heat and mass transfer into account and including both drying, devolatilization, and char burn-out. Calculations using the non-isothermal model indicated significantly longer reaction times compared to those of the corresponding isothermal model for particles exceeding a few hundred microns in diameter. Similarly Groenli and Melaan [2] developed a single particle model for large particles (2–3 cm) and found that the addition of secondary cracking reactions are necessary in order to capture the ratio between gas, tar, and char formed for variations in the heating conditions. Bharadwaj et al. [3] mathematically investigated the influence of particle internal heat and mass transport and concluded that the drying and devolatilization to some extent was controlled by heat transport alone. Johansen et al. [4] showed through high heating rate experiments of particles less than 125 μm in diameter that the time scale for particle heat-up is comparable to that of complete devolatilization at high temperatures. Wagenaar et al. [5] combined slow heating rate thermogravimetric methods with flash pyrolysis drop tube experiments, and they were able to derive a single set of kinetic parameters capable of describing the pyrolysis of both set-ups at temperatures below 873 K.

* Corresponding author.
** Corresponding author.
E-mail addresses: jjoha@kt.dtu.dk (J.M. Johansen), pgl@kt.dtu.dk (P. Glarborg).
[1] www.kt.dtu.dk.

http://dx.doi.org/10.1016/j.energy.2015.11.025
0360-5442/

The objective of this work is to describe the rate of total devolatilization process at suspension firing conditions for non-isothermal particles using a zero-dimensional model with a global kinetic expression correcting for the heat transport limitations. This approach will reduce the computational cost of implementing single-dimensional particle models to CFD (computational fluid dynamics) simulations of larger systems, providing a method to do complex multiphase calculations with modest hardware requirements. The work provides a link between the complex multidimensional models found in the single particle literature and the isothermal assumption often made in burner simulations.

This work is divided into the following parts listed in chronological order:

1. Model description
2. Acquisition of validation material (literature study)
3. Model validation
4. Calculation of averaged devolatilization conversion and temperature profiles for non-isothermal particles (model output)
5. Single step, first order reaction devolatilization kinetic fitted to the calculated averaged conversions for different particle sizes

2. Modeling

In the present work the devolatilization of a fuel particle of spherical shape is described by a pyrolysis and a drying model coupled with a heat transport model taking both external and internal particular transport limitations into account.

The modeling is based on the following assumptions:

1. The model is solved in one dimension
2. Only primary pyrolysis takes place
3. The heat of pyrolysis sums to zero
4. No convective heat transport takes place inside the particle
5. There are no mass transfer limitations
6. Particles are spherical
7. Only the reactor walls contribute to the radiative external heat flux

The assumptions are generally accepted in the particle modeling literature [1,5–7]. Although some of the assumptions have been suggested to play an influence, e.g. multidimensional spread of energy, momentum, and mass [8], the influence of secondary reactions and heat of pyrolysis [9,10], the level of assumptions is generally considered valid for mass loss simulations similar to the objective of the current study.

2.1. Governing equations

The drying of the particles is described by a kinetic model [11]:

$$\dot{w} = k_Y(Y^* - Y(t))\rho_w \tag{1}$$

where $\dot{w}$ is the rate of water evaporation, ρ_w is the density of water, and Y^* and Y are the water content of the virgin fuel and the released amount of water at time t. The rate constant, k_Y, is expressed as:

$$k_Y = A_Y T_p^{1/2} \exp\left[\frac{-E_{a,Y}}{RT_p}\right] \tag{2}$$

where A_Y and $E_{a,Y}$ are the pre-exponential factor and the activation energy for the water evaporation model and T_p and R are the local particle temperature and the universal gas constant.

The devolatilization is solely driven by the thermal breakdown of the organic structure and is described by a single global reaction:

$$\text{parent fuel} \xrightarrow{k} \text{solid} + \text{volatiles} \tag{3}$$

As such, only the primary pyrolysis [12,13], is taken into account neglecting any secondary reactions [14,15].

The rate of reaction is described by a single SFOR (step first order reaction)

$$\frac{dV(t)}{dt} = k(V^* - V(t)) \tag{4}$$

where V and V^* are the fraction of volatile matter released and the ultimate fraction of volatile matter respectively. V^* has been obtained experimentally in entrained flow reactors to yield the true high temperature, high heating rate value which is known to deviate significantly from low temperature, low heating rate experiments often used in fuel characterization standards [16].

The rate constant, k, obeys an Arrhenius type expression

$$k = A \exp\left[\frac{-E_a}{RT_p}\right] \tag{5}$$

where A and E_a are the pre-exponential factor and the activation energy respectively, for the pyrolysis step while R and T_p denote the universal gas constant and the local temperature of the solid.

The heat balance accommodates the intra-particular heat transport limitations coupled with a transport model for the external heat flux. If a quasi-steady-state is considered and the heat transport is described by Fourier's law, then

$$c_P\rho\frac{\partial T(t,r)}{\partial t} = \frac{2\lambda}{r}\frac{\partial T(t,r)}{\partial r} + \lambda\frac{\partial^2 T(t,r)}{\partial r^2} - \dot{w}_w\Delta_{vap}H \tag{6}$$

describes the heat transport through the particle. Here c_P, ρ, and λ are the specific heat capacity, density, and thermal conductivity of the solid phase, respectively.

The initial condition is given by the particle temperature at time zero, T_0:

$$T(0,r) = T_0 \tag{7}$$

The boundary conditions are defined as adiabatic behavior at the particle center, and the heat flux from the surrounding to the particle, q_{ext}, given by the total contribution from a convective flux, q_c, and a radiative flux, q_r. This yields the spatial boundaries of the particles as:

$$\lambda\frac{\partial T}{\partial r}\Big|_{r=0} = 0 \tag{8}$$

$$\lambda\frac{\partial T}{\partial r}\Big|_{r=R} = q_{ext} \tag{9}$$

2.2. Algebraic equations

In addition to the governing equation describing the energy balance of the system, a number of algebraic equations must be defined in order to describe the transport properties of the transient system.

2.2.1. Heat of evaporation of water

Because the model aims at describing particles used for suspension fired boilers, only bound water is taken into consideration.

The moisture content of the fuels used for these purposes is assumed not to exceed the fiber saturation point.

The energy needed to evaporate bound water, $\Delta_{vap}H$, is found as the sum of the heat of desorption of the bound water, $\Delta_{ds}H$, and the subsequent evaporation of liquid water, $\Delta_l H$:

$$\Delta_{vap}H = \Delta_l H + \Delta_{ds}H \tag{10}$$

2.2.2. Particle material properties

Each of the material specific properties, c_p, ρ, and λ changes linearly with conversion, χ [2], as

$$\varphi_i(\chi_i) = \chi_i\varphi_a + (1-\chi_i)\varphi_b \tag{11}$$

where index i indicates the discretization in the radial direction. The radiative contribution is introduced through an effective thermal conductivity, λ_{eff}, found as the sum of conduction in the solid, λ_s, and gas phase, λ_g, as well as the radiative, λ_r, contribution:

$$\lambda_{eff} = \lambda_g + \lambda_s + \lambda_r \tag{12}$$

The intraparticular heat transport by radiation, λ_r, is correlated from previous studies [17] and is proportional to the cubed particle temperature, thus, especially important at elevated temperatures [18]:

$$\lambda_r = \frac{\left(\chi d_{pore,c} + (1-\chi)d_{pore,f}\right)\sigma T_p^3}{\varepsilon} \tag{13}$$

here d_{pore} denotes the pore diameter of the char and the parent fuel respectively. ε is the particle emissivity and σ is the Stefan–Boltzmann constant.

2.2.3. External transport

The radiative heat flux to the particle, q_r, is given by the Stefan–Boltzmann law [19], while the convective heat transport is driven by the difference between the bulk gas temperature, T_g, and the particle surface temperature, $T_p|_{r=R}$, correlated by the heat transfer coefficient, h, which is calculated for a spherical particle based on the flow conditions [20].

$$h = \frac{\lambda Nu}{2R} = \frac{\lambda\left(2 + 0.6Re^{\frac{1}{2}}Pr^{\frac{1}{3}}\right)}{d_p} \tag{14}$$

$$Re = \frac{d_p v_g \rho_g}{\mu_g} \tag{15}$$

$$Pr = \frac{c_{P,g}\mu_g}{\lambda_g} \tag{16}$$

where Nu, Re, and Pr denote the Nusselt, Reynold, and Prandtl number, respectively. The slip velocity between gas and particle is denoted v_g. The gas density, ρ_g, specific heat capacity, $c_{P,g}$, viscocity, μ_g, and thermal conductivity, λ_g, are empirically correlated to the temperature [21].

The net contribution of heat, q_{ext}, used in (9) can then be expressed by:

$$q_{ext} = h\left(T_g - T_p|_{r=R}\right) + \varepsilon\sigma\left(T_w^4 - T_p^4|_{r=R}\right) \tag{17}$$

where T_w is the temperature of a radiating wall, assumed to be equally visible from all angles.

2.2.4. Shrinking

A 20% reduction in particle size was observed during devolatilization experiments of wood particles [22]. This is assumed to primarily affect the external heat transport to the particle. The convective contribution is corrected by correlating the heat transport coefficient, h, to the reduction in particle diameter as function of conversion. The radiative contribution is reduced through a factor scaling with the reduction in surface area. A linear correlation between mass averaged conversion and particle size reduction is assumed. The development in morphology of a given particle as it undergoes thermal conversion is ambiguous [1] and detailed modeling of the physical progress of a generic fuel lies beyond the scope of this work. A shrinking correction has been included in order to recognize the observations of the original experimental data [22] to which the model has been fitted.

2.3. Particle properties

The particle is described as a sphere and correlated to experimental data from literature of non-spherical particles by using a fixed V/A-ratio in order to balance the external heat flux and particle heat capacity. The thermophysical data used in the model is listed in Table 1.

2.4. Drying and devolatilization kinetics

Because of the low moisture content (<10 wt.%) in fuels used for suspension fired combustion purposes, all of the inherent water is treated as bound water. The release of bound water is controlled by a kinetic expression derived by Chan et al. [23] who determined the kinetic parameters as listed in Table 2.

The devolatilization kinetics will in this work need to cover both a wide range of temperatures (300–1850 K) and heating rates ($10–10^5$ K/s). This is notoriously difficult using a global mechanism such as the one employed in equation (3). This challenge motivated the development of the DAEM (distributed activation energy model); however, even for these infinite parallel reaction models, the validation material often stem from low heating rate thermogravimetric experiments [24–26].

The devolatilization kinetics needed to evaluate equation (3) at high heating rates are obtained from previous work on high heating rate, high temperature experiments on biomass devolatilization [4]. The work was aimed at developing devolatilization SFOR kinetics for isothermal particles at conditions similar to suspension firing. These results ($E_{a,1} = 21{,}305$ J/mol, $A_1 = 18.9 \times 10^3$ 1/s) will in this work be employed as intrinsic kinetics which coupled with the heat transport model will yield a conversion rate for non-isothermal particles.

For low heating rates, i.e. larger particles, the kinetics derived by Wagenaar et al. [5] have been used. They used a two step mechanism: A primary pyrolysis with three competing reactions forming gas, tar, and char followed by a consecutive step cracking the tar to gas as illustrated in Fig. 1. These kinetic data have previously been used with success for larger particles of around 11 mm in diameter [1].

Because equation (3) assumes that the char yield is independent of the devolatilization conditions, the net devolatilization rate constant can be found as:

$$k_2 = k_V + \min(k_T; k_{V2}) \tag{18}$$

The model adopts the approach of Simone et al. [27] introducing a critical temperature separating the high from the low temperature pyrolysis kinetics. The separation is necessary in order for the SFOR mechanism to remain valid in the entire temperature interval. A critical temperature of around 800 K matches the typical reported

Table 1
Thermophysical properties used in the model.

Symbol	Unit	Description	Expression	Ref
$c_{p,f}$	$J\cdot(kg\cdot K)^{-1}$	Specific heat capacity	$\frac{1000R}{7.72}(g(z_1(T))+2g(z_2(T)))$	[2,36]
$c_{p,c}$			$\frac{1000R}{11.3}(g(z)+2g(z))$	[36]
			$g=\frac{z_i^2\exp^{z_i}}{(\exp^{z_i}-1)^2}$	
			$z_1=380/T$, $z_2=1800/T$	
$c_{P,g}$	$J\cdot(mol\cdot K)^{-1}$		$31.2-14.6\times10^{-3}T+32.9\times10^{-6}T^2$ $-20.9\times10^{-9}T^3+4.36\times10^{-12}T^4$	[21]
λ_f	$J\cdot(m\cdot K\cdot s)^{-1}$	Thermal conductivity	$0.13+3\times10^{-4}(T-273), T\leq1006$ K $0.3, T>1006$ K	[2,37,38]
λ_c			$0.08-(T-273)\times10^{-4}, T\leq943$ K $0.013, T>943$ K	[37,39]
λ_g			0.0258	[38]
λ_r		*	$d_{pore}\sigma T_p^3/\varepsilon$	[17]
λ_{eff}		*	$(1-\chi)\lambda_f+\chi\lambda_c+\lambda_g\varphi+\lambda_r$	[2,38]
$\lambda_{g\ ext}$			$-1.72\times10^{-4}+1.03\times10^{-4}\ T$ $-5.67\times10^{-8}T^2+2.68\times10^{-11}\ T^3$ $-4.92\times10^{-15}\ T^4$	[21]
μ	Pa·s	Viscosity	$3.98\times10^{-7}+7.24\times10^{-8}\ T$ $-4.81\times10^{-11}T^2+2.28\times10^{-14}\ T^3$ $-4.20\times10^{-18}\ T^4$	[21]
$d_{por,f}$	m	Pore diameter	3.2×10^{-6}	[2]
$d_{por,c}$			10^{-4}	[2]
ε	–	Particle emissivity	0.85	
σ	$J\cdot(m^2\cdot K^4\cdot s)^{-1}$	Stenfan-Boltzmann	5.6704×10^{-8}	[40]
ρ_f	$kg\cdot m^{-1}$	Density (Wood/wood pellet)	700/1180	[32]
ρ_c			$\rho_f\times(1\text{-vol})$	
ρ_g			$362.65\ T^{-1.006}$	[21]
$\Delta_l H$	$J\cdot kg^{-1}$	Heat of evaporation	$(3179.0-2.5\ T)1000$	[41]
$\Delta_{ds}H$		Heat of desorption	$400\Delta_l H\left(1-\frac{Y}{Y_{fsb}}\right)^2$	[42]
Y_{fsb}	–	Fibre saturation point	$0.598-0.001\ T$	[43]

*In this study the porosity, φ, has been assumed to vary linearly with the conversion, χ.

shift in first order kinetics [27,28] as illustrated in Fig. 2. The large particles (11 mm) experience heating rates on the order of 10 K/s [1], while the small particles (~100 μm) are heated much faster on the order of 10^5 K/s [4]. Thus, the influence of each reaction constant is a function of particle diameter.

3. 1D model validation

The 1D model is validated against data from three different studies, each presenting devolatilization data of woody fuel at different particle sizes (0.063–10.9 mm) and different heating rates (30–10^5 K/s). An overview of the key characteristics of the experimental validation data is given in Table 3. The validation has been included in appendix Appendix A.

Table 2
Kinetic parameters used for the non-isothermal particle modeling.

Parameter	Unit	Constant	Reference
High temperature kinetics			
A_1	s^{-1}	18.9×10^3	[4]
$E_{a,1}$	$kJ\cdot mol^{-1}$	21.305	
Low temperature kinetics			
A_V	s^{-1}	1.11×10^{11}	[5]
$E_{a,V}$	$kJ\cdot mol^{-1}$	177	
A_T	s^{-1}	9.28×10^9	[5]
$E_{a,T}$	$kJ\cdot mol^{-1}$	149	
A_{V2}	s^{-1}	4.28×10^6	[5]
$E_{a,V2}$	$kJ\cdot mol^{-1}$	108	
Water evaporation			
A_Y	$s^{-1}\cdot K^{-1/2}$	4.4×10^6	[23]
$E_{a,Y}$	$kJ\cdot mol^{-1}$	88	

4. Results and discussions

A set of kinetic parameters that can be used in a simple isothermal model, accounting for both the influence of heat transfer and kinetic limitations, are derived based on the calculations using the detailed 1D model.

The following algorithm is used to derive apparent devolatilization kinetics for non-isothermal particles:

1. The non-isothermal 1D model, combining heat transfer, water release, and devolatilization is used to generate conversion profiles of a specific particle size at a given temperature.
2. The conversion profile (from step 1) is superimposed on an isothermal devolatilization model (equation (19)) and the corresponding particle temperature history is calculated.
3. The combination of the non-isothermal conversion profile (step 1) and the isothermal temperature history (step 2) is used to derive a set of apparent devolatilization kinetics corrected for heat transport limitations.

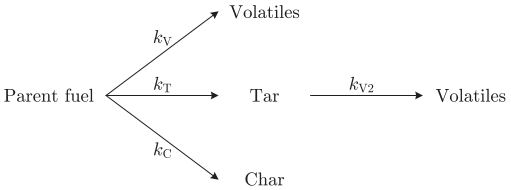

Fig. 1. Two-step semi-global reaction mechanism [5].

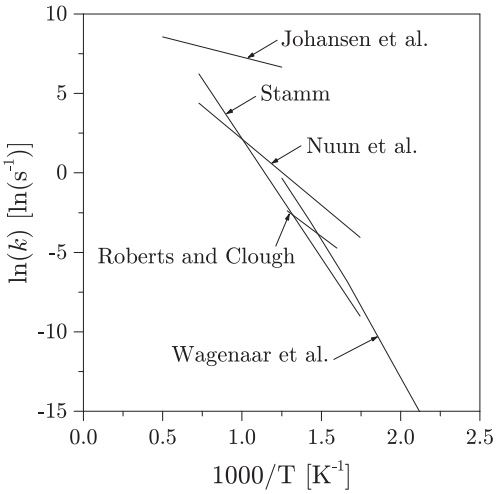

Fig. 2. Kinetic data for the devolatilization of different biomasses (author?) [4,5,28,44,45]. The rate constant for Wagenaar et al. is the net rate given by equation (18).

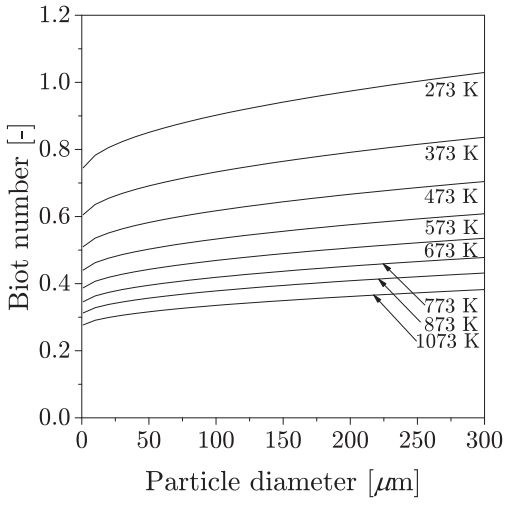

Fig. 3. A Biot number ($Bi = hd_p/(2\lambda)$) of a biomass particle analysis based on the physical properties listed in Table 1. The heat transfer coefficient, h, is calculated on averaged values of gas properties at temperatures between 1400 and 1700 K and at a slip velocity of 2 m/s. The temperatures indicate particle temperatures.

The isothermal model used to derived heat transport corrected devolatilization kinetics shares all of the thermophysical data with the non-isothermal model, cf. Table 1. The temperature history is computed by solving a heat balance:

$$m_p c_p \frac{dT_p}{dt} = hA_p(T_g - T_p) + \varepsilon_p A_p \sigma\left(T_w^4 - T_p^4\right) \quad (19)$$

where m_p, c_p, ε_p, and A_p are the mass, specific heat, emissivity, and surface area of the particle. T_p, T_g, and T_w are the particle, bulk gas, and radiation temperatures, respectively. σ and h are the Stefan–Boltzmann constant and the gas phase heat transfer number.

4.1. Identification of characteristic particle sizes

One of the most widely used methods to categorize a particle as being thermally thin or thermally thick is by assessing the Biot number. For inert particles the transition from iso-thermal to non-isothermal regime is commonly known to occur at $Bi = 0.1$. However, for transient models where the thermophysical properties change as a function of temperature and solid composition, the problem becomes somewhat more ambiguous.

Bryden et al. [29] used a Biot number analysis based on the parent fuel properties and correlated the output to their transient model for solid fuel thermal degradation. They found that a Biot number of 0.2 indicates the transition from the thermally thin to the thermally thick regime also, as suggested by Borman and Ragland [30]. They included the contribution from external radiation by assuming a particle surface temperature equal to that of the bulk gas phase. Knowing that this would overestimate the radiative heat transfer they corrected the total heat transfer coefficient by dividing it by a factor of 2. They concluded that their method was valid within a 25% accuracy.

However, because the contribution from external radiation depends on the particle surface temperature to the power of 4, this term will change significantly as the particle undergoes heat up from ambient to the final temperature. In addition, the contribution from radiation for smaller particles will be small compared to the influence of convective heat transport.

A conventional Biot number analysis is illustrated in Fig. 3. It shows how the requirement of $Bi \ll 1$ will never be satisfied for conditions relevant to suspension fired combustion, even at very small particle sizes due to the slow heat internal heat transfer. The implication is that on dimensionless time scales, the temperature gradients inside a particle cannot be neglected, regardless of particle size. However, the necessary time for devolatilization scales with particle size. Thus, the nominal time difference between an isothermal and a non-isothermal approach for very small particles may be insignificant when compared to the time scale for complete devolatilization.

Instead of a Biot number analysis or similar analyses, e.g. *Py*' number analysis [31], the present work will evaluate the heat transfer inside and external to the particle by using 1D model calculations. By analyzing the radial conversion and temperature profiles of the particles, three distinct categories can be defined depending on particle size, cf. Fig. 4:

Table 3
Overview of the set-ups used for validation data.

#	Set-up	Particle size mm	Heating rate K/s	Peak temperature K	Reference
A	Entrained flow reactor	0.063–0.090	10^5	1405–1667	[4]
B	Single particle combustor	1.79–5.8	10^2–10^3	1480–1831	[22]
C	Single particle combustor	10.9	30	1050–1267	[1]

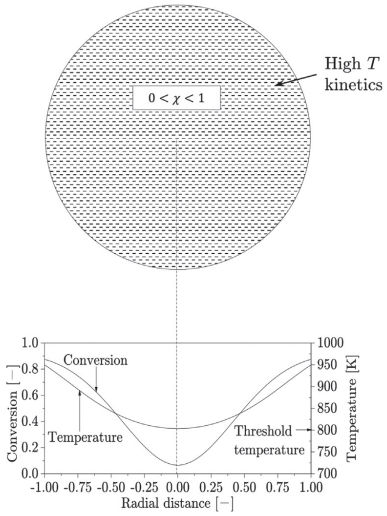

(a) Small particle.

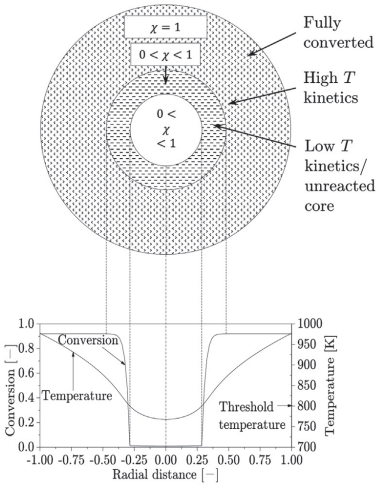

(b) Medium particle.

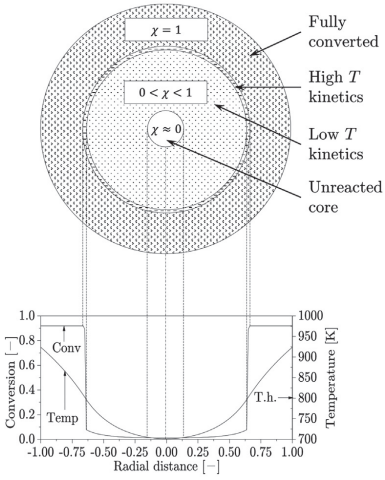

(c) Large particle.

Fig. 4. Definition of the three characteristic particle sizes. Fig. 4a: small particles: The entire particle is being converted in the high temperature kinetic regime. Fig. 4b: medium particles: The outer part of the particle reaches full conversion before the temperature in the center exceeds the critical threshold separating low from high temperature pyrolysis kinetics. Fig. 4c: large particles: The heat transport through the particle is slow. Thus, the outer part will reach full conversion while the core is still unreacted. The heat front propagates slowly, leaving only a thin shell of high temperature kinetics, while a large part of the particle is converted in the low temperature kinetics regime. The calculations are carried out with $T_g = 1405$ K and $T_w = 1000$ K, and particle properties given in Table 6.

1. Small particles, cf. Fig. 4a: Nearly isothermal particles. The internal heat transport occurs fast and as a result, the core of the particle reaches elevated temperatures before the outer part of the particle is fully devolatilized. The heat up is fast, thus the devolatilization process is primarily controlled by the high temperature devolatilization kinetics.
2. Medium size particles, cf. Fig. 4b: The particle size is sufficiently large as to introduce non-negligible temperature gradients.

Table 4
Definitions of the transitions between the three particle size devolatilization categories. T_p is the local particle temperature, T_c is the threshold temperature separating low and high temperature devolatilization kinetics, r is the normalized radial distance going from center to surface, χ is the local devolatilization conversion, and $|_t$ denotes a given time step.

Transition	Description	Mathematical description
–Small	From zero length to the critical particle diameter where the outer part of the particle reaches full conversion before the core reaches the critical temperature threshold separating low from high temperature kinetics.	$T_p > T_c \quad r\in[0;1]$ $\wedge$ $\chi < 1 \quad r\in[0;1]$
Small–medium	From small particles to where the outer shell reaches full conversion before devolatilization has begun at the core.	$T_p < T_c \quad r\in[0;r1]$ $\wedge$ $T_p > T_c \quad r\in[r1;1]$ $\wedge$ $\chi < 1 \quad r\in[0;r1]$
Medium–	From medium particles and up.	

Table 5
Effective particle diameter for each particle bin. Heat transport corrected devolatilization kinetics specific to the class size.

Size bin	Interval μm	Diameter μm	A s^{-1}	E_a kJ·mol^{-1}
Small	0–112	89	8.56×10^{10}	171.8
Medium	112–616	490	3.99×10^{9}	162.3
Large	616–2000	1603	2.62×10^{6}	118.7

However, the heat transport still occurs relatively fast. Thus, as the outer part of the particle reaches full devolatilization, the temperature of the core has risen sufficiently to initiate devolatilization. The relative increase in internal thermal resistance compared to small particles results in a primary share of the conversion taking place in the high temperature kinetic regime.

3. Large particles, cf. Fig. 4c: The internal heat transport is significantly slower compared to the smaller particle sizes. As a result, an unreacted core remains even as the outer part of the particle reaches full conversion. The heat propagates slowly through the particles resulting in a broad reaction zone controlled by the low temperature kinetics. This is directly followed by a narrow shell of high temperature kinetics.

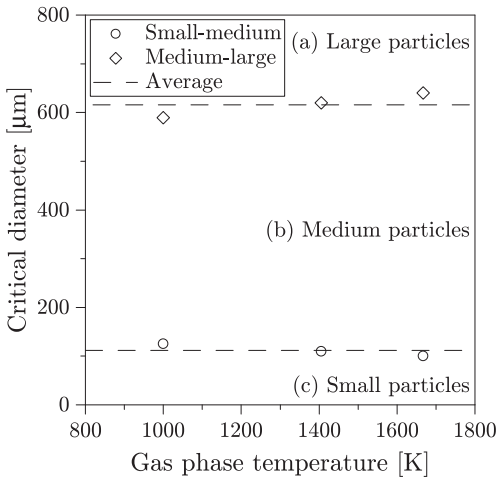

Fig. 5. The critical particle diameters satisfying the conditions given in Table 4. The average values are used as a generic measure for particle size classification. Average values: Small-medium 112 μm, medium–large 616 μm.

The transition between the three categories of particle sizes can be defined on a conceptual basis as described in Table 4.

Fig. 5 shows the transition diameters as function of the gas temperature. The critical diameters vary only slightly with temperature. For a generically applicable discretization of a given size distribution, the mean values are used to define the small, medium, and large particles.

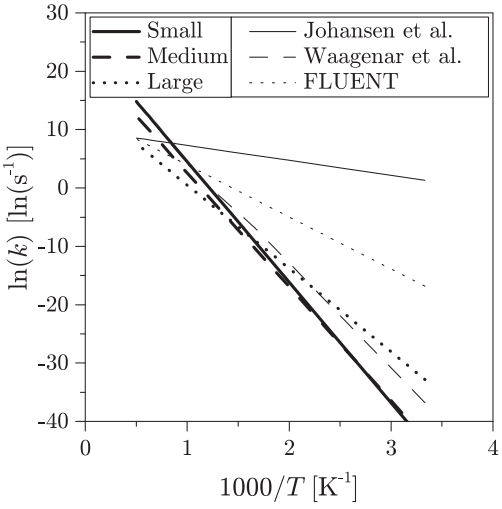

Fig. 6. The resulting kinetics for the heat transport corrected characteristic particles sizes. Compared to the literature values of Wagenaar et al. [5], Johansen et al. [4], and the FLUENT® default values for wood devolatilization.

Table 6
Particle characterization.

Parameter	Unit	Value	Reference
Moisture	wt. %	0.0	
Volatiles		91.9	[4]
Char		7.90	[4]
Ash		0.200	[4]
Density	kg·m^3	1180	[32]

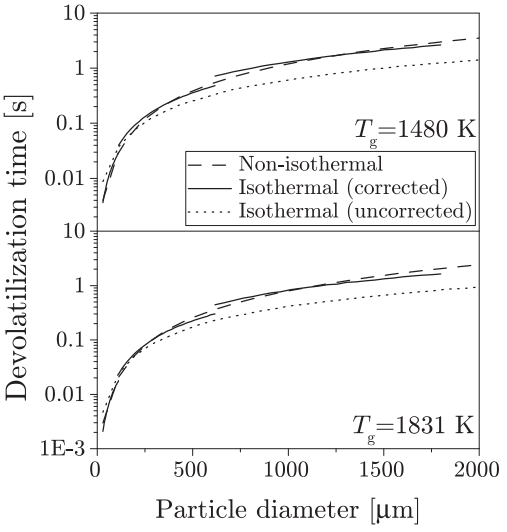

Fig. 7. A direct comparison on the predicted total devolatilization time between the non-isothermal and isothermal model using heat transport corrected and uncorrected devolatilization kinetics as a function of initial particle diameter. Temperatures indicate gas phase temperatures.

4.2. Conversion profiles for characteristic particle sizes

Following the particle sizes, defined in Fig. 5, conversion profiles are calculated for a single particle size representing the different particle size bins. The characteristic particle diameter is chosen as the diameter equivalent to half of the net volume of the corresponding size bin. The average particle diameter for the large particle bin is calculated using 2 mm as the largest particle diameter. This corresponds to a typical 95% quantile for pulverized biomass used in suspension fired boilers.

In Fig. 6, the resulting heat transport corrected kinetics are compared to the literature values of Wagenaar et al. [5] and Johansen et al. [4]. The ANSYS® FLUENT® default values for wood devolatilization ($E_a = 74\,\mathrm{kJ\cdot mol^{-1}}$ and $A = 312 \times 10^3\ \mathrm{s^{-1}}$) are also represented and will be used as a literature reference in the following comparison of kinetics, cf. Figs. B.12–B.14. Fig. 6 clearly shows why the combination of the low (Wagenaar et al. [5]) and the high (Johansen et al. [4]) temperature kinetics is necessary in order to describe the devolatilization across different heating rates. The differences in the rate of devolatilization are significant, especially at low temperatures.

The fuel properties used for the calculations are listed in Table 6. Since the work aims to facilitate large numerical simulations of pulverized biomass fired boilers, the density is chosen as that of a typical wood pellet [32]. To simplify data interpretation, the calculations have been carried out on dry particles.

Fig. 7 shows the direct comparison between the predicted total devolatilization time (for 95% conversion) using the non-isothermal 1D model and the isothermal model with and without the heat transport correction in the devolatilization kinetics. A noticeable better fit is achieved by applying the heat transport corrected devolatilization kinetics in the appropriate size categories. The time resolved results are included in appendix ??

5. Conclusion

A method has been developed that increases the accuracy of the predicted time dependent volatile release for biomass particle sizes relevant for suspension fired combustion <2 mm. The method makes it possible to simulate heat transport limited pyrolysis in zero dimensions using a simple conversion mechanism and a set of heat transport corrected reaction rates. This allows one to carry out multiphase fluid dynamics calculations (CFD) without having to implement computational heavy single or multi-dimensional calculations of the discrete phase.

Comparison of the 0D modeling approach to a 1D model (including heat transport and kinetic limitations) shows that using uncorrected pyrolysis kinetics will overestimate the total pyrolysis time of small particles (89 μm) by 50–80%. For larger particles (1603 μm) the uncorrected pyrolysis kinetics will lead to a predicted devolatilization time of under half of that predicted by the 1-dimensional model.

The method taking for heat transport limitations into account by correcting the devolatilization kinetics, is easily implemented into most CFD commercial codes. It avoids the requirement for demanding multidimensional computations of the discrete phase while still providing a more accurate prediction of the time resolved release of volatiles.

The non-isothermal 1D model has been developed based on time resolved empiric conversion data for very small particles (<200 μm) and large particles of 10.9 mm. The model performance for particles within this interval has been evaluated based on the total devolatilization time, and a critical temperature at which the rate constant changes from low to high temperature kinetics has been assigned. Thus, the time dependent release of the volatiles may not be accurately predicted by the model. This could be improved by introducing a blending option based on multiple parallel reactions [33] or alternatively by an implementation of a more detailed devolatilization mechanism, e.g. the distributed activation energy model [24,34]. The computational penalty should however be kept in mind [35].

Acknowledgement

This work is part of the Power Generation from Renewable Energy (GREEN) Research Centre funded by the Danish Council for Strategic Research who are gratefully acknowledged.

Appendix A. 1D model validation

This supplementary material covers the validation of the one dimensional, non-isothermal devolatilization model developed in the main text. The 1D model is validated against data from three different studies, each presenting devolatilization data of woody fuel at different particle sizes (0.063–10.9 mm) and different heating rates (30–10^5 K/s).

Appendix A.1. Small particles, validation set-up A

Set-up A has been used previously by the authors [4], and the reactor description and experimental procedure can be found

within that study. It is a laminar flow reactor operating at high peak temperatures (1405–1667 K) and the particles experience heating rates on the order of 10^5 K•s^{-1}. The reactor was operated at laminar (bulk flow) conditions with an understoichiometric CH_4/H_2-flame [4]. The solid fuel feed rate was kept at 10–20 mg h^{-1} ensuring single particle conditions. Particles were collected at different residence times by a movable probe. The work provided time resolved devolatilization profiles, where particle temperature and residence time data were determined from CFD (computational fluid dynamics) simulations. In these experiments, isothermal particle behavior is assumed.

Fig. A.8 shows a comparison between measurements and results for the 1D model at 1405 and 1667 K. It compares the effect of using the kinetic data from Johansen et al. [4] who used small particles to derive high heating rate kinetics, data from Wagenaar et al. [5] who used a combination of drop tube furnace and TGA equipment to derive pyrolysis kinetics. The use of slow heating rate TGA kinetics (Wagenaar et al. [5]) leads to an overprediction of the devolatilization time of the small particles. Contrary, the kinetics derived at high heating rates ((Johansen et al.) [4]) capture the high temperature experiment well. The combined kinetic expression used in this work predicts slightly higher reaction times than the experimental data, however, still the agreement is still found to be reasonable, considering the time scales.

Appendix A.2. Medium size particles, validation set-up B

Set-up B is a single particle combustor heated by a non-premixed gas flame. The particle is rapidly exposed to the hot environment and the devolatilization and char burn-out processes are analysed by visual methods [22].

The measured devolatilization times compile the work of Jensen [46] and Jepsen [47]. They worked on devolatilization experiments using cubic wood particles. The particle sizes range from Ref. 1.8–5.8 mm (corresponding spherical diameter) and the temperature interval from 1458 to 1831 K. The reactor is a convective single particle reactor heated by a flat flame burner. The particle is introduced to the burner fixed on a platinum wire and shielded by a removable ceramic tube. A high speed camera (65 Hz) captures the devolatilization and combustion phases through a view port in the side of the reactor. The set-up has previously been used in other work and a detailed description can be found elsewhere [22].

Fig. A.9 compares the observed residence time required for complete devolatilization (including heating and drying) to the model results. The devolatilization time has been defined in the experimental work as the time from which the particle is exposed to the hot reactor and to the point where a flame is no longer visible around the particle. In the 1D model the time for complete devolatilization has been defined as the time when 95% of the original volatile matter has left the particle.

The model is able to predict the total devolatilization times well. The model will in general slightly under predict the required residence times. The results are, however, well within the uncertainty of the experimental material.

Appendix A.3. Large particles, validation set-up C

The set-up is based on the same principles as set-up B but includes a scale which allows for time resolved analysis of the mass loss during devolatilization and char burn-out. The experiments include single particle pyrolysis of large biomass particles of 10.9 mm. The data are obtained from the work of Lu et al. [1] and include temporal data of mass loss as well as surface and center particle temperatures. The mass loss is obtained by a micro scale, the surface temperature by two-line thermometry, and the center temperature by thermocouple measurements. Figs A.10 and A.11 show the comparison of the 1D model results to the experimental data. The model is able to predict both the conversion profile and the surface temperature well. The conversion (drying and devolatilization) is predicted to initiate slightly later than the measured data and reach completion slightly before the measured data. The particle core temperature is significantly under estimated at low degrees of conversion. This is, however, believed to originate partly from experimental artifacts, e.g. by heat conduction through the thermocouple itself.

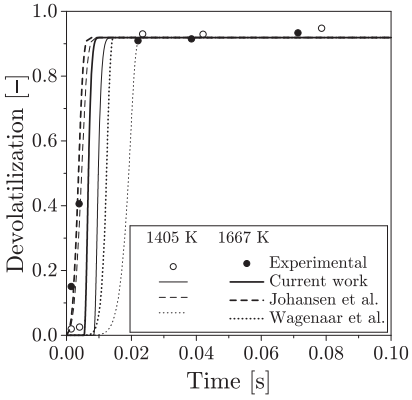

Fig. A.8. Comparison of the 1D model to the laminar entrained flow reactor devolatilization experiments. The devolatilization profiles obtained by using kinetic data obtained by Johansen et al. [4] and Wagenaar et al. [5] is also compared to the kinetics derived in this work. A single particle diameter of 78.9 μm has been used for the simulations corresponding to the Rosin-Rammler mean diameter of the experiments. The illustrated conversion is the mass averaged conversion.

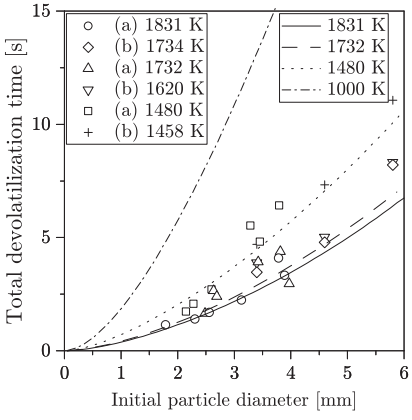

Fig. A.9. Comparison between measured single wood particle devolatilization times and the corresponding simulations using the 1D model. The devolatilization times includes particle heat up, drying, and devolatilization. Experimental data: [46,47].

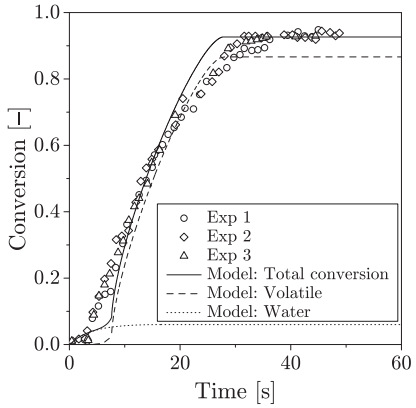

Fig. A.10. Conversion comparison between single particle measurements and the 1D model. $T_g = 1050$ K, $T_w = 1276$ K, $d_p = 10.9$ mm. Exp 1–3 are triple determination experiments.

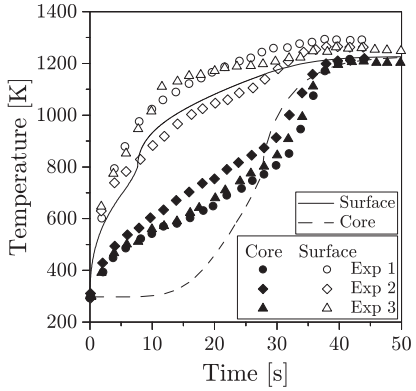

Fig. A.11. Comparison between single particle temperature measurements and the 1D model. $T_g = 1050$ K, $T_w = 1276$ K, $d_p = 10.9$ mm. Exp 1–3 are triple determination experiments.

Appendix B. Time resolved conversion profiles

Figs B.12–B.14 present a model comparison of devolatilization profiles for two gas phase temperatures at each of the characteristic particle size classes. The figures compare the results of the non-isothermal 1D model, the isothermal model using FLUENT® default values, and the isothermal model using heat transport corrected devolatilization kinetics, as seen in Table 5. Both pre-exponential factor and activation energy are allowed to change during the parameter fitting, making the physical interpretation ambiguous. However, the qualitatively relates to the temperature at which the reaction is allowed to take place at a significant rate while the pre-exponential factor relates to the rate at which the reaction is allowed to accelerate.

Fig. B.12 presents the results from the small particle size ($d_p = 89$ μm). It shows a longer devolatilization time using the default FLUENT® values, increasing the required residence time for complete devolatilization by around 30%.

This trend is reversed for the medium and large particle classes, cf. Figs B.13 and B.14. The isothermal model using the uncorrected kinetics under predicts the required time for devolatilization, most pronounced for larger particles. The heat transport corrected kinetics used in the isothermal model is capable of predicting approximately the same time for complete devolatilization as the non-isothermal model.

The discontinuous behavior of the conversion profile produced by the non-isothermal model is a consequence of using two sets of kinetics for different temperature intervals. Thus, the conversion levels amongst the models are different for low degrees of conversion.

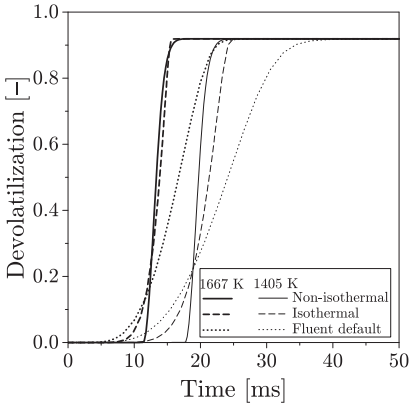

Fig. B.12. Small particles: $d_p = 89$ μm. Comparison between the non-isothermal and the isothermal model using the heat transport corrected devolatilization kinetics and the default FLUENT® values.

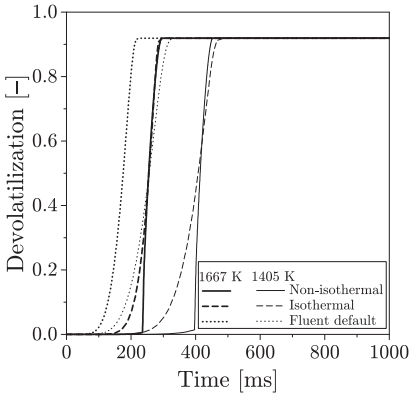

Fig. B.13. Medium particles: $d_p = 489.9$ μm. Comparison between the non-isothermal and the isothermal model using the heat transport corrected devolatilization kinetics and the default FLUENT® values.

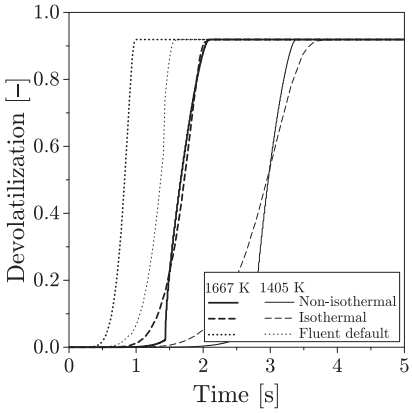

Fig. B.14. Large particles: $d_p = 1603$ μm. Comparison between the non-isothermal and the isothermal model using the heat transport corrected devolatilization kinetics and the default FLUENT® values.

References

[1] Lu H, Robert W, Peirce G, Ripa B, Baxter LL. Comprehensive study of biomass particle combustion. Energy Fuels 2008;22(4):2826–39. http://dx.doi.org/10.1021/ef800006z. http://pubs.acs.org/doi/abs/10.1021/ef800006z.

[2] Grønli MG, Melaaen MC. Mathematical model for wood pyrolysiss comparison of experimental measurements with model predictions. Energy Fuels 2000;14(4):791–800.

[3] Bharadwaj A, Baxter LL, Robinson AL. Effects of intraparticle heat and mass transfer on biomass devolatilization: experimental results and model predictions. Energy Fuels 2004;18(4):1021–31. http://dx.doi.org/10.1021/ef0340357.

[4] Johansen JM, Gadsbøll R, Thomsen J, Jensen PA, Glarborg P, De Martini N, et al. Devolatilization of woody biomass at short residence times and high heating rates and peak temperatures. 2015.

[5] Wagenaar BM, Prins W, van Swaaij WPM. Flash pyrolysis kinetics of pine wood. Fuel Process Technol 1993;36:291–8.

[6] Panton RL, Rittmann JG. Pyrolysis of a slab of porous material. Proc Combust Inst 1971;13(1):881–91. http://dx.doi.org/10.1016/S0082-0784(71)80089-9. http://linkinghub.elsevier.com/retrieve/pii/S0082078471800899.

[7] Mehrabian R, Scharler R, Obernberger I. Effects of pyrolysis conditions on the heating rate in biomass particles and applicability of TGA kinetic parameters in particle thermal conversion modelling. Fuel 2012;93:567–75. http://dx.doi.org/10.1016/j.fuel.2011.09.054. http://linkinghub.elsevier.com/retrieve/pii/S0016236111006144.

[8] Di Blasi C. Processes of flames spreading over the surface of charring fuels: effects of the solid thickness. Combust Flame 1994;97:225–39.

[9] Kung H-C, Kalelkar AS. On the heat of reaction in Wood pyrolysis. Combust Flame 1973;20(1):91–103. http://dx.doi.org/10.1016/S0010-2180(73)81260-X. http://dx.doi.org/10.1016/S0010-2180(73)81260-X.

[10] Rath J, Wolfinger MG, Steiner G, Krammer G, Barontini F, Cozzani V. Heat of wood pyrolysis. Fuel 2003;82:81–91.

[11] Benkoussas B, Consalvi J-L, Porterie B, Sardoy N, Loraud J-C. Modelling thermal degradation of woody fuel particles. Int J Therm Sci 2007;46(4):319–27. http://dx.doi.org/10.1016/j.ijthermalsci.2006.06.016. http://linkinghub.elsevier.com/retrieve/pii/S1290072906001657.

[12] Janse A, Westerhout R, Prins W. Modelling of flash pyrolysis of a single wood particle. Chem Eng Process Process Intensif 2000;39(3):239–52. http://dx.doi.org/10.1016/S0255-2701(99)00092-6. http://linkinghub.elsevier.com/retrieve/pii/S0255270199000926.

[13] Blasi CD, Di Blasi C. Analysis of convection and secondary reaction effects within porous solid fuels undergoing pyrolysis. Combust Sci Technol 1993;90(5–6):315–40. http://dx.doi.org/10.1080/00102209308907620.

[14] Liden AG, Berruti F, Scott DS. A kinetic-model for the production of liquids from the flash pyrolysis of biomass. Chem Eng Commun 1988;65:207–21.

[15] Boroson ML, Howard JB, Longwell JP, Peters WA. Product yields and kinetics from the vapor phase cracking of Wood pyrolysis tars. AIChE J 1989;35(1):120–8. http://dx.doi.org/10.1002/aic.690350113. http://doi.wiley.com/10.1002/aic.690350113.

[16] Bonvicini G, Coraggio G, Faleni M. Biofuels devolatilization and char combustion characterization with the IPFR. Tech. Rep. December, international flame research foundation. 2013.

[17] Di Blasi C, Russo G. Modeling of transport phenomena and kinetics of biomass pyrolysis. Adv Thermochem Biomass Convers 1993;2:906–21.

[18] Brown LE. An experimental and analytical study of wood pyrolysis [Phd thesis]. University of Oklahoma; 1972. https://shareok.org/handle/11244/3250.

[19] Bird RB, Steward WE, Lightfoot EN. Transport phenomena. 2nd ed. New York: John Wiley & Sons, Inc.; 2007.

[20] Richter A, Nikrityuk P a. Drag forces and heat transfer coefficients for spherical, cuboidal and ellipsoidal particles in cross flow at sub-critical Reynolds numbers. Int J Heat Mass Transf 2012;55(4):1343–54. http://dx.doi.org/10.1016/j.ijheatmasstransfer.2011.09.005. http://dx.doi.org/10.1016/j.ijheatmasstransfer.2011.09.005.

[21] Perry R. Perry's chemical engineers' handbook. McGraw-Hill; 2007.

[22] Momeni M, Yin C, Kær SK, Hansen TB, Jensen PA, Glarborg P. Experimental study on effects of particle shape and operating conditions on combustion characteristics of single biomass particles. Energy Fuels 2013;27(1):507–14. http://dx.doi.org/10.1021/ef301343q. http://pubs.acs.org/doi/abs/10.1021/ef301343q.

[23] Chan W-CR, Kelbon M, Krieger BB. Modelling and experimental verification of physical and chemical processes during pyrolysis of a large biomass particle. Fuel 1985;64(11):1505–13. http://dx.doi.org/10.1016/0016-2361(85)90364-3. http://linkinghub.elsevier.com/retrieve/pii/0016236185903643.

[24] Cai J, He F, Yao F. Nonisothermal nth-order DAEM equation and its parametric study use in the kinetic analysis of biomass pyrolysis. J Math Chem 2007;42(4):949–56. http://dx.doi.org/10.1007/s10910-006-9151-4. http://link.springer.com/10.1007/s10910-006-9151-4.

[25] Miura K. A new and simple method to estimate f(E) and k0(E) in the distributed activation energy model from three sets of experimental data. Energy Fuels 1995;9(2):302–7.

[26] Sonobe T, Worasuwannarak N. Kinetic analyses of biomass pyrolysis using the distributed activation energy model. Fuel 2008;87(3):414–21. http://dx.doi.org/10.1016/j.fuel.2007.05.004. http://linkinghub.elsevier.com/retrieve/pii/S0016236107002177.

[27] Simone M, Biagini E, Galletti C, Tognotti L. Evaluation of global biomass devolatilization kinetics in a drop tube reactor with CFD aided experiments. Fuel 2009;88(10):1818–27. http://dx.doi.org/10.1016/j.fuel.2009.04.032. http://linkinghub.elsevier.com/retrieve/pii/S0016236109002087.

[28] Nunn TR, Howard JB, Longwell JP, Peters WA. Product compositions and kinetics in the rapid pyrolysis of sweet gum hardwood. Ind Eng Chem Process Des Dev 1985;24:836–44.

[29] Bryden KM, Ragland KW, Rutland CJ. Modeling thermally thick pyrolysis of wood. Biomass Bioenergy 2002;22(1):41–53. http://dx.doi.org/10.1016/S0961-9534(01)00060-5. http://linkinghub.elsevier.com/retrieve/pii/S0961953401000605.

[30] Borman GL, Ragland KW. Combustion engineering. McGraw-Hill; 1998.

[31] Pyle DL, Zaror CA. Heat transfer and kinetics in the low temperature pyrolysis of solids. Chem Eng Sci 1984;39(1):147–58.

[32] Obernberger I, Thek G. Physical characterisation and chemical composition of densified biomass fuels with regard to their combustion behaviour. Biomass Bioenergy 2004;27(6):653–69. http://dx.doi.org/10.1016/j.biombioe.2003.07.006. http://linkinghub.elsevier.com/retrieve/pii/S0961953404001072.

[33] Niksa S, Lau CW. Global rates of devolatilization for various coal types. Combust Flame 1993;94(3):293–307. http://dx.doi.org/10.1016/0010-2180(93)90075-E.

[34] Braun RL, Burnham AK. Analysis of chemical reaction kinetics using a distribution of activation energies and simpler models. Energy Fuels 1987;1(2):153–61. http://dx.doi.org/10.1021/ef00002a003.

[35] Flynn JH. The "Temperature integral" — Its use and abuse. Thermochim Acta 1997;300:83–92.

[36] Merrick D. Mathematical models of the thermal decomposition of coal heats and heats of reaction. Fuel 1983;62:540–6.

[37] Koufopanos CA, Papayannakos N, Maschio G, Lucchesi A. Studies on kinetics, thermal and heat transfer effects. Can J Chem Eng 1991;69:907–15.

[38] Grønli MG. A theoretical and experimental study of the thermal degradation of biomass [Phd thesis]. The Norwegian University of Science and Technology; 1996. http://www.diva-portal.org/smash/get/diva2:321540/FULLTEXT01.pdf.

[39] Zhang X, Dukhan A, Kantorovich II, Bar-Ziv E. The Thermal conductivity and porous structure of char particles. Combust Flame 1998;113:519–31.

[40] Lide DR, Haynes WM, editors. Handbook of chemistry and physics. 90th ed. Boca Raton, Florida: CRC Press; 2010.

[41] Ražnjević K. Handbook of thermodynamic tables and charts. Hemisphere Pub Corp 1976. http://books.google.dk/books?id=VIRUAAAAMAAJ.

[42] Stanish MA, Schajer GS, Kayihan F. A mathematical model of drying for hygroscopic porous media. AIChE J 1986;32(8):1301–11. http://dx.doi.org/10.1002/aic.690320808. http://doi.wiley.com/10.1002/aic.690320808.

[43] Siau JF. Transport processes in wood. In: Springer series in wood science. Springer-Verlag; 1984. http://books.google.dk/books?id=DVTxAAAAMAAJ.

[44] Stamm AJ. Thermal degradation of wood and cellulose. Ind Eng Chem 1956;48(3):413–7.

[45] Roberts AF, Clough G. Thermal decomposition of wood in an inert atmosphere. Proc Combust Inst 1963;9(1):158–66.

[46] Jensen P. Combustion and modeling of alternative fuels. Master's thesis. The Technical University of Denmark; 2011. www.orbit.dtu.dk.

[47] Jepsen MS. Pyrolysis of large biomass particles in a single particle combustion reactor. Master's thesis. The Technical University of Denmark; 2014. www.orbit.dtu.dk.

Nomenclature

χ: conversion
$\Delta_{ds}H$: heat of bound water desorption
$\Delta_{l}H$: heat of liquid water evaporation
$\Delta_{vap}H$: net heat of evaporation
$\dot{w}$: rate of water evaporation
λ: thermal conductivity
λ_{eff}: effective thermal conductivity
λ_g: gas phase conductivity
λ_g: gas phase contribution to the thermal conductivity
λ_r: radiative contribution to the thermal conductivity
λ_s: solid phase contribution to the thermal conductivity
μ_g: gas phase viscosity
ρ: density
ρ_g: gas phase density
σ: Stefan–Boltzmann constant
ε: emissivity
φ: arbitrary property
A: pre-exponential factor
A: surface area
A_Y: pre-exponential factor for water evaporation
Bi: biot number
$c_{P,g}$: gas phase specific heat capacity
c_P: specific heat capacity
$d_{pore,c}$: char pore diameter
$d_{pore,f}$: parent fuel pore diameter
d_p: particle diameter
$E_{a,Y}$: activation energy for water evaporation
E_a: activation energy
$g(z)$: dummy function
h: external heat transfer number
k: rate constant (devolatilization)
k_Y: rate constant (water evaporation)
m_p: mass of the particle
Nu: Nusselts number
Pr: Prandtls number
q_c: convective contribution to the external heat flux
q_{ext}: external heat flux
q_r: radiative contribution to the external heat flux
R: gas constant
r: particle radius
Re: Reynolds number
t: time
T_c: critical temperature
T_g: gas phase temperature
T_p: particle temperature
T_w: wall temperature
V: particle volume
V: volatile fraction
V^*: volatile fraction in the parent fuel
v_g: gas slip velocity
Y: water fraction
Y^*: water fraction in the parent fuel
Y_{fsb}: fibre saturation point

APPENDIX C

AMV Full-Scale: Plant Operating Conditions

In the current appendix a graphical presentation of the operating conditions during the AMV full-scale campaign is presented. Plant data are reported every 10 minutes in this report.

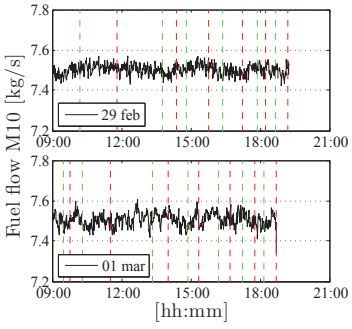

Figure C.1 Total fuel flow through mill 10. This is distributed to all four burners on level 10.

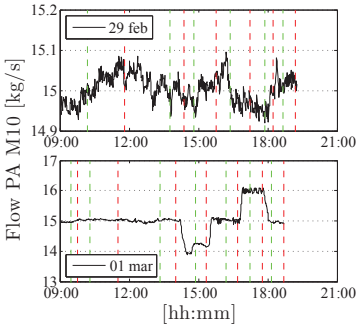

Figure C.2 Total flow of PA to mill 10. This is distributed to all four burners on level 10.

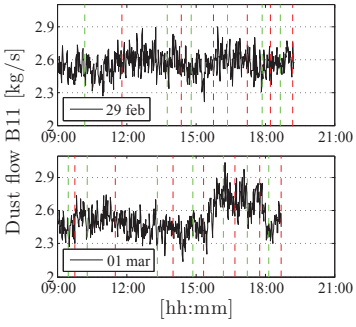

Figure C.3 Total dust flow to burner #11 on level 10.

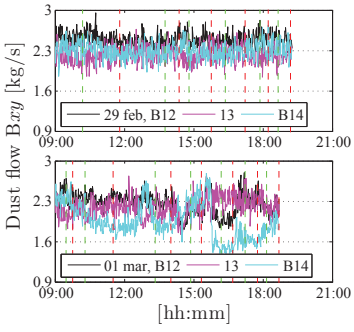

Figure C.4 Individual dust flows to level 10 burners.

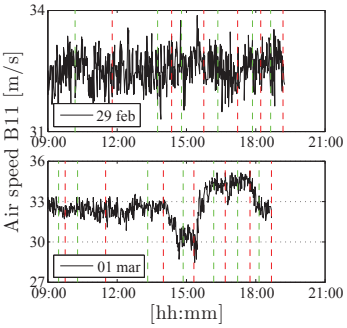

Figure C.5 Air speed to burner #11.

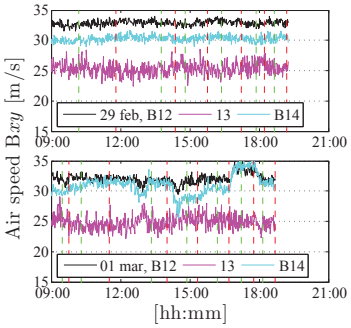

Figure C.6 Air speed to level 10 burners.

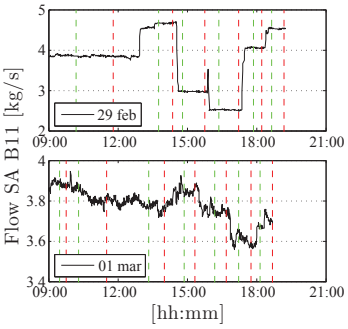

Figure C.7 Measured flow of SA to burner #11.

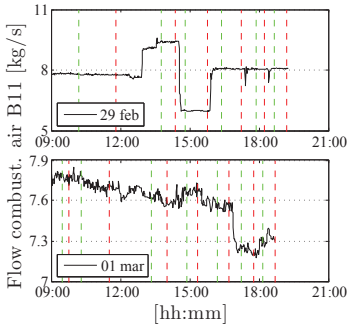

Figure C.8 Total flow of combustion air ($SA + TA$) to burner #11.

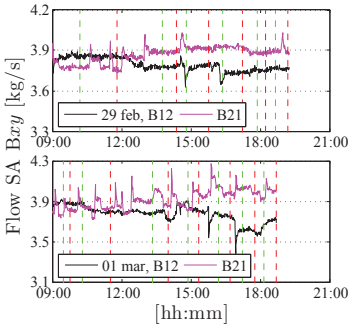

Figure C.9 Measured flow of SA to level 10 burners.

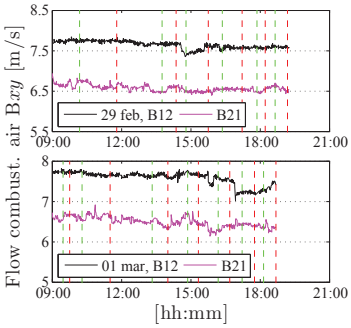

Figure C.10 Total flow of combustion air ($SA+TA$) to level 10 burners.

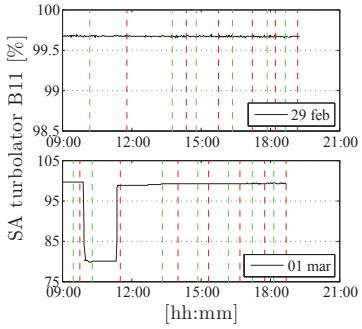

Figure C.11 SA turbulator setting. Percentage of the physical position.

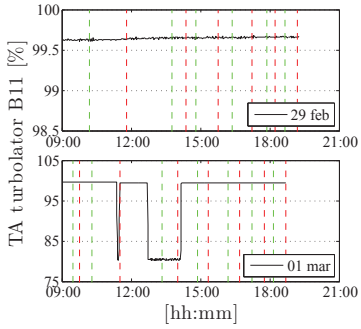

Figure C.12 TA turbulator setting. Percentage of the physical position.

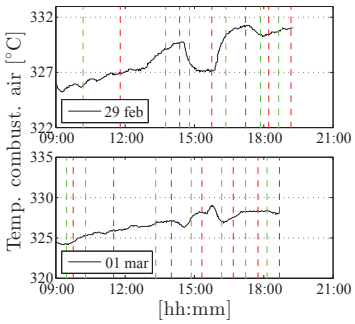

Figure C.13 Temperature of the combustion air: both SA and TA.

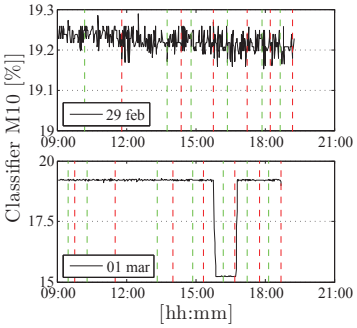

Figure C.14 Classifier frequency, percentage of speed.

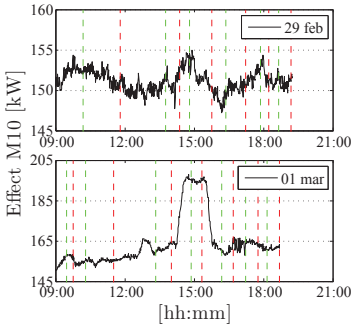

Figure C.15 Mill effect.

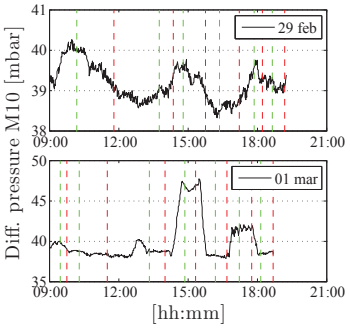

Figure C.16 Pressure drop across mill 10.

The production of heat and power from the thermal conversion of biomass has gained global interest with the desire to lower the anthropogenic emission of potentially harmful gases. Development and implementation of high efficiency biomass combustion technology is arguably the best near-term solution to provide stable and CO_2-neutral centralized power and district heating.

The present study contributes to the construction of a scientific basis for the development of the next generation of biomass burner technology. The work combines experimental and modeling work in lab-, pilot-, and full-scale and aims to improve the predictive tools for biomass devolatilization at conditions relevant to suspension fired bio-dust combustion. It provides new methods for the extrapolation of simple pyrolysis models across scales and operating conditions. The results are readily implementable to commercial CFD softwares and provide potentially signficant simulation improvements over the currently available models without adding additional strain to the computational requirements.

The studies of the fundamental processes are supplemented by comprehensive full-scale flame measurements at operating power plants firing 100 % bio-dust. The campaigns are build from systematic changes in the operating conditions and characterization of central flame parameter thus linking quantified flame responses to specific operating conditions. As such, the present work provides both improvements to the predictive tools as well as evaluation material for complex burner simulations.

Combustion and Harmful Emission Control Research Centre
Department of Chemical and Biochemical Engineering
Technical University of Denmark

Søltofts Plads
Bygning 229
2800 Kgs. Lyngby

Tlf. 45 25 28 00
Fax 45 88 22 58
E-mail kt@kt.dtu.dk
Web www.kt.dtu.dk